Convective transport from drops in complex shearing flows

Sabarish V N

Engineering Mechanics Unit

JNCASR

This dissertation is submitted for the degree of

M.S.(Engg.)

July 2021

To my Parents and my Grandparents......

Declaration

I hereby declare that the matter embodied in the thesis entitled "**Convective transport from drops in complex shearing flows**"is the result of investigations carried out by me at the *Engineering Mechanics Unit, Jawaharlal Nehru Centre for Advanced Scientific Research*, Bangalore, India under the supervision of **Prof. Ganesh Subramanian** and that it has not been submitted elsewhere for the award of any degree or diploma.

In keeping with the general practice in reporting scientific observations, due acknowledgment has been made whenever the work described is based on the findings of other investigators.

Sabarish V N

Certificate

I hereby certify that the matter embodied in this thesis entitled "**Convective transport from drops in complex shearing flows**" has been carried out by **Mr. Sabarish V N** at the *Engineering Mechanics Unit, Jawaharlal Nehru Centre for Advanced Scientific Research*, Bangalore, India under my supervision and that it has not been submitted elsewhere for the award of any degree or diploma.

Prof. Ganesh Subramanian
(Research Supervisor)

Acknowledgements

It gives me immense pleasure to take this opportunity to acknowledge the people who have made this thesis possible. First and foremost, it has been a real privilege to work with *Prof. Ganesh Subramanian* over the past three years. A neophyte to the field of theoretical fluid mechanics, I have been extremely lucky to have been initiated into this wonderful branch of physics by him. His depth of understanding, clarity of thought and physical intuition and reasoning have awed me at several instances and I can only aspire to have such qualities, something that I hope to achieve in the long run. Working with him has been an intellectually rewarding experience and I would have never been able to learn and appreciate applied (and sometimes pure) mathematics if not for him. From being the most approachable person I have ever known to being a constant source of encouragement, he has been an ideal advisor throughout my stay at JNCASR. He has never prevented me from doing things the way I wanted and ensured that I complete the procedural requirements for my degree on time. Importantly, he taught me the uncanny knack of laying bare mathematical errors by physically motivated reasoning rather than just staring at the equations unrelentingly, something that has made my understanding of the subject (slightly) better. Above all, thanks are due to his incredible course on Fluid Dynamics, without which this thesis would not have been possible. I attended the course as a student and also as the TA for three straight years and it has been a life-altering experience for me. More than anything, the course made me appreciate applied mathematics and has motivated me to learn and explore the field further. Being the workaholic that I am, I couldn't have asked for a better mentor.

I wish to thank all the faculty members at the *Engineering Mechanics Unit, JNCASR* for their teaching and support. I had great fun doing experiments as part of the *Heat Transfer* course offered by *Prof. K R Sreenivas.* Fresh out of my B.E, with almost no experience in theory, his course was the one which offered a breather in an otherwise mathematically loaded curriculum. Being an astute experimentalist, his way of teaching focused on practical aspects of a problem from which I learned plenty. I would also like to thank him for his support for my PhD applications which was both timely and generous. *Prof. Meheboob Alam*'s Advanced Mathematics course was a blessing in disguise for the theoretically uninitiated in EMU, covering a broad range of topics which I needed to know in my research. For his lucid presentations and especially his lenient evaluations of the final exam, I give him my thanks. *Prof. Santosh Ansumali*'s course on Advanced Computational Techniques and *Prof. Diwakar Vengadesan*'s course on Basic Computational Science (often taught in tandem) was a great learning experience for me. Through them I finally understood what many of my CSc buddies in CEG were talking about all the time. Their lectures on parallel numerical solvers for PDEs and quadrature integrator were extremely helpful in my own work for doing BEM and LD simulations. Their classrooms always had a jovial ambience, filled with lots of discussions and fun and it was an enthralling experience. Finally, I would also like to thank *Prof. Rajesh Ganapathy* of *ICMS*, for his enthralling soft-matter course. How he unravelled a field as diverse and exciting as soft matter in a one-credit course is completely beyond me. He introduced me to a lot of path-breaking work in soft matter and motivated me to pursue my PhD in this field by supporting me with my applications. I thank him for his support and encouragement. Thanks to all these individuals, for making EMU a fun place to work in, with their extremely jovial and yet driven approach to research.

No words can describe the love and gratitude I owe my family, *My Parents* and two sisters *Sandhya* and *Sanjana*. Every researcher knows the importance of support from the family and mine has never vacillated from their support and, most importantly, never showed any skepticism towards my ambitions and encouraged me to work towards them. If not for their unconditional love and support for everything I do, this thesis would not be possible.

This list cannot be complete without *Aishwarya*, the one person to whom I owe the most. She has been my only source of sanity in JNCASR, being there for me whenever I needed her and has always managed to cheer me up, sometimes simply by being with me!! Most of the moments I cherish during my stay in JNC revolve around her; the outings, long-distance trips, movies and the late-night maggi at utility. Her support during my PhD applications and through the pandemic was the only thing keeping me going. If not for her love and support, I highly doubt I would be sane now and I very much look forward to receiving the same from her for the rest of my life.

I would like to thank my friends, *Mohit, Akshay, Ashish and Anjana*, for all the full-filled treks, cycling trips, in-house celebrations and numerous outings. They have been a vital tonic to my otherwise mundane routine at JNC. Mohit has been a chill roommate, understanding of my OCDs and has always helped me maintain a clean ambiance in our room. We have had a lot of cherish-able moments together, especially with our pet hamster. We have been lucky to get a huge room to share that let us both feel at home and I was also lucky that I got to share the room with him during the quarantine period of the pandemic when everyone else in JNC was getting fed-up of loneliness. Akshay has been a cool person to hang-out with, sharing my own enthusiasm for fluid dynamics and physics. He introduced me to the JNC football community and I have had a lot of fun playing with him and other enthusiasts, These two also shared my enthusiasm for quizzing and winning the second place in the JNC quiz right at the termination of all our tenure, in the midst of a ranging pandemic, was one of the silver-linings of that dreadful period. Thanks are due to Anjana for all the "Christmas-special" pastries and sweets and other savories she has so generously cooked for the rest of us. My stay at JNC would not have been the joy-ride that it was, but for these wonderful people.

Finally, I would like to thank my friends at EMU, especially my lab-mates, *Prateek, Piyush, Arun, Pulkit, Sankalp and Raksha*. They provided a simulating and interactive ambience in lab and have never shied away from helping me in my need. They were also very helpful during my PhD applications, providing me with a lot of inputs and perspectives to think on. All of them were my seniors except for Raksha, who joined fairly recently, but nevertheless, helped me a lot with my PhD admissions with her suggestions. Piyush has been a towering figure in lab, with incredible depth of knowledge, intuition and clarity on several topics and has helped me on several occasions with my work. Prateek and Arun are equally towering personas, always open to debate every issue under the sky and share my love of movies, politics, football and history. Prateek is also the quintessential foodie, often trying out different restaurants and pubs with his protegé *Saumyakantha* my junior and they saw fit to grace me with occasional invitations to their adventures, which I quite cherished, especially the last one that was just a few days before the peak of the pandemic; eating fancy food and chilling in an over-crowded restaurant, easily the most dangerous stunt I have performed yet. *Shaurya, Praveen, Rafi and Vybhav* are some of the people I shared the EMU building with and I would like to thank them for their help at various points during my stay; Shaurya and Rafi especially for providing me with their bicycles for my cycling trips and Vybhav for his help with my experiments for the heat transfer course. I am quite sure, there are numerous others that I have left out here for the want of brevity, but I would very much like to thank all of them for their support and I dedicate this thesis to all these individuals who made this work possible directly and indirectly.

Abstract

This work broadly deals with transport in two-phase systems. The two-phase system of direct relevance to this study is an emulsion, where one of the phases is dispersed as droplets in the other (ambient/continuous) phase. In this work, we analyse the transport in such a system, where we analytically calculate the transport rate in the convection dominant regime (as characterised by large Péclet numbers, $Pe \gg 1$) from a single neutrally buoyant drop suspended in an ambient three-dimensional linear flow, for an arbitrary value of the drop-to medium viscosity ratio (λ). The scenario we are interested in pertains to the Stokesian regime ($Re = 0$) or near-Stokesian regime ($Re \ll 1$) and the transport rate is calculated as a dimensionless Nusselt number (Nu), which depends on the geometry of the flow (as characterized by the streamline topology) on the surface of the drop. Correspondingly, we consider two separate scenarios where the surface streamlines on the drop are either open or closed. The emphasis in our study is on being able to tailor the transport-rate (Nu) calculation to non-trivial surface or near-surface streamline topologies; in contrast to examples from textbooks, or those in the existing literature, that are restricted to simple symmetric ambient flow configurations. The results of this study are categorised into five chapters and a brief description of them follows.

We begin with an introduction to the problem and a comprehensive survey of literature relevant to our study in *Chapter 1*. This is followed by *Chapter 2*, which deals with transport in the open streamline regime, and wherein we develop a framework to calculate Nu for a drop in an arbitrary incompressible $3D$ linear flow that is parameterized by four dimensionless parameters namely $\epsilon, \alpha, \theta_\omega$ and ϕ_ω and show that the calculation for this case is a straightforward extension of the analysis for two simpler sub-cases: (i) $3D$ extension with inclined vorticity (parameterized by ϵ and α) and (ii) axisymmetric extension with inclined vorticity (parameterized by α and θ_ω). For both these cases, as is typical for flows with open streamlines, transport is enhanced in the large Pe limit by the formation of an asymptotically thin boundary layer ($\delta_{BL} \sim O(Pe^{-1/2})$) and the enhancement is a function of the drop-to-medium viscosity ratio λ. For each of the aforementioned two-parameter families of ambient linear flows, we begin with a complete analysis of the surface streamline topology which are obtained from the three-dimensional velocity field that is a solution of the Stokes equations. Although the equations governing the surface streamlines are nonlinear, the equation is recognized to be a projection, onto the drop surface (a unit sphere), of an *auxiliary linear system* which can be solved in closed-form. These solutions can then be projected back onto the drop surface to obtain closed-form expressions for the surface streamlines. We analyse the streamline topologies based on the cubic-discriminant and the invariants of the velocity-gradient tensor associated with this auxiliary linear system. We use the insights from this analysis, together with the solutions of the auxiliary system, to develop a flow-aligned non-orthogonal coordinate system, the $C - \tau$ system, with C being a streamline label and τ the phase along the streamline. This novel coordinate system allows one to evaluate Nu analytically for a drop immersed in an arbitrary three-dimensional linear flow for $Pe \gg 1$. One finds, $Nu = f(P, \lambda)Pe^{1/2}$, where the parameter P is the set of parameters identified above ($P \equiv (\epsilon, \alpha)$, $P \equiv (\theta_\omega, \alpha)$ for the two families considered), and $f(P, \lambda)$ is given by a two-dimensional integral which can be readily evaluated numerically.

In *Chapter 3*, we digress a bit from the main theme underlying the thesis (transport) and follow up

on an interesting result from our analysis of the surface streamline topologies in the open-streamline regime in Chapter 2. Our analysis has revealed the existence of novel planar linear flows that occupy a three-dimensional subspace of the four-dimensional parameter space that characterizes $3D$ incompressible linear flows. This is in contrast to the canonical one-parameter family of planar linear flows that has been extensively researched in the context of problems in microhydrodynamics. We term these novel flows 'eccentric planar linear flows', where the eccentricity arises from there being a non-trivial rate of extension perpendicular to the plane of the flow. The eccentric planar linear flows include both eccentric elliptic and eccentric hyperbolic linear flows that are separated by degenerate linear flows with parabolic streamlines (and that are the generalizations of the canonical simple shear flow). These flows correspond to a zero cubic invariant (R) of the velocity gradient tensor, with the degenerate flows with parabolic streamlines corresponding to the quadratic invariant (Q) also being zero. The region of existence of these flows is visualised via a pair of three-dimensional sub-spaces: (i) The $\epsilon - \phi_\omega - \theta_\omega$ space, and (ii) The $\epsilon - \phi_\omega - (1/\alpha)$ space of the full $4D$ parameter space. From the transport perspective, the eccentric elliptic linear flows are of interest because while the auxiliary flow at these points contains closed streamlines, the actual ambient flow does not. This implies that while the surface streamlines are closed, those off the surface of the drop are not. Therefore, the drop is expected to behave in a manner similar to a solid particle as far as transport enhancement is concerned. Correspondingly, one anticipates Nu to scale as $Pe^{1/3}$ for $Pe \to \infty$ (and therefore, $Nu/Pe^{1/2} \to 0$). The first step towards an analytical description of the aforementioned phenomena is developed in this chapter, which involves deriving the equation of the elliptic surface streamlines in the aforementioned flow-aligned $C - \tau$ coordinates. These coordinates should enable an asymptotic calculation of the transport rate at large Pe for such flows, thereby determining the proportionality factor in the Nu-$Pe^{1/3}$ relationship above, as a function of the flow parameters.

The domain of existence of these linear flows, in a space spanned by the flow-type parameters, may be considered as an alternate to the conventional classification scheme of incompressible $3D$ linear flows based on scalar invariants Q, R of the velocity-gradient tensor. The $Q - R$ scheme has a degeneracy owing to both eccentric and canonical planar flows corresponding to $Q = 0$, while the $3D$ sub-spaces avoid this issue. For compressible $3D$ flows, an analogous classification along the line mentioned above does not exist. In this chapter, we take an initial step towards this by developing an alternate classification scheme for $2D$ linear flows (compressible and incompressible), which are traditionally classified using a $P - Q$ scheme, that does not allow for finding relative position between the flow topologies. The resulting classification is in an analogous two-dimensional parameter space (the dimensionless parameters being named χ and ζ), which is finite in extent and allows one to locate the various flow topologies relative to each other.

In calculating the Nu for the drop in the open-streamline regime, we assume the drop surface to be isothermal in the boundary-layer analysis. This is a rather restrictive assumption which requires one to neglect resistance to interior transport. It is known from several studies in the literature that the interior streamlines for a general ambient linear flow may be chaotic, leading to reduced transport resistance. In *Chapter 4*, we show the existence of chaotic interior streamlines and also calculate the Nusselt number in the interior by performing Langevin Dynamics simulations and show for the first time the enhancement of transport due to chaos for general linear flows. We find that the extent of chaotic regions in the interior is dependent on the ambient linear flow and these regions are interspersed with islands of regular streamlines the boundary of which , constitutes an invariant surface in the interior. We also note that there are certain threshold parameter values where the chaos is maximum and space-filling which leads to a significant enhancement in Nu by more than an order of magnitude. For the most chaotic interior flows, the enhancement implies the existence of a boundary layer in the interior of the drop. Such a boundary layer, if it exists, can easily be accounted for in the original transport-rate calculation. We show for the first time, the existence of such a boundary layer by calculating the steady-state profiles from our transient simulations and end this chapter with a brief account (from earlier studies) on how the framework of Chapter 1 can be extended to include an interior boundary layer so that the con-

jugate problem with finite transport resistances both in the interior and exterior of the drop can be solved.

Finally, we return to the exterior transport problem in *Chapter 5*, where we focus on the closed-streamline regime. It is known that, in the Stokesian regime, for a subset of the planar linear flows (the canonical one-parameter family of hyperbolic and elliptic planar linear flows separated by simple shear), the streamlines around the drop are either open or closed. These canonical flows are characterized by a single parameter, $\hat{\alpha}$, and the transition from closed to open near-surface streamlines occurs when $\hat{\alpha}$ exceeds a λ-dependent threshold. The closed-streamline topology leads to Nu approaching an $O(1)$ value for $Pe \to \infty$, implying diffusion-limited transport. Thus, convective enhancement for large Pe is only possible with corrections to the Stokesian field that alter the streamline topology. In our study, this correction arises from drop deformation; inertia can also lead to an altered streamline topology, and has been analyzed before. The deformation of the drop is controlled by either the Capillary number (Ca) or the viscosity ratio (λ) and we re-derive the corrections to the leading order Stokesian field for both cases and analyze the exterior streamline topology, revealing a non-trivial alteration. The originally closed streamlines are transformed to spiralling ones, with a fraction of these spiralling streamlines being densely winding around nested tori. We develop an analytical framework in terms of the pair of Stokesian streamline labels C and E. These labels are are constants of fluid motion for $Re = Ca = 0$, but are slowly varying functions of time for small but finite deformation, termed adiabatic invariants. The characteristic time scale of this variation is $O(\dot{\gamma}^{-1} Ca^{-1})$ or $O(\dot{\gamma}^{-1} \lambda)$, that is much larger than the $O(\dot{\gamma}^{-1})$ ($\dot{\gamma}$ being the shear rate) flow time scale characterizing circulation around a given closed Stokesian streamline. We use the method of averaging, to derive the closed-streamline-averaged equations governing the aforementioned pair of adiabatic invariants to represent the topology in an equivalent $C - E$ space and analyse them. We also perform Boundary Element (BEM) simulations, to support the conclusions, from the method of averaging, of an alteration of alteration of streamline topology due to drop deformation, which had been ruled out in earlier studies. The reminder of the chapter briefly discusses the streamline topology obtained when both inertia and deformation are considered simultaneously, where we show, rather surprisingly, that the nested tori configuration is preserved.

Table of Contents

List of Figures

List of Tables

Chapter 1

Introduction

The transport of heat or mass from liquid drops, freely suspended in a flowing fluid medium is a problem of both fundamental and immense practical significance. The physical scenario corresponds to a disperse two-phase system, the disperse phase being the drops, and such systems are ubiquitous in both nature and industry; transport of heat or mass generated by a chemical reaction, for instance, occurs across the interface between the two phases, and the primary objective is usually to determine the rate of this transport. A particular example from the industrial context is the process of suspension polymerization (Vivaldo-Lima et al. (1997); Brooks (2010)), where the process starts with the liquid monomer in the form of suspended drops in an ambient fluid. As the exothermic polymerization process progresses, heat is released from the drop, and needs to be convected away efficiently (by stirring of the ambient fluid), even as the viscosity ratio between the drop fluid and ambient increases as a function of time due to the polymerization reaction. Other industrial examples include vaporization of fuel drops, following injection into a turbulent environment, that occurs in internal combustion engines (Law (1982))) where the rate of vaporization may have a direct impact on the efficiency and emission levels of the engine. Examples of natural phenomena include cloud formation, where one has the formation of water drops in the turbulent atmosphere via the transfer of heat from and mass to water drops (Beard and Pruppacher (1971), Duguid and Stampfer (1971), Kinzer and Gunn (1951)). Applications may also be found in biological systems where the uptake of nutrients and other biochemicals by cells in complex flows is of interest (Magar et al. (2003); Guasto et al. (2012); Stocker (2012)).

In this work, we analyse the problem of convective heat or mass transfer from an isolated drop (with density ρ_d) suspended in another fluid (of density ρ_a), the ambient, that may be subjected to an imposed flow, which is the fundamental problem underlying the various scenarios described above. This physical system can give rise to two different scenarios depending on the ratio of densities of the two phases (ρ_a and ρ_d). The first one corresponds to the case with a density mismatch, where we have a *settling or rising drop* (depending on whether $\rho_d/\rho_a > 1$ or $\rho_d/\rho_a < 1$ respectively), leading to a net slip between the two phases. The second case is when $\rho_d/\rho_a = 1$, which corresponds to a *neutrally buoyant drop* with zero slip. The rate of transport in each of these cases depends on which of the mechanisms, convection vis-a-vis diffusion, is dominant. The relative importance of convective to diffusive transport is measured by the Peclet number (Pe). The velocity scale in Pe depends on whether the slip-induced translation or the effect of the ambient shear dominates. We will assume the latter to be the case (which is always true for the case of a neutrally buoyant drop quoted above), in which case Pe is defined as $Pe = \dot{\gamma}a^2/D$, where D is the diffusivity of heat or mass in the ambient fluid and $\dot{\gamma}$ is the shear rate, with its inverse ($\dot{\gamma}^{-1}$) serving as the characteristic time scale associated with the shearing flow. The two extremes of Pe serve as natural bounds for the rate of transport. One has diffusion-dominant transport for $Pe \ll 1$, with the rate of transport in general increasing to a convection-dominant limit for $Pe \gg 1$. Apart from Pe, the dimensionless rate of transport, in the aforementioned physical system may also be influenced by the following dimensionless governing parameters:

- *Reynolds number* (Re), which is a measure of the relative importance of inertial and viscous forces in momentum transport and is defined as $Re = \dot{\gamma}a^2/\nu$, ν is the kinematic viscosity of the ambient fluid, and is related to the ambient viscosity μ of the ambient phase as $\nu = \mu/\rho$, and a is the drop radius.

- *Capillary number* (Ca), which is a measure of the relative importance of viscous and surface tension forces and is defined as $Ca = \mu\dot{\gamma}a/\sigma$, where σ is the coefficient of interfacial tension between the two phases.

- *Drop-to-medium viscosity ratio* (λ), which is defined as $\lambda = \hat{\mu}/\mu$, where $\hat{\mu}$ is the viscosity of the drop phase. Note that both Ca and λ control the extent of deformation of the drop under the action of ambient flow.

- P, which denotes a set of parameters that characterize the geometry of the ambient flow. We shall restrict ourselves to ambient flows that are incompressible $3D$ linear flows and for this case, P will be seen to denote a group of four dimensionless parameters.

Thus, our problem involves a multi-dimensional parameter space and one expects a wide range of possibly complex behavior. The principal aim of this thesis is to derive an expression for the Nusselt number Nu (ratio of the actual rate of transport to that due to diffusion alone, and hence a dimensionless measure of transport rate in diffusion units), as a function of these aforementioned parameters as:

$$Nu = f(Re, Ca, Pe, \lambda, P). \tag{1.1}$$

Note that we have used the parlance pertaining to heat transport in Eq.1.1. Although we will continue to retain this notation, it is worth noting that Nu is replaced by Sh (Sherwood number) in the chemical engineering literature, when it comes to problems involving mass transport. In the interest of an analytical study, we move to a reduced parameter space based on the following assumptions:

- We consider the limit $Pe \gg 1$, corresponding to the convection-dominant regime. This is precisely the regime where computation becomes difficult, and an asymptotic analysis comes in handy.

- Viscous effects dominate momentum transport i.e. $Re \ll 1$. This assumption of small Re which translates to small-sized drops, combined with neutral buoyancy, justifies the assumption of an ambient linear shearing flow (since the non-linear dependence on position, of the velocity field, becomes smaller by a factor that is the ratio of the drop size to the characteristic flow length scale). Hence as mentioned above, P in Eq.1.1 will turn out to be a set of four dimensionless parameters.

- The deformation of the drop, subject to the flow of the ambient fluid is small. The deformation is governed by the Capillary number Ca or the viscosity ratio λ and small deformation translates to $Ca \ll 1$ or $\lambda \gg 1$.

Therefore, the baseline scenario, in light of the above assumptions, is the case of a (spherical) drop immersed in an arbitrary linear flow for $Re = Ca = 0$ (with arbitrary λ).

We begin this chapter by first providing a brief survey of relevant earlier work which starts off with the aforementioned baseline scenario. We will only summarise efforts which have focused on the problem of transport from a single drop or a single particle, and in doing so elucidate some aspects of the underlying physics. The overwhelming majority of efforts that exist in the literature focus on transport from particles or drops of a sufficiently simple shape (cylinders or spheres), and importantly, in relatively simple flows which possess a high degree of symmetry. The main result in these efforts is an expression for the Nusselt number Nu, as a function of Pe, since the overall heat transfer is usually the primary quantity of interest. All of the analytical efforts are restricted to small or large Pe, $Re \ll 1$ and $Ca = 0$ (for drops), with only numerical efforts probing arbitrary values of these parameters. It is the large Pe limit that is relevant to this thesis.

1.1 Transport from Solid Particles

For solid particles, the Capillary number Ca and viscosity ratio λ do not enter the functional relation given in Eq.1.1 and the only relevant parameters are therefore Pe, Re and P. In the discussion that follows, we shall briefly review some of the studies in the literature that have attempted to calculate Nu as a function of these parameters under suitable assumptions, beginning with the case of a non-neutrally buoyant particle that translates relative to the ambient owing to the density mismatch.

1.1.1 Transport from non-neutrally buoyant (translating) particles

For a translating particle, the heat transport problem is best analyzed in a reference frame moving with the particle, in which case the particle is stationary, and there is an ambient uniform flow at infinity. Acrivos and T. D. Taylor (1962) first solved the problem of heat transfer from a solid sphere in a uniform flow, for small Pe, in the Stokes regime ($Re \ll 1$). They realized that, even in the limit of small Pe, the conduction approximation is a not a uniformly valid one in an unbounded domain since, at distance of $r \sim O(aPe^{-1})$ from the particle (a being the particle length scale), the so-called convection screening length, convection effects will eventually become comparable to conduction. Thus, a regular series expansion of the temperature field in Pe will lead to an ill-posed system at $O(Pe)$, where the boundary condition at ∞ cannot be satisfied for any choice of the solution. Therefore, the analysis of the effect of small Pe requires a matched asymptotic expansions approach, with separate expansions for the temperature field in the inner ($r < O(a)$), and the outer ($r > O(aPe^{-1})$) regions. This procedure led to a solution of the form $Nu = 2 + (1/2)Pe + (1/4)Pe^2 \log Pe$, where the $(1/2)Pe$ correction comes entirely from the outer region. The analogous problem in two dimensions, a single infinite cylinder in uniform flow, will lead to a Nusselt number of the form $Nu \sim O(\log Pe)^{-1}$. This logarithmic scaling arises on account of the Stokes' paradox in two dimensions. Acrivos and T. D. Taylor (1962) also show that, the inertial effects due to small values of Re, do not enter the solution at $O(Pe)$, thereby making the solution applicable for particles with weak inertia at large Pe. Later, Brenner (1963), generalised the small Pe result for a particle of arbitrary shape in uniform flow and, rather surprisingly, found that the contribution of the inner region, associated with an arbitrary shaped particle, still vanishes uniformly despite despite the absence of fore-aft symmetry, and the convective enhancement, at O(Pe), still comes solely from the outer region. Batchelor (1979) extended and unified much of the prior work in the small Pe regime by adopting a simple procedure to calculate the leading term in the convective correction to the pure diffusion rate based on the insight offered by earlier efforts, where it was shown that the convective correction depends only on the ambient flow in the outer region. Batchelor's work mainly focused on scalar transport from a spherical particle suspended in an ambient shearing flow (which leads to a $Pe^{1/2}$ leading order correction for $Pe \ll 1$, as explained in a later section) in both small and large Pe regimes, while treating uniform flow as a separate special case, but nevertheless showed that the procedure works for both classes of problems. Later, Brunn (1984) considered the effect of inertia (Re small but finite) on scalar transport in the low Pe regime and established that, Nu is independent of Re and depends only on the structure of the incident flow up to to first order in Pe. The inertial correction only enters the expansion at $O(Pe^2)$, leading to a solution of the form $Nu = 2 + (1/2)Pe + (1/4)Pe^2 \log Pe + g(Pr)Pe^2$, where g is a function of the Prandtl number, $Pr = Pe/Re$. More recently Pozrikidis (1997) had considered the unsteady transport from particles of arbitrary shapes, in the small Pe regime, based on arguments similar to those used by Batchelor. For particles suddenly introduced into a steady uniform flow, the transient decay of Nu to steady state is exponential. He also solves for the mean rate of transport from an oscillating flow and reports that the mean transport rate is significantly reduced due to oscillation-induced convective mixing, that decreases the gradients in the scalar field.

In the large Pe limit ($Pe \gg 1$), convective effects dominate everywhere in the flow, except for a thin thermal boundary layer next to the surface of the body, where they are comparable to diffusion. Acrivos

and T. D. Taylor (1962) again were the first to obtain the Nusselt number for transport from an isothermal sphere in uniform Stokes ($Re \ll 1$) flow, the relation being of the form $Nu = 0.991(Pe^{1/3}) + O(1)$ for $Pe \gg 1$. This result arises only from the limiting form of the Stokesian velocity field in the thermal boundary layer, which can be justified by the fact that the velocity gradients near the surface change over a length scale $O(a)$, while the temperature (or concentration) gradients change rapidly over a distance of $O(aPe^{-1/3})$. The $Pe^{1/3}$ scaling for the thermal boundary layer in the limit of large Pe can be derived in a straightforward manner. For a solid particle, owing to no-slip condition on the surface, the convective time scale is $a^2/(U\delta_{BL})$, where U is the velocity scale and δ_{BL} is the the thermal boundary layer thickness; so, $U\delta_{BL}/a$ is the simple shear flow in the vicinity of the particle surface. The diffusion time scale is δ_{BL}^2/D, and matching the two time scales yields $\delta_{BL} \sim Pe^{-1/3}$. Acrivos and Goddard (1965) later extended this by calculating higher order corrections to the Nusselt number as $Nu = Pe^{1/3}(0.991 + 0.461Pe^{-1/3} + o(Pe^{-1/3}))$ for $Pe \gg 1$. The last term in this expansion denotes higher order contributions that arise due to the full fluid motion. The calculation of the $O(Pe^{1/3})$ contribution to Nu for axisymmetric particles (spheroids) in uniform flows was provided by Sehlin (1969). More recently Dehdashti and Masoud (2020) have considered the problem of heat transfer in both the small and large Pe limit from a solid particle of arbitrary shape in a uniform flow with a constant heat flux condition at the boundary. For $Pe \ll 1$ and arbitrary Re, their results are analogous to the one derived by Brenner (1963), which was $Nu = 2 + (1/2)Pe$ up to leading order. For large Pe, they use Green's functions to provide expressions for the temperature field up to the second order, in terms of multidimensional integrals (which are evaluated numerically), for axisymmetric and $2D$ particles at small or moderate Re, and derive exact result for Nu for spheroids in Stokes flow ($Re = 0$) as a special case.

There have been several numerical studies focused on scalar transport in uniform flow past axisymmetric objects (spheres and spheroids), almost all of which have typically dealt with Pe and Re values comparable to each other. Following the analytical developments mentioned above, Masliyah and Epstein (1972) numerically solved the diffusion equation for Re ranging from 1 to 100 and with Pe ranging from $1 - 70$ at a constant $Pr = 0.7$, for both spheroids and spheres in uniform flow using finite difference scheme and matched their simulations with the relevant asymptotic results. Several works have focused on heat transfer from solid spheres in unsteady flows in moderate ranges of Pe and Re (Konpoliv and Sparrow (1970); Konpoliv and Sparrow (1971); Konpoliv and Sparrow (1972); Abramzon and Elata (1984); Feng and Michaelides (2000a); Blackburn (2002)), and steady and unsteady heat transfer from spheroids (Kishore and Sai (2011); Ke et al. (2018); Ma and Zhao (2020)). Many of these works validate the asymptotic relations derived by earlier efforts, discussed above for spheres and spheroids, in a uniform flow at $Re \ll 1$. To our knowledge, there are far fewer numerical studies on translating spheres and spheroids at high Pe and low Re (Karp-Boss et al. (1996); Pahlow et al. (1997)). This may be due to the need to resolve an asymptotically thin boundary layer.

To summarise this survey on transport from non-neutrally buoyant particles for $Re \ll 1$, the dimensionless transport rate Nu has two distinct dependencies on Pe, depending on the dominant mechanism of transport. For three dimensional flows, in the diffusion-dominant regime ($Pe \ll 1$), $Nu = 2 + O(Pe)$, while in the convection dominant regime ($Pe \gg 1$), $Nu \sim O(Pe^{1/3})$. While, we have restricted our survey to the case of $Re \ll 1$, studies of transport have also been carried out for $Re \gg 1$. In this case, there is a laminar boundary layer that forms around the particle, with the boundary layer separating for bluff bodies. Provided one has an attached boundary layer (as is the case for an aligned flat plate, for example), one may use scaling arguments to infer the Nu dependence. Since the simple shear flow on the particle surface now has a velocity gradient of $O(Re^{1/2})$, a scaling argument along the lines of that mentioned above leads to $Nu \sim Re^{1/2}Pr^{1/3}$ for $Pr \gg 1$ and to $(RePr)^{1/2}$ for $Pr \ll 1$; interested readers are directed to G. L. Leal (2007) for further information. We now shift our focus to transport from neutrally-buoyant solid particles immersed in an ambient linear shearing flow.

1.1.2 Transport from neutrally buoyant solid particles

When a small $(a/L \ll O(1))$ isolated particle is neutrally buoyant, it acts like a passive tracer and faithfully follows the ambient flow. Therefore, the problem of transport from such a particle is again best analysed in a coordinate frame moving with the local velocity of the particle. In such a coordinate frame, the flow that the particle sees is a linear flow at leading order in a/L. In effect, one has to now calculate transport from a stationary particle at the origin of an ambient linear shearing flow. Three dimensional incompressible linear flows are characterized by four dimensionless parameters (see Chapter 2). The simplest of these linear flows are the canonical one-parameter (denoted by $\hat{\alpha}$, which is a measure of the relative magnitudes of extension and vorticity; a precise definition is given in Eq.3.3)) family of planar linear flows, which have been widely studied in the past; the extremal members of this family consisting of solid-body rotational flow ($\hat{\alpha} = -1$) and planar extensional flow ($\hat{\alpha} = 1$), with simple shear flow ($\hat{\alpha} = 0$) as a marginal member separating flows with dominant extension from those with dominant rotation. Cox et al. (1968) analysed the streamline patterns associated with the Stokesian velocity field, around a force-free and freely rotating circular cylinder and sphere subject to an ambient simple shear flow ($\hat{\alpha} = 0$). His analysis revealed the existence of closed streamlines around the particle in both cases. This was later confirmed by experiments (Cox et al. (1968); Robertson and Acrivos (1970a) and numerical simulations (Kossack and Acrivos (1974)). Kao et al. (1977) later extended this analysis to the entire one-parameter family of canonical planar linear flows. They found that there were regions of both closed and open streamlines for planar linear flows between simple shear and planar extensional flow whereas all streamlines were closed for those between solid-body rotation and simple shear. There are no closed streamlines for planar extension. They also derived an expression for the radial extent of the separatrix surface which separates regions of closed and open streamlines. Unlike the case of particles in a uniform flow, near-field closed streamlines exert a significant influence on scalar transport at large Pe. Accordingly, one has two fundamentally distinct scenarios associated with particles in a linear shearing flow, one where the near-field contains closed streamlines and another where these streamlines are open.

1.1.2.1 Transport in the Closed Streamline Regime

Frankel and Acrivos (1968) were the first to study, theoretically, the heat transfer from small spheres and cylinders freely rotating in a shear flow at both small and large Pe. In the low Pe regime they predicted Nu to increase as $O(logPe)^{-1}$ for a cylinder, just as for uniform flow, while the increase scales as $O(Pe^{1/2})$ for a sphere. The $O(Pe^{1/2})$ scaling arises because of the existence of a convective screening length, which for the ambient linear flow, is $O(aPe^{-1/2})$. In the large Pe regime, the authors found, surprisingly, Nu to be independent of Pe. For a cylinder, this asymptotic value is 5.73. The authors were not able to obtain a closed form expression for this asymptotic value, for a sphere, owing to the complicated three-dimensional nature of the flow. In a later effort, Acrivos (1971), via an approximate analysis, found this asymptotic value to be 4.5. Yu-Fang and Acrivos (1968) later showed Nu to be independent of Pe for the general case of scalar transport across a $2D$ closed streamline field, implying the absence of any boundary layer enhancement. The presence of closed streamlines makes even strong convection ineffective in carrying away heat from the body thereby making the transport diffusion limited. Later, Poe and Acrivos (1976) extended the theoretical analysis to the case of sphere in a canonical planar linear flow, and found that except in the case of a planar extensional flow, Nu is independent of Pe, for $Pe \gg 1$. A sphere, in any one of the canonical planar linear flows, exhibits diffusion-limited transport at large Pe, with the order unity large-Pe asymptote that arises depending on flow type. One would expect this asymptote to increase with decreasing thickness of the closed-streamline region, eventually scaling in an inverse manner with the ratio of the thickness of the closed-streamline region to the particle size, and thereby, diverging to infinity in the limit of planar extension.

The existence of diffusion-limited transport at large Pe, for a freely rotating cylinder, was confirmed experimentally by Robertson and Acrivos (1970b) who performed experiments on a freely rotating cylin-

der in a shear flow apparatus. The authors found that, for $Pe > 70$, the Nusselt number was indeed independent of Pe. On the other hand, when the cylinder was held fixed and not allowed to rotate, they found that the Nusselt number did scale with Pe as $Nu \sim Pe^{1/3}$ in agreement with the existence of a thermal boundary layer. Another set of experiments were carried out by Poe and Acrivos (1975), who considered freely rotating spheres in a simple shear flow. The authors found that, just as in the case of a cylinder, the sphere appeared to be surrounded by a region of closed streamlines. Again, for a sphere that is held fixed, the streamlines adjacent to the body are open, and as we saw before, can contribute effectively to the transport through the formation of a thermal boundary layer.

The above discussions have mainly looked at heat transfer in the low Reynolds number limit where the Stokes approximation is assumed valid. For ambient flows which lead to open streamlines in the vicinity of the particle (like uniform flow, planar extension, axisymmetric extension etc., which we describe in the section that follows), the effect of inertia will enter as a regular perturbation about a leading order Stokesian contribution. But when the streamlines around the particle are closed, inertia has a singular effect and determines the transport rate at leading order for sufficient large Pe. Subramanian and Koch (2006a) showed that, in the case of small spheres freely suspended in a planar linear flow, weak inertia has a fundamental effect on the heat transfer by destroying the region of closed streamlines which existed at $Re = 0$ (Acrivos (1971); Robertson and Acrivos (1970a); Poe and Acrivos (1975)). The inertial streamlines, for small Re, have a tightly spiralling character, with new channels of convection being opened up due to inertia. The authors showed, in the limit $Re \ll 1$ and $Re.Pe \gg 1$, that Nu again increases with Pe as:

$$Nu = 0.33(Re.Pe)^{1/3} \tag{1.2}$$

for simple shear flow, with the scaling arising due to a thermal boundary layer forming on account of the inertial flow. Subramanian and Koch (2006b) extended this analysis for a general planar linear flow and derived an expression for Nu which is given by:

$$Nu = 0.33(1 + \hat{\alpha})^{2/3}(RePe)^{1/3}. \tag{1.3}$$

Yang et al. (2011) have carried out simulations of heat transfer from spheres at finite Re which find good agreement, in the relevant asymptotic limit of large Pe, with the theoretical predictions above.

1.1.2.2 Transport in the Open streamline regime

Almost all linear flows, apart from the canonical planar linear flows lead to open streamlines in the vicinity of a spherical particle. There have been a few efforts analysing transport from a particle in the Stokesian regime. The large-Pe convective transport from a particle (and a drop), in an axisymmetric extensional flow, was examined by Gupalo and Riazantsev (1972). The analogous analysis for a particle (and drop) in a planar extensional flow was done by Polyanin (1984). Batchelor (1979), generalised all these efforts by analysing scalar transport from a sphere subject to a general linear ambient flow at large Pe. In the high Pe calculation, of relevance to the work in this thesis, he considered two broad classes of ambient linear flows. The first were linear extensional flows where the particle remains stationary owing to the ambient flow being irrotational. For these flows, Batchelor used a flow-aligned orthogonal coordinate system along with a suitable transformation of the independent variables to derive a similarity solution for this boundary layer problem. By suitably defining the Peclet number based on the parameters of the linear flow, the Nusselt number for an arbitrary extensional flow was shown to be given by:

$$Nu = 0.90 \left(\frac{a^2 E}{D}\right)^{1/3} \tag{1.4}$$

where E is the characteristic strength of extension ($E = \sqrt{E_1^2 + E_2^2 + E_3^2}$, where E_1, E_2 and E_3 are the principal components of extension; this choice for the scale makes the numerical pre-factor of Nu in Eq.1.4

for axisymmetric and planar extensions lie within 1% of each other); the result (Eq.1.4) reduces to the earlier simpler in appropriate limits. The second class of flows were the linear flow with vorticity, the vorticity vector being inclined at an arbitrary angle to the principal axes of the rate of strain. For this case, a freely suspended spherical particle rotates with the angular velocity ($\boldsymbol{\omega}/2$) of the vortical part of the flow. Unlike the case of a planar linear flow, where the streamlines adjacent to the sphere would be closed, here the contribution from the extensional component of the velocity gradient, along the axis of rotation, causes the streamlines to become tightly wound spirals. Fluid elements therefore follow helical paths with a drift along the axis of the rotation. But, Batchelor argued that owing to the rotation of the solid particle, the velocity field in the boundary layer due to the extensional component is $O(Pe^{-1/3})$ smaller than that arising from rotation. This ensures that averaging over a single turn of a streamline (ϕ) would work, leading to a steady field with only $\boldsymbol{E} : \boldsymbol{\omega}\boldsymbol{\omega}$, the component along the axis of rotation which leads to the aforementioned drift, as the only relevant component of extension that governs heat transport at large Pe. For this second class of linear flows the expression for the Nusselt number was found to be:

$$Nu = 0.968 \left(\frac{a^2 E_\omega}{D}\right)^{1/3} \tag{1.5}$$

with the conditions that $|\boldsymbol{\omega}|$ is not smaller than $O(Pe^{-1/3})$, in which case the spirals would cease to be tightly wound. When E_ω is zero, the drift which contributed to the heat transfer vanishes and we recover the results obtained earlier by Acrivos and coworkers for diffusion-limited transport in planar linear flows.

Until recently, analogous results for non-spherical particles suspended in linear shearing flows were not available. Lawson (2020), extended Batchelor's results for a spheroid in a general linear flow by using a flow-aligned orthogonal coordinate system, where the dynamic behavior of spheroids in these flows, namely spinning and tumbling, as well as the aspect ratio have been shown to considerably influence scalar transport at large Pe. The author also uses a second-order finite-volume scheme to solve the convection-diffusion equation to find heat transfer rate from spheres and spheroids in planar and axisymmetric extensional flows for Pe ranging from $1 < Pe < 10^4$, which validates the asymptotic relations derived by him and Batchelor (1979). Previously they had only been numerically studied by Karp-Boss et al. (1996) and Pahlow et al. (1997), who explored transport from spheres and spheroids in simple shear flow for the moderate range of $Pe < 1000$.

This concludes our brief review of studies on transport from solid particles. We have kept our focus on the Stokesian regime $Re \ll 1$ which eliminates Re from the functional relation of Nu for most of the cases considered. Thus, in this regime $Nu = f(Pe, P)$. Further, in the Stokesian regime, we identified two distinct regimes of transport namely the diffusion-dominant ($Pe \ll 1$) and convection dominant ($Pe \gg 1$) and we saw that these two regimes lead to different functional relations for Nu. In the former regime we obtained $Nu = 2 + O(Pe)$ for translating particles and $Nu = 2 + O(Pe^{1/2})$ for neutrally-buoyant ones. The latter regime, gave us $Nu \sim O(Pe^{1/3})$ for both translating and neutrally buoyant particles, except when there were regions of closed streamlines around it. We also saw that in majority of the cases (with open streamlines), inertia has a perturbative effect on the above result. However, for linear flows that lead to near-field closed streamlines, inertia has a singular effect and lead to a Nusselt number of the form $Nu \sim O(RePe)^{1/3}$. This then summarizes the dependence of Nu on the relevant dimensionless parameters for solid particles.

1.2 Transport from Drops

While it is evident that the problem of transport from solid particles has received a great deal of attention, the analogous problem for drops in an ambient linear flow has been less widely studied. This is because the problem of transport from viscous drops is significantly more complicated than the solid particle case.

Note that all the studies mentioned earlier on transport from solid particles have assumed the particle surface to have a uniform temperature, an assumption that is valid for highly conducting particles; the assumption is not a limiting one in the mass transport scenario. On the other hand, for drops, one has to worry about the relative magnitudes of the transport resistances in the drop and exterior phases, and the aforementioned uniform temperature (or concentration) boundary condition neglects the drop phase resistance. Thus, one may classify the transport analyses for drops according to the phase contributing to the dominant transport resistance, and accordingly, we discuss the relevant efforts from the literature in the following order: (1) those concerning the exterior transport problem (2) those focusing on the internal transport problem and, (3) the studies that deal with comparable resistances in the interior and exterior, the so-called conjugate transport problem.

1.2.1 The Exterior Transport Problem

In the exterior transport problem, one does not have to account for the flow or temperature gradient in the interior of the drop and simply assume an isothermal boundary (interface). In this case, studies have focused on estimating Nu as a function of relevant physical parameters, which for the case of drop include Pe, Re, Ca, λ and the flow parameters as given in Eq.1.1. Much like the case of solid particles, majority of the analytical studies assume a spherical drop ($Ca = 0$) in the Stokesian regime ($Re \ll 1$). Here again, one has two scenarios depending on the value of the density ratio between the drop and the ambient phase. We first look at the non-neutrally buoyant case ($\rho_a = \rho_d$) which is equivalent to a stationary drop subject to a uniform flow in the exterior.

1.2.1.1 Transport from a non-neutrally buoyant (translating) drop

For the case of an isolated spherical drop suspended in a uniform flow, $Nu = 2 + O(Pe)$ (Newman (1931)) for $Pe \ll 1$ and $Nu = (3\lambda/(4(1 + \lambda)))(Pe^{1/2})$ for $Pe \gg 1$ (Levich (1962); Feng and Michaelides (1996); Feng and Michaelides (2000b)). Note here that these relations correspond to $Re \ll 1$ and $Ca = 0$. The $Pe^{1/2}$ scaling can again be understood in a straightforward manner as follows. Unlike the solid particle, the drop surface allows for a finite slip. This implies that the time scale associated with convection is a/U, where a is the drop length scale and U is the slip velocity scale. Similarly, the diffusion time scale is δ_{BL}^2/D, and comparison of the two time scales gives $\delta_{BL} \sim O(aPe^{-1/2})$. This leads to the $Pe1/2$ scaling above. Note that this scaling implies that the heat transport from a drop is asymptotically larger than that from a solid particle at the same Pe, since the no-slip boundary condition in the latter case weakens convective effects. Given that a translating drop is surrounded by open streamlines (as given by the Hadamard-Rybzinski solution (G. L. Leal (2007)), neither weak inertia ($Re < O(1)$) nor deformation ($Ca \neq 0$) can affect the leading order solution.

The translating drop problem has also been studied numerically by several authors, staring with the work of Abramzon and Fishbein (1977), who calculated the transport rate in the Stokesian range numerically, for $Pe \leq 1000$. The simulations provided a satisfactory match with the analytical predictions of Newman (1931) and Levich (1962). Feng and Michaelides (2000b), numerically analysed the transport from a spherical drop of an arbitrary viscosity ratio λ, again assuming a Stokesian velocity field in the exterior. Based on their results in the range $10 < Pe < 10^4$, the authors suggested a correlation of the form $Nu = Pe^n$ where $n = 0.322 + (0.113\lambda/(0.361 + \lambda))$. The value of this exponent lies between the asymptotic limits $Pe^{1/3}$ for solid particles and $Pe^{1/2}$ for drops, predicted by theory. In a related work, Feng and Michaelides (2001) calculate the transport rate from a spherical drop with $1 < Re < 500$ and $10 < Pe < 10^4$, with the velocity field being numerically evaluated from the Navier-Stokes equations. They find that for small values of Re, their simulation matches well with the asymptotic solution of $Pe^{1/2}$, but for finite Re, the exponent is a function of λ. Also, for a given Pe, the Nusselt number at steady state increases with Re, except for $Pe \ll 1$, where, Nu at higher Re collapse to a constant value

that is greater than the corresponding Stokesian value. To our knowledge, there have been no analytical or numerical studies on transport from a deformed drop in uniform flow at low Re and high Pe.

1.2.1.2   Transport from a neutrally buoyant drop

Similar to a solid particle, this problem may be reduced to that of a stationary drop in an ambient linear flow. As mentioned earlier, these flows in general are governed by four dimensionless parameters, but in literature majority of the studies have focused on simple, symmetric flow configurations that include the one-parameter family of canonical planar linear flows and axisymmetric extensional flows. Recall that the streamlines in the vicinity of the solid particles suspended in planar linear flows were open or closed depending on the flow parameter $\hat{\alpha}$. For a drop the viscosity ratio λ also governs the transition between open and closed streamlines. Torza et al. (1971) analysed the streamlines in the interior and exterior of a drop in a simple shear flow, a member of the aforementioned one-parameter family. Their theoretical analysis predicted closed streamlines adjacent to the drop as well as open streamlines further away, and the existence of a λ-dependent limiting separatrix surface which separates these two regions. Additionally, Torza et al. (1971) performed experiments which appeared to confirm the existence of a closed streamline region. The theoretical analysis of both interior and exterior streamlines was extended to the aforementioned one-parameter family of planar linear flows by Powell (1983). It was shown that extent of the closed streamline region and the limiting surface depended on both the linear flow parameter ($\hat{\alpha}$) as well as the viscosity ratio (λ). There is a critical viscosity ratio, $\lambda_c = 2\hat{\alpha}/(1-\hat{\alpha})$, that separates regions of closed and open streamlines in the ($\hat{\alpha}, \lambda$) plane. One therefore expects the Nu-surface ($Nu/Pe^{1/2}$) plotted as a function of $\hat{\alpha}$ and λ) to be sensitive to the variation in the streamline topology across the aforementioned critical curve. We note that $\lambda \to \infty$ corresponds to a solid particle, in which case, as seen earlier, streamlines remain open only in the case of planar extensional flow.

Transport in the open-streamline regime

The drop transport problem has only been solved for specific ambient flows, with a high degree of symmetry; a general expression for the Nusselt number, along the lines of that obtained by Batchelor (1979) for a solid particle, is not available. Among the cases considered are a neutrally buoyant drop in an axisymmetric extensional flow by Gupalo and Riazantsev (1972), for which the analysis proceeds in a manner similar to the translation problem (Newman (1931), Levich (1962)). Gupalo, Riazantsev, and Ulin (1975) have carried out the analysis for an ambient flow which is a sum of an axisymmetric extension and a uniform flow, aligned with the axis of symmetry of extension, again an axisymmetric problem. The only case of a non-axisymmetric ambient flow that we are aware is the case of planar extension which was analyzed by Polyanin (1984) using the approach used by Batchelor (1979) for the case of a rigid particle. For all these cases, the flow field adjacent to the drop is entirely composed of open streamlines, and in the limit of high Pe, Nu scales as $Pe^{1/2}$.

The first step towards the analysis of transport from a neutrally buoyant drop in a general incompressible linear flow for $Pe \gg 1$ was taken by Krishnamurthy and Subramanian (2018a), who developed a framework to analytically calculate Nu for a drop in two one-parameter linear flow families - the canonical planar linear flows and $3D$ extensional flows. Their work begins with developing a flow-aligned non-orthogonal coordinate system for the case of planar linear flows, where, as was already mentioned, there are two fundamentally distinct regimes with respect to near-field streamlines. The first is an open-streamline regime which exists for $\lambda < \lambda_c$, and where a boundary-layer-enhanced heat transfer leads to $Nu \sim O(Pe^{1/2})$ for large Pe. In the other regime, which exists for $\lambda > \lambda_c$, the drop is completely surrounded by closed streamlines and the heat transfer is diffusion limited at $Re = 0$ even as $Pe \to \infty$. Krishnamurthy and Subramanian (2018a) start with the analysis for the open streamline regime, $\lambda > \lambda_c$, where, they demonstrate an important result that the surface streamlines on the drop surface on the drop surface may still be regarded as Jeffery orbits (Jeffery (1922)), but with an imaginary aspect ratio

that is now a function of both the flow parameter ($\hat{\alpha}$) and λ. Based on this knowledge they develop a flow-aligned, non-orthogonal surface coordinate system, termed the $C - \tau$ system (originally developed to described Jeffery orbits with real-valued aspect ratios in the context of the orientation dynamics of anisotropic particles; see L. G. Leal and Hinch (1971)), to solve for Nu in closed form given by:

$$Nu = \mathcal{F}(\hat{\alpha}, \lambda)Pe^{1/2} \tag{1.6}$$

where $\mathcal{F}(\hat{\alpha}, \lambda)$ is given by a definite integral that can be readily evaluated numerically. In their formulation, C denotes a streamline label while τ denotes the phase along a given streamline. They extend their analysis to study another one-parameter family of linear flows, the $3D$ extensional flow parameterized by ϵ, for which they again use the $C - \tau$ formalism to find Nu as:

$$Nu = \frac{\mathcal{G}(\epsilon)}{(1 + \lambda)^{1/2}}Pe^{1/2} \tag{1.7}$$

where $\epsilon = E_3/E_2$ and E_3 and E_2 are the principal rates of strain. The results reduce to the known ones quoted above for planar (Polyanin (1984)) and axisymmetric (Gupalo and Riazantsev (1972)) for $\epsilon = 0$ and $\epsilon = 1$, respectively. Interestingly, one may also define a $C - \tau$ coordinate system for a rigid particle, with C acting as a label for the surface shear-stress-lines, rather than streamlines. Krishnamurthy and Subramanian (2018a) show, in an Appendix, based on such a coordinate system, that one may also recover the results of Batchelor (1979). Note that that the dependence on λ can be incorporated into a rescaled Peclet number, and so, the Nusselt number Nu can be scaled with the viscosity ratio λ, unlike the previous case. Finally, Krishnamurthy and Subramanian (2018a) also point out the possibility of generalizing their results, obtained for the exterior problem, to the conjugate problem in the limit that there exists a boundary layer, of thickness $O(Pe^{1/2})$, in the interior of a drop. The existence of a interior boundary layer is, however, not obvious, and it is shown here that the emergence of an interior boundary layer, with the conventional scaling, is sensitively dependent on the chaotic nature of the interior streamlines.

There have been a couple of efforts that have examined the role of drop deformation on transport in the open-streamline regime. Favelukis and Lavrenteva (2013), Favelukis and Lavrenteva (2014) analysed the problem of transport from a drop, for finite Ca, in an ambient uniaxial and biaxial extension, respectively; note that, for small Ca, the deformed drop takes the form of a prolate and an oblate spheroid in the aforementioned flows. The authors solve the transport problem in the corresponding spheroidal coordinates and observe that the Nusselt number decreases by about 10% from the corresponding value for a spherical drop ($Ca = 0$), when Ca increases by five times. They also find that the decrease in Nu increases with increase in the viscosity ratio at a given Ca, with the case of inviscid drop having the minimal decrease in Nu from the value corresponding to that of a spherical drop. These results are consistent with the statement made earlier that deformation only has a perturbative effect on transport in the open-streamline regime and the trend reported by the authors can be expected to occur for drop in other ambient flows as well.

Transport in the closed-streamline regime

When $\lambda > \lambda_c$ for a drop in planar linear flow, the streamlines around the drop are closed and it leads to diffusion-limited transport for $Re = Ca = 0$ and $Pe \to \infty$. The closed surface streamlines are true Jeffery orbits, with real-valued aspect ratios that are again functions of $\hat{\alpha}$ and λ. As for the case of rigid particles, inertia is expected to destroy the closed-streamline topology, in turn leading to a convectively enhanced transport, as reflected in a Nu growing with Pe for $Pe \to \infty$. Krishnamurthy and Subramanian (2018b) analyzed the inertial streamline topology in the exterior of the drop based on the velocity field derived earlier by Raja et al. (2010). Their analysis reveals that the original closed Stokesian streamlines are modified into spiralling ones. They also find that the nature of spiralling is again a function of λ, and there exists another $\hat{\alpha}$-dependent threshold λ_{bif}. While all finite-Re streamlines near the drop spiral in

along the vorticity axis, and leave close to the flow-gradient plane for $\lambda > \lambda_{bif}$, for $\lambda_c < \lambda < \lambda_{bif}$, the inertial streamlines leave the drop at an intermediate angle after spiralling in from both the flow-gradient plane and the vorticity axis. This implies that, in the large-Pe transport problem, the thermal wake bifurcates off the flow-gradient plane at $\lambda = \lambda_{bif}$. Krishnamurthy and Subramanian (2018b) followed up their analysis of streamline topology with the calculation of Nu, by using the $C - \tau$ formalism, analogous to that developed for the open-streamline regime. The authors calculated the Jeffery-orbit-averaged drift due to inertia and obtained the rate of transport in the limit that there is a thin boundary layer with a thickness of $O(Re^{-1/2}Pe^{-1/2})$ on the drop surface. While the analysis is more intricate than the open-streamline one, they show that the three-dimensional heat transfer problem for this case can, in fact, be simplified to a one-dimensional one using the above coordinate system. In effect, the use of the coordinate system transforms the original non-axisymmetric problem to an axisymmetric one, akin to that solved for a solid particle by (Subramanian and Koch (2006b)). They show that the Nusselt number for this case is given by:

$$Nu = \mathcal{H}(\hat{\alpha}, \lambda)Re^{1/2}Pe^{1/2} \tag{1.8}$$

in the limit of $Pe \gg 1$ and $RePe \gg 1$. The prefactor $\mathcal{H}(\hat{\alpha}, \lambda)$ has been evaluated by the authors by performing a one-dimensional C integral numerically. The combination of the open and closed streamline analyses in Krishnamurthy and Subramanian (2018a), Krishnamurthy and Subramanian (2018b) yielded a Nu-surface singular along the critical curve $\lambda_c(\hat{\alpha})$. However, the authors comment on how the true Nu-surface would connect smoothly across the critical curve for any finite Pe. So far, no analogous study has considered the effect of deformation on transport in the closed streamline regime, probably due to the fact that the experiments of Torza et al. (1971) suggested that the streamlines around the drop remain closed even for weak deformation of the drop.

One may now summarize the results for the exterior problem as follows. The primary inference from this survey should be the functional form of Nu corresponding to the low and high Pe limit in the Stokesian regime. For $Pe \ll 1$, $Nu = 2 + O(Pe)$ for flows with a relative slip between the drop and the ambient (translating drop) and $Nu = 2 + O(Pe^{1/2})$ for flows with no relative slip (neutrally-buoyant drop), analogous to a solid particle. For $Pe \gg 1$, we saw that $Nu \sim O(Pe^{1/2})$ provided the streamlines in the near-field remain open. When the streamlines in the near-field are closed, then the transport is diffusion-limited, unless closed streamlines are opened up. Weak inertia achieves this and for this case, $Nu \sim O(RePe)^{1/2}$.

1.2.2   The Interior Transport Problem

As already mentioned above, the interior transport problem corresponds to the dominant transport resistance being within the drop phase, and one may assume the interface to be isothermal. For $Pe = 0$, the time dependent temperature profile may be analytically determined. In contrast to the exterior problem, for small Pe, the correction to the diffusive limit is $O(Pe^2)$. The first effort to consider the transport of heat or mass in the $Pe \gg 1$ regime was the classical work of Kronig and Brink (1950), for a translating spherical drop. Recognizing that the streamlines at large Pe are isothermal at leading order, the authors solved obtained Nu from the solution of a diffusion problem in a streamline-aligned coordinate system, and finding Nu to be about 2.7. Thus, transport at large Pe is again diffusion limited, and this limitation arises from the streamlines, in the interior of a translating drop, being closed curves in any meridional plane; heat has to diffuse across these isothermal streamlines at the steady state even as Peclet number becomes large ($Pe \gg 1$). One expects an analogous diffusion limitation for a neutrally buoyant drop in simple linear flows such as axisymmetric or planar extension, although an analytical solution for the plateau value of Nu is not available for these flows; this is because the coefficients of the diffusion equation, in streamline coordinates, are not known in closed form. Nevertheless, computations performed by Christov and Homsy (2009) show that Nu, for axisymmetric extension, asymptotes to 4.5 for $Pe \gg 1$.

The diffusion-limited transport in the above flows arises owing to the interior streamlines being simple closed curves. Overcoming diffusion limitation requires the interior streamlines to open up. This is, however, not a sufficient condition. For instance, diffusion limitation persists even when one has open streamlines winding around indefinitely around invariant tori, as is the case for axisymmetric extension with vorticity aligned with the symmetry axis. Thus, the only possible way for the interior region to exhibit convective enhancement of transport is through Lagrangian chaos (Aref et al. (2017)). This implies a chaotic state in the interior of the drop bought about by a steady deterministic velocity field (Bohr et al. (1998)). The existence of such steady chaotic streamlines in bounded domains were first shown by Bajer and Moffat (1990), who analysed the flow field in the interior of a spherical drop subject to an arbitrary quadratic velocity field. Stone et al. (1991) were the first to show, by numerical simulations, that chaotic streamlines inside the drop are possible with the cubic interior field associated with ambient axisymmetric extensional flows with inclined vorticity, (which is a two-parameter family of linear flow, as we shall see later). Kroujiline and Stone (1999) followed it up and showed that Lagrangian chaos is again possible for a translating drop subject to a rotation along an axis not aligned with the direction of translation. Apart from these cases, Bryden and Brenner (1999) considered non-neutrally buoyant drop subjected to simple shear flow and found that it too exhibits chaotic streamlines. This serves to indicate that when a drop is suspended in a general $3D$ linear flow field, the streamlines in the interior can exhibit chaos. Although not relevant to the transport study here, Ward and Homsy (2001) and Christov and Homsy (2009) have reported the presence of chaotic streamlines inside a electrohydrodynamically driven translating drop, subject to oscillatory electric fields. In this case, chaotic dynamics arises even when field is axisymmetric (on account of the directions of translation and the electric field being aligned) because of the additional time dependence.

While it is now well established that both unsteady two-dimensional flows and steady three-dimensional ones exhibit Lagrangian chaos (Aref et al., 2017), that such chaotic streamlines can lead to transport enhancement was first shown to be true by Bryden and Brenner (1999), for the case of a translating drop in a simple shear flow. The authors solved the governing equations numerically, using finite difference method, and showed that the Nusselt number does not plateau for large Pe, although their simulations were restricted to a moderate range of $1 < Pe < 1000$. The restricted range of Pe prevented the authors from extracting a scaling behavior for Nu. Ward and Homsy (2001) and Christov and Homsy (2009) also showed by numerical simulations that convective enhancement of transport rate occurs in the case of an electrohydrodynamically driven translating drop subject to oscillatory electric fields, when the amplitude of the oscillation crosses a certain threshold. Although, as indicated above, there exist multiple studies on chaotic interior streamlines arising within a drop immersed in an ambient shearing flow, there has been no systematic effort to analyze the effect of chaos on the rate of transport, and on the interior temperature/concentration field, especially from the point of view of demonstrating a connection between chaos-induced enhanced transport and the emergence of interior boundary layers.

1.2.3 The Conjugate Transport Problem

While the external and internal transport problem has been studied analytically for certain special cases, the conjugate transport problem has only been explored through approximate and numerical techniques as it involves solving a coupled system of convection-diffusion equations, with the continuity of temperature and flux being satisfied at the interface. The case of $Pe = 0$ was analysed by Philip (1964), Brown (1965) and Cooper (1977), who solve the problem of transient conduction from a stationary fluid at $Pe = 0$, accounting for both internal and external resistances. Levich et al. (1965) and Chen (1969) independently solved the conjugate heat transfer problem for a translating drop in the large Pe limit which is valid for very short times, smaller than the characteristic relaxation time for heat transfer, when the concentration at the edge of the boundary layer can be assumed constant and equal to the initial concentration. They use similarity transformation to solve the conjugate transport problem and find that the Nusselt number

scales as $Nu = (1/(1 + \kappa))Pe^{1/2}$, where $\kappa = (D_e/D_i)^{1/2}$, the ratio of diffusivities of the external and internal phase. Following this work, Brounshtein et al. (1970), suggested an alternative approach to solve the Nusselt number for the conjugate problem, where the solution of the internal problem proceeds in a manner similar to Kronig and Brink (1950), with a modified surface boundary condition that takes into account the resistance of the external phase. Their solution involve the Biot number (Bi) as an additional parameter.

Abramzon and Borde (1980), numerically analysed the unsteady conjugate heat transfer problem for a translating drop in the Stokesian regime for $1 < Pe < 1000$ and found that their simulations matched well with the asymptotic expressions of Levich et al. (1965) and Chao (1969). Recently, Alexandrova et al. (2014), Saboni et al. (2016) have studied the effect of Re and viscosity ratio (λ) on conjugate transport for a translating drop for $1 < Pe < 1000$. The results from these studies are similar to those observed in the case of external and internal transport problem, with Nu and Pe related through a scale factor that is a function of λ and Re and the steady state transfer rates at a given Pe increasing with Re and decreasing with λ. A review of the relevant numerical studies on conjugate transport problem has been provided by Michaelides (2006). Far fewer studies have focused on the conjugate transport problem for drops in ambient shearing flows. One such effort is by Liu et al. (2019) who study the unsteady conjugate transport problem from a drop in uni-axial extension for $1 \leq Pe \leq 10^3$. The predicted Nusselt numbers is again found to dependent on κ, the ratio of diffusivities and they have validated their simulations with the well known case of external transport from a drop in axisymmetric extension (Gupalo and Riazantsev (1972)). For topologically complex ambient shearing flows, there have been no studies yet on the conjugate transport problem.

1.3   The focus of this thesis

With the background provided in the previous section on the state of affairs pertaining to the problem of transport from drops, we now describe the focus and organisation of this thesis and where it fits in amongst the existing literature. From the survey of literature, it is evident that the calculation of transport rate from a neutrally buoyant drop in an arbitrary $3D$ linear flow still remains unsolved, whereas the analogous problem for solid particles had been solved by Batchelor (1979) four decades ago. The reason for this is the non-trivial topology of the streamlines in the thermal boundary layer on the drop surface. For solid particles, any arbitrary linear flow can be placed into one of the two categories: (i) flows without vorticity and, (ii) flows with vorticity. Batchelor showed that in the first case, the surface streamlines are simply open trajectories that run along the surface shear-stress lines on the surface, and for which analysis can be carried out in the orthogonal von-Mises coordinates. Crucially for the second case, owing to the rotation of the solid body and no-slip boundary condition, the extensional velocity components in the boundary layer are asymptotically ($O(Pe^{-1/3})$) smaller than the rotational component. And so, one can consider a ϕ-averaged steady state where, the only relevant extensional component was E_ω, the one along the axis of rotation, which resulted in tightly wound spirals as the surface-streamlines. Thus any arbitrary linear ambient flow only results in either of these two surface-streamline topologies which can be easily analysed. But for drops, we no longer have the luxury of smallness of the extensional components in the boundary layer; the surface slip allows for a non-zero rate of extension on the drop surface. Therefore, the analogous problem for the drops considerably more complicated, and all possible surface-streamline topology associated with an arbitrary linear flow needing to be accounted for. However, we saw in the last section that there have been recent efforts (Krishnamurthy and Subramanian (2018a), Krishnamurthy and Subramanian, 2018b) which have taken an initial step towards solving this problem using a non-orthogonal coordinate system.

The first part of this thesis will build upon these recent efforts, specifically Krishnamurthy and Subramanian (2018a), to move closer to a solution of the drop transport problem. In **Chapter 2**, we begin

our study by calculating the Nusselt number from an isolated spherical drop suspended in a pair of two-parameter families of incompressible linear flows: (i) $3D$ extension with aligned vorticity, and (ii) Axisymmetric extension with inclined vorticity. The first flow is parameterized by two dimensionless quantities $P = \{\epsilon, \alpha\}$, while the latter one is parameterized by $P = \{\alpha, \theta_\omega\}$. These two flows naturally constitute the next level in the hierarchy of $3D$ incompressible linear flows following the one-parameter family of canonical planar linear flows and $3D$ extensional flows, which were considered by Krishnamurthy and Subramanian (2018a) in their analysis. Our analysis largely builds on their effort, where we use the flow-aligned non-orthogonal coordinate system, the $C-\tau$ system, developed by them and extend it to these two-parameter flows. As we shall see, this extension requires a thorough analysis of surface-streamline topologies, which we perform by using the critical-point techniques introduced by Perry and Chong (1987). We then proceed to calculate the Nu as $Nu = \mathcal{F}_1(\alpha, \epsilon, \lambda)Pe^{1/2}$ and $Nu = \mathcal{F}_2(\alpha, \theta_\omega, \lambda)Pe^{1/2}$ for the two aforementioned families. An important aspect to emphasize is that, for the linear flows considered in the Nu-calculations above, the complexity of the streamline topologies significantly exceeds those that have been analyzed in the literature thus far.

Our analysis of the streamline topology for the aforementioned two-parameter families of linear flows has revealed the existence of exceptional linear flow topologies that have closed surface streamlines, where the Nu deviates from the $Pe^{1/2}$ relation mentioned earlier and instead scales as $Pe^{1/3}$ for $Pe \gg 1$, just like a solid particle. These flows, as it will be shown, have a non-trivial rate of extension orthogonal to the plane of flow with the canonical one-parameter family of planar flows (governed by $\hat{\alpha}$) constituting a special case of these flows, with the extensional component normal to the plane of flow being identically zero. We term these flows the *eccentric planar linear flows*, and they include both eccentric elliptic and eccentric hyperbolic linear flows that are separated by degenerate linear flows with parabolic streamlines (and that are the generalizations of the canonical simple shear flow, just like the eccentric elliptic and hyperbolic flows are generalizations of the corresponding canonical analogs). They are so named, for they give rise to eccentric elliptic and hyperbolic streamlines on the drop surface. In **Chapter 3**, we study the properties of these newly-discovered flows and show that they occupy a three-dimensional subspace in the $4D$ parameter space of arbitrary $3D$ linear flows. We again use critical point techniques to show that these flows constitute a three-parameter family, and correspondingly construct two complementary three-dimensional sub-spaces: (i) the $\epsilon - \phi_\omega - \theta_\omega$ space and, (ii) the $\epsilon - \phi_\omega - 1/\alpha$ space, which can be used in conjunction to locate the planar flows. We recognise that the projections of these linear flow stream-lines onto the surface of a unit sphere are the solutions of the equations governing the orientation vector of a spheroid suspended in these flows and as such, these projections (the surface streamlines), specifically those of eccentric planar elliptic flows, constitute generalisations of Jeffery orbits (Jeffery (1922)). Using geometric arguments, we derive the equation of these generalised Jeffery orbits, which has several important applications that we mention in the chapter. The domain of existence in the two sub-spaces mentioned above, can also be interpreted as a classification scheme for the incompressible $3D$ linear flows, which demarcate the eccentric and canonical planar flows and allows for finding the distance between the various flow topologies. An analogous classification does not exist for compressible linear flows, and the conventional classification based on scalar invariants P, Q, R of the velocity-gradient tensor, do not distinguish the canonical and eccentric flows. Such a distinction is crucial in applications, where these flows result in qualitatively different scenarios. Therefore, we take an initial effort in addressing this issue by developing an alternative classification scheme for the $2D$ linear flows, where one can find the relative positions of each topology with respect to one another.

In **Chapter 4**, we briefly address the interior transport problem. Earlier studies (Kronig and Brink (1950)) had established that the rate of transport in the interior of the drop suspended in uniform flows, neglecting exterior phase resistance, is diffusion-limited. This is again related to the streamline topology in the interior, where regular, closed streamlines result in diffusion-limitation. However, studies by Stone et al. (1991), Bryden and Brenner (1999) and Christov and Homsy (2009), have shown that the interior of

the drop exhibits chaotic streamlines for certain ambient linear flow configurations. Stone et al. (1991) in particular, show that interior streamlines are chaotic for axisymmetric extensions with inclined vorticity. Chaotic interior streamlines are expected to lead to convectively enhanced transport, and this has been shown in Bryden and Brenner (1999), Ward and Homsy (2001) and Christov and Homsy (2009). This convective enhancement will again happen through the formation of an internal boundary layer. In this chapter, we quantify the effect of chaos on transport rate and the resulting internal temperature field using Langevin Dynamics simulations. It is shown that the streamlines are chaotic for both the two-parameter families and for the general linear flow. We calculate the Nu for a few representative cases and show that Nu grows as Pe^β, where β is a flow-dependent scaling exponent. This in turn implies, and we show, that there is an internal boundary layer of thickness $\sim O(Pe^{-\beta})$. Importantly, we observe that the nature of chaos in the interior is highly dependent on the ambient flow and also affects the growth rate of Nu. While certain cases lead to regions of non-chaotic islands (containing regular streamlines) interspersed within the chaotic region, other cases lead to completely (space-filling) chaotic interior. Recall from the discussion on the flow-aligned coordinate system that, it can be generalised to solve the conjugate transport problem, should there exist a boundary layer (of thickness $\sim O(Pe^{-1/2})$) in the interior (Krishnamurthy and Subramanian (2018a)). The results of our simulations suggest that, for cases where chaos is space-filling in the interior the Nusselt number grows as $Pe^{1/2}$ for $Pe \to \infty$, much like the exterior problem. This suggests for certain cases which lead to space-filling chaos in the interior, one can solve the conjugate problem analytically using the $C - \tau$ system.

Another aspect of the drop transport problem that has remained unexplored is the effect of drop deformation on transport. The deformation of a drop in ambient flow is controlled by two parameters namely Ca, the Capillary number, and λ, the viscosity ratio. Much like inertia (Subramanian and Koch (2006a); Subramanian and Koch (2006b); Krishnamurthy and Subramanian (2018b)), deformation can also be expected to fundamentally alter the closed-streamline topology, opening new channels for convection. Although both Ca and λ affect the drop deformation, only Ca is responsible for a qualitative alteration in the streamline topology since surface tension alone (and not the viscosity ratio) is responsible for a deviation from the reversible Stokesian scenario. The studies that exist for this problem, both experimental (Torza et al. (1971)) and computational (Kennedy and Pozrikidis (1994)), rather surprisingly, appear to indicate that the streamlines in the vicinity of the drop continue to remain closed even for finite Ca. In chapter 5, we re-derive the deformation-induced ($O(Ca)$) correction, in the limit of small Ca, to the Stokesian velocity field of earlier studies Barthes-Biesel and Acrivos (1973), (Greco (2002)), and use it to analyse the exterior streamline topology. In contrast to the conclusions of the aforementioned studies, we find that drop deformation alters the streamline topology in a highly non-trivial fashion. This alteration of streamline topology is also confirmed using BEM simulations. We show that the closed streamline topology in the exterior is transformed to one consisting of spiralling streamlines, and and unlike the inertial case, a significant fraction of these spiralling streamlines end up winding (densely) around invariant tori. It is worth mentioning that such invariant tori have not been noticed in earlier simulations (Singh and Sircar (2011)) that have considered both the effect of inertia and drop deformation via numerical simulations. It is well known that the Stokesian streamlines around a spherical may be parameterized by a pair of variables, say C and E, that are, by definition, constants of fluid motion for $Re = Ca = 0$. We show rigorously, by using the method of averaging, that the finite-Ca exterior streamline topology may be characterised by means of trajectories in the $C - E$ plane, obtained from integrating the closed-streamline-averaged equations. This analysis shows that the originally invariant streamline labels C and E are adiabatic invariants of the finite-Ca field, in that they vary slowly over a time scale of $O(\dot{\gamma}^{-1}Ca^{-1})$, which is much larger than the flow time scale characterizing circulation around a given closed Stokesian streamline ($O(\dot{\gamma}^{-1})$, $\dot{\gamma}$ being the shear rate). The nested tori appear as closed curves in the C-E plane, and the method of averaging shows that such closed curves exist for all values of $\hat{\alpha}$ right up to $\hat{\alpha}_c$, regardless of λ. The closed curves (and, therefore, the invariant tori) are preserved even with the addition of inertia, where the spatial extent of the domain of closed curves is a function of the

parameter Re/Ca. When the deformation is limited by the large drop viscosity, and is therefore $O(1/\lambda)$, the effects of irreversibility, that are responsible for the alteration of the closed streamline topology, still depend on Ca. The derivation of the exterior velocity field to $O(1/\lambda) shows that, for \lambda.Ca of O(1)$, the streamline topology is altered at $O(1/\lambda)$, as expected; however, when $\lambda.Ca \gg 1$, the alteration occurs at $O(1/\lambda^2.Ca)$, with the streamlines at $O(1/\lambda)$ still being closed (despite the drop deformation). Although consideration of the $O(1/\lambda)$ alteration of the streamline topology is also possible, within the framework of the method of averaging, the derivation of the corresponding adiabatic invariants is more involved since one has to account for the drop deformation and is beyond the scope of this thesis. Finally, we conclude the chapter by discussing the implications of this non-trivial streamline topology for transport from the deformed drop and suggest directions for future work.

Chapter 2

Transport in the Open-Streamline Regime

In this chapter, we study transport from a neutrally buoyant Newtonian drop suspended in another Newtonian fluid in the convection dominant regime ($Pe \gg 1$). The ambient fluid is assumed to undergo an arbitrary $3D$ linear flow. We take the Reynolds number based on drop radius for this case to be very small ($Re \ll 1$), where Re is defined as $Re = |\mathbf{\Gamma}|a^2/\nu$; with $|\mathbf{\Gamma}|$ being the characteristic scale of the velocity-gradient tensor, a being the drop radius and ν, the kinematic viscosity of the ambient medium. This corresponds to the Stokesian regime. There are certain exceptional linear flows where the assumption of small Re is not equivalent to $Re = 0$, owing to a qualitative alteration of the streamline topology and the resulting effect on convective transport. Such exceptional flows are discussed in Chapter 5. We note that the small length scale of the drop compared to the length scale over which the ambient velocity gradients vary, and also the fact that the drop is neutrally buoyant, are directly related to the assumption above of an ambient linear flow. Any complicated flow appears, in a frame of reference moving with the drop, as a linear flow at leading order in the ratio of drop size to flow length scale. Finally, we consider the limit where surface tension forces dominate viscous forces leading to the drop interface remaining spherical at all times. This corresponds to a regime where the Capillary number (Ca) is infinitesimally small ($Ca \ll 1$), where $Ca = \mu|\mathbf{\Gamma}|a/\sigma$, and μ is the dynamic viscosity of the ambient fluid, σ is the interfacial tension between the drop and ambient fluid. Again it's shown that there are exceptional linear flows where a small Ca leads to a qualitative change in streamline topology; this is again discussed in Chapter 5. The main objective of this chapter of the thesis is to determine the Nusselt number as a function of the ambient linear flow parameters (P) and the drop-to-medium viscosity ratio (λ)[1]. The onset of drop deformation at finite Ca or weak inertia (finite Re) will not qualitatively alter the conclusions of our analysis, as it only has a perturbative effect to the baseline scenario corresponding to $Re = Ca = 0$ and the key qualitative features of this Nusselt number surface will remain insensitive to the effects of small drop deformation. Even with these assumptions, we get a problem rich in physics and relevant to several practical applications.

While we wish to study transport from a drop suspended in an arbitrary ambient linear flow, we proceed in a hierarchical fashion, wherein we first consider an ambient flow of relatively simple topology and then move on to more complex flows. The simplest non-trivial linear flow families without obvious symmetries are the one-parameter family of canonical planar linear flows and $3D$ extensional flows, both of which have already been considered by Krishnamurthy and Subramanian (2018a). Therefore, our analysis will begin with the next rung in complexity: a pair of two-parameter families of linear flows, where the surface streamline patterns are significantly more complex than the flows considered by Krishnamurthy and Subramanian (2018a). There are two distinct two-parameter families, both of which connect in an

---

[1]Recall Eq.1.1 from Chapter 1.

appropriate limit to the aforementioned one-parameter families. The simplest of these two families is the family of $3D$ extensional flows with vorticity aligned along a principal component o extension, while the more involved one corresponds to axisymmetric extension with vorticity inclined to the axis of symmetry. For these two families, we analyse the surface streamline topology in the aforementioned limit. While this analysis is of fundamental interest, this characterization will also lay the foundation for the heat transfer analysis that follows it. As we shall see, this analysis of surface streamline topology will enable us to define a surface-streamline-aligned non-orthogonal coordinate system, which demonstrates the existence of a similarity solution to the convection-diffusion equation, in turn, enabling us to evaluate Nu in closed form. We shall use this procedure for both the two-parameter families mentioned above. Importantly, we argue that the Nusselt number surface for a drop in an arbitrary linear flow, shares features of the corresponding surfaces of the two-parameter families. This implies that the aforementioned two-parameter families can be thought of as building blocks of an arbitrary linear flow. We finally conclude this chapter by providing a few future research directions that arise from the analysis carried out in this chapter.

2.1   3D Incompressible Linear Flows

Linear flows, despite their analytical simplicity, are an indispensable analytical tool for the fluid dynamicist. Linear flows provide the local approximation to the flow field at a point of interest and are extremely useful in visualising complex three-dimensional flow fields, and serve as the building-blocks of a complex $3D$ flow field (Perry and Chong (1987), Chong et al. (1990)). They are also of immense practical importance, for they constitute the canonical flows in a rheometer, and are thus relevant in the rheological characterisation of complex fluids as they control the response of small microstructural elements. Therefore are relevant in several other microhydrodynamic phenomena including deformation and breakup of drops (G. I. Taylor (1934), Bentley and L. G. Leal (1986)), coil-stretch dynamics of polymeric molecules (Shaqfeh (2005)), orientation dynamics of anisotropic particles (Jeffery (1922), Marath and Subramanian (2018), Anand et al. (2020)). From a dynamical systems perspective, linear flows are the solution trajectories of $3D$ autonomous system of linear ODEs, and so the critical points in the flow can be analysed in terms of their dynamical behavior (Chong et al. (1990)).

$3D$ linear flows may be written in the form:

$$\boldsymbol{u} = \dot{\boldsymbol{x}} = \boldsymbol{\Gamma}.\boldsymbol{x} \tag{2.1}$$

where $\boldsymbol{\Gamma}$ is the transpose of the velocity-gradient tensor. From linear algebra, any second rank tensor can be written as a sum of its symmetric and anti-symmetric parts. Thus we may write:

$$\boldsymbol{\Gamma} = \boldsymbol{E} + \boldsymbol{\Omega} \tag{2.2}$$

where $\boldsymbol{E}$ is the rate-of-strain tensor denoting the extensional component and $\boldsymbol{\Omega}$ is the vorticity tensor, denoting the rotational component. This in turn implies that a linear flow, in general, is a superposition of extensional and rotational components, where $\boldsymbol{E}$ represents the extensional elements in the flow and $\boldsymbol{\Omega}$ represents the rotational counterpart. At the face of it, linear flows are characterised by 9 parameters, the elements of $\boldsymbol{\Gamma}$ which has a $3x3$ matrix representation; as we show below, however, for incompressible linear flows, this governing set can be reduced to just four dimensionless parameters, based on the following arguments. The first condition is that of incompressibility, which imposes a constraint of zero trace of $\boldsymbol{\Gamma}$. Next, by shifting to a coordinate system, aligned with the principal components of extension, one may further reduce the number of parameters by three; the rate-of strain tensor is diagonal in this coordinate system, with the elements given by $\{E_1, E_2, E_3\}$. The scalar rate of transport is evidently independent of the choice of coordinate system. Finally, the overall scale for the characteristic velocity gradient, given by $|\boldsymbol{\Gamma}|$, may be incorporated into the definition of the Peclet number (Pe), which further reduces the

number of parameters, by one, to four. Therefore, we see that a $3D$ incompressible linear flow is governed by four dimensionless parameters, and a convenient choice for the four-parameter set P is:

$$P = \{\epsilon, \alpha, \theta_\omega, \phi_\omega\}. \tag{2.3}$$

These four parameters are defined as follows:

- ϵ is the ratio of one of the principal components of extension to another. In our work it is defined as $\epsilon = \frac{E_3}{E_2}$. This definition also implies that the characteristic scale of $\mathbf{\Gamma}$, $|\mathbf{\Gamma}| = E_2$. Note that with this scaling, $E_2 = 1$, $E_3 = \epsilon$ with the third principal component E_1 being given by $-(1+\epsilon)$, due to incompressibility. This parameter is a measure of the departure of extension from axisymmetry.

- α is the ratio of the vorticity magnitude to a principal component of extension, given by $\alpha = \frac{|\boldsymbol{\omega}|}{E_2}$, where $|\boldsymbol{\omega}|$ is the magnitude of the vorticity vector.

- θ_ω and ϕ_ω, denote the orientation of the vorticity vector $\boldsymbol{\omega}$, relative to the principal axis (of $\boldsymbol{E}$)-aligned coordinate system. θ_ω is inclination measured relative to E_3 and ϕ_ω to E_1.

Based on these definitions, a $3D$ incompressible linear flow is written as:

$$\dot{\boldsymbol{x}} = \bar{\mathbf{\Gamma}}.\boldsymbol{x} \tag{2.4}$$

where,

$$\bar{\mathbf{\Gamma}} = \begin{bmatrix} -(1+\epsilon) & -\frac{\alpha\cos\theta_\omega}{2} & -\frac{\alpha\sin\theta_\omega\sin\phi_\omega}{2} \\ \frac{\alpha\cos\theta_\omega}{2} & 1 & -\frac{\alpha\sin\theta_\omega\cos\phi_\omega}{2} \\ \frac{\alpha\sin\theta_\omega\sin\phi_\omega}{2} & \frac{\alpha\sin\theta_\omega\cos\phi_\omega}{2} & \epsilon \end{bmatrix} \tag{2.5}$$

in terms of these four dimensionless parameters. The geometry of the flow, as given by Eq.2.5, is given in Figure.2.1, where the vorticity vector (red) has an arbitrary orientation with respect to the principal components of extension.
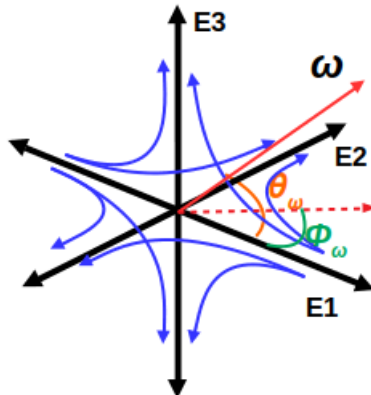
Figure 2.1: The geometry of an arbitrary incompressible $3D$ linear flow

Having defined $\bar{\mathbf{\Gamma}}$, we now look at the various sub-families that correspond to limiting values of these parameters.

- The first sub-family is the one-parameter family of canonical planar linear flows. They correspond to $\epsilon = 0$ and $\theta_\omega = 0$ or equivalently to $\epsilon = -1$, $\theta_\omega = \pi/2$ and $\phi_\omega = 0$. The parameter α ranges from $\alpha \in [0, \infty]$, where $\alpha = 0$ corresponds to planar extension and the other limit corresponds to solid

body rotation. Simple shear corresponds to $\alpha = 2$. In order to be consistent with standard range of the governing parameter associated with these flows (Bentley and L. G. Leal (1986)), we define a new parameter:

$$\hat{\alpha} = \frac{1 - (\alpha/2)}{1 + (\alpha/2)} \tag{2.6}$$

This new parameter will now include the whole spectrum of canonical flows in the range $\hat{\alpha} \in [-1, 1]$, and going outside this interval will result in the same flows in the interval. Now, $\hat{\alpha} = -1$ corresponds to solid-body rotation, $\hat{\alpha} = 1$ corresponds to planar extension and $\hat{\alpha} = 0$ is simple shear, consistent with the range used in earlier studies.

- The second case is also a one-parameter family, namely $3D$ extension, for which $\alpha = 0$ (so, $\theta_\omega, \phi_\omega$ are irrelevant). Here the fundamental range of ϵ is $\epsilon \in [0, 1]$, and going outside this range will again lead to the same flow topologies. Here, $\epsilon = 0$ corresponds to planar extension and $\epsilon = 1$ corresponds to axisymmetric extension. The aforementioned one-parameter families were considered by Krishnamurthy and Subramanian (2018a) in his analysis of transport from a drop. Our work, in particular this chapter, can be considered an extension of their results to relatively complex flow topologies corresponding to the two-parameter families, which constitute the next rung in this hierarchy.

- The next sub-family in the hierarchy is the two-parameter family of non-axisymmetric extension with vorticity aligned along a principal component of extension. This corresponds to either $\theta_\omega = 0$ or $\theta_\omega = \pi/2$, $\phi_\omega = 0$ or $\theta_\omega = \pi/2$, $\phi_\omega = \pi/2$, depending on the principal component along which vorticity is aligned. Based on the choice of $\theta_\omega, \phi_\omega$, the range of ϵ covering all possible flow topologies will be different and we shall see later that this range will be an extended one compared to pure three-dimensional extension, on account of addition of vorticity. The other parameter α will have the range $\alpha \in [0, \infty]$. The limiting cases of this family correspond to $3D$ extension for $\alpha = 0$ and solid-body rotation for $\alpha = \infty$.

- The last sub-family is again, a two-parameter family - axisymmetric extension with vorticity inclined to the axis of symmetry. This corresponds to $\epsilon = 1$ or equivalently to $\epsilon = -2$. In both cases, the governing parameters range from $\theta_\omega \in [0, \pi/2]$ and $\alpha \in [0, \infty]$. The limiting cases correspond to axisymmetric extension for $\alpha = 0$ and solid-body rotation for $\alpha = \infty$.

Finally, we conclude our discussion on linear flows by noting that the characteristics of an arbitrary linear flow is, qualitatively, a combination of the characteristics of the aforementioned two-parameter families. In the first family, the vorticity vector is aligned along a principal component of extension while the extension is three-dimensional and in the latter case, the extension is axisymmetric while the vorticity vector is inclined at an angle to the axis of symmetry. Thus, an arbitrary linear flow can be considered a combination of these two flows. Therefore, we will begin our analysis with the aforementioned two-parameter families as the ambient flow in which the drop is suspended. We also note that, the number of parameters that we use to characterise a $3D$ incompressible linear flow is four, which is in contrast to the characterisation of Chong et al. (1990), where these flows are parameterized by the two scalar invariants Q and R of $\boldsymbol{\Gamma}$. This is because our classification recognises the geometry of the flow, which does not enter a classification based solely on the scalar invariants.

2.2 Governing Equations and Boundary Conditions

We denote the viscosities and densities of the fluids inside and outside the drop as $\hat{\mu}, \mu, \hat{\rho}$ and ρ, with the variables with carets corresponding to the former. Neutral buoyancy implies that $\hat{\rho} = \rho$. The governing equations for fluid motion in the low-Reynolds-number limit are the Stokes equation and the equation of continuity given by:

$$-\boldsymbol{\nabla} p + \mu \nabla^2 \boldsymbol{u} = 0$$
$$\boldsymbol{\nabla}.\boldsymbol{u} = 0 \tag{2.7}$$

where $\boldsymbol{u}$ and p are the velocity and pressure fields. To render these equations dimensionless, we use the undeformed drop radius as a characteristic length scale ($l_c = a$); an ambient flow based scale for the velocity ($u_c = |\boldsymbol{\Gamma}|a$) for the velocity scale; and the viscous scaling for the interior and exterior pressure fields ($p_c = \hat{p}_c = \mu u_c/l_c$). Using these scales, the governing equations in dimensionless form for the flow inside and outside the drop are given by:

$$\nabla.\mathbf{u} = 0$$
$$\nabla^2\mathbf{u} = \nabla p \qquad (Exterior\ Problem) \qquad\qquad \begin{aligned}\nabla.\hat{\mathbf{u}} = 0\\ \lambda\nabla^2\hat{\mathbf{u}} = \nabla\hat{p}\end{aligned} \qquad (Interior\ Problem) \qquad (2.8)$$

where $\lambda = \hat{\mu}/\mu$ is the drop to ambient fluid viscosity ratio. It is convenient to split the exterior velocity field as:

$$\boldsymbol{u} = \bar{\boldsymbol{\Gamma}}.\boldsymbol{x} + \boldsymbol{u}' \tag{2.9}$$

where $\boldsymbol{u}'$ is the disturbance velocity that vanishes at large distances from the drop. Since any linear flow (with a trivial pressure field) is a solution of the Stokes equations, the disturbance field also satisfies Eq. 2.8. The boundary conditions for the interior and exterior fields are given by;

$\mathbf{u}' \to 0$ as $r \to \infty$ (disturbance velocity decays off at infinity)

$\hat{\mathbf{u}} = \bar{\boldsymbol{\Gamma}}.\boldsymbol{x} + \boldsymbol{u}'$ at $r = 1$ (continuity of velocity at interface)

$\mathbf{u}.\mathbf{n} = \hat{\mathbf{u}}.\boldsymbol{n} = 0$ at $r = 1$ (stationary spherical interface)

$(\boldsymbol{\sigma}.\mathbf{n}).(\mathbf{I} - \mathbf{nn}) = (\hat{\boldsymbol{\sigma}}.\mathbf{n}).(\mathbf{I} - \mathbf{nn})$ at $r = 1$ (continuity of tangential stress at the interface).

where $\boldsymbol{\sigma}$ and $\hat{\boldsymbol{\sigma}}$ are the stress tensors in the exterior and interior fluid, respectively. Note that the boundary conditions are imposed on a spherical interface and this assumption also enters in taking $\boldsymbol{n}$ to be a unit radial vector. As stated earlier, this assumption is valid for $Ca = 0$. In this limit, the normal stress balance at $r = 1$ is not required to determine the velocity and pressure fields. One may, in principle, make these fields as the leading order approximation in small-Ca expansion (provided $\lambda \sim O(1)$; see Chapter 5). The higher order corrections may then be solved for in a systematic manner. For instance, the normal stress balance above may be used to determine the small, $O(Ca)$, drop deformation on account of viscous stresses. In turn, one may use this $O(Ca)$ interfacial deformation to determine the $O(Ca)$ correction to the velocity and stress fields; the normal stress balance may then be used to calculate the $O(Ca^2)$ deformation, and so on, in what is essentially an asymptotic expansion for small Ca. For this procedure, the BCs also need to be modified by accounting for drop deformation. For both the two-parameter family of flows considered here and for majority of $3D$ linear flows, the exterior streamlines in the near-field are open. In fact it is well known from Krishnamurthy and Subramanian (2018a) and Powell (1983), that except for a vanishingly small subset of the one-parameter family of canonical planar linear flows, the exterior streamlines in the near-field are always open. The higher order corrections associated with deformation, will only have a perturbative effect on the velocity field and hence the transport rate for these flows with open streamlines. But for the flows with closed streamlines, deformation has a singular effect, and qualitatively changes the streamline topology and transport rate (see Chapter 5).

The Stokes equations (Eq. 2.8) subject to the above boundary conditions can be solved to yield the well-known results for both the interior and exterior velocity fields (G. L. Leal (2007), Cox (1969)) as:

$$\boldsymbol{u} = \dot{\boldsymbol{x}} = C_1\boldsymbol{E}.\boldsymbol{x} + \boldsymbol{\Omega}.\boldsymbol{x} + C_2(\boldsymbol{E}:\boldsymbol{xx})\boldsymbol{x} \tag{2.10}$$

where C_1 and C_2 are given by:

$$\text{Interior}\begin{cases} C_1 &= \frac{-3\lambda}{2(1+\lambda)} + \frac{5\lambda}{2(1+\lambda)}r^2 \\ C_2 &= \frac{-\lambda}{1+\lambda}r^2 \end{cases} \qquad \text{Exterior}\begin{cases} C_1 &= 1 - \frac{\lambda}{(1+\lambda)r^5} \\ C_2 &= \frac{5\lambda}{2(1+\lambda)r^7} - \frac{(5\lambda)+2}{2(1+\lambda)r^5} \end{cases} \qquad (2.11)$$

The surface velocity field is obtained from Eq.2.10, by setting $r = 1$ in either the interior or exterior fields and is of the form:

$$\dot{\boldsymbol{n}} = \boldsymbol{\Omega}.\boldsymbol{n} + G(\lambda)\left((\boldsymbol{E}:\boldsymbol{nn})\boldsymbol{n} + \boldsymbol{E}.\boldsymbol{n}\right) \qquad (2.12)$$

where $G(\lambda) = \frac{1}{1+\lambda}$. With the known expression for the surface velocity field, one now needs to solve $\frac{d\boldsymbol{n}}{dt} = \boldsymbol{u}(\boldsymbol{n})$ on the unit sphere, to obtain, analytically, the form of the surface streamlines; this is required in the calculation of transport rate at large Pe, which is governed by the surface flow relevant to the convection boundary layer. Now, for the one parameter family of flows discussed in Krishnamurthy and Subramanian (2018a), substituting for $\boldsymbol{E}$ and $\boldsymbol{\Omega}$, one may easily find the solutions to this governing equation in closed form, but for an arbitrary linear flow and for the two-parameter families considered here, the solutions in closed-form by solving the governing system of differential equations is not obvious because the equations are non-linear. Thus we take a different approach to write down the solutions in closed form.

Observing that Eq. 2.12 has the same form as the equation governing Jeffery orbits (L. G. Leal and Hinch (1971), Jeffery (1922)), which are the trajectories traced out by the orientation vector of an axisymmetric particle suspended in linear shearing flows (see Chapter 3), we conclude that the surface streamlines must be generalisations of Jeffery orbits, and as will be seen later, generalisation of the so-called natural coordinates introduced by L. G. Leal and Hinch (1971) constitute a convenient choice to analyse the drop transport problem. Importantly, we realize that Eq.2.12 is the projection, onto the unit sphere (drop surface), of the linear equation given by:

$$\dot{\boldsymbol{x}} = \boldsymbol{\Omega}.\boldsymbol{x} + G(\lambda)\left(\boldsymbol{E}.\boldsymbol{x}\right) = \hat{\boldsymbol{\Gamma}}.\boldsymbol{x}, \qquad (2.13)$$

where, $\boldsymbol{n} = \boldsymbol{x}/|\boldsymbol{x}|$. The solutions of the surface-streamline equations (Eq.2.12) can be alternatively obtained by solving the linear system given by Eq.2.13, which we term the '*auxiliary linear flow*', and then projecting the solutions onto the unit sphere (drop surface). The advantage of this method is the fact that the auxiliary flow, being a linear system, is exactly solvable, implying that one can always obtain the surface-streamline equations in closed form. As we will see later, this approach is more useful when we consider linear flows of relatively complex topologies. For the case of $3D$ extension with aligned vorticity, we can solve the full non-linear equations for surface streamlines in closed form, however, they are not decoupled in spherical coordinates for the other two-parameter family of axisymmetric extension with inclined vorticity. Therefore, for this case, one needs to use the auxiliary flow solutions to obtain closed-form expressions for surface-streamline equations. With this background of the problem, we now move on to analyse the first two-parameter family, three-dimensional extension with vorticity aligned along one of the principal components of extension (hereafter called aligned-vorticity family).

2.3   Drop in 3D Extension with Aligned Vorticity

The velocity-gradient tensor for the aligned-vorticity family is given by:

$$\bar{\boldsymbol{\Gamma}} = \begin{bmatrix} -(1+\epsilon) & -\frac{\alpha}{2} & 0 \\ \frac{\alpha}{2} & 1 & 0 \\ 0 & 0 & \epsilon \end{bmatrix} \qquad (2.14)$$

The geometry of the flow given by Eq.2.14 is shown in Fig.2.2, where we have taken the vorticity vector to be aligned along E_3 and $\epsilon = E_3/E_2$.
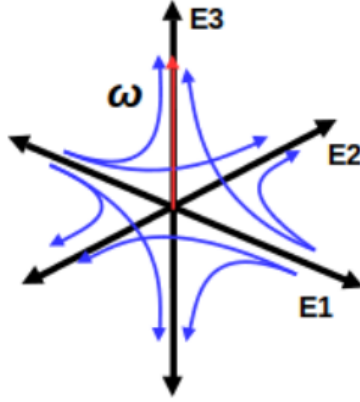
Figure 2.2: The geometry of $3D$ extension with aligned vorticity.

Recall from earlier discussion that when $\alpha = 0$, the range of ϵ needed to cover all possible flow configurations is $\epsilon \in [0, 1]$ (Krishnamurthy and Subramanian (2018a)), on account of invariance of transport rate to flow reversal (Brenner (1963)). However, with the addition of vorticity, one needs an extended range to cover the entirety of flow topologies. Also recall, that the range of ϵ is dependent on the principal axis along which vorticity is aligned. For the configuration given in Fig.2.2, one can easily show that $\epsilon \in [-2, 0]$ covers the full spectrum of topologies, to within flow reversals, with values outside the interval corresponding to the time-reversed versions of the topologies inside it. Owing to the analysis of Brenner (1963), we can, therefore, restrict ourselves to this range. In our analysis, we choose a coordinate system that is coincident with the principal extensional components, with x_1, x_2, x_3 along E_1, E_2, E_3, as shown in Figure. 2.3, which shows the system under consideration.
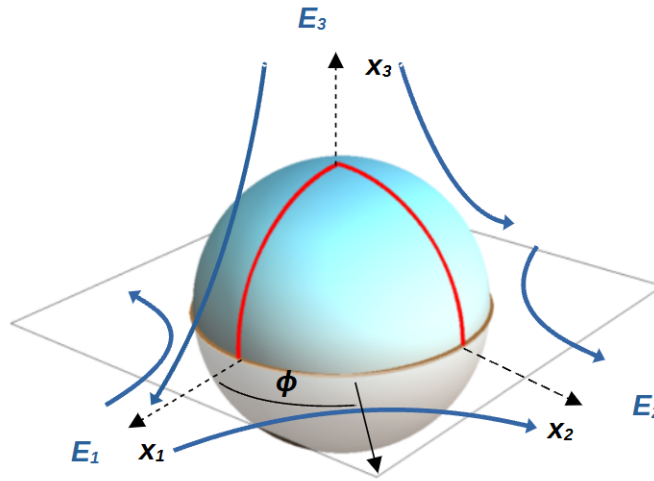
Figure 2.3: Schematic of the coordinate system used showing the three axes aligned along the three principal components of extension.

The range of ϵ includes several special cases as listed below:

- $\epsilon = -2$ corresponds to axisymmetric compressional flow, with vorticity aligned along the axis of symmetry (the x_3 axis). Here the extensional components are $E_1 = E_2 = 1$ and $E_3 = -2$.

- $\epsilon = -0.5$ corresponds to an axisymmetric extensional flow with the extensional components given

by $E_1 = E_3 = -0.5$ and $E_2 = 1$. Although the extension corresponds to the time-reversed version of the compressional flow above, the vorticity is perpendicular to the axis of symmetry in this case.

- $\epsilon = -1$ corresponds to a planar extension in the $x_2 - x_3$ plane and, with vorticity vector present in the plane of flow. Note that, this flow is planar (planar extension) only when $\alpha = 0$ and for non-zero α, the flow is three-dimensional.

- $\epsilon = 0$ is the final special case which corresponds to the one-parameter family of canonical planar linear flows, with the flow taking place in the $x_1 - x_2$ plane and vorticity perpendicular to it. Recall that this special case was already analysed by Krishnamurthy and Subramanian (2018a) in an earlier effort.

We begin our analysis for this case by writing down the solutions of the surface streamlines, which lets us analyse the organisation of the surface streamline topology using critical-point techniques. The analysis of this topology directly leads to our definition of the flow-aligned affine coordinate system, the $C - \tau$ system. We then describe the characteristic features of this coordinate system and then show that it enables us to solve the governing equation for transport using a similarity transformation.

2.3.1 Surface Streamline Topology - Organisation

For the two-parameter family under consideration, the velocity field (Eq.2.10) is given in spherical coordinates as,

$$u_r = r(C_1 + C_2 r^2) \left(\epsilon \cos^2 \theta - \frac{1}{2}(\epsilon + (2 + \epsilon) \cos 2\phi) \sin^2 \theta \right) \tag{2.15}$$

$$u_\theta = \frac{-1}{4} r \, C_1 \left(3\epsilon + (2 + \epsilon) \cos 2\phi \right) \sin 2\theta \tag{2.16}$$

$$u_\phi = \frac{1}{2} r \, \sin \theta (\alpha + C_1(2 + \epsilon) \sin 2\phi) \tag{2.17}$$

where C_1 and C_2 are defined in Eq. 2.11. On the drop surface $(r = 1)$, the radial velocity is identically zero, and the surface streamlines are trajectories on the unit sphere determined by the velocity components in the θ and ϕ directions, which lead to the following ODEs from Eq.2.15 - Eq.2.17:

$$\frac{d\theta}{dt} = \frac{-(3\epsilon + (2 + \epsilon) \cos 2\phi) \sin 2\theta}{4(1 + \lambda)} \tag{2.18}$$

$$\frac{d\phi}{dt} = \frac{((1 + \lambda)\alpha + (2 + \epsilon) \sin 2\phi)}{2(1 + \lambda)} \tag{2.19}$$

For this two-parameter family, the above system of equations may be solved owing to the equation for $d\phi/dt$ being independent of θ. These solutions of are given by:

$$\tan \phi = -\frac{A \tanh \left(\frac{A(t+c_0)}{2(1+\lambda)} \right) + (2 + \epsilon)}{\alpha(1 + \lambda)} \tag{2.20}$$

$$\tan \theta = C\alpha(1 + \lambda) \left(\frac{(\tan^2 \phi + 1)}{1 - \left(\frac{(2+\epsilon) - (1+\lambda)\alpha \tan \phi}{A} \right)^2} \right)^{1/2} e^{\frac{-3\epsilon t}{2(1+\lambda)}} \tag{2.21}$$

where $A = \sqrt{(2 + \epsilon)^2 - (1 + \lambda)^2 \alpha^2}$. The above procedure does not work in any obvious manner once the system of equations are fully coupled. But the auxiliary flow approach always gives a closed form expression for the surface velocity field by solving the auxiliary linear system and projecting the solutions

onto the unit sphere. To do this, we begin with the velocity-gradient tensor for the auxiliary flow ($\hat{\mathbf{\Gamma}}$) given by:

$$\hat{\mathbf{\Gamma}} = \begin{bmatrix} -\frac{(1+\epsilon)}{1+\lambda} & -\alpha/2 & 0 \\ \alpha/2 & \frac{1}{1+\lambda} & 0 \\ 0 & 0 & \frac{\epsilon}{1+\lambda} \end{bmatrix}. \tag{2.22}$$

where, in comparison with Eq.2.13, we see that $G(\lambda) = 1/(1+\lambda)$. Then we solve Eq.2.13, to get solutions for $\boldsymbol{x} = \{x_1, x_2, x_3\}$ as:

$$x_1 = \frac{e^{\frac{\epsilon+A}{2(1+\lambda)}} \left(\left(2 + \epsilon + A - e^{\frac{tA}{1+\lambda}}(2+\epsilon-A) \right) x_1^0 - \left(-1 + e^{\frac{tA}{1+\lambda}} \right)(1+\lambda)\alpha x_2^0 \right)}{2A} \tag{2.23}$$

$$x_2 = \frac{e^{\frac{\epsilon+A}{2(1+\lambda)}} \left(\left(e^{\frac{tA}{1+\lambda}}(2+\epsilon+A) - ((2+\epsilon)-A) \right) x_2^0 + \left(-1 + e^{\frac{tA}{1+\lambda}} \right)(1+\lambda)\alpha x_1^0 \right)}{2A} \tag{2.24}$$

$$x_3 = e^{\frac{t\epsilon}{1+\lambda}} x_3^0 \tag{2.25}$$

where A is again $\sqrt{(2+\epsilon)^2 - (1+\lambda)^2\alpha^2}$ and x_1^0, x_2^0 and x_3^0 are the initial points. This can be projected onto the unit sphere by simply dividing each of the expressions by $r = \sqrt{x_1^2 + x_2^2 + x_3^2}$ and then converting the resulting expressions into spherical coordinates. We can easily show, that this approach gives us the same expressions as in Eq.2.20 and 2.21, where one can write the hyperbolic functions in both the equations in terms of the exponential function, which would then lead us to expressions of the form:

$$\tan\phi = \frac{(A-B) + e^{\frac{At}{(1+\lambda)}}\tan\phi_0(A+B)}{(A+B)\tan\phi_0 + e^{\frac{At}{(1+\lambda)}}(A-B)} \tag{2.26}$$

$$\tan\theta = \frac{C}{2A}(1 + \tan^2\phi)e^{\frac{-t(A+3\epsilon)}{2(1+\lambda)}} \left((A+B) + e^{\frac{At}{(1+\lambda)}}(A-B) \right) \tag{2.27}$$

where $B = (2+\epsilon) - (1+\lambda)\alpha$ and $\tan\phi_0 = x_2^0/x_1^0$. Note from Eqns.2.20-2.21 and 2.26-2.27, that when $2+\epsilon < (1+\lambda)\alpha$, the hyperbolic functions become trigonometric ones and correspondingly the exponentials become complex, suggesting that the streamlines are spirals for this case. But otherwise, they will be open trajectories as we will see later. We use these solutions to plot the surface streamlines and analyse them.

In our analysis, we organise the surface streamlines by using the scalar invariants (P,Q and R) and discriminant (Δ) associated with the characteristic equation of the velocity-gradient tensor ($\hat{\mathbf{\Gamma}}$) of the auxiliary linear flow (to be defined in the following sub-section). Such an organisation of linear flows has already been carried out by Chong et al. (1990) and Perry and Chong (1987), who used these invariants in the so-called $P - Q - R$ classification, to characterise the streamline patterns motivated, in part, by the need to understand the structure of sub-Kolmogorov turbulence. In Figure 2.4 below, we show a plot from their work, where the organisation of the streamline topology is shown in the $Q - R$ plane (relevant to incompressible flows). Particularly, note that, when there is a change in the sign of the discriminant (Δ), there is a qualitative change in the streamline topology. The streamlines change from spiralling to non-spiralling ones when the discriminant changes from positive to negative values. The cubic invariant R of $\hat{\mathbf{\Gamma}}$ is also crucial, as $R = 0$ (the Q axis) corresponds to planar flow topologies. As we shall see later these features are observed in our analysis too and they help us understand and organise the streamline topologies better.
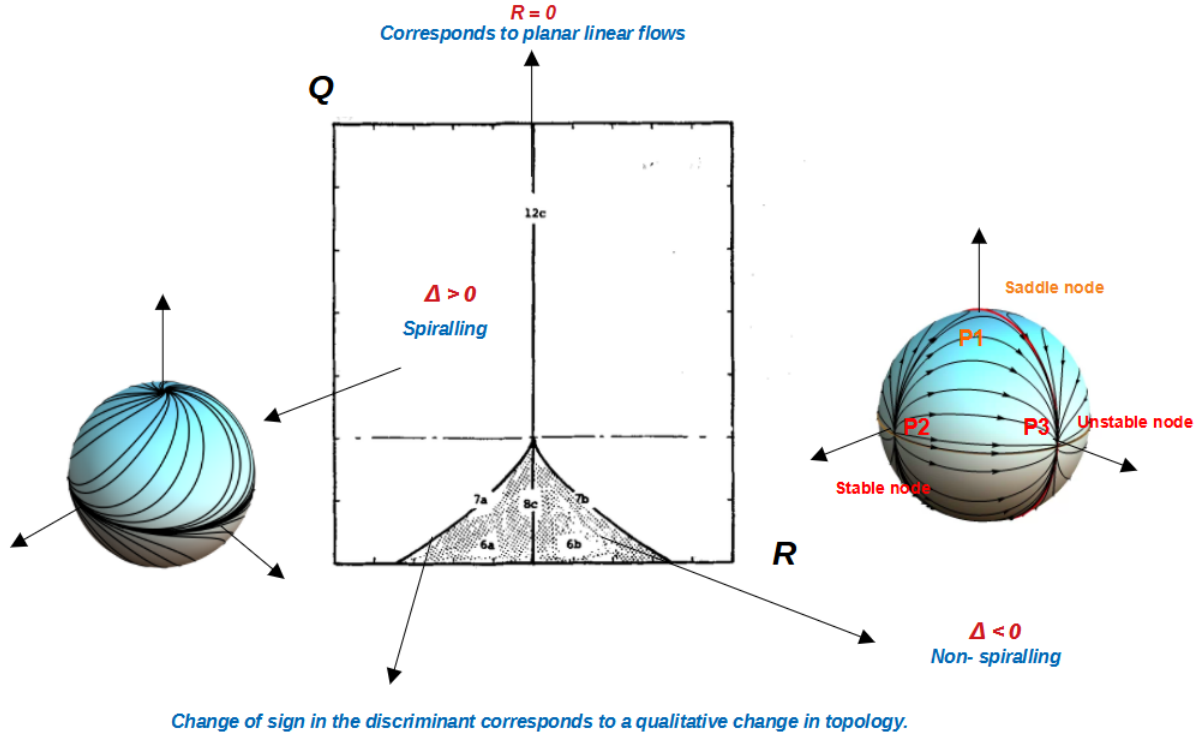
Figure 2.4: Organisation of the linear flow topologies in the $Q - R$ plane.

2.3.1.1 Invariants of the Auxiliary linear flow

The scalar invariants that we use to organise the streamline topology correspond to the coefficients that occur in the cubic characteristic equation satisfied by the eigenvalues μ of $\hat{\mathbf{\Gamma}}$ given by,

$$\mu^3 + Q\mu + R = 0 \tag{2.28}$$

The discriminant of the cubic equation, which determines the nature of the roots (eigenvalues) is given by $\Delta = 4Q^3 + 27R^2$ (see Section 2.4.2). As already indicated Δ determines the spiralling or non-spiralling character of flow (Chong et al. (1990)), as the nature of the trajectories is related to the nature of the eigenvalues. The linear invariant P (that would occur as the coefficient of μ^2) is zero for incompressible flows, $Q = (1/2)(tr(\hat{\mathbf{\Gamma}})^2 - tr((\hat{\mathbf{\Gamma}})^2))$ is the quadratic invariant, and $R = det(\hat{\mathbf{\Gamma}})$ is the cubic invariant. $R = 0$ corresponds to a planar linear flow configuration and the sign of Q when $R = 0$ determines the elliptic or hyperbolic character of the planar flow. For Eq.2.28, these invariants are given by:

$$\Delta = \frac{-((2 + \epsilon)^2 + (1 + \lambda)^2 \alpha^2)(4(1 + \epsilon - 2\epsilon^2) + (1 + \lambda)^2 \alpha^2)^2}{16(1 + \lambda)^6} \tag{2.29}$$

$$Q = \frac{-4(1 + \epsilon + \epsilon^2) + (1 + \lambda)^2 \alpha^2}{4(1 + \lambda)^2} \tag{2.30}$$

$$R = \frac{\epsilon(4 + 4\epsilon - (1 + \lambda)^2 \alpha^2)}{4(1 + \lambda)^3}. \tag{2.31}$$

We observe that λ can be scaled of these quantities by writing α as $\alpha' = (1+\lambda)\alpha$, $\Delta' = (1+\lambda)^6\Delta$, $Q' = (1+\lambda)^2 Q$ and $R' = (1+\lambda)^3 R$. The rescaled invariants are given by:

$$\Delta' = \frac{-((2+\epsilon)^2 + \alpha'^2)(4(1+\epsilon-2\epsilon^2) + \alpha'^2)^2}{16} \tag{2.32}$$

$$Q' = \frac{-4(1+\epsilon+\epsilon^2) + \alpha'^2}{4} \tag{2.33}$$

$$R' = \frac{\epsilon(4+4\epsilon - \alpha'^2)}{4}. \tag{2.34}$$

This suggests that the viscosity ratio does not affect the surface streamline topology and therefore, it is enough to analyse the topology in terms of the scaled quantities. Note that the scaled quantities are identical to the original ones for $\lambda = 0$. So for a bubble, the auxiliary and ambient linear flows are identical. Note that the discriminant and invariants only involve α'^2, implying that changing the direction of the vorticity does not affect the topology and is consistent with the time-reversal symmetry of Stokes flows, where changing the direction of vorticity is equivalent to reversing time. In the following analysis, we will examine plots of Δ', R' and Q', as a function of α' (with the domain being $\alpha' \geq 0$, owing to the aforementioned symmetry argument) for different values of ϵ and the plots will be correlated to the changes in the surface streamline topology (changes in the topology are qualitative). To begin with, we note that $\Delta' = 0$, which separated the two qualitatively different topologies in the $Q - R$ plane (fig.2.4), has two solutions given by:

$$\alpha'_{th1} = (2+\epsilon) \tag{2.35}$$

$$\alpha'_{th2} = 2(1+\epsilon-2\epsilon^2)^{1/2} \tag{2.36}$$

where, α'_{th1} is real-valued for all ϵ in the range $-2 \leq \epsilon \leq 0$ and is a zero crossing but α'_{th2} is real-valued only for $-0.5 \leq \epsilon \leq 0$ and is a doubly degenerate point (that is, a point of tangency), owing to the fact that it occurs under a square. Similarly, we observe that R' has a zero crossing given by:

$$\alpha'_{th3} = 2\sqrt{1+\epsilon} \tag{2.37}$$

which is real-valued for $-1 \leq \epsilon < 0$. For the special case of canonical planar linear flows (i.e. $\epsilon = 0$), R' is uniformly zero for all α' (consistent with the cubic invariant-based classification; see Chong et al. (1990)). Thus, it is prudent to analyse the streamline topology in different ranges of ϵ, which correspond to the aforementioned cases, that also includes the special cases ($\epsilon = -2$, $\epsilon = -1$, $\epsilon = -0.5$ and $\epsilon = 0$) discussed in the beginning of this section.

2.3.1.2   Cases with a single zero in Δ'

The first interval we consider is the range $-2 \leq \epsilon \leq -1$, where Δ' only has a single zero crossing. In this interval, we first look at the limiting case of $\epsilon = -2$, that corresponds to an axisymmetric extension with vorticity along the axis of symmetry. Representative plots of Δ' and R' for this case, together with the surface streamline topologies at key points are shown in Fig.2.5. For $\epsilon = -2$, Δ' starts off with zero at $\alpha' = 0$ and increases monotonically with α'. The point $\alpha' = 0$ is doubly degenerate, that is, it's a point of tangency, and from our earlier discussion, it corresponds to $\alpha'_{th2} = 0$. At this point, the streamlines are meridional, with the meridians being organised by a ring of fixed points and a pair of diametrically opposite stable and unstable nodes. This ring of fixed points is orthogonal to the nodes and the existence of this ring (a degenerate configuration) implies that the topology is structurally unstable. The streamlines corresponding to positive Δ' have a spiralling character, the spiralling trajectories being organised on the

unit sphere by a pair of unstable foci (located on the x_3 axis) and an entraining equatorial limit cycle (on $x_1 - x_2$ plane). The nature of spiralling is such that in the vicinity of $\alpha' = 0$, the spirals are tightly wound near the focus and the limit cycle and are stretched out in the region between them. As $\alpha' \to \infty$, the spirals become more tight, taking multiple turns on the hemisphere between the focus and the limit cycle, eventually becoming circular streamlines for $\alpha' = \infty$, corresponding to solid-body rotation.
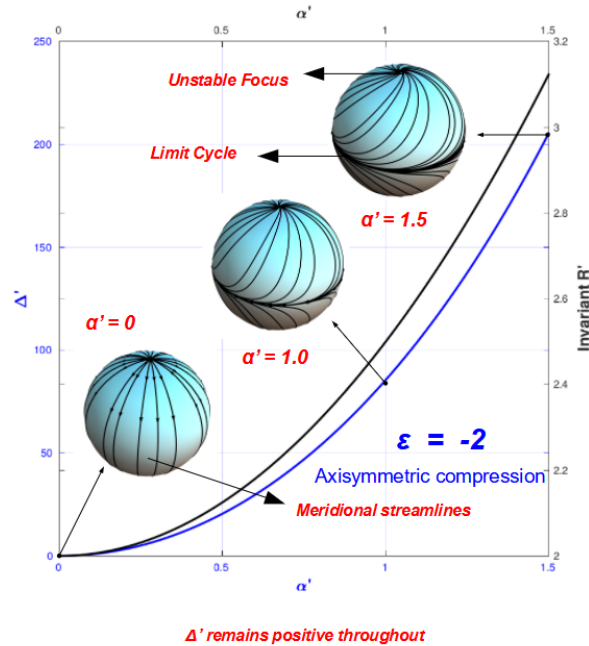
Figure 2.5: Plot of Δ' and R' versus α' for $\epsilon = -2$. The insets in the plots shows the surface streamline topology corresponding to different values of Δ' and R'.

The next streamline topology we encounter corresponds to $-2 < \epsilon \leq -1$, for which the discriminant Δ' only suffers a single zero-crossing and there are no points of tangency. Representative plots of Δ' and R' for an ϵ in the aforementioned range, together with the surface streamline topologies at key points are shown in Fig.2.6. Here, Δ' starts off negative when $\alpha' = 0$ and increases monotonically with α' crossing zero at α'_{th1}. The streamline topology for negative Δ' is non-spiralling, and the surface streamlines are organised on the drop surface by three pairs of fixed points: (i) a pair of saddles, and (ii) a pair each of stable and unstable nodes, conserving Euler characteristic. The stable and unstable manifolds of the saddle node terminate at the unstable and stable nodes on the equator respectively, splitting the drop surface into eight octants. With increasing α', i.e. as $\alpha' \to \alpha'_{th1}$ where $\Delta' = 0$, two of the octants on an hemisphere shrink in size relative to the other two with the stable node and saddle approaching each other. Right at α'_{th1}, these nodes merge in a (inverted) saddle-node bifurcation, with the unstable node transitioning into an unstable focus across this point. Beyond α'_{th1}, $\Delta' > 0$, and the the streamlines on the surface have a spiralling character, which have the same features mentioned for $\epsilon = -2$. For the other limiting value of $\epsilon = -1$, Δ' does not have any degenerate points, and so the sequence of topologies is the same as above with an exception mentioned below.
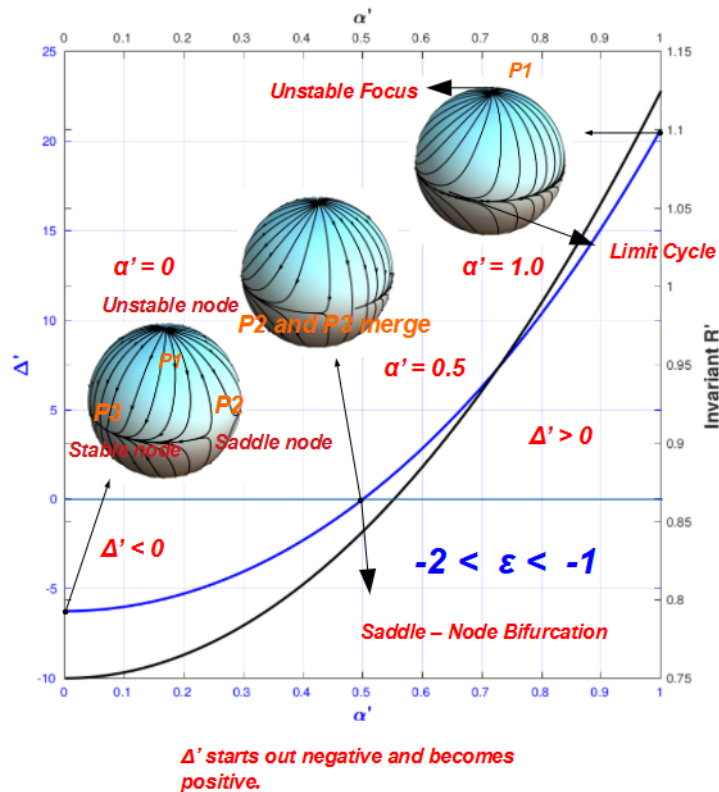
Figure 2.6: Plot of Δ' and R' versus α' for $-2 < \epsilon \leq -1$ along with corresponding surface-streamline topologies. Here Δ' suffers a zero crossing, while R' does not.

The cubic invariant R' for both the aforementioned cases, starts off with a positive value at $\alpha' = 0$ and increases monotonically. Therefore, there are no zero-crossings and so, the auxiliary flow is three-dimensional for all α'. The only exception to this is $\epsilon = -1$, $\alpha' = 0$, that corresponds to planar extension. But this qualitative difference in the $3D$ streamline topology at this point, does not affect the surface-streamline topology as we shall see below.

The next surface-streamline topology that we encounter corresponds to the range $-1 < \epsilon < -0.5$, for which the representative plots of Δ' and R' for a given ϵ in the range is shown in Fig.2.7, along with the streamline topologies at key points. In this case, the behavior of Δ' is similar to the previous case, with the exception that it is non-monotonic. Nevertheless, the minimum in the Δ' curve does not lead to any qualitative change to the sequence of streamline topologies. The key difference is that the cubic invariant R' suffers a zero crossing (α'_{th3}), unlike the case examined above. This implies that the auxiliary flow at α'_{th3} has a planar and the nature of the flow can be seen to be hyperbolic from the plot of Q' shown in Fig.2.8, which is negative at α'_{th3}, consistent with the earlier $Q - R$ classification (Fig.2.4). The figure also contrasts the surface-streamline topology associated with this planar flow with that of a $3D$ non-spiralling one, from which one can see that the qualitative change in the $3D$ streamline topology does not affect the surface-streamline topology.

A crucial aspect of these planar flows is that they are not members of the canonical family of hyperbolic planar flows and unlike the canonical case, there is a non-zero component of extension normal to the plane of flow. We label these "novel" flows, the '*eccentric planar hyperbolic flows* ', the reason for which will be clear later. These flows are generalisations of the canonical family and is identified here for the first time. A detailed exposition on these flows is presented in a separate chapter (Chapter 3) in the thesis.
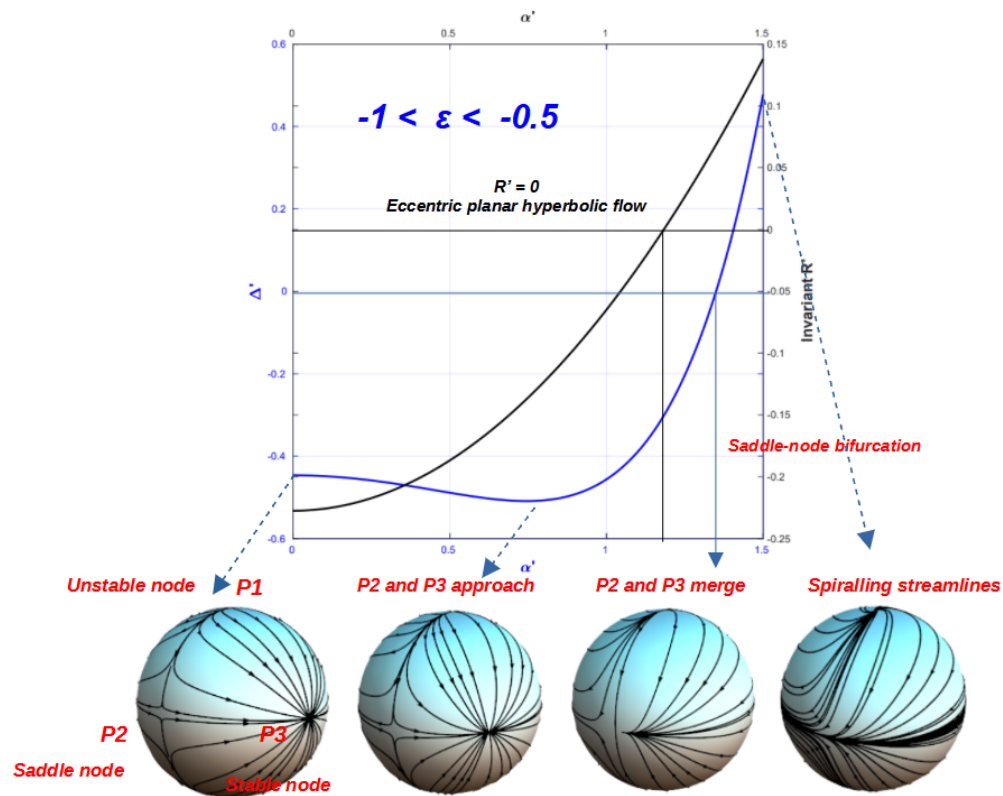
Figure 2.7: Plot of Δ' and R' versus α' for $-1 < \epsilon < -0.5$ along with corresponding surface-streamline topologies. Here Δ' behavior is the same as the previous case, but R' suffers a zero crossing unlike the other cases.
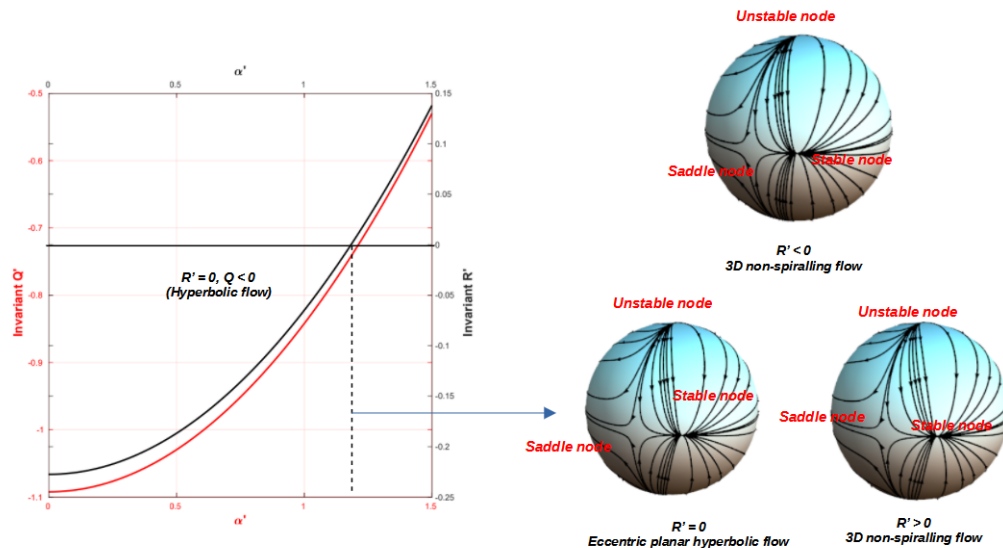
Figure 2.8: (a) Plot of R' and Q' versus α' for $-1 < \epsilon < -0.5$. Q' is negative at the point where $R' = 0$, implying hyperbolic character of the planar flow. (b) Comparison of surface-streamline topologies corresponding to cases, where the auxiliary linear flow is a hyperbolic planar flow and $3D$ extensional flows.

2.3.1.3 Cases with two zeros in Δ'
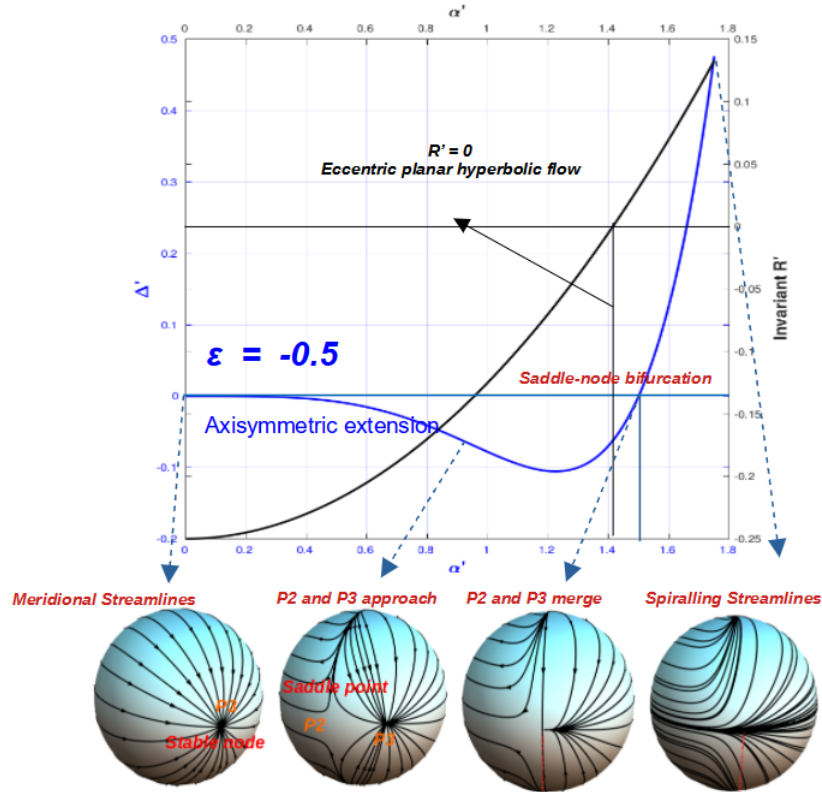
Figure 2.9: Plot of Δ' and R' versus α' for $\epsilon = -0.5$ along with corresponding surface-streamline topologies. Here Δ' starts with a doubly degenerate point much like Figure.2.5 and is negative until α'_{th1}. R' suffers a zero-crossing, leading to an eccentric planar hyperbolic flow topology.

We now begin examining cases where the plot of Δ' against α' has two zeros, namely α'_{th1} and α'_{th2}; the latter corresponds to a point of tangency. As already indicated above, this corresponds to the range $-0.5 \leq \epsilon < 0$. We first consider the transition value $\epsilon = -0.5$, which corresponds to an axisymmetric extension like $\epsilon = -2$, but with the vorticity vector perpendicular to the axis of symmetry. The plot of Δ' and R' against α' for this case is shown in Fig.2.9. Here, the discriminant starts off with zero at $\alpha' = 0$ and decreases initially with increasing α'. The starting point of α' is also the point of tangency for this case, i.e. $\alpha'_{th2} = 0$, and at this point, the streamlines are meridional, with the meridians being organised by a ring of fixed points and a pair of diametrically opposite stable and unstable nodes, just like the case of $\epsilon = -2$. For $\alpha' > \alpha'_{th2} > 0$, Δ' is negative and non-monotonic and therefore the surface-streamline topology is similar to the non-spiralling topology encountered in the previous cases. Δ' suffers a zero crossing at α'_{th1} and it corresponds to a saddle-node bifurcation beyond which the streamlines on the drop surface have a spiralling character as the earlier cases. In this case too, we encounter eccentric planar hyperbolic flows (Fig.2.9), and as was already mentioned, it's existence is incidental as far as the transport problem is concerned.

Next we move on to the range $-0.5 < \epsilon < 0$. Here, all of the features described above for $\epsilon = -0.5$ hold, with the exception that the point of tangency α'_{th2} has now moved to a finite positive value, separating two regions of negative Δ'; in each region, the surface-streamlines have a non-spiralling character, with the fixed points exchanging identities across the point of tangency. The point of tangency itself corresponds to a degenerate meridional topology, again with a ring of fixed points, but this is a non-orthogonal meridional topology unlike the previous cases. As α' increases beyond α'_{th2}, Δ' crosses zero and becomes positive,

with the surface streamlines again becoming spirals.
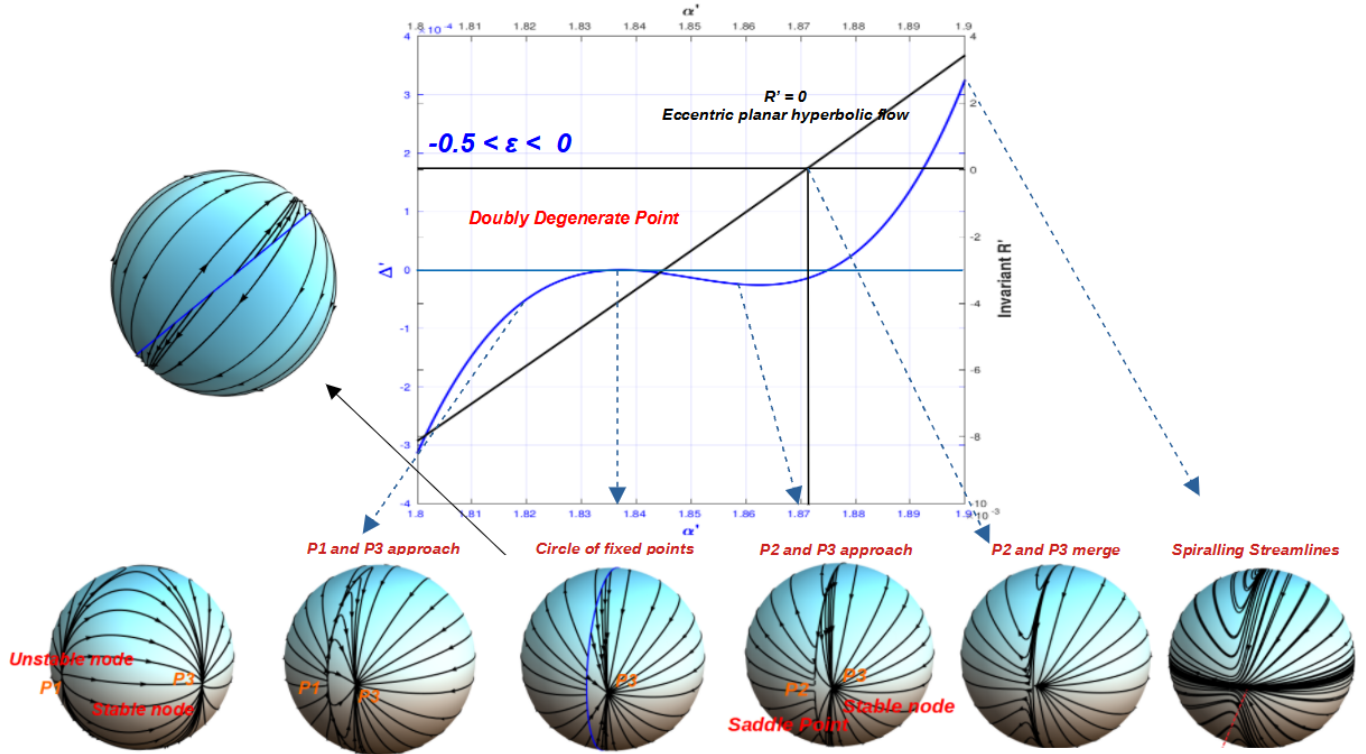
Figure 2.10: Plot of Δ' and R' versus α' for $-0.5 < \epsilon < 0$ along with corresponding surface-streamline topologies. Δ' behavior is the same as the previous case, but it starts with a negative value and the point of tangency has moved to a finite positive α'. R' suffers a zero-crossing like the previous case.

2.3.1.4 Case with a triply degenerate zero in Δ'

Finally, we look at $\epsilon = 0$, which corresponds to the canonical planar linear flows in the ambient. The plots of Δ' and R' are shown in Fig.2.11, where we see that $R' = 0$ for all α', which is consistent with the fact that these flows are planar flows. Here, the discriminant starts off negative, with surface streamlines corresponding to the non-spiralling topology and only has a single zero crossing which is a triply-degenerate point ($\alpha'_{TD} = 2$), with $\Delta' = \frac{d\Delta'}{s\alpha'} = \frac{d^2\Delta'}{d\alpha'^2} = 0$. This point corresponds to the coalescence of α'_{th1} (a simple zero-crossing) and α'_{th2} (a doubly degenerate point) to give α'_{TD}, a triply degenerate zero. This is also seen from the plot shown in Fig. 2.12, where we see that as $\epsilon \to 0$ from $\epsilon = -0.5$, α'_{th1} and α'_{th2} approach each other. The surface-streamlines at this point are meridional, but the meridians are organised only by a ring of fixed points unlike the earlier meridional topology we encountered. Beyond this point, we see that the surface streamlines on the drop are closed.

This case was already analysed by Krishnamurthy and Subramanian (2018a) in their work, but their governing parameter was $\hat{\alpha}$, defined as $\hat{\alpha} = (E - \Omega)/(E + \Omega)$. Comparing our results with theirs, we see that the triply degenerate point corresponds to $\hat{\alpha}_c = \lambda/(2 + \lambda)$ in their work, which is a λ-dependent threshold separating open and closed streamline regimes. Here, this λ dependency has been scaled out, but it is straightforward to show that α'_{TD} is the same as $\hat{\alpha}_c$, provided one uses the relation given in Eq.2.6, relating $\hat{\alpha}$ and α. Recall that the scaled variable α' is the same as α for $\lambda = 0$. For the same value of λ, Krishnamurthy and Subramanian (2018a) report $\hat{\alpha}_c = 0$. Thus substituting $\alpha'_T = 2$ in Eq.2.6, gives us $\hat{\alpha} = 0 = \hat{\alpha}_c$, validating our results. Apart from this validation, we will use Eq.2.6 in the heat transfer analysis to validate our Nu calculation with that of Krishnamurthy and Subramanian (2018a).
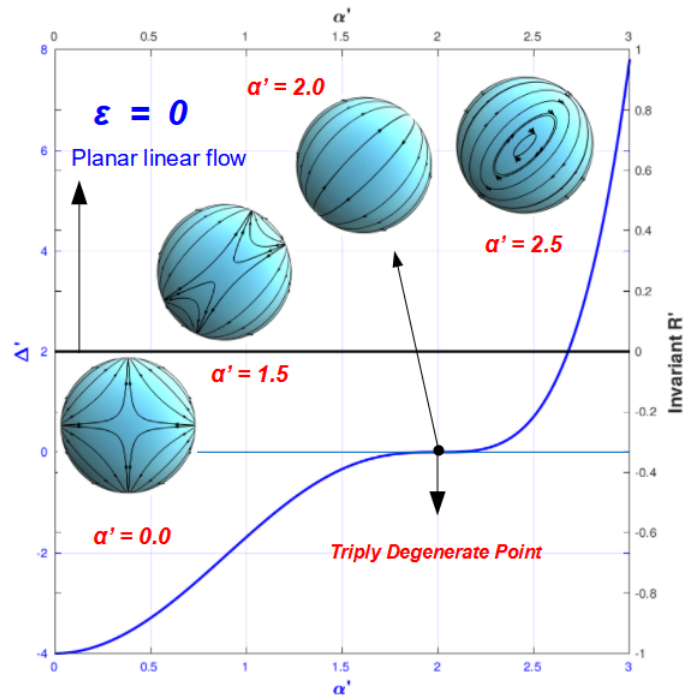
Figure 2.11: Plot of Δ' and R' versus α' for $\epsilon = 0$ along with corresponding streamline topologies. Here the Δ' behavior is the same as the previous case, but with a triply degenerate point, beyond which we observe closed streamlines. Note R' is identically 0 for this case.
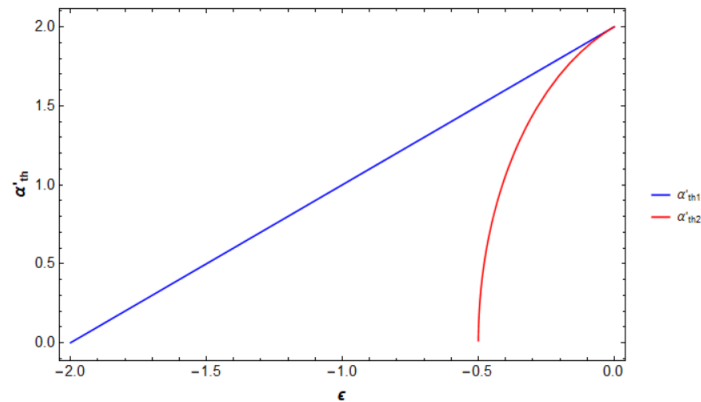
Figure 2.12: Plot α'_{th1} and α'_{th2} with ϵ. The thresholds approach each other as $\epsilon \to 0$.

With this, we conclude the section on streamline topology organisation. In the next section, we quantify the various features we encountered in this section using fixed point analysis, before moving on to the heat transfer analysis.

2.3.2 Surface Streamline Topology - Fixed Point Analysis

In this subsection, we use fixed point analysis to establish quantitatively what was described in the last section. Specifically, the surface-streamline topologies seen earlier were organised by fixed points, and the transition from one topology to other involved bifurcations (local) that are accompanied by a change in the nature of the fixed points. Herein, we confirm the nature of fixed points via calculation of the

corresponding eigenvalues. We consider both auxiliary flow for which the origin is always a sole fixed point and the equation governing the surface streamlines, which on account of non-linearity, allow for multiple fixed points and/or limit cycles. We begin by noting that the eigenvalues of the auxiliary flow, governed by a velocity-gradient tensor $\hat{\mathbf{\Gamma}}$, which are given by:

$$\mu_1 = \epsilon \tag{2.38}$$

$$\mu_2 = \frac{-\epsilon - \sqrt{(2+\epsilon)^2 - \alpha'^2}}{2} \tag{2.39}$$

$$\mu_3 = \frac{-\epsilon + \sqrt{(2+\epsilon)^2 - \alpha'^2}}{2}. \tag{2.40}$$

completely characterise the surface-streamline topology, since the surface streamlines are projections of the auxiliary flow streamlines, onto the drop surface. For instance, the surface-flow will have spiralling character only if the auxiliary flow contains spiralling streamlines, for which the eigenvalues are complex. We also examine the eigenvalues of the non-linear surface velocity field about the fixed points on the drop surface, by linearising the field about these points. The coordinates of these fixed points, obtained by solving $\boldsymbol{u}|_{r=1} = 0$ is:

$$\{P_1, P_2, P_3\} = \begin{cases} (0, 0, \pm 1) \\ \left(\pm\sqrt{\frac{(2+\epsilon)+A'}{2(2+\epsilon)}}, \pm\sqrt{\frac{(2+\epsilon)-A'}{2(2+\epsilon)}}, 0 \right) \\ \left(\pm\sqrt{\frac{(2+\epsilon)-A'}{2(2+\epsilon)}}, \pm\sqrt{\frac{(2+\epsilon)+A'}{2(2+\epsilon)}}, 0 \right) \end{cases} \tag{2.41}$$

where $A' = \sqrt{(2+\epsilon)^2 - \alpha'^2}$. Here, the $\pm$ before these coordinates corresponds to the fact there are a pair of diametrically opposite fixed points, owing to the fact that the surface-streamline topology satisfies the $\boldsymbol{x} \leftrightarrow -\boldsymbol{x}$ symmetry, since this applies to ambient linear flow. Alternatively, one can find the positions of these fixed points by using the eigenvectors of the auxiliary system. Note that when the streamlines are spirals, the auxiliary system involves a real eigenvector and two complex conjugate eigenvectors. The intersection of the real eigenvector with the unit sphere gives the position of the focus, while the real and imaginary parts of one of the complex eigenvectors span the plane of the limit cycle. When the streamlines are not spirals, the system has three real and distinct eigenvectors, with each eigendirection containing one of the three pairs of fixed points. Thus their intersection with the unit sphere gives the location of all six fixed points on the unit sphere. These fixed points have been marked in the streamline topology plots shown earlier and we investigate the nature of these fixed points using their eigenvalues. To do this, we linearise the surface velocity field about these points, which we can again represent as $\boldsymbol{u}_S = \hat{\mathbf{\Gamma}}'.\boldsymbol{n}$. The eigenvalues of the surface velocity field about the fixed points can be easily evaluated to be:

$$\{\mu_{P_1}^1, \mu_{P_1}^2\} = \begin{cases} \frac{-3\epsilon+A'}{2} \\ \frac{-3\epsilon-A'}{2} \end{cases} \qquad \{\mu_{P_2}^1, \mu_{P_2}^2\} = \begin{cases} A' \\ 3\epsilon + A' \end{cases} \qquad \{\mu_{P_3}^1, \mu_{P_3}^2\} = \begin{cases} -A' \\ 3\epsilon - A' \end{cases} \tag{2.42}$$

These eigenvalues, change sign when one moves from a given fixed point to the diametrically opposite one. In the discussion that follows, we plot these eigenvalues as a function of α' for different values of ϵ, in the various ranges of ϵ encountered earlier, in order to determine the nature of the fixed points.

2.3.2.1 Cases with a single (non-degenerate) zero in Δ'

The first scenario again pertains to $-2 < \epsilon \leq -1$. For this case, the eigenvalues of the auxiliary system are plotted in Fig. 2.13. The eigenvalues are all real until α'_{th1} (the zero crossing of Δ') after which two of them become complex while the third one remains real and negative. Real eigenvalues imply that the streamlines are non-spiralling and complex ones imply spiralling topologies. This can be correlated to the

discriminant plot in Fig.2.6, where the region where Δ' is negative is also the region where the eigenvalues are real and when $\Delta' > 0$, the eigenvalues are complex. When the streamlines are non-spiralling, they run between fixed points on the drop surface, and from Eqs.2.41, we see that three pairs of fixed point exist for $\alpha' < \alpha'_{th1}$ and only one pair ($P1$) exists for $\alpha' > \alpha'_{th1}$. From the plots of eigenvalues about these fixed points Fig.2.14(a)-(c), we see that the eigenvalues about $P1$ (Fig.2.14(a)) are real and are of same sign until α'_{th1}, beyond which they becomes complex with a positive real part. This suggests that the $P1$ is a pair of unstable nodes for $\alpha' < \alpha'_{th1}$ and unstable foci above α'_{th1}. Similarly, from Fig.2.14(b)-(c), for $\alpha' < \alpha'_{th1}$, we observe that the pair $P2$ and $P3$ are saddles and stable nodes respectively, since the eigenvalues about $P2$ are real and oppositely signed, while about $P3$, they are both real and negative. Beyond α'_{th1}, these points no longer exist and have therefore merged into a limit cycle, right at α'_{th1} (Fig.2.15). Thus the surface streamline topology consists of open streamlines organised by three pairs of fixed points below α'_{th1} and spiralling streamlines above α'_{th1}.
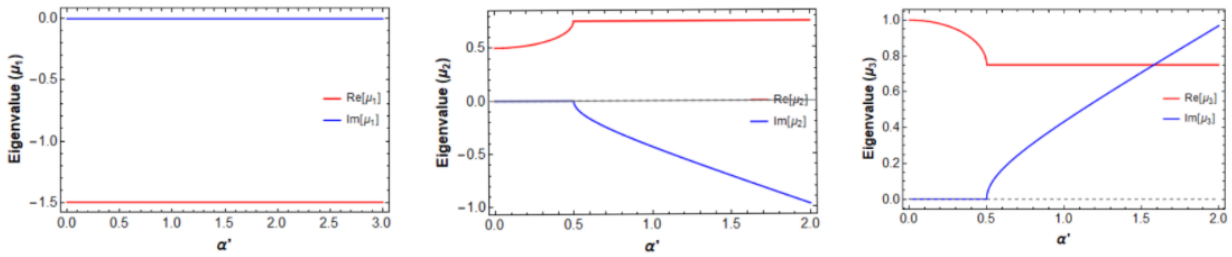
Figure 2.13: Plot of eigenvalues μ_i of the auxiliary linear flow for $-2 < \epsilon \leq -1$.
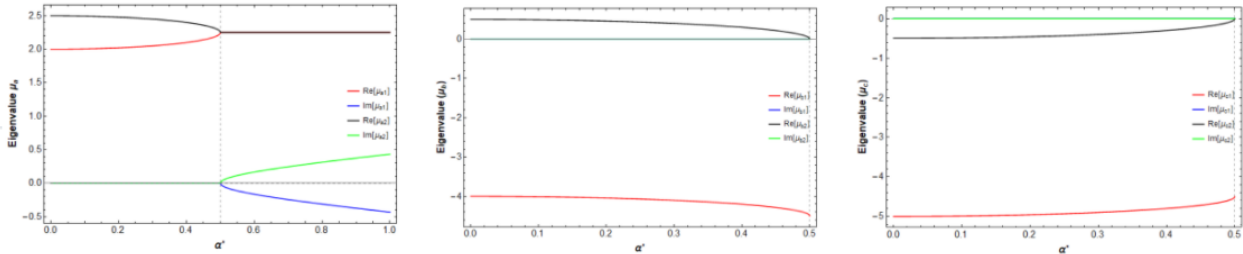
Figure 2.14: Plot of eigenvalues of the linearised surface velocity field about $P1, P2$ and $P3$ for $-2 < \epsilon \leq -1$. The vertical grid line corresponds to α'_{th1}.
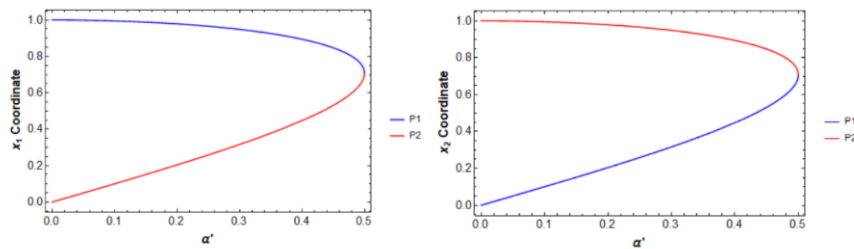
Figure 2.15: Plot of the x_1 and x_2 coordinates of $P2$ and $P3$ with α'. They merge together at α'_{th1}.

The second case in this scenario corresponds to $-1 < \epsilon < -0.5$, where we encountered a non-canonical planar flow topology corresponding to $R' = 0$, the eccentric planar hyperbolic topology, whose existence

can be confirmed using the fixed point analysis. From the plot of eigenvalues of the auxiliary system, we see that right at the point where the eccentric planar flows occur (α'_{th3}), one of the eigenvalues is 0, while the other two are real and oppositely signed, confirming the planar hyperbolic character of the auxiliary flow. The behavior of the eigenvalues of the linearised system, about the fixed points, is again similar to the previous case, where $P2$ and $P3$ merge at α'_{th1} (saddle-node bifurcation), beyond which $P1$ becomes an unstable focus and thus these plots are not shown for this case.
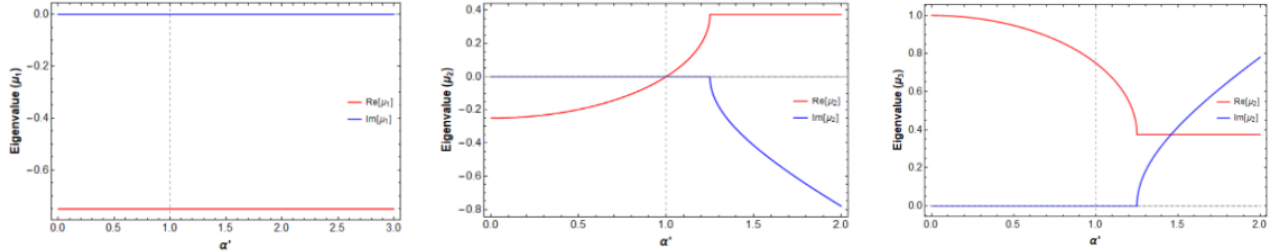
Figure 2.16: Plot of eigenvalues of the auxiliary linear flow for $-1 < \epsilon < -0.5$. The vertical grid line marks the point of occurrence of eccentric planar hyperbolic flow (α'_{th3}).

2.3.2.2 Cases with two zeros in Δ'

This scenario corresponds to $-0.5 \leq \epsilon < 0$. For this case, as was pointed out before, there is an intermediate meridional topology at α'_{th2}, across which the fixed points change identities (except for $\epsilon = -0.5$, where the meridional topology occurs at $\alpha'_{th2} = 0$). This can be shown from the plots of eigenvalues of the auxiliary system shown in Fig.2.17, where at α'_{th2}, two of the three eigenvalues are equal. The presence of eccentric planar hyperbolic flows for this case can again be shown from the eigenvalue plots of the auxiliary linear system at α'_{th3}, where one of the eigenvalues become identically zero and the other two eigenvalues are oppositely signed. Apart from these special points, the nature of the eigenvalues and their correlation to streamline topology are similar to the previous cases, where real eigenvalues imply non-spiralling topology and complex ones imply a spiralling topology. From Fig.2.18 showing the eigenvalues of the linearised surface velocity field about the fixed points $P1, P2$ and $P3$, we see that the eigenvalues about $P1$ and $P2$ change sign at α'_{th2}, the point of occurrence of meridional topology, implying the swap of identities of these fixed points. Apart from this exception, the plot and it's implications to the surface-streamline topology are identical to the earlier cases.
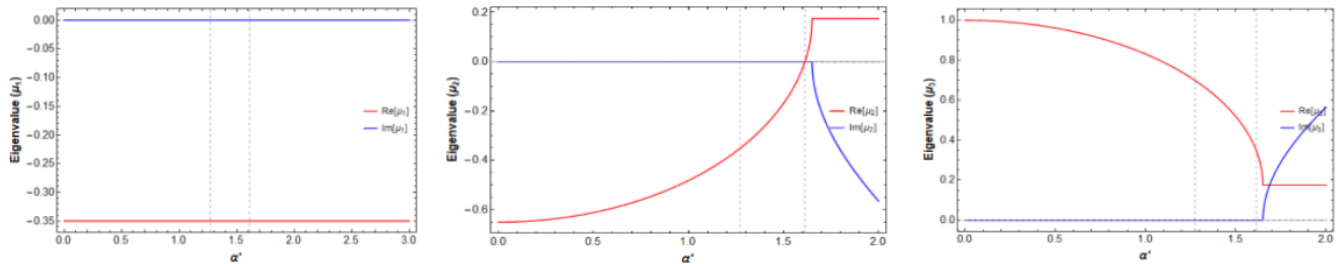
Figure 2.17: Plot of eigenvalues of the auxiliary linear flow for $-0.5 \leq \epsilon < 0$. The first vertical grid line marks α'_{th2} corresponding to skewed meridional topology and the second one marks the point of occurrence of eccentric planar hyperbolic flow (α'_{th3}).
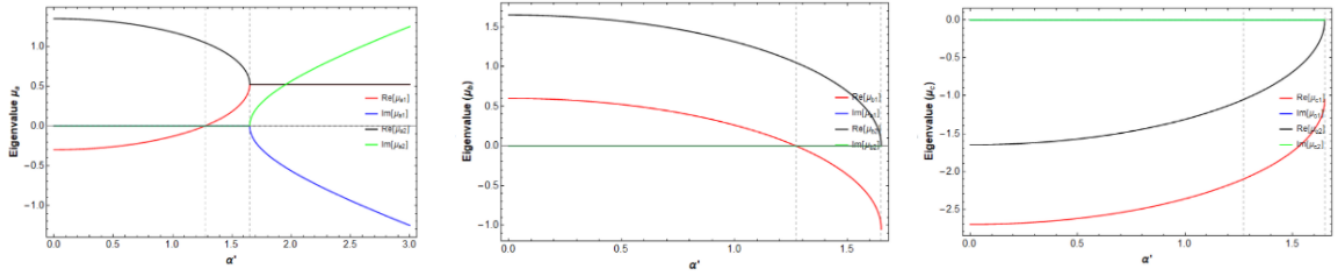
Figure 2.18: Plot of eigenvalues $\mu_{P_i}^{1,2}$ of the linearised surface velocity field about the fixed points $P1$, $P2$, $P3$ for $-0.5 \leq \epsilon < 0$. The vertical grid lines correspond to α'_{th2} and α'_{th1}.

For the transition point corresponding to $\epsilon = -0.5$, the eigenvalues of the auxiliary system and the eigenvalues of the non-linear velocity field about the fixed points, behave the same way as the aforementioned case, but, with the meridional topology occurring at $\alpha'_{th2} = 0$. So the plots for $\epsilon = -0.5$ are not shown.

2.3.2.3 Cases with a single (degenerate) zero in Δ'

For $\epsilon = -2$, we see that two of the three eigenvalues of the auxiliary linear system are complex valued, whereas the third one is real and negative (Fig.2.19). At $\alpha' = 0 = \alpha'_{th2}$, the eigenvalues are real and two of the eigenvalues are equal with the third being the negative of their sum. This, once again, corresponds to the meridional topology organised by a ring of fixed points and a pair of diametrically opposite nodes. The eigenvalues of the linearised surface velocity field about the focus, at $P1 = (0, 0, \pm1)$, are shown in Fig.2.20, where we see that they are complex numbers with a positive real part for $\alpha' > 0$, implying that the focus is an unstable one. We also note that, for this case, the fixed points $P2$ and $P3$ (given by Eq.2.41) do not exist for $\alpha' > 0$, implying the presence of a limit cycle. This establishes that the streamline topology for this case has a spiralling character for all values of α', starting from an unstable focus and terminating at a limit cycle.
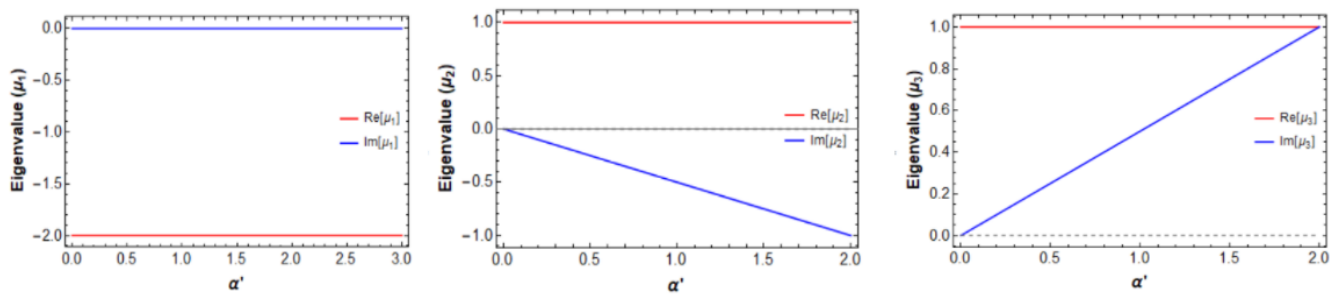
Figure 2.19: Plot of eigenvalues μ_i of the auxiliary linear flow for $\epsilon = -2$.
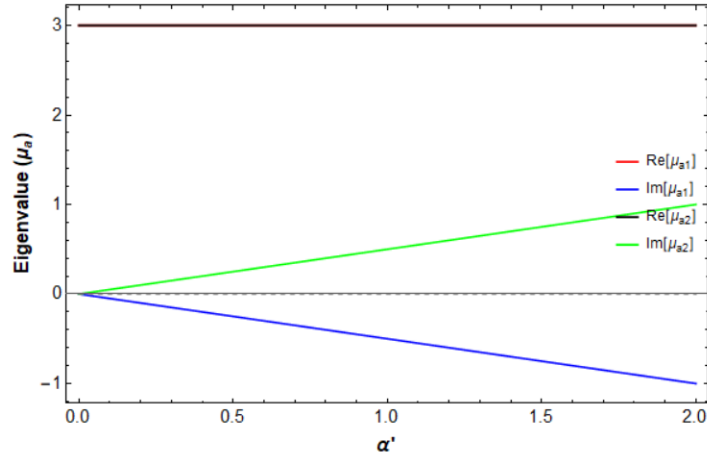
Figure 2.20: Plot of eigenvalues $\mu_{P_i}^{1,2}$ of the linearised surface velocity field about the fixed points $P1$ for $\epsilon = -2$. $P2$ and $P3$ do not exist for $\alpha' > 0$.

For $\epsilon = 0$, the canonical planar linear flows, we see from the plot of eigenvalues of the auxiliary system that in Fig.2.21, one of the eigenvalues is zero for all α, consistent with the planar flow topology of this case. For $\alpha' < \alpha'_{TD}$, the non-zero eigenvalues are real and are equal and opposite, implying the auxiliary flow is a planar hyperbolic flow and for $\alpha' > \alpha'_{TD}$, they are complex, implying planar elliptic flows. At the triply degenerate point α'_{TD}, all eigenvalues are zero, implying that the auxiliary flow is simple shear. Correspondingly at this point, the surface-streamline topology is meridional, but unlike the meridional topologies encountered above, this topology is organised only by a ring of fixed points. This can also be seen from Fig.2.22, showing the plots of eigenvalues of the non-linear system about the fixed points. The eigenvalues about all three fixed points are zero at α'_{TD}, consistent with the nature of the meridional topology described above. In the cases examined above, the meridional topology was associated with non-zero eigenvalues about one pair of fixed points ($P3$ in fig.2.18 and $P1$ in Fig.2.20), and so these meridional topologies were organised by a fixed ring and a pair of fixed points. For $\alpha' < \alpha'_{TD}$, all three pairs of fixed points exist, giving rise to a non-spiralling topology organised by these points and for $\alpha' > \alpha'_{TD}$, only $P1$ exists and the eigenvalues about it are purely imaginary, implying that it is a center. Thus the streamline topology is closed for $\alpha' > \alpha'_{TD}$.
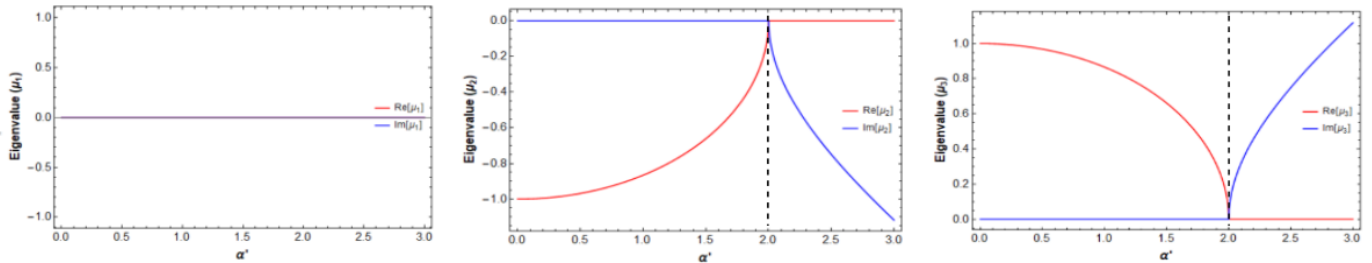
Figure 2.21: Plot of eigenvalues μ_i of the auxiliary linear flow for $\epsilon = 0$.
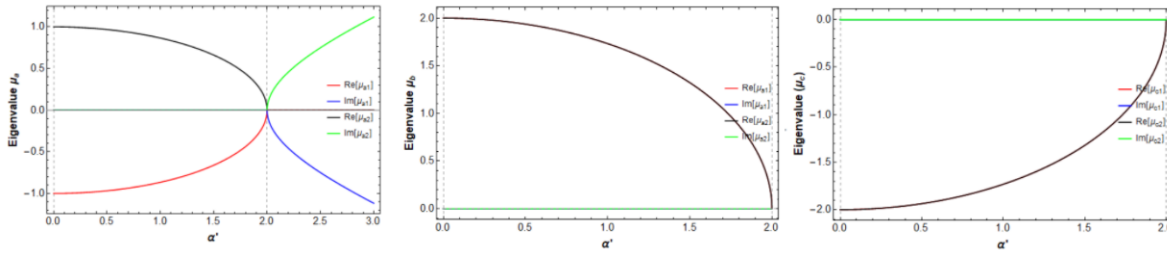
Figure 2.22: Plot of eigenvalues $\mu_{P_i}^{1,2}$ of the linearised surface velocity field about the fixed points $P1$, $P2$, $P3$ for $\epsilon = 0$.

Having completed the streamline topology analysis, we now move on to the transport problem for which we first define the surface-flow aligned coordinate system, the $C - \tau$ system. In the next section, we define and discuss the salient features of this coordinate system and show how it leads to an analytical evaluation of Nu.

2.3.3   Heat Transfer Analysis

In this section, we will set up the heat transfer problem for a drop suspended in $3D$ extensional flows with aligned vorticity, the first two-parameter family of linear flows that we consider, in the limit of large Pe [2]. Almost all the members of this two-parameter family have open streamlines in the vicinity of the drop, with the exception of $\epsilon = 0$, that corresponds to canonical planar linear flows, for which, depending on λ, the streamlines in the vicinity may be closed and one expects diffusion-limited transport at large Pe (Krishnamurthy and Subramanian (2018a)). The drop surface is assumed to be at a constant temperature T_0 and is suspended in an ambient fluid of temperature T_∞. The presence of open streamlines near the drop surface implies that in the limit of large Péclet ($Pe \gg 1$), there is formation of a thin thermal boundary layer across which almost the entire temperature drop occurs. The convection induced enhancement in transport is characterised via the Nusselt number, which is the dimensionless rate of heat transfer defined as the ratio of total heat transfer rate to the transfer rate due to conduction alone ($Nu = 1$ for purely conductive heat transfer):

$$Nu = \frac{Ql}{4\pi a^2 \ k \ (T_0 - T_\infty)} \tag{2.43}$$

where Q is the total heat transfer rate, k the thermal conductivity of the ambient fluid, l is the characteristic length scale and $4\pi a^2$ is the surface area of the spherical drop across which the heat transfer occurs, where a, the drop radius, is the characteristic length scale of the problem. For a thermal boundary layer near a solid surface, the boundary layer thickness scales as $Pe^{-1/3}$. This can be seen by comparing the time scales of convective transport given by $a^2/(Uy)$ and diffusive transport given by y^2/D as shown in Fig.2.23a. The convective time scale has this form since the no-slip boundary condition for the velocity at the solid surface makes the flow inside the thermal boundary layer appear locally linear (a simple shear flow). This scaling for the boundary layer thickness leads to the Nusselt number scaling as $Nu \sim Pe^{1/3}$ (Acrivos and Goddard (1965), Acrivos (1971), Acrivos (1980), Batchelor (1979)). For a drop, on the other hand, the thermal boundary layer forms at a fluid-fluid interface. The convective time scale in this case is just a/U, where the interfacial slip is $O(U)$. The diffusive time scale for a drop is again given by y^2/D, giving us a boundary layer thickness scaling as $Pe^{-1/2}$, and the Nusselt number scaling as $Nu \sim Pe^{1/2}$ (see Fig.2.23b)[3]. Clearly, the existence of an interfacial slip velocity implies that the Nu for a drop is

---

[2]We note here that our analysis is equally applicable for heat or mass transfer, and we henceforth restrict ourselves to the former. The large Pe limit, however, naturally pertains to mass transfer since the Schmidt number ($Sc = \nu/D$) (specially for liquids) is much larger than unity.

[3]In the scaling arguments above, which was also briefly discussed in Chapter 1, the Nusselt number is related to the inverse of the thermal boundary layer thickness, because the dominant heat transfer from the drop occurs across the thin boundary

(a) Solid particle   (b) Drop
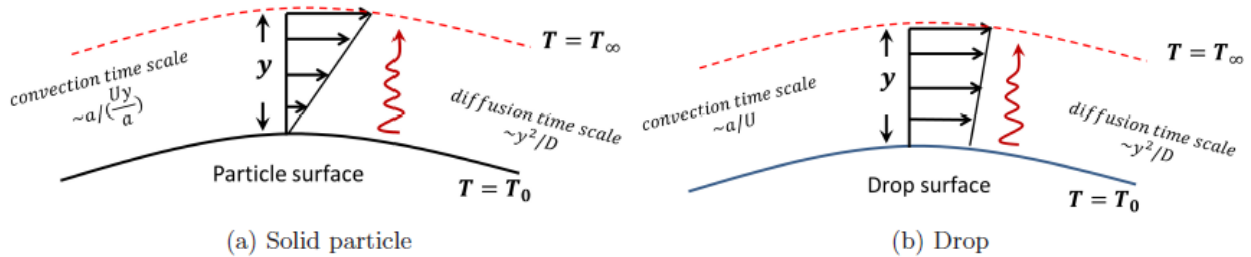
Figure 2.23: Schematic representations of the thermal boundary layer (a) near a solid particle and (b) near a drop or liquid interface. The scaling of the boundary layer thickness and hence the dimensionless heat transfer with Péclet number can be inferred by taking a ratio of the time scales of convection and diffusion

asymptotically larger than that for a solid particle at the same (large) Pe.

2.3.3.1   Governing Equations

The heat transfer problem is governed by the convection-diffusion equation for energy conservation, with convection being driven by the Stokesian velocity field. We assume that the heat transfer is decoupled from the momentum conservation equations, as is typical of forced convection problem (which is equivalent to assuming that an appropriate Grashof number based on $(T_0 - T_\infty)$ is small) and further assume that changes in temperature do not cause variations in the fluid properties. The convection-diffusion equation can be written in dimensionless form as:

$$Pe(\boldsymbol{u}.\boldsymbol{\nabla}\Theta) = \nabla^2\Theta \tag{2.44}$$

where we have used the non-dimensional temperature $\Theta = (T - T_\infty)/(T_0 - T_\infty)$. The boundary conditions are given by:

$$\Theta = 1 \quad \text{at } r = 1 \text{ (Isothermal drop surface)} \tag{2.45}$$

$$\Theta = 0 \quad \text{as } r \to \infty \text{ (Ambient temperature is } T_\infty \text{ at infinity)} \tag{2.46}$$

As mentioned earlier, we will solve this system of equations in the limit of $Pe \gg 1$.

2.3.3.2   The $C - \tau$ Coordinate System

In this section, we define and describe the surface-streamline-aligned coordinate system that we use to solve for the Nusselt number (Nu). The equations governing the surface streamlines is written in invariant form in Eq.2.12. Krishnamurthy and Subramanian (2018a) made the important observation that Eq.2.12 was identical in form to the following equation:

$$\dot{\boldsymbol{p}} = \boldsymbol{\Omega}.\boldsymbol{p} + \frac{\gamma'^2 - 1}{\gamma'^2 + 1}\left[\boldsymbol{E}.\boldsymbol{p} - (\boldsymbol{E} : \boldsymbol{pp})\boldsymbol{p}\right], \tag{2.47}$$

that governs the trajectories of an axisymmetric particle in a linear flow; for simple shear flow, these trajectories are known as Jeffery orbits (Jeffery (1922)). While the shape of the original Jeffery orbits depended on a geometric parameter (the so-called Bretherton constant) that is a function of the particle

---

layer. This is no longer true in the vicinity of certain points or singular curves where the boundary layer approximation breaks down, implying the presence of a thermal wake. Unlike the large Re momentum wake, the thermal wake at large Pe occupies a vanishingly small portion of the drop's surface, and therefore, contributes negligibly to the heat / mass transfer.

shape (this being the aspect ratio), in the present case of a drop, as seen from Eq.2.12, its place is taken by an effective Bretherton constant G which depends on the flow parameters and λ. This insight allows us to define a new coordinate system on the drop surface to describe the surface streamlines analogous to the so-called natural coordinates developed for the Jeffery orbits (L. G. Leal and Hinch (1971)). Note that in Krishnamurthy and Subramanian (2018a), the Bretherton constant was a function of λ and a single flow parameter, since the authors only examined a pair of one-parameter families. The authors go on to show that the convection-diffusion equation admits a similarity solution in the asymptotic limit of $Pe \gg 1$, in a non-orthogonal surface-streamline-aligned coordinate system.

In this section, we shall extend the analysis of Krishnamurthy and Subramanian (2018a) to the two-parameter family of $3D$ extension with aligned vorticity, by defining a non-orthogonal coordinate system, the $C - \tau$ system, in order to solve the convection-diffusion equation. We start by rewriting Eq.2.20 and Eq.2.21 by introducing a new variable $\tau = At/2(1 + \lambda)$ to get:

$$\tan \phi = -\frac{A \tanh (\tau) + (2 + \epsilon)}{\alpha(1 + \lambda)} \tag{2.48}$$

$$\tan \theta = C(1 + \lambda)\alpha \left(\frac{(\tan^2 \phi + 1)}{1 - \left(\frac{(2+\epsilon) - (1+\lambda)\alpha \tan \phi}{A} \right)^2} \right)^{1/2} e^{\frac{-3\epsilon\tau}{A}} \tag{2.49}$$

where $A = \sqrt{(2 + \epsilon)^2 - (1 + \lambda)^2 \alpha^2}$. Note here that A becomes imaginary when $\alpha > \frac{2+\epsilon}{1+\lambda}$, which corresponds to the threshold value $(1 + \lambda)\alpha'_{th1}$ (the zero-crossing of Δ') encountered earlier. Recall that above this threshold, the streamlines on the drop surface are spiralling and thus it leads to a different expression for $\tan \phi$ and $\tan \theta$, which we will see later. These definitions are derived from the solutions of the surface streamline equation, whereby one of the constants of integration (c_0, from the ϕ integration) was set to a constant, according to our convenience (as $c_0 = 0$) and the other constant (from integration of θ) is used as a coordinate variable (i.e. $c_1 = C$), which labels the streamlines. The freedom of choosing an arbitrary ϕ_0 corresponds, physically, to choosing a point on a streamline that corresponds to $t = 0$ (essentially, choosing an origin for the variable t). The modified time variable, now named as τ, denotes the phase along these streamlines. The aforementioned choice of initial conditions conforms to the Jeffery orbit solutions (see for instance L. G. Leal and Hinch (1971), Krishnamurthy and Subramanian (2018a)). These equations define the $C - \tau$ coordinate system that is aligned with the surface-streamlines. This is a coordinate system where the coordinate lines C and τ are in general not orthogonal to one another. Physically, as seen in Fig.2.24, the C coordinate defines a given trajectory (or orbit if the streamline is closed), while the τ coordinate gives the phase along that trajectory (orbit). Following L. G. Leal and Hinch (1971), the metric factors h and k and the skewness angle $\alpha 1$ ($\alpha 1$ would be $\pi/2$ in an orthogonal coordinate system) are:

$$h = g_{CC} = \theta_C \tag{2.50}$$

$$k = g_{\tau\tau} = \left(\theta_\tau^2 + \sin^2 \theta \ \phi_\tau^2 \right)^{1/2} \tag{2.51}$$

$$g_{C\tau} = \theta_C \theta_\tau \tag{2.52}$$

$$\sin \alpha 1 = \sin \theta \ \phi_\tau \left(\theta_\tau^2 + \sin^2 \theta \ \phi_\tau^2 \right)^{-1/2} \tag{2.53}$$

where θ_C, θ_τ etc. denote partial derivatives with respect to the subscript variables and g_{CC}, $g_{\tau\tau}$ and $g_{C\tau}$ are the components of the metric tensor of the (C, τ) coordinate system on the unit sphere surface, as per the conventional notation (Aris (2012)). The contravariant unit vectors of the (C, τ) coordinate system (i.e the unit vectors along the coordinate lines) in terms of the conventional spherical coordinates unit

vectors are given by:

$$\hat{\boldsymbol{C}} = \hat{\boldsymbol{\theta}} \tag{2.54}$$

$$\hat{\boldsymbol{\tau}} = \cos\alpha 1 \ \hat{\boldsymbol{\theta}} + \sin\alpha 1 \ \hat{\boldsymbol{\phi}} \tag{2.55}$$

We note that $\hat{\boldsymbol{C}}$ is still along the meridional direction, but $\hat{\boldsymbol{\tau}}$ is along the streamline, rather than along the azimuth, which leads to the non-orthogonality. The (C, τ) coordinate system is depicted in Fig.2.24, for a representative member of the two-parameter family considered here, with non-spiralling topology. The components of the velocity field on the drop surface, in the (C, τ) coordinate system are given by:

$$\boldsymbol{u} = u_C \hat{\boldsymbol{C}} + u_\tau \hat{\boldsymbol{\tau}} \tag{2.56}$$

where,

$$u_C = u_\theta - \frac{u_\phi \theta_\tau}{\phi_\tau \sin\theta} \tag{2.57}$$

$$u_\tau = \frac{k u_\phi}{\phi_\tau \sin\theta} \tag{2.58}$$

Since we are using a surface-streamline aligned coordinate system, the velocity along $\hat{\boldsymbol{C}}$ is:

$$u_C = 0 \tag{2.59}$$

where we have used the expressions for u_θ and u_ϕ given in Eq.2.18 and 2.19, respectively. The above result is because the τ coordinate is aligned along the surface streamlines. This reduction of the surface velocity field in the (C, τ) coordinate system to a one-component field, is helpful in proceeding towards a solution of the heat transfer problem, both in the open and closed streamline regimes, which we solve in the next section. This reduction to a one-component field is readily achievable for the familiar flows such as translation or axisymmetric extensional flow. The $C - \tau$ coordinate system achieves this regardless of the topology of the surface streamlines. We now show that our definition of the (C, τ) coordinate system, enables a natural means of distinguishing the non-spiralling and spiralling surface streamline topology that arises on either side of α'_{th1}.
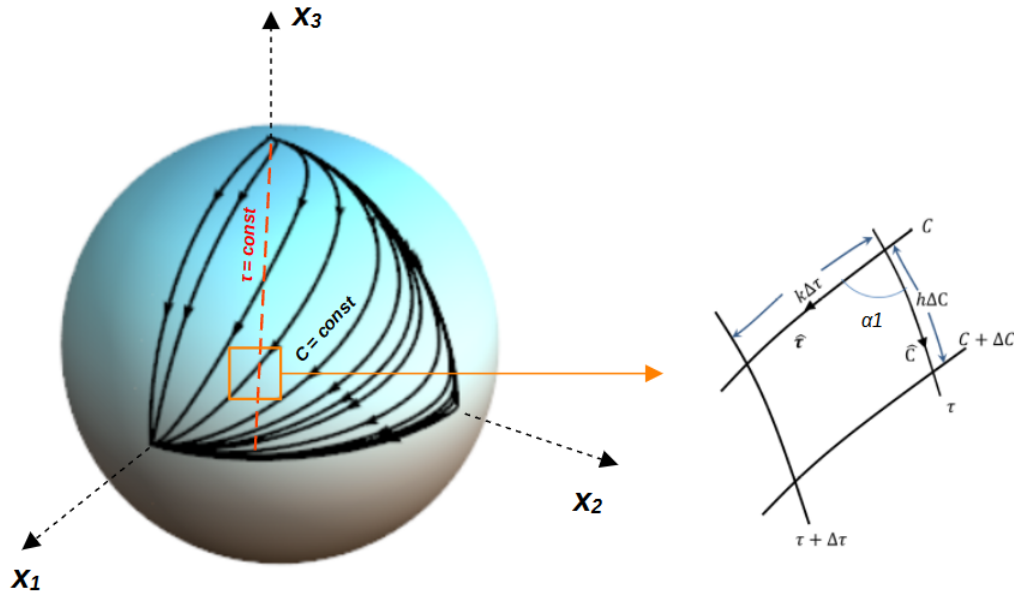
Figure 2.24: Depiction of the coordinate system on the drop surface showing the mapping to streamlines on the drop. The plot on the right shows the unit vectors and metrics of the (C, τ) coordinate system.

The Non-Spiralling (Open) Regime: $\alpha < (2 + \epsilon)/(1 + \lambda)$

In this regime, the surface streamlines are open trajectories running from a stable node to an unstable one (see Fig.2.24). Correspondingly, our $C - \tau$ definition for this scenario contains real exponential or hyperbolic functions in their definitions as given in Eq.2.48 and Eq.2.49. We use these definitions given in Eq.2.48 and Eq.2.49, to map the $C - \tau$ coordinates to the spherical coordinates. From these equations, we can denote C and τ as,

$$C = \frac{e^{\frac{3\epsilon\tau}{A}} \tan\theta \left(1 - \left(\frac{(2+\epsilon)-(1+\lambda)\alpha\tan\phi}{A}\right)^2\right)^{1/2}}{\alpha(1+\lambda)\sqrt{1+\tan^2\phi}} \tag{2.60}$$

$$\tau = -\tanh^{-1}\left(\frac{(1+\lambda)\alpha\tan\phi + (2+\epsilon)}{A}\right) = \frac{1}{2}\log\left(\frac{\hat{\gamma}_0 - \tan\phi}{\hat{\gamma}_1 + \tan\phi}\right) \tag{2.61}$$

where $\hat{\gamma}_0 = \frac{A-(2+\epsilon)}{(1+\lambda)\alpha}$ and $\hat{\gamma}_1 = \frac{A+(2+\epsilon)}{(1+\lambda)\alpha}$. From the expression for τ, the branch points of the logarithm correspond to the numerator and denominator being individually equal to 0, which gives us the two limiting ϕ directions, given by:

$$\phi^{(1)} = \tan^{-1}\left(\frac{(1+\lambda)\alpha}{A - (2+\epsilon)}\right) \tag{2.62}$$

$$\phi^{(2)} = \tan^{-1}\left(\frac{(1+\lambda)\alpha}{A + (2+\epsilon)}\right) \tag{2.63}$$

The other two fixed points ($\phi^{(3)}$ and $\phi^{(4)}$) can be found by simply rotating $\phi^{(1)}$ and $\phi^{(2)}$ by π, as they conform to the inversion symmetry of Stokes flow. These fixed points divide the hemisphere into four distinct regions. In regions 1 and 3, when $-\phi^{(1)} < \phi < \phi^{(1)}$ and $\phi^{(2)} < \phi < \phi^{(3)}$, the argument of the logarithm is positive and thus τ is purely imaginary. From Eq.2.60, we see that C is real in these regions. The other two regions (2 and 4), lie in the range $\phi^{(1)} < \phi < \phi^{(2)}$ and $\phi^{(3)} < \phi < \phi^{(4)}$, respectively. Here, the argument of the logarithm is negative and thus we rewrite it as:

$$\tau = \frac{1}{2}\log\left(\frac{\tan\phi - \hat{\gamma}_0}{\tan\phi + \hat{\gamma}_1}exp(\imath\pi)\right), \tag{2.64}$$

where $(\tan\phi - \hat{\gamma}_0)/(\tan\phi + \hat{\gamma}_1)$ is positive. Expanding this, we get:

$$\tau = \frac{1}{2}\log\left(\frac{\tan\phi - \hat{\gamma}_0}{\tan\phi + \hat{\gamma}_1}\right) + \frac{\imath\pi}{2} \tag{2.65}$$

where $\tau - (\imath\pi/2)$, is now purely real. Therefore, we can introduce a new variable:

$$\hat{\tau} = \tau - \frac{\imath\pi}{2} \tag{2.66}$$

where $\hat{\tau}$ is purely real. Thus, in both the regions, we have redefined the τ coordinate such that the phase variable along a trajectory is always real, and we further define:

$$\tau = \tau' \tag{2.67}$$
$$\hat{\tau} = \tau' \tag{2.68}$$

in the regions 1 and 2, respectively, such that τ' is real in both regions. From Eq.2.60, we see that in regions 2 and 4, the trajectory constant C is purely imaginary. We had earlier noted that C is real in the regions 1 and 3. This motivates us to define,

$$C = \imath\hat{C} \tag{2.69}$$

in regions 2 and 4, which makes $\hat{C}$ real in all regions concerned. Thus we have the following mapping for the $C - \tau$ system:

- In regions 1 and 3: $(C, \tau) \equiv (C, \tau')$.

- In regions 2 and 4: $(C, \tau) \equiv (i\hat{C}, \tau' + \frac{\iota\pi}{2})$.

The mapping of this coordinate system is depicted in Fig.2.25a and 2.25b, and the mapping can be viewed as follows:

- In a given octant, $\tau' = \infty$ corresponds to the stable node regardless of C and $\tau' = -\infty$ corresponds to the unstable node, again, regardless of C.

- $C = 0$, corresponds to the two meridians passing through $\phi = \tan^{-1}(\phi^{(1)})$ and $\phi = \tan^{-1}(\phi^{(2)})$. These two meridians intersect at $\theta = 0$, which is also a solution for $C = 0$. Thus, these two meridians along with the fixed point corresponding to $\theta = 0$ (i.e. $\boldsymbol{x} = \{0, 0, 1\}$), are marked by $C = 0$. When this fixed point on the polar axis is the saddle point (when $-0.5 < \epsilon \le 0$ and $\alpha' < \alpha'_{th2}$), $C = 0$ marks the stable and unstable manifolds of the saddle. Otherwise, it marks the stable manifold and the meridional trajectory connecting unstable and stable node, when the saddle happens to be at the equator.

- $C = \infty$, corresponds to the trajectory on the equatorial plane that connects the two fixed points on the equator. Again this is the trajectory connecting the stable and unstable node when saddle point is on the polar axis. Otherwise, it corresponds to the unstable manifold of the saddle.

We had earlier mentioned, that an equivalent definition of C and τ is possible from the solutions of auxiliary linear flow equations, which were given in Eq.2.26 and Eq.2.27. Rewriting these equations again using the new variable $\tau = At/(1 + \lambda)$, we have:

$$\tan\phi = \frac{(A - B) + e^\tau(A + B)}{(A + B) + e^\tau(A - B)} \tag{2.70}$$

$$\tan\theta = \frac{C}{2A}(1 + \tan^2\phi)e^{\frac{-\tau(A+3\epsilon)}{2A}}\left((A + B) + e^\tau(A - B)\right) \tag{2.71}$$

where, we have set $\tan\phi_0 = 1$. This value is chosen for the sake of convenience. These definitions only help in covering one of the four regions in a hemisphere, namely region 1. In order to have a definition that is consistent for the adjacent region, region 2, we simply set $\tan\phi_0 = -1$, which is ϕ_0 rotated by $\pi/2$. Thus, the definitions compatible with region 2 is given by:

$$\tan\phi = -\frac{(A - B) + e^\tau(A + B)}{(A + B) + e^\tau(A - B)} \tag{2.72}$$

$$\tan\theta = \frac{C}{2A}(1 + \tan^2\phi)e^{\frac{-\tau(A+3\epsilon)}{2A}}\left[(A + B) + e^\tau(A - B)\right] \tag{2.73}$$

These definitions have the advantage that, unlike the earlier definitions, we do not need a complex number formulation to represent the different regions on the drop surface. This is because, in the earlier definitions, we had set the constant of integration associated with ϕ integration ($c_0 = 0$), and, as was pointed out, it corresponds to us choosing a point on the streamline at $t = 0$. But, doing so puts the initial point in one of the four regions mentioned earlier. Thus, with the same choice of initial point, one had to resort to a complex number formulation to shift to the other quadrants. But in the aforementioned equations, we merely choose different initial conditions for different regions (Regions 1 and 2 to be specific). These definitions also result in the same mapping of the $C - \tau$ coordinates that we saw before. Owing to the simplicity of these new definitions, that result from the solutions of the auxiliary linear system, we shall be using them in our Nu calculation.
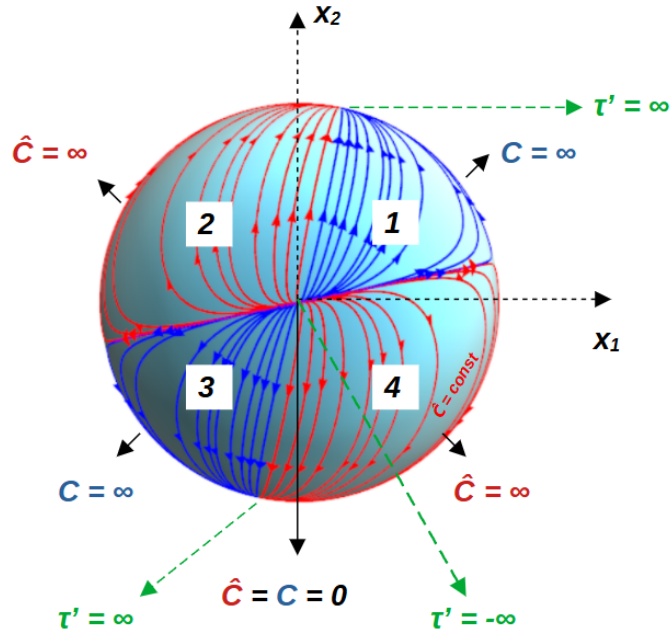
(a) Trajectories on the unit sphere : View along the polar axis.
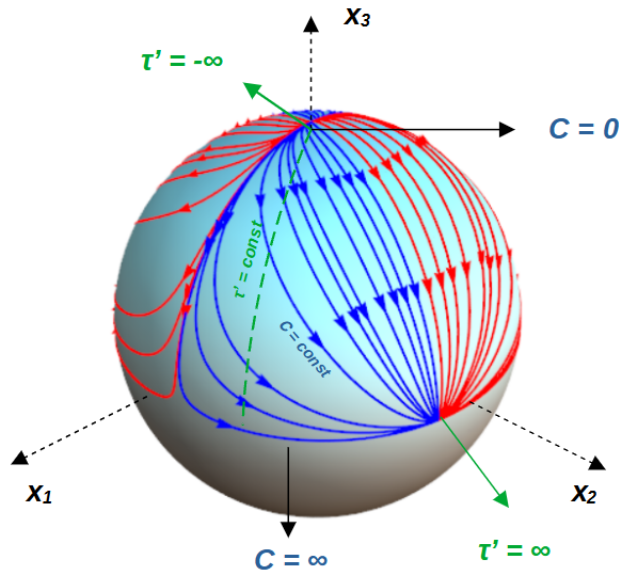
(b) Trajectories on the unit sphere : Isometric view.

Figure 2.25: Depiction of the (C, τ) coordinate system on the drop surface in the open streamline regime. The four regions are marked 1 through 4, where regions $1, 3$ and $2, 4$ are inversions of each other. The streamline trajectories begin at the unstable node and culminate at the stable node (on the equatorial great circle). The phase variable for the position along a given trajectory is given by τ' and varies from $-\infty$ at the inlet to ∞ at the outlet. The trajectories are labelled by C and $\hat{C}$, in region 1 and 2 respectively. These vary from 0 at the poles to ∞ at the equatorial plane

The $C - \tau$ definitions given above, however, have a singular limit corresponding to $\epsilon \to -2$. The streamlines are near-meridional as $\epsilon \to -2$, and these meridians emanate and terminate at the poles on the polar axis. Such meridional streamlines do not lend themselves to a $C - \tau$ characterization, as both

ϕ and τ don't vary along a streamline and thereby preventing an invertible transformation between the two. Thus close to this ϵ, we need to rely on numerical extrapolation of our Nu results.

The Spiralling Regime: $\alpha > (2 + \epsilon)/(1 + \lambda)$

Here, the streamlines on the drop surface are spiralling. Correspondingly, one needs to use $C-\tau$ definitions that reflect this spiralling character. We see from Eq.2.48 and Eq.2.49 that, when $\alpha > (2 + \epsilon)/(1 + \lambda)$, A becomes imaginary. Accordingly, we rewrite the equations as:

$$\tan \phi = \frac{A' \tan (\tau) - (2 + \epsilon)}{\alpha(1 + \lambda)} \tag{2.74}$$

$$\tan \theta = C(1 + \lambda)\alpha \left(\frac{(\tan^2 \phi + 1)}{1 + \left(\frac{(2+\epsilon)+(1+\lambda)\alpha \tan \phi}{A'} \right)^2} \right)^{1/2} e^{\frac{-3\epsilon\tau}{A'}} \tag{2.75}$$

where $A = iA' = i\sqrt{(1 + \lambda)^2\alpha^2 - (2 + \epsilon)^2}$ and leads to a trigonometric (periodic) dependence on τ, consistent with the spiralling nature of the streamlines. These definitions, unlike the earlier ones for the open trajectories, are valid for the whole hemisphere, since the streamlines are not restricted to a particular region in the hemisphere. The mapping of the unit hemisphere in $C - \tau$ coordinates is shown in Fig.2.26. Here $C = 0$ corresponds to the unstable focus for any arbitrary τ and $C = \infty$ corresponds to the equatorial limit cycle. The τ mapping can be inferred from Eq.2.74 where, we see that, ϕ is periodic and varies from 0 to 2π, while τ is continuous and varies between $-\infty$ and ∞. But, this range of τ will result in over-counting the area of the hemisphere, on account of the streamlines being spirals. Thus, in order to cover the unit sphere, one needs, $C \in (-\infty, \infty)$ and $\tau \in [\tau^*, \tau^* \mod 2\pi]$, that corresponds to a single 2π turn of a given streamline. Alternatively, one can cover the unit sphere in an alternative way, where τ ranges from $-\infty$ to ∞, with C ranging from C^* to $C^* e^{\frac{6\epsilon\pi}{A'}}$. With this choice for the range of C and τ, the equatorial limit cycle corresponds to $\tau \to \infty$ and $\tau \to -\infty$ marks the unstable focus with, C in the range specified above, covering all streamlines spiralling between the focus and limit cycle.

One can also use the solutions of auxiliary flow equations (Eq.2.70 and Eq.2.71) to write the definitions of C and τ in this regime as:

$$\tan \phi = \frac{(\imath A' - B) + e^{\imath\tau}\imath A' + B)}{(\imath A' + B) + e^{\imath\tau}(\imath A' - B)} \tag{2.76}$$

$$\tan \theta = \frac{C}{2\imath A'}(1 + \tan^2 \phi)e^{\frac{-\tau(\imath A'+3\epsilon)}{2A'}} \left((\imath A + B) + e^{\imath\tau}(\imath A - B)\right) \tag{2.77}$$

which is the same as the definitions given earlier. In order to be consistent with the non-spiralling regime, we use the aforementioned definitions in our Nu calculation, which is discussed next. In our calculations, the range of C and τ correspond to, $\tau \in (\infty, \infty)$, with $C \in [C^*, C^* e^{\frac{6\epsilon\pi}{A'}}]$.
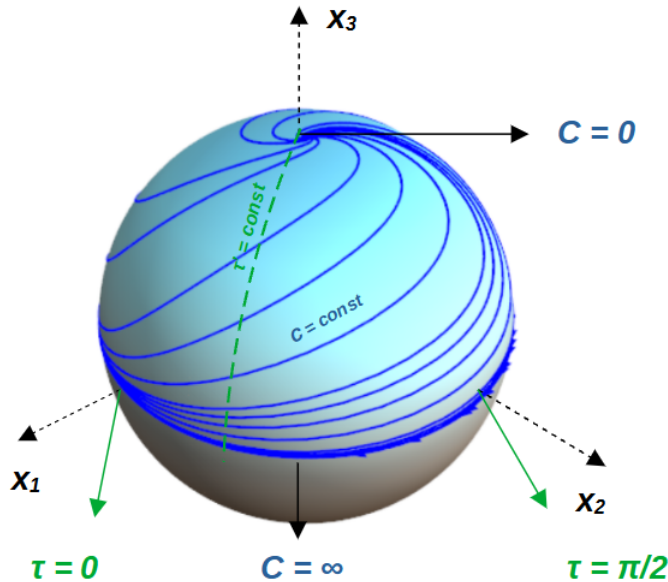
Figure 2.26: Depiction of the $C-\tau$ coordinate system on the drop surface showing mapping to streamlines on the drop in the spiralling regime. Unlike the previous case, this regime requires a single definition for C and τ that is uniformly applicable throughout the hemisphere.

A general feature of the definition of C and τ corresponding to both the regimes is that, τ changes at a constant rate with respect to t along all streamlines, where the constant is a function of λ and the flow parameters as is shown in the subsequent section. This fact, as we shall see later, plays a crucial role in simplifying the heat transfer analysis when the problem is cast in terms of the (C, τ) coordinate system. Note that a particular special case that warrants attention corresponds to $\epsilon = 0$, which leads to closed streamlines on the drop surface and the $C-\tau$ definitions for this case is the same as natural coordinates associated with the Jeffery orbits (Krishnamurthy and Subramanian (2018a). As we shall see later, the presence of closed streamlines on the drop result in $Nu = 0$, implying diffusion-limited transport.

2.3.3.3 Boundary Layer Analysis

We have examined the $C - \tau$ coordinate system in detail; the definitions of C and τ are given by the relations Eq.2.70-2.73 in the non-spiralling regime and by Eqs.2.76-2.77 in the spiralling regime. The unit hemisphere has been mapped in terms of these coordinates, in both these regimes. We now use these coordinates to solve the convection-diffusion equation for large Pe, so as to obtain the temperature field in the thermal boundary layer and hence solve for the non-dimensional rate of transport defined by the Nusselt number.

As a first step, we write the convection-diffusion equation in the $C - \tau$ coordinates, which is given by:

$$u_r^{(0)} \frac{\partial \Theta}{\partial r} + \frac{u_C}{h} \frac{\partial \Theta}{\partial C} + \frac{u_\tau}{k} \frac{\partial \Theta}{\partial \tau} = \frac{1}{Pe} \nabla^2 \Theta \tag{2.78}$$

where $u_r^{(0)}$ is the radial velocity, and the tangential components $u_C^{(0)}$ and $u_\tau^{(0)}$ are defined by Eq.2.57 and 2.58, respectively. As already seen, and as must be the case $u_C^{(0)}$ by definition of the coordinate C (Eq.2.59). Thus, the equation simplifies to:

$$u_r^{(0)} \frac{\partial \Theta}{\partial r} + \frac{u_\tau}{k} \frac{\partial \Theta}{\partial \tau} = \frac{1}{Pe} \frac{\partial^2 \Theta}{\partial r^2} \tag{2.79}$$

where we have now assumed radial diffusion to be dominant on account of a thin thermal boundary layer on the drop surface. Since it is only the velocity field near the drop surface which is relevant to the heat transfer analysis, we define the boundary layer coordinate, $y = r - 1$, and retain the leading order terms in u_r and u_τ (from Eqs.2.15 and 2.58 expressed in terms of C and τ), which are given by:

$$u_r^{(0)} = \frac{3 \left(e^{\frac{3\epsilon\tau}{A}} \epsilon B + C^2 \left(\epsilon((1+\lambda)\alpha - (2+\epsilon)\cosh\tau) + (2+\epsilon)A\sinh\tau \right) \right)}{(1+\lambda) \left(e^{\frac{3\epsilon\tau}{A}} B + 2C^2((2+\epsilon)\cosh\tau - (1+\lambda)\alpha) \right)} y + O(y^2)$$

$$= h_r(\tau, C, \epsilon, \alpha, \lambda) y + O(y^2) \tag{2.80}$$

$$\frac{u_\tau}{k} = \frac{A}{(1+\lambda)} + O(y)$$

$$= h_\tau(\epsilon, \alpha, \lambda) + O(y) \tag{2.81}$$

where A and B have been defined in Eq.2.21. We note that the dependence of h_r and h_τ on λ and α has a specific form; an implicit dependence via the combination $(1 + \lambda)\alpha$, which, recall was the definition of α' from the streamline analysis and an overall prefactor $1 + \lambda$. This suggests that we can pull $(1 + \lambda)^{-1}$ into the definition of Pe, thereby resulting in Nu being a function of α'. Another crucial feature is the constancy of $h_\tau = u_\tau/k$, implying that τ changes with the dimensionless time t at a constant rate independent of the streamline. This considerably simplifies the Nu calculation, by rendering the analysis in $C - \tau$ coordinate system analogous to that of a solid particle in spherical coordinates (where u_ϕ is constant on account of uniform rotation of the particle (Subramanian and Koch (2006b)).

Now, rescaling the boundary layer coordinate as $Y = Pe^m y$, where m is an exponent which gives the boundary layer thickness scale and Y is $O(1)$, we get:

$$h_r Y \frac{\partial\Theta}{\partial Y} + h_\tau \frac{\partial\Theta}{\partial\tau} = \frac{Pe^{2m}}{Pe} \frac{\partial^2\Theta}{\partial Y^2} \tag{2.82}$$

where the leading order balance implies $m = 1/2$ giving the expected the boundary layer thickness scaling as $y \sim Pe^{-1/2} Y$. From here on, the analysis is standard (G. L. Leal (2007)). Defining a similarity variable $\eta = Y/g(C, \tau)$, where $g(C, \tau)$ characterizes the dependence of the boundary layer thickness on the position on the drop surface, the non-dimensional temperature is found to satisfy:

$$\frac{d^2\Theta}{d\eta^2} + 2\eta \frac{d\Theta}{d\eta} = 0 \tag{2.83}$$

where

$$h_\tau g \frac{dg}{d\tau} - h_r g^2 = 2. \tag{2.84}$$

The boundary conditions for the non-dimensional temperature are given by:

$$\Theta = 1 \quad \text{at } \eta = 1 \tag{2.85}$$

$$\Theta = 0 \quad \text{as } \eta \to \infty \tag{2.86}$$

Solving Eqs.2.83 using 2.85 and 2.86, we get,

$$\Theta(\eta) = 1 - \frac{2}{\sqrt{\pi}} \int_0^\eta e^{-s^2} ds \tag{2.87}$$

Next, we need to solve the boundary layer thickness equation given by Eq.2.84. Introducing $f = g^2/2$, we get:

$$h_\tau \frac{df}{d\tau} - 2h_r f = 2. \tag{2.88}$$

This is a linear equation which can be solved by using an integrating factor given by:

$$Q = \exp\left[\int \frac{-2h_r}{h_\tau} d\tau\right].$$

(2.89)

Thus the formal solution for g can be written as:

$$g = \frac{2}{h_\tau^{1/2}} \left(Q^{-1} \int_{\tau_{inlet}}^{\tau} Q \, d\tau_1\right)^{1/2}$$

(2.90)

where τ_{inlet} is determined from the constraint that the boundary-layer thickness be finite at the inlet stagnation points. This finiteness arises from the fact that at the inlets, the local flow is a linear extension convecting heat towards the stagnation point, balancing the outward diffusion, which leads to a finite thickness of the boundary layer. From this point on, one may use the closed-form expression for Q, based on the aforementioned exponential form. This was the procedure followed by Krishnamurthy and Subramanian (2018a), in determining Nu for the canonical one-parameter family of planar linear flows (in the open-streamline regime). Unfortunately, the exponential form doesn't lend itself to closed-form expressions for more complicated linear flows. For instance, while one may adopt a procedure analogous to Krishnamurthy and Subramanian (2018a) for the aligned-vorticity family under consideration, this does not hold true for the axisymmetric extension with inclined vorticity case considered next. The same also holds for a general linear flow. So, it is of interest to come up with an alternate procedure to evaluate Q in closed form for an arbitrary ambient linear flow. Interestingly, the $C - \tau$ system guarantees a closed form expression for Q, owing to the crucial feature of h_τ being independent of C and τ. To show this, we start from the continuity equation in the boundary layer coordinate system (y, C, τ), which is of the form:

$$\frac{\partial(hk\sin\alpha 1 u_r^{(0)})}{\partial y} + \frac{\partial(k\sin\alpha 1 u_C^{(0)})}{\partial C} + \frac{\partial(h\sin\alpha 1 u_\tau^{(0)})}{\partial \tau} = 0.$$

(2.91)

where h, k are the metric factors and $\alpha 1$ is the skewness angle of the coordinate system, which are defined in Eq.2.50 - 2.53. Again, using the expansions of u_r and u_τ given in Eqs. 2.80 and 2.81, and the fact that $u_C^{(0)} = 0$, one obtains:

$$\frac{\partial(hk\sin\alpha 1 h_r y)}{\partial y} + \frac{\partial(hk\sin\alpha 1 h_\tau)}{\partial \tau} = 0.$$

(2.92)

Now, using the fact that $h_r \neq f(y)$ and $h_\tau = const$, we can rewrite the above equation as:

$$hk\sin\alpha 1 h_r = -h_\tau \frac{\partial(hk\sin\alpha 1)}{\partial \tau}$$

(2.93)

and so we have,

$$-\frac{h_r}{h_\tau} = \frac{\partial \log(hk\sin\alpha 1)}{\partial \tau}.$$

(2.94)

Now, substituting this into the definition of Q, we get,

$$Q = \left(\frac{hk\sin\alpha 1}{(hk\sin\alpha 1)_0}\right)^2$$

(2.95)

where $(hk\sin\alpha 1)_0$ is $hk\sin\alpha 1$ evaluated at $\tau = \tau_{inlet}$. Thus to within a constant, we can write the integrating factor as,

$$Q \sim (hk\sin\alpha 1)^2$$

(2.96)

which suggests that the integrating factor can always be calculated in terms of the metric factors of the coordinate system given in Eq.2.50 - 2.53. As we will see later, this also offers another huge numerical advantage in calculating the Nusselt number Nu. From this juncture, we use the appropriate relations for Q, corresponding to the spiralling and non-spiralling regimes to calculate the Nusselt number.

Non-Spiralling Regime: $\alpha < (2+\epsilon)/(1+\lambda)$

In this regime, the expression for Q in regions 1 and 3 can be obtained by substituting Eqs.2.70-2.71 in Eqs.2.95, 2.50 and 2.51, which after manipulations is given by :

$$Q_I = \frac{e^{\frac{3\epsilon\tau}{A}}}{\left(e^{\frac{3\epsilon\tau}{A}}B + 2C^2((2+\epsilon)\cosh\tau - (1+\lambda)\alpha)\right)^3} \tag{2.97}$$

Using this, the the relation for boundary layer thickness is given by:

$$g = \frac{2(1+\lambda)}{A}e^{\frac{-3\epsilon\tau}{2A}}\left(e^{\frac{3\epsilon\tau}{A}}B + 2C^2((2+\epsilon)\cosh\tau - (1+\lambda)\alpha)\right)^{3/2}$$

$$\left(\int_{\tau_{inlet}}^{\tau} \frac{e^{\frac{3\epsilon\tau1}{A}}}{\left(e^{\frac{3\epsilon\tau1}{A}}B + 2C^2((2+\epsilon)\cosh\tau1 - (1+\lambda)\alpha)\right)^3}d\tau1\right)^{1/2} \tag{2.98}$$

From the above equation, one can see that at the inlet, i.e. $\tau \to -\infty$, $Q_I \sim \exp\left[(3\epsilon\tau/A)\right]$ and $Q_I^{-1} \sim \exp\left[(-3\epsilon\tau/A)\right]$, with their product g being finite. On the other hand, $g(C,\tau)$ diverges at the outlet as $\tau \to \infty$, indicative of a thermal wake. We can similarly show the same features for the regions 2 and 4, in which, Q is defined as:

$$Q_{II} = \frac{e^{\frac{3\epsilon\tau}{A}}}{\left(e^{\frac{3\epsilon\tau}{A}}B + 2C^2((2+\epsilon)\cosh\tau + (1+\lambda)\alpha)\right)^3} \tag{2.99}$$

Again, we can easily see that the boundary layer thickness is finite at the inlet and diverges at the outlet. A representative plot of the boundary layer thickness is shown in Fig.2.27a for the parameter values given by $\epsilon = -1.5$, $\lambda = 1$, $\alpha = 0.1$. The plot shows the thickness calculated in both regions 1 and 2.

Spiralling Regime: $\alpha > (2+\epsilon)/(1+\lambda)$

In this regime, we use the appropriate definitions of $C - \tau$ (Eq.2.72-2.73) in Eq.2.95, to get:

$$Q = \frac{e^{\frac{3(\epsilon+\imath A')\tau}{A'}}}{\left(e^{\frac{3(\epsilon+\imath A')\tau}{A'}}B + 2C^2((2+\epsilon)\cos\tau - (1+\lambda)\alpha)\right)^3} \tag{2.100}$$

where A' is real as was previously defined. Again substituting this into the equation for boundary layer thickness, we see that the thickness is finite at the inlet as $Q \sim \exp[(3\epsilon\tau/A')]$ and $Q^{-1} \sim \exp[-(3\epsilon\tau/A')]$ as $\tau \to -\infty$, keeping g finite and the thickness diverges as $\tau \to \infty$. A representative plot for this regime showing $g(C,\tau)$ and its behavior is shown in Fig.2.27b. We now make use of these expressions to calculate the Nusselt number.
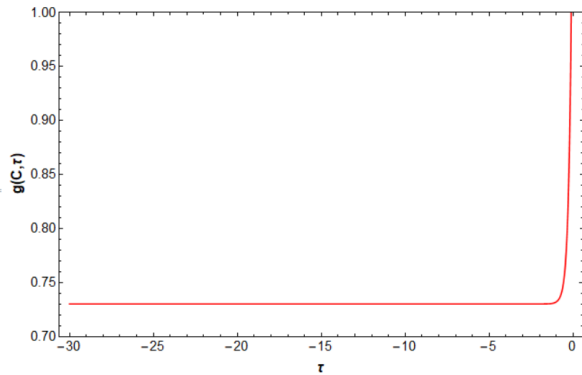
(a) $g(C, \tau)$ for the non-spiralling regime.
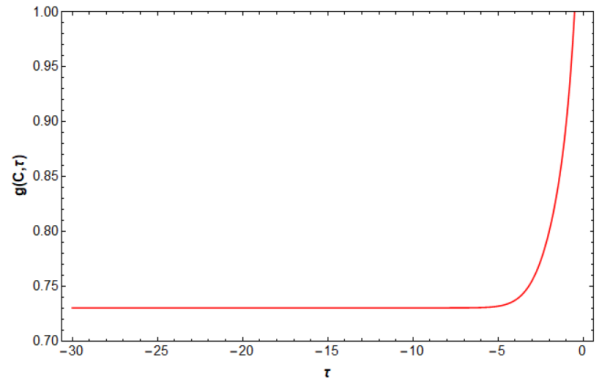
(b) $g(C, \tau)$ for the non-spiralling regime.

Figure 2.27: Plot of Boundary layer thickness $g(C, \tau)$ for $\epsilon = -1.25, \lambda = 0$ in (a) the non-spiralling regime when $\alpha = 0.5$ ($< \alpha_{th1} = 0.75$) and (b) the spiralling regime for which $\alpha = 3$ ($> \alpha_{th1} = 0.75$). The thickness is finite at the inlet corresponding to $\tau \to -\infty$ and diverges at the wake $\tau \to \infty$. Both the plots are for a trajectory constant $C = 1$.

2.3.3.4   The Nusselt Surface

Having calculated the boundary-layer thickness as a function of C and τ on the drop surface, the dimensionless rate of heat transfer, the Nusselt number (Nu), is given by:

$$Nu = \frac{-1}{4\pi} \int_S \left(\frac{\partial \Theta}{\partial y} \right)_{y=0} dS = -\frac{Pe^{1/2}}{4\pi} \int_S \left(\frac{\partial \Theta}{\partial Y} \right)_{Y=0} dS \tag{2.101}$$

where S denotes the surface area of the drop. Rewriting this in terms of the similarity variable η, we get:

$$Nu = \frac{-1}{4\pi} \int_S \frac{1}{g} \left(\frac{d\Theta}{d\eta} \right)_{\eta=0} dS = \frac{Pe^{1/2}}{2\pi^{3/2}} \int_S \frac{dS}{g(C, \tau)} \tag{2.102}$$

From Eq.2.102, Nu is just proportional to the areal average of the inverse boundary layer thickness. In $C - \tau$ coordinates, the differential areal element is given by $hk \sin \alpha 1 \ dC \ d\tau$, accounting for the non-orthogonality. Thus Nu is given by:

$$Nu = \frac{Pe^{1/2}}{2\pi^{3/2}} \int_S \frac{hk \sin \alpha 1 \ dC \ d\tau}{g(C, \tau)} \tag{2.103}$$

As for the boundary layer thickness, we first derive a general expression for Nu, based on the properties of the coordinate system and then use expressions pertaining to the two parameter family under consideration. Krishnamurthy and Subramanian (2018a) have mentioned Eq.2.103 as the generic expression for Nu, this is a four-dimensional integral, where the integrand involves $g(C, \tau)$ which itself involves two further integrations, one of them required to evaluate the integrating factor. The four-dimensional integration may be avoided by using the relation in Eq.2.95. Substituting for $hk \sin \alpha 1$ from Eq.2.95 in terms of Q, we have:

$$Nu = \frac{Pe^{1/2} h_\tau^{1/2}}{2\pi^{3/2}} \int_S \frac{Q^{1/2} (hk \sin \alpha 1)_0 \ dC \ d\tau}{2 \left(Q^{-1} \int_{\tau_{inlet}}^{\tau} Q \ d\tau_1 \right)^{1/2}}, \tag{2.104}$$

We can reduce it further by noting that the τ integrand reduces to an exact differential as,

$$Nu = \frac{Pe^{1/2}h_\tau^{1/2}}{2\pi^{3/2}} \int_S \frac{Q \left(\int_{\tau_{inlet}}^\tau Q\, d\tau_1\right)^{-1/2} (hk\sin\alpha 1)_0\, dC\, d\tau}{2}$$

$$= \frac{Pe^{1/2}h_\tau^{1/2}}{2\pi^{3/2}} \int_C \int_{\tau_{inlet}}^{\tau_{outlet}} \frac{d}{d\tau} \left(\int_{\tau_{inlet}}^\tau Q\, d\tau_1\right)^{1/2} (hk\sin\alpha 1)_0\, d\tau\, dC. \tag{2.105}$$

After integrating over τ, we can write Nu as,

$$Nu = \frac{Pe^{1/2}h_\tau^{1/2}}{2\pi^{3/2}} \int_C (hk\sin\alpha 1)_0 \left(\int_{\tau_{inlet}}^{\tau_{outlet}} Q\, d\tau_1\right)^{1/2} dC \tag{2.106}$$

where $\tau_{inlet} = -\infty$ and $\tau_{outlet} = \infty$, corresponding to the inlet and wake of the boundary layer. This equation only involves two nested integrals, as opposed to four in Eq.2.103. Thus Eq.2.106 provides one with an effective means to calculate Nu with minimal computational effort for an arbitrary linear flow. Now, we substitute the appropriate Q expressions corresponding to the spiralling and non-spiralling regimes of the aligned-vorticity family under consideration, in order to calculate Nu.

Non-Spiralling Regime: $\alpha < (2+\epsilon)/(1+\lambda)$

In this regime, we know that the hemisphere is divided into four regions, $I \equiv (1,3)$ and $II \equiv (2,4)$, where the pair $I = (1,3)$ conforms to the inversion symmetry of linear flows and likewise for the other pair. Thus we can write Nu as the sum of two integrals, namely:

$$Nu = (2)\frac{Pe^{1/2}h_\tau^{1/2}}{2\pi^{3/2}} \int_C (hk\sin\alpha 1)_0 \left(\int_{\tau_{inlet}}^{\tau_{outlet}} (Q_I + Q_{II})\, d\tau_1\right)^{1/2} dC$$

$$= 2(Nu_I + Nu_{II}) \tag{2.107}$$

where the prefactor of two is included, since the drop surface is divided into four regions, two of which are equivalent to $I = (1,3)$ and two to $II = (2,4)$; the integrals Nu_I, Nu_{II} denote integrations over I and II, respectively. Note that $(hk\sin\alpha 1)_0$ has been factored out as it is the same for I and II, since they have a common inlet. Considering the Nusselt number contribution from regions $I = (1,3)$, and substituting for Q from Eq.2.97, and $hk\sin\alpha 1$ which is given by $\frac{CA}{(1+2C^2)^{3/2}B}$, one obtains:

$$Nu_I = \frac{Pe^{1/2}h_\tau^{1/2}}{2\pi^{3/2}} \int_C (hk\sin\alpha 1)_0 \left(\int_{\tau_{inlet}}^{\tau_{outlet}} Q_I\, d\tau_1\right)^{1/2} dC$$

$$= \frac{Pe^{1/2}A^{3/2}}{2\pi^{3/2}B(1+\lambda)^{1/2}} \int_0^\infty \frac{C}{(1+2C^2)^{3/2}} \left(\int_{-\infty}^\infty \frac{e^{\frac{3\epsilon\tau}{A}}}{\left(e^{\frac{3\epsilon\tau}{A}}B + 2C^2((2+\epsilon)\cosh\tau - (1+\lambda)\alpha)\right)^3} d\tau_1\right)^{1/2} dC. \tag{2.108}$$

Similarly for regions $II = (2,4)$, substituting for Q_{II} from Eq.2.99, we can write down the expression for Nu as,

$$Nu_{II} = \frac{Pe^{1/2}h_\tau^{1/2}}{2\pi^{3/2}} \int_C (hk\sin\alpha 1)_0 \left(\int_{\tau_{inlet}}^{\tau_{outlet}} Q_{II}\, d\tau_1\right)^{1/2} dC$$

$$= \frac{Pe^{1/2}A^{3/2}}{2\pi^{3/2}B(1+\lambda)^{1/2}} \int_0^\infty \frac{C}{(1+2C^2)^{3/2}} \left(\int_{-\infty}^\infty \frac{e^{\frac{3\epsilon\tau}{A}}}{\left(e^{\frac{3\epsilon\tau}{A}}B + 2C^2((2+\epsilon)\cosh\tau + (1+\lambda)\alpha)\right)^3} d\tau_1\right)^{1/2} dC. \tag{2.109}$$

These integrals can be readily evaluated numerically. Note that, Nu can be scaled with λ by pulling the $(1+\lambda)^{1/2}$ into the definition of Pe and redefining Pe as $\hat{Pe} = Pe/(1+\lambda)$. The λ dependence on the RHS appears as the combination $(1+\lambda)\alpha$ which, recall is the definition of α'. Thus the λ dependence on the Nusselt number can be scaled out if we calculate Nu as a function of $\hat{Pe}$ and α'.

Spiralling Regime: $\alpha > (2+\epsilon)/(1+\lambda)$

In this regime, for which Q is given by Eq.2.100 and $hk \sin \alpha 1$ is given by $\frac{CA'}{(1+2C^2)^{3/2}B}$, we can write the Nusselt number as:

$$
Nu = \frac{Pe^{1/2}h_\tau^{1/2}}{2\pi^{3/2}} \int_C (hk \sin \alpha 1)_0 \left(\int_{\tau_{inlet}}^{\tau_{outlet}} Q \, d\tau_1 \right)^{1/2} dC
$$

$$
= \frac{Pe^{1/2}A'^{3/2}}{2\pi^{3/2}B(1+\lambda)^{1/2}} \int_C \frac{C}{(1+2C^2)^{3/2}} \left(\int_{-\infty}^{\infty} \frac{e^{\frac{3(\epsilon+\iota A')\tau}{A'}}}{\left(e^{\frac{3(\epsilon+\iota A')\tau}{A'}} B + 2C^2((2+\epsilon)\cos\tau - (1+\lambda)\alpha) \right)^3} d\tau_1 \right)^{1/2} dC.
$$
(2.110)

Here, the τ limit runs from $-\infty$ to ∞ as before, while the C limit only runs from C^* to $C^* \exp[(6\epsilon\pi)/A']$, to avoid double-counting of the spiralling streamlines; equivalently, one may also use the limits C going from 0 to ∞, with τ ranging from τ^* to $\tau^* \mod 2\pi$. As was already mentioned, the effect of λ on Nu can be scaled out by writing it is a function of $\hat{Pe}^{1/2}$ and α'.

Discussion

The surface plot of $Nu/\hat{Pe}^{1/2}$ is shown in Fig.2.28, where the Nusselt number is plotted as a function of ϵ and α'. The plot displays an increasing trend of $Nu/\hat{Pe}^{1/2}$ as ϵ decreases from 0 to -2 at a given α'. At $\epsilon = 0$, the Nusselt number surface discontinuously drops to 0, owing to the presence of closed streamlines on the drop. This corresponds to the special case of planar linear flows analysed by Krishnamurthy and Subramanian (2018a), which we discuss below. The plot also contains another special case corresponding to $\epsilon = -2$, which is the case of axisymmetric extension with the vorticity along the axis of symmetry. We see that for this case Nu is independent of α'. This can also be shown analytically, and is done below as a part of the discussion on special cases.

For all ϵ, except $\epsilon = 0$, the Nu surface smoothly continues from the non-spiralling to spiralling regime; this threshold corresponds to $\alpha' = \alpha'_{th1}$. The value of Nu along this threshold ($\alpha' = \alpha'_{th1}$) can be calculated by setting $2 + \epsilon = \alpha'$, in all our definitions, which gives:

$$
\frac{Nu_{th}}{\hat{Pe}^{1/2}} = \frac{4\alpha'}{\pi^{3/2}} \int_0^\infty \frac{C}{(1+2C^2)^{3/2}} \left(\int_{-\infty}^{\infty} \frac{e^{3\tau(-2+\alpha')}}{\left(e^{3\tau(-2+\alpha')} + 2C^2(1+\tau^2\alpha'^2) \right)^3} d\tau \right)^{1/2} dC
$$
(2.111)

This value matches with our numerical evaluation of the Nusselt number (given in Eq.2.107 and Eq.2.110) when approaching the threshold from either side (that is, from spiralling or non-spiralling regime). For $\epsilon = 0$, for which $\alpha' \to 2$, the expression above reduces to,

$$
\frac{Nu_{th}}{\hat{Pe}^{1/2}} = \frac{2^{3/4}3^{1/2}}{\pi} \int_0^\infty \left(\frac{C}{(1+C^2)^{5/2}} \right)^{1/2} dC = 2\sqrt{\frac{3}{\pi}} \frac{\Gamma(\frac{3}{4})}{\Gamma(\frac{1}{4})},
$$
(2.112)

where Γ denotes the Gamma function. The aforementioned expression matches with the expression given in Eq.3.69 of Krishnamurthy and Subramanian (2018a), barring their definition of α. Beyond this threshold Nu drops to zero for $\epsilon = 0$.
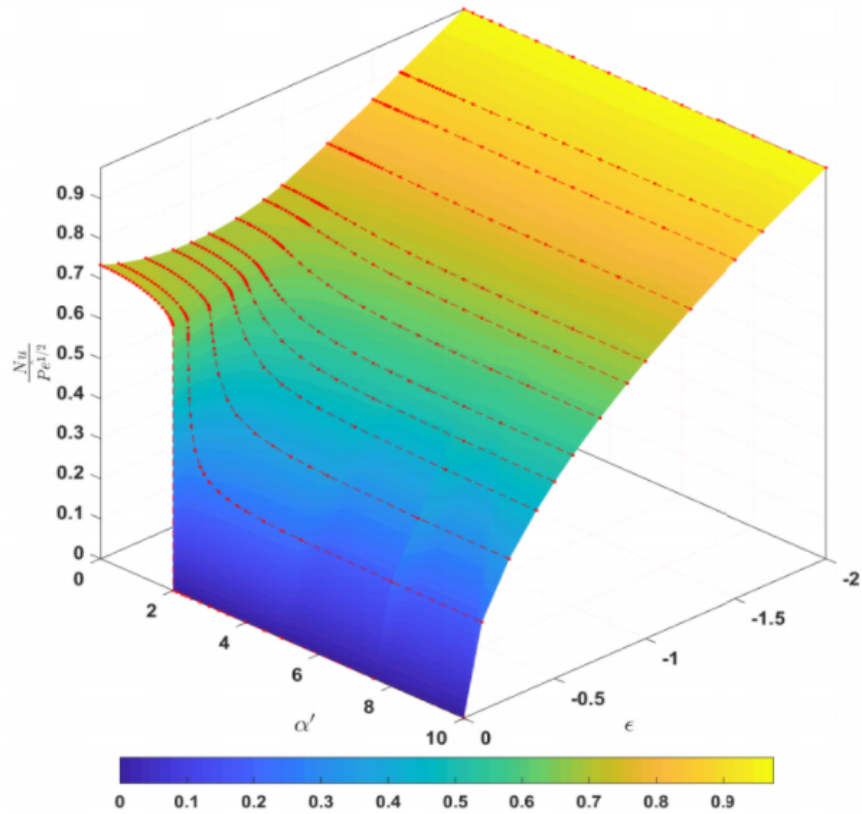
Figure 2.28: Plot of $Nu/P\hat{e}^{1/2}$ as a function of α' and ϵ. The Nu for an arbitrary λ, α can be calculated from this surface by using $Nu/Pe^{1/2} = (Nu/P\hat{e}^{1/2})/(\sqrt{1+\lambda})$, at an α given by $\alpha'/(1+\lambda)$ and ϵ.

(a) $\lambda = 0.5$ (b) $\lambda = 1$ (c) $\lambda = 5$
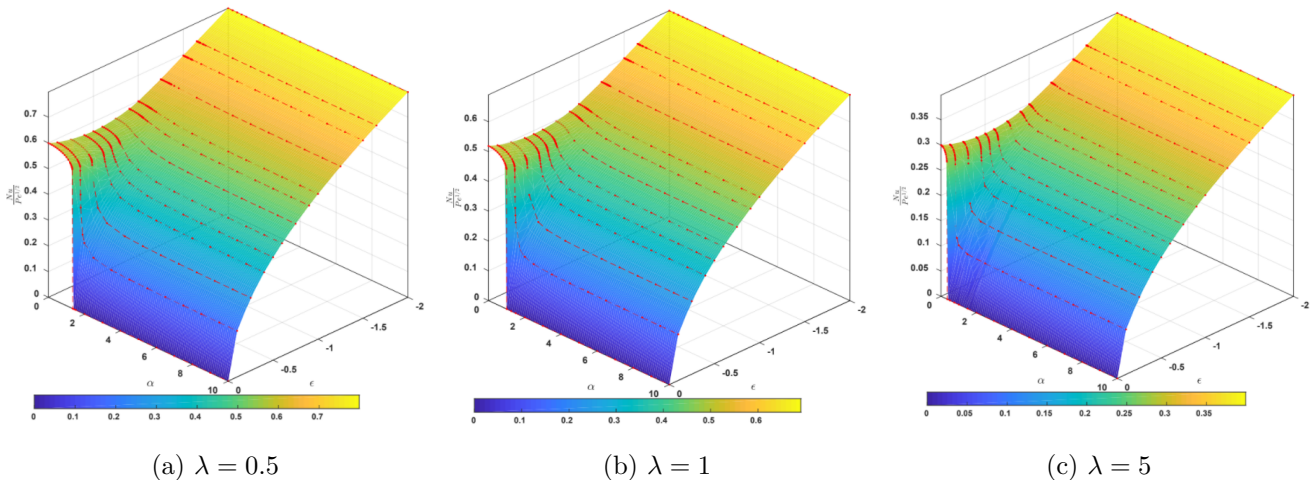
Figure 2.29: Plot of Nu against α, ϵ for (a) $\lambda = 0.5$, (b) $\lambda = 1$ and, (c) $\lambda = 5$, which constitutes the actual Nusselt number.

In Fig.2.29(a)-(c), we plot $Nu/Pe^{1/2}$ as a function of α and ϵ for three different λ's. As expected, as λ increases, the Nusselt number decreases at a given (α, ϵ). Also note that the threshold curve α_{th1} moves to smaller values as λ increases. Both these features are consistent with our λ-based rescaling $Nu/\hat{Pe}^{1/2} = (Nu/Pe^{1/2})(1+\lambda)$ and $\alpha' = \alpha(1+\lambda)$. We now discuss the limiting special cases one

encounters for the two-parameter family examined.

Special Cases

- The first case is $\epsilon = 0$, which corresponds to the one-parameter family of canonical planar linear flows. This case was already analysed by Krishnamurthy and Subramanian (2018a), where they use the same label α for their governing flow parameter. To avoid confusion, we call it $\hat{\alpha}$, which is related to our α by the relation given in Eq.2.6. Note that the definition of $\hat{\alpha}$ in their case, led them to a Nu relation that could not be completely scaled with λ (see their Eq.3.62), as it involved a constant $\gamma = ((1 - \hat{\alpha})(1 + \lambda) + (1 + \hat{\alpha}))/((1 - \hat{\alpha})(1 + \lambda) - (1 + \hat{\alpha}))$ (related to the aspect ratio). Using Eq.2.6, we can reduce this quantity into $\gamma = (\alpha' + 2)/(\alpha' - 2)$, and thereby make $Nu = f(\hat{Pe}^{1/2}, \alpha')$. The authors present a Nu surface as a function of $\hat{\alpha}$ and λ (see Fig.7 of Krishnamurthy and Subramanian (2018a)), where the Nu drops to zero discontinuously beyond a critical curve in the $\hat{\alpha} - \lambda$ plane given by:

$$\lambda_c = \frac{2\hat{\alpha}}{1 - \hat{\alpha}}. \tag{2.113}$$

For the sake of comparison we also calculate Nu given in Eqs.2.108-2.109 for $\epsilon = 0$, as a function of $\hat{\alpha}$ and λ, where we use Eq.2.6 to convert between α and $\hat{\alpha}$, in Fig.2.30a and 2.30b, and the results match with that of Krishnamurthy and Subramanian (2018a). Note that for comparing our results with theirs, we also should redefine our Pe number using their velocity scale, which leads to the following relation between the two Pe numbers:

$$Pe = \frac{Pe_{Deepak}}{1 + \alpha} \tag{2.114}$$
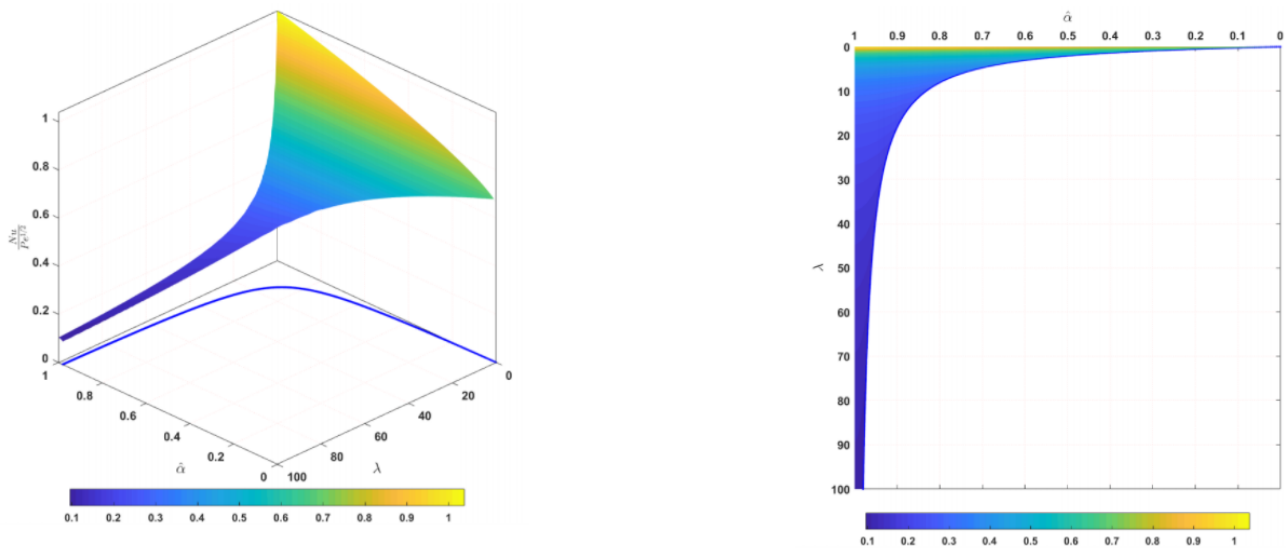
(a) Perspective view.   (b) Top view.

Figure 2.30: Plot of $Nu/Pe^{1/2}$ as a function of $\hat{\alpha}$ and λ for $\epsilon = 0$. Note that to compare with the results of Krishnamurthy and Subramanian (2018a), we have redefined our Pe according to Eq.2.114. These surfaces are analogous to the plot given in Fig. 7 of Krishnamurthy and Subramanian (2018a).

To understand the Nu surfaces for other ϵ better, one can consider this case ($\epsilon = 0$) as the baseline scenario, where Nu drops to zero discontinuously across the critical curve as shown in Fig.2.30. For other ϵ, they cross this curve whilst still remaining finite, and gradually decrease to 0 as $\hat{\alpha}$ increases.

The Nusselt surface decreases rapidly, but in a continuous fashion, across the critical curve, for small but finite ϵ. The decrease is gradual for larger ϵ. This has been shown in Fig.2.31a - 2.31c, where the case of $\epsilon = 0$, has been compared with other ϵ.

(a) $\epsilon = 0$ (b) $\epsilon = -0.25$ (c) $\epsilon = -0.5$
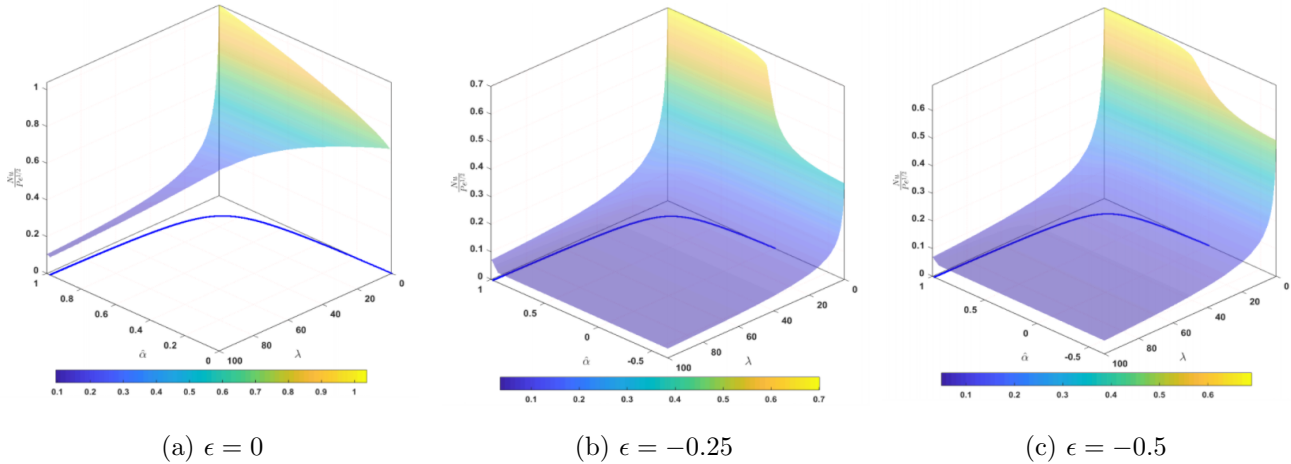
Figure 2.31: Plot of $Nu/Pe^{1/2}$ as a function of $\hat{\alpha}$ and λ for different ϵ. The plot shows the critical curve in the $\hat{\alpha} - \lambda$ plane beyond which (a) Nu discontinuously drops to zero for $\epsilon = 0$ and (b) continue past the critical curve before gradually decreasing 0 for $\epsilon = -0.25$ and (c) $\epsilon = -0.5$.

- The second special case corresponds to $\epsilon = -2$, which is axisymmetric extension with the vorticity vector along the axis of symmetry. For this case, we can again show analytically that Nu is independent of α' and is a constant, which is equal to Nu for the case of axisymmetric extension (Gupalo and Riazantsev (1972)). To show this, we rewrite our expression for Q in Eq.2.100, for $\epsilon \to -2$, which gives us:

$$Q = \frac{(1+2C^2)^3 e^{\frac{12\tau}{\alpha'}}}{\left(1 + 2C^2 e^{\frac{6\tau}{\alpha'}}\right)^3} \tag{2.115}$$

Similarly, we have $(hk \sin \alpha 1)_0 = \frac{C}{(1+2C^2)^{3/2}}$ and $h_\tau = \frac{\alpha'}{1+\lambda}$. Substituting these values into the expression for Nu, we get,

$$
\begin{aligned}
Nu &= \frac{\hat{P}e^{1/2} \alpha'^{1/2}}{\pi^{3/2}} \int_{C*}^{C*e^{6\pi/\alpha'}} \frac{C}{(1+2C^2)^{1/2}} \left(\int_{-\infty}^{\infty} \frac{(1+2C^2)^3 e^{\frac{12\tau}{\alpha'}}}{\left(1 + 2C^2 e^{\frac{6\tau}{\alpha'}}\right)^3} \, d\tau \right)^{1/2} dC \\
&= \frac{\hat{P}e^{1/2}}{\pi^{3/2}} \int_{C*}^{C*e^{6\pi/\alpha'}} \left(\frac{\alpha'}{4\sqrt{3}C} \right)^{1/2} dC \\
&= \frac{\hat{P}e^{1/2} 3^{1/2}}{\pi^{1/2}}
\end{aligned}
\tag{2.116}
$$

which is the same value given in Gupalo and Riazantsev (1972) and is independent of α'.
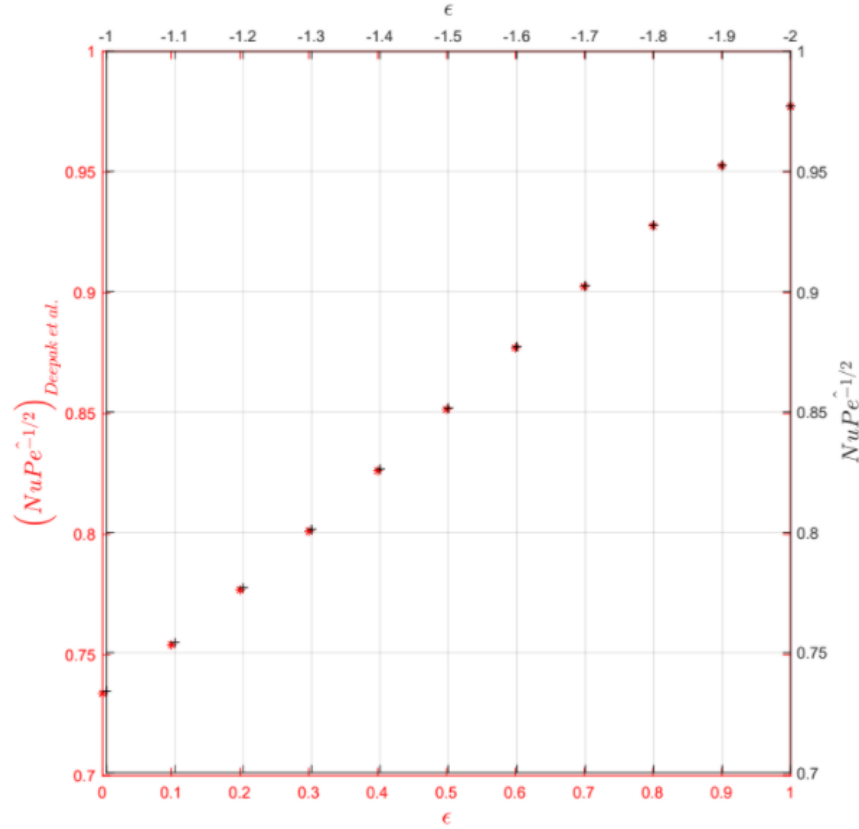
Figure 2.32: Plot of $Nu/P\hat{e}^{1/2}$ as a function of ϵ for pure extensional flows. The data in red corresponds to that of Krishnamurthy and Subramanian (2018a), while the data in black corresponds to our calculation, which matches exactly withe the former.

- The final case pertains to pure extensional flows, which translates to ϵ varying over the entire interval with $\alpha' = 0$. The Nusselt number for this case has also been calculated by Krishnamurthy and Subramanian (2018a) with which we compare our values. Note that Krishnamurthy and Subramanian (2018a) have used ϵ ranging from 0 to 1. In our case, this is equivalent to any of the intervals $-2 \leq \epsilon \leq -1$ or $-0.5 \leq \epsilon \leq -1$ or $-0.5 \leq \epsilon \leq 0$, all of which are equivalent for $\alpha' = 0$. For the latter two intervals, Pe has to be redefined to accommodate a numerical factor, that results from the magnitude of the velocity-gradient scale associated with these two. In order to facilitate a direct comparison with the results of Krishnamurthy and Subramanian (2018a), we use the first range of ϵ to compare our results with theirs, which is plotted in Fig.2.32. The value for $\epsilon = 0$ (planar extension), has also been previously calculated by Polyanin (1984) who used an orthogonal coordinate system to calculate Nu for drop in a planar extension, which cannot be extended to complex linear flows, for which the non-orthogonal $C - \tau$ system must be used.

2.4 Drop in Axisymmetric Extension with Inclined Vorticity

Having analysed the heat transfer in the first two-parameter family, we now move on to the second one: Axisymmetric extension with vorticity inclined to the axis of symmetry. The two parameters that govern this family are α and θ_ω, where θ_ω is the angle of inclination of the vorticity vector to the axis of symmetry and α, as before, is the ratio of vorticity magnitude to the magnitude of extension (same as the previous case). A schematic showing the geometry of this family of linear flows is given in Fig.2.33, where the axis

of symmetry of the extension has been taken to be the x_1 axis.
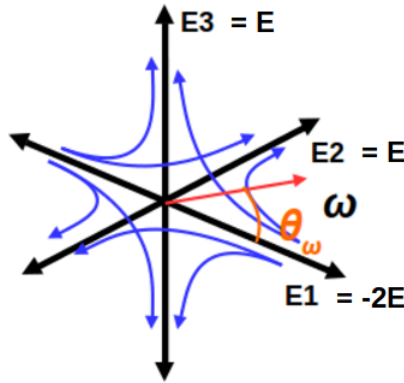
Figure 2.33: The geometry of axisymmetric extension with inclined vorticity.

Analogous to the previous case, we first begin by writing down the velocity-gradient tensor associated with this two-parameter family which is given by:

$$\bar{\Gamma} = \begin{bmatrix} -2 & -\frac{\alpha \sin \theta_\omega}{2} & 0 \\ \frac{\alpha \sin \theta_\omega}{2} & 1 & -\frac{\alpha \cos \theta_\omega}{2} \\ 0 & \frac{\alpha \cos \theta_\omega}{2} & 1 \end{bmatrix} \tag{2.117}$$

For this two-parameter family the range of the parameters that cover all possible flow configurations are: $\theta_\omega \in [0, \pi/2]$ and $\alpha \in [0, \infty]$. The limiting case $\theta_\omega = 0$, where the vorticity vector is aligned along the axis of symmetry, was already encountered in the earlier two-parameter family, where it corresponded to $\epsilon = -2$. For the other limiting case, $\theta_\omega = \pi/2$, the vorticity vector is perpendicular to the axis of symmetry and it corresponds to the time-reversed scenario associated with $\epsilon = -0.5$ of the earlier two-parameter family. For α, the limiting cases correspond to axisymmetric extension ($\alpha = 0$) and solid-body rotation ($\alpha = \infty$). Analogous to the previous case, we begin our analysis by writing down the velocity field on the drop surface and the governing equations for the surface streamlines. Then we analyse and organise the surface-streamline topology using the scalar invariants of the auxiliary linear system associated with this flow. Finally, we write down the solutions of the surface-streamline equations, which, once again lets us define a surface-streamline-aligned coordinate system to analyse the transport problem in the exterior, assuming negligible resistance in the interior of the drop.

2.4.1   Surface Streamline Topology - Organisation

For the two-parameter family under consideration, the Stokesian velocity field (Eq.2.9) in spherical coordinates are:

$$u_r = r(C_1 + C_2 r^2) \left(\cos^2 \theta - \frac{1}{2}(1 + 3\cos 2\phi) \sin^2 \theta \right) \tag{2.118}$$

$$u_\theta = \frac{-1}{4} r \, C_1 \left((3 + 3\cos 2\phi) \sin 2\theta \right) + \frac{1}{4} r \left(\alpha \cos \theta_\omega \sin \phi \right) \tag{2.119}$$

$$u_\phi = \frac{1}{2} r \, \sin \theta (3C_1 \sin 2\phi) + \frac{1}{4} r \left(\alpha \sin \theta_\omega \, \sin \theta - \alpha \cos \theta_\omega \, \cos \phi \cos \theta \right) \tag{2.120}$$

where C_1 and C_2 are given in Eq.2.10. On the drop surface these components reduce to:

$$\frac{d\theta}{dt} = \frac{-1}{4(1+\lambda)}\left((3 + 3\cos 2\phi)\sin 2\theta\right) + \frac{1}{4}\left(\alpha \cos \theta_\omega \sin \phi\right) \tag{2.121}$$

$$\sin\theta\frac{d\phi}{dt} = \frac{1}{2(1+\lambda)}\sin\theta(3\sin 2\phi) + \frac{1}{4}\left(\alpha \sin\theta_\omega \, \sin\theta - \alpha\cos\theta_\omega \, \cos\phi\cos\theta\right). \tag{2.122}$$

Unlike the aligned vorticity case, these equations are not obviously solvable in closed form by direct integration of Eqs.2.121-2.122. So, we have to use the auxiliary flow equations to construct the solutions for surface-streamlines. Recall that the auxiliary linear system is given by:

$$\dot{\boldsymbol{x}} = \hat{\boldsymbol{\Gamma}}.\boldsymbol{x}, \tag{2.123}$$

where the velocity-gradient tensor for the auxiliary flow ($\hat{\boldsymbol{\Gamma}}$) is given by:

$$\hat{\boldsymbol{\Gamma}} = \begin{bmatrix} -\frac{2}{1+\lambda} & -\frac{\alpha \sin\theta_\omega}{2} & 0 \\ \frac{\alpha\sin\theta_\omega}{2} & \frac{1}{1+\lambda} & -\frac{\alpha\cos\theta_\omega}{2} \\ 0 & \frac{\alpha\cos\theta_\omega}{2} & \frac{1}{1+\lambda} \end{bmatrix}, \tag{2.124}$$

for the two-parameter family under consideration. The solution to Eq.2.123, can be written in a straight-forward manner as:

$$\boldsymbol{x} = \boldsymbol{S}^{-1}\hat{\boldsymbol{D}}\boldsymbol{S}(\boldsymbol{x_0}). \tag{2.125}$$

Here, $\boldsymbol{S}$ is the matrix of eigenvectors given by $\boldsymbol{S} = [\vec{\boldsymbol{\mu_1}}, \vec{\boldsymbol{\mu_2}}, \vec{\boldsymbol{\mu_3}}]^T$, where $\vec{\boldsymbol{\mu_i}}$ are the eigenvectors associated with the eigenvalues μ_i of $\hat{\boldsymbol{\Gamma}}$. The matrix $\hat{\boldsymbol{D}}$ is the matrix of exponentials of eigenvalues which is given by:

$$\hat{\boldsymbol{D}} = \begin{bmatrix} e^{\mu_1 t} & 0 & 0 \\ 0 & e^{\mu_2 t} & 0 \\ 0 & 0 & e^{\mu_3 t} \end{bmatrix} \tag{2.126}$$

and $\boldsymbol{x_0}$ are the initial values. This solution $\boldsymbol{x}$ is then projected onto the unit sphere by dividing it by the norm i.e. $\boldsymbol{x}/|\boldsymbol{x}|$, which gives us the surface-streamline solutions in terms of the eigenvalues and eigenvectors of the auxiliary linear system. We shall use these solutions to define our $C - \tau$ coordinate system which will enable us to calculate Nu using a similarity transformation. But first, we use the invariants of $\hat{\boldsymbol{\Gamma}}$, to organise the streamline topologies in just the same manner done for the aligned-vorticity case.

2.4.1.1 Invariants of the Auxiliary System

The scalar invariants used to organise the streamline patterns are again the discriminant Δ, the cubic invariant R and the quadratic invariant Q which, for the case of axisymmetric extension with inclined vorticity, are given by:

$$\Delta = \frac{3\left(((1+\lambda)\alpha^2 - 12)^3 + 27(-8 + (1+\lambda)^2\alpha^2(1 - 3\cos^2\theta_\omega))^2\right)}{16(1+\lambda)^6} \tag{2.127}$$

$$Q = \frac{(1+\lambda)^2\alpha^2 - 12}{4(1+\lambda)^2} \tag{2.128}$$

$$R = \frac{-8 + (1+\lambda)^2\alpha^2(1 - 3\cos^2\theta_\omega)}{4(1+\lambda)^3}. \tag{2.129}$$

Much like the aligned-vorticity case, here too one may scale all these invariants with λ by defining $\Delta' = (1+\lambda)^6\Delta$, $R' = (1+\lambda)^3 R$, $Q' = (1+\lambda)^2 Q$ and $\alpha' = (1+\lambda)\alpha$, the scaled invariants being given by:

$$\Delta' = \frac{3\left((\alpha'-12)^3 + 27(-8+\alpha'^2(1-3\cos^2\theta_\omega))^2\right)}{16} \tag{2.130}$$

$$Q' = \frac{\alpha'^2 - 12}{4} \tag{2.131}$$

$$R' = \frac{-8 + \alpha'^2(1-3\cos^2\theta_\omega)}{4}. \tag{2.132}$$

This again suggests that one would have the same spectrum of topologies that are distributed across different regions of the two-parameter plane for different λ. Note that one could have arrived at the same conclusion in an alternate manner by pulling out the factor $1/(1+\lambda)$ from $\hat{\Gamma}$ and incorporating it into the velocity scale, which then enters the definition of the Peclet number Pe. This new velocity scale would now be $E/(1+\lambda)$, instead of just E, where E is the magnitude of extension, and the new Peclet number is now given by $\hat{Pe} = Pe/(1+\lambda)$, as for the aligned-vorticity case. This λ-rescaled $\hat{\Gamma}$ is given by:

$$\hat{\Gamma}_\lambda = \begin{bmatrix} -2 & -\frac{\alpha'\sin\theta_\omega}{2} & 0 \\ \frac{\alpha'\sin\theta_\omega}{2} & 1 & -\frac{\alpha'\cos\theta_\omega}{2} \\ 0 & \frac{\alpha'\cos\theta_\omega}{2} & 1 \end{bmatrix} \tag{2.133}$$

where $\alpha' = (1+\lambda)\alpha$. The invariants calculated for this redefined $\hat{\Gamma}_\lambda$, will have the same form given in Eq.2.130 - 2.132. This also implies that λ dependence of Nu can be scaled out provided we also scale α as α'.

The definition of Δ' (Eq.2.130) suggests that it has two roots given by α'_{th1} and α'_{th2} given by:

$$\alpha'_{th1} = \frac{3\sqrt{1+9\cos^2\theta_\omega(2-3\cos^2\theta_\omega) - \sqrt{(-1+\cos^2\theta_\omega)(-1+9\cos^2\theta_\omega)}}}{\sqrt{2}}, \tag{2.134}$$

$$\alpha'_{th2} = \frac{3\sqrt{1+9\cos^2\theta_\omega(2-3\cos^2\theta_\omega) + \sqrt{(-1+\cos^2\theta_\omega)(-1+9\cos^2\theta_\omega)}}}{\sqrt{2}}, \tag{2.135}$$

which are plotted as a function of θ_ω in Fig.2.34a (recall that the sign of Δ' determines the spiralling or non-spiralling character of the surface streamlines). From the plot, we see that they only exist beyond a critical θ_ω given by $\theta_\omega^{th2} = \tan^{-1}2\sqrt{2}$. We also plot R' as a function of α' for different θ_ω in the same figure (Fig.2.34b), from which we see that there is another critical θ_ω given by $\theta_\omega^{th1} = \tan^{-1}\sqrt{2}(<\theta_\omega^{th2})$, above which R' suffers a zero crossing, implying the occurrence of a planar linear flow. This zero-crossing in R' is labelled α'_{th3}, consistent with the earlier section of aligned-vorticity case. It is therefore convenient to analyse the streamline topologies corresponding to the following three distinct ranges of θ_ω between the two thresholds:(i) $0 \leq \theta_\omega < \theta_\omega^{th1}$, (ii) $\theta_\omega^{th1} < \theta_\omega < \theta_\omega^{th2}$ and finally, (iii) $\theta_\omega^{th2} < \theta_\omega \leq \pi/2$. We now use the aforementioned invariants to organise our streamline topology in these three classes and then move on to analysing it using fixed-point techniques.

(a) α'_{th1} and α'_{th2} vs θ_ω (b) R' vs α'
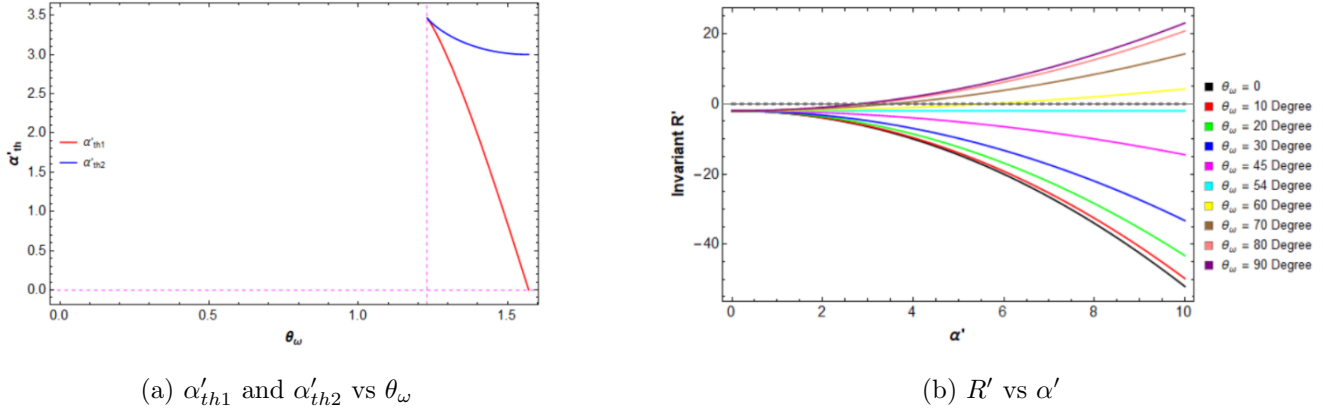
Figure 2.34: Plot of (a) α'_{th1} and α'_{th2} as a function of θ_ω where the vertical line marks $\theta_\omega^{th2} = \tan^{-1}\sqrt{2} \sim 70°$ and (b) the cubic invariant R' as a function of α' for multiple θ_ω. The $\theta_\omega^{th1} = \tan^{-1}\sqrt{2} \sim 54°$ plot corresponds to the (cyan) horizontal line, above which all R' plots exhibit a simple zero crossing (α'_{th3}).

2.4.1.2   Case 1 - $0 \leq \theta_\omega < \theta_\omega^{th1}$

The first case corresponds to θ_ω in the range $0 < \theta_\omega^{th1}$, for which, the plot of Δ' and R' are shown in Fig.2.35 along with the surface-streamline topologies corresponding to chosen values of α'. Δ' starts off from zero at $\alpha' = 0$ (a point of tangency) and increases monotonically implying the absence of any zero crossing. Correspondingly, the streamline topology starts off at $\alpha' = 0$ with a degenerate meridional configuration before becoming a spiralling topology, the spiralling trajectories being organised on the unit sphere by a pair of unstable foci and an entraining limit cycle. The spiralling becomes tighter with increasing α', approaching circular streamlines corresponding to the solid-body rotation topology for $\alpha' \to \infty$. The cubic invariant R' for this case starts off with a finite (negative) value and decreases monotonically with α', implying that R' also does not have a zero crossing. Thus in this case, there are no planar flow configurations. Note that the case of $\theta_\omega = 0$ is a special case that was already encountered in the previous section, where the vorticity vector was aligned with the axis of symmetry of extension $(\epsilon = -2)$. For $\theta_\omega = 0$, the positions of the fixed points (the pair of unstable foci for $\alpha' \neq 0$) remain invariant with increasing α'. In contrast, for all non-zero θ_ω (in the interval under consideration), while the surface-streamline topology does not change with α', the fixed points move from the axis of extension, at $\alpha' = 0$, to the vorticity axis with increasing α'. The same is true of the axis of limit cycle, which changes its orientation from being aligned with the axis of extension, at $\alpha' \ll 1$, to aligned with the vorticity axis for $\alpha' \to \infty$. The limit cycle is always a great circle regardless of it's orientation, on account of the underlying symmetry of the ambient linear flow.
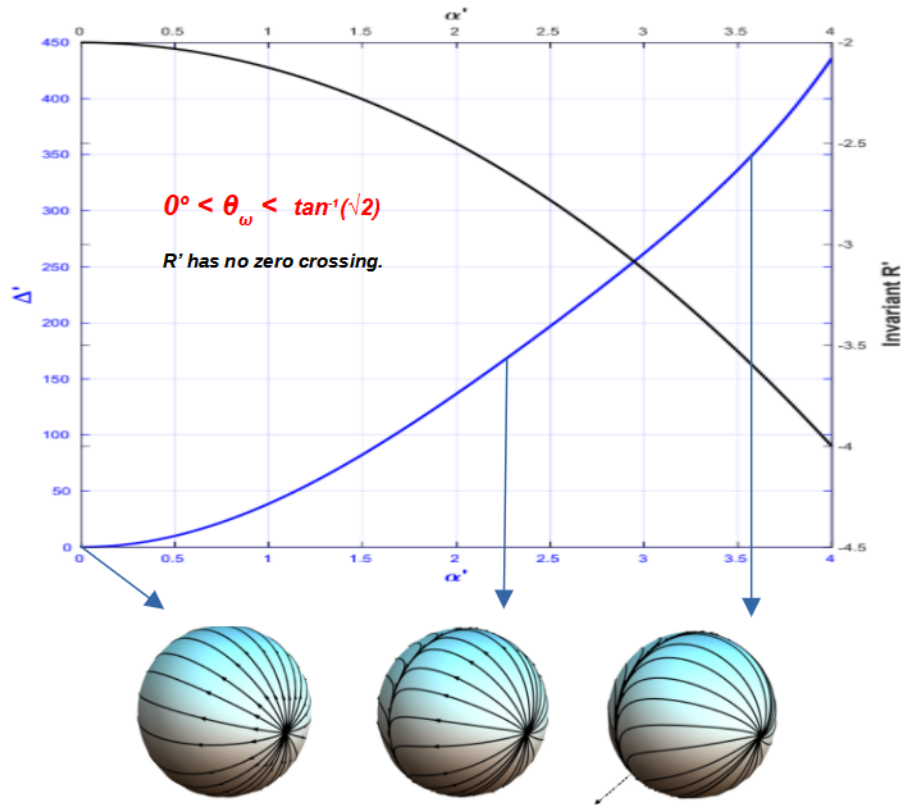
Figure 2.35: Plot of Δ' and R' versus α' for $0 \leq \theta_\omega < \theta_\omega^{th1}$. The discriminant is positive throughout suggesting spiralling streamlines on the drop surface. The finiteness of R' indicates that there are no planar flow configurations in this case.

2.4.1.3   Case 2 - $\theta_\omega^{th1} \leq \theta_\omega \leq \theta_\omega^{th2}$

In this interval, between the two threshold values of θ_ω, Δ' still does not exhibit a zero-crossing but R' does. A representative plot of Δ' and R' as a function of α' along with the surface-streamline topologies corresponding to chosen values of α' is shown in Fig.2.36. In this case too, the streamlines start off as meridians at $\alpha' = 0$, when $\Delta' = 0$. As α' increases, the streamlines acquire a spiralling character, as already seen in Case 1. As one approaches the critical α' (α'_{th3}) corresponding to the zero-crossing of R', remarkably, the spirals become closed orbits. they reflect the fact that the auxiliary linear flow at this point itself has closed elliptical streamlines. These flows are also members of the eccentric planar family which we encountered before and owing to their elliptic character, these flows are named, '*eccentric planar elliptic flows*'. As α' increases beyond this critical point, the unstable foci become stable ones, with the limit cycle now acting as the source. therefore, across the eccentric elliptic flow configuration, the direction of spiralling is reversed. As for the previous case, with further increase of α', the spirals become more tighter and approach a closed streamline configuration for $\alpha' \to \infty$.
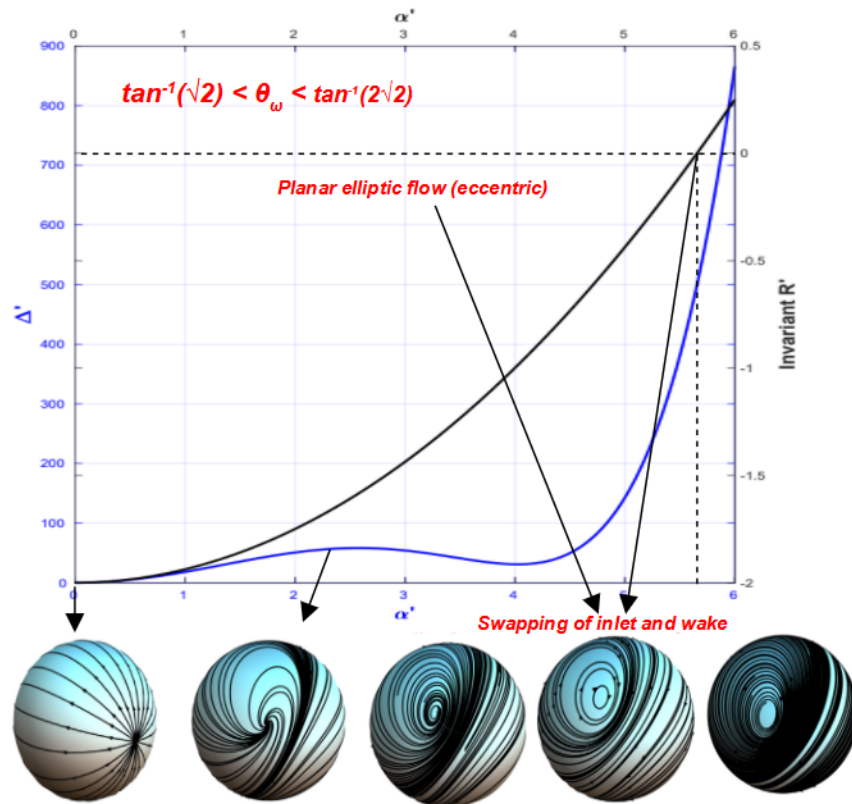
Figure 2.36: Plot of Δ' and R' versus α' for $\theta_\omega^{th1} < \theta_\omega < \theta_\omega^{th2}$. Δ' is positive throughout suggesting spiralling streamlines on the drop surface. At α'_{th3}, R' suffers a zero crossing indicating that there is a planar flow configuration at this point, which happens to be elliptic flows leading to closed streamlines on the drop. This closed-streamline topology mediates a change in the direction of spiralling.

The fact that the flow at $R' = 0$ contains elliptic streamlines is also corroborated by the plot in Fig.2.37, where the quadratic invariant Q' is plotted along with R' and we see that $Q' > 0$ when $R' = 0$, just like it is for the canonical elliptic flows. The eccentric elliptic flows are generalisations of the canonical planar elliptic flows, much like their hyperbolic counterpart that we encountered before. These flows also have the unique property that they remain planar despite the existence of a non-trivial extensional component perpendicular to the plane of flow. However, note that the occurrence of planar hyperbolic flows was merely incidental as far transport is concerned, but as we shall see later, the eccentric elliptic flows, profoundly influence the transport rate.
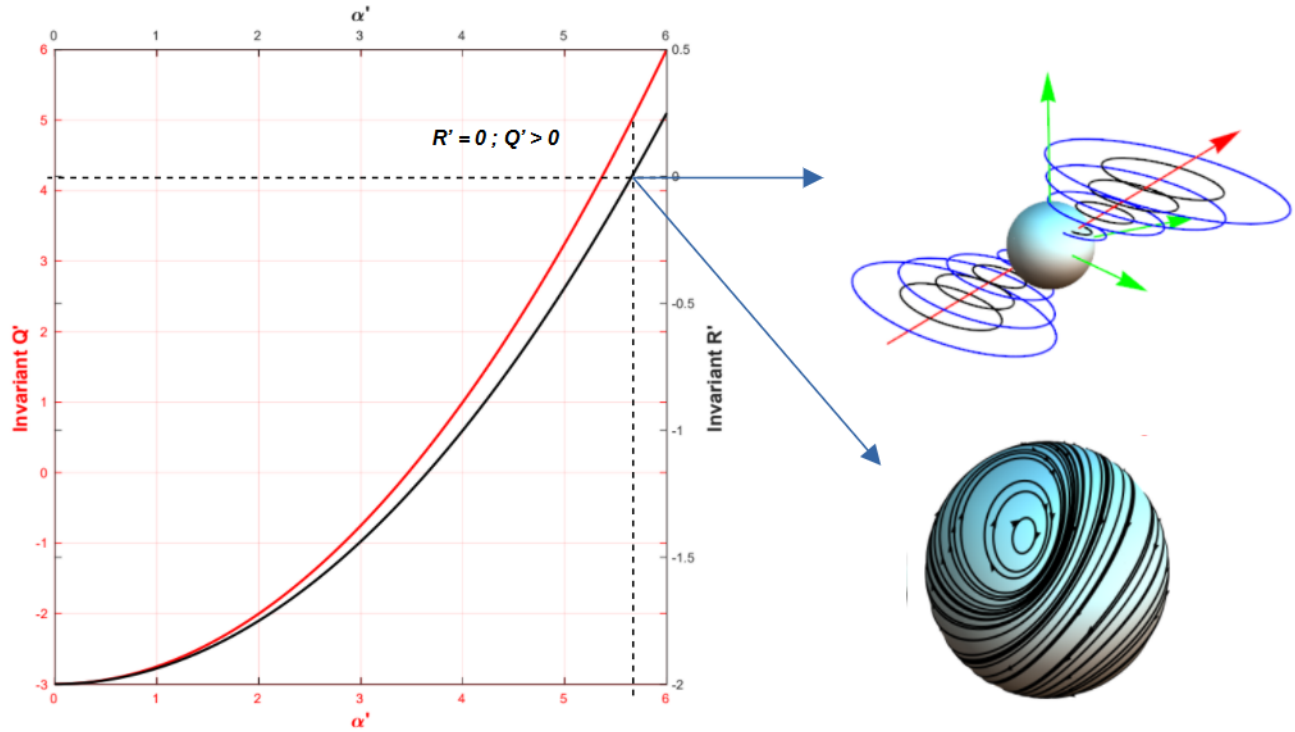
Figure 2.37: Plot of Q' and R' versus α' for $\theta_\omega^{th1} < \theta_\omega < \theta_\omega^{th2}$. Q' is positive when $R' = 0$, suggesting that the planar flow topology is elliptic. The figure on top shows the $3D$ auxiliary linear flow, consisting of elliptic streamlines situated on two different double cones, whose projection on the drop surface leads to the topology shown below, with eccentrically located elliptic streamlines.

We now examine the transition values of θ_ω associated with this interval, starting with $\theta_\omega = \theta_\omega^{th1} = \tan^{-1}\sqrt{2}$. Here, the behavior of Δ' and R' are the same as for the other values θ_ω in this interval. The streamlines remain spiralling throughout, starting off with a degenerate meridional topology, and become closed streamlines at $\alpha' = \infty$. However, the other transition value, θ_ω^{th2} is non-trivial. Given that we have encountered generalisations of the canonical elliptic flows above and hyperbolic planar flows, it is natural to seek the existence of a generalisation of the canonical simple shear flow, which we encounter in the transition case of $\theta_\omega = \theta_\omega^{th2} = \tan^{-1} 2\sqrt{2}$. Recall that this is the threshold value at which Δ' exhibits a zero, which in this case is a doubly degenerate point ($\Delta' = d\Delta'/d\alpha' = 0$; a point of tangency). While majority of the features associated with the surface streamlines mentioned above, hold true for this case, the point at which $R' = 0$ (α'_{th3}) also happens to be the point at which $\Delta' = 0$, which leads to the fact that the flow topology associated with this point is planar and has parabolic streamlines (see Fig.2.38). This flow is the 'planar parabolic flow' and is the generalisation of the canonical simple shear flow, for Q' is also 0 at this point. This flow also mediates a change in the direction of spiralling, much like the eccentric planar elliptic flows. Thus, we see that the generalisations of the canonical planar flow family has quadratic curves for streamlines, but, with the neutral direction (zero velocity) inclined non-trivially to the plane of flow.
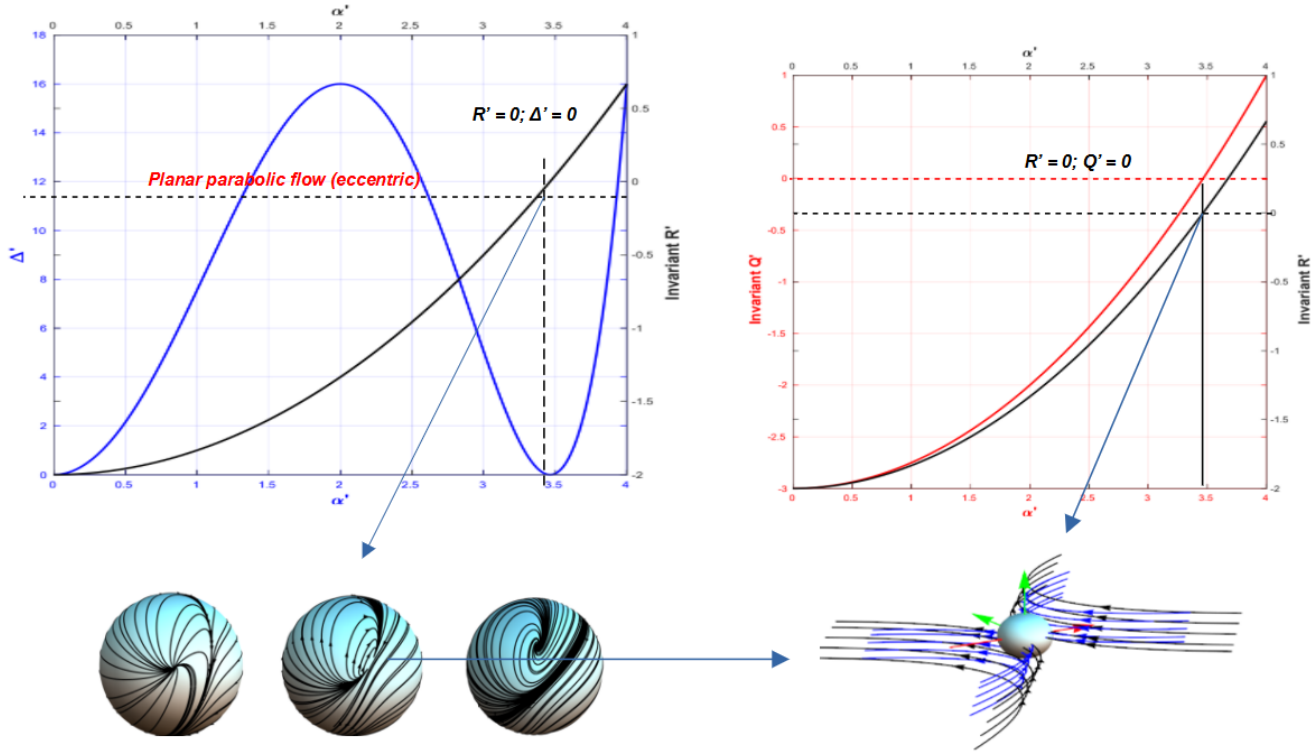
Figure 2.38: Plot of (a) Δ' and R' versus α' and (b) Q' and R' versus α' for $\theta_\omega = \theta_\omega^{th2}$. Δ' is positive throughout without any zero-crossing. At $\alpha'_{th3} = 2\sqrt{3}$, R' suffers a zero crossing indicating that there is a planar flow configuration at this point, which happens to be a parabolic flow, as $Q' = 0$. This leads to parabolic (open) streamlines on the drop. This topology again mediates a change in the direction of spiralling. The bottom right figure shows the $3D$ auxiliary flow streamlines at this point which are parabolas.

2.4.1.4 Case 3 - $\theta_\omega^{th2} < \theta_\omega \leq \pi/2$

In this final case, Δ' suffers two zero-crossings at α'_{th1} and α'_{th2}, between which Δ' is negative. As can be seen in Fig.2.39, it starts off from 0 at $\alpha' = 0$, and is positive as α' increases up to α'_{th1}. At this first zero-crossing Δ' changes sign and remains negative until the second crossing at α'_{th2}, beyond which it is positive again. In the regions where Δ' is positive, the surface-streamlines have a spiralling character, similar to the spiralling topologies encountered in the previous cases. The streamline topology corresponding to $\Delta' < 0$ consists of non-spiralling streamlines organised by three pairs of fixed points; a pair of saddles and a pair each of unstable and stable nodes, with the streamlines running from the stable to unstable node. The manifolds of the saddle points, divide the sphere into eight unequal octants, which, unlike the non-spiralling configuration of the aligned-vorticity case, is highly skewed, with the saddle points, no longer situated along a line orthogonal to the great circle containing the stable and unstable nodes. The axis of the great circle is itself inclined to the axis of symmetry of extension in a non-trivial fashion. This region of non-spiralling streamlines now mediate a change in the spiralling direction, with the spirals running from an unstable focus to a limit cycle below α'_{th1} and from the limit cycle to a stable focus after the zero-crossing at α'_{th2}. In this case too R' suffers a zero-crossing and the planar flow configuration that we encounter is the eccentric planar hyperbolic flows, which are irrelevant from the transport perspective, just like the eccentric planar hyperbolic topologies encountered in the aligned-vorticity case. The limiting scenario in this case is $\theta_\omega = \pi/2$, which was already encountered in the aligned-vorticity case, where it corresponded to $\epsilon = -0.5$, with the vorticity vector perpendicular to the axis of symmetry.
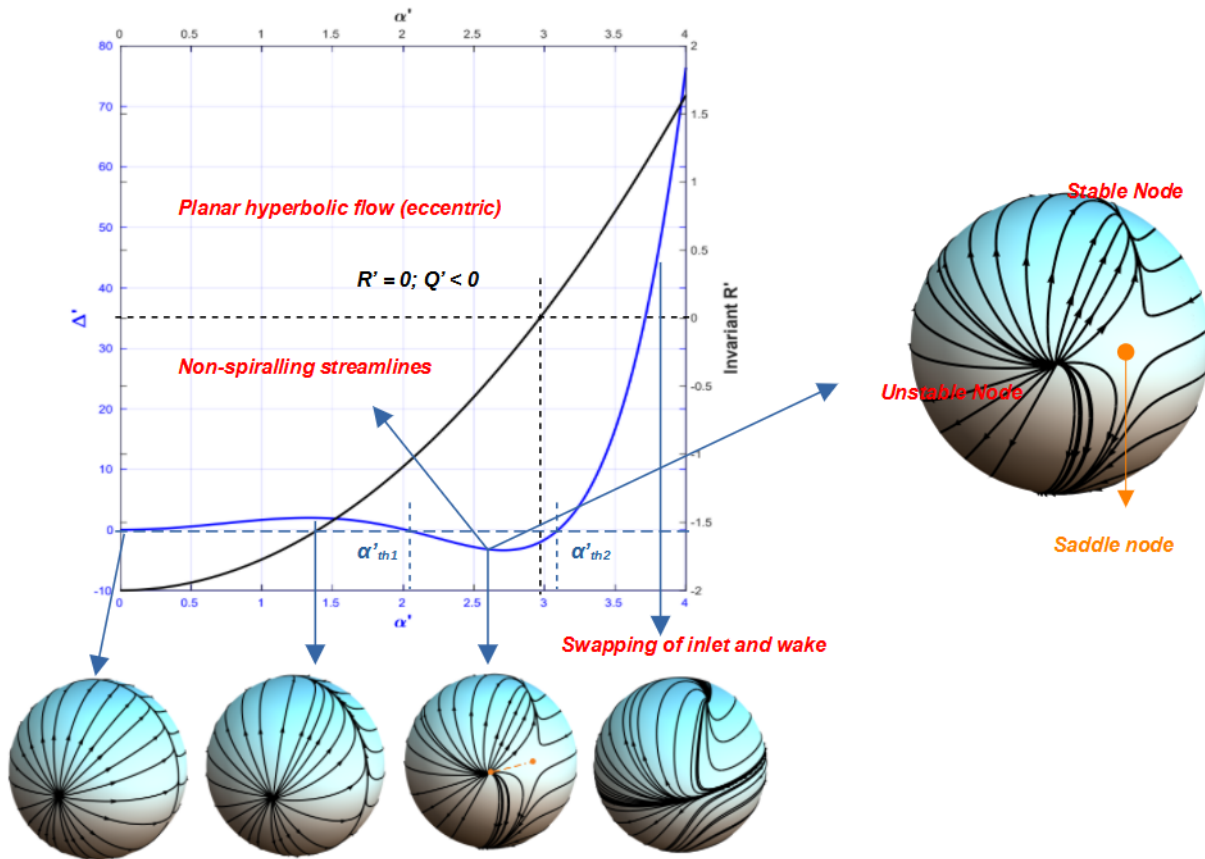
Figure 2.39: Plot of Δ' and R' versus α' for $\theta_\omega^{th2} < \theta_\omega \leq \pi/2$. Δ' is non-monotonic and suffers two zero-crossings at α'_{th1} and α'_{th2}. Between these two points, the streamlines are organised by three pairs of fixed points (see inset) which are topologically equivalent (but are significantly skewed) to the non-spiralling topology encountered in the aligned-vorticity case and they also mediate a change in the spiralling direction. R' suffers zero-crossing leading to eccentric planar hyperbolic flows at α'_{th3}.

This concludes our organisation of streamline topology. We now move on to the eigenvalue analysis that corroborates the features we discussed above and then move to the $C - \tau$ formulation for Nu calculation.

2.4.2 Surface-Streamline Topology - Eigenvalue Analysis

In this section, we analyse the eigenvalues of the auxiliary linear system to support the conclusions drawn in the previous section regarding the streamline topology. The eigenvalues of $\hat{\boldsymbol{\Gamma}}$, can be calculated as solutions of the characteristic equation given by:

$$\mu^3 + Q'\mu + R' = 0 \tag{2.136}$$

where Q' and R' are the scalar invariants defined in Eq.2.131 and Eq.2.132 respectively and μ is the eigenvalue. Unlike the aligned-vorticity case, the cubic equation is not factorisable and so the solution is derived using Cardano's method (Arfken et al. (2012)) of solution of a cubic equation. According to this method, we assume an ansatz of the form, $\mu = u + v$, which when substituted in Eq.2.136 yields,

$$u^3 + v^3 + (u + v)(3uv + Q') + R' = 0. \tag{2.137}$$

Setting $3uv + Q' = 0$ in the above equation we get the system of equations:

$$u^3 + v^3 = -R' \tag{2.138}$$

$$u^3 v^3 = -Q'^3/27 \tag{2.139}$$

where the second equation is obtained by cubing the condition $3uv = -Q'$. The above system of equations suggest that u^3 and v^3 are such that they have $-R'$ as the sum and $-Q'^3/27$ as their product, which immediately tells us that u^3 and v^3 are solutions of the quadratic equation,

$$t^2 + R't - Q'^3/27 = 0, \tag{2.140}$$

for which the solutions are given by:

$$u^3 = \frac{-R' + \sqrt{R'^2 + \frac{4Q'^3}{27}}}{2} \tag{2.141}$$

$$v^3 = \frac{-R' - \sqrt{R'^2 + \frac{4Q'^3}{27}}}{2}. \tag{2.142}$$

Thus the eigenvalues are given by the sum of the cube roots of u^3 and v^3 (i.e. $\mu = (u^3)^{1/3} + (v^3)^{1/3}$), which also involves the cube roots of unity $(1, \omega = \frac{1+\imath\sqrt{3}}{2}, \omega^2 = \frac{1-\imath\sqrt{3}}{2})$. Thus, we have nine possible solutions (the nine combinations involving u, $u\omega$, $u\omega^2$ and v, $v\omega$, $v\omega^2$), of which six solutions are degenerate and the three valid ones correspond to those combinations that satisfy $uv = -Q'/3$. Substituting for R', Q' and realising that $\Delta' = 4Q'^3 + 27R'^3$, we get:

$$u^3 = \frac{-\left(\frac{-8+\alpha'^2(1-3\cos^2\theta_\omega)}{4}\right) + \frac{1}{3\sqrt{3}}\sqrt{\frac{3((\alpha'^2-12)^3+27(-8+\alpha'^2(1-3\cos^2\theta_\omega))^2)}{16}}}{2} \tag{2.143}$$

$$v^3 = \frac{-\left(\frac{-8+\alpha'^2(1-3\cos^2\theta_\omega)}{4}\right) - \frac{1}{3\sqrt{3}}\sqrt{\frac{3((\alpha'^2-12)^3+27(-8+\alpha'^2(1-3\cos^2\theta_\omega))^2)}{16}}}{2} \tag{2.144}$$

We use these expressions along with the constraint $uv = -Q'/3$, to get the correct set of eigenvalues and plot them as a function of α' for different values of θ_ω (belonging to the three intervals seen before) and correlate them to the surface-streamline topology. We note here that, while in principle, the non-degenerate eigenvalues that satisfy this constraint can be written as $u + v$, $u\omega + v\omega^2$, $u\omega^2 + v\omega$, where u and v are real, finding u and v using the symbolic manipulation package $Mathematica^{\circledR}$, which we have used in our study, was not possible. This is because the software does not factor out the real solution from $(1)^{1/3}$ when finding the cube root of Eq.2.143-2.144. So, we are not able to provide closed-form expressions for u and v (and hence the eigenvalues) at this point. To analyse the nature of the fixed points in the streamline topology, we need the eigenvalues of the non-linear surface velocity field about these fixed points. But, since the streamline topologies encountered for this case are distorted versions of the aligned-vorticity ones, the analysis does not convey anything new about the nature of the fixed points. So, we only show a representative calculation for a single value of θ_ω for the want of brevity.

2.4.2.1   Case 1 - $0 \leq \theta_\omega < \theta_\omega^{th1}$

In this range, recall that the streamline topology consisted entirely of spiralling streamlines, which originate at a pair of unstable foci and terminate at a limit cycle (Fig.2.35). Correspondingly, in Fig.2.40, for the case of $\theta_\omega = \pi/4$, we see that the a pair of eigenvalues are imaginary and the other one is real valued. The real part of both imaginary eigenvalues are positive and the real eigenvalue is negative, which implies that the streamline topology is spiralling.
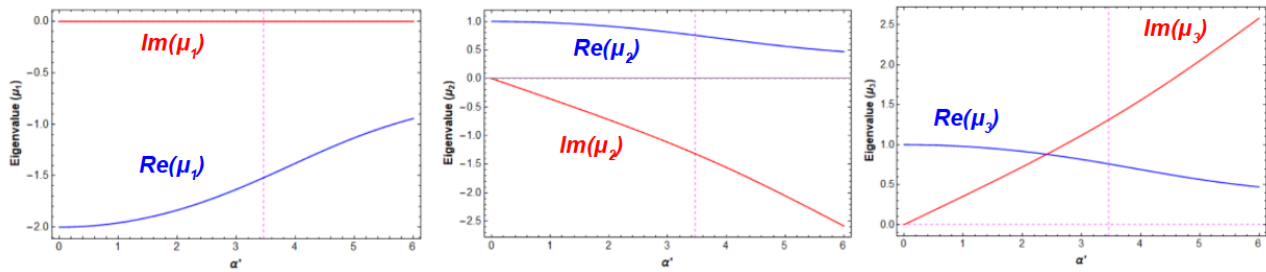
Figure 2.40: Eigenvalues of the auxiliary flow for $0 \leq \theta_\omega < \theta_\omega^{th1}$, where μ_1 is purely real (negative) and μ_2, μ_3 are complex, with positive real parts, consistent with the streamline topology encountered for this case. The vertical line marks $\alpha' = \sqrt{12}$ where the valid set of eigenvalues change to a different combination.

We also plot the eigenvalues about the focus, for the same value of parameters ($\theta_\omega = \pi/4$, and at specific values of α'), which suggests that the focus is an unstable one as both the eigenvalues are complex with a positive real part as seen in Fig.2.41a. Therefore, this confirms that the surface-streamline topology consists of spiralling streamlines originating at a pair of unstable foci and terminating at a limit cycle. This real part approaches 0 as $\alpha' \to \infty$, implying that it becomes a center at $\alpha' = \infty$, consistent with the fact that it corresponds to solid-body rotation with concentric circles as surface streamlines. As noted in the discussion on streamline topology, the fixed point(focus), moves from the axis of extension, at $\alpha' = 0$, to the vorticity axis ($\theta_\omega = \pi/4$ in this illustration) for $\alpha' \to \infty$. This can be seen by tracking the orientation of the real eigenvector (whose intersection with the unit sphere gives the location of the fixed point) with respect to axis of symmetry of extension as a function of α' and this has been plotted in Fig.2.41b, where we see that as $\alpha' \to \infty$, the eigenvector approaches $\theta_\omega = \pi/4$. Also, the limit cycle changes its orientation with α' starting off orthogonal to the axis of symmetry of vorticity axis as $\alpha' \to \infty$. This has also been portrayed in Fig.2.41b, where the orientation of the normal to the plane of the limit cycle with x_1 axis is plotted as a function of α'. These two inclinations are different suggesting that the topology is skewed.
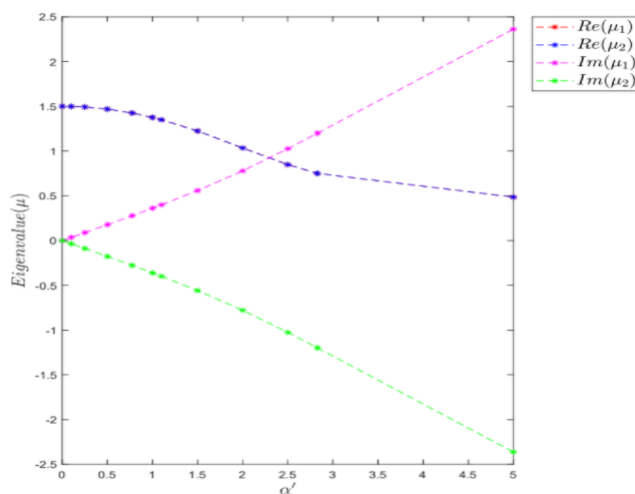
(a) Eigenvalues about the focus.
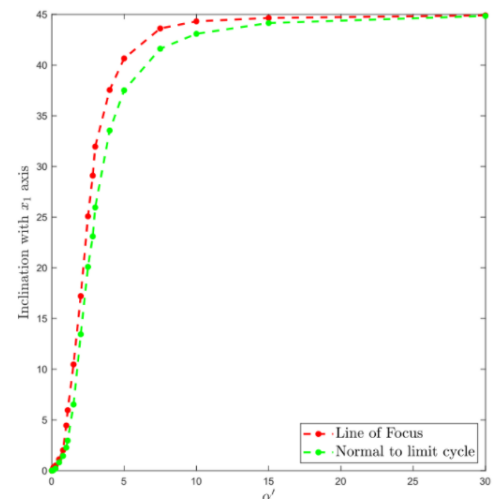
(b) Inclination of focus and limit cycle.

Figure 2.41: Plot of (a) Eigenvalues of the auxiliary flow about the fixed point (focus) for $\theta_\omega = \pi/4 < \theta_\omega^{th1}$, where the eigenvalues are both complex numbers with a positive real part. (b) Angle of inclinations of the line passing through the focus and the normal to limit cycle with x_1 axis (axis of symmetry), which are different, showing the underlying skewness of the topology. As $\alpha' \to \infty$, the inclination of both approach $\pi/4$, where both vectors align with vorticity axis at $\alpha' = \infty$.

2.4.2.2 Case 2 - $\theta_\omega^{th1} \leq \theta_\omega \leq \theta_\omega^{th2}$

The streamline topology in this interval still exhibits a spiralling character with the exception of the topologies associated with the eccentric planar flows, which mediate a change in the direction of spiralling (Fig.2.36). Correspondingly, the eigenvalues of the auxiliary linear system are similar to the previous case until the point of occurrence of eccentric planar flow (α_{th3}'). This can be seen in Fig.2.42, where two of the eigenvalues are complex with positive real parts while the third one is real and negative until this point, consistent with a spiralling topology organised by a pair of unstable foci and an entraining limit cycle. At $\alpha' = \alpha_{th3}'$, the real eigenvalue is zero, while the complex ones are purely imaginary, consistent with the elliptic planar flow configuration. Beyond α_{th3}', the direction of spiralling is reversed as the eigenvalues change sign at this point. So the foci have become stable ones with the limit cycle acting as the source.

The transition value of $\theta_\omega = \theta_\omega^{th1}$, as we saw earlier, is qualitatively similar to any other θ_ω in the interval with the exception that there is no zero-crossing in R'. Therefore, the eigenvalues of the auxiliary system for this case would exhibit a similar behavior, except that there will be no critical point (α_{th3}') across which the eigenvalues change sign. So the streamline topology will have a spiralling character for all α', with no change in the spiralling direction.

For the other transition case of $\theta_\omega = \theta_\omega^{th2}$, we saw earlier that a planar parabolic flow mediates the change in spiralling direction (Fig.2.38) and this too can be seen from the plot of auxiliary flow eigenvalues shown in Fig.2.43. Unlike the previous case, at $\alpha' = \alpha_{th3}'$, the eigenvalues are all identically zero, implying that the planar flow topology has parabolic streamlines, which is a generalisation of simple shear flow. In this interval, again, the focus and the normal to the plane of limit cycle continue to change their orientation with α', eventually aligning with the vorticity direction at $\alpha' = \infty$.
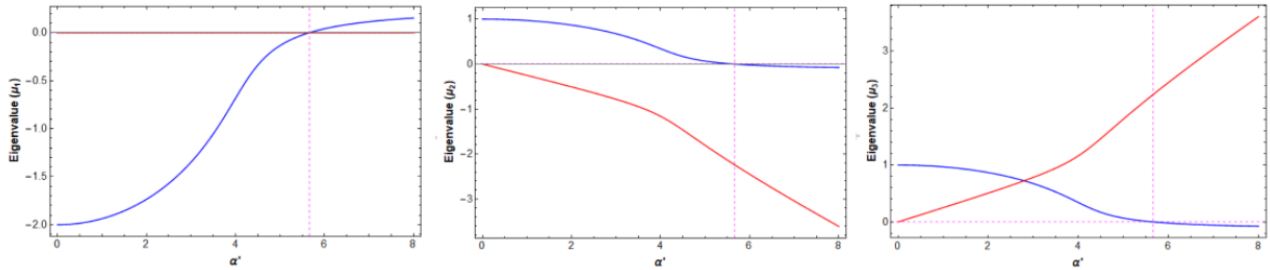
Figure 2.42: Eigenvalues of the auxiliary flow for $\theta_\omega^{th1} < \theta_\omega < \theta_\omega^{th2}$, where μ_1 is purely real and μ_2, μ_3 are complex. At α_{th3}', the eigenvalues are purely imaginary, indicating the presence of eccentric planar elliptic flows and beyond this point, the eigenvalues change signs indicating a change in spiralling direction.
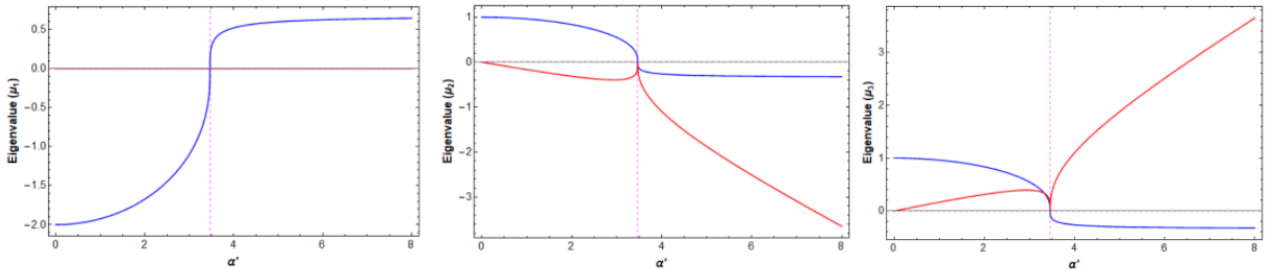
Figure 2.43: Eigenvalues of the auxiliary flow for $\theta_\omega = \theta_\omega^{th2}$, where at α_{th3}', the eigenvalues are all identically zero, implying the presence of eccentric planar parabolic flow, which is a generalisation of simple shear flow.

2.4.2.3 Case 3 - $\theta_\omega^{th2} < \theta_\omega \leq \pi/2$

In this final interval of θ_ω, we saw that the discriminant suffers two zero-crossings (α'_{th1} and α'_{th2}) leading to an intermediate region of non-spiralling streamlines on the drop surface (Fig.2.39). Correspondingly, as seen from Fig.2.44, the eigenvalues of the auxiliary flow, exhibit an intermediate region (again between α'_{th1} and α'_{th2}) where all eigenvalues are real. For $\alpha' < \alpha'_{th1}$ and $\alpha' > \alpha'_{th2}$, two of the eigenvalues are complex and the third one is real. The eigenvalue μ_1 which was real before α'_{th1}, becomes complex after α'_{th2}. Similarly μ_3, which was a complex value before α'_{th1} becomes real after α'_{th2}. μ_2 is the only eigenvalue that remains complex for $\alpha' < \alpha'_{th1}$ and $\alpha' > \alpha'_{th2}$. However, the real part of μ_2 changes beyond α'_{th2}. These features are consistent with the streamline topology that we encountered, where the intermediate region with all three real eigenvalues, mediate a change in direction of spiralling. We see that in this intermediate region, there is an α'_{th3}, corresponding to $R' = 0$, where one of the eigenvalues is zero, while the other two are equal and opposite, making this the point of occurrence of eccentric planar hyperbolic flows.
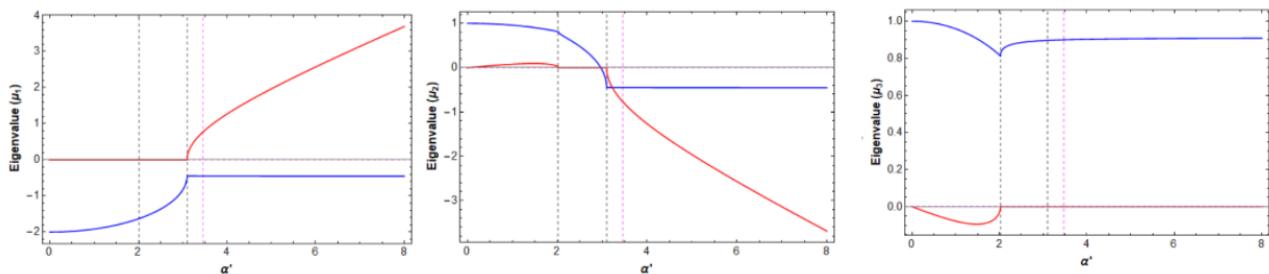
Figure 2.44: Eigenvalues of the auxiliary flow for $\theta_\omega^{th2} < \theta_\omega \leq \pi/2$, where the eigenvalues are purely real for $\alpha'_{th1} < \alpha' < \alpha'_{th2}$ (marked by the two black vertical lines). In this region, the streamlines are non-spiralling. In this intermediate region μ_2 crosses zero at α'_{th3} where, the other two eigenvalues are equal and opposite, corresponding to the point of occurrence of eccentric planar hyperbolic flows.

This concludes the section on streamline topology analysis. As noted earlier, the surface-streamline topologies of this two-parameter family are distorted versions of the topologies encountered for the aligned-vorticity case, and are therefore topologically equivalent to them. This implies that the $C - \tau$ formulation developed for the aligned-vorticity case can be extended to this case as well, which we discuss next.

2.4.3 The $C - \tau$ Coordinate System

In this section, we derive the $C - \tau$ coordinate system for the case of inclined vorticity with axisymmetric extension. Unlike the previous case, where the $C - \tau$ definitions were derived from the solutions to the surface-velocity field in spherical coordinates, here we derive it from the solutions of the auxiliary flow. The solutions to the auxiliary flow can be formally written as a function of eigenvalues and eigenvectors (Eq.2.125), which are in turn related to the flow parameters (see Eqs.2.143-2.144). This formal solutions is available in terms of the Cartesian coordinates, but the $C - \tau$ definitions shown earlier (Eqs.2.70-2.73, Eqs.2.76-2.77) are in terms of the spherical coordinates. Thus it is imperative to revisit the $C - \tau$ definitions of the aligned-vorticity case, in order to gain further insights that would aid in defining the $C - \tau$ system for the inclined-vorticity case.

As a first step, we note the following features of the $C - \tau$ definitions given in Eqs.2.70-2.73, Eqs.2.76-2.77. In these definitions, we see that:

$$\phi \sim f(\tau) \tag{2.145}$$

$$\theta \sim f(C, \tau). \tag{2.146}$$

The definitions that lead to these features, arise from the integration of the surface streamline equations, which involves two constants of integration. As already noted, one of the constants (ϕ_0) can be set to any convenient numerical value that corresponds to $\tau = 0$ along any surface streamline. This is because the surface streamline equations are an autonomous system of equations, in a coordinate system with its polar axis passing through a fixed point (focus, if the streamlines are spiralling, and any of the three fixed points if they are not; in our case it is the saddle). In the spiralling regime, there is no restriction on this choice, while there is a mild restriction in the non-spiralling regime; in that ϕ_0 cannot correspond to the special values that demarcate the octant boundaries on the hemisphere. Given such a choice of ϕ_0, the variable τ ranges from $-\infty$ to ∞ along any given surface streamline; in the spiralling regime $\tau \to -\infty$ corresponds to the unstable focus and $\tau \to \infty$ to the limit cycle, whereas, in the non-spiralling regime, $\tau \to -\infty$ corresponds to the unstable node and $\tau \to \infty$ to the stable node. With this choice of ϕ_0, the other constant of integration can be chosen as $C \sim \tan\theta_0$ (where θ_0 is the value of θ associated with a given streamline at this ϕ_0). For the aligned-vorticity case, we had chosen $\phi_0 = \pi/4$. Note that, all of the surface-streamline topology for the aligned vorticity case have the location of the (pair) saddles (or foci for spiralling regime) being invariant to a change of flow parameters. The line connecting the saddles (or foci) is always along the normal to the plane containing the other fixed points (or the limit cycle). Thus in a spherical coordinate system, the obvious choice for the polar axis is the line passing through the saddle (or focus), in which case, the plane of the great circle connecting the other two fixed points (or the limit cycle)[4], corresponds to $\pi/2$. Thus using the above methodology immediately leads to saddles (or foci) being mapped to $C = 0$ and the great circle (or limit cycle) to $C = \infty$. We now make use of the aforementioned insights to define the $C - \tau$ system for the inclined-vorticity case, where, in general, the polar axis (containing the saddle (or focus)) is not coincident with the normal to plane of the limit circle.

A typical spiralling streamline topology for our case is shown in Fig.2.45, where the polar axis of original spherical coordinate system does not contain the focus. In the figure on the right, we have rotated the original system, such that the polar axis passes through the focus to be consistent with the aligned-vorticity case. However, in general, it will still not coincide with the normal to the plane of limit cycle. If we choose an arbitrary ϕ as the initial arc, we see that the limit cycle will not necessarily correspond to $\theta = \pi/2$, thereby corresponding to a finite C value, inconsistent with the previous case. But this can be addressed as follows: Taking an arbitrary ϕ_0, we first find the θ value corresponding to the limit cycle along this initial arc (θ_0'). This will correspond to a C value given by $C^* \sim \tan(\theta_0')$. We can then simply rescale C as:

$$C' = \frac{CC^*}{(C + C^*)} \tag{2.147}$$

Now, using C' as the new arbitrary constant for the θ integration, will lead to a scenario where $C = \infty$ will correspond to the limit cycle. This ensures continuity with the aligned-vorticity case and satisfies both the criteria highlighted in Eq.2.145-2.146. The same procedure can be extended to the non-spiralling case, where the position of the great circle (C^*) can be found by choosing a suitable ϕ_0 that doesn't coincide with any of the special curves. But this procedure has to be repeated for each of the octants individually. With this clarification, we will now see how to enforce these conditions using the solutions of the auxiliary flow equations.

---

[4]Recall from Section. 2.3.3.2, that the inversion symmetry implies that the limit cycle must always be a great circle
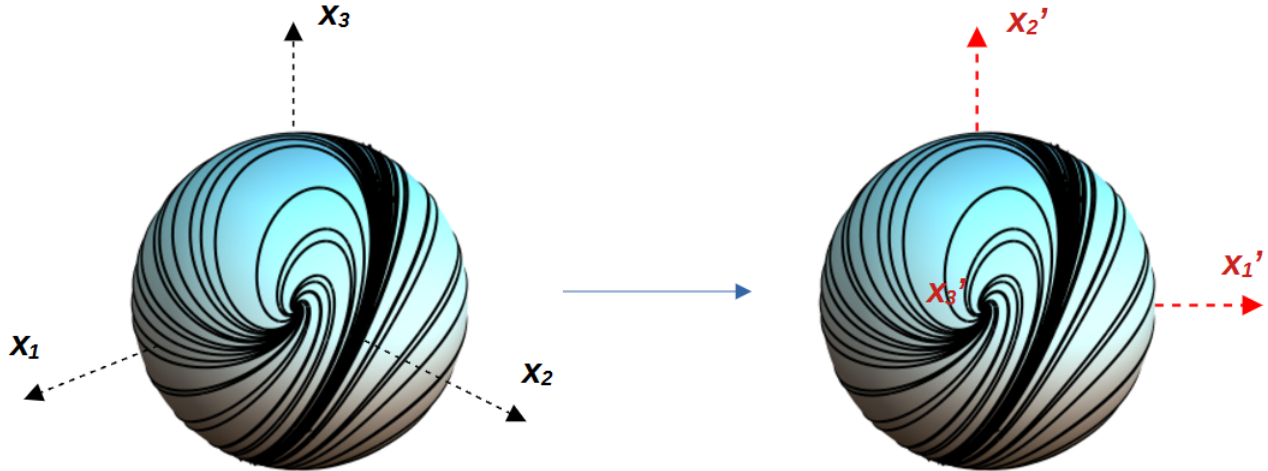
Figure 2.45: Typical spiralling streamline topology for the case of axisymmetric extension with inclined vorticity, showing how the topology is oriented to the original coordinate system (x_1, x_2, x_3) and the new coordinate (x'_1, x'_2, x'_3) system with its polar axis through the focus.

The solutions to the auxiliary flow for this case is written in terms of the eigenvalues and eigenvectors as given in Eq.2.125. In the rotated coordinate system, the solutions will have the same form (x'_1, x'_2, x'_3), with the exception being that the eigenvectors have to calculated for the rotated velocity-gradient tensor $\hat{\Gamma}' = M^{-1}\hat{\Gamma}M$, where M is the matrix of transformation. The matrix M is rotates the polar axis of the original coordinate system to align with the real eigenvector of $\hat{\Gamma}$, whose intersection with the unit circle gives the focus. Thus, we can represent the solutions in the rotated coordinate system as:

$$x' = S'^{-1}\hat{D}'S'(x'_0) \tag{2.148}$$

where the primed quantities are now in the rotated frame. The vector $x'_0 = [x'_{10}, x'_{20}, x'_{30}]^T$ marks the initial points in the Cartesian system. In spherical coordinate system, they can be used to define the initial ϕ' and θ' as:

$$\phi'_0 = \tan^{-1}\left(\frac{x'_{20}}{x'_{10}}\right) \tag{2.149}$$

$$\theta'_0 = \tan^{-1}\left(\frac{(x'^2_{10} + x'^2_{20})^{1/2}}{x'_{30}}\right) \tag{2.150}$$

Thus choosing a ϕ_0 or θ_0 is equivalent to assigning values for the initial Cartesian coordinates. In our case, we choose $\phi_0 = \pi/4$, implying that $x'_{10} = x'_{20} = 1$ and θ_0 should be set such that it satisfies the criteria $\theta_0 \sim \tan^{-1} C'$. Thus we set $x'_{30} = 1/C' = (C + C^*)/CC^*$. This implies that our solution is given by:

$$x' = \begin{bmatrix} x'_1 \\ x'_2 \\ x'_3 \end{bmatrix} = S'^{-1}\hat{D}'S' \begin{bmatrix} 1 \\ 1 \\ \frac{C+C^*}{CC^*} \end{bmatrix} \tag{2.151}$$

where the matrix $\hat{D}'$, contains the time variable which we simply rename τ. We can then project the

solutions onto the unit sphere merely by writing it in terms of spherical coordinates θ' and ϕ' as:

$$\tan \phi' = \frac{x'_2}{x'_1} = f(\tau) \tag{2.152}$$

$$\tan \theta' = \frac{(x_1'^2 + x_2'^2)^{1/2}}{x'_3} = f(C, \tau) \tag{2.153}$$

which defines the relation between the spherical and $C - \tau$ system for this case. In this formulation, the τ variable ranges from $-\infty$ to ∞, regardless of the regime under consideration, just like the aligned-vorticity case. In the next section, we make use of this formalism to calculate Nu for various parameter values corresponding to the different streamline topologies we encountered.

2.4.4 Heat Transfer Analysis

Having derived the $C - \tau$ equations from the solutions of auxiliary system, we can readily use them to calculate Nu as given in Eq.2.106. We do this Nu calculation numerically, for a fixed θ_ω, corresponding to the three distinct intervals we encountered in the surface-streamline topology analysis (Section 2.4.1), and calculate Nu as a function of α'. For each (θ_ω, α') pair, we first calculate the eigenvalues and eigenvectors in a coordinate system with its polar axis along one of the foci (for spiralling streamlines) and along the one of the saddle points (for non-spiralling ones), then use them to construct the auxiliary flow solutions, which are then projected onto the unit sphere by writing the solutions in terms of the spherical coordinates θ', ϕ', whilst substituting for the initial points as shown in Eq.2.151. These equations then define the $C - \tau$ system (where τ is just the dimensionless time variable t), which we substitute in the expression for Nu. Note that the integrating factor Q can be calculated in terms of $hk \sin \alpha 1$, which is written as a function of θ' and ϕ' as:

$$hk \sin \alpha 1 = \frac{\partial(\tan \theta')}{\partial C} \frac{d(\tan \phi')}{d\tau} \frac{\tan \theta}{(1 + \tan^2 \phi')(1 + \tan^2 \theta')^{3/2}} \tag{2.154}$$

using chain rule of differentiation and the definitions of τ and C. Then one can substitute the aforementioned expression into Eq.2.106 to calculate Nusselt number. Note that, if the streamline topology has a spiralling character, then the limits on C integration run from C^* to $C^* f(\nu)$, where ν is the period of τ, corresponding to a single 2π turn of the streamline. This period is again dependent on the flow parameters α' and θ_ω and an explicit form for this is not known for arbitrary values of these parameters, but is rather obtained by substituting for the specific flow parameters as,

$$\phi'(\tau = \nu) = \phi'_0. \tag{2.155}$$

The function $f(\nu)$ can be evaluated as:

$$f(\nu) = \frac{1}{C^*} \frac{\tan \theta'(\nu, C^*)}{\tan \theta'(0, C^*)} \tag{2.156}$$

For the non-spiralling case, $C \in [0, \infty]$, while $\tau \in [-\infty, \infty]$. We will use this procedure to calculate Nu as a function of α' at a given θ_ω, which are chosen from the three distinct intervals in which we analysed the surface-streamline topology.

Before we set out to do this calculation, we derive the asymptotes of Nu for small and large α'. This is possible since the solutions for $\alpha' = 0$ and $\alpha' = \infty$ are canonical ones, corresponding to axisymmetric extension and solid-body rotation respectively, for which the Nusselt number for $Pe \gg 1$ is well known (Gupalo and Riazantsev (1972), G. L. Leal (2007)). For $\alpha' = 0$, we saw from the previous section on aligned-vorticity, that $Nu = P\hat{e}^{1/2}\sqrt{3/\pi})$ and for solid-body rotation, owing to closed-streamlines in the

boundary layer, we have $Nu/\hat{Pe}^{1/2} = 0$. For small α', we can calculate Nu as an asymptotic correction to the Nu for the axisymmetric extension case and for large α', we can perturb the velocity field associated with solid-body rotation to calculate Nu. In both these limits, the leading order velocity field is a function of λ, but for the sake of convenience in readily using the asymptotic results in validating the Nusselt surface calculated using the $C - \tau$ formulation, we set $\lambda = 0$. This is because, the Nusselt surface in the $C - \tau$ formulation, is plotted as a function of the rescaled Peclet number $\hat{Pe}$, which is the same as the original, unscaled definition Pe for $\lambda = 0$. While these asymptotic calculations serve as validations for our numerical evaluation of Nu, they are also indispensable, as the nature of spiralling in both these limits makes evaluation of Nu using the $C - \tau$ formalism infeasible. This is due to the fact that for $\alpha' \ll 1$, the streamlines are tightly wound near the focus and the limit cycle and are stretched in the hemispherical region between them, where they do not even complete one visible turn. This implies that the limits of integration $C^* f(\nu)$ (in Eq.2.106), will either be exponentially small or large and it is extremely difficult to carry out numerical integrations with such small or large limits even with double floating-point accuracy. In the other limit, the tight nature of spiralling implies that the lower (C^*) and upper ($C^* f(\nu)$) limits of integration approach each other (i.e. $f(\nu) \ll 1$)close to each other and the numerical evaluations break down again. So, we will begin with the calculation of small α' asymptote and then move on to the other limit, before coming back to the evaluation of Nu surface using $C - \tau$ coordinate system. Note that for both these asymptotes, the result derived is valid for arbitrary θ_ω, since, $\alpha' = 0$, where there is no vorticity, θ_ω is irrelevant and for $\alpha' = \infty$, the focus has approached the axis of the limit cycle.

2.4.4.1   The Nu-Asymptote for $\alpha' \ll 1$

In the limit of small α', we calculate Nu, by expanding it in powers of α', starting from axisymmetric extension ($\alpha' = 0$) as the leading order approximation. The exact solution for the leading order scenario has already been calculated by Gupalo and Riazantsev (1972), who used spherical coordinates to solve the convection-diffusion equation. In order to calculate corrections to the leading order solution, one needs to solve a inhomogeneous convection-diffusion equation using a boundary layer (BL) approximation, which requires the Green's function associated with the operator; which is not available for an arbitrary linear flow. However, Acrivos and Goddard (1965), in the context of finding higher-order corrections to the leading order approximation for Nu, had obtained the Green's function of the convection-diffusion operator (in its BL form) for an arbitrary axisymmetric flow. This Green's function can also be used in the present context, the only difference being that, the forcing functions in our case, at higher orders, are associated with departure from axisymmetry (rather than from non-BL contributions).

We begin with the convection-diffusion equation in the BL form given by:

$$u_y \frac{\partial \Theta}{\partial y} + u_\theta \frac{\partial \Theta}{\partial \theta} + \frac{u_\phi}{\sin\theta} \frac{\partial \Theta}{\partial \phi} = \frac{1}{\hat{Pe}} \frac{\partial^2 \Theta}{\partial y^2} \tag{2.157}$$

where $y = r - 1$, is the distance normal to the surface in the boundary layer and approximation to the Laplacian on the RHS reflects dominance of radial diffusion. This can be written as:

$$P\Theta = 0 \tag{2.158}$$

where P is the differential operator given by:

$$u_y \frac{\partial}{\partial y} + u_\theta \frac{\partial}{\partial \theta} + \frac{u_\phi}{\sin\theta} \frac{\partial}{\partial \phi} - \frac{1}{\hat{Pe}} \frac{\partial^2}{\partial y^2}. \tag{2.159}$$

We can now expand the quantities involved as a power series in α', leading to the following expansions for the differential operator and the BL temperature field as,

$$P = P_0 + \alpha' P_1 + \alpha'^2 P_2 + O(\alpha'^3) \tag{2.160}$$

$$\Theta = \Theta_0 + \alpha' \Theta_1 + \alpha'^2 \Theta_2 + O(\alpha'^3) \tag{2.161}$$

which leads to the following hierarchy of equations:

$$O(1): \ P_0\Theta_0 = 0 \tag{2.162}$$

$$O(\alpha'): \ P_0\Theta_1 + P_1\Theta_0 = 0 \tag{2.163}$$

$$O(\alpha'^2): \ P_0\Theta_2 + P_1\Theta_1 + P_2\Theta_0 = 0 \text{ and so on} \tag{2.164}$$

Now, the velocity field that appears in P has the form,

$$u_r = u_{r0} + \alpha' u_{r1} \tag{2.165}$$
$$u_\theta = u_{\theta 0} + \alpha' u_{\theta 1} \tag{2.166}$$
$$u_\phi = u_{\phi 0} + \alpha' u_{\phi 1} \tag{2.167}$$

where the $O(1)$ quantities correspond to axisymmetric extensional flow, and the $O(\alpha')$ quantities are the terms involving vorticity, which is inclined at an angle θ_ω to the axis of symmetry. Eqs.2.165-2.167 are the exact expressions for the velocity field, and so, as far as the velocity field is concerned, the small-α' expansion terminates at first order. Therefore in the expansion of P, $P_i = 0 \ \forall i \geq 2$ and so in the hierarchy of equations that result from Eq.2.158, $P_0\Theta_i + P_1\Theta_{i-1} = 0$ for $i \geq 2$. Thus, the governing equation at $O(\alpha^2)$ (Eq.2.164) reduces to,

$$P_0\Theta_2 + P_1\Theta_1 = 0. \tag{2.168}$$

We can now substitute for the velocity field in the governing equation at $O(1)$, in order to derive Θ_0.

The velocity field at $O(1)$, corresponding to the drop in an axisymmetric extensional flow, can be written in terms of a Stokes streamfunction ψ_s, given by:

$$\psi_s = \left(\frac{7}{4} - \frac{3}{4r^2} - r^3\right) \cos\theta \sin^2\theta \tag{2.169}$$

with,

$$u_{r0} = -\frac{1}{r^2 \sin\theta} \frac{\partial \psi_s}{\partial \theta} \tag{2.170}$$

$$u_{\theta 0} = \frac{1}{r \sin\theta} \frac{\partial \psi_s}{\partial r}. \tag{2.171}$$

The $O(\alpha')$ components u_{r1} (which is 0), $u_{\theta 1}$ and $u_{\phi 1}$, for the case of drop in an axisymmetric extensional flow with inclined vorticity are given by:

$$u_{\theta 1} = -\frac{1}{2} \sin\theta_\omega \sin\phi, \tag{2.172}$$

$$u_{\phi 1} = \frac{1}{2}(\cos\theta_\omega \sin\theta - \sin\theta_\omega \cos\theta \cos\phi), \tag{2.173}$$

where, the contribution from axisymmetric extension has been accounted for at $O(1)$. The stream function ψ_s can again be expanded in terms of the radial coordinate y, which gives:

$$\psi_s = \psi_s^{(0)}y + \psi_s^{(1)}y^2 + ... \tag{2.174}$$

with $\psi_s^{(0)}$ being:

$$\psi_s^{(0)} = \frac{3}{2} \cos\theta \sin^2\theta \tag{2.175}$$

Using these quantities into P, we get for P_0:

$$P_0 = \frac{\partial \psi_s^{(0)}}{\partial \theta} y \frac{\partial}{\partial y} - \psi_s^{(0)} \frac{\partial}{\partial \theta} - \frac{1}{\hat{P}e} \sin \theta \frac{\partial^2}{\partial y^2}. \tag{2.176}$$

We can now assume an ansatz of the form $y = Y \hat{P}e^{-1/2}$, which eliminates $\hat{P}e$ from the equation and is consistent with the $\hat{P}e^{1/2}$ scaling for Nu for a drop at large $\hat{P}e$. Thus the governing equation at $O(1)$ becomes:

$$\frac{\partial \psi_s^{(0)}}{\partial \theta} Y \frac{\partial \Theta_0}{\partial y} - \psi_0 \frac{\partial \Theta_0}{\partial \theta} - \sin \theta \frac{\partial^2 \Theta_0}{\partial Y^2} \tag{2.177}$$

with the boundary conditions given by:

$$\lim_{Y \to 0} \Theta_0 = \mathcal{H}(\theta) \tag{2.178}$$

$$\lim_{\theta \to 0} \Theta_0 = 0 \tag{2.179}$$

where the first condition with the Heaviside function, pertains to an isothermal drop surface. From this point onwards, we closely follow along the lines of Acrivos and Goddard (1965), by first using a coordinate transformation from of the form:

$$z' = \psi_s^{(0)} Y \tag{2.180}$$

$$t' = \int_0^\theta \psi_s^{(0)}(\theta') \sin \theta' d\theta' \tag{2.181}$$

Using this transformation, the governing equation can be shown to reduce to:

$$\frac{1}{J} \left[\frac{\partial}{\partial t'} - \frac{\partial^2}{\partial z'^2} \right] \Theta_0 = 0 \tag{2.182}$$

where J is the Jacobian of the transformation given by, $J = (\sin \theta (\psi_0^{(0)})^2)^{-1}$. The boundary conditions under this transformation are given by:

$$\lim_{t' \to 0} \Theta_0 = 0 \tag{2.183}$$

$$\lim_{z' \to 0} \Theta_0 = \mathcal{H}(t - 0) \tag{2.184}$$

This operator P_0 in this coordinate system (Eq.2.176), is similar to the diffusion operator, for which the Green's function can be calculated using the method of images. This Green's function is already reported in the paper by Acrivos and Goddard (1965), where it is reported for a generic case, with our specific case of drop corresponding to their n being equal to 1. This quantity n denotes the order of the zero of $\psi_s^{(0)}$ as $Y \to 0$, which in our case is one as can be seen from Eq.2.175. This expression, however, has a typographical error where, in their Eq.4.9, the denominator is missing the quantity $\tau = t - t^*$. The correct Green's function for this case is then given by:

$$G = \frac{(z'z'^*)^{1/2}}{2(t' - t^*)} \exp \left[-(\zeta^2 + \zeta^{*2}) \right] \mathcal{I}_{1/2}(2\zeta\zeta^*) \tag{2.185}$$

where, $\zeta = z'/(2t'^{(1/2)})$, $\zeta^* = z'^*/(2t'^{(1/2)})$ and $\mathcal{I}_{1/2}$ is the Bessel function of order 1/2. Using this Green's function, we can calculate the temperature field Θ_0 as:

$$\Theta_0 = \int_0^{t'} \left[\frac{\partial G(z^*, t^*, z', t')}{\partial z^*} \right]_{z^* \to 0} \mathcal{H}(t' - t^*) dt^* \tag{2.186}$$

where $t^* = 0$ in our case. One can show that the leading temperature field from the above equation reduces to:

$$\Theta_0 = \frac{\Gamma(1/2, \zeta^2)}{\Gamma(1/2)} \tag{2.187}$$

where $\Gamma(1/2, \zeta^2)$ is the incomplete Gamma function given by, $\Gamma(1/2, \zeta^2) = \int_{\zeta^2}^\infty e^{-S} S^{(1/2)-1} dS$. Using this temperature field in the definition for average Nusselt number, Nu_0, we get, at leading order:

$$Nu_0 = \int_0^{t'_m} \int_0^{2\pi} \left(\frac{d\Theta_0}{dz} \right)_{z=0} dt\, d\phi = \sqrt{\frac{3}{\pi}} \tag{2.188}$$

which matches with the value given in Gupalo and Riazantsev (1972), Krishnamurthy and Subramanian (2018a) and our own calculation for axisymmetric extension (Eq.2.116). Here $t'_m = \int_0^{\pi/2} \psi_s^{(0)}(\theta') \sin \theta' d\theta' = 3/8$. We can now use this temperature field in the governing equation at next order given in Eq.2.163. As a first step, we need to derive the operator P_1, which we obtain by substituting for u_{r1} (which is 0), $u_{\theta 1}$ and $u_{\phi 1}$ from Eqs.2.172-2.173 into P, which gives:

$$P_1 = -\frac{\eta}{2} \sin \phi \frac{\partial}{\partial \theta} + \frac{1}{2} \left((1 - \eta^2)^{1/2} - \eta \cot \theta \cos \phi \right) \frac{\partial}{\partial \phi} \tag{2.189}$$

where $\eta = \sin \theta_\omega$. We can rewrite this in terms of the new coordinates z' and t' as:

$$P_1 = -\frac{\eta}{2} \sin \phi \left(\left(\frac{\dot{\psi}_0 z}{\psi_0} \right) \frac{\partial}{\partial z'} + (\psi_0 \sin \theta) \frac{\partial}{\partial t'} \right) + \frac{1}{2} \left((1 - \eta^2)^{1/2} - \eta \cot \theta \cos \phi \right) \frac{\partial}{\partial \phi} \tag{2.190}$$

Thus, the equation to solve at this order for finding Θ_1 is given by:

$$P_0 \Theta_1 = -P_1 \Theta_0 = q(z', t') \tag{2.191}$$

where now P_1 and Θ_0 are given by Eq.2.190 and Eq.2.187 respectively. Both the surface and far-field boundary conditions are homogeneous and are given by:

$$\lim_{t' \to 0} \Theta_1 = \lim_{z' \to 0} \Theta_1 = 0 \tag{2.192}$$

The formal solution of Eq.2.191 can be written in terms of the Green's function above as (Acrivos and Goddard (1965)):

$$\Theta_1 = \int_0^{t'} \int_0^\infty G(z^*, t^*, z', t') J(t^*) q(t^*, z^*)\, dz^*\, dt^* \tag{2.193}$$

After several manipulations, this can be shown to be:

$$\Theta_1 = \frac{e^{-\zeta^2} \left(\sqrt{3} \psi_0 + 2\sqrt{3} t - 3\sqrt{2} t^{1/2} \right) z \eta \sin \phi}{4\sqrt{3\pi} \psi_0 t^{3/2}} \tag{2.194}$$

The Nusselt number at this order is:

$$Nu_1 = \int_0^{t'_m} \int_0^{2\pi} \left(\frac{d\Theta_1}{dz} \right)_{z=0} dt\, d\phi = 0, \tag{2.195}$$

where the RHS is identically zero from the integration of $\sin \phi$ in Eq.2.194. This is expected, since Nu should not change with the reversal in the direction of rotation and thus for all odd orders of α', the Nusselt number should be zero and the first non-zero correction to Nu comes from $O(\alpha'^2)$. Repeating the same procedure for $O(\alpha'^2)$, for which the governing equation is given by,

$$P_0 \Theta_2 = -P_1 \Theta_1 = q(t', z') \tag{2.196}$$

with P_1 and Θ_1 given by Eq.2.190 and Eq.2.194. The formal solution can again be written as:

$$\Theta_2 = \int_0^{t'} \int_0^{\infty} G(z^*, t^*, z', t') J(t^*) q(t^*, z^*) \, dz^* \, dt^* \tag{2.197}$$

which could not be evaluated in closed form. But, substituting this formal expression in the definition of Nu, we get a closed form expression for Nu_2 as:

$$Nu_2 = f(\theta_\omega)\alpha'^2 = \frac{\sqrt{\tfrac{3}{2}}\pi^{3/2}(-2244608 + 222075\pi^2)\sin^2\theta_\omega}{41943040}\alpha'^2 \tag{2.198}$$

The plot of this numerical coefficient $f(\theta_\omega)$ is shown in Fig.2.46, where we see that it is zero at $\theta\omega = 0$, consistent with the fact that Nu is independent of α' at $\theta_\omega = 0$ and it is maximum for $\theta_\omega = \pi/2$.
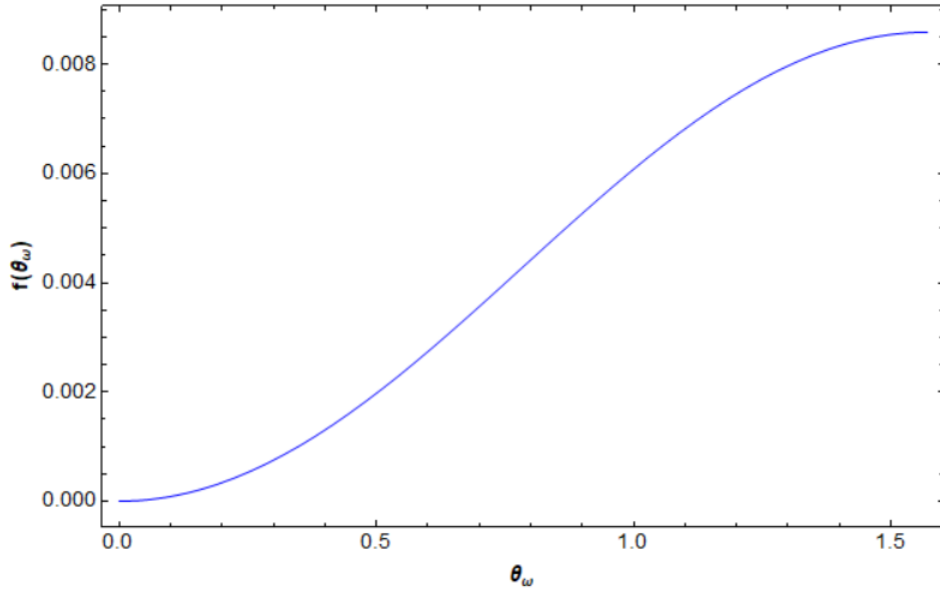
Figure 2.46: Plot of the numerical coefficient $f(\theta_\omega)$ as a function of θ_ω. It is seen that f is 0 at $\theta_\omega = 0$, consistent with the independence of Nu from α' at this value of inclination.

2.4.4.2 The Nu-Asymptote for $\alpha' \gg 1$

In the limit of $\alpha' \to \infty$, the ambient flow is that of solid-body rotation. To calculate the limiting value of Nu in this limit, we follow a procedure akin to that followed in Subramanian and Koch (2006b), where the authors calculate the inertial correction to the Nusselt number for a particle suspended in a planar linear flow. In their case, the leading order Stokesian velocity field is similar to that of solid-body rotation, on account of the streamlines being closed. In their case, the deviation from closed streamlines arises from a weak bi-axial extension at $O(Re)$ driven by inertia. In our case, this weak extension arises on account of $\alpha' \gg 1$. The starting point is again the convection-diffusion equation in BL form given in Eq.2.157. Similar to the previous case, we expand u_r, u_θ and u_ϕ in $1/\alpha'$ as:

$$u_r = u_{r0} + \frac{1}{\alpha'}u_{r1} \tag{2.199}$$

$$u_\theta = u_{\theta 0} + \frac{1}{\alpha'}u_{\theta 1} \tag{2.200}$$

$$u_\phi = u_{\phi 0} + \frac{1}{\alpha'}u_{\phi 1} \tag{2.201}$$

with $u_{r0} = u_{\theta 0} = 0$ and $u_{\phi 0} = -\frac{1}{2}(1+y)\sin\theta$. The $O(1/\alpha')$ corrections are complicated functions of θ_ω and are not reported here, but we report the ϕ-averaged expressions for these quantities at a later stage. Writing the velocity field in this form, suggests that the Péclet number definition for this case is different from the one we have used in the $C - \tau$ formalism. Since the leading order velocity field is that of solid body rotation, the Peclet number in this limit is defined as $Pe' = |\boldsymbol{\omega}|a^2//D$, whereas our original definition is $\hat{P}e = E_2 a^2/(D(1+\lambda))$. So the two definitions are related by $Pe' = \hat{P}e\,\alpha'$, where recall that $\alpha' = (1+\lambda)(|\boldsymbol{\omega}|/E_2)^5$.

From the leading order velocity field we see that $u_{\phi 0}$ is the only contribution on the LHS of Eq.2.157 and since y is of the order of boundary layer thickness at large Pe', the equation at leading order reduces to:

$$\frac{\partial\Theta}{\partial\phi} = 0 \tag{2.202}$$

Thus, to a first approximation, the azimuthal dependence of the temperature field may be neglected and the temperature can be expanded as:

$$\Theta = \Theta_0(r,\theta) + f(Pe',\alpha')\Theta_1(r,\theta,\phi) + ... \tag{2.203}$$

where $f(Pe',\alpha') \ll 1$. Substituting this into the convection-diffusion equation, we get at the first order:

$$(u_{r0} + \frac{1}{\alpha'}u_{r1})\frac{\partial\Theta_0}{\partial y} + \left(\frac{u_{\theta 0} + \frac{1}{\alpha'}u_{\theta 1}}{r}\right)\frac{\partial\Theta_0}{\partial\theta} + f(Pe',\alpha')\left(\frac{u_{\phi 0} + \frac{1}{\alpha'}u_{\phi 1}}{r\sin\theta}\right) = \frac{1}{Pe'}\frac{\partial^2\Theta_0}{\partial y^2} \tag{2.204}$$

Further, averaging over ϕ-coordinate and using the result that the leading order field has closed streamlines, one obtains:

$$\frac{1}{\alpha'}\left(\int_0^{2\pi}\frac{1}{2\pi}u_{r1}d\phi\right)\frac{\partial\Theta_0}{\partial y} + \frac{1}{\alpha'}\left(\int_0^{2\pi}\frac{1}{2\pi}u_{\theta 1}d\phi\right)\frac{\partial\Theta_0}{\partial\theta} = \frac{1}{Pe'}\frac{\partial^2\Theta_0}{\partial y^2} \tag{2.205}$$

The quantities inside the braces, the ϕ-averaged velocity components are given by:

$$\int_0^{2\pi}\frac{1}{2\pi}u_{r1}d\phi = -\frac{3}{8}(1+3\cos(2\theta))(1+3\cos(2\theta_\omega)) \tag{2.206}$$

$$\int_0^{2\pi}\frac{1}{2\pi}u_{\theta 1}d\phi = \frac{3}{8}\sin(2\theta)(1+3\cos(2\theta_\omega)) \tag{2.207}$$

From these expressions, we observe that $\int_0^{2\pi}u_{r1}d\phi \sim O(y)$ and $\int_0^{2\pi}u_{\theta 1}d\phi \sim O(1)$, and thus the leading order balance between the convective and diffusive terms become $(1/\alpha') \sim Pe'^{-1}/y^2$, which gives $y \sim (Pe'/\alpha')^{-1/2}$, consistent with the $Pe'^{-1/2}$ scaling for the boundary layer thickness. Now, following along the lines of Subramanian and Koch (2006b), and introducing a rescaled boundary-layer coordinate $\eta = y(Pe'/\alpha')^{1/2}$, we get:

$$\eta\hat{f}_1\frac{\partial\Theta_0}{\partial\eta} + \hat{g}_1\frac{\partial\Theta_0}{\partial\theta} = \frac{\partial^2\Theta_0}{\partial\eta^2} \tag{2.208}$$

where

$$\hat{f}_1 = \frac{1}{2\pi}\int_0^{2\pi}u_{r1}d\phi = -\frac{3}{8}(1+3\cos(2\theta))(1+3\cos(2\theta_\omega)) \tag{2.209}$$

$$\hat{g}_1 = \frac{1}{2\pi}\int_0^{2\pi}u_{\theta 1}d\phi = \frac{3}{8}\sin(2\theta)(1+3\cos(2\theta_\omega)) \tag{2.210}$$

---

[5]Note that we have set $\lambda = 0$ and so $\alpha' = \alpha = |\boldsymbol{\omega}|/E_2$.

From this point, the ensuing analysis is standard (Subramanian and Koch (2006b)); defining a similarity variable $s = \eta/g(\xi)$ with $\xi = \cos\theta$ and $g(\xi)$ characterizing the angular dependence of the boundary layer thickness, we can reduce Eq.2.208 to,

$$\frac{\partial^2 \Theta_0}{\partial s^2} + 2s\frac{\partial \Theta_0}{\partial s} = 0 \tag{2.211}$$

where

$$g^2 \hat{f}_1 + \frac{\hat{g}_1}{2}(1-\xi^2)^{1/2}\frac{dg^2}{d\xi} = -2 \tag{2.212}$$

with the boundary conditions being:

$$\Theta_0 = 1 \ at \ s = 0 \tag{2.213}$$

$$\Theta_0 \to 0 \ as \ s \to \infty \tag{2.214}$$

Solving Eq.2.211, subject to aforementioned BCs, we get,

$$\Theta_0 = 1 - \frac{2}{\Gamma(1/2)}\int_0^s e^{-t^2} dt \tag{2.215}$$

for the temperature field, which is again a standard result (G. L. Leal (2007)). The upper limit in the integration above can be found by solving the equation for boundary-layer thickness $g(\xi)$ given in Eq.2.212, for which the solution is:

$$g(\xi) = \sqrt{\frac{4}{3|(1+3\cos(2\theta_\omega))|}}\frac{1}{\xi} \tag{2.216}$$

We can now calculate the Nusselt number, which is given by:

$$\begin{aligned} Nu &= \frac{2(Pe'/\alpha')^{1/2}}{\Gamma(1/2)}\left(\sqrt{\frac{4}{3|(1+3\cos(2\theta_\omega))|}}\right)^{-1}\int_0^1 \xi \, d\xi \\ &= \sqrt{\frac{3|(1+3\cos(2\theta_\omega))|}{4\pi}}(Pe'/\alpha')^{1/2} \\ &= h(\theta_\omega)(Pe'/\alpha')^{1/2} = h(\theta_\omega)\hat{P}e^{1/2} \end{aligned} \tag{2.217}$$

where, as already noted above, $\hat{P}e = Pe'\alpha'$. This equation gives the expression for the numerical prefactor that the Nusselt number plateaus to at large α'. This prefactor is plotted in Fig.2.47. From the figure, we see that this prefactor goes to zero at $\theta_\omega = \tan^{-1}\sqrt{2} = \theta_\omega^{th1}$, which marks the inclination above which, the cubic invariant R' crosses zero. We see that the prefactor at $\theta_\omega = 0$ is given by $h = \sqrt{3/\pi}$, which is the Nusselt number for axisymmetric extensional flow with vorticity aligned along the axis of symmetry, for which Nu is independent of α' and is equal to the value corresponding to pure axisymmetric extension.
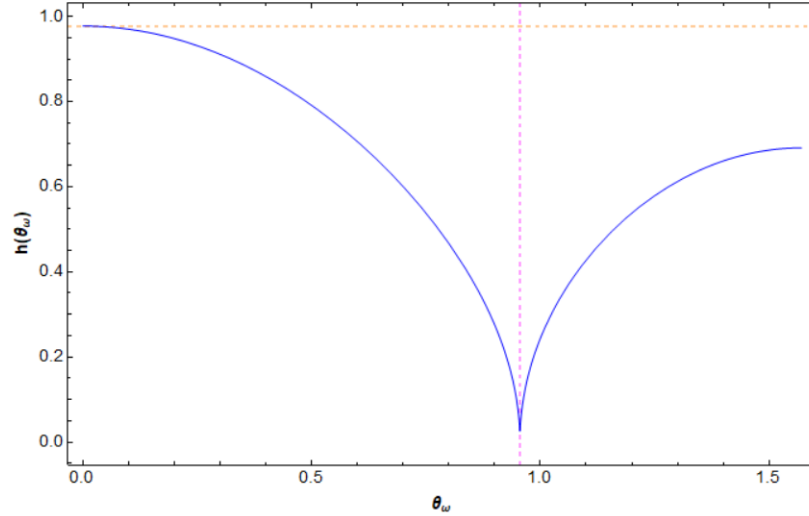
Figure 2.47: Plot of the numerical coefficient $h(\theta_\omega)$ as a function of θ_ω. It is seen that h is 0 at $\theta_\omega = \theta_\omega^{th2}$, where R' approaches zero as $\alpha' \to \infty$.

The numerical coefficient, specifically the dependence on θ_ω could have been inferred apriori, by using the same arguments used by Batchelor (1979), where, he shows that for ambient flows with vorticity, especially in axisymmetric extensional flows, the transfer rate Nu remains unaffected by the velocity distribution that varies with ϕ and is asymptotically same as for an axisymmetric extensional flow, with the extension along the axis of symmetry being $\boldsymbol{E} : \boldsymbol{\omega\omega}/|\boldsymbol{\omega}|^2$. This modified rate of extension is given by $1 + 3\cos(2\theta_\omega)$, which is the same as $h(\theta_\omega)$. With the expressions for the asymptotes in place, we now proceed to calculate the Nusselt number (Nu) using the $C - \tau$ formulation.

2.4.4.3 The Nusselt Number

In this section, we show the results for Nu, calculated from Eq.2.106, using the $C - \tau$ formulation described above, for different values of flow-type parameters (θ_ω, α'). We calculate Nu for specific values of θ_ω as a function of α', and plot them along with the asymptotes at small and large α' that we discussed in the last two sections (Eq.2.198 and Eq.2.217). Finally, we put together the Nu vs α' curves for different θ_ω so as to construct a Nusselt surface (i.e. $Nu/\hat{P}e^{1/2}$), similar to what was done for the aligned-vorticity case (Fig.2.28). Note that this would be the λ-rescaled surface, since, both $\hat{P}e$ and α' are related to the original parameters with appropriate forms of $(1 + \lambda)$.

To begin with, we split the Nu calculation into three cases, akin to the surface-streamline topology analysis, where each case corresponds to an interval of θ_ω, with the threshold values of θ_ω^{th1} and θ_ω^{th2} as the transition points between the intervals.

Case 1 - $0 \leq \theta_\omega < \theta_\omega^{th1}$

For any θ_ω in this interval, $Nu/\hat{P}e^{1/2}$ monotonically decreases with increasing α', owing to a progressively tighter spiralling of the surface streamlines, and it asymptotes to a plateau at large α'. This can be seen in Fig.2.48a, where we plot $Nu/\hat{P}e^{1/2}$ for $\theta_\omega = \pi/6 < \theta_\omega^{th1}$. The existence of a plateau implies that, Nu in the limit of large α', where the spiralling surface streamlines have an asymptotically small pitch, is only controlled by the rate of extension (since $\hat{P}e$ only involves E_2). This is analogous to the results of Batchelor (1979) for a solid particle, however for a solid particle Nu scales as $Pe^{1/3}$ for $Pe \gg 1$, unlike a drop, for which, $Nu \sim O(Pe^{1/2})$. In Fig.2.48b, we plot $(Nu - Nu_0)/\hat{P}e^{1/2}$ against α' for the

same value of θ_ω, on a logarithmic scale, Nu_0 being the asymptote at small α', to show the correctness of our calculations, where the α'^2 scaling for $\alpha' \ll 1$ is clearly visible. For $\alpha' \to \infty$, we shall see later that $Nu - Nu_\infty \sim O(1/\alpha'^2)$, where Nu_∞ is the large-α' plateau. From these plots, we observe that the numerical integrations for Nu match well with the asymptotic values at both limits. Particularly note that, the numerical integrations match with the asymptote (at small α') over a large interval of α', but as we shall see this interval of agreement shrinks with increasing θ_ω.
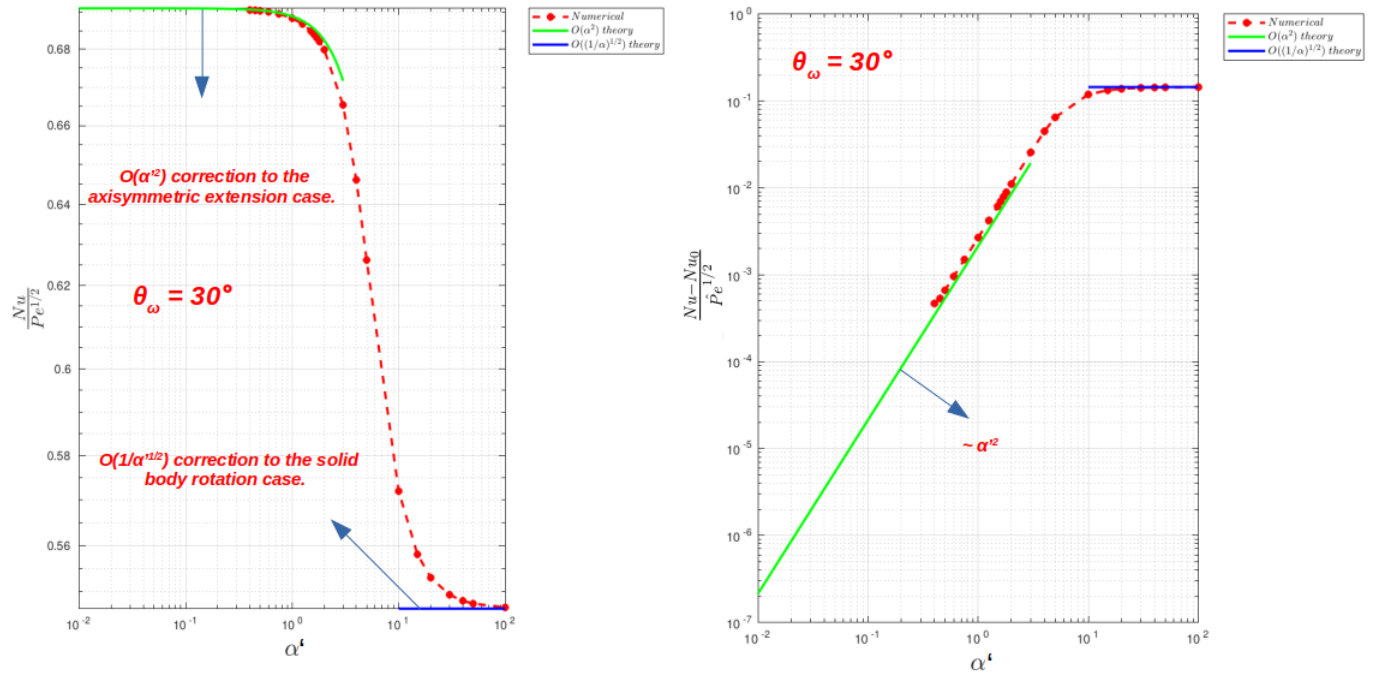
Figure 2.48: Plot of $Nu/\hat{P}e^{1/2}$ for $\theta_\omega = \pi/6 < \theta_\omega^{th1}$ with the asymptotes shown. We see that Nu decreases with increase in α' and our calculations match exactly with the asymptotic predictions.

Case 2 - $\theta_\omega^{th1} \leq \theta_\omega \leq \theta_\omega^{th2}$

In this interval, the streamlines were spirals except at critical values of α', at which R' suffered a zero-crossing (α'_{th3}), which resulted in a closed streamline topology on the drop (Fig.2.36). Correspondingly, $Nu/Pe^{1/2}$ decreases with α' until α'_{th3}, at which point, $Nu/\hat{P}e^{1/2}$ drops to zero owing to the presence of closed streamlines on the drop surface. Beyond this point, Nu rises again before eventually plateauing at large α', going through a local maximum. Thus the plot of $Nu/\hat{P}e^{1/2}$ for this interval is non-monotonic as can be seen in Fig.2.49, corresponding to $\theta_\omega = \pi/6$. Note that the large-α' plateau of Nu is still lower than the value at $\alpha' = 0$, even though Nu rises beyond α'_{th3}. The plot on the logarithmic scale (Fig.2.49(b)) shows the $O(\alpha'^2)$ scaling behavior at small α' and the plateau at large α', where, we shall later see that $Nu - Nu_\infty \sim O(1/\alpha'^2)$, like the previous case. These results again matches well with our asymptotic predictions. We shall see later that $Nu/\hat{P}e^{1/2} \sim O(|\alpha' - \alpha'_{th3}|^{1/2})$ as $\alpha' \to \alpha'_{th3}$, which can be easily shown using scaling arguments.
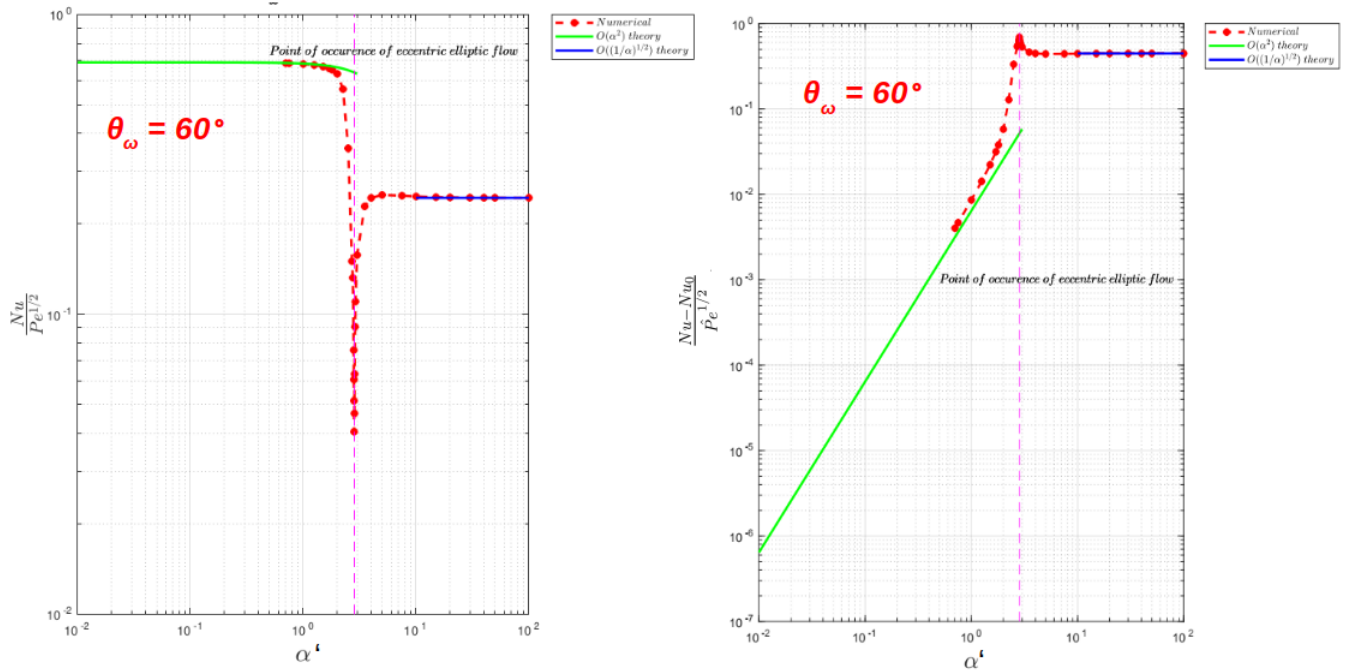
Figure 2.49: Plot of $Nu/\hat{P}e^{1/2}$ for $\theta_\omega = \pi/3$ with the asymptotes shown. $Nu/\hat{P}e^{1/2}$ drops to zero at $\alpha'_{th3} = 4\sqrt{2}$, that corresponds to $R' = 0$, which is the point of occurrence of eccentric planar elliptic flow.
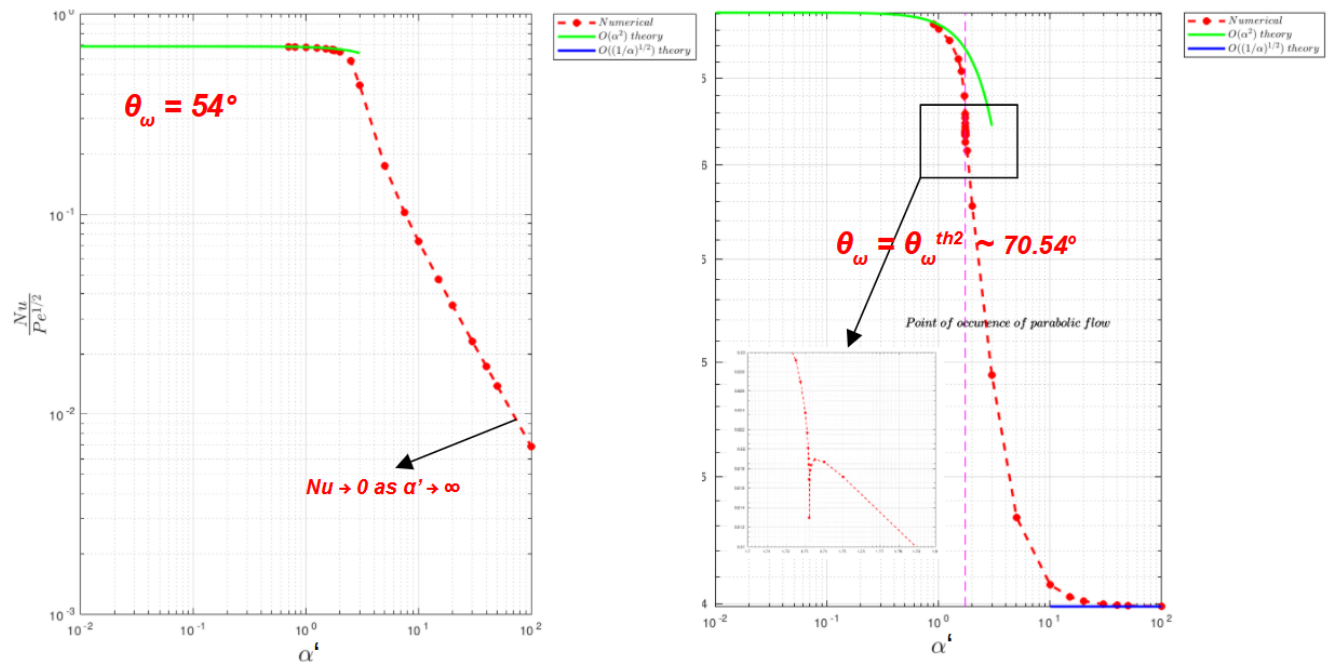
Figure 2.50: Plot of $Nu/\hat{P}e^{1/2}$ for θ_ω^{th1} and θ_ω^{th2}. In the first case, $Nu/\hat{P}e^{1/2}$ drops to zero at $\alpha' = \infty$, consistent with our asymptotic calculation. In the second case, Nu drops down to a finite value at α'_{th3}, before rising again to reach the large-α' plateau, which is consistent with the presence of eccentric parabolic streamlines on the drop surface at this point.

There are two limiting cases, each corresponding to each of the threshold values of θ_ω bounding this

interval, where Nu variation differs from that shown in Fig.2.49. At θ_ω^{th1}, Nu decreases monotonically and approaches zero as $\alpha' \to \infty$. From our earlier analysis of surface-streamline topology, recall that R' approaches zero as $\alpha' \to \infty$ and our asymptotic analysis (Eq.2.217) revealed that for this value of inclination, Nu should be zero at $\alpha' = \infty$, which our calculations also conform to, as seen in Fig.2.50(a). Importantly, we shall see later, that for this case alone, $Nu - Nu_\infty \sim O(1/\alpha')$ as $\alpha' \to \infty$. In Fig.2.50(b), we have plotted the results for $\theta_\omega = \theta_\omega^{th2}$, from which we see that $Nu/\hat{P}e^{1/2}$, dips down to a finite value at $\alpha' = \alpha'_{th3} = 2\sqrt{3}$, before going through a local maximum to reach the large-α' plateau. At α'_{th3} for this inclination, we encountered planar parabolic flows (see Fig.2.38), owing to $R' = \Delta' = 0$ at this point. The Nu behavior is again consistent with the fact that at the point of occurrence of planar parabolic flows, the streamlines on the drop-surface are still open and hence, we get a finite value of Nu at this point. This finiteness of Nu for planar parabolic flows is also consistent with the fact that Nu for its canonical counterpart, simple shear, is again finite. However, we see that α'_{th3} is located at a cusp, with the slope of the Nu curve on either side of this point changing from positive to negative ∞.

Case 3 - $\theta_\omega^{th2} < \theta_\omega \leq \pi/2$

In this final case, Δ' suffers two zero crossings and therefore, there is an intermediate region of non-spiralling streamlines between regions of spiralling streamlines. From the plot in Fig.2.51 for $\theta_\omega = 4\pi/9$, we see that $Nu/\hat{P}e^{1/2}$ again decreases with α', and does so monotonically unlike the cases with closed streamline topologies. The Nu curve continues smoothly across the two zero-crossings of Δ' implying no discontinuity in slopes, and importantly, the point of occurrence of eccentric planar hyperbolic flows (between the zero-crossings) leads to no qualitative change in Nu behavior, just like the aligned-vorticity case. In the intermediate region of non-spiralling streamlines, the procedure for calculation of Nu is the same as for the non-spiralling case, but with both C and τ limits running till ∞.
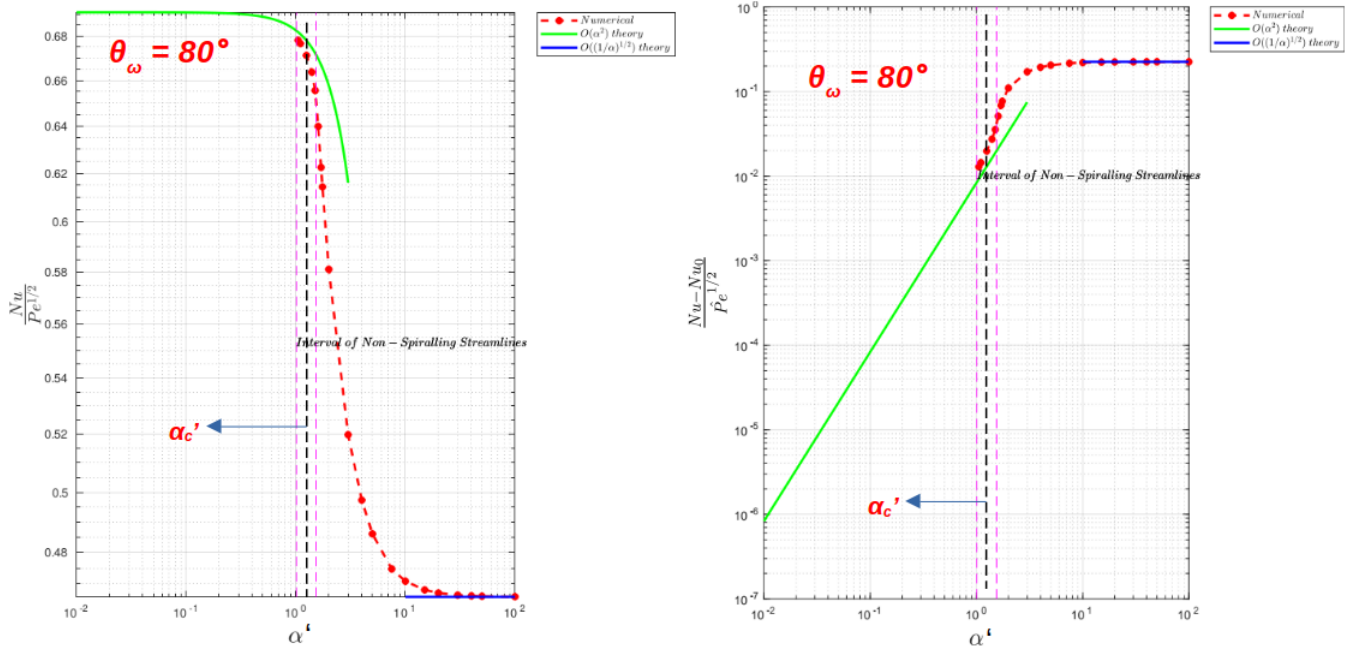
Figure 2.51: Plot of $Nu/\hat{P}e^{1/2}$ for $\theta_\omega = 80°$ with the asymptotes shown. $Nu/\hat{P}e^{1/2}$ changes continuously across the zero-crossings of Δ' and at α'_{th3}, which is the point of occurrence of eccentric planar hyperbolic flow, there is no qualitative change in Nu behavior.

The Nusselt Surface

Having looked at the behavior of $Nu/\hat{P}e^{1/2}$ across a range of θ_ω, we can now put all of them together to build a Nusselt surface as was done for the aligned-vorticity case. This surface is shown in Fig.2.52, where we see that in the range of θ_ω, between the two thresholds (the red dashed lines), there are singular dips of Nu to zero at the corresponding α'_c (the blue dashed lines). But overall, we see that Nu decreases with increasing α' reaching finite plateaus at large α', except at θ_ω^{th1}, where it approaches zero as $\alpha' \to \infty$. In this plot, we have normalised both the x and y axes in order to generate a uniform grid ($\bar{\alpha}' = \alpha'/\alpha'_{max}$ and $\bar{\theta}_\omega = \theta_\omega/(\pi/2)$). Note that, since our $Nu/\hat{P}e^{1/2}$ is scaled with λ, we can use this surface to calculate Nu for an arbitrary λ by dividing Nu by $(1 + \lambda)^{1/2}$, provided we also divide α' by $(1 + \lambda)$, much like the aligned-vorticity case, as shown in Fig.2.53(a)-(c) for three different values of λ. Here again, we see that $Nu/Pe^{1/2}$ decreases with λ and, they correspond to smaller values of α as λ increases, a trend consistent with our scaling.
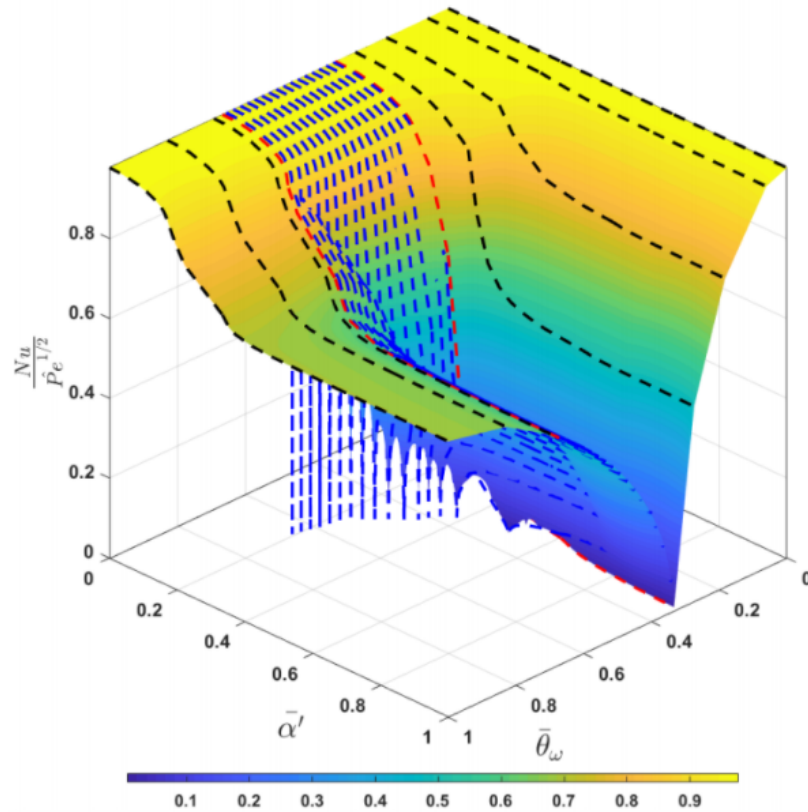
Figure 2.52: The Nusselt ($Nu/\hat{P}e^{1/2}$) surface for axisymmetric extension with inclined vorticity as a function of $\bar{\theta}_\omega = \theta_\omega/(\pi/2)$ and $\bar{\alpha}' = \alpha'/\alpha'_{max}$, where α'_{max} in our calculations was 100. The dips in the plot (blue dashed lines) correspond to the points of occurrence of eccentric planar elliptic flows, where $Nu \sim O(Pe^{1/3})$. The red dashed lines correspond to the threshold values of θ_ω.

(a) $\lambda = 0.5$ (b) $\lambda = 1$ (c) $\lambda = 5$
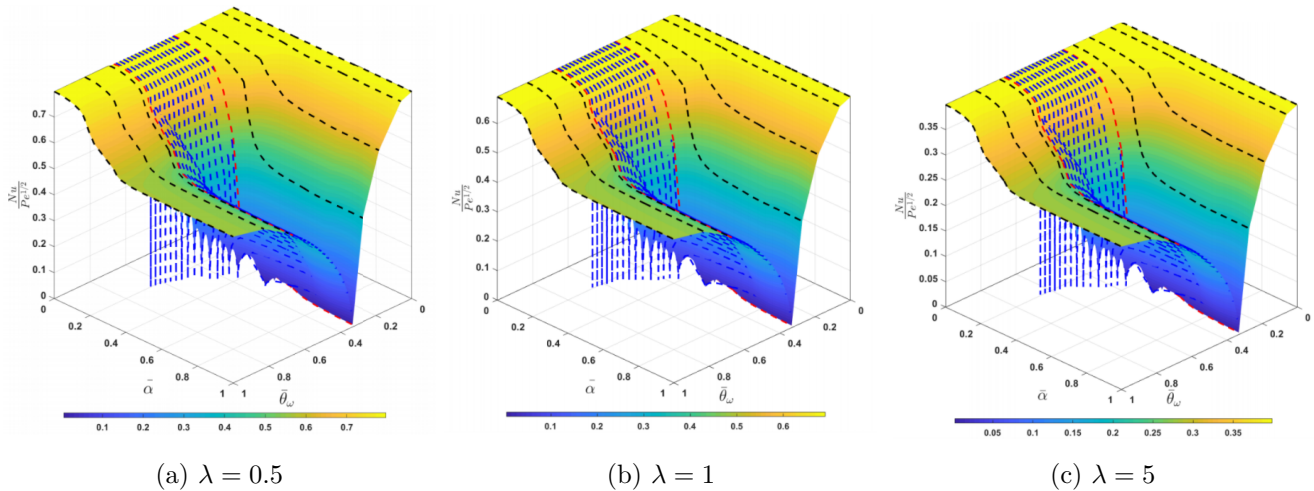
Figure 2.53: Plot of $Nu/Pe^{1/2}$ against $\bar{\alpha}$, $\bar{\theta}_\omega$ for (a) $\lambda = 0.5$, (b) $\lambda = 1$ and, (c) $\lambda = 5$, which constitutes the actual Nusselt number.

Discussion

In the Nusselt surface (Fig.2.52) above, we see that $Nu/\hat{P}e^{1/2}$ is along on the curve, that constitutes the loci of α'_{th3}. This however does not imply that Nu is identically zero, as it is known that the near-surface streamlines for the eccentric elliptic linear flows, are not closed, even though the surface streamlines on the drop are closed. This implies that, right at α'_{th3}, the velocity across the closed orbits (drift velocity) on the drop-surface is zero, but in the immediate vicinity of the surface, this drift velocity is non-zero. This situation is analogous to that of a rotating rigid particle in any ambient $3D$ linear flow (with vorticity), where the surface streamlines are closed (circular, in fact) while the near-surface streamlines are not. We know that, for such a rigid particle, $Nu \sim O(Pe^{1/3}$ for $Pe \gg 1$. This immediately suggests that for a drop suspended in a,linear flow, at $\alpha' = \alpha'_{th3}$ (with $\theta_\omega^{th1} < \theta_\omega < \theta_\omega^{th2}$), $Nu \sim O(Pe^{1/3})$. Therefore, as far as transport is concerned, a spherical drop, at the point of occurrence of eccentric planar elliptic flows, behaves like a solid particle! In contrast, for a drop in canonical elliptic flows, $Nu \sim O(1)$ for $Pe \gg 1$, owing to the presence of closed near0surface streamlines.

While we have seen that $Nu/\hat{P}e^{1/2} \to 0$ at $\alpha' = \alpha'_{th3}$, it is also of interest to examine the manner in which it approaches zero. As pointed out before, the drift velocity across the streamlines at α'_c is zero. But in the vicinity of this point, the drift velocity would be $O(|\alpha' - \alpha'_c|)$. Based on this fact, we can show that $\hat{P}e$, would be replaced by $\hat{P}e(|\alpha' - \alpha'_c|)$ in the scaling relation, using a procedure akin to that followed by Subramanian and Koch (2006b), by using a $C - \tau$ coordinate system for the closed-streamline topology of the leading order surface velocity field, in which $u_C = 0$ (note that Subramanian and Koch (2006b) had used a spherical coordinate system, where the tangential component $u_{\theta 0}$ of the leading order field was zero and they had Re as the perturbation parameter, which in our case is $|\alpha' - \alpha'_c|$). Therefore, one can expect Nu to scale as $(|\alpha' - \alpha'_c|)^{1/2}$ on either side of the critical value. We confirm this scaling behavior by plotting $Nu/\hat{P}e^{1/2}$ against $\alpha' - \alpha'_c$ for $\theta_\omega^{th1} < \theta_\omega < \theta_\omega^{th2}$ where the eccentric elliptic flows occur. In fig.2.54, one such plot for $\theta_\omega = \pi/3$ is shown, which confirms the aforementioned scaling behavior on either side of α'_c. In the following chapter, we write down the exact expressions for the definitions of C and τ coordinates for the surface-streamlines associated with the eccentric elliptic flows, which forms the starting point of the aforementioned asymptotic calculation. Before moving to the discussion of the large α' limit, we briefly note that the $Pe^{1/3}$ scaling for drops in an eccentric elliptic flow suggests that, unlike the other cases, where drops have an asymptotically larger transport rate than solid particles (owing to the $Pe^{1/2}$ scaling) at large Pe, there are linear flows where a solid particle may be more efficient than a

drop in transporting passive scalars. The heat transfer analysis associated with drops in eccentric elliptic flows, shall be the subject of a separate investigation in the future.
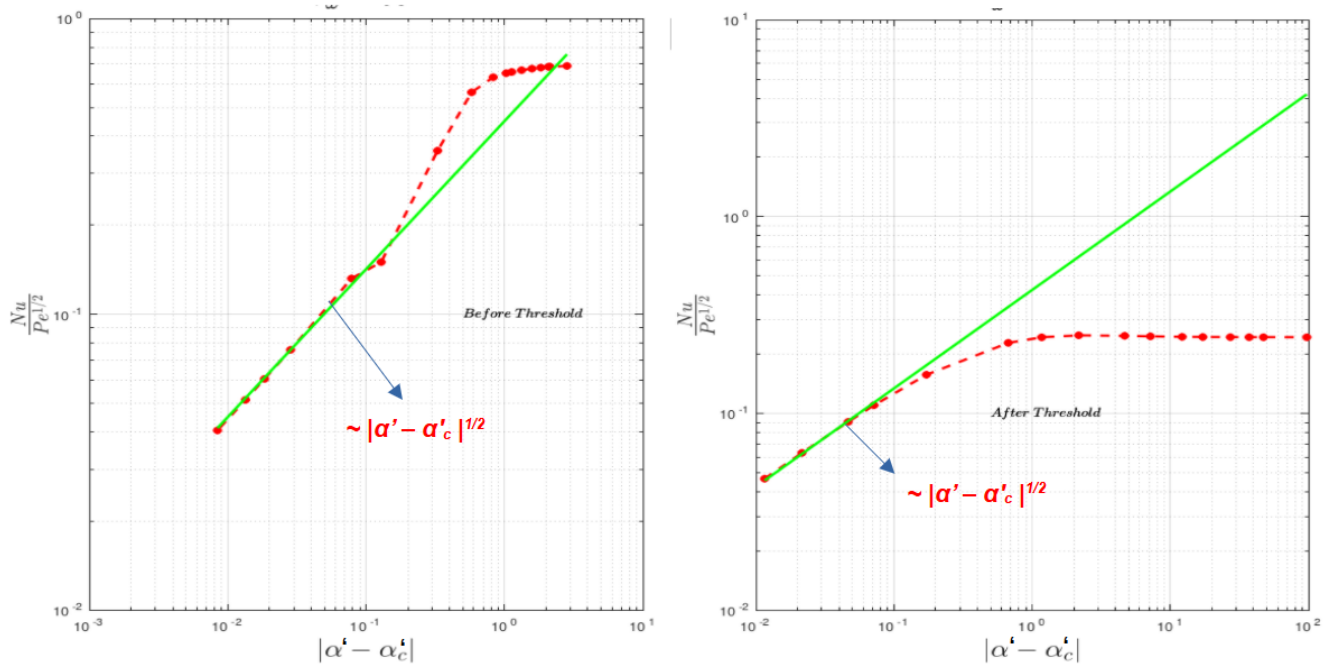
Figure 2.54: Plot of $Nu/\hat{P}e^{1/2}$ against $\alpha' - \alpha'_{th3}$ on either side of the critical value, showing the scaling behavior of Nu in the vicinity of the critical points.

In the limit of large α', we now examine the manner in which $Nu/\hat{P}e^{1/2}$ asymptotes to the large-α' plateau (Nu_∞). In Fig.2.55, we have plotted $(Nu - Nu_\infty)/\hat{P}e^{1/2}$, against α', and we see that it scales as $O(\alpha'^{-2})$ for all θ_ω except for θ_ω^{th1}, where the scaling is $O(\alpha'^{-1})$. Going back to the calculation of the Nu-asymptote for $\alpha' \gg 1$, these scaling relations imply that, for θ_ω^{th1}, the asymptotic expansion of $Nu/Pe'^{1/2}$, with $Pe' = \hat{P}e\,\alpha'$, has the form:

$$\frac{Nu}{Pe'^{1/2}} = \frac{h(\theta_\omega)}{\alpha'^{1/2}} + \frac{h^{(1)}(\theta_\omega)}{\alpha'} + \frac{h^{(2)}(\theta_\omega)}{\alpha'^{3/2}} + ... \tag{2.218}$$

where $h(\theta_\omega) = h^{(1)}(\theta_\omega) = 0$, with the first non-zero correction appearing at $O(1/\alpha'^{3/2})$. Eq.2.218 suggests that for this critical value of inclination, the weak extension at $\alpha' \gg 1$, is a singular perturbation about the solid-body rotation. Note that the scaling should actually be $1/|\alpha'|$, in order to satisfy the invariance of Nu with the direction of fluid motion. For, $\theta_\omega \neq \theta_\omega^{th1}$, the $1/\alpha'^2$ scaling implies that the extension is a regular perturbation of the closed streamlines associated with solid-body rotation. To exactly calculate the numerical prefactor, one can use a procedure analogous to the calculation of small-α' asymptote, using Green's function of the leading-order convection-diffusion operator to derive the exact expansion. This will be taken up in the near future, but for now, our calculations already give indications of the scaling to be expected.
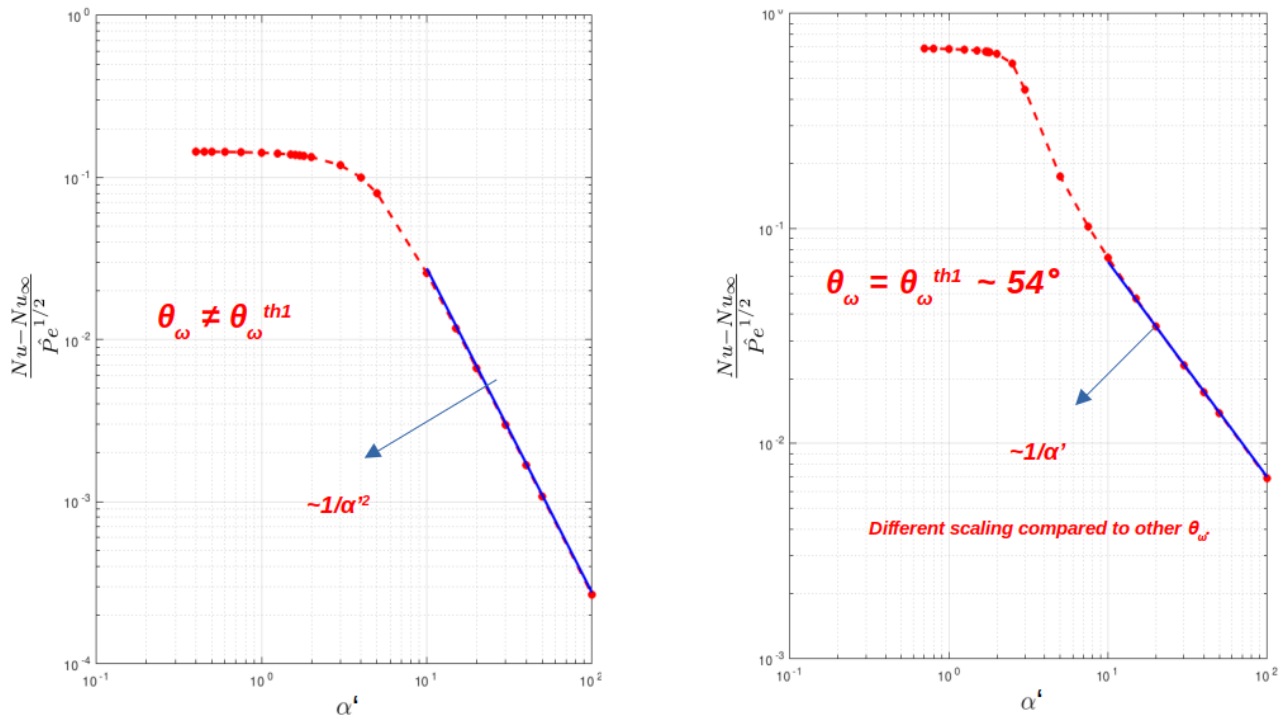
Figure 2.55: Plot of $(Nu - Nu_\infty)/\hat{P}e^{1/2}$ against α', showing the scaling behavior of Nu in the vicinity of $\alpha' = \infty$.

Special Cases

There are two special cases that one encounters in this two-parameter family, and the first of these corresponds to $\theta_\omega = 0$, for which $Nu/\hat{P}e^{1/2}$ is constant and is equal to $\sqrt{3/\pi}$ as seen in Fig.2.52. The second case is that of $\theta_\omega = \pi/2$, which corresponds to $\epsilon = -0.5$ in the aligned-vorticity case. Our calculations for the latter case, using the $C - \tau$ formalism of both aligned and inclined-vorticity cases match exactly, validating our approach.

This concludes our discussion on transport from a spherical drop in axisymmetric extension with inclined vorticity. We now summarise the results obtained in this chapter and their implications.

2.5   Concluding Remarks

In this chapter, which forms the bulk of this thesis, we have developed a framework to calculate Nu analytically, for a drop suspended in a couple of two-parameter families of linear flows, using a surface-streamline aligned non-orthogonal coordinate system. We saw the characteristics of this coordinate system and it's advantage in enabling a closed-form solution for Nu. One can show that this $C - \tau$ formulation can be easily extended to the case of a drop suspended in an arbitrary $3D$ linear flow (governed by four parameters $P = \{\epsilon, \alpha, \theta_\omega, \phi_\omega\}$). This argument is based on the fact that, the surface-streamline topologies encountered in the two-parameter families are the only topologies possible, that respect the constraints imposed by incompressibility and the time-reversal symmetry of the Stokesian field. So, for a drop in an arbitrary linear flow the surface streamline topology will again be a spiralling or a non-spiralling one. Since an arbitrary linear flow has no underlying symmetry, the streamline topologies are similar to the ones obtained for the second two-parameter family, where the spiralling and non-spiralling topologies were skewed versions of the symmetrical ones observed in the aligned-vorticity case. In our analysis, we saw

that one can define a surface-streamline aligned coordinate system $(C - \tau)$ in either case to solve the convection-diffusion equation. Therefore, extending such an analysis to the case of a drop in an arbitrary linear flow is straightforward.

To illustrate our argument, we plot Δ' and R' with the corresponding streamline topologies at chosen points in Fig.2.56, for representative cases of $\epsilon = -1.6, \phi = 23°, \theta_\omega = \pi/4$ and $\epsilon = -1.6, \phi = 23°, \theta_\omega = \pi/3$. From the plots, one can see that the behavior of Δ' is, loosely speaking, a combination of the behavior observed for the two two-parameter families. Δ' starts off with a negative value, and then becomes positive, passing through a saddle-node bifurcation. Moreover, the Δ' curves are non-monotonic when $\Delta' > 0$ and exhibits a critical topology corresponding to $R' = 0$, where the ambient flow is an eccentric planar elliptic flow (in Fig.2.56(a)) or a planar parabolic flow (Fig.2.56(b)). These features were similar to the ones observed for the two-parameter families and confirms our argument one can obtain the nature of the Nu-curve for a drop in arbitrary linear flow, by piecing together specific Nu-curves already shown earlier for the two-parameter families. A detailed analysis of this case, however, is out of the scope of this thesis and will be carried out at a later stage.
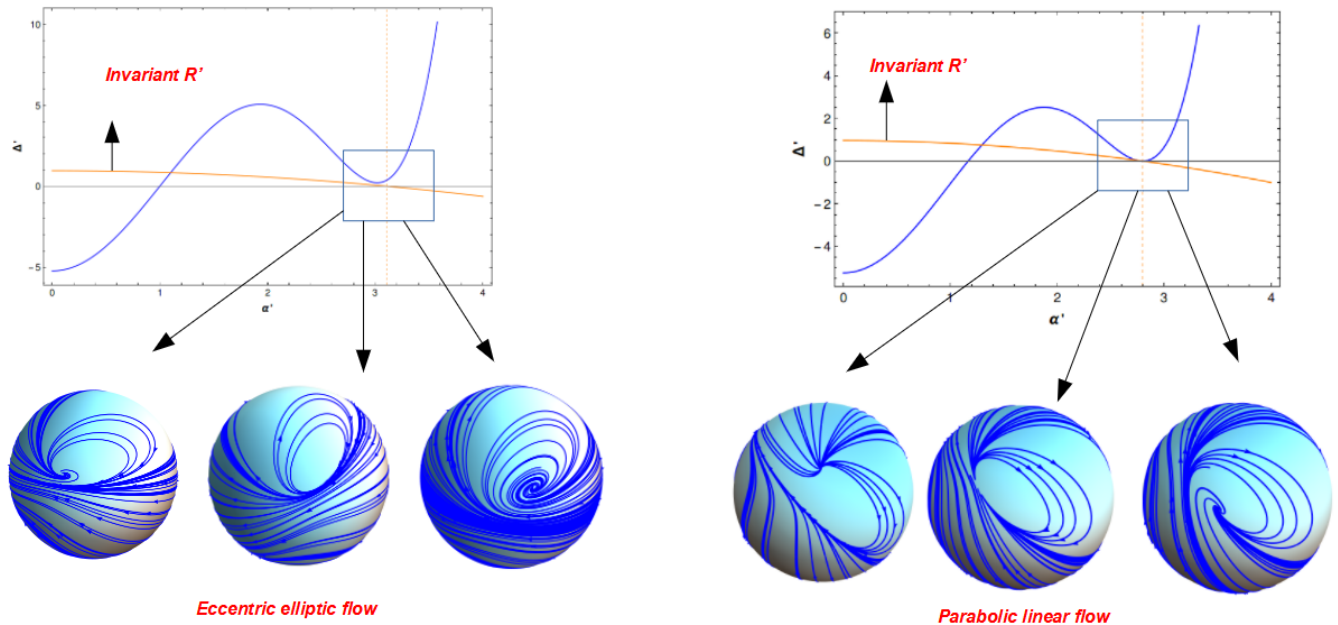
Figure 2.56: Plot of scalar invariants along with streamline topology for $\epsilon = -1.6, \phi = 23°$ with (a) $\theta_\omega = 60°$ and (b) $\theta_\omega = 70.5°$. The behavior of Δ' can be seen as a combination of the behavior encountered in the two two-parameter cases discussed before. Importantly, we see that eccentric planar flows exist (at α'_{th3}) even in the four-parameter family of linear flows.

In our analysis on the two-parameter families, we also identified a novel class of planar linear flows, the eccentric family of planar flows, that are generalisations of their canonical counterparts. Moreover, from Fig.2.56, one can infer that these flows exist in the four-dimensional parameter space associated with a general linear flows. This suggests that, these planar flows may be characterised by at most three parameters, unlike the one-parameter family of canonical planar linear flows. As we shall see in detail in Chapter 3, they occupy a three-dimensional sub-volume in the four-dimensional parameter space. From the transport perspective, it is clear that the regions where eccentric planar elliptic flows occur $Nu/\hat{P}e^{1/2}$ will be zero. But these flows, also have implications for other microhydrodynamic phenomena, and we will be discussing the eccentric planar linear flows and their implications in the next chapter.

Chapter 3

The General Class of Planar Linear Flows

This chapter marks a slight digression from the overall aim of this thesis, an analysis of the transport problem. Here we follow up on the serendipitous result revealed by the analysis in the previous chapter - the discovery of 'eccentric' planar linear flow configurations. The term "eccentric" is used on account of there being a non-trivial component of extension normal to the plane of flow, as opposed to the canonical planar flows, where this normal component of extension is zero (G. L. Leal (2007)). These flows are therefore, generalisations of the canonical planar flows, which constitute a one-parameter family (Bentley and L. G. Leal (1986); Subramanian and Koch (2006b)). In the first part of this chapter, we analyse these flows in greater detail, by comparing the various geometrical properties of these flows to the canonical ones and identify their region of existence in the four-dimensional space of incompressible linear flows. The streamlines of the canonical elliptic planar flows, when projected onto a unit sphere lead to trajectories identical to Jeffery orbits (Jeffery (1922)). Note that Jeffery orbits refer to the trajectories on the unit sphere, of an axisymmetric particle in an ambient simple shear flow; analogous trajectories are obtained across a range of canonical planar linear flows as shown by L. G. Leal and Hinch (1972). These trajectories are spherical ellipses, with an eccentricity that is a function of both the particle aspect ratio and the flow-type. For the canonical elliptic planar flows, the eccentricity is a function of the lone flow-type parameter $\hat{\alpha}$. In all the cases, the Jeffery orbits are characterised by an orbit constant. We show that the projection of these 'eccentric' elliptic planar flows onto the unit sphere give rise to generalised Jeffery orbits, and derive an expression for the generalised orbit constant. A closed-form expression for this constant is directly relevant to the solution of the transport problem in the $C - \tau$ coordinate system used in Krishnamurthy and Subramanian (2018a), as this expression serves as the starting point for the calculation of Nu in the vicinity of these eccentric (elliptic) flows, where we saw earlier that $Nu \sim O(Pe^{1/3})$, as opposed to $Nu \sim O(Pe^{1/2})$ everywhere else. Apart from this, we also identify other problems in microhydrodynamics where these flows are relevant.

The final part of this chapter is again motivated by our finding of the eccentric plane linear flows above. In the traditional classification scheme of linear flows, the $P - Q_R$ scheme (Chong et al. (1990)), all of the incompressible linear flows occupy the Q axis. Thus, there is no distinction between the eccentric and canonical linear flows despite the obvious differences associated with them in microhydrodynamics problems. For instance, for the drop transport problem in particular, the eccentric linear flow of the ambient phase leads to different Nu scaling for $Pe \gg 1$ than the canonical flows. Thus, it is important to develop an alternate classification scheme which retains a notion of distance between different linear flows - an element absent in the aforementioned classification, which is solely based on the real or complex nature of the eigenvalues of the velocity-gradient tensor associated with a linear flow. This remains true of the original $P - Q$ classification of compressible planar linear flows (Perry and Chong (1987)). In this

part of the chapter, we take the initial step towards this end by developing a new scheme with two new parameters χ and ζ, which lets one find the relative position of the planar linear flows with respect to each other. This scheme is finite in extent, and occupies a bounded region in the $\chi - \zeta$ plane that takes the shape of a diamond. The hope is to extend this idea to develop a new framework in a higher-dimensional setting, for classifying planar linear flows, that demarcates the eccentric and canonical flows, while also giving their relative positions with respect to one another.

3.1 The Canonical Family of Planar Linear Flows

In the first section, we briefly review the canonical planar linear flows. This family governed by a single parameter, constitutes an important class of flows in fluid dynamics. Being a $2D$ linear flow, the behavior of a suspended phase can be easily analysed in these flows and, they also serve as local first approximations to $2D$ shearing flows. These qualities make them indispensable to the field of rheology and microhydrodynamics, as these flows include the standard rheometric flow of simple shear, and have been extensively examined both experimentally and theoretically in this regard. For instance, Olbricht et al. (1982) study the behavior of deformable, directed microstructure in these flows theoretically and classify the flows based on their level of influence on the microstructure dynamics. Another instance is the study of coil-stretch transition of single long polymeric chains suspended in these flows, which are relevant to biological processes involving DNA strands (Shaqfeh (2005)). G. I. Taylor (1934), in a seminal work, studied the deformation and breakup of an isolated drop in canonical planar flows, which were generated using a four-roll mill; miniature versions of this device have also been developed in recent years (Hudson et al. (2004), Lee et al. (2007)) for extensional rheometry. Since then, there have been several efforts which have focused on the deformation and breakup of droplets (Bentley and L. G. Leal (1986), Guido et al. (1999)), vesicles and other deformable particles. These flows are also used in theoretical studies characterising the rheology of a suspension made of such droplets (Cox (1969), Frankel and Acrivos (1970), Barthes-Biesel and Acrivos (1973), Rallison (1980)), solid particles (Batchelor and Greene (1972), Kao et al. (1977)) and even microorganisms like bacteria and plankton (Nambiar et al. (2017), Nambiar et al. (2019)), owing to their analytical simplicity. Other applications include the analysis of microscopic dynamics of particles or drops (of various shapes) suspended in these flows, starting with the pioneering effort of Jeffery (1922), who studied the orientation dynamics of axisymmetric objects in shear flows. Several other works have followed this effort spanning an entire century, with Marath and Subramanian (2018) comprehensively analysing the inertial orientation dynamics of spheroids in planar linear flows fairly recently. Such studies have direct relevance in atmospheric sciences, where the sedimenting ice crystals in clouds are subject to similar dynamics in a turbulent fluid (provided they are smaller than Kolmogorov scale) (Anand et al. (2020)). In another line of work, these flows have also been extensively analysed in calculating the transport rate (both at small and large Pe) from both solid particles (Batchelor (1980)) and drops (Krishnamurthy and Subramanian (2018a)). Owing to their linearity, these flows can been used as building blocks, to geometrically visualise several complicated flow topologies in the vicinity of stagnation points of a flow field, as was shown by Perry and Chong (1987). In their work, the authors have developed an extensive technique to analyse the flow-topologies. The key idea behind these techniques is the fact that these flows are equivalent to the solution trajectories near the fixed (critical) point of a $2D$ autonomous dynamical system and thus they can be analysed in the purview of dynamical systems theory.

These canonical planar linear flows have the extensional component lying in the plane of flow and the vorticity vector perpendicular to it. They can be represented by:

$$\boldsymbol{u} = \boldsymbol{\Gamma}.\boldsymbol{x} \tag{3.1}$$

with

$$\mathbf{\Gamma} = \begin{bmatrix} 0 & 1 & 0 \\ \hat{\alpha} & 0 & 0 \\ 0 & 0 & 0 \end{bmatrix} \tag{3.2}$$

being the (transpose of the) velocity gradient tensor, and $\mathbf{\Gamma} = \mathbf{E} + \mathbf{\Omega}$. Here, $\hat{\alpha}$ is the dimensionless parameter the governs the planar linear flow. $\mathbf{E}$ is symmetric and will have $(1 + \hat{\alpha})/2$ as it's elements and $\mathbf{\Omega}$ is anti-symmetric having $(1 - \hat{\alpha})/2$ as it's elements. Equating the elements of $\mathbf{E}$ to the normalised strength $E/E + \Omega$ will yield:

$$\hat{\alpha} = \frac{E - \Omega}{E + \Omega} \tag{3.3}$$

as the definition of $\hat{\alpha}$. It is easy to see that $\hat{\alpha} \in [-1, 1]$ will cover all the possible flows (going outside this interval will reproduce same the family of flows) with the limiting members being solid-body rotation ($E = 0$; with concentric circles as streamlines) for $\hat{\alpha} = -1$ and planar extension ($\Omega = 0$; with rectangular hyperbolas as streamlines) for $\hat{\alpha} = 1$. When the magnitudes of extension and vorticity are equal, one obtains simple shear flow, which therefore corresponds to $\hat{\alpha} = 0$ and is the only linear flow with straight streamlines. It is easily shown that the streamlines are concentric ellipses when $-1 < \hat{\alpha} < 0$ and hyperbolas when $0 < \hat{\alpha} < 1$. Correspondingly, the flows with $-1 < \hat{\alpha} < 0$ are termed elliptic planar linear flows and the other family is termed the hyperbolic planar linear flows (Bentley and L. G. Leal (1986), Subramanian and Koch (2006b)). A schematic of this one-parameter family is shown in Fig.3.1.
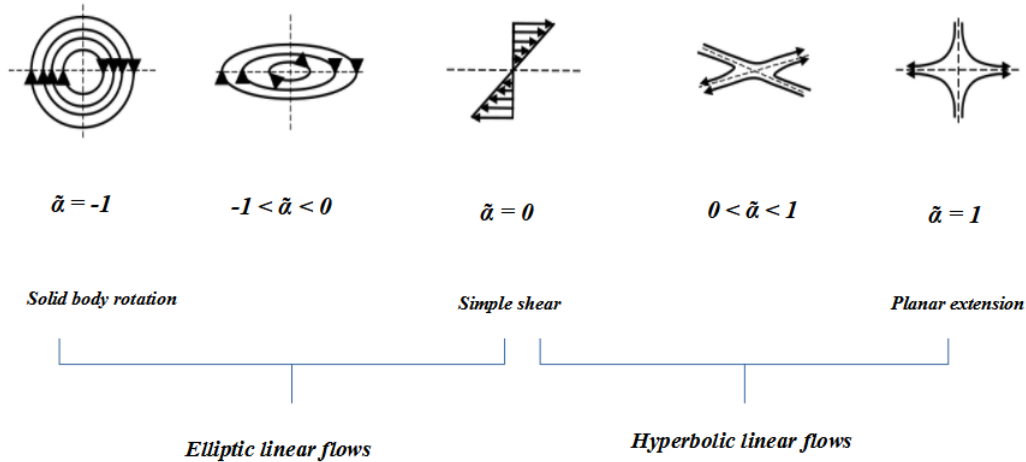
Figure 3.1: Schematic of the canonical planar linear flows, with their flow topologies and the corresponding values of $\hat{\alpha}$.

Recall that, the canonical planar flows are analogous to the solution trajectories of $2D$ autonomous (linear) dynamical systems. Hence, the various characteristics of the flow can be analysed using critical-point techniques, introduced by Perry and Chong (1987). On account of linearity, the critical fixed point in our case is just the origin and the associated eigenvalues completely characterise the streamline pattern. The eigenvalues and the eigenvectors are:

$$(\mu_1, \mu_2, \mu_3) = (0, -\sqrt{\hat{\alpha}}, \sqrt{\hat{\alpha}}) \tag{3.4}$$

and the corresponding eigenvectors can be shown to be:

$$\boldsymbol{v_1} = \{0, 0, 1\} \tag{3.5}$$

$$\boldsymbol{v_2} = \{-\frac{1}{\sqrt{\hat{\alpha}}}, 1, 0\} \tag{3.6}$$

$$\boldsymbol{v_3} = \{\frac{1}{\sqrt{\hat{\alpha}}}, 1, 0\} \tag{3.7}$$

As can be seen from these expressions, the eigenvalues (μ_2, μ_3) and hence the eigenvectors ($\boldsymbol{v_2}$ and $\boldsymbol{v_3}$) are complex when $\hat{\alpha} < 0$, corresponding to the elliptic linear flows, with $\boldsymbol{v_1}$, the only real eigenvector, along the direction of vorticity vector. The eigenvalues (μ_2, μ_3) are equal and oppositely signed for hyperbolic linear flows ($\hat{\alpha} > 0$), as required by incompressibility, with the corresponding eigenvectors ($\boldsymbol{v_2}$ and $\boldsymbol{v_3}$), lying on the flow-gradient plane for all $\hat{\alpha} > 0$. They are orthonormal only for $\hat{\alpha} = 1$, consistent with the streamlines being rectangular hyperbolas for this case. For the special case of simple shear ($\hat{\alpha} = 0$), the eigenvalues are all identically zero with any arbitrary vector along the flow-vorticity plane ($x_1 - x_3$ plane) being the eigenvector. Thus $\{0, 0, 1\}$ (the vorticity vector) and $\{1, 0, 0\}$ (flow-direction) and any linear combination of them are eigenvectors.

One can also calculate the scalar invariants of the tensor $\boldsymbol{\Gamma}$, which are the coefficients in the characteristic equation of the system given by:

$$\mu^3 - \hat{\alpha}\mu = 0. \tag{3.8}$$

The linear invariant P, is only non-zero for compressible flows, and is zero for the canonical planar linear flows. From Eq.3.8, the quadratic invariant $Q = -\hat{\alpha}$ and the cubic invariant $R = 0$. Therefore, the elliptic flows correspond to $Q > 0$ and the hyperbolic flows correspond to $Q < 0$, with simple shear having $Q = R = 0$. We shall see later that these same properties are also satisfied by the eccentric planar flows and therefore, both canonical and eccentric flows occur along the Q axis. With this brief introduction to canonical planar linear flows, we now move to analyse the eccentric planar flows.

3.2 Eccentric Planar Linear Flows

In this section, we study the properties of the eccentric planar linear flows and find their region of existence in the four-dimensional parameter space of $3D$ incompressible linear flows. Next, in the context of the projected surface streamlines, we discuss the relation of eccentric planar elliptic flows to Jeffery orbits and derive an equation for the generalised orbit constant.

3.2.1 Properties of Eccentric Planar Linear Flows

Recall from Chapter 2 that, we had identified the eccentric planar linear flows when analysing the surface-streamline patterns. These surface-streamlines were found to be the projections of the solutions of an auxiliary linear flow, with a velocity-gradient tensor $\bar{\boldsymbol{\Gamma}} = f(\lambda, P = \{\epsilon, \alpha, \theta_\omega, \phi_\omega\})$. We saw that the auxiliary flow can be made independent of the viscosity ratio (λ) by redefining the vorticity magnitude as $\alpha' = \alpha(1 + \lambda)$ and the velocity scale as $E_3/(1 + \lambda)$. In this rescaled form, the auxiliary flow is the same as the linear flow of the ambient fluid at infinity. This is also equivalent to setting $\lambda = 0$ in the auxiliary flow, which reduces it to the ambient linear flow at infinity. Therefore, we shall use the velocity-gradient tensor $\bar{\boldsymbol{\Gamma}}$ associated with the ambient $3D$ incompressible linear flow (rather than the λ-dependent one), as the starting point of our analysis of planar linear flows. This tensor is given by:

$$\bar{\boldsymbol{\Gamma}} = \begin{bmatrix} -(1+\epsilon) & -\frac{\alpha\cos\theta_\omega}{2} & -\frac{\alpha\sin\theta_\omega\sin\phi_\omega}{2} \\ \frac{\alpha\cos\theta_\omega}{2} & 1 & -\frac{\alpha\sin\theta_\omega\cos\phi_\omega}{2} \\ \frac{\alpha\sin\theta_\omega\sin\phi_\omega}{2} & \frac{\alpha\sin\theta_\omega\cos\phi_\omega}{2} & \epsilon \end{bmatrix} \tag{3.9}$$

and is parameterized by four non-dimensional quantities, the definitions of which were given in the previous chapter. It is important to note that in general the flows characterised by Eq.3.9 are three-dimensional in nature except when the cubic invariant $R = 0$, which points to one or more of the eigenvalues associated with $\bar{\Gamma}$ being zero, in turn pointing to a planar linear flow. Thus, the eccentric planar linear flows are parameterized by at most three parameters corresponding to a three-dimensional sub-space. Recall from the previous chapter that, in the two-parameter family of axisymmetric extension with inclined vorticity, all three types of eccentric planar flows occur (Fig.2.35-2.39). This subset of eccentric planar linear flows was governed by a single parameter, with the value of the other parameter set by the equation $R = 0$. In this section, we analyse the eccentric planar flows that belong to the aforementioned family in detail. These results are representative of the more general eccentric planar linear flows characterised by three parameters.

For the case of axisymmetric extension with inclined vorticity, $\bar{\Gamma}$ is given by:

$$\bar{\Gamma} = \begin{bmatrix} 1 & -\frac{\alpha \cos \theta_\omega}{2} & 0 \\ \frac{\alpha \cos \theta_\omega}{2} & 1 & -\frac{\alpha \sin \theta_\omega}{2} \\ 0 & \frac{\alpha \sin \theta_\omega}{2} & -2 \end{bmatrix} \tag{3.10}$$

for which the the three scalar invariants are,

$$P = 0 \tag{3.11}$$

$$Q = \frac{\alpha^2 - 12}{4} \tag{3.12}$$

$$R = \frac{-8 + \alpha^2(1 - 3\cos^2(\theta_\omega))}{4}. \tag{3.13}$$

We can find the locus of the one-parameter subset of the eccentric planar linear flows by solving $R = 0$, to get

$$\alpha = \frac{2\sqrt{2}}{\sqrt{1 - 3\cos^2(\theta_\omega)}} \tag{3.14}$$
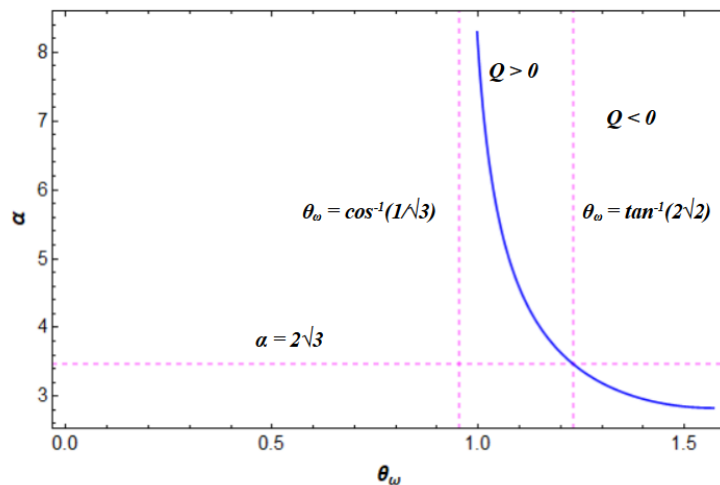
Figure 3.2: Domain of existence of eccentric planar linear flows in the $\theta_\omega - \alpha$ plane. For $\theta_\omega = \cos^{-1}\left(\frac{1}{\sqrt{3}}\right)$, the eccentric flow occurs at $\alpha = \infty$ which corresponds to solid-body rotation and at a point $(\theta_\omega, \alpha) = (\tan^{-1}(2\sqrt{2}), 2\sqrt{3})$, $Q = R = 0$ implying that the eccentric planar flow is parabolic.

This is plotted in the $\alpha - \theta_\omega$ plane in Fig.3.2. From Eq.3.14, we see that the solutions for α exist only for $\theta_\omega > \cos^{-1}\left(\frac{1}{\sqrt{3}}\right)$, which was labelled θ_ω^{th1} in the previous chapter. From Eq.3.12 for Q, we see that

it is positive for $\alpha > 2\sqrt{3}$ and negative below it. For $\alpha = 2\sqrt{3}$, one finds $\theta_\omega = \tan^{-1}(2\sqrt{2})$, (which was labelled θ_ω^{th2} in Chapter 2). This pair of (θ_ω, α) corresponds to $Q = R = 0$ and a planar parabolic flow, while the other cases correspond to eccentric planar elliptic or hyperbolic flows depending on whether $Q > 0$ (eigenvalues are complex conjugates) or $Q < 0$ (eigenvalues are oppositely signed). Based on the aforementioned information, we conclude that the eccentric planar linear are (i) elliptic for $\cos^{-1}\left(\frac{1}{\sqrt{3}}\right) \leq \theta_\omega < \tan^{-1}(2\sqrt{2})$, (ii) parabolic at $\theta_\omega = \tan^{-1}(2\sqrt{2})$, and (iii) hyperbolic for $\tan^{-1}(2\sqrt{2}) < \theta_\omega \leq 90°$. We now proceed to calculate the various characteristics of these flows, and compare them against the characteristics of canonical planar linear flows mentioned earlier.

(a) Eccentric planar eliptic flow

(b) Eccentric planar parabolic flow

(c) Eccentric planar hyperbolic flow
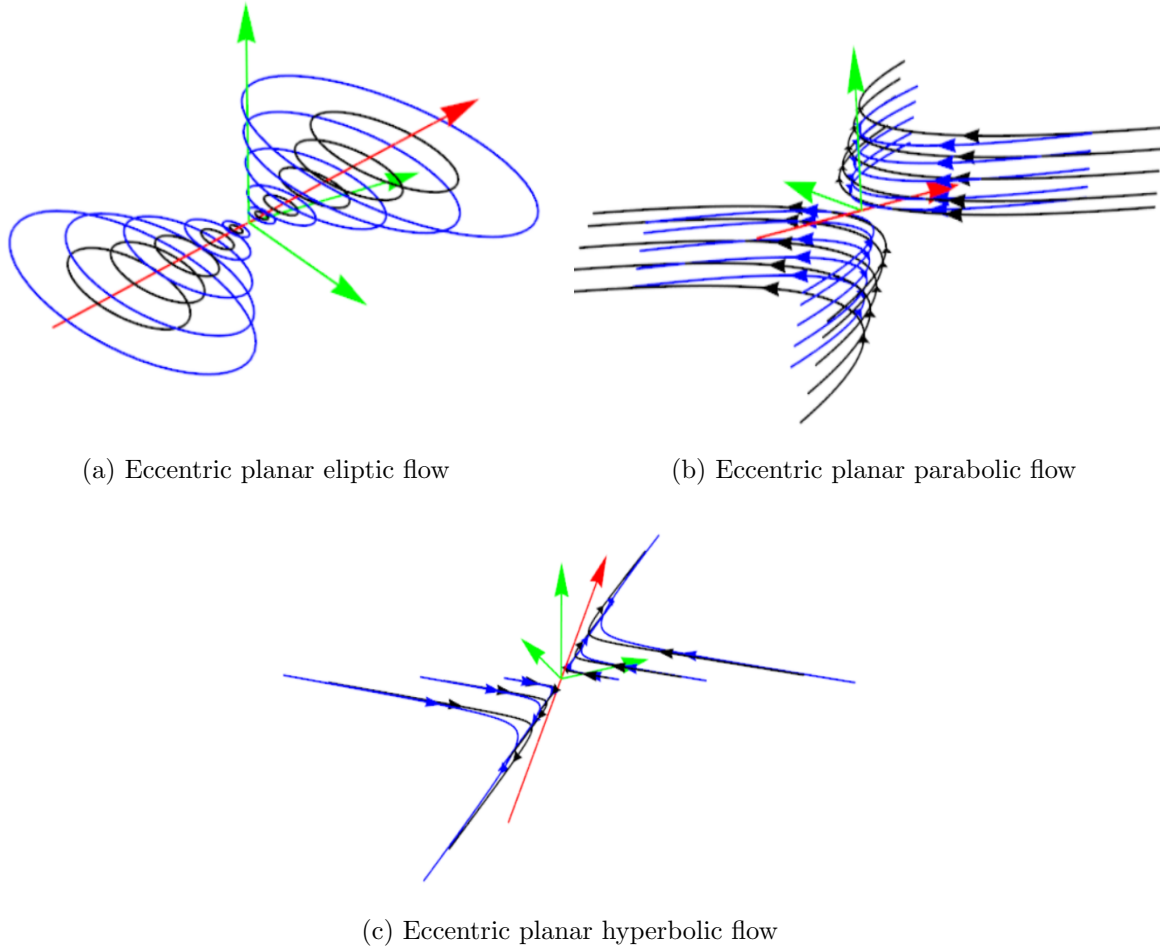
Figure 3.3: Representative plots of the streamlines associated with *eccentric planar* (a) elliptic, (b) parabolic and, (c) hyperbolic flows. All the streamlines are drawn in a coordinate frame with it's polar axis normal to the plane of flow (green axes) and the red arrow corresponds to the neutral direction (eigenvector) associated with $\bar{\mathbf{\Gamma}}$. The two colors (black and blue) represent streamlines corresponding to different values of the arbitrary constant C, where all streamlines having the same color correspond to a unique projection onto a unit sphere (see Section 3.3 for more details).

The first property we calculate is the eccentricity of the streamlines. The typical streamline topologies for eccentric planar flows are shown in Fig.3.3, where we see that the plane of flow is not orthogonal to the neutral direction (eigenvector corresponding to the zero eigenvalue). We calculate the eccentricity of these streamlines, noting that for a given (θ_ω, α) pair at which these flows occur, the streamlines across multiple planes exhibit the same properties and thus it suffices to calculate all the quantities in one of

the planes. We observe that the major and minor axes changes across the streamlines on the same plane but their ratios remain constant. Therefore, the eccentricity of the streamlines of eccentric planar flows are constant for a given (θ_ω, α) pair. The eccentricity of these streamlines which is defined as:

$$
e = \begin{cases}
\sqrt{1 - \frac{b^2}{a^2}} & \text{for ellipses} \\
\\
\sqrt{1 + \frac{b^2}{a^2}} & \text{for hyperbolas}
\end{cases} \tag{3.15}
$$

where b and a are the major and minor axes. The eccentricity is plotted against θ_ω in Fig.3.4. From this figure, we see that $e < 1$ for $\cos^{-1}\left(\frac{1}{\sqrt{3}}\right) \leq \theta_\omega < \tan^{-1}(2\sqrt{2})$ corresponding to the elliptic flows and, $e > 1$ for $\tan^{-1}(2\sqrt{2}) < \theta_\omega \leq \pi/2$ corresponding to hyperbolic flows. The eccentricity $e = 1$ for $\theta_\omega = \tan^{-1}(2\sqrt{2})$ for the parabolic flow. We also note that $e = \sqrt{2}$ for $\theta_\omega = \pi/2$, implying that the streamlines of this limiting hyperbolic flow are rectangular hyperbolas. Thus, this flow is a rotational linear flow with the same streamline pattern as the canonical planar extension. However, this limiting hyperbolic flow, does not always have rectangular hyperbolas as streamlines, for the sequence of eccentric planar linear flows corresponding to other values of the flow parameter. The other limiting flow in this sequence is the canonical planar linear flow of solid-body rotation corresponding to $\theta_\omega = \cos^{-1}(\frac{1}{\sqrt{3}})$. This is the only canonical flow in this sequence. However, as we shall see later, solid-body rotation will not always be a limiting flow of the eccentric planar flow sequence corresponding to other values of the flow parameters.
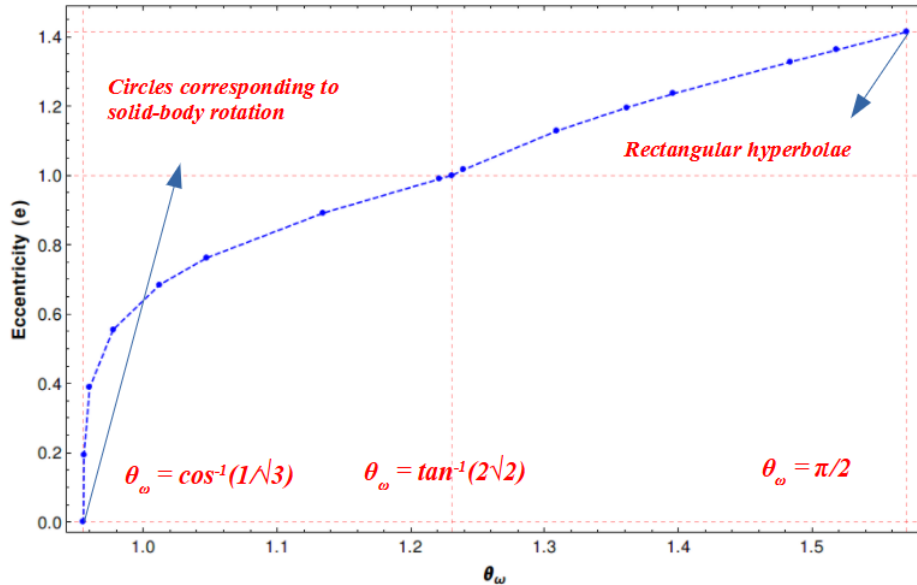
Figure 3.4: Eccentricity e of the streamlines of eccentric planar linear flows. The elliptic flows with $e < 1$ correspond to $\cos^{-1}\left(\frac{1}{\sqrt{3}}\right) \leq \theta_\omega < \tan^{-1}(2\sqrt{2})$ and the hyperbolic flows with $e > 1$ correspond to $\tan^{-1}(2\sqrt{2}) < \theta_\omega \leq 90°$. The parabolic flow, which serves as the bridge between the two, has $e = 1$ corresponding to the point $\theta_\omega = \tan^1(2\sqrt{2})$.

The next property we calculate is the angle between the normal to the plane of flow and the eigenvector corresponding to the neutral direction. In the case of canonical flows, we saw that this direction was always orthogonal to the plane of flow. Recall that for elliptic flows, there is only one real eigenvector, whereas for the hyperbolic ones, there are three, two of which lie on the lane of flow, along the asymptotes of the hyperbolas. For the special case of parabolic flows, there is a unique non-degenerate real eigenvector, along

the axis of the parabolas, unlike the simple shear flow, where we have an entire plane (flow-vorticity plane) of neutral directions. In Fig.3.5, we see that the angle of inclination between the neutral direction and the plane of flow is non-trivial, except for $\theta_\omega = \cos^{-1}\left(\frac{1}{\sqrt{3}}\right)$, which corresponds to solid-body rotation. For the case of parabolic flows, we see that the inclination is $\pi/2$ consistent with the fact that the eigenvector is along the plane of flow. A consequence of these results is the fact that there is a non-trivial component of extension normal to the plane of flow. We see that in Fig.3.6, where the component of extension along a normal to the plane of flow is plotted. We see that this is zero, again, only for the case of solid-body rotation, but remains non-zero for every other member of the sequence.
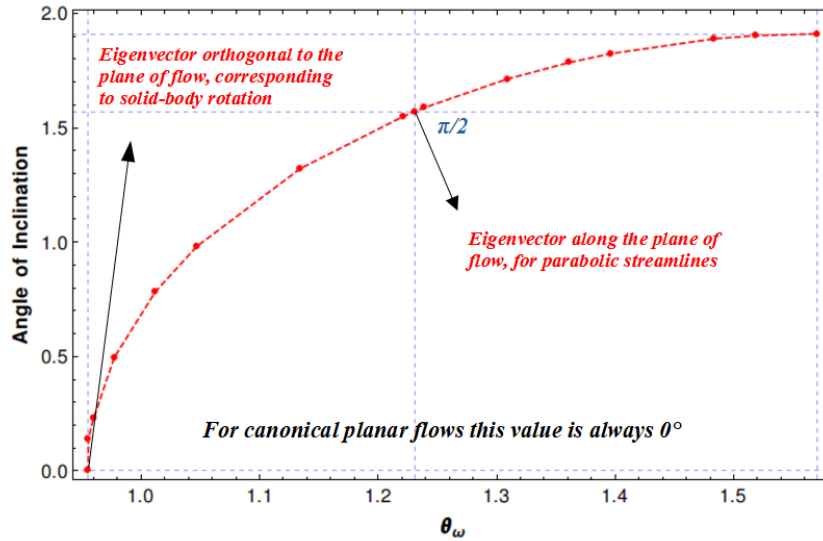
Figure 3.5: Angle of inclination between the normal to the plane of flow and the neutral direction for the eccentric planar linear flows. All these flows have a non-trivial inclination as opposed to the canonical flows.
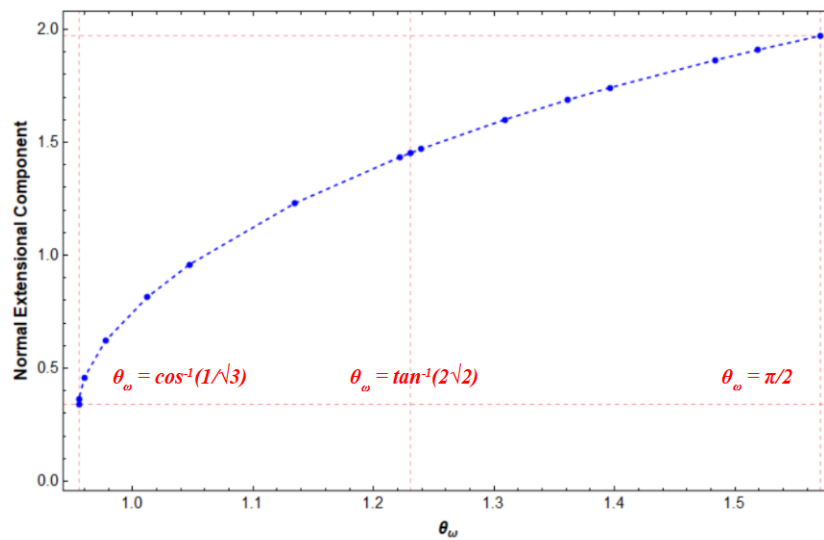
Figure 3.6: The component of extension normal to the plane of flow against θ_ω. All flows have a finite component of extension normal to the plane of flow again in contrast to the canonical flows for which this value is identically zero.

The fact that the flows are planar despite there being a non-trivial normal component of extension can be explained easily in the context of elliptic flows, where the streamlines are periodic orbits. For these flows, the neutral direction lies on the face of a right circular cone, whose axis coincides the vector along which the magnitude of extension is maximum. Thus, within this conical region, we have extension and outside it we have compression. When vorticity is added to it, there is a critical inclination at which, a line element in the space will be subject to alternate extension and compression such that it executes a periodic motion, where at the end of one cycle, it comes back to it's original length. This gives rise to a closed-streamline topology, which is the eccentric elliptic flow topology and the critical inclination corresponds to $R = 0$.

These properties show how the eccentric planar flows differ from the actual ones and more specifically highlight the fact that the canonical planar linear flows are special cases of these flows, which constitute a more general class of planar linear flows. Note that even though we have calculated these values for a particular sequence of one-parameter family of eccentric planar flows, and we shall comment on these properties for a more general sequence at a later stage. In the next section, we identify the domain of existence of these flows in the $4D$ parameter space of general linear flows and show that this domain occupies a three-dimensional volume in the $4D$ hyperspace, much like the plot in Fig.3.2, where the one-parameter family of eccentric planar flows lie on a line ($1D$ volume) in the $\theta_\omega - \alpha$ plane ($2D$ space).

3.2.2   Domain of Existence of Eccentric Planar Linear Flows

As indicated earlier, the one-parameter sequence of eccentric planar linear flows is only a projection of the three-dimensional sub-space onto the $\theta_\omega - \alpha$ space. In order to characterise the full space of eccentric planar linear flows in the four-dimensional parameter space of incompressible linear flows, we return to the general form of the velocity-gradient tensor given in Eq.3.9. The scalar invariants P, Q and R are of this tensor are given by:

$$P = 0 \tag{3.16}$$

$$Q = \frac{\alpha^2}{4} - (1 + \epsilon + \epsilon^2) \tag{3.17}$$

$$R = \frac{\epsilon \left(16(1 + \epsilon) - \alpha^2(1 + 3\cos 2\theta_\omega)\right) + 2(2 + \epsilon)\alpha^2 \cos 2\phi_\omega \sin^2 \theta_\omega}{16} \tag{3.18}$$

In order to find the region of existence of planar flows, we again for $R = 0$. As mentioned above, the eccentric planar linear flows occupy a three-dimensional sub-space of $4D$ hypersurface which cannot be directly visualised. We therefore visualise this sub-space by looking at projections of this volume onto a pair of $3D$ spaces: (i) $\epsilon - \phi_\omega - \theta_\omega$ space and (ii) $\epsilon - \phi_\omega - \alpha$ space. In each of these spaces, we choose an (ϵ, ϕ_ω) pair and find the critical values of θ_ω and α that demarcate the different linear flows using the properties of these invariants. As a result we obtain the surfaces in each of these sub-spaces that demarcate the different eccentric planar flows. We first describe the construction of these surfaces in the $\epsilon - \phi_\omega - \theta_\omega$ space and then move on to the other space.

3.2.2.1   The $\epsilon - \phi_\omega - \theta_\omega$ Space

Recall from Section 2.2 that, in order to cover all possible linear flow configurations, ϵ should range from $-2 \leq \epsilon \leq 0$, and ϕ_ω from $0 \leq \phi_\omega \leq \pi/2$ on account of the four-fold symmetry in the azimuthal angle. The surface on which the parabolic flows occur is first found by solving $Q = 0$ and $R = 0$ simultaneously. The first of these equations gives,

$$\alpha = 2\sqrt{1 + \epsilon + \epsilon^2} \tag{3.19}$$

This can then be substituted into R to find the equation of the surface in the $\epsilon - \phi_\omega - \theta_\omega$ sub-space as:

$$\theta_\omega = \frac{1}{2}\cos^{-1}\left(1 - \frac{4\epsilon^3}{(1 + \epsilon + \epsilon^2)(3\epsilon + (2 + \epsilon)\cos 2\phi_\omega)}\right) \tag{3.20}$$

This solution does not exist outside the range of cosine function and thus setting the constraint that the argument inside the cosine should lie within $(-1, 1)$, gives us:

$$\phi_\omega \in [0, \pi/2] \quad \text{for } \epsilon = 0 \tag{3.21}$$

$$\phi_\omega \geq \frac{1}{2}\cos^{-1}\left(\frac{\epsilon(1 + \epsilon + \epsilon^2) - 2\epsilon(2 + 2\epsilon + \epsilon^2)}{(1 + \epsilon + \epsilon^2)(2 + \epsilon)}\right) = \phi_\omega^{cr1} \quad \forall \, \epsilon \neq 0 \tag{3.22}$$

The first of these equation corresponds to the special case of $\epsilon = 0$ for which the solution is simply, $\theta_\omega = 0$ regardless of ϕ_ω. From Eq.3.22, as $\epsilon \to 0$, $\phi_\omega^{cr1} \to \pi/4$, so the critical curve bounding the domain of existence in the $\epsilon - \phi_\omega$ space meets the $\epsilon = 0$ axis at $\phi_\omega = \pi/4$ and from Eq.3.20, $\theta_\omega = \pi/2$ all along this critical curve. Also from Eq.3.22, there is no constraint on ϕ_ω for $\epsilon < -1$.

Using these results, we can plot the parabolic flow surface two views of which are shown in Fig.3.7, where we see that the surface is smooth for all non-zero values of ϵ. For $\epsilon = 0$, the solution of Eq.3.20 is $\theta_\omega = 0°$, which is disjoint from the solution surface corresponding to non-zero ϵ (Eq.3.22). Therefore, the surface asymptotes to a critical curve in the shape of an inverted T ($\perp$) defined by the combination of curves $\theta_\omega = 0$, $0 \leq \phi_\omega \leq \pi/2$ and $0 \leq \theta_\omega \leq \pi/2$, $\phi_\omega = \pi/4$. The first of these curves (horizontal line) is populated by canonical planar linear flows regardless of ϕ_ω, with the flow taking place in the $x_1 - x_2$ plane and vorticity along x_3 (see Eq.3.9). The vertical line is populated by eccentric planar flows for all θ_ω. It will be seen later that all the surfaces (which bound the region of existence of eccentric planar linear flows) intersect at this critical curve, implying that along these lines of intersection (the red lines), the particular type of planar flow is determined by α alone. This projection of a hypersurface therefore leads to an apparent contradiction in that distinct points in the full four-dimensional space appear connected in this projection. The other special case is $\epsilon = -1$, which again corresponds to one of the extensional components being zero (planar extension). For this case, $\theta_\omega = 90°$ and $\phi_\omega = 0°$ again corresponds to canonical planar linear flows (for all values of α). The final limiting case corresponds to $\epsilon = -2$, for which we see that the θ_ω at which the eccentric parabolic flows occur is independent of ϕ_ω, consistent with what we have already seen in Section 2.4. Keep in mind that this surface marks the transition from elliptic to hyperbolic flow, and therefore serves as a bounding surface for both eccentric elliptic and hyperbolic flows.

Region where eccentric planar parabolic flows do not exist.

(a) Top View

Surface on which eccentric planar parabolic flows exist.

Points of occurrence canonical planar flows   Points of occurrence eccentric planar flows

(b) Isometric View
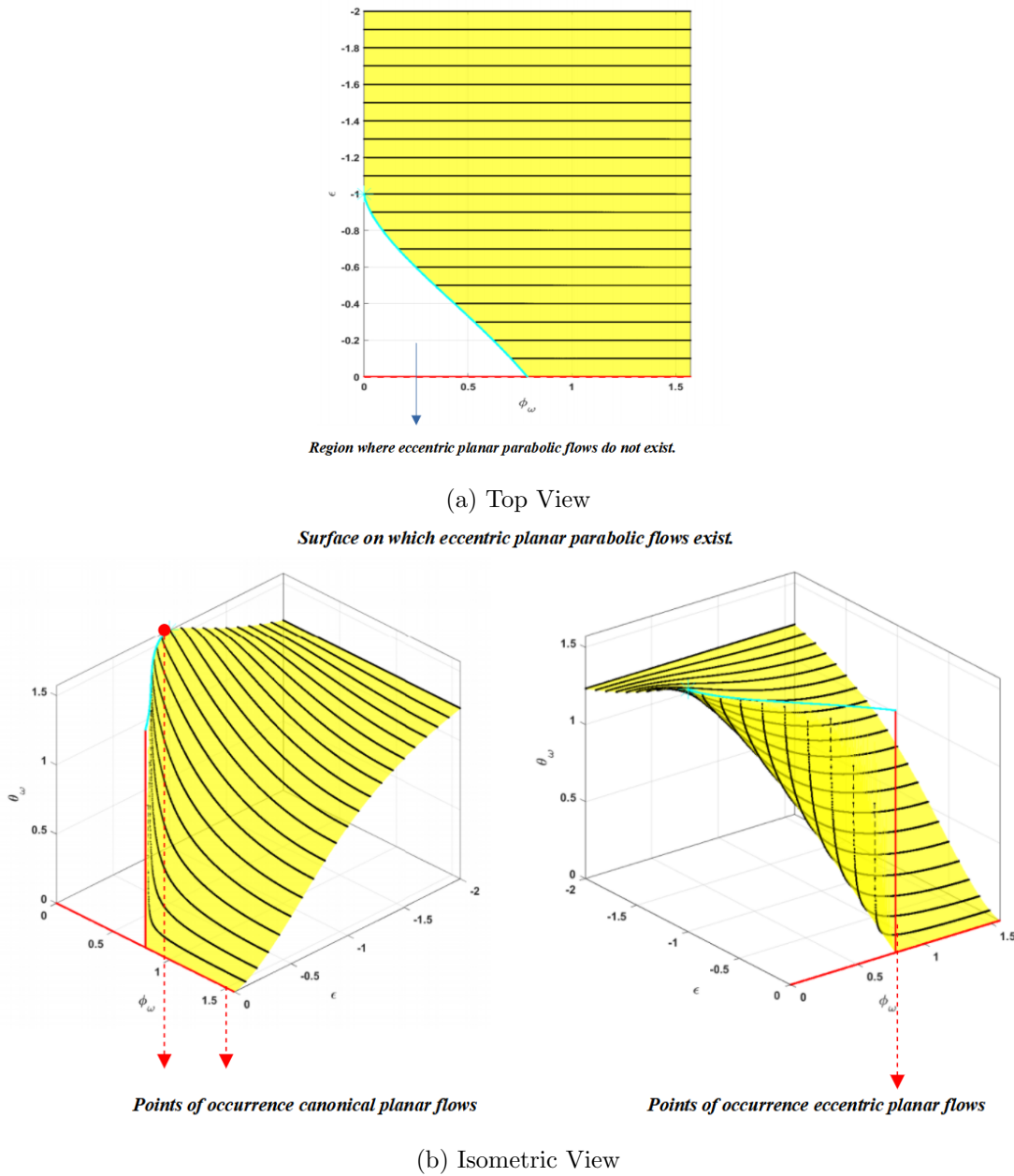
Figure 3.7: A view showing the surface on which the eccentric planar parabolic flows occur in the $\epsilon-\phi_\omega-\theta_\omega$ space. The blue line in (a) marks the boundary of the region where these flows do not exist in the $\epsilon-\phi_\omega$ plane. The horizontal and vertical lines in (b) are the critical curves that form the asymptote of the surface, along which the type of planar flow is determined by α alone.

Now, we move on to find the projected view of the second surface, in the $\epsilon-\phi_\omega-\theta_\omega$ space, that marks the boundary of eccentric elliptic linear flows. We again solve $R=0$ for α and we find the solution to be:

$$\alpha = \frac{2\sqrt{\epsilon(1+\epsilon)}}{\sqrt{\epsilon\cos^2\theta_\omega - \frac{1}{2}(\epsilon+(2+\epsilon)\cos 2\phi_\omega)\sin^2\theta_\omega}} \tag{3.23}$$

A real-valued α is possible only when the quantity inside the square root is positive, which gives:

$$\theta_\omega = \frac{1}{2}\cos^{-1}\left(1 - \frac{4\epsilon}{3\epsilon+(2+\epsilon)\cos 2\phi_\omega}\right) \tag{3.24}$$

as the expression for the limiting value of θ_ω corresponding to a zero-crossing in R. In other words, this value of θ_ω causes α in Eq.3.24 to diverge, which from our earlier analysis of surface streamline topology, we know to be the critical value of inclination above or below which R suffers zero crossing (Fig.2.34b).

Region where solid-body rotation flows do not exist.   *Region where eccentric planar elliptic flows do not exist.*

(a) Top View

Surface on which solid-body rotation flow topology exists.

Points of occurrence canonical planar flows   *Points of occurrence eccentric planar flows*

(b) Isometric View
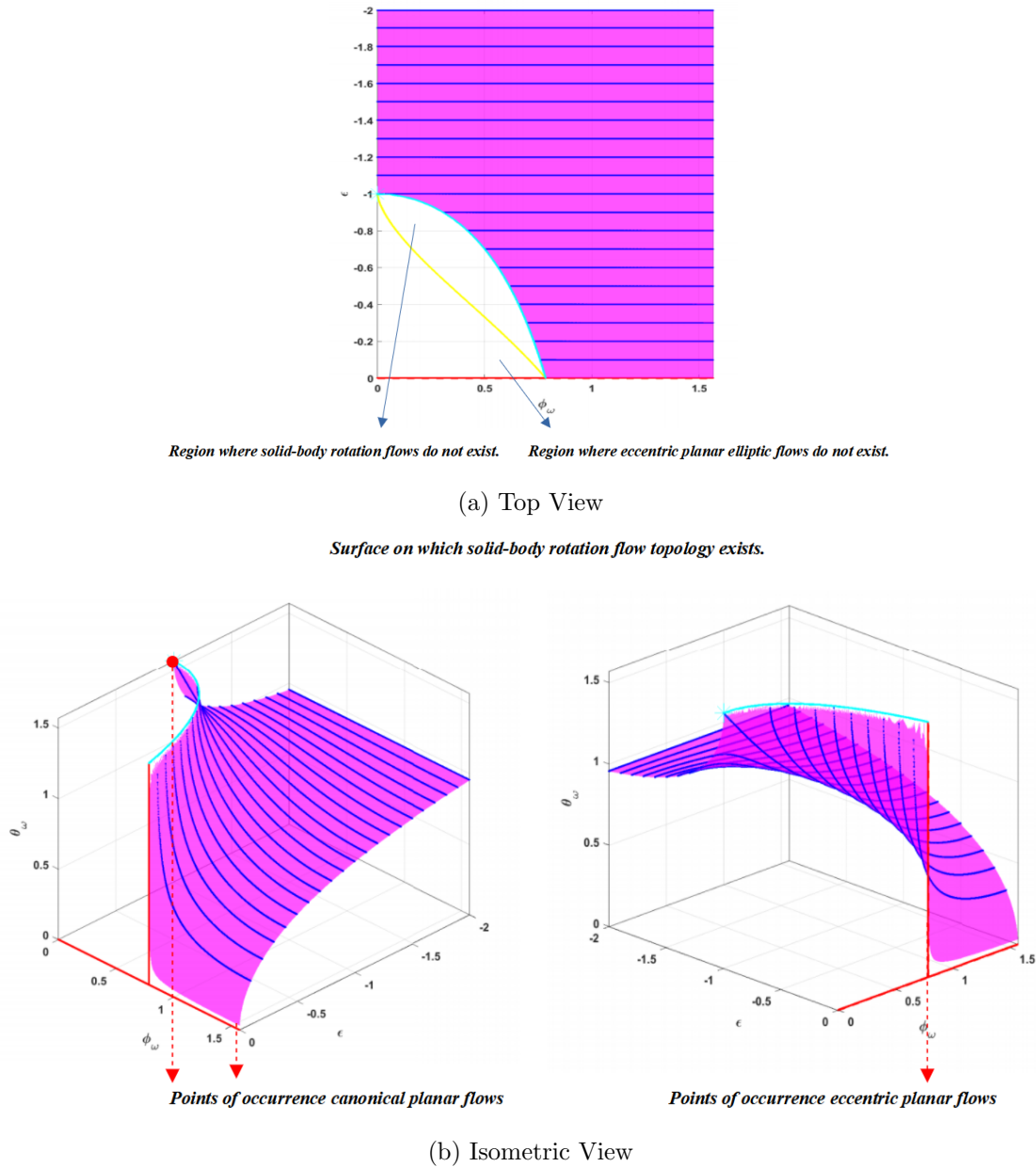
Figure 3.8: The $\epsilon - \phi_\omega - \theta_\omega$ space with the surface that marks the bounding surface of eccentric planar elliptic flows. All points on this surface correspond to canonical solid-body rotation. In (a), the blue line marks the boundary of the region where these flows do not exist and, the yellow line corresponds to the threshold below which parabolic flows do not exist (Eq.3.22). So, the region between the blue and yellow lines have eccentric elliptic flows as limiting ones. The horizontal and vertical lines are the critical curves that form the asymptote of the surface, same as in Fig.3.7a.

Therefore, Eq.3.24 marks the surface bounding the eccentric planar elliptic flows, with all the points on it corresponding to solid-body rotations ($\alpha = \infty$). The inverse cosine function in the equation, again sets

a constraint on θ_ω, which gives us the domain of existence of this surface in the $\epsilon - \phi_\omega$ plane to be:

$$\phi_\omega \in [0, \pi/2] \quad \text{for } \epsilon = 0 \tag{3.25}$$

$$\phi_\omega \geq \frac{1}{2} \cos^{-1}\left(\frac{-\epsilon}{2+\epsilon}\right) = \phi_\omega^{cr2} \quad \forall \, \epsilon \neq 0 \tag{3.26}$$

From Eq.3.26, as $\epsilon \to 0$, $\phi_\omega^{cr2} \to \pi/4$, so the critical curve bounding the domain of existence in the $\epsilon - \phi_\omega$ space meets the $\epsilon = 0$ axis at $\phi_\omega = \pi/4$ and from Eq.3.24, $\theta_\omega = \pi/2$ all along this critical curve just like the critical curve of the parabolic flow surface. Also from Eq.3.26, we see that there is no constraint on ϕ_ω for $\epsilon < -1$ and so $\phi_\omega \in [0, \pi/2]$ for $\epsilon < -1$.

The elliptic flow surface is plotted in Fig.3.8, where, we see that the same features observed in the parabolic flow surface are also observed in this case. The surface is smooth for $\epsilon \neq 0$ and asymptotes to the same singular curve as the parabolic flow surface when $\epsilon \to 0$. For this case too, the curve $\theta_\omega = 0$ is the solution of Eq.3.24 for $\epsilon = 0$, which is disjoint from the solution surface (Eq.3.26) corresponding to non-zero ϵ. Owing to these features, the two surfaces (Eq.3.22 and 3.26) intersect at this singular $\perp$-shaped line. Also, we see that, both Eq.3.20 and Eq.3.24 reduce to $\theta_\omega = \frac{1}{2} \cos^{-1}\left(1 + \frac{4}{\cos 2\phi_\omega - 3}\right)$ for $\epsilon = -1$, implying that these two surfaces have another intersection at $\epsilon = -1$. As noted before, along these lines of intersection, the particular type of planar flow is determined by α alone. And finally, at the other limiting value of $\epsilon = -2$, the elliptic flow surface asymptotes to a horizontal line, and is therefore independent of ϕ_ω, just like the surface of parabolic flows.

We can equivalently make use use of the behavior of the cubic invariant R as a function of θ_ω, α at a given (ϵ, ϕ_ω) pair to arrive at Eq.3.24. We observe from the plots of R against α, that there is a critical $\theta_\omega = \theta_\omega^{th1}$ above which R suffers zero crossing. This is shown in Fig.3.9 for certain specific values of ϵ and ϕ_ω, but the same is true for (almost[1]) all other values of ϵ, ϕ_ω. This plot gives us a crucial insight which can be utilised to find the bounding surface in the $\epsilon - \phi_\omega - \theta_\omega$ space. This is based on the fact that, in the plot of R against α, the curve for θ_ω^{th1} is horizontal (implying that it crosses zero at $\alpha = \infty$). So to find this critical θ_ω^{th1}, we merely differentiate R with α and solve $dR/d\alpha = 0$ for θ_ω^{th1}, which gives the same result as in Eq.3.24.

Finally, we plot the last surface that remains to be found, which is the bounding surface for the eccentric planar hyperbolic flows. This can be found based on the behavior of R as a function of θ_ω and α shown in Fig.3.9. Our detailed analysis reveals that the starting value of R at $\alpha = 0$ (corresponding to a pure $3D$ extensional flow) changes sign at $\epsilon = -1$ (where it is zero). This implies that all the curves corresponding to θ_ω greater than θ_ω^{th1} will suffer a zero crossing when $\epsilon < -1$ (see Fig.3.9b) and the curves corresponding to $\theta_\omega < \theta_\omega^{th1}$ will do so when $\epsilon > -1$ (see Fig.3.9a). Since θ_ω ranges from 0 and $\pi/2$, the boundary surface corresponds to $\theta_\omega = \pi/2$ for $\epsilon < -1$ and $\theta_\omega = 0$ for $\epsilon > -1$. Note that there is nothing special about the hyperbolic flows that correspond to points on these limiting surfaces (except at few special values to be discussed later). Also note that these hyperbolic surfaces are not limiting in the sense that, they also form a boundary of the original $4D$ space for general linear flows. Notwithstanding degeneracy, crossing this boundary surface would land us outside the original $4D$ space, outside the domain of existence of linear flows, let alone planar linear flows. The same holds true for points beyond the pair of critical curves on the roof ($\theta_\omega = \pi/2$. Nevertheless, one can always change α at this limiting value of θ_ω and it will lead to $3D$ linear flows. In addition to this, we also observe that in the plane $\epsilon = -1$ and $\epsilon = 0$, regardless of ϕ_ω and θ_ω, $\alpha = 0$ is a planar extension flow topology. But

---

[1]This implies the (ϵ, ϕ_ω) pair, for which the limiting flow is solid-body rotation. As seen from Fig.3.8a, there is a region in (ϵ, ϕ_ω) plane where these flows do not exist we will observe a different kind of behavior of the invariant R in this region, which is explained later.

the curves of intersection of these bounding surfaces in the aforementioned planes are shared by parabolic and elliptic flows as well. Therefore, both planes ($\epsilon = -1$ and $\epsilon = 0$), are part of the overall surface on which hyperbolic flows (specifically, planar extensional flows) occur. Putting these surfaces together will give us the bounding surface on which eccentric planar hyperbolic flows occur.

(a) $-1 < \epsilon < 0$ (b) $-2 \leq \epsilon < -1$
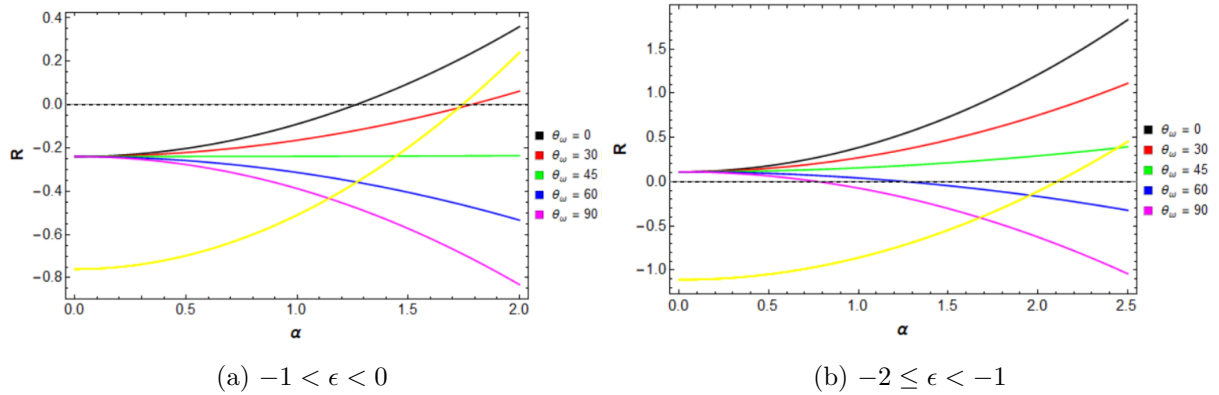
Figure 3.9: Plot of the cubic invariant R against α as a function of θ_ω for (a)$-1 < \epsilon < 0$ and (b)$-2 \leq \epsilon < -1$. This plot suggests that θ_ω bounding the eccentric hyperbolic flows is 0 for (a) and $\pi/2$ for (b). The yellow curve corresponds to the quadratic invariant Q.

We can now put the three limiting surfaces together to get the region of existence of eccentric planar linear flows in $\epsilon - \phi_\omega - \theta_\omega$ space, with the transitions between the different types of linear flows marked. This is done in Fig.3.10. From the plot, we see that all the surfaces intersect at $\epsilon = -1$ and $\epsilon = 0$, whose implication is explained in the previous paragraph. We note that, when $\phi_\omega^{cr1} < \phi_\omega < \phi_\omega^{cr2}$, where the magenta surface is absent, no solid-body rotations occur. We also observe that, there is a range of values in $\epsilon - \phi_\omega - \theta_\omega$ space where only eccentric hyperbolic flows occur (when $\phi_\omega < \phi_\omega^{cr1}$), owing to the absence of parabolic and elliptic bounding surfaces. For the sake of clarity, we have not included the $\epsilon = 0$ plane, which is a part of the (green) bounding surface populated by eccentric hyperbolic flows. This plot only completes one half of the picture, and one also needs the region in $\epsilon - \phi_\omega - \alpha$ space in conjunction with Fig.3.10, to uniquely map the planar linear flow topologies.
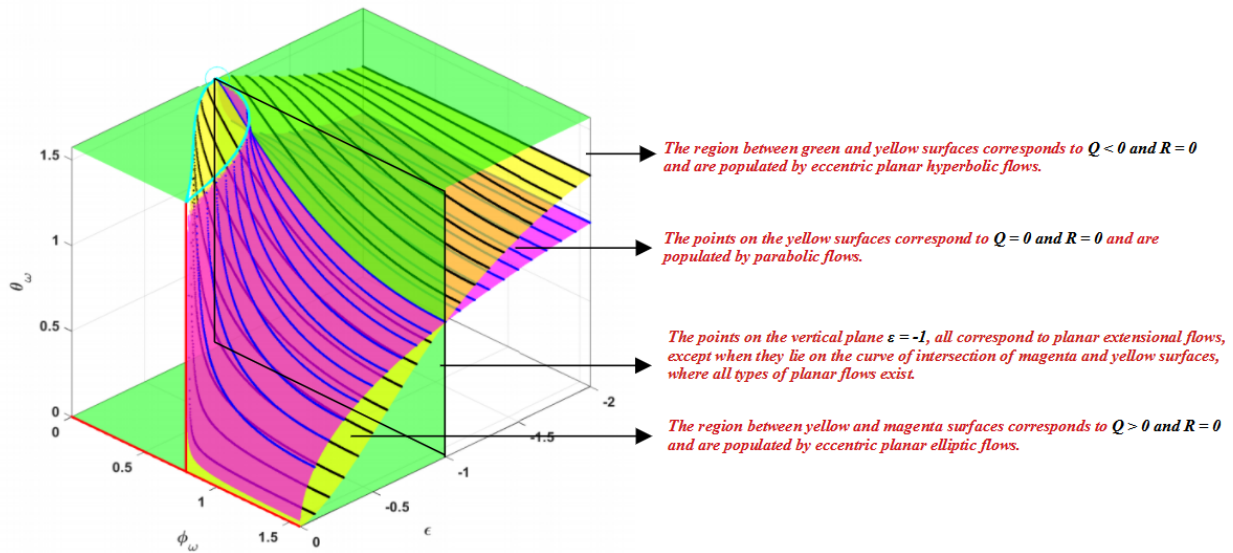
(a) The region of existence of eccentric planar flows and their bounding surfaces.
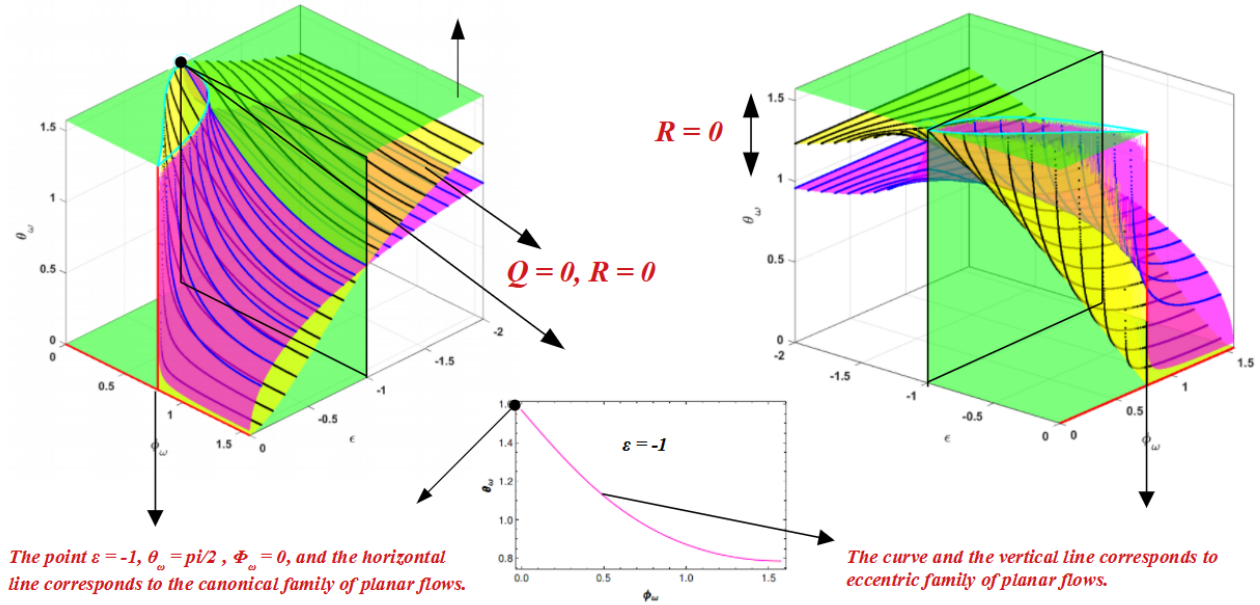
(b) Special points and lines in the region of existence.

Figure 3.10: The region of existence of eccentric planar flows in the $\epsilon - \phi_\omega - \theta_\omega$ space with (a) the values of invariants associated with the bounding surfaces, (b) the special points and lines in the region, which correspond to intersections of the bounding surfaces. The magenta and yellow lines in the bottom plane correspond to the critical curves given by Eq.3.26 and Eq.3.22 respectively.

3.2.2.2 The $\epsilon - \phi_\omega - \alpha$ Space

The bounding surfaces of the eccentric planar linear flows in the $\epsilon - \phi_\omega - \theta_\omega$ space are projections of hypersurfaces bounding a three-dimensional volume in a $4D$ parameter space. As a result these projections tend to be degenerate, wherein distinct points on the full $4D$ space appear connected in these projections, which show up as the singular curves in the $\epsilon - \phi_\omega - \theta_\omega$. Therefore, to uniquely map a distinct planar flow, one also needs another independent projection of the original hypersurface onto another $3D$ space,

namely the $\epsilon - \phi_\omega - \alpha$ space, where of ϵ and ϕ_ω are again the independent coordinates, with the third coordinate being α. Keeping in mind that solid-body rotation corresponds to $\alpha = \infty$, we set the third coordinate as $1/\alpha$ instead.

In the $\epsilon - \phi_\omega - 1/\alpha$ space, we again find the surface corresponding to eccentric planar parabolic flows first, by $Q = 0$, with Q given in Eq.3.17. This equation suggests that Q is independent of ϕ_ω and θ_ω, which gives the solution as:

$$\frac{1}{\alpha} = \frac{1}{2\sqrt{1 + \epsilon + \epsilon^2}} \tag{3.27}$$

Recall, from the analysis carried out in the $\epsilon - \phi_\omega - \theta_\omega$ space, that this same solution was used find the parabolic flow surface in that sub-space, and so, in the $\epsilon - \phi_\omega - 1/\alpha$ space, the parabolic flow surface automatically satisfies $R = 0$. We also noted that, this solution does not exist when $\phi_\omega < \phi_\omega^{cr1}$ (Eq.3.22) so long as $\epsilon \neq 0$. Thus, excluding this region leads to the surface of existence shown in Fig. 3.11, where the same color scheme used for the solution surfaces in the complementary space has been used to avoid confusion. We see from the plot that this surface is smooth and continuous. For the limiting value of $\epsilon = 0$, the solution given in Eq.3.27 tends to a constant value equal to $1/\alpha = 1/2$ (corresponding to simple shear flow) independent of ϕ_ω as expected. Therefore the domain of existence of parabolic flows includes the yellow surface and the asymptote (red line) at $\epsilon = 0$ which are disjoint, just like in domain of existence in the complementary space.
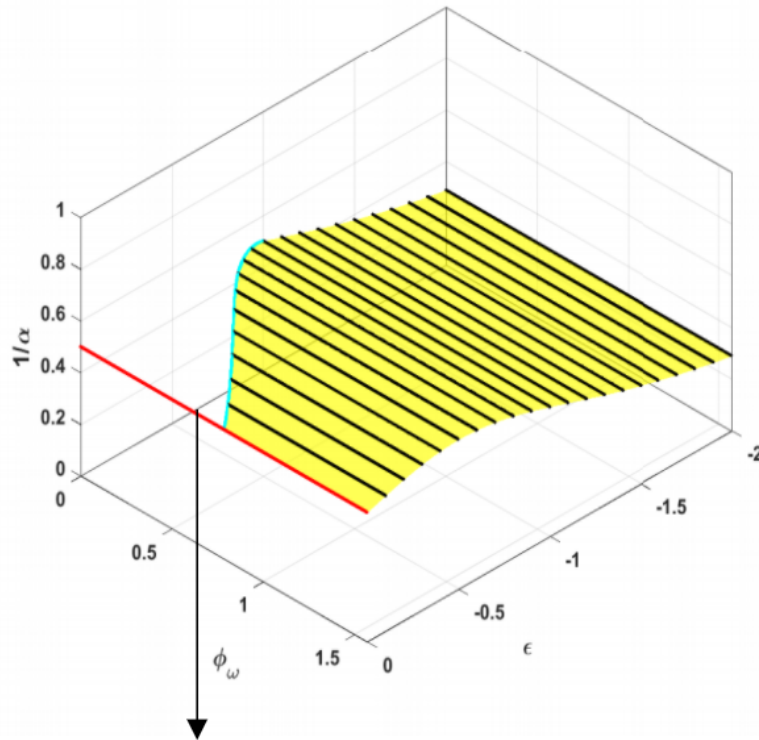
Line along which canonical flow occurs and in this case, the canonical flow is simple shear.

Figure 3.11: The surface on which eccentric planar parabolic flows occur. The cyan curve marks the boundary beyond which this solution is not valid and it is the same critical curve corresponding to Eq.3.22 which also appeared in the $\epsilon - \phi_\omega - \theta_\omega$ space. The red line corresponding to $\epsilon = 0$ is also a solution along which simple shear flows occur.

The surface lifts up from zero implying the absence of solid-body rotation topologies.
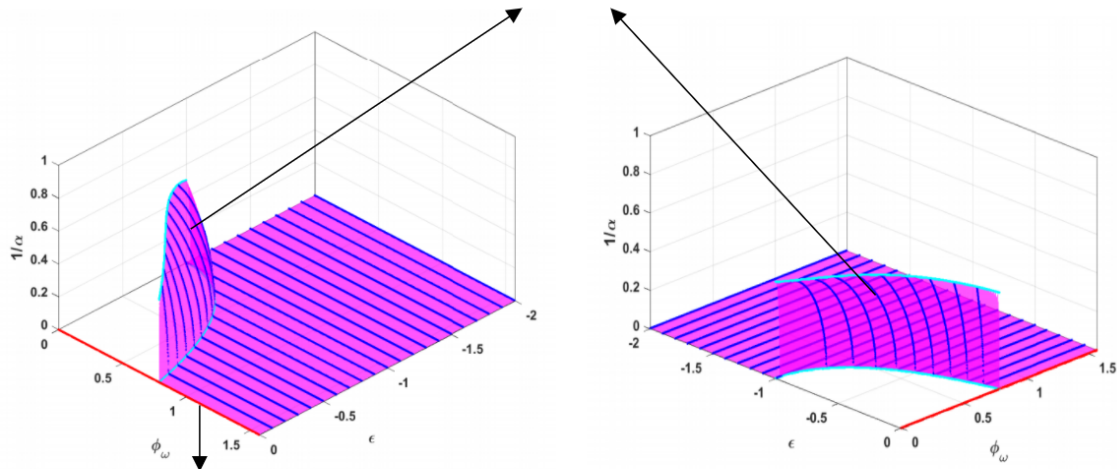
Line along which canonical flow occurs and in this case, the canonical flow is solid-body rotation.

(a) Isometric View.
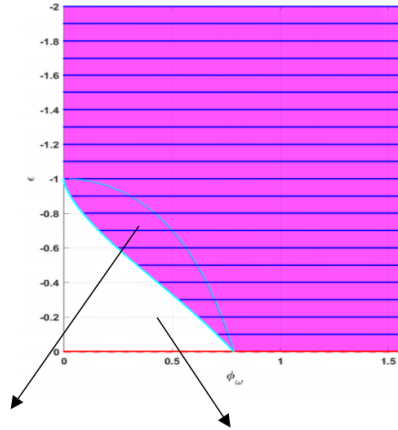
Region where solid-body rotation flows do not exist.   Region where eccentric planar elliptic flows do not exist.

(b) Top View.

Figure 3.12: The surface that bounds the eccentric planar elliptic flows. $1/\alpha = 0$ corresponds to solid-body rotations and when $1/\alpha \neq 0$, eccentric elliptic flows populate the surface. The cyan curves mark the two critical curves (ϕ_ω^{cr1}, ϕ_ω^{cr2}) between which solid-body rotations do not exist and for $\phi_\omega < \phi_\omega^{cr1}$, elliptic flows do not occur except at $\epsilon = 0$. The red line marks the asymptote of the bounding surface populated by solid body rotations.

We now move on to the bounding surface corresponding to eccentric planar elliptic flows. Recall again, from the discussion on $\epsilon - \phi_\omega - \theta_\omega$ space, that the limiting flow of solid-body rotation occurs for almost all $\epsilon - \phi_\omega$ pair except in the region where $\phi_\omega^{cr1} < \phi_\omega < \phi_\omega^{cr2}$ (the two cyan curves bounding the magenta and yellow surfaces in Fig.3.10a), provided $\epsilon \neq 0$. In this region, as already mentioned, the limiting topology of the eccentric elliptic flow is not solid-body rotation but rather an elliptic flow itself. In this region, these eccentric elliptic flows occurs at a finite α for a given θ_ω. This is in contrast to the solid-body rotation topology, which occurs when $1/\alpha = 0$. Therefore in the $\epsilon - \phi_\omega - 1/\alpha$ space, the bounding surface containing solid-body rotation corresponds to $1/\alpha = 0$ for all (ϵ, ϕ_ω), except in the region $\phi_\omega^{cr1} < \phi_\omega < \phi_\omega^{cr2}$, where the bounding surface will lift up from zero to a finite value of $1/\alpha$, and, will merge with the parabolic flow surface at $\phi_\omega = \phi_\omega^{cr1}$. This finite value of α can be found from the plot

of R against α as a function of θ_ω in this region, which is shown in Fig.3.13(a). From the figure, we see that this finite value of α corresponds to the last zero-crossing suffered by R and it happens for the curve with $\theta_\omega = \pi/2$. Thus this surface can be found by simply solving $R = 0$ with $\theta_\omega = \pi/2$, which gives us:

$$\frac{1}{\alpha} = \frac{\sqrt{\epsilon + (2 + \epsilon)\cos 2\phi_\omega}}{2\sqrt{2}\sqrt{-\epsilon(1 + \epsilon)}} \quad \text{for} \quad \phi_\omega^{cr1} < \phi_\omega < \phi_\omega^{cr2} \tag{3.28}$$

From the equation above, we see that $\frac{1}{\alpha} \to 0$ as $\phi_\omega \to \phi_\omega^{cr2}$ (the inner cyan curve in Fig.3.12b) and $\frac{1}{\alpha} \to \frac{1}{2\sqrt{1+\epsilon+\epsilon^2}}$ as $\phi_\omega \to \phi_\omega^{cr1}$ (the outer cyan curve in Fig.3.12b), which is the equation of the parabolic flow surface given in Eq.3.27. The bounding surface is plotted in Fig.3.12, where we see that the surface lifts from $1/\alpha = 0$ between the two boundaries (cyan curves). For the limiting value of $\epsilon = 0$, $1/\alpha = 0$ is the solution for $R = 0$, independent of ϕ_ω, and it again corresponds to solid-body rotations. This asymptote is therefore part of the solution surface, wherein it is again disjoint from the elliptic flow surface given Eq.3.28.

Finally, we plot the surface which bounds the eccentric planar hyperbolic flows. This surface is again constructed with insights from the R versus α plots as a function of θ_ω like the ones shown in Fig.3.9 and 3.13. However, finding the α values that bound the hyperbolic flows is more involved than in the $\epsilon - \phi_\omega - \theta_\omega$ subspace (Fig.3.10). In order to explain the construction of this surface, we first need to thoroughly understand the behavior of the cubic invariant R as a function of α. A part of this behavior is already highlighted in Fig.3.9, where we have plotted R against α for different θ_ω at a specific value of ϕ_ω and ϵ. However, we also observe that for certain values of (ϵ, ϕ_ω), the cubic invariant exhibits a completely different behavior as shown in Fig.3.13. The key to construct the bounding surface is in understanding the difference between these two kinds of behavior.

The first case corresponds to the behavior of R shown in Fig.3.9, which was already discussed in the previous section. Recall that, in this case there is a critical θ_ω^{th1}, for which R is horizontal (implying that it crosses zero at $\alpha = \infty$; corresponds to solid body rotations) and the final θ_ω that crosses zero is either $0°$ or $90°$ depending on whether $\epsilon > -1$ or $\epsilon < -1$. Also, the zero-crossing of the quadratic invariant Q coincides with the zero-crossing of R corresponding to a second critical θ_ω^{th2} between $(0°, \theta_\omega^{th1})$ or $(\theta_\omega^{th1}, 90°)$. Thus, for this scenario, which we label **Type 1**, we have all three types of eccentric planar flows with solid-body rotation occurring at θ_ω^{th1} and $\alpha = \infty$; the hyperbolic flows above (or below) θ_ω^{th2} and, the parabolic flow occurring at θ_ω^{cr2}. This is exactly what we observed for the case of axisymmetric extension with inclined vorticity ($\epsilon = -2, \phi_\omega = [0, 2\pi]$) in Section 3.2.1.

In the second scenario corresponding to Fig.3.13, we see that R is never horizontal. This behavior corresponds to $\phi_\omega < \phi_\omega^{cr2}$, where there are no solid-body rotations. We label this scenario **Type 2**. Therefore, $\phi_\omega = \phi_\omega^{cr2}$, marks the boundary that demarcates Type 1 and Type 2 behavior. In Type 2, the zero-crossing of R for all θ_ω is finite, implying the lower and upper bounding surfaces in the $1/\alpha$ space needs to finite. Here, there is still two further possibilities:

- The zero-crossing of the quadratic invariant Q coincides with that of R for a $\theta_\omega \in (0, \pi/2)$. In this scenario, again all three types of flows exist and they are bounded by finite bounding surfaces. We label this scenario **Type 2A**.

- The zero-crossing of Q and R does not coincide for any $\theta_\omega \in [0, \pi/2]$. From Figs.3.13(c) and 3.13(d), we see that α corresponding to the zero-crossing of Q is greater than the largest α value at which R crosses zero. This largest value may either correspond to $\theta_\omega = 0°$ or $\theta_\omega = 90°$. Therefore, here only hyperbolic flows exist. This scenario is labelled **Type 2B**. Recall that this is precisely what was observed in the region $\phi_\omega < \phi_\omega^{cr1}$, from Fig.3.10. Therefore, the boundary that demarcates Type 2A and Type 2B is $\phi_\omega = \phi_\omega^{cr1}$.

Further in Type 2B scenario shown in Fig.3.13(c), 3.13(d), we see that the maximum value of the R zero-crossing (α_{max}^{zc}), corresponds to $\theta_\omega = \pi/2$ above a critical value of ϕ_ω and to $\theta_\omega = 0°$ below it. Right at this critical value, R is independent θ_ω. Therefore, this critical value can be found by solving $dR/d\theta_\omega = 0$, which gives us:

$$\phi_\omega^{cr3} = \frac{1}{2} \cos^{-1}\left(\frac{-3\epsilon}{2+\epsilon}\right) \tag{3.29}$$
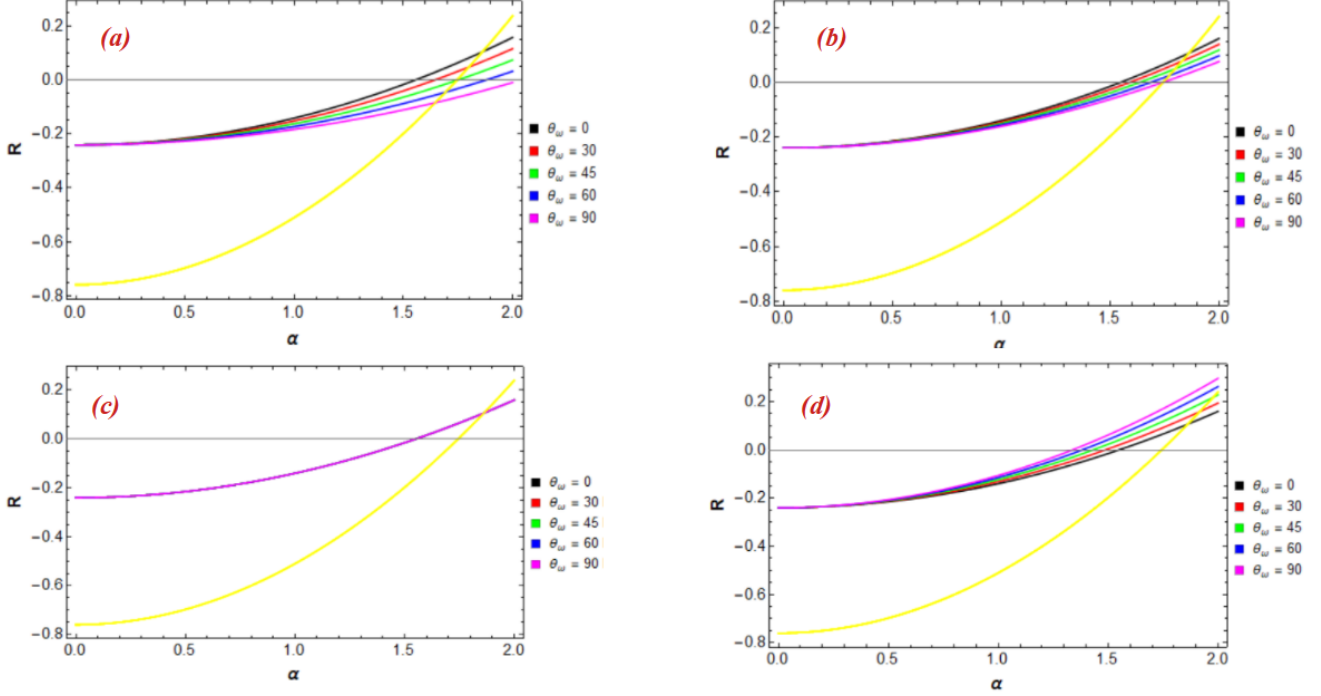
Figure 3.13: Plot of the cubic invariant R against α as a function of θ_ω corresponding to Type 2 scenario ($\phi_\omega < \phi_\omega^{cr2}$). In plot (a) $\phi_\omega > \phi_\omega^{cr1}$, in (b) $\phi_\omega = \phi_\omega^{cr1}$, (c) corresponds to $\phi_\omega = \phi_\omega^{cr3}$ and, (d) to $\phi_\omega < \phi_\omega^{cr3}$. Plots (a) and (b) correspond to Type 2A scenario, where all planar flows exist and (c) and (d) correspond to Type 2B, where only hyperbolic flows exist. Plot (b) corresponds to the boundary demarcating Type 2A and 2B and plot (c) corresponds to the critical value (ϕ_ω^{cr3}), across which the limiting θ_ω corresponding to α_{max}^{zc} changes. The yellow curve again corresponds to the quadratic invariant Q.

The information presented above can be used to plot the bounding surface in $1/\alpha$ space populated by hyperbolic flows. The equation of this surface associated with the three scenarios that was explained in the previous paragraphs are shown below.

- For **Type 1** scenario ($\phi_\omega > \phi_\omega^{cr2}$), we note that the limiting hyperbolic flow occurs at an α, where $R = 0$, for $\theta_\omega = \pi/2$ (when $\epsilon < -1$) and $\theta_\omega = 0$ (when $\epsilon > -1$). This value of α is the minimum of all zero-crossings in R (note that the maximum value of $\alpha = \infty$ corresponds to the bounding elliptic flow surface consisting of solid-body rotation). We therefore have:

$$\frac{1}{\alpha} = \begin{cases} \frac{\sqrt{\epsilon+(2+\epsilon)\cos 2\phi_\omega}}{2\sqrt{2}\sqrt{-\epsilon(1+\epsilon)}} & (\epsilon < -1) \\ \frac{1}{2\sqrt{1+\epsilon}} & (\epsilon > -1) \end{cases} \tag{3.30}$$

The second equation is only valid when $\epsilon \neq 0$. For $\epsilon = 0$, the solution is $1/\alpha = \infty$.

- For Type 2A behavior, the equation again corresponds to,

$$\frac{1}{\alpha} = \frac{1}{2\sqrt{1+\epsilon}} \tag{3.31}$$

as this behavior is observed only when $\epsilon > -1$ and when $\phi_\omega^{cr1} < \phi_\omega < \phi_\omega^{cr2}$ where, both the maximum and minimum zero-crossings of R are finite, with Q having a solution in between these two values. This solution is also valid only for non-zero ϵ and the solution is ∞ when $\epsilon = 0$.

- In Type 2B behavior, both maximum (α_{max}) and minimum (α_{min}) values of the solution of $R = 0$ correspond to hyperbolic flows and therefore there are two surfaces here bounding a region with only eccentric hyperbolic flows in between them. For this case, the solution is:

$$\frac{1}{\alpha_{min}} = \begin{cases} \frac{\sqrt{\epsilon + (2+\epsilon)\cos 2\phi_\omega}}{2\sqrt{2}\sqrt{-\epsilon(1+\epsilon)}} & (\phi_\omega < \frac{1}{2}\cos^{-1}\left(\frac{-3\epsilon}{2+\epsilon}\right)) \\ \frac{1}{2\sqrt{1+\epsilon}} & (\phi_\omega > \frac{1}{2}\cos^{-1}\left(\frac{-3\epsilon}{2+\epsilon}\right)) \end{cases} \tag{3.32}$$

$$\frac{1}{\alpha_{max}} = \begin{cases} \frac{\sqrt{\epsilon + (2+\epsilon)\cos 2\phi_\omega}}{2\sqrt{2}\sqrt{-\epsilon(1+\epsilon)}} & (\phi_\omega > \frac{1}{2}\cos^{-1}\left(\frac{-3\epsilon}{2+\epsilon}\right)) \\ \frac{1}{2\sqrt{1+\epsilon}} & (\phi_\omega < \frac{1}{2}\cos^{-1}\left(\frac{-3\epsilon}{2+\epsilon}\right)) \end{cases} \tag{3.33}$$

provided $\epsilon \neq 0$. The solutions at $\epsilon = 0$ are given by:

$$\frac{1}{\alpha_{min}} = \infty \quad \forall \, \phi_\omega \tag{3.34}$$

$$\frac{1}{\alpha_{max}} = \frac{1}{2} \quad \forall \, \phi_\omega \tag{3.35}$$

This implies that the solution in the first relation of Eq.3.32 asymptotes to the vertical line $\phi_\omega = \pi/4$ running between $1/\alpha = 1/2$ (simple shear) to ∞ (planar extension) as $\epsilon \to 0$, while the second relation suffers a discontinuous jump to $1/\alpha = \infty$ at $\epsilon = 0$.

The bounding surface populated by eccentric planar hyperbolic flows has been plotted in Fig.3.14, by using the aforementioned equations. From the plot, we see that the surface diverges at $\epsilon = -1$, which implies that the minimum value of α at which hyperbolic flows occur, for $\epsilon = -1$, is $\alpha = 0$. Note that the special case of $\epsilon = -1$, $\alpha = 0$, corresponds to canonical planar extensional flows for all values of ϕ_ω and θ_ω, because of the absence of vorticity. As mentioned in Eq.3.34-3.35, for $\epsilon = 0$, again $\alpha = 0$ (which is not shown in Fig.3.14), but this solution is disjoint from the surface when $\phi_\omega > \frac{1}{2}\cos^{-1}\left(\frac{-3\epsilon}{2+\epsilon}\right)_{\epsilon=0} = \frac{\pi}{4}$, which was also observed for the other bounding surfaces.
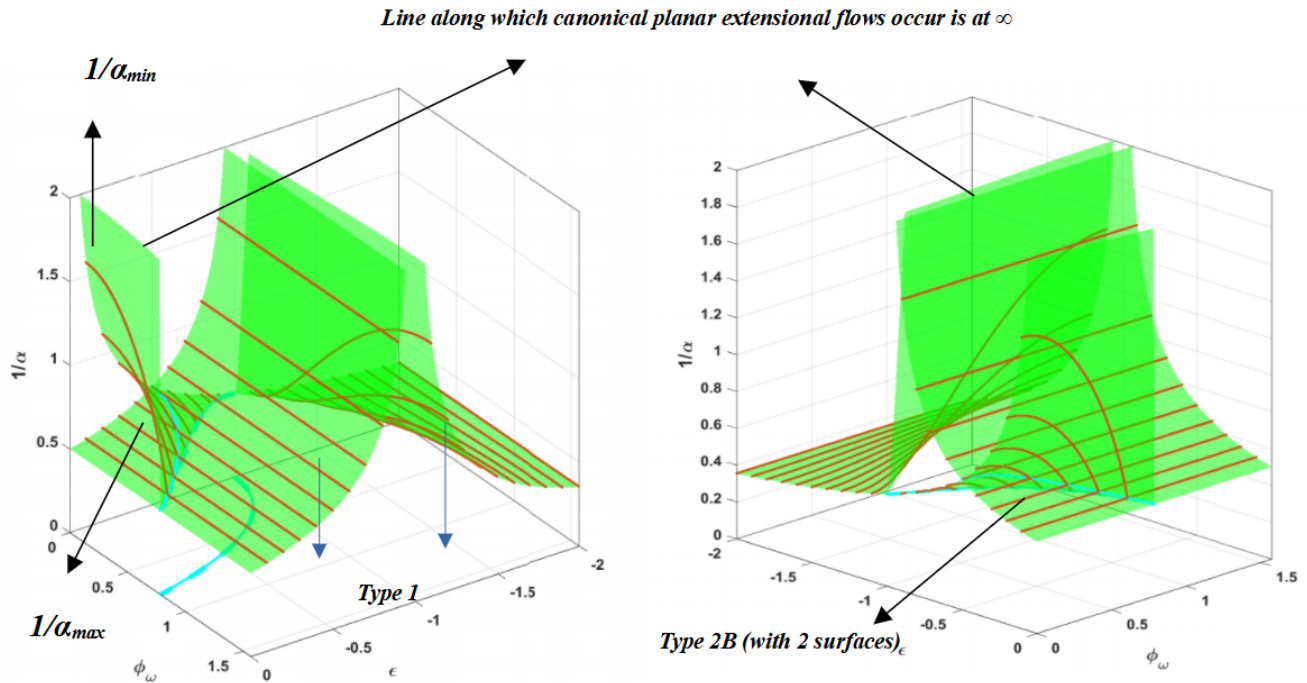
(a) Isometric View.
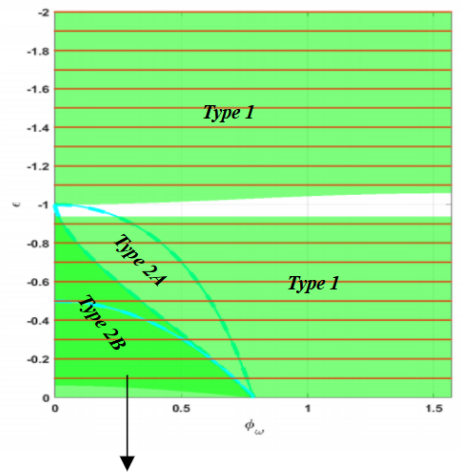
(b) Top View.

Figure 3.14: The bounding surface of eccentric planar hyperbolic flows highlighting the regions corresponding to the three scenarios Type 1, Type 2A and Type 2B. The surface diverges at $\epsilon = -1$, suggesting that at $1/\alpha = \infty$, $R = 0$ regardless of ϕ_ω and θ_ω and it corresponds to planar extension. At $\epsilon = 0$, $1/\alpha = \infty$ for all ϕ_ω (the line is not shown). The top view (b) shows the boundaries that separate the regions associated with Type 1, Type 2A and Type 2B.

We are now in a position to include all the three surfaces in Fig.3.11,3.12,3.14 together to show the region of occurrence of the general class of planar linear flows, with the transitions from one flow type to another, in the $\epsilon - \phi_\omega - 1/\alpha$ space and this has been implemented in Fig.3.15. In the next section, we show how to use the surfaces in Fig.3.10 and Fig.3.14 in conjunction, to locate a planar linear flow, and comment on the geometrical features and, the special limiting cases.
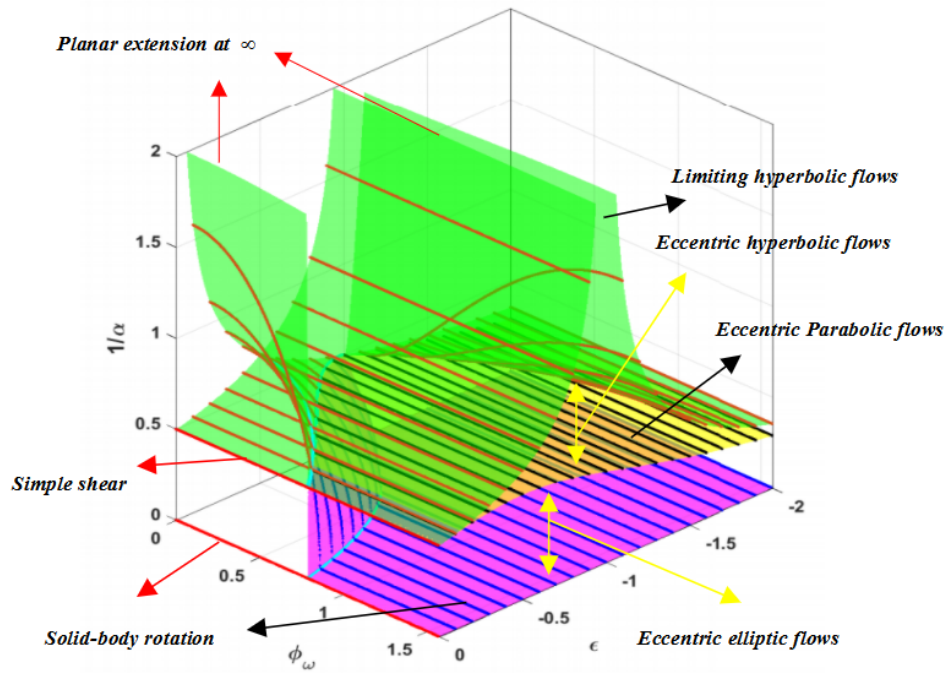
(a) Isometric View.
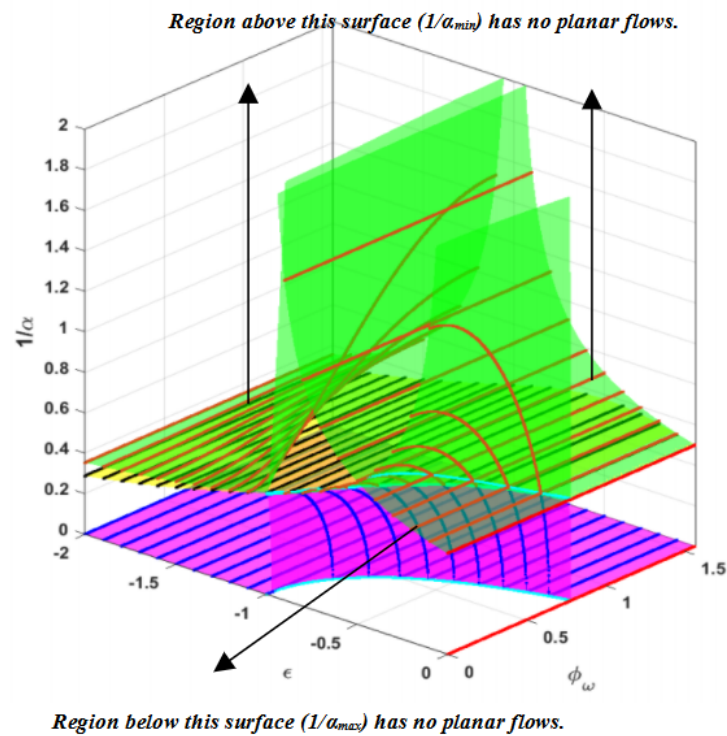
(b) Isometric View

Figure 3.15: The domain of existence of eccentric planar linear flows in $\epsilon - \phi_\omega - 1/\alpha$ space with the various flow types and their region of existence highlighted.

3.2.2.3 Locating a Planar Linear Flow

In order to locate a planar linear flow, one needs to use both the $\epsilon - \phi_\omega - \theta_\omega$ and $\epsilon - \phi_\omega - 1/\alpha$ spaces in conjunction. We now illustrate how choosing a (ϵ, ϕ_ω) pair gives us the planar linear flows and their locations as (θ_ω, α) coordinates. In our example, we choose the plane $\phi_\omega = 0.5$ and take cross-sectional views of both the sub-spaces above (Fig.3.16(a) and (b)). We choose this value of ϕ_ω because it includes all the scenarios we encountered in the earlier subsection. We then proceed by choosing a value of ϵ corresponding to each of these scenario and explain how to locate the planar linear flows in each of these cases.
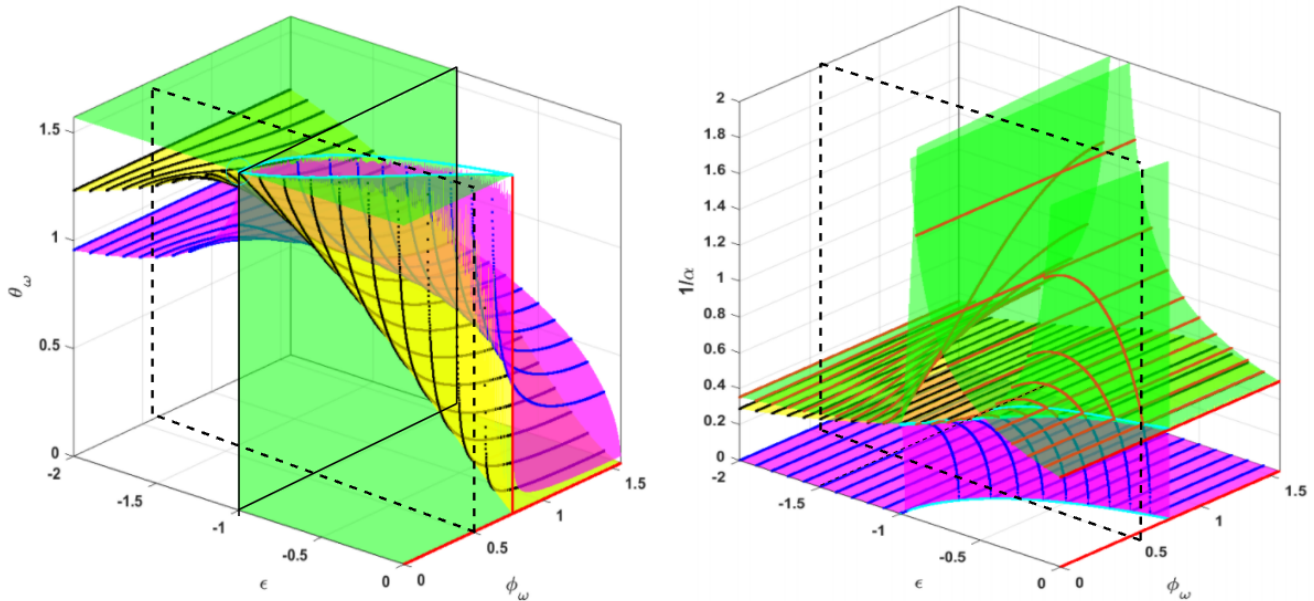
Figure 3.16: The domain of existence of eccentric planar flows in the $\epsilon - \phi_\omega - \theta_\omega$ space and the $\epsilon - \phi_\omega - 1/\alpha$ space, where we have chosen the plane $\phi_\omega = 0.5$ to explain the procedure for locating a planar flow.

$\epsilon < -1$

This interval corresponds to the Type 1 scenario mentioned earlier. We choose a value of $\epsilon = -1.5$ and we draw a vertical line through this value of ϵ in Fig.3.17a, where the points of intersection of this line with the magenta (bounding surface of elliptic flows), yellow (parabolic flow surface) and, green (bounding surface of hyperbolic flows) surfaces are labelled $P1, P2$, and $P3$ in the θ_ω space and $P1', P2'$ and $P3'$ in the $1/\alpha$ space. We have also shown the R versus α plots for the chosen value of $(\epsilon, \phi_\omega) = (-1.5, 0.5)$ in Fig.3.17b. One can understand the sequence of planar flows along this line as follows: In the $\epsilon - \phi_\omega - \theta_\omega$ space, as one moves along this vertical line from $\theta_\omega = 0$, one does not encounter planar flows until $P1$ corresponding to a $\theta_\omega \approx 57°$. At this value of $\theta_\omega = P1 = 57°$, the planar flow occurs at $1/\alpha = P1' = 0$. Therefore for $(\theta_\omega, 1/\alpha) = (P1, P1') = (57°, 0)$, we have solid-body rotation. As we move along the vertical line from $P1$ to $P2$ in the $\epsilon - \phi_\omega - \theta_\omega$ space, there are eccentric planar elliptic flows occurring at the corresponding interval $1/\alpha \in (P1', P2')$ in the $\epsilon - \phi_\omega - 1/\alpha$ space. At $(\theta_\omega, 1/\alpha) = (P2, P2') \sim (72°, 0.36)$, we have planar parabolic flows. Similarly, when $\theta_\omega \in (P2, P3)$ and $1/\alpha \in (P2', P3')$, eccentric planar hyperbolic flows occur. Note that $(\theta_\omega, 1/\alpha) = (P3, P3')$ correspond to the pair of parameter values for which the zero-crossing in R (like the ones shown in Fig.3.9 and 3.13) occurs at the minimum possible α which is $1/P3'$. Thus, once an (ϵ, ϕ_ω) pair is chosen, the eccentric planar linear flows occur between the magenta and green surface in both sub-spaces and their coordinates are the corresponding points on the two sub-spaces.
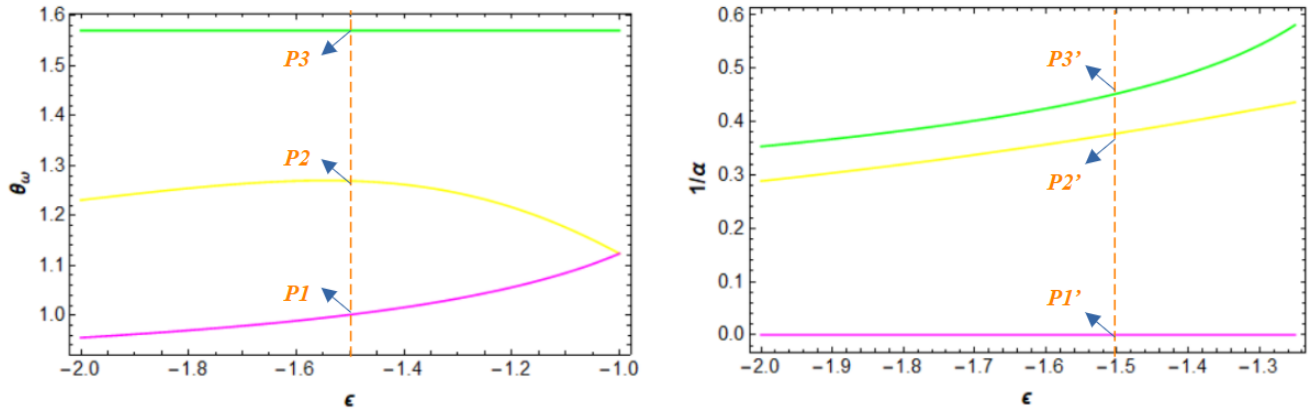
(a) Cut section of Fig.3.16 along $\phi_\omega = 0.5$ for $\epsilon < -1$
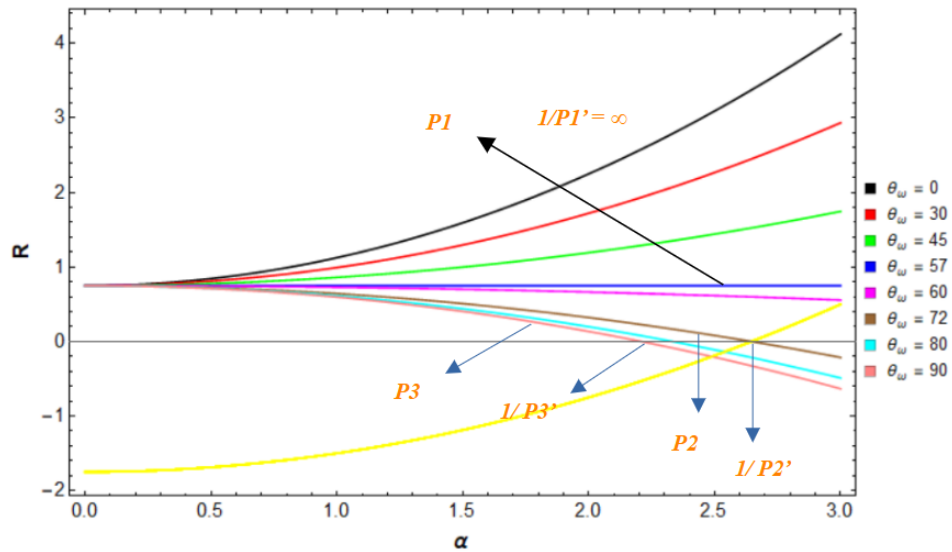
(b) Plot of R against α for $(\epsilon, \phi_\omega) = (-1.5, 0.5)$

Figure 3.17: Plot showing the locations of eccentric planar linear flows for $\epsilon < -1$, in cut-sections of the two sub-spaces. This corresponds to the Type 1 scenario.

$\epsilon > -1$

When $\epsilon > -1$, we see from the cut-section plot in Fig.3.18, that all three scenarios are encountered. We shall explain each scenario on a case-by-case basis.

(A) Type 1

In scenario Type 1, motion along a vertical line corresponding to a particular value of ϵ gives the same kind of results that was observed when $\epsilon < -1$ (Fig.3.17a). The only exception is that, here the order of the surfaces encountered as one moves from $\theta_\omega = 0°$ to $\theta_\omega = 90°$ is inverted, in that we encounter $P3$ (limiting hyperbolic flow) first in the $\epsilon - \phi_\omega - \theta_\omega$ space followed by $P2$ (parabolic flow) and $P1$ (solid-body rotation). But, the order remains the same as the previous case in $\epsilon - \phi_\omega - 1/\alpha$ space. This can be seen in Fig.3.19, for the vertical line labelled (a). In this scenario, we encounter all three types of eccentric

planar flows, with the limiting elliptic flow being a solid-body rotation, just like the previous case for $\epsilon > -1$.
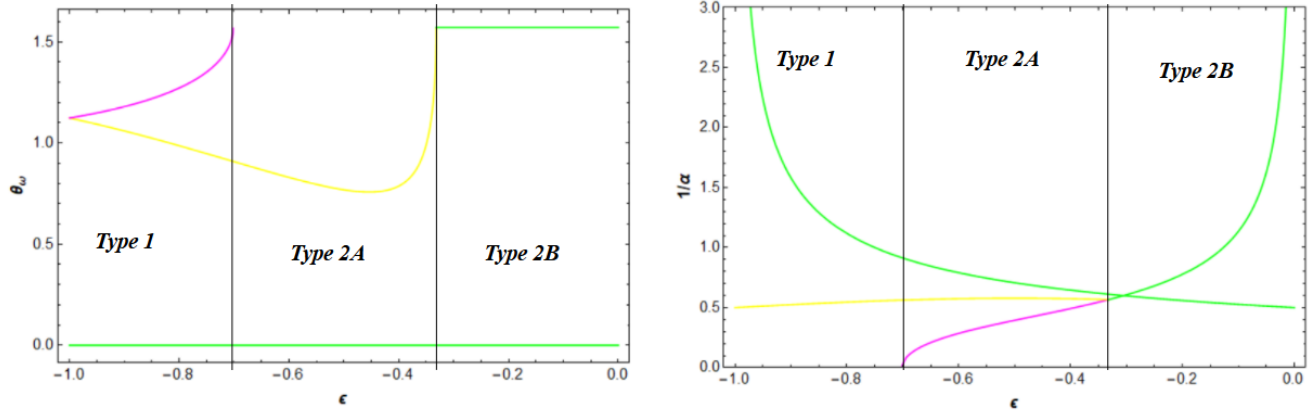
Figure 3.18: Cut section of Fig.3.16(a) and (b) along $\phi_\omega = 0.5$ when $\epsilon > -1$

(B) Type 2A

In this scenario, marked by the vertical line (b) in Fig.3.19, the magenta surface (corresponding to solid-body rotation) no longer exists in the θ_ω space and correspondingly in the $1/\alpha$ space, it lifts off from zero. Therefore,in this scenario $P1 = 90°$, which is merely the limiting value of the parameter θ_ω and $P1' \neq 0$. This implies that along this vertical line, the limiting planar linear flow corresponds to an eccentric elliptic flow and not solid-body rotation. The rest of the features remain the same for this case. Therefore, for this case, as one travels along a vertical line i the θ_ω space from $0°$ to $90°$, one encounters hyperbolic flows between $P3 = 0°$ and $P2$ and parabolic flow at $P2$ and eccentric elliptic flows between $P2$ and $P1 = 90°$. Correspondingly, in the $1/\alpha$ space, the elliptic flows lie between $P1' \neq 0$ and $P2'$,, parabolic flow at $P2'$ and eccentric hyperbolic flows between $P2'$ and $P3'$.

(C) Type 2B

In this case, there are three different scenarios possible. These three scenarios are each marked by the vertical lines labelled (c), (d), and (e) respectively. This scenario is characterised by the fact that there are only hyperbolic flows present along any vertical line and no other planar flow topologies exist. We see this across all three vertical lines mentioned above. Along line (c) in the θ_ω space, there is no $P1$ and $P2$, instead the line starts from $P3 = 0°$ and terminates at $P4 = 90°$, running between the two limits of the parameter θ_ω. Correspondingly in the $1/\alpha$ space. the vertical line (c) encounters the first hyperbolic planar flow at $P3'$ and the last hyperbolic flow at $P4'$ below $P3'$ and above $P4'$, there are no planar flow topologies and the limiting eccentric hyperbolic flows are given by the coordinates $(\theta_\omega, 1/\alpha) = (0°, P3')$ and $(90°, P4')$.

Along line (d), which is on the boundary given in Eq.3.29, which marks to the flip between the values of θ_ω corresponding to the maximum and minimum values of α at which $R = 0$, i.e. a flip between $P3$ and $P4$, all θ_ω along the line (d), exhibit an eccentric planar hyperbolic flow topology at the same $1/\alpha = P3' = P4'$. This means that the location of the hyperbolic flow is given by $(\theta_\omega, 1/\alpha) = ([0°, 90°], P3' = P4')$. This is seen clearly in Fig.3.20, which is a magnified image of Fig.3.19b.

Finally, along the line (e) in the θ_ω space, $P3$ and $P4$ are flipped and are now equal to $P3 = 90°$ and $P4 = 0°$. This flip implies that the the θ_ω for which the zero-crossing in R (α value) is minimum and

maximum are flipped. This is again seen in Fig.3.19a. In this case too there are only eccentric hyperbolic flow topologies and the limiting flows correspond to $(\theta_\omega, 1/\alpha) = (90°, P3')$ and $(0°, P4')$.

(a) Cut section of $\epsilon - \phi_\omega - \theta_\omega$ space.

(b) Cut section of $\epsilon - \phi_\omega - 1/\alpha$ space.
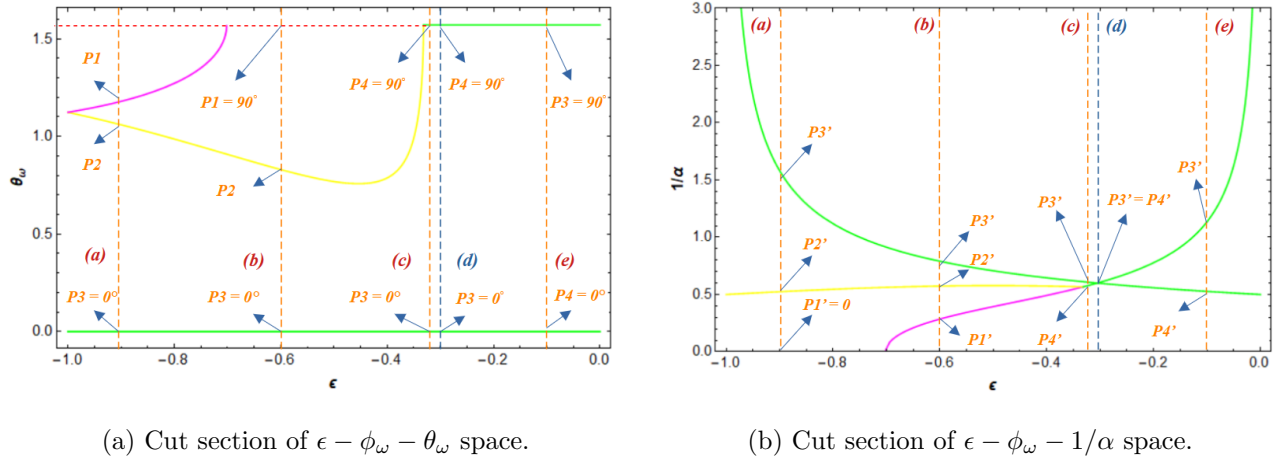
Figure 3.19: Cut section of Fig.3.16 along $\phi_\omega = 0.5$ showing the vertical lines corresponding to different types of scenarios. Line $(\boldsymbol{a})$ corresponds to Type 1, line $(\boldsymbol{b})$ to Type 2A and lines $(\boldsymbol{c})$, $(\boldsymbol{d})$, and $(\boldsymbol{e})$ to Type 2B scenario respectively.
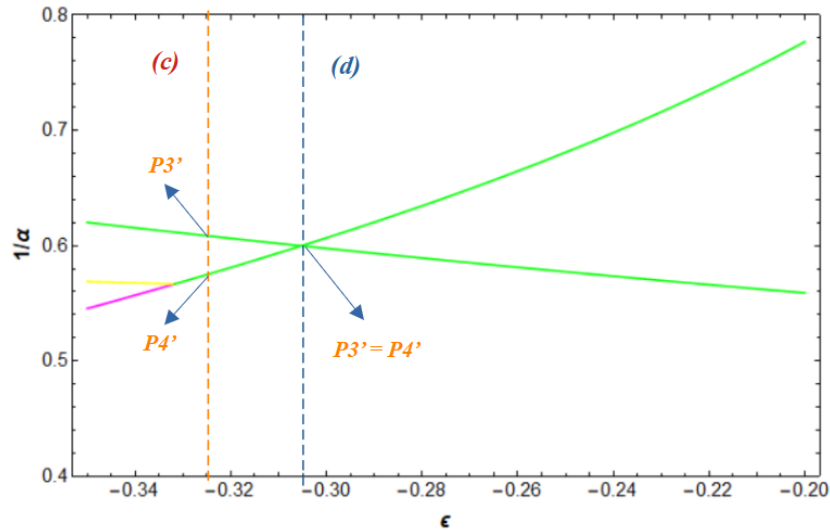
Figure 3.20: Magnified view of the cut section of Fig.3.19b.

This discussion concludes the brief introduction to the procedure for locating planar linear flows. We now move on to study the special points in Fig.3.16 and how to identify the flows and their corresponding locations in the two sub-spaces in which these flows are represented.

3.2.2.4   Special Limiting Cases in $\epsilon - \phi_\omega - \theta_\omega$ and $\epsilon - \phi_\omega - 1/\alpha$ Spaces

In the section we briefly analyse the limiting special cases, corresponding to $\epsilon = -1$, $\epsilon = 0$ and $\epsilon = -2$ in detail.

(A) $\epsilon = -2$

The simplest of the special cases is $\epsilon = -2$, which corresponds to axisymmetric extension with inclined vorticity. This was one of the cases analysed in Chapter 2 on heat transfer. To see how the eccentric planar flows are located for this case, we take the cut-section of the surface at $\epsilon = -2$ which is shown in Fig.3.21. From the plot, we see that the solution curves (magenta, yellow and green) in both spaces are independent of ϕ_ω as it should be owing to the axisymmetry involved. This value also corresponds to the Type 1 scenario, for which the procedure for locating the planar flows is detailed in the last section. We note that for this case, all three types of eccentric planar flows exist at unique values of (θ_ω, α) with solid-body rotation and eccentric rectangular hyperbolic flows being the limiting streamlines. It is for this special case that the properties in Section 3.2.1 were calculated. But, we had already noted in that section that the limiting values of those properties may not always hold true for other sequences of flows. We can now see that the limiting value of eccentricity is not always -1, and for sequences of flows corresponding to scenarios Type 2, the limiting value is not the same. The same is also true of the other limiting value of $e = \sqrt{2}$. This limiting value will be $0 < e < 1$ for an arbitrary sequence in either Type 1 or type 2 scenario. The same is also true of the angle of inclination between the neutral direction and the normal to the plane of flow. However, for any arbitrary sequence in Type 1 and Type 2A, the inclination will be $\pi/2$ for the parabolic flows. For a sequence corresponding to Type 2B scenario, the eccentricity will be $0 < e < 1$ and the inclination will be greater than $\pi/2$ as there will be no elliptic and parabolic flows in this sequence.

(a) Cut section of $\epsilon - \phi_\omega - \theta_\omega$ space. (b) Cut section of $\epsilon - \phi_\omega - 1/\alpha$ space.
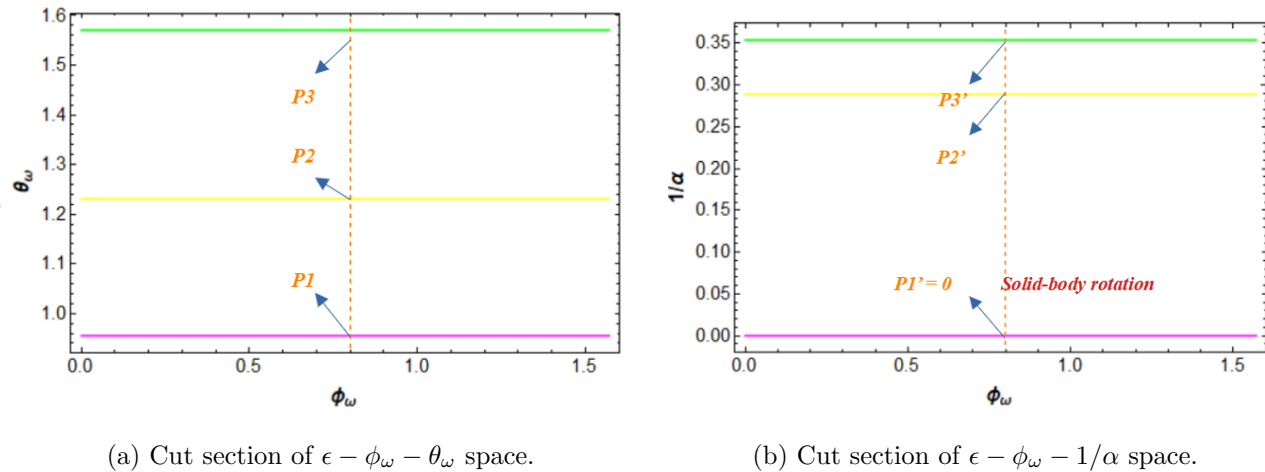
Figure 3.21: Cut section of Fig.3.16 along $\epsilon = -2$ showing that the limiting surfaces are independent of ϕ_ω consistent with the axisymmetric nature of the flow. This value of ϵ corresponds to Type 1 scenario.

(B) $\epsilon = -1$

This case corresponds to planar extension with inclined vorticity and it was shown in the earlier sections that the entire plane $\epsilon = -1$ in the θ_ω space was a bounding surface populated by hyperbolic flows, specifically canonical planar extensions. We also observed that on this plane, which is already a bounding surface populated by hyperbolic flows, there is a line along which, the surfaces populated by both solid-body rotations and parabolic flows intersect. Thus this line is the line of intersection of all three surfaces, as a result of which it is populated by all three types of eccentric planar flows, with the type being determined by the complementary coordinate $1/\alpha$. Thus for any point on this line, there is an infinity of points on the plane $\epsilon = -1$ in the $1/\alpha$ space which, together give the coordinates of eccentric planar flows. This is shown in Fig.3.22, where, for a point on the red line (in the θ_ω space corresponding to a specific (ϵ, ϕ_ω) pair, eccentric planar flows exist for the entire range of $1/\alpha$ on the $\epsilon = -1$ plane, i.e. $(\theta_\omega, 1/\alpha) = (P, [0, \infty])$ are coordinates for which planar flows exist with eccentric elliptic flows

between $(\theta_\omega, 1/\alpha) = (P, [0, P'))$, eccentric hyperbolic flows between $(\theta_\omega, 1/\alpha) = (P, (P', \infty])$ and eccentric parabolic flow at $(\theta_\omega, 1/\alpha) = (P, P)$. For the special case of $P = \pi/2$, i.e. $(\epsilon, \phi_\omega, \theta_\omega) = (-1, 0, \pi/2)$, the aforementioned ranges correspond to canonical elliptic and hyperbolic flows, with simple shear at $(\theta_\omega, 1/\alpha) = (\pi/2, P')$. For any other point P^* on the plane (not on the red line) in the θ_ω space, the complementary coordinate at which the planar extensional flows occur is given by $(\theta_\omega, 1/\alpha) = (P^*, \infty)$.
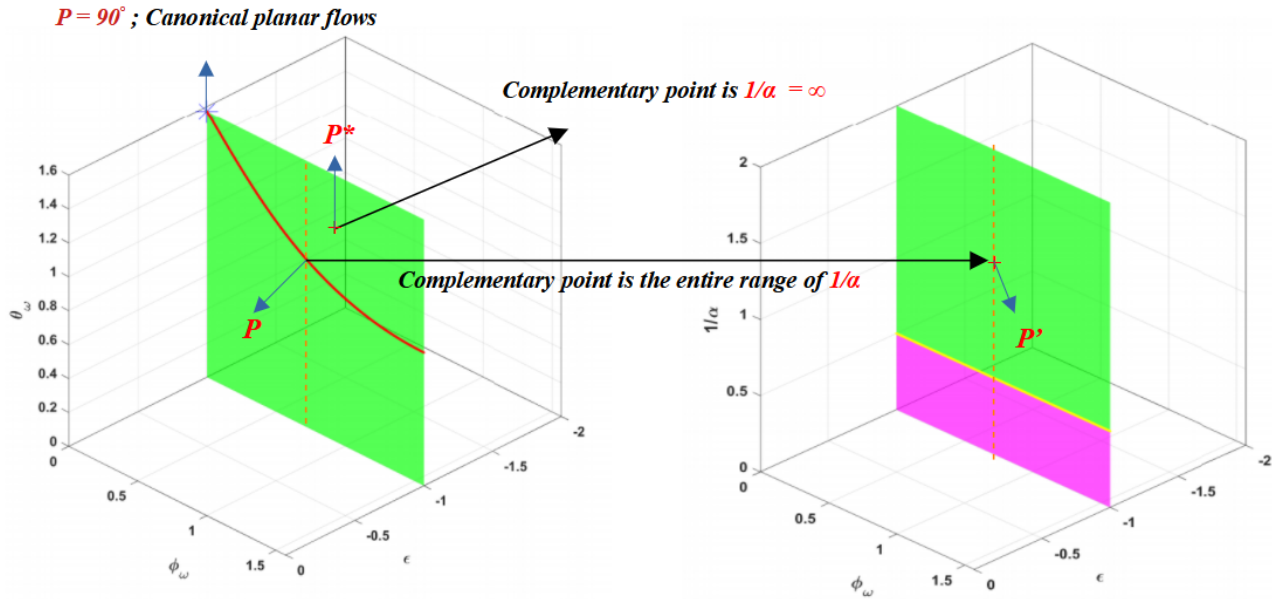
Figure 3.22: Location of eccentric planar flows in the special plane $\epsilon = -1$. For points on the line of intersection, eccentric planar flows exist for the entire range of $1/\alpha$ and for points not on the line, canonical planar extension exists at $1/\alpha = \infty$.

(C) $\epsilon = 0$

The final special case again corresponds to another planar extensional configuration with $\epsilon = 0$. In this case, we had noted that the entire plane is again a surface populated by hyperbolic flows, specifically planar extensions, and that there are two lines on this plane where all three surfaces intersect in the θ_ω space. These lines are $\theta_\omega = 0$ and $\phi_\omega = \pi/4$, shown in red in Fig.3.23. For this case too, the location of planar flows is similar to the case of $\epsilon = -1$. For a point P^* not on these two lines in the θ_ω space, planar extensional flows exist at $1/\alpha = \infty$, i.e. $(\theta_\omega, 1/\alpha) = (P^*, \infty)$ is always canonical planar extension. For a point P on either of the two lines, the complementary point P' in the $1/\alpha$ space is the entire range, i.e. $P' \in [0, \infty]$. The key exception is that, when this point P is on the line $\theta_\omega = 0$, thereby making $P = 0$, the planar flows are canonical planar flows, but when P is on the line $\phi_\omega = \pi/4$, with $P \in (0, \pi/2]$, the flows are eccentric planar flows.
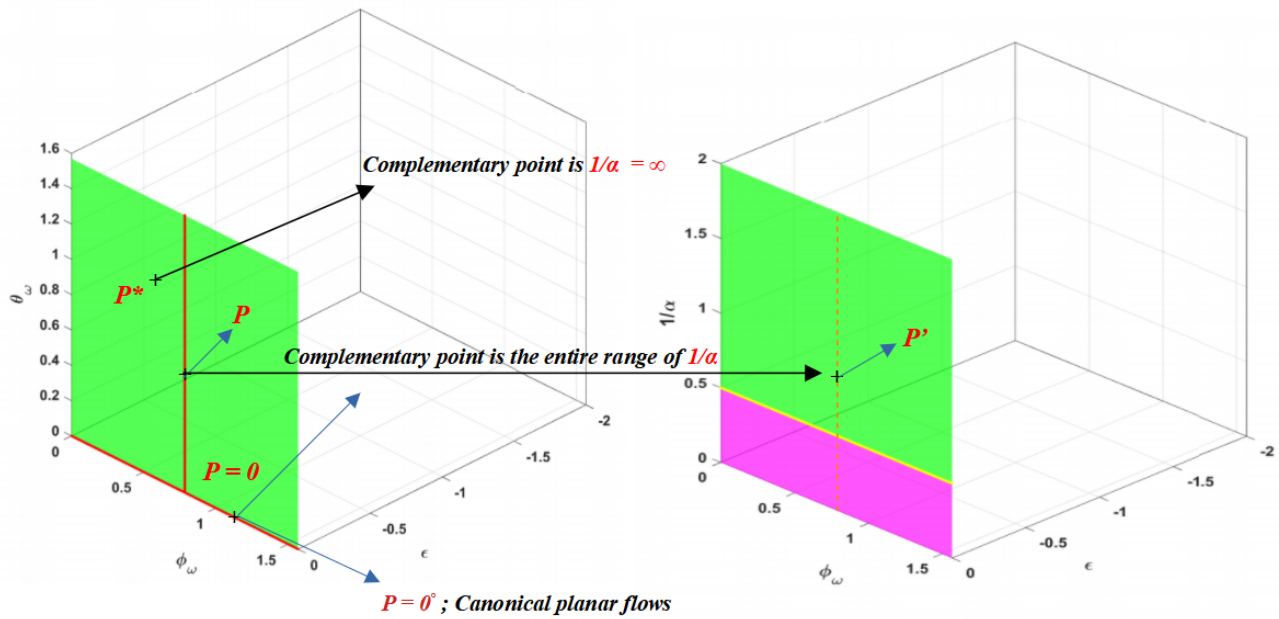
Figure 3.23: Location of eccentric planar flows in the special plane $\epsilon = 0$. For points on the two lines of intersection (red), eccentric planar flows exist for the entire range of $1/\alpha$ and for points not on the line, canonical planar extension exists at $1/\alpha = \infty$.

With this discussion, we conclude the section on the eccentric planar linear flows. We have successfully identified their region of existence in the four-dimensional parameter space of $3D$ incompressible linear flows. We observe that these flows occupy a finite volume in the parameter space as opposed to the canonical planar flows, which constitute an infinitesimally small subset, within the set of $3D$ linear flows. Thus these eccentric planar flows are crucial and relevant to many applications, a few of which we list in the conclusion. In the next section, we focus on the relationship between the eccentric elliptic flows and Jeffery orbits and derive an expression for the generalised orbit constant, which forms the starting point of the asymptotic analysis of heat transfer in the vicinity of such eccentric elliptic flows.

3.3   Surface streamlines as Generalised Jeffery Orbits

The motion of a single, small particle suspended in a Newtonian fluid which is undergoing a simple shear flow has been the subject of a considerable number of theoretical and experimental investigations which have spanned approximately a century. Interest in this problem stems mainly from its central role in the determination of the bulk properties of a dilute suspension composed of a large number of such particles in an ambient fluid. In a simple imposed shearing motion of the ambient fluid, the increased rate of dissipation which occurs due to the presence of a non-spherical particle is highly dependent upon its orientation, so that the rate of working for a given bulk motion of a dilute suspension will depend on the probability distribution of orientations among all the suspension particles. The starting point for most of these studies is the seminal work of Jeffery (1922), who analytically solved the Stokesian motion of a small rigid force-free and torque-free spheroid suspended in a uniform shear flow of the ambient Newtonian fluid. His solutions showed that the unit orientation vector (it's axis of rotation) rotates in one of the infinite number of one-parameter family of elliptic orbits traced on the surface of a unit sphere. These orbits are spherical ellipses defined by a orbit constant C. His analysis revealed that the orbit traced by the orientation vector is purely a function of the initial orientation and the orientation vector remains on that orbit indefinitely. The shape of the orbits themselves is a function of the aspect ratio of the spheroid,

where this function is called the Bretherton constant β given by:

$$\beta = \frac{\kappa^2 - 1}{\kappa^2 + 1} \tag{3.36}$$

where, κ is the geometric aspect ratio of a spheroid. Jeffery's analysis was extended by various authors at a later stage by accounting for the effects of inertia (Mason and Manley (1956)), Brownian motion (L. G. Leal and Hinch (1971)) and particle-particle interactions Anczurowski and Mason (1967). These effects will lead to a slow drift of the orientation vector across the orbits before it settles in a steady state orbit.

Although many of these studies have restricted themselves to simple shear flow, the Stokesian orientation dynamics of a spheroid suspended in canonical planar linear flows of the ambient was given by L. G. Leal and Hinch (1972), who observed that when the parameter governing the planar flow ($\hat{\alpha}$) was greater than an aspect-ratio-dependent critical value, then the orbits are no longer closed and become open trajectories. Thus the Bretherton constant governing these orbits now become a function of both κ and the flow-parameter $\hat{\alpha}$. Recently, Marath and Subramanian (2018) extended this work by accounting for particle inertia and analysed the inertial effect on orientation dynamics of spheroids in planar linear flows. Recently, Krishnamurthy and Subramanian (2018a) showed that the Jeffery orbits are the same as the surface streamlines on an undeformed drop suspended in a planar linear flow where the Bretherton constant is now a function of the viscosity ratio (λ) of the drop and the flow parameter $\hat{\alpha}$. The fact that the Stokesian surface streamlines and Jeffery orbits are one and the same should not be a surprise, as the governing equations for both are derived using the same symmetry arguments. The authors go on to exploit this fact and define a flow-aligned coordinate system, using the solutions of Jeffery orbit equations, with the orbit constant C serving as one of the coordinates, to to analyse the problem of convective transport from the drop to the ambient.

All of the aforementioned generalisations, result in the Bretherton constant, governing the eccentricity of the orbits, being a function of a parameter other than the aspect ratio, while the orbits remain spherical ellipses. However, the equivalence between surface streamlines and Jeffery orbits, suggest that the projections of the streamlines of eccentric planar elliptic flows described earlier in the chapter, onto a unit sphere (which gives the surface streamlines), are generalisations of the well-known Jeffery orbits, where now the orbits will no longer remain spherical ellipses. This therefore constitutes a true generalisation of the canonical Jeffery orbits in just the same respect, as the eccentric planar flows were generalisations of the canonical ones. In this section, we derive the equations governing these generalised Jeffery orbits based on geometrical arguments and show that they reduce to the well-known equations of the canonical Jeffery orbits when the eccentricity of the ambient planar flow vanishes.

3.3.1   The Canonical Jeffery Orbit Equation - Geometric Approach

In this section, we begin with a discussion on the governing equation of the canonical Jeffery orbits and it's solution and show that this solution can be derived alternatively using purely geometrical argument. The governing equation of the Jeffery orbits, which are trajectories traced by the unit orientation vector of a spheroid of aspect ratio κ, suspended in an ambient simple shear flow are (L. G. Leal and Hinch (1971)):

$$\dot{\boldsymbol{p}} = \boldsymbol{\Omega}.\boldsymbol{p} + \frac{\kappa^2 - 1}{\kappa^2 + 1}\left(\boldsymbol{E}.\boldsymbol{p} - (\boldsymbol{E}:\boldsymbol{pp})\boldsymbol{p}\right) \tag{3.37}$$

where $\boldsymbol{E}$ and $\boldsymbol{\Omega}$ correspond to the ambient shearing flow in which the spheroid is suspended and are given by:

$$\boldsymbol{E} = \begin{bmatrix} 0 & \frac{1}{2} & 0 \\ \frac{1}{2} & 0 & 0 \\ 0 & 0 & 0 \end{bmatrix} \qquad\qquad \boldsymbol{\Omega} = \begin{bmatrix} 0 & \frac{1}{2} & 0 \\ \frac{-1}{2} & 0 & 0 \\ 0 & 0 & 0 \end{bmatrix} \qquad (3.38)$$

and the constant multiplying the strain-rate tensor contributions is called the Bretherton constant (Eq.3.36). This governing equation can be written down using symmetry arguments based on the time-reversal symmetry of Stokesian regime and the linearity of the ambient flow (L. G. Leal and Hinch (1972)). Substituting these values into Eq.3.37 gives the governing equation in spherical coordinates as:

$$\frac{d\theta}{dt} = \frac{\kappa^2 - 1}{4(\kappa^2 + 1)} \sin(2\theta) \sin(2\phi) \qquad (3.39)$$

$$\frac{d\phi}{dt} = \frac{1}{\kappa^2 + 1} \left(\kappa^2 \cos^2 \phi + \sin^2 \phi \right) \qquad (3.40)$$

One can easily integrate the equations to get the solutions as:

$$\tan \phi = \kappa \tan \left(\frac{t}{\kappa + (1/\kappa)} \right) \qquad (3.41)$$

$$\tan \theta = \frac{C\kappa}{(\kappa^2 \cos^2 \phi + \sin^2 \phi)} \qquad (3.42)$$

From this equation, we see that the trajectories traced by the unit orientation vector are spherical ellipses with a period $T = 2\pi \left(\kappa + \frac{1}{\kappa} \right)$, where the constant C labels a particular elliptic orbit on the spherical surface. Here $C = 0$ corresponds to the spinning trajectory (the point of intersection of the polar axis with unit sphere) and $C = \infty$ is the tumbling orbit (the great circle on the equatorial plane) (Marath and Subramanian (2018)). The eccentricity of these elliptic orbits are a function of the aspect ratio, precisely, the Bretherton constant β (Eq.3.36). As already mentioned, the analysis leading to the orbit equations cannot be used to determine the orbit constant C for a single particle, there being no inherent preference for one orbit over any other within the framework of Jeffery's theory, and so the orbit that forms the trajectory of the vector is a function of the initial orientation and the vector remains on that orbit indefinitely.

We now show how the solution given in Eq.3.42 can be derived using a simple geometrical argument. Note that while Jeffery orbits were identified as the trajectories traced by unit orientation vector of a spheroid in a shear flow, they also arise in another context, where they are the projections, onto a unit sphere, of the three-dimensional streamlines associated with a canonical (elliptic) planar linear flow. We shall use this fact to illustrate our geometric approach. Note that in this context, the governing equations for the Jeffery orbits become:

$$\dot{\boldsymbol{n}} = \boldsymbol{\Omega}.\boldsymbol{n} + (\boldsymbol{E}.\boldsymbol{n} - (\boldsymbol{E} : \boldsymbol{nn})\boldsymbol{n}) \qquad (3.43)$$

which is exactly the projection of the velocity field associated with an ambient linear flow $\dot{\boldsymbol{x}} = \boldsymbol{\Gamma}.\boldsymbol{x} = (\boldsymbol{E} + \boldsymbol{\Omega}).\boldsymbol{x}$, onto the unit sphere surface. Here $\boldsymbol{E}$ and $\boldsymbol{\Omega}$ are by:

$$\boldsymbol{E} = \begin{bmatrix} 0 & \frac{1+\hat{\alpha}}{2} & 0 \\ \frac{1+\hat{\alpha}}{2} & 0 & 0 \\ 0 & 0 & 0 \end{bmatrix} \qquad\qquad \boldsymbol{\Omega} = \begin{bmatrix} 0 & \frac{1-\hat{\alpha}}{2} & 0 \\ \frac{\hat{\alpha}-1}{2} & 0 & 0 \\ 0 & 0 & 0 \end{bmatrix} \qquad (3.44)$$

where, $\hat{\alpha}$ is the flow-parameter governing the canonical planar linear flow and the elliptic flows correspond to $\hat{\alpha} < 1$. Given that the streamlines of this ambient canonical elliptic flow are concentric ellipses in planes orthogonal to the polar axis, we can directly write down the solution as described below.

Consider the the canonical planar elliptic flow, whose streamlines are shown in Fig.3.24, where the streamlines are shown for a particular plane, with the streamlines in all parallel planes (displaced along x_3) are the same. We can therefore construct a right-elliptic cone with an arbitrary cone angle whose vertex is at the origin and with its face bound by the elliptic streamlines across the planes as shown in Fig.3.25a. It is easy to see that the projection of this cone onto the unit sphere will result in a Jeffery orbit (Fig.3.25b), as it is the projection of the auxiliary flow onto the unit sphere. Mathematically, this is equivalent to finding the intersection between the arbitrary elliptic cone given by:

$$\frac{x_1^2}{a^2} + \frac{x_2^2}{b^2} = x_3^2 \tag{3.45}$$

and the unit sphere:

$$x_1^2 + x_2^2 + x_3^2 = 1. \tag{3.46}$$

Real eigenvector is along x_3 normal to the plane of flow.
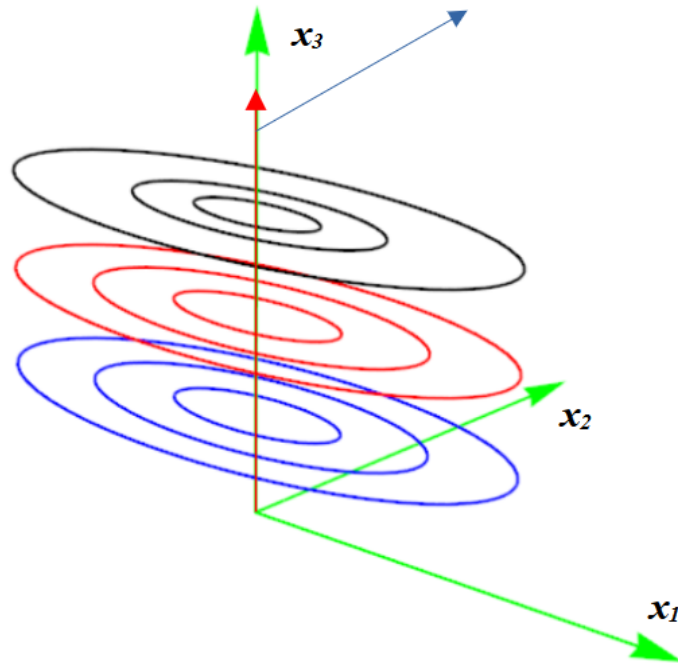
Figure 3.24: Plot of the streamlines, on multiple x_3 planes, for the canonical elliptic planar flows. The flow is in planes parallel to the $x_1 - x_2$ plane, with both vorticity and real eigenvector along x_3 and therefore the real eigenvector is normal to the plane of flow.

In Eq.3.45, a and b are the normalised semi-major and semi-minor axes of the elliptic section and they are the arbitrary parameters that set the angle of the cone. These ellipses have an eccentricity $e = \sqrt{1 - (b^2/a^2)}$. Note that in writing down this equation of the cone, we have assumed a coordinate system with the polar axis x_3, normal to the plane of flow and x_1 and x_2 along the major and minor axes of the ellipse. In this coordinate system, the solution that satisfies Eq.3.46 is simply the unit spherical coordinates: $x_1 = \sin\theta\cos\phi$, $x_2 = \sin\theta\sin\phi$ and $x_3 = \cos\theta$. Substituting this into Eq.3.45 gives us:

$$\tan\theta = \frac{a\sqrt{1 - e^2}}{\left((1 - e^2)\cos^2\phi + \sin^2\phi\right)^{1/2}} \tag{3.47}$$

We see that this equation has the same form as one of the Jeffery orbit equation given in Eq. 3.42 and is therefore the expected solution of Eq.3.43, which we have derived without having to integrate it.
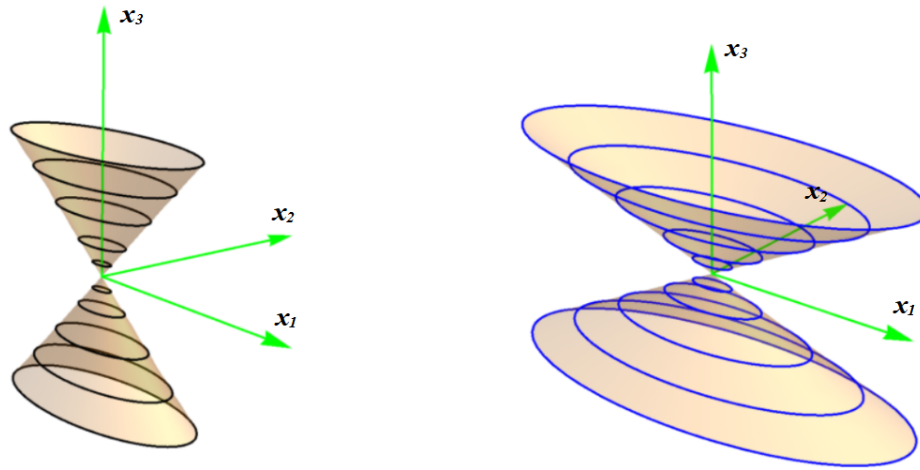
(a) Elliptic cones with two different open angles bound by streamlines across different x_3 planes.
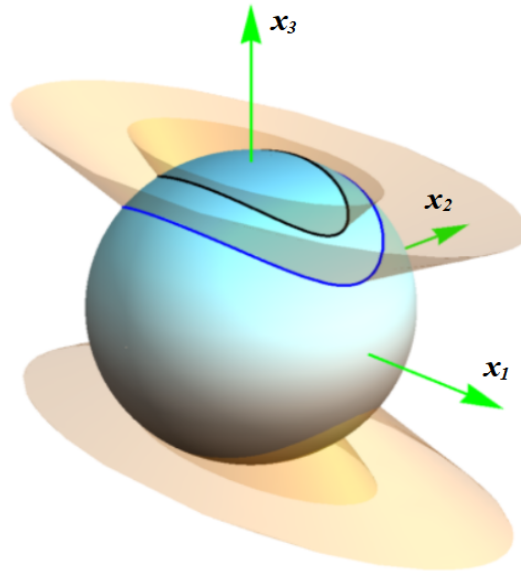
(b) Projection of the cones onto a unit sphere.

Figure 3.25: Plot of (a) cones of two different open angles bound by streamlines across multiple x_3 planes. The first cone has $c = 1$ and the second one has $c = 1/2$ for a specific choice of a and $b = a\sqrt{1 - e^2}$ and (b) projection of the aforementioned cones onto a unit sphere result in Jeffery orbits with two different orbit constants set by a and c.

The only thing that remains, is to rewrite the constants that appear in Eq.3.47 in terms of the flow parameter $\hat{\alpha}$. To do this we first separate out the arbitrary constants from the flow-dependent ones. We had already mentioned that a and b, which determine the angle of cone is arbitrary, so that cannot be related to any flow-dependent constants. So a is an arbitrary constant in Eq.3.47 and so we can rename it C, so as to be consistent with the constant of integration that appears in the solution of Eq.3.39. This

only leaves us with e, the eccentricity of the ellipses. This constant is not arbitrary, for even though the major and minor axes of the ellipses change, they have the same eccentricity owing to their concentric nature, for a given flow parameter $\hat{\alpha}$. Thus, this is the only flow-dependent parameter, which needs to be written in terms of $\hat{\alpha}$.

In order to do that, we recognise that e, being a constant has to be related to the invariants of the auxiliary linear flow, which are the eigenvalues and eigenvectors. We further realise that e is related to the ratio of two lengths (along two vectors: the major and minor axes) and so must be related to the eigenvectors of the flow. The eigenvectors of the auxiliary flow velocity-gradient tensor,

$$\mathbf{\Gamma} = \frac{1}{2} \begin{bmatrix} 0 & 1 & 0 \\ \hat{\alpha} & 0 & 0 \\ 0 & 0 & 0 \end{bmatrix} \tag{3.48}$$

are given by:

$$\boldsymbol{p_1} = \left\{ \iota \sqrt{-\frac{1}{\hat{\alpha}}}, 1, 0 \right\} \tag{3.49}$$

$$\boldsymbol{p_2} = \left\{ -\iota \sqrt{-\frac{1}{\hat{\alpha}}}, 1, 0 \right\} \tag{3.50}$$

$$\boldsymbol{p_3} = \{0, 0, 1\} \tag{3.51}$$

One can easily show that the eccentricity e of the elliptic streamlines are given by:

$$e = \left(1 - \frac{1}{|\text{Im}[\boldsymbol{p_1}]|^2} \right)^{1/2} = (1 + \hat{\alpha})^{1/2} \tag{3.52}$$

where $|\text{Im}[\boldsymbol{p_1}]|$ is the norm of the imaginary part of the eigenvector $\boldsymbol{p_1}$ which is the same as that of $\boldsymbol{p_2}$. Substituting for e in Eq.3.47, we get:

$$\tan\theta = \frac{C\gamma}{\left(\gamma^2 \cos^2\phi + \sin^2\phi \right)^{1/2}} \tag{3.53}$$

with $\gamma^2 = -\hat{\alpha}$, the effective aspect ratio governing the nature of the Jeffery orbit and $C = a$. We now see, by comparing Eq.3.42 and Eq.3.53 that, the Bretherton constant associated this scenario is only a function of the flow parameter $\hat{\alpha}$. To get the other solution, governing the phase along the orbit τ, we simply substitute for θ from Eq.3.53 into Eq.3.43, which gives us:

$$\tan\phi = \gamma \tan\left(\frac{2\gamma t}{\gamma^2 + 1} \right) = \gamma \tan\tau \tag{3.54}$$

which is the other solution given in Eq.3.41. In the solutions above $\hat{\alpha} < 0$ and so the trajectories are periodic orbits, which become open trajectories for $\hat{\alpha} > 0$. Therefore, using simple geometrical arguments, we have derived the equations of Jeffery orbits and in the next section, we show that we can easily extend this to derive the equations of generalised Jeffery orbits, which are the trajectories traced by the orientation vector of a spheroid, suspended in an eccentric planar elliptic flow, on a unit sphere. Before that, however, we briefly look at the Jeffery orbits that occur in the context of the heat transport problem that was analysed by Krishnamurthy and Subramanian (2018a), who identified that the surface streamlines on a spherical drop suspended in an ambient canonical elliptic linear flow are also Jeffery

orbits, whose eccentricity is again governed by a Bretherton constant, which is now a function of both $\hat{\alpha}$ and the viscosity ratio $\hat{\lambda}$. For this case the governing equation is:

$$\dot{\boldsymbol{n}} = \boldsymbol{\Omega}.\boldsymbol{n} + \frac{1}{1+\lambda}(\boldsymbol{E}.\boldsymbol{n} - (\boldsymbol{E}:\boldsymbol{nn})\boldsymbol{n}). \tag{3.55}$$

The solutions for the surface streamline equation above, are again given by Eq.3.53 and Eq.3.54, with $\gamma^2 = ((1-\hat{\alpha})\lambda - 2\hat{\alpha})/((1-\hat{\alpha})\lambda + 2))$. Therefore Eq.3.43 is a special case of Eq.3.55 with $\lambda = 0$. In this case, the orbits are ellipses when $\gamma^2 > 0$ and so there exists a critical curve in the $\hat{\alpha} - \lambda$ plane given by $\lambda_c = 2\hat{\alpha}/(1-\hat{\alpha}$, below which the trajectories are open. This equivalence of surface streamlines with Jeffery orbits were used by the authors to solve the transport problem using a Jeffery orbit aligned coordinate system. But this dependence on λ is an apparent one, as was shown in Chapter 2, and it can be scaled out by suitably redefining the velocity scale and the vorticity magnitude of $\boldsymbol{\Gamma}$, where the rescaled quantities now involve $1+\lambda$ in their definitions. Using these rescaled quantities, $\gamma^2 = -\alpha'$, where $\alpha' = (1+\lambda)\alpha = 2(1+\lambda)((1-\hat{\alpha})/(1+\hat{\alpha}))$.

3.3.2 The Generalised Jeffery Orbit Equation
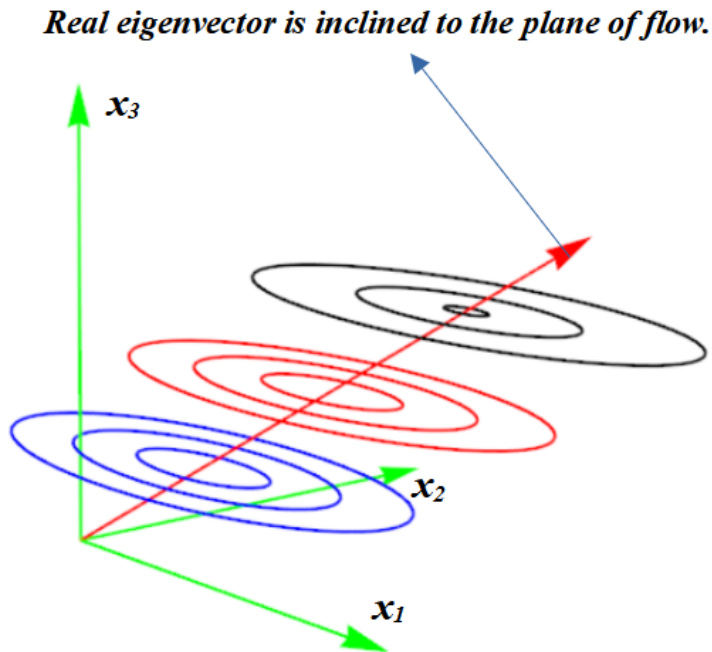
Figure 3.26: Plot of the streamlines in multiple x_3 planes, for the eccentric planar elliptic flows. The flow is in planes parallel to the $x_1 - x_2$ plane, with the real eigenvector (red arrow) inclined to the plane of flow.

The geometric approach used to derive the Jeffery orbit equation can be easily extended to find the equation of generalised Jeffery orbits, which are the same as the projection of an eccentric planar elliptic flow onto a unit sphere. The only difference in this case is that the elliptic cone whose intersection with the unit sphere gives the Jeffery orbit, has an axis that passes through the centers of all elliptical cross-sections along the neutral direction, which is no longer orthogonal to the plane of flow. Therefore the cone is no longer a right-elliptic one as shown in Fig.3.26. This is because the eccentric planar flows are characterised by the neutral direction having a non-trivial inclination with the normal to the plane of flow. Therefore in

a coordinate system with it's polar axis along the normal to the plane of flow, the elliptic cone whose vertex lies at the origin and whose face is bound by the eccentric elliptic streamlines across planes, has its axis (the neutral direction) inclined to the polar axis. Note here that the streamlines on a particular x_3 planar are similar in that their eccentricity is fixed (for a given set of flow parameters), just like the canonical case.
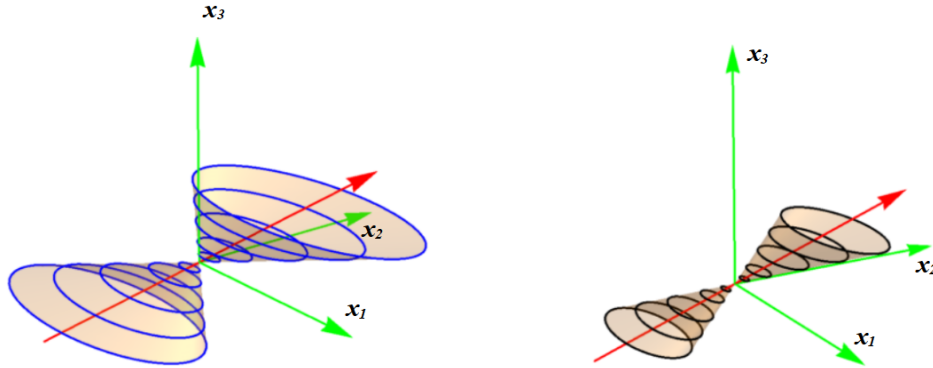
(a) Oblique cones with two different open angles bound by streamlines across x_3 planes.
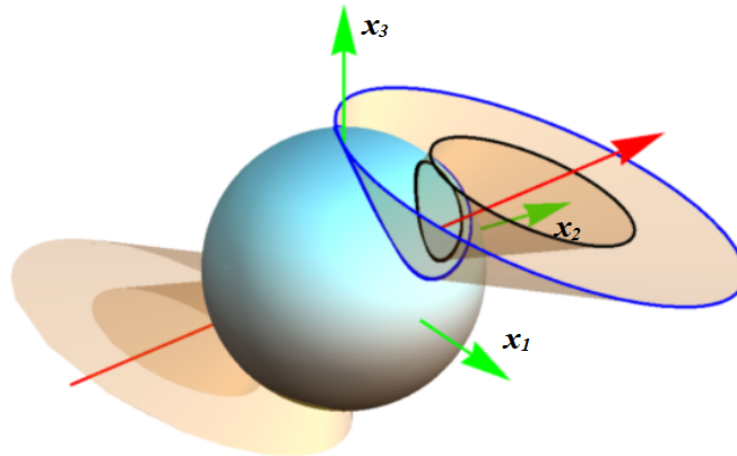
(b) Projection of the cones onto a unit sphere.

Figure 3.27: Plot of (a) oblique elliptic cones of two different open angles bound by streamlines across multiple x_3 planes. The first cone has $a = 1$ and the second one has $a = 2$ for a specific choice of e and (b) projection of the aforementioned cones onto a unit sphere result in Jeffery orbits with two different orbit constants set by the values of a.

One can immediately see that the projection of this cone onto the unit sphere will lead to eccentric elliptic orbits on the surface (Fig.3.27b). The equation of such an elliptic cone, based on the construction diagram in Fig.3.28, can be easily shown to be:

$$\frac{(x_1 - x_1^0)^2}{a^2} + \frac{(x_2 - x_2^0)^2}{b^2} = x_3^2 \tag{3.56}$$

where a, b and c correspond to the usual definition and x_1^0 and x_2^0 are location of the centre of the ellipses along the neutral direction. The intersection of this cone again with the unit sphere (Eq.3.46) can be

found by substituting $x_1 = \sin\theta\cos\phi$, $x_2 = \sin\theta\sin\phi$ and $x_3 = \cos\phi$, which gives us:

$$\frac{(\sin\theta\cos\phi - x_1^0)^2}{a^2} + \frac{(\sin\theta\sin\phi - x_2^0)^2}{b^2} = \cos^2\theta \tag{3.57}$$

Since x_1^0 and x_2^0 lie along the neutral direction, they can be represented in terms of the inclination of the neutral direction, θ' and ϕ' as:

$$x_1^0 = x_3 \, \tan\theta' \cos\phi' = \cos\theta \, \tan\theta' \, \cos\phi' = \cos\theta \, \hat{\delta} \tag{3.58}$$

$$x_2^0 = x_3 \, \tan\theta' \sin\phi' = \cos\theta \, \tan\theta' \sin\phi' = \cos\theta \, \hat{\gamma} \tag{3.59}$$

based on the construction shown in Fig.3.28. Here $\hat{\delta} = \tan\theta'\cos\phi'$ and $\hat{\gamma} = \tan\theta'\sin\phi'$. This can be substituted into Eq. 3.57 along with $b^2 = a^2(1 - e^2)$ to get:

$\tan\theta =$

$$\frac{C}{\left(\frac{1}{1-e^2}\left[(\sin^2\phi - \hat{\gamma}^2) + \csc^2\theta(\hat{\gamma}^2 - \hat{\gamma}\sin\phi\sin 2\theta)\right] + \left[(\cos^2\phi - \hat{\delta}^2) + \csc^2\theta(\hat{\delta}^2 - \hat{\delta}\cos\phi\sin 2\theta)\right]\right)^{1/2}} \tag{3.60}$$

where $C = a$ again. Here $C = 0$ again corresponds to the spinning orbit, which is now along the neutral direction and not the polar axis as before and $C = \infty$ is again, the great circle on the equatorial plane (tumbling orbit). This is the desired equation of the generalised Jeffery orbits. Note that in this equation, all the constants (except for C) are in terms of the flow parameters, with e being related to the imaginary eigenvectors and, $\hat{\gamma}$ and $\hat{\delta}$ being related to the real eigenvector (associated with zero eigenvalue) of the auxiliary flow tensor. However, given the complicated nature of these expressions, we do not present them here. Also note that this equation reduce to the canonical Jeffery orbit equation (Eq.3.43, when $\hat{\delta} = \hat{\gamma} = 0$, which are the values of these constants for the canonical elliptic flows.
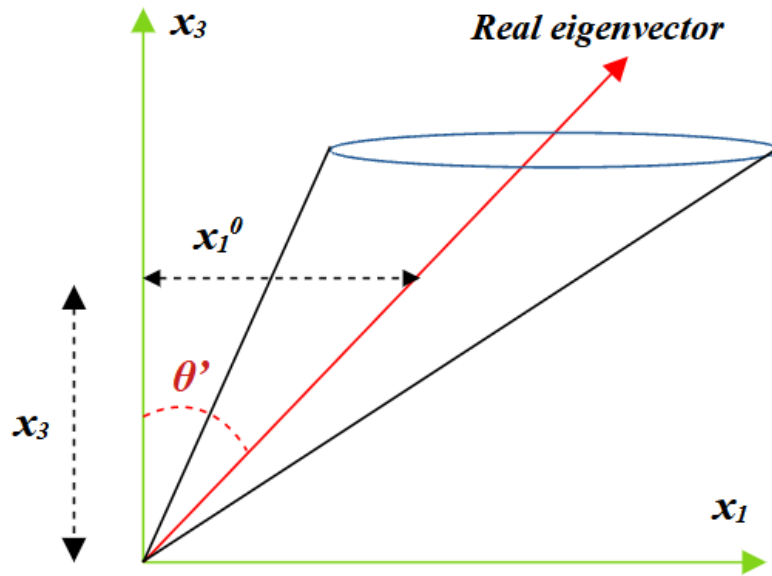
Figure 3.28: Construction diagram showing the relation between the centre of an ellipse at a height x_3 with the orientation of the real eigenvector θ' and ϕ'.

In order to find the other solution, which gives us the phase along the orbit, one must simply substitute for this θ into the azimuthal velocity field on the surface of the unit sphere and integrate it to find the phase t. So, we rewrite Eq.3.60, so as to get an explicit relation between θ and ϕ. This can be done by writing all trigonometric functions involving θ in the equation in terms of $\tan\theta$, which gives us after a few manipulations:

$$f_1(\phi)\tan^2\theta - 2f_2(\phi)\tan\theta + (f_3(\phi) - C^2) = 0 \tag{3.61}$$

which is a quadratic equation in $\tan\theta$. This can be solved to get:

$$\tan\theta = \frac{f_2(\phi) \pm \sqrt{f_2(\phi)^2 - f_1(\phi)(f_3(\phi) - C^2)}}{f_1} \tag{3.62}$$

with,

$$f_1(\phi) = \sin^2\phi + (1 - e^2)\cos^2\phi \tag{3.63}$$

$$f_2(\phi) = \hat{\gamma}\sin\phi + (1 - e^2)\,\delta\cos\phi \tag{3.64}$$

$$f_3(\phi) = \hat{\gamma}^2 + (1 - e^2)\,\hat{\delta}^2 \tag{3.65}$$

Eq.3.62 suggests that there are two possible roots for $\tan\theta$, whose significance may be appreciated as follows: We see that when $C > C^* = f_3 - (f_2^2/f_1) = \mathcal{F}(\phi)$, the solutions are complex. Since C is a constant, we can invert this condition as $\phi < \mathcal{F}^{-1}(C)$. For $C > C^*$, the condition is satisfied by the whole domain of ϕ ($\phi \in [0, \infty] \mod 2\pi$). But when $C < C^*$, the range of ϕ that satisfies this condition is $\phi \in [\phi_1, \phi_2]$, where $\phi_2 - \phi_1 < 2\pi$. Thus, there is a critical C^*, below which ϕ is oscillatory and above which it is a continuous function. This is reminiscent of the generalised position variable in the phase space of the simple pendulum, which runs between two finite limits within the separatrix (corresponding to the critical energy magnitude) and running from $-\infty$ to ∞ outside the separatrix. Here $C = C^*$ is the critical C value that serves the role of the separatrix for the phase variable. For $C > C^*$, both roots of the solution Eq.3.62, give the same trajectory. But for $C < C^*$, the two roots together make up a single trajectory, where each branch runs from ϕ_1 to ϕ_2, as we shall illustrate with an example later. In order to find the other solution ϕ or equivalently, the phase t, we substitute the expression for θ in Eq.3.62 into the azimuthal surface velocity field of associated with the linear flow.

The azimuthal component of the surface velocity field can be derived from Eq.3.43, although, one should first ensure to write $\boldsymbol{\Gamma}$ in a coordinate system with it's polar axis normal to plane of flow. In the original coordinate system, the velocity-gradient tensor is given by:

$$\boldsymbol{\Gamma} = \begin{bmatrix} -(1+\epsilon) & \frac{1}{2}\alpha\cos\theta_\omega & \frac{1}{2}\alpha\sin\theta_\omega\sin\phi_\omega \\ -\frac{1}{2}\alpha\cos\theta_\omega & 1 & \frac{1}{2}\alpha\sin\theta_\omega\cos\phi_\omega \\ -\frac{1}{2}\alpha\sin\theta_\omega\sin\phi_\omega & -\frac{1}{2}\alpha\sin\theta_\omega\cos\phi_\omega & \epsilon \end{bmatrix} \tag{3.66}$$

where the four parameters ϵ, α, θ_ω and ϕ_ω have the usual definitions. This needs to be rotated to a coordinate system whose polar axis is normal to the plane of flow and the other two axes are along the major and minor axes of the ellipses. Denoting this rotation matrix by $\boldsymbol{M}$, we then have,

$$\hat{\boldsymbol{\Gamma}} = \boldsymbol{M}^{-1}\bar{\boldsymbol{\Gamma}}\boldsymbol{M} \tag{3.67}$$

using which we can write down the azimuthal surface velocity field u_ϕ which will be a function of θ, ϕ. After substituting for θ from Eq.3.62, we will have $u_\phi = f(C, \phi) = \frac{d\phi}{dt}$, which we can integrate as,

$$\int_{\phi_1}^{\phi_2} \frac{d\phi}{u_\phi} = \int dt \tag{3.68}$$

to get the phase t for an orbit C. Note that, the limits of ϕ integration here will be between ϕ_1 and ϕ_2 for $C < C^*$ and between 0 to ∞ for $C > C^*$.

We now illustrate the aforementioned features by choosing specific values of the flow parameters. We choose $\epsilon = -2, \phi_\omega = 0°, \theta_\omega = 60°$ and $\alpha' = 2\sqrt{2}$, which is a point of occurrence of eccentric elliptic planar flow according to the surfaces in Fig.3.16. Substituting these parameter values we get:

$$\hat{\delta} = \frac{2}{5}(\sqrt{6} + 1) \tag{3.69}$$

$$\hat{\gamma} = \frac{2}{5}(\sqrt{6} - 1) \tag{3.70}$$

$$1 - e^2 = \frac{1}{5}(7 - 2\sqrt{6}) \tag{3.71}$$

which when substituted into Eq.3.62 gives:

$\tan\theta =$

$$\frac{10(1 - \sqrt{6})(\cos\phi + \sin\phi))}{5((\sqrt{6} - \cos 2\phi)(1 - \sqrt{6}))}$$

$$\pm \frac{\sqrt{5\left((4(28\sqrt{6} - 73) + 25(7 - 2\sqrt{6})C^2)\cos^2\phi + 20(7 - 2\sqrt{6})\sin 2\phi + 25(-4 + 5C^2)\sin^2\phi\right)}}{5((\sqrt{6} - \cos 2\phi)(1 - \sqrt{6}))}$$

$$\tag{3.72}$$

The azimuthal surface velocity field in the rotated coordinate system (where the polar axis is normal to the plane of flow and the other two axes along major and minor axes) is given by:

$$\frac{u_\phi}{\sin\theta} = \frac{d\phi}{dt} = -\sqrt{6} + \cos 2\phi + \frac{2}{\tan\theta}(\cos\phi + \sin\phi) \tag{3.73}$$

the solution for which can be written as the integral,

$$\int_{\phi_1}^{\phi_2} \frac{d\phi}{\left(-\sqrt{6} + \cos 2\phi + \frac{2}{\tan\theta}(\cos\phi + \sin\phi)\right)} = \int_{t_1}^{t_2} dt \tag{3.74}$$

which can be integrated numerically. We observe that depending on C, the integrand on the LHS is real for all ϕ between 0 and ∞ when $C > C^* \sim 1.05$ and it is real only for a range of ϕ when $C < C^*$ (see Fig.3.29a). Note that when $C < C^*$, the integrand on the LHS corresponding to both the roots of $\tan\theta$ (Eq.3.72) exist only for ϕ between ϕ_1 to ϕ_2, implying that these two solutions make up two halves of a given orbit C. The orbits corresponding to these solutions in Eq.3.72 and 3.74 are shown in Fig.3.29b, where we see that for $C < C^*$, the two roots (blue and red halves of an orbit) together constitute a single Jeffery orbit. The equations given in Eq.3.62 and Eq.3.68, therefore constitute the generalised Jeffery orbit equations. Again, in the context of heat transfer, these generalised orbits are also the surface streamlines on the drop suspended in eccentric planar elliptic flows, for which the governing equation is given in Eq.3.55. We had observed in Chapter 2 that these surface-streamlines are independent of the viscosity ratio (λ) when one rescales the velocity field by $(1 + \lambda)$ and redefines the vorticity magnitude as $\alpha' = (1 + \lambda)\alpha$ in Eq.3.66. So Eqs.3.62 and 3.68 also describe the surface streamlines on the drop, provided one replaces α with α'. Following Krishnamurthy and Subramanian (2018a), the Eqs.3.62 and Eq.3.68 constitute the definitions of the $C - \tau$ coordinate system, which we couldn't write down in closed form for the case of axisymmetric extension with inclined vorticity in Chapter 2.
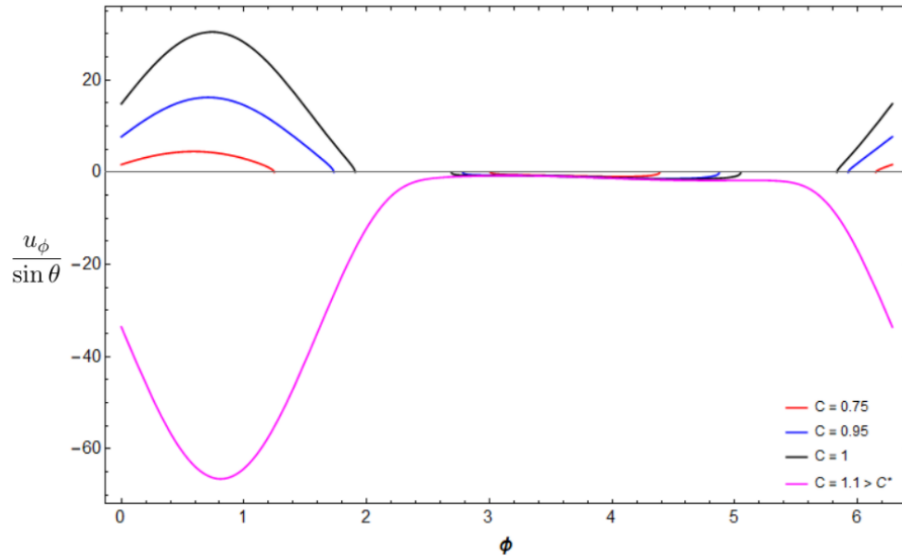
(a) The integrand $u_\phi/\sin\theta$ in Eq.3.74 against ϕ for different C
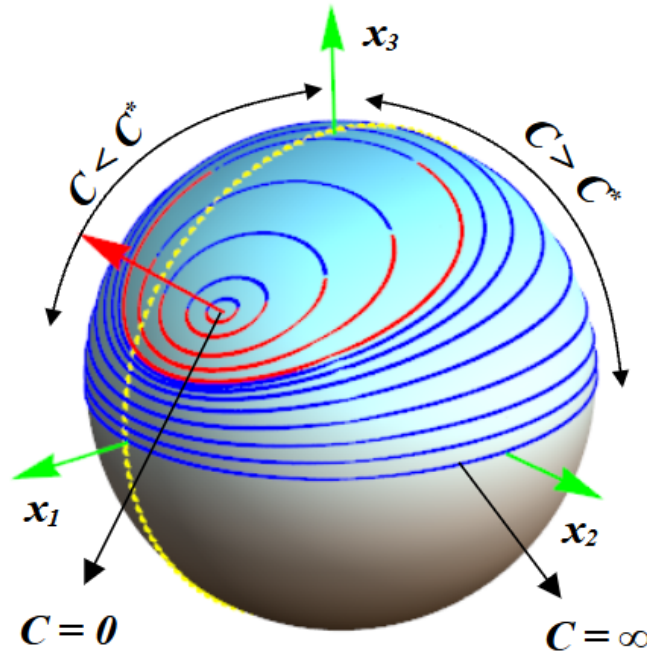
(b) The generalised Jeffery orbits on the surface of the sphere.

Figure 3.29: Plot of (a) the integrand $u_\phi/\sin\theta$ against ϕ for different C. We see that the integrand only exists for a range of ϕ when $C < C^*$ and exists everywhere in the domain when $C > C^*$ and (b) The generalised Jeffery orbits on the surface of the unit sphere. When $C < C^*$, both the roots of $\tan\theta$ in Eq.3.72 exist only for $\phi \in [\phi_1, \phi_2]$ with $\phi_2 - \phi_1 < 2\pi$ and together make up a single orbit (red part corresponds to positive root and blue to the negative root). When $C > C^*$, both roots exist for $\phi \in [0, 2\pi]$ and give the same orbit.

Note that these $C - \tau$ definitions are only valid for the eccentric elliptic flow topologies encountered in this case and not for the spiralling streamline topologies. Nevertheless, these equations form the starting point of the asymptotic analysis of heat transfer in the vicinity of these eccentric elliptic flows. Recall that,

owing to the closed streamlines on the surface at these points, $Nu \sim O(Pe^{1/3})$ instead of $Nu \sim O(Pe^{1/2})$ at these points and so $Nu/Pe^{1/2} \to 0$ as we approach these points. The asymptote of this decay was found to be $|\alpha - \alpha_c'|^{1/2}$ at a given $\theta_\omega = \theta_\omega'$, α_c' being the value at which these eccentric elliptic flow occurs. In order to show this, one must solve the convection-diffusion equation asymptotically with $\theta_\omega', \alpha_c'$ as the base state where $u_C = 0$ by definition and for small deviation from α_c' at the same θ_ω', $u_c \sim O(|\alpha' - \alpha_c'|)$. Using this in the convection- diffusion equation, one can easily show, following the same procedure given in Subramanian and Koch (2006b), that $Nu \sim (Pe|\alpha' - \alpha_c'|)^{1/2}$. A detailed calculation of this is out of the scope of this thesis and will be taken up in the near future.

This concludes the first part of this chapter which focused on the eccentric planar linear flows and their implications. In the next part we comment on the conventional classification scheme of canonical planar linear flows and its drawbacks and provide a new scheme which addresses these limitations.

3.4 Classification of $2D$ Linear Flows

Linear flows have been widely studied because of their fundamental and practical relevance. As was pointed out in the introduction of this chapter, these flows include the canonical rheometric flows (simple shear, planar/axisymmetric extension) which are indispensable to the field of rheology. Moreover, they also serve as local approximations to the flow field in the neighborhood of point of interest. For instance, in the context of turbulent flows, the local flows on length scales smaller than the Kolmogorov scale η_k, (the smallest length scale in turbulence, which is isotropic) may be regarded as linear flows and the statistics of such linear flows is crucial to the development of consistent theoretical framework for turbulence, and towards the response of suspended microstructure elements including drops, polymer molecules, micro-swimmers etc. (Meneveau (2011)). Thus, it is of interest to organise these flows in a sensible manner and this organisation might itself be a function of the problem of interest. order to effectively use and analyse them in various contexts. The first such classification was developed by Perry and Chong (1987) for planar linear flows, based on the fact that the streamlines of these flows are analogous to the solution trajectories of $2D$ autonomous system of ODEs in the neighborhood of fixed points (Strogatz (1994)). Accordingly, the authors classified the linear flows according to their behavior in the vicinity of these critical points. This behavior is governed by the two scalar invariants (P, Q) of the velocity-gradient tensor. Later Chong et al. (1990) extended this classification to include $3D$ linear flows in the $P - Q - R$ space, R being the third scalar invariant. The usefulness of the classification was shown by Gulitski (2007), who used this classification scheme to analyse the bias in the distribution of linear flows in sub-Kolmogorov scale incompressible turbulence. The bias is revealed by a characteristic tear drop shaped locus in the $Q - R$ plane, a fact that was initially shown by Ashurst et al. (1987) and has been confirmed by several other experiments and simulations (see Meneveau (2011)).

In the previous sections, we showed that there is a class of incompressible planar linear flows, namely the eccentric planar linear flows, which occupy a $3D$ sub-space in the four-dimensional parameter space of incompressible $3D$ linear flows. As mentioned therein, these flows occupy the same sub-space (the Q axis) as the canonical linear flows in the aforementioned classification. Thus, in terms of these invariants, one cannot distinguish between the canonical and eccentric planar flows. However, doing so is important from the microhydrodynamic perspective, as, in the context of the transport problem for instance, the eccentric elliptic flows, which occupy the same position in the $P - Q - R$ classification as the canonical elliptic flows, lead to an entirely different behavior as far as transport is concerned. The same is true for other microhydrodynamic phenomena like orientation dynamics of spheroids (Jeffery (1922)) and coil-stretch transitions (Shaqfeh (2005)). So, even though this classification has been useful in the interpretation of sub-Kolmogorov turbulence, one needs to beyond this for other applications. This degeneracy in the organisation is because, the $P - Q - R$ classification does not account for the geometry of these flows, as characterised by the eigenvectors. Recall, that the crucial difference between the canonical and eccentric

planar flows is the inclination of the invariant vector to the plane of flow. This geometric parameter, however, does not enter an eigenvalue based classification, such as the $P - Q - R$ scheme. Moreover, there is another drawback in the $P - Q - R$ classification in that there is no means to find the relative position of the various flow topologies in this scheme. For instance, all the canonical flows exist along the Q axis, with hyperbolic flows corresponding to $Q < 0$, elliptic flows to $Q > 0$ and simple shear to $Q = 0$. But, one cannot find the distance (in suitable units) between two, say, elliptic flows of different eccentricity, as Q is a scalar invariant that does not account for the geometry of these flows. This notion of distance is also a desired feature to have in all the applications of interest listed above. These drawbacks are also true of the original $P - Q$ classification of planar linear flows introduced by Perry and Chong (1987).

It is therefore important to develop an alternate framework for classifying the various linear flows taking into account the points mentioned in the previous paragraph. The earlier section achieves this, albeit in a restricted context of planar linear flows. In the section that follows, we develop another version of this classification, again in the restricted context of compressible (canonical) planar linear flows. In other words we develop an alternative to the original $P - Q$ classification, that maps each planar flow to a unique point in the parametric plane. By introducing the notion of distance between the different flows, it enables one to find the relative position between various flow topologies. Note that, introducing a notion of distance in the classification of $3D$ linear flows, will lead us to a hypersurface with more than three-dimensions (as we saw in the earlier section). So we address this issue in the simpler context of $2D$ linear flows as an initial step, with hopes of extending this in the future to a scheme that also demarcates between the canonical and eccentric planar linear flows.

3.4.1 The $P - Q$ Classification for $2D$ Linear Flows

Before introducing the new classification scheme, we briefly describe the conventional $P - Q$ scheme for $2D$ linear flows. By $2D$ flows, we mean the canonical case, where there is no component of extension normal to the plane of flow. Recall that $2D$ linear flows are represented by a velocity-gradient tensor of the form

$$\mathbf{\Gamma} = \begin{bmatrix} a & b \\ c & d \end{bmatrix}. \tag{3.75}$$

The characteristic equation of this $2x2$ matrix is given by:

$$\mu^2 + P\mu + Q = 0 \tag{3.76}$$

where $P = -(\mu_1 + \mu_2)$, is the negative of the trace (sum of eigenvalues) and $Q = \mu_1\mu_2$, the determinant (product of eigenvalues). The cubic invariant is , of course, $R = 0$. The eigenvalues are given by:

$$\mu_{1,2} = \frac{-P \pm \sqrt{P^2 - 4Q}}{2} \tag{3.77}$$

where the quantity $P^2 - 4Q$ is the discriminant. If $P^2 > 4Q$, we have real eigenvalues and if $P^2 < 4Q$, we have complex ones. When $P^2 = 4Q$, the eigenvalues are equal corresponding to degenerate cases. When $P = 0$, the sum of eigenvalues is zero, implying that the flow is incompressible. Thus, the canonical planar linear flows (the one parameter family) occupy the entire Q axis in this scheme, with simple shear corresponding to $Q = 0$. This is shown in Fig.3.30, which is a reproduction of Fig.2 from Perry and Chong (1987). In this $P - Q$ plane, off the Q axis, all the flows correspond to compressible planar flows. They are broadly arranged into type types of topologies:

- If $P^2 > 4Q$, the eigenvalues are real, and the topology obtained is a node or a saddle, depending on whether the two eigenvalues are of the same or opposite sign. Thus, $P^2 > 4Q$, $Q > 0$ corresponds to nodes and $Q < 0$ corresponds to saddles. Further, for nodes, when $P > 0$, both eigenvalues are negative, leading to stable nodes and when $P < 0$, it leads to unstable nodes.

- If $P^2 < 4Q$, the eigenvalues are complex (the region only exists for $Q > 0$), the topology gives rise to a focus, with streamlines spiralling to or from it. A stable focus corresponds to $P > 0$ and unstable one to $P < 0$.
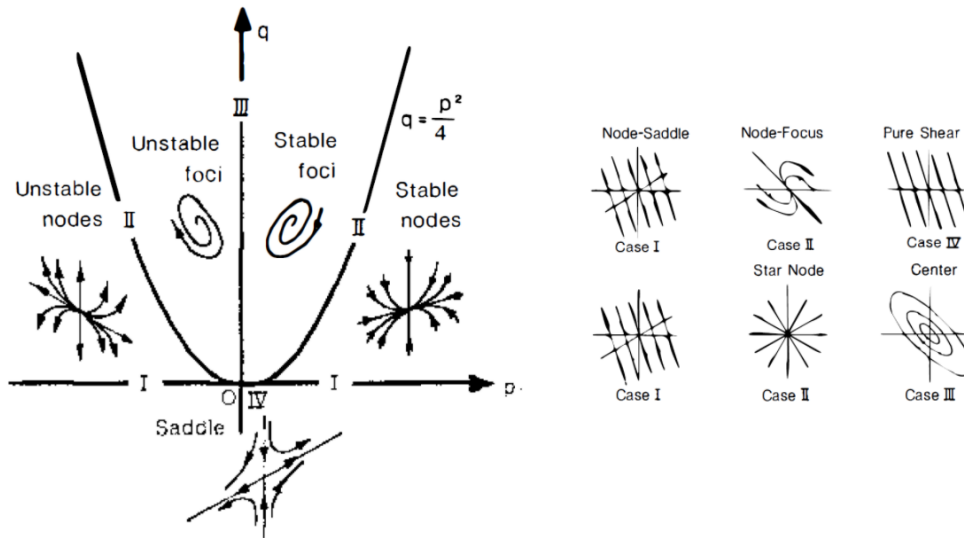
Figure 3.30: The $P - Q$ classification scheme with the flow topologies associated with different regions and the boundaries of the $P - Q$ plane. (Image reproduced from Perry and Chong (1987)).

There a few special points (or lines) in the $P - Q$ plane, which form boundaries of this plane, and correspond to degenerate scenarios. The first is, as already discussed, the Q axis. The second is the parabola $P^2 = 4Q$, which corresponds to both of the eigenvalues of the flow being equal. The points on this parabola correspond to what are called the degenerate node topology, and there are two types of these degenerate nodes: (i) star - nodes; when there are two independent eigenvectors and, (ii) node-focus; when there is only one eigenvector. The third case corresponds to the P axis ($Q = 0$). This immediately implies one of the eigenvalues is zero and therefore leads to node-saddle topologies, also termed line sources or sinks, depending on whether $P < 0$ or $P > 0$. Finally, we have simple shear, which lies at the intersection of the aforementioned degenerate boundaries. For this flow, both eigenvalues are zero and there is a plane of degenerate eigendirections associated with this flow, as already mentioned.

This classification scheme above does not, however, provide any information on the relative positions of the different flow topologies in a given region (for instance, the location on $P^2 = 4Q$, corresponding to a particular star-node topology). This issue is addressed by introducing a new classification scheme, the $\chi - \zeta$ scheme which is introduced in the next section.

3.4.2 The $\chi - \zeta$ Classification scheme

The starting point of this new classification scheme is to write down the (normalized) velocity-gradient tensor in Eq.3.75, as a sum of the three elementary constituents that make up any $2D$ linear flow multiplied by constants χ and ζ (which are non-dimensional) as:

$$\mathbf{\Gamma} = \zeta \begin{bmatrix} 1 & 0 \\ 0 & 1 \end{bmatrix} + (1 - |\zeta|) \left(\chi \begin{bmatrix} 1 & 0 \\ 0 & -1 \end{bmatrix} + (1 - \chi) \begin{bmatrix} 0 & 1 \\ -1 & 0 \end{bmatrix} \right) \tag{3.78}$$

where the three elementary constituents correspond to pure dilatation, planar extension and solid-body rotation (all normalised in suitable units). Note that the latter two components characterize the usual

canonical linear flows. We then attempt to construct a region in the $\chi - \zeta$ plane where all possible $2D$ linear flows exist. Based on Eq.3.78, an intuitive guess for the boundaries of the region would be the lines $\chi = \pm 1$ and $\zeta = \pm 1$, which encloses a square with side of length 2. This region is shown in Fig.3.31.
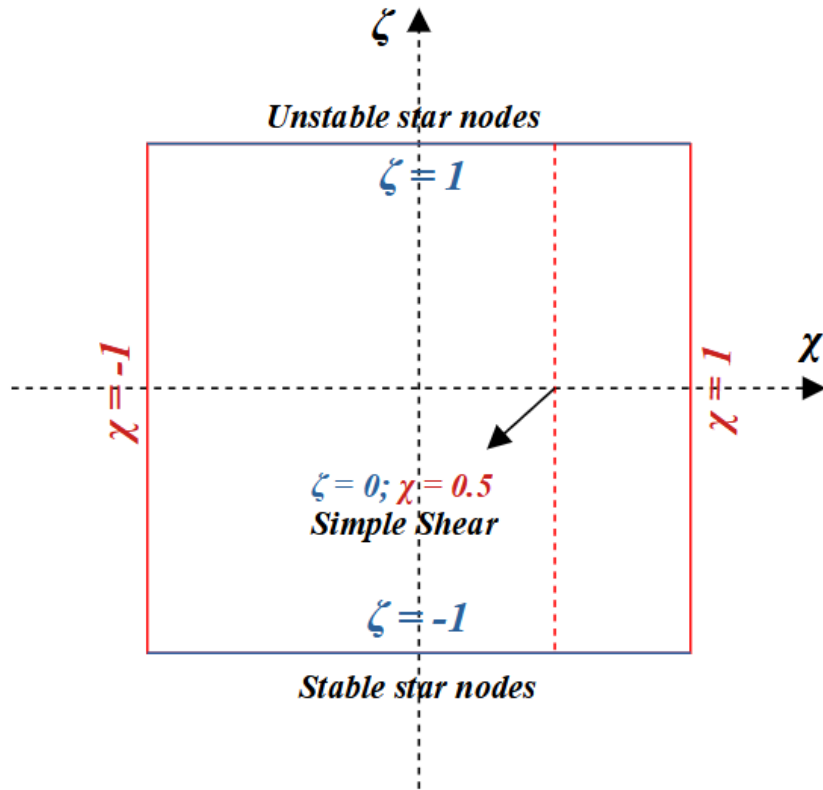
Figure 3.31: The $\chi - \zeta$ classification scheme based on Eq.3.78, which is degenerate owing to the presence of star nodes along the entire boundary $\zeta = \pm 1$. In this scheme the simple shear is at the point $(\chi, \zeta) = (0.5, 0)$.

From the figure, we see that, while $\chi = \pm 1$ still corresponds to different flow topologies depending on ζ, the same is not true for $\zeta = \pm 1$, as each of these boundaries is populated by the same topology - pure dilatation (star node topology), or in fluid dynamics parlance, source for $\zeta = 1$ and $\zeta = -1$. The resulting classification will be degenerate. This degeneracy was not an issue in the case of eccentric planar linear flows, since the degeneracy arose only in lower-dimensional projections. However, in the present case we only have a two-dimensional parameter space. Therefore, we need to reshape this region such that the star node topologies correspond to points. This can be achieved by simply collapsing the lines $\zeta = \pm 1$, to the point $(\chi, \zeta) = (0, \pm 1)$, which changes the shape of the region from a square to a diamond. Mathematically, this implies that the line $\chi = \pm 1$ should be rewritten as $\chi = f(\zeta)$, which achieves a tilt such that they meet $\chi = 0$ at $\zeta = \pm 1$. Further, in the present scheme, simple shear corresponds to $\chi = 0.5$. For purposes of symmetry (also keeping in mind the location of simple shear in the $P - Q$ scheme) we wish to rescale the coefficients such that simple shear occurs at $\chi = 0$. All these may be achieved by rewriting the velocity-gradient tensor as:

$$\mathbf{\Gamma} = \zeta \begin{bmatrix} 1 & 0 \\ 0 & 1 \end{bmatrix} + (1 - |\zeta|) \left(\frac{(2\chi - |\zeta| + 1)}{2(1 - |\zeta|)} \begin{bmatrix} 1 & 0 \\ 0 & -1 \end{bmatrix} + (1 - \frac{(2\chi - |\zeta| + 1)}{2(1 - |\zeta|)}) \begin{bmatrix} 0 & 1 \\ -1 & 0 \end{bmatrix} \right) \tag{3.79}$$

Rewritten this way, one can easily show that the boundary of the region in the $\chi - \zeta$ plane is now the parallelogram, with boundaries given by $\zeta = \pm(1 + 2\chi)$ and $\zeta = \pm(1 - 2\chi)$, with $\chi \in [-0.5, 0.5]$ and

$\zeta \in [-1, 1]$. In this scheme, there are no degeneracies and simple shear flow occurs at $(\chi, \zeta) = (0, 0)$, with planar extension and solid-body rotation occurring at $(\chi, \zeta) = (0.5, 0)$ and $(\chi, \zeta) = (-0.5, 0)$ respectively. This region is shown in Fig.3.32a.

Now we identify special curves, which corresponded to the degenerate boundaries in the $P - Q$ classification. To do this, we write the characteristic equation of $\mathbf{\Gamma}$, as given in Eq.3.79:

$$\mu^2 - (2\zeta)\mu + (\zeta^2 + 2\chi(|\zeta| - 1)) = 0 \tag{3.80}$$

which gives the eigenvalues as:

$$\mu_{1,2} = \frac{-\zeta \pm \sqrt{2\chi(1 - |\zeta|)}}{2\zeta}. \tag{3.81}$$

The discriminant is now $\chi(1 - |\zeta|)$ and the curve corresponding to the discriminant being zero, which was the parabola $P^2 = 4Q$ in the $P - Q$ classification, is now $\chi = 0$ (the end points of this segment corresponds to $\zeta = \pm 1$). The Q axis ($P = 0$) in the $P - Q$ classification is now the line $\zeta = 0$. Finally, the P axis ($Q = 0$), where one of the eigenvalues was zero, is given by the equation: $\zeta^2 + 2\chi(|\zeta| - 1) = 0$. All these curves are plotted in the $\chi - \zeta$ plane shown in Fig.3.32b. Based on the aforementioned information, one can immediately identify the various flow topologies associated with the various sub-regions in the $\chi - \zeta$ plane.
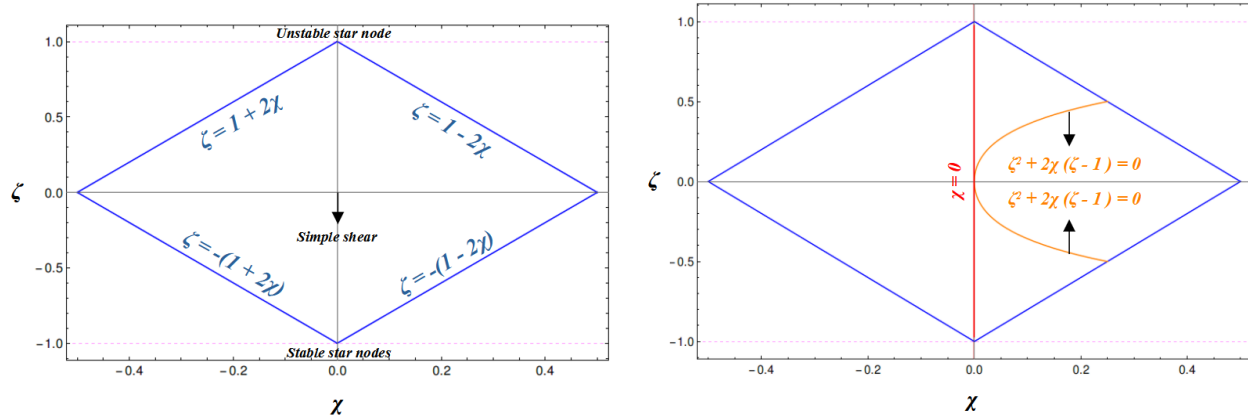
(a) The classification scheme in $\chi - \zeta$ plane.

(b) Special curves in $\chi - \zeta$ plane.

Figure 3.32: Plot of (a) the classification scheme in the $\chi - \zeta$ plane without degeneracy. In this scheme, $\zeta = 0$ corresponds to incompressible planar linear flows with $\chi = 0$ corresponds to simple shear; $\chi = -0.5$ to solid-body rotation and $\chi = 0.5$ to planar extension. The star nodes now correspond to the point $(\chi, \zeta) = (0, \pm 1)$ and (b) the special curves in the plane that corresponds to the degenerate scenarios. The red line $\chi = 0$ corresponds to degenerate critical points corresponding to zero discriminant and the orange curves correspond to one of the eigenvalues being zero.

The region bounded between $\chi = 0$ and $\zeta = \pm(1 + 2\chi)$, where the discriminant is negative, corresponds to topologies with stable focus for $\zeta < 0$ and unstable focus for $\zeta > 0$ respectively. Similarly, the region bounded between $\chi = 0$, $\zeta = \pm(1 - 2\chi)$ and $\zeta^2 + 2\chi(|\zeta| - 1) = 0$ correspond to stable ($\zeta < 0$) and unstable ($\zeta > 0$) node topologies; while the region between $\zeta^2 + 2\chi(|\zeta| - 1) = 0$ and $\zeta = \pm(1 - 2\chi)$ corresponds to saddles. The horizontal line $\chi = 0$ is populated by the canonical planar incompressible linear flows and the vertical line $\chi = 0$, where the discriminant is zero, is populated by the degenerate node-foci topologies (both stable and unstable). Finally, along the curve $\zeta^2 + 2\chi(|\zeta| - 1) = 0$, where one of the eigenvalues is zero, we have line sources and sinks (node-saddles). Thus we see that all possible flow topologies are covered in this scheme, which also allows for the notion of distance between the flow

topologies, as each flow corresponds to a unique point in this scheme. We now plot the flow topologies along several trajectories in the $\chi - \zeta$ plane, which are shown in Fig.3.33a-3.33e, and the flows along these trajectories are shown in Table 3.1.

(a) Trajectory 1

(b) Trajectory 2

(c) Trajectory 3

(d) Trajectory 4
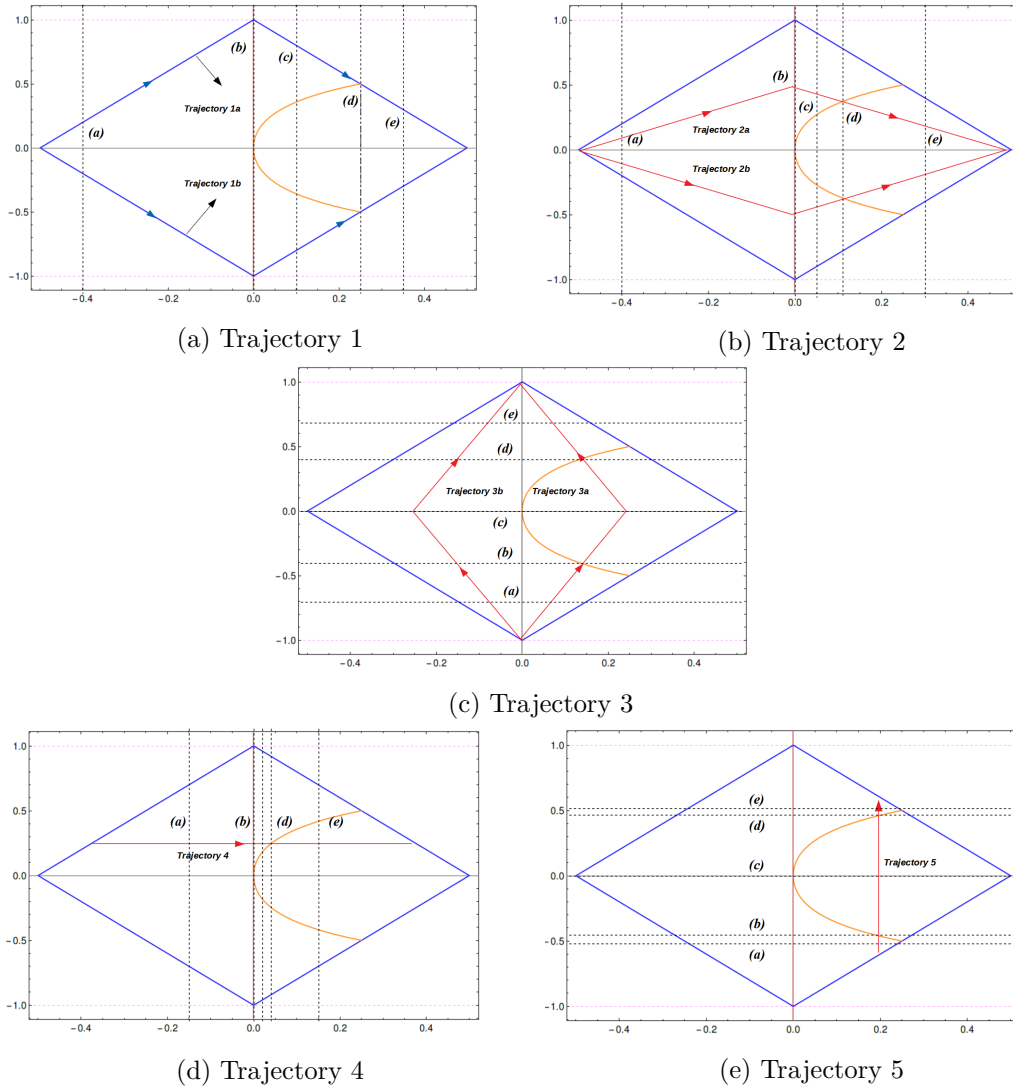
(e) Trajectory 5

Figure 3.33: The trajectories along which streamlines are plotted in Table 3.1. They are plotted at five different points $((a) - (e))$, corresponding to the points of intersection of the vertical black lines with the a chosen trajectory.

For the trajectories in Fig.3.33a, which are along the boundaries of the region, and for the trajectories in Fig.3.33b, the starting and ending points correspond to solid-body rotation and planar extension. Also note, that the topologies along the trajectories $1a$ and $1b$ ($2a$ and $2b$) are the same except that the critical points are unstable for $1a(2a)$ and stable for $1b(2b)$. We also observe that the (real) eigenvectors of the flow (when $\chi > 0$, given by green and red arrows in Table.3.1), are always along the coordinate axes $((0,1)$ and $(1,0))$ for the trajectory along the boundary. Another feature we observe is that, when a trajectory runs between the two star nodes (like the ones in Fig.3.33c, trajectory $3a$), the eigenvectors of flow remain constant along the entire trajectory. Note that whenever any trajectory crosses $\chi = 0$, we have a node-focus topology and whenever they cross the orange curves ($\zeta^2 + 2\chi(|\zeta| - 1) = 0$), the flow corresponds to a node-saddle topology as is consistent. Also note that for trajectories that are vertical lines (like Fig.3.33e), when they correspond to $\chi > 0.25$, only saddles are obtained, as they will not

intersect the orange curves. Similarly, when the trajectory is horizontal (like Fig.3.33d) and corresponds to $\zeta > 0.5$ or $\zeta < -0.5$, we only encounter nodes for $\chi > 0$, again because, we do not intersect the orange curves populated by node-saddle flows.

No. a	b	c	d	e
1a Unstable focus	Star Node	Unstabe node	Node-Saddle	Saddle
2a Unstable foci	Node-Focus	Unstable node	Node-Saddle	Saddle
3a Stable node	Node-saddle	Saddle	Node-Saddle	Unstable node
3b Stable focus	Stable focus	Elliptic flow	Unstable focus	Unstable focus
4 Untable focus	Node-focus	Unstable Node	Node-saddle	Saddle
5 Stable node	Node - Saddle	Saddle	Node saddle	Unstable focus

Table 3.1: Flow topologies at points along the trajectories in the $\chi - \zeta$ scheme shown in Fig.3.33(a)-3.33(e)

These information from the plots in Table.3.1 can be used to demarcate the different planar flows in the $\chi - \zeta$ plane as shown in Fig.3.34. We have therefore, come up with a classification for $2D$ linear flows, that is both finite in extent and also gives the distance between various flow topologies. Note that the domain of occurrence of incompressible planar flows (Fig.3.16), can also be considered one such classification, as the governing parameters are defined taking the geometry of the flows into account, and therefore the domain demarcates eccentric and canonical planar linear flows, unlike the $Q - R$ classification based on scalar invariants. Therefore it is natural to extend these ideas to develop a broader classification scheme for $3D$ linear flows (including compressible flows) that demarcates the eccentric planar linear flows from the canonical ones. At present, this is out of the scope of this work and will be taken up in the future.
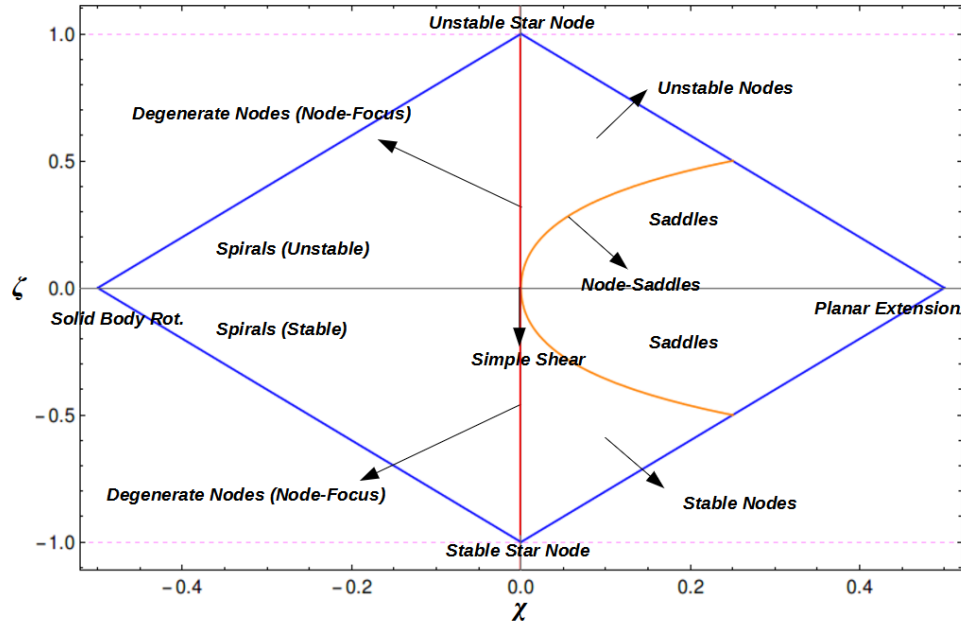
Figure 3.34: The $\chi - \zeta$ classification scheme highlighting the regions corresponding to the different planar flow topologies.

3.5 Concluding Remarks

In this chapter, we have discussed the general class of incompressible planar linear flows, the eccentric planar linear flows, in significant depth and identified their domain of existence in the four-dimensional parameter space of incompressible $3D$ linear flows. We showed that these flows occupy a $3D$ sub-volume in the hyperspace and this has implications in several microhydrodynamic phenomena. One such application was already encountered i the context of convective transport from drops suspended in these flows, specifically the eccentric elliptic planar flows, for which we showed using scaling arguments that $Nu \sim O(Pe^{-1/6}) \to 0$ as $|\alpha_c' - \alpha'|^{1/2}$ with α_c' being the point of occurrence of these elliptic flows. This immediately implies that, at these special points for drops, $Nu \sim Pe^{1/3}$, and they behave like solid particles, which have crucial implications. Another interesting application is the orientation dynamics of spheroids in these flows, which will lead to generalised Jeffery orbits, for which we have derived an expression using geometrical arguments. It is however more crucial to see how this orientation dynamics change as a function of spheroid aspect ratio when they are suspended in eccentric planar linear flows. A direct extrapolation from the behavior in canonical planar flows (L. G. Leal and Hinch (1972)), would imply that in eccentric parabolic and hyperbolic flows, the trajectories will no longer be closed orbits, but would be open curves. This transition from closed orbits to open ones, will be marked by a three-dimensional hypersurface that is a function of the flow-type parameters and aspect ratio and will be mediated by a critical topology, which for the case of spheroids in canonical linear flows were meridians. Another application where these flows will play a crucial role is the coil-stretch dynamics of polymeric molecules, like single-strand DNA, suspended in these flows. As with the other applications cited, the dynamics of this problem in canonical planar flows are well known (Shaqfeh (2005)). But coil-stretch dynamics can also be solved in the context of eccentric planar flows, which is another avenue worth pursuing in the future, for its relevance in various biological processes.

Chapter 4

Transport in the Interior of a Drop

In this chapter, we turn our attention to the problem of transport in the interior of a spherical drop suspended in an ambient linear flow. In calculating the Nusselt number in the exterior in Chapter 2, we had assumed an isothermal drop surface as our boundary condition. Such a boundary condition requires the resistance to transport within the interior to be negligibly small, a restrictive condition rarely realised in practice, since this requires the interior thermal conductivity (k_i) to be much larger than the one (k_e) in the ambient phase. This makes it a restrictive assumption. As shown in Krishnamurthy and Subramanian (2018a), it is possible to generalise the $C - \tau$ formulation to a less restrictive scenario where the interior conductivity is comparable to the exterior, the so called conjugate transport problem, provided that there also exists a boundary layer in the interior of the drop at large Pe. The rate of transport is now a function of k_i/k_e, and an expression for Nu was derived by the authors for the one-parameter family of linear flows. The existence of this internal boundary layer, however, is not obvious and is dependent on the nature of flow inside the drop. For a drop subject to the one-parameter family of canonical planar linear flows in the ambient, it is well known that the streamlines in the interior are closed (Powell (1983), Krishnamurthy and Subramanian (2018a)), which leads to diffusion-limited transport and thus there will be no boundary layer in the interior. The same is also true for the other one-parameter family, three-dimensional extensional flow (Krishnamurthy and Subramanian (2018a)). In such cases, the assumption of an isothermal boundary, amounts to the restriction on the interior thermal conductivity mentioned above. But, Stone et al. (1991), had shown using computer simulations that for one of the two-parameter family of flows, the axisymmetric extension with inclined vorticity, the streamlines inside the drop are chaotic. There are also other instances, where the drop interior exhibits chaos, which are reported in literature (Kroujiline and Stone (1999), Bryden and Brenner (1999), Ward and Homsy (2001), Christov and Homsy (2009)). The presence of chaotic streamlines imply that the interior is well mixed and therefore the transport is no longer diffusion limited. Such a condition in the interior would lead to the formation of an internal boundary layer, where the resistance to transport is localised.

In this chapter, we briefly review the literature on the various known instances that lead to so-called Lagrangian chaos in the drop interior, before turning the focus on our case, a spherical drop in a $3D$ linear flow. We then study the nature of streamlines inside the drop numerically, and show, by using Poincaré sections, that the interior streamlines are chaotic for both the two-parameter families examined in Chapter 2 and one therefore expects the same for the general $3D$ linear flow. We then use Langevin simulations, to analyse the tracer concentration profiles and calculate the transport rate for the interior problem, where now the external phase is assumed to have negligible transport resistance. Although earlier efforts have calculated the chaos-induced transport enhancement, none of them have obtained the implied scaling behavior in the asymptotic limit of large Pe, in particular if chaos leads to the expected $Pe^{1/2}$ enhancement due to the formation of an internal boundary layer. In this chapter we show, for the first time, the presence of an internal boundary layer and find that, the implied scaling of Nu at large Pe is dependent on the linear flow. We conclude this chapter by discussing how this boundary layer can be

incorporated into our $C - \tau$ analysis to solve the conjugate transport problem, for certain special cases.

4.1 Lagrangian Chaos in Drop Interior - A Brief Review

Suspensions of drops in an ambient phase has been extensively studied in literature since the seminal works of G. I. Taylor (1934), G. I. Taylor, 1932, who analysed the rheology and deformation of a drop suspended in a shearing flow. Following this, several authors have extended Taylor's original results by calculating higher order corrections to drop deformation and the associated rheology (Cox (1969), Frankel and Acrivos (1970), Barthes-Biesel and Acrivos (1973)). These studies however, did not focus on the nature of streamlines, particularly in the interior or exterior of the drop. Such efforts came later, starting with the work of Torza et al. (1971), who analysed the streamlines in the interior and exterior of a drop suspended in an ambient simple shear. Powell (1983) extended this analysis to the whole one-parameter family of canonical planar linear flows. In the 1980's, there were studies by Aref and co-workers (Aref et al. (2017), Aref and Balachandar (1986)) and Ottino (Ottino (1990)), on the ability of simple $2D$ time-dependent flow fields to generate chaotic pathlines. This chaos is termed Lagrangian chaos, which describes the chaotic motion of the fluid particle, and distinguishes it from Eulerian chaos, where the underlying velocity field at a fixed point, is itself chaotic or random (Bohr et al. (1998))). Thus, Lagrangian chaos can be considered a deterministic chaos, where the underlying dynamical equations are deterministic. Passive tracers in such a chaotic field would produce large areas of mixing, as shown by Kaper and Wiggins (1993), Kumar and Homsy (1996) for the specific case of chaos in eccentric journal bearings and in cavities (Ottino (1990)). A material volume of passive tracer typically undergoes a process of folding and stretching, making it unrecognizable from its initial shape. The explanation for the phenomenon stems from theory based on chaos in dynamical systems, where, chaos leads to exponential divergence of the trajectories of two initially nearby fluid elements. All these aforementioned scenarios involve two-dimensional and unsteady flows. Following these efforts, there have been studies that have considered steady $3D$ flows and their ability to generate chaotic pathlines, an example of which is the flow in the interior of a spherical drop suspended in an ambient flow. Bajer and Moffat (1990), were the first to treat general bounded quadratic flows within a spherical domain and showed that, such a flow can be decomposed into two integrable flows with closed streamlines, namely a quasi-rigid rotation and a twisting flow. They observed that, these flows can exhibit 'stretch-twist-fold' kinematics, leading to chaotic advection. They showed using the method of averaging that, the asymptotic limits of a general quadratic flow, where the limits corresponded to rotation-dominant and twist-dominant flow fields, the streamlines of the flow were localised near the adiabatic invariants of the system (closed curves) and for arbitrary strengths of these two components, especially when the twist component dominates over the rotation, computer-generated Poincaré sections showed that, the adiabatic invariants break down leading to a chaotic interior. Vainshtein et al. (1996) used the method of averaging to analytically show this breakdown of adiabatic invariants and concluded that it is their repeated quasi-random scattering near separatrix surfaces, that eventually led to the chaotic state.

Following the work of Bajer and Moffat (1990), several authors have identified multiple instances in which chaos occurs in such a confined setting, notably inside droplets. Stone et al. (1991), first showed using numerical analysis that, chaotic streamlines exist in the interior of a spherical drop subject to axisymmetric extensional flows with inclined vorticity in the ambient, one of the two-parameter families we encountered in Chapter 2, where, unlike the case of Bajer and Moffat (1990), the velocity field has a cubic non-linearity. Later, Kroujiline and Stone (1999) considered two possible three-dimensional internal velocity fields. The first consisted of a drop translating due to buoyancy forces and the second a drop in an extensional flow. The addition of a vorticity vector that is not aligned to the axis of each of these velocity fields produced steady three-dimensional chaotic streamlines. A computational parametric study of the mixing was performed through an analysis of Poincaré maps. Bryden and Brenner (1999) considered a buoyant drop subjected to simple shear and found that it too exhibits chaotic streamlines.

In the aforementioned studies, chaos in a steady $3D$ field is bought about by the incompatibility between the symmetries of two integrable sub-components of the $3D$ field, which again results in the breakdown of adiabatic invariants, as shown rigorously by Neishtadt et al. (1998), using the method of averaging, for the flow field considered by Stone et al. (1991). In their particular case, the incompatibility is bought about by the non-trivial inclination between the axes of symmetry of two axisymmetric flow-fields, axisymmetric extension and rigid-rotation, while in the case of Bryden and Brenner (1999), the two incompatible fields are translation and simple shear. The aforementioned efforts serves to indicate that when a drop is suspended in an arbitrary, steady $3D$ linear flow field, the streamlines in the interior can exhibit chaos. More recently, Ward and Homsy (2001) and Christov and Homsy (2009) have reported the presence of chaotic streamlines inside a electrohydrodynamically driven translating drop, subject to oscillatory electric fields, where Lagrangian chaos in the former case, again results from the non-trivial inclinations of the axes of symmetry of the two underlying components (translation and extension due to Maxwellian stresses on a charged drop) and in the latter, from the unsteadiness of the underlying flow field.

While all the aforementioned studies have shown the ability of chaos to bring about an effective mixing, leading to a uniform concentration in the interior, the implication for the transport rate is not immediately obvious and only a handful of studies have focused on this issue. It is well-known that without chaotic streamlines in the interior, transport from the drop is always diffusion-limited, when the dominant transport resistance lies in the drop phase, regardless of the magnitude of Peclet number (Kronig and Brink (1950), Christov and Homsy (2009), Oliver and DeWitt (1993)). For the cases with chaotic streamlines in the interior, Bryden and Brenner (1999) were the first to consider the enhancement of mass transfer inside a drop by chaotic advection in a steady three-dimensional Stokes flow. Their problem consists of a drop translating due to buoyancy subjected to a steady shear flow. The parameters include the angle between the velocity vector and vorticity vectors, different viscosity ratios, and a dimensionless magnitude of shear. The authors show that, in the parameter regime in which chaotic streamlines nearly fill the drop, the mass transfer rates become convection dominated. The mass transfer coefficient that the authors calculate is, however, only an approximate measure of chaos-induced convective enhancement, as the authors assume a constant flux at the interface, governed by a finite conductivity of the ambient phase, and therefore, the resulting coefficient is not a true measure of the chaotic enhancement. Christov and Homsy (2009), similarly show the enhancement of transport rate from a charged drop translating in an oscillating electric field. While their calculations assume negligible exterior resistance, their underlying velocity field is axisymmetric and their calculations do not extend to very large values of Pe. Therefore their study offers no insight into the existence of an internal boundary layer and the implied scaling at this asymptotic limit.

To our knowledge, there have been no formal studies that calculate the Nusselt number and the implied scaling at $Pe \gg 1$, in the interior of a drop suspended in complex three-dimensional linear flows, under the conditions of chaotic mixing. In this chapter, we make a preliminary effort in this direction, the objective being to demonstrate the existence (at large Pe) of a thermal or concentration boundary layer in the interior and to characterise the resulting transport rate from a drop subject to complex three-dimensional linear flows. In our study, we assume the exterior phase resistance to be negligible, which is necessary to calculate the true measure of chaos-induced convective enhancement. The existence of a thermal boundary layer would pave the way for the $C - \tau$ analysis described in Chapter 2, to be extended for the analysis of conjugate transport problem under certain special conditions, as shown by Krishnamurthy and Subramanian (2018a).

4.2   Drop in a General $3D$ Linear Flow - Lagrangian Chaos

In this section, we analyse the nature of the streamlines in the interior of a spherical drop in an ambient linear flow. As already stated in the context of the exterior transport problem, the study pertains to the

Stokesian regime ($Re \ll 1$). The interior velocity field in this limit is given by:

$$\boldsymbol{u} = \frac{1}{2(1+\lambda)} \left[(5r^2 - 3)\boldsymbol{E}.\boldsymbol{x} - 2(\boldsymbol{E} : \boldsymbol{xx})\boldsymbol{x} \right] + \boldsymbol{\Omega}.\boldsymbol{x} \tag{4.1}$$

where $\boldsymbol{E}$ and $\boldsymbol{\Omega}$ are the symmetric and anti-symmetric parts of the velocity gradient tensor $\boldsymbol{\Gamma}$, which for a $3D$ linear flow, in terms of dimensionless quantities is given by:

$$\boldsymbol{\Gamma} = \begin{bmatrix} -(1+\epsilon) & -\frac{\alpha \cos \theta_\omega}{2} & -\frac{\alpha \sin \theta_\omega \sin \phi_\omega}{2} \\ \frac{\alpha \cos \theta_\omega}{2} & 1 & -\frac{\alpha \sin \theta_\omega \cos \phi_\omega}{2} \\ \frac{\alpha \sin \theta_\omega \sin \phi_\omega}{2} & \frac{\alpha \sin \theta_\omega \cos \phi_\omega}{2} & \epsilon \end{bmatrix} \tag{4.2}$$

where the quantities $\epsilon, \alpha, \theta_\omega, \phi_\omega$ are the four dimensionless parameters that govern an arbitrary $3D$ linear flow and they have the same definitions mentioned in Chapter 2. In this chapter too, we proceed in an hierarchical fashion, starting our analysis with the two-parameter families of flows, before analysing the general linear flow. In our analysis, we shall make use of the Poincaré sections obtained by numerically integrating the aforementioned interior velocity field, to demonstrate the presence or absence of chaos. The Poincaré sections in our study are generated by marking the points where the streamlines corresponding to a given initial point intersect a chosen plane ($x_1 - x_3$ plane in our case) from one particular direction ($x_2 \to 0^+$). We begin our analysis by first considering the ambient linear flows, which produce regular streamlines in the interior. By regular streamlines, we mean, either simple closed curves or where the trajectories densely wind around nested tori.

4.2.1 Flows with Regular Interior Streamlines

For this class of flows, the Nusselt number is independent of Pe for $Pe \gg 1$, implying that the transport is diffusion-limited. The first case we consider is that of a translating drop, which is best analysed in a frame of reference moving with the drop.

4.2.1.1 Translating Drop

This case does not correspond to a linear flow in the ambient, but nevertheless is a widely studied one, which we shall use later in validating our simulations. Therefore, we study this case here, the results of which will be used at a later stage, while discussing the numerical calculation of transport rate. In a frame of reference moving with a drop, a translating drop is equivalent to a drop subject to a uniform velocity $\boldsymbol{U}$ motion in the ambient. This leads to a velocity field in the interior given by:

$$\boldsymbol{u}(\boldsymbol{x}) = \frac{\boldsymbol{U}}{2(1+\lambda)} \cdot \left((2r^2 - 1)\boldsymbol{I} - \boldsymbol{xx} \right) \tag{4.3}$$

We have taken $\boldsymbol{U} = \boldsymbol{1_3}$, which is along the x_3 direction. The aforementioned velocity field is axisymmetric and therefore, it can be characterised by a single invariant, the Stokes streamfunction ψ_s, which is given by:

$$\psi_s = 4r^2(1 - r^2)\sin^2 \theta \tag{4.4}$$

The surfaces given by $\psi_s = constant$, correspond to a family nested tori, that fill up the entire region inside the drop. The streamlines correspond to closed trajectories in the cross-sectional planes of constant-ϕ. The surface $\psi_s = 0$ corresponds to the limiting tori, that is coincident with the drop surface. All streamlines in the interior correspond to $\psi_s > 0$, while $\psi_s < 0$ implies $r > 1$, which is irrelevant to our case. The other limiting tori corresponds to a ring of stagnation points, which is given by $\psi_s = 1$. The streamlines in the interior have two cells and are closed as shown in Fig.4.1, where the Poincaré section was obtained by integrating the velocity field in Eq.4.3 using a fourth-order Runge-Kutta scheme (RK(4)) with a time step of 10^{-4}. The integrations were carried out for a total time of 10^5, and each curve in the section,

which correspond to different initial conditions, contains more than 10^5 points. The curves of same color correspond to initial conditions which are mirror images about the x_3 axis. As was already mentioned, we choose the $x_1 - x_3$ plane to plot the Poincaré section, which corresponds to the plane $\phi = 0$. Note that for this case, the streamlines lie entirely on a given constant-ϕ plane and therefore, to plot the Poincaré section, one must choose initial points that lie on the $x_1 - x_3$ plane and the resulting section in this case will give us the actual streamlines, rather than the points at which a streamline intersects the plane as it approaches it from a particular direction. Thus, the closed curves in the section correspond to cut-sections along the $\phi = 0$ plane, of the nested tori.
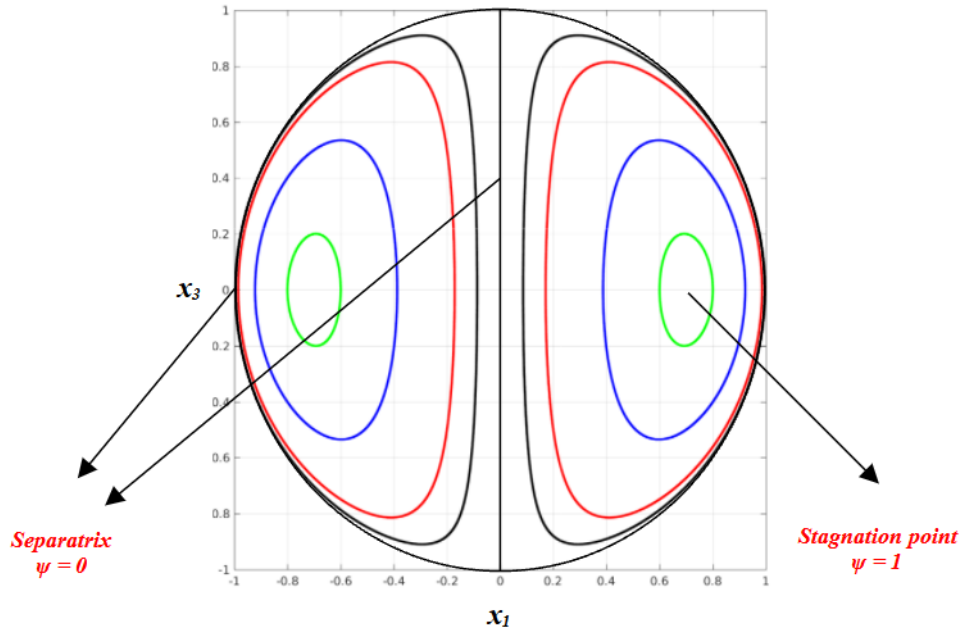
Figure 4.1: Poincaré section for a translating drop in the meridional plane ($x_1 - x_3$ plane). The velocity field (Eq.4.3) leads to two cells of nested closed streamlines in the interior.

The nature of the velocity field for this case implies that, the fluid particles cannot jump from one torus to another, and therefore there is no chaos. The addition of a perturbation to this base state, destroys the stability of these structures, thereby leading to chaotic streamlines. One such perturbation is the addition of another axisymmetric field, in such a way that the axes of symmetry of both the underlying fields are not coincident with one another. This was the case that was analysed by Bryden and Brenner (1999), where the authors observed that the addition of simple shear to translation leads to chaos, when the neutral directions of both the fields are inclined non-trivially to each other.

4.2.1.2 Drop in Axisymmetric Extension

The next case we consider is the case of drop in axisymmetric extension, which is the limiting case of the cubic family of flows considered by Stone et al. (1991). The velocity-gradient tensor for this case is:

$$\mathbf{\Gamma} = \begin{bmatrix} -2 & 0 & 0 \\ 0 & 1 & 0 \\ 0 & 0 & 1 \end{bmatrix} \tag{4.5}$$

and the resulting (Cartesian) components of the velocity field are:

$$u_1 = \frac{1}{2(1+\lambda)} \left[-2(5r^2 - 3)x_1 - 2(x_2^2 + x_3^2 - 2x_1^2)x_1 \right] \tag{4.6}$$

$$u_2 = \frac{1}{2(1+\lambda)} \left[(5r^2 - 3)x_2 - 2(x_2^2 + x_3^2 - 2x_1^2)x_2 \right] \tag{4.7}$$

$$u_3 = \frac{1}{2(1+\lambda)} \left[(5r^2 - 3)x_3 - 2(x_2^2 + x_3^2 - 2x_1^2)x_3 \right] \tag{4.8}$$

The term $(1 + \lambda)$ can again be absorbed into the velocity scale, rendering the streamline topology independent of λ. For the cases with vorticity, this implies that $(1 + \lambda)\alpha$ can be treated as the re-scaled vorticity magnitude α', same as what was done in the exterior transport problem. The same velocity field can be rewritten in spherical coordinates as:

$$u_r = \frac{3}{4}r(1 - r^2)(1 + 3\cos 2\theta) \tag{4.9}$$

$$u_\theta = \frac{3}{4}(5r^2 - 3)\sin 2\theta \tag{4.10}$$

$$u_\phi = 0 \tag{4.11}$$

Owing to the absence of swirl (Eq.4.11), one can again introduce a Stokes' streamfunction that characterises the full velocity field, which is given by:

$$\psi_s = \frac{3}{4}r^3(1 - r^2)\cos\theta \sin^2\theta \tag{4.12}$$
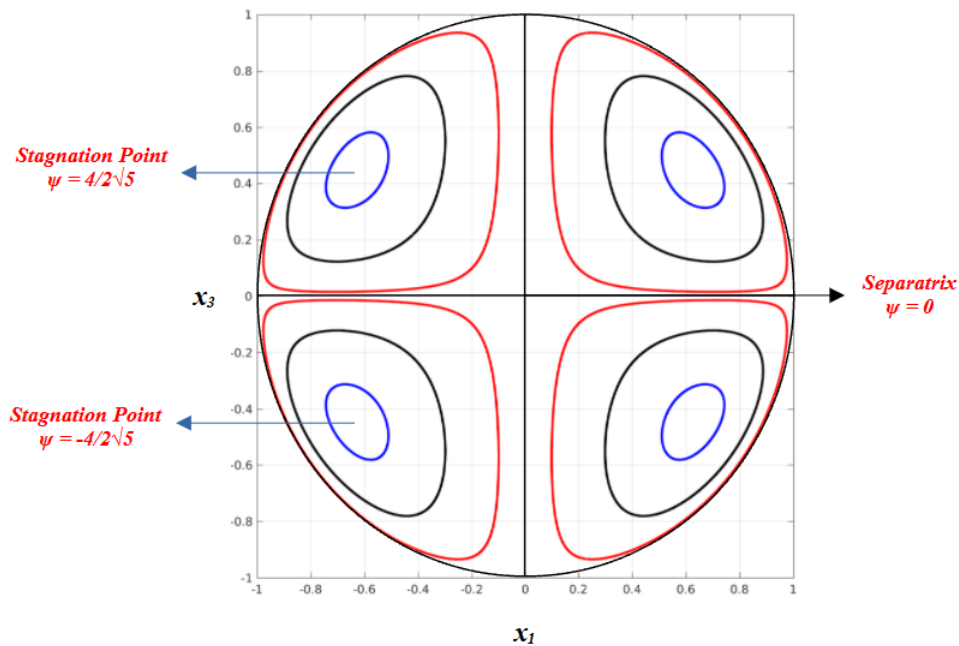
Figure 4.2: Poincaré section for a drop in an axisymmetric extensional flow ($x_1 - x_3$ plane). The topology consists of four cells of nested closed curves as streamlines, in any plane passing through the axis of symmetry.

Being an axisymmetric field, this case is analogous to the case of a translating drop, where the stream-surfaces $\psi_s(r, \theta) = constant$, correspond to a family of nested tori, symmetric about the equatorial plane plane ($x_3 = 0$). The streamlines correspond to the closed paths in the cross-sectional planes of constant-ϕ, just like the previous case. Here, $\psi_s = 0$ denotes the separatrix, which forms the limiting curve, part of which lies on the drop surface and the equatorial plane. The streamlines in the interior correspond to $\psi_s > 0$ for $x_3 > 0$, and to $\psi_s < 0$ when $x_3 < 0$ and have four cells. There is a ring of stagnation points associated with this flow, which are centers, and their position is given by $\psi_s = \pm 4/(2\sqrt{5})$. The Poincaré sections for this case is shown in Fig.4.2, where the streamlines were obtained by integrating the velocity field in Eq.4.6 - 4.8, again, using a RK(4) scheme with same parameters as before. Just like the case of a translating drop, the streamlines corresponding to this case do not jump from one constant-ϕ plane to another and owing to this constraint, the Poincaré sections were generated by choosing initial points that lie on the $x_1 - x_3$ plane. Therefore, the closed curves in the Poincaré section are the cut-sections of the nested tori and so, correspond to the actual streamlines, rather the points of intersection of a streamline with the plane.

Just like the case of translation, the velocity field for this case does not lead to chaos, as fluid particles are confined to the surface of a tori. In this case too, the addition of a perturbation can destroy the stability of this base state. The perturbation for this case can be in the form of vorticity, that is inclined to the axis of symmetry of the base state. However, when vorticity is aligned along the axis of symmetry, we again observe the same Poincaré section as in Fig.4.2, because the underlying velocity field gives rise to the same streamfunction with the exception that the particle paths now evolve according to $\phi(t) = \omega t + \phi_0$, implying that the streamlines now densely wind around the nested tori, which gives rise to the same Poincaré section as in Fig.4.2. As was already mentioned, this also constitutes a regular streamline topology. But, when vorticity is inclined to the axis of symmetry, some of the tori are destroyed and the interior becomes chaotic, as first reported by Stone et al. (1991).

Apart from the aforementioned flows, the one-parameter family of canonical planar linear flows also exhibit closed streamlines in the interior (Powell (1983), Krishnamurthy and Subramanian (2018a)), where the closed streamlines are now characterised by a pair of invariants, unlike the previous cases (where ψ_s was the only invariant), owing to the non-axisymmetry of the velocity field. In all these cases, we have only considered a spherical drop. However, drop deformation may play a non-trivial role in destabilising this regular topology into a chaotic one, the consideration of which is out of the scope of this study.

4.2.2 Flows with Chaotic Streamlines in the Interior

In this section, we shall look at the linear flows which lead to chaotic streamlines in the interior of the drop. These linear flows include both the two-parameter families of flows analysed in Chapter 2 and this remains true for the general four-parameter family of arbitrary linear flows, all of which have non-zero vorticity. For the case of drop in an arbitrary linear flow, chaos is the rule rather than the exception, as almost all these flows are devoid of any underlying symmetry and hence would result in chaos.

4.2.2.1 Drop in $3D$ Extensional flow with Aligned Vorticity

This was the first two-parameter family that was considered in our exterior heat transfer analysis. To our knowledge, there have been no studies in literature analysing the nature of interior streamlines for this case. We observe that members of this family exhibit chaotic streamlines in the interior. In Fig.4.3, we have shown the Poincaré sections for $\epsilon = -0.25$, at different α', where we see that the Poincaré sections exhibit both chaotic and non-chaotic regions. This section was obtained by numerically integrating the velocity field using a RK(4) scheme with $dt = 10^{-4}$, for different initial conditions and for a total time of 10^9. This guarantees that the both chaotic and regular trajectories have more than 10^5 points of intersection in the section. The plots of different color in the sections correspond to different initial conditions. For

instance, the blue points in the section are generated by a single wandering streamline associated with a particular initial condition. From the plots, we see that, the extent of chaotic region increases with α' and the section becomes more complicated with multiple islands of regular flow springing up inside the chaotic region. The islands on the same hemisphere, for instance, the red curve on all the sections in the upper hemisphere, belong to the same torus located in the upper hemisphere. With further increase in α', the extent of chaotic region shrinks, ultimately becoming regular for $\alpha' \to \infty$. This is consistent with the fact that $\alpha' \to \infty$, corresponds to the case of solid-body rotation for which there is no chaos. Although not shown here, $\alpha' = 0$ for all ϵ exhibits regular streamline topology in the interior as it corresponds to $3D$ extensional flow without vorticity. One crucial point to note here is that, the equatorial plane $(x_3 = 0)$ remains an invariant surface for all values of α', owing to the underlying symmetry of this case, that arises from the alignment of vorticity vector along one of the principal components of extension. Thus, any fluid particle in the upper hemisphere $(x_3 > 0)$, never crosses into the lower one, even if it is on a chaotic trajectory. Although the plot corresponds to a particular value of ϵ, we have verified the presence of chaotic streamlines inside the drop for other values ϵ, except $\epsilon = -2$, that corresponds to axisymmetric extension with vorticity aligned along the axis of symmetry, for which the streamlines are regular as already mentioned.

$\alpha' = 0.5$ $\alpha' = 1.0$ $\alpha' = 1.5$ $\alpha' = 2$ $\alpha' = 10$
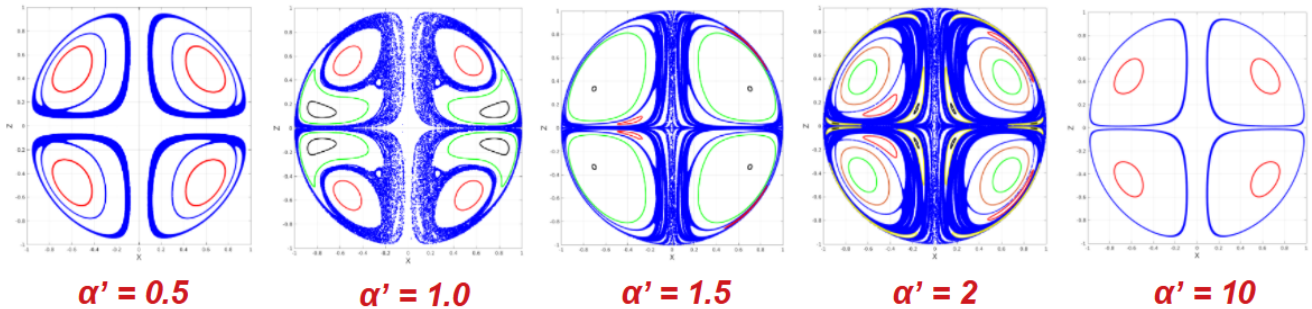
Figure 4.3: Poincaré section for drop in $3D$ extensional flow with aligned vorticity for $\epsilon = -0.25$. The spatial extent of chaotic streamlines exhibit a non-monotonic dependence on α'.

The chaos in the interior can be understood as follows: The three-dimensional extension with aligned vorticity can be considered a flow with canonical planar hyperbolic flow as a base state and, the third component of extension along the vorticity axis, added as a perturbation. The interior streamlines corresponding to this base state is known to contain heteroclinic orbits connecting the saddle points in the interior field (Powell (1983)). Taken together, these orbits form a cycle, called the *heteroclinic cycle*. Perturbations of such cycles offer a classical mechanism for generation of global chaos (Wiggins (1988)), which is what results when the third component of extension is added to this base state leading to a three-dimensional chaotic flow-field. For small magnitudes of this perturbation, one can analytically characterise this chaos using the method of averaging, following along the lines of Stone et al. (1991), but such a characterisation is not undertaken in this study, so as to keep our focus on the objective of this study; the calculation of the enhancement of transport rate. The existence of regular islands can also be explained in a similar fashion. Note from Fig.4.3 that, these islands are localised in the vicinity of the stagnation points (centers) and the invariant plane in the interior and thus they are significantly more stable than other regions and preserve their stability despite the breakdown of heteroclinic cycle, which leads to chaos in other parts of the interior. However, an exact analytic description on the location of these islands and their stability is beyond the scope of this study.

4.2.2.2   Drop in axisymmetric Extension with Inclined Vorticity

This was the case originally considered by Stone et al. (1991), who first showed that the interior streamlines are chaotic, when vorticity is added to axisymmetric extension (for which we saw in Fig.4.2 that, the streamlines were regular), where the vorticity is inclined to the axis of symmetry at an angle θ_ω and has a magnitude α'. The authors noted that chaotic streamlines exist for any $\theta_\omega \neq 0$ and $\alpha' \neq 0$. In this case too, the chaotic region is interspersed with non-chaotic islands, except at certain critical values of the parameters. The Poincaré sections corresponding to $\theta_\omega = 36°$ at different α' is shown in Fig.4.4. These sections were again generated by numerically integrating the velocity field using the same method and parameters mentioned for the previous case. These simulations, however, required smaller total times ($5 * 10^8$) for generating similar number of points of intersection (10^5 points) of a given streamline with the $x_1 - x_3$ plane, as the previous case. All the sections in Fig.4.4 are generated by a single wandering streamline starting at the same initial condition, except for the last section, where the red set of points correspond to a different streamline. From the plot, we see that the section contains regular and chaotic regions, where the regular islands belong to the same torus (Stone et al. (1991)). At a given inclination, the extent of chaotic region increases with increasing α', spans the entire drop at a critical value of $\alpha' \sim 1.75$. where the dominant island of regular streamlines (in the neighbourhood of the stagnation point, which is an elliptic fixed point seen in Fig.4.2) is broken and then starts decreasing again. Importantly, unlike the previous case, there are no invariant planes and the chaotic trajectory wanders over the entire drop, which is evident from Fig.4.4. For $\alpha' \to \infty$, the streamlines again become regular.
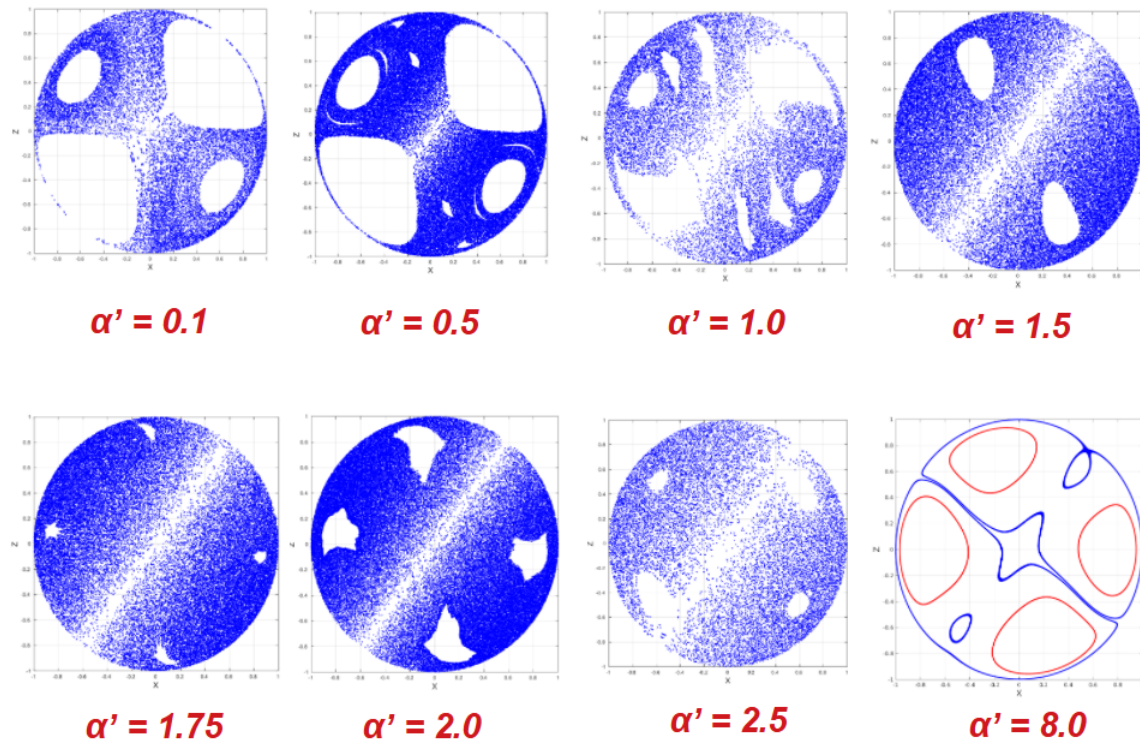
Figure 4.4: Poincaré section for drop in an axisymmetric extensional flow with inclined vorticity. The plot corresponds to $\theta_\omega = 36°$. The extent of chaotic streamlines exhibit a non-monotonic behavior with α', just like in Fig.4.3.

Similarly, one can fix a value of α' and change θ_ω, for which one again observes a similar trend as shown in Fig.4.5, where the Poincaré sections are plotted for $\alpha' = 0.1$ at different inclinations of vorticity (θ_ω). The streamlines are regular for $\theta_\omega = 0$ (which as we saw in Section 4.2.1, is axisymmetric extension with vorticity along the axis of symmetry, that results in a regular flow in the interior) and the region

of chaotic streamlines increases with increasing orientation and practically occupies the entire drop at a critical $\theta_\omega \sim 55°$. Beyond this, the structure becomes qualitatively complicated, with multiple islands of regular streamlines co-existing with chaotic regions. This shows an interesting result that, chaos in the interior can be space-filling even for small magnitudes of vorticity $\alpha' = 0.1 \ll 1$. Stone et al. (1991) had used the method of averaging in the asymptotic limit of $\alpha' \ll 1$, to analytically estimate the value of this critical θ_ω, and find that their numerical results match with the analysis. The rationale behind this analysis is that, for small values of vorticity magnitude, the system exhibits two widely separated time scales, the time scale of circulation associated with the base flow ($t_b \sim O(1)$) and the time scale of vorticity induced drift ($t_d \sim O(1/\alpha')$), with $t_d \gg t_b$ and so the system can be analysed in an averaged sense by integrating out the effect of the fast time scale.
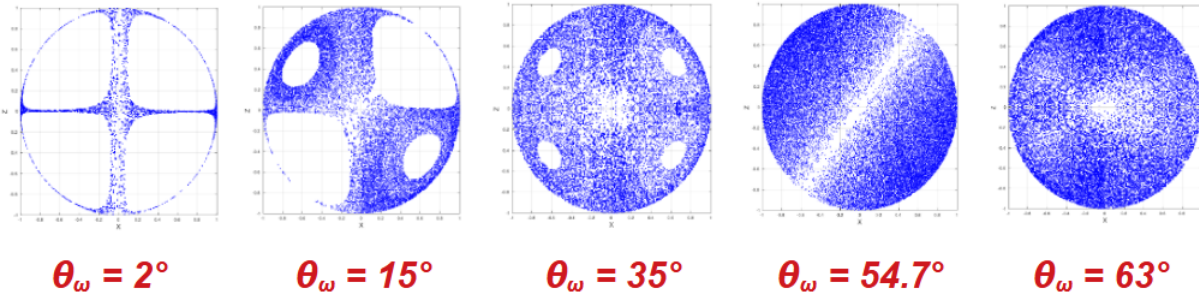
Figure 4.5: Poincaré section for drop in an axisymmetric extensional flow with inclined vorticity. The plot corresponds to $\alpha' = 0.1$. The extent of chaotic streamlines initially increases with θ_ω, reaches a maximum about $\theta_\omega \sim 55°5$.

The chaos can again be attributed to the perturbation of heteroclinic cycles, where for this case, as seen in Fig.4.2, the cycle comprises of heteroclinic orbits that connect the poles (a saddle), to the equator (which is actually a ring of saddles) via the origin (also a saddle point). The perturbation is bought about by vorticity, which is added at an arbitrary inclination to the axis of symmetry. The regular islands are again localised in the vicinity of the elliptic stagnation points as can be seen in Fig.4.4.

4.2.2.3 Drop in General $3D$ Linear Flow

Finally, we move on to the case of a spherical drop in an arbitrary $3D$ linear flow. From the results for the two-parameter families presented before, it is appropriate to expect the streamlines to be chaotic in the interior when the drop is suspended in a general linear flow. In Fig.4.6, we show one such instance. The plot shows Poincaré sections corresponding to $\epsilon = -0.25, \phi_\omega = 10°$ and $\theta_\omega = 36°$ for different α'. These sections were again obtained using the same numerical procedure and each section is generated by a single wandering streamline starting with the same initial condition, except for the last section, where the red set of points correspond to a different streamline. All the sections contain more than 10^5 points of intersection. The important thing to note here is that, the Poincaré sections qualitatively resemble the ones obtained by Stone et al. (1991) for axisymmetric flow with inclined vorticity. Here too, there are no invariant surfaces and the fluid particle that is part of a chaotic trajectory wanders both the hemispheres of the drop. This is crucial because an $\epsilon = -0.25$ is significantly far from the axisymmetric case ($\epsilon = -0.5$). But despite that, the Poincaré sections look similar to the case with an axisymmetric base state. Importantly, comparing Fig.4.3 and Fig.4.6, we see that chaos is more space-filling for corresponding values of α' for the arbitrary flow case than for the axisymmetric case. This implies that, the non-axisymmetry of extension leads to greater chaos and possibly a greater enhancement of transport at large Pe. This dependence of Nu on ϵ at large Pe requires a more detailed investigation that is beyond the scope of this study. But, as far as the transport problem is concerned, the preliminary results presented here give strong evidence

for a potential enhancement in the transport rate, which we seek to calculate numerically.
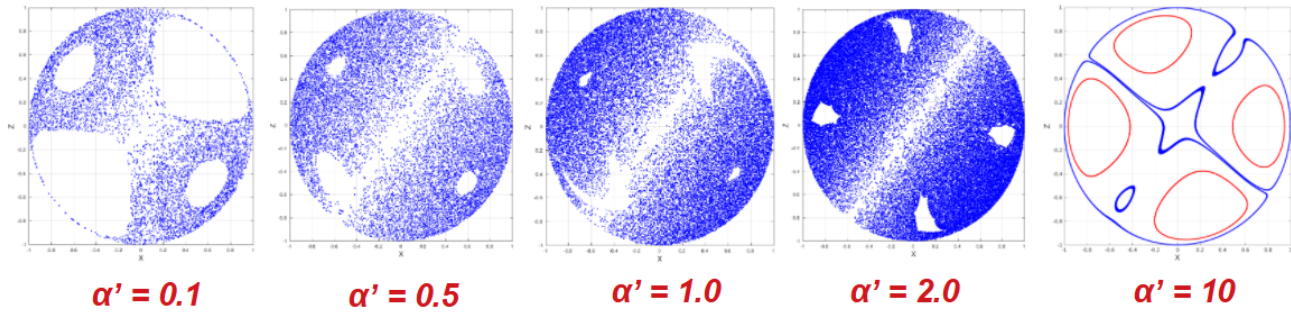
Figure 4.6: Poincaré section for drop in a general linear flow. The plot corresponds to $\epsilon = -0.25, \theta_\omega = 36°, \phi_\omega = 10°$. The Poincaré sections are qualitatively similar to those obtained by Stone et al. (1991) for drop in axisymmetric extension with inclined vorticity, but stronger chaos results at corresponding values of α', owing to the non-axisymmetry of extension.

4.3   Calculation of Transport Rate

This section focuses on the calculation of the non-dimensional transport rate Nu, of heat or mass from the drop, when the dominant resistance to transport is in the interior phase. We assume that the exterior phase resistance is negligible and this corresponds to an isothermal surface. This is the analog of the exterior transport problem addressed in Chapter 2. The difference in this case is, of course, that this calculation will be a numerical one on account of the chaotic streamlines. In the last section, we saw that when vorticity is present in the ambient linear flow in addition to extensional flow, it breaks the symmetry of the underlying extensional flow and leads to chaotic streamlines in the interior of the drop. This is true for almost all cases, except for some special cases, when the vorticity is aligned along the axis of symmetry or its magnitude is very large. As already mentioned in the introduction, such a chaotic, well-mixed state in the interior leads to enhancement of transport rate (Ottino (1990), Bryden and Brenner (1999)). But these efforts do not address the scaling of such a convectively enhanced transport in the asymptotic limit ($Pe \to \infty$) and restrict their calculations to moderate Pe ($1 < Pe < 2000$). To our knowledge, the one effort that addresses the scaling behavior is by *Chaotic Mixer for Microchannels* (2002), whose work deals with the effect of chaos in mixing a micro-channel flow, and they show that the length of the channel scales logarithmically with Pe in the asymptotic limit. But we are not aware of any efforts along those lines to find the scaling behavior of Nu in the interior problem with chaotic flows. Here, we attempt this for the first time, by calculating the transport rate Nu, for the cases which exhibit chaotic streamlines in the interior.

Recall that when the streamlines are closed (either in the interior or exterior), transport will be diffusion limited. This implies that a plot of Nu versus Pe will plateau to a finite value as $Pe \to \infty$. This has been shown to be true by Poe and Acrivos (1976), who considered the problem of (exterior) transport from a sphere in a planar linear flow (with vorticity), where the sphere rotation leads to closed streamlines in the immediate neighborhood, which leads to a plateau in the Nusselt number (with $Nu \approx 4.5$ for $Pe \gg 1$ for simple shear flow). An analogous scenario prevails for the interior case, when there are closed streamlines present. For instance, Kronig and Brink (1950), were the first to calculate the rate of extraction of mass from a translating droplet (that exhibits closed streamlines in the interior as seen in Fig.4.13), and they found that $Nu \approx 2.7$ for $Pe \gg 1$. The same is true for axisymmetric extension (which also has closed streamlines; see Fig.4.4), where $Nu \approx 4.5$ as $Pe \gg 1$, as verified numerically by Christov and Homsy (2009). At large Pe, shear enhanced diffusion causes the closed streamlines to isothermalise

at a time scale of $O((a^2/D)Pe^{-1/3})$ and thus, at longer times the transport rate is determined by diffusion across these isothermal streamlines. It is this transport rate associated with diffusion problem[1], that determines the infinite-Pe plateau of Nu (Krishnamurthy and Subramanian (2018a)). But for cases with chaotic streamlines, the Nusselt number will not reach a plateau as $Pe \to \infty$. This is somewhat analogous to what happens in the exterior case, when there are open streamlines present. However, in the interior, we also have islands of regular flow inside the chaotic regions (Fig.4.4-4.6), across which heat or mass has to diffuse. This distribution of resistance within the chaotic islands and a boundary layer near the interface, where diffusion effects are not negligible, complicates the situation and one cannot apriori expect a $Pe^{1/2}$ scaling of Nu for $Pe \gg 1$, unlike the exterior case, where the diffusion effects are localised to a BL of thickness $O(Pe^{-1/2})$. Thus, the presence of islands of closed-streamlines add to the complexity and in general leads to a boundary layer of thickness $Pe^{-\beta}$, where the exponent β has to obtained on a case-to-case basis numerically. These ideas are summarised in Fig.4.7, where typical plots of Nu versus Pe are shown for both non-chaotic and chaotic cases.
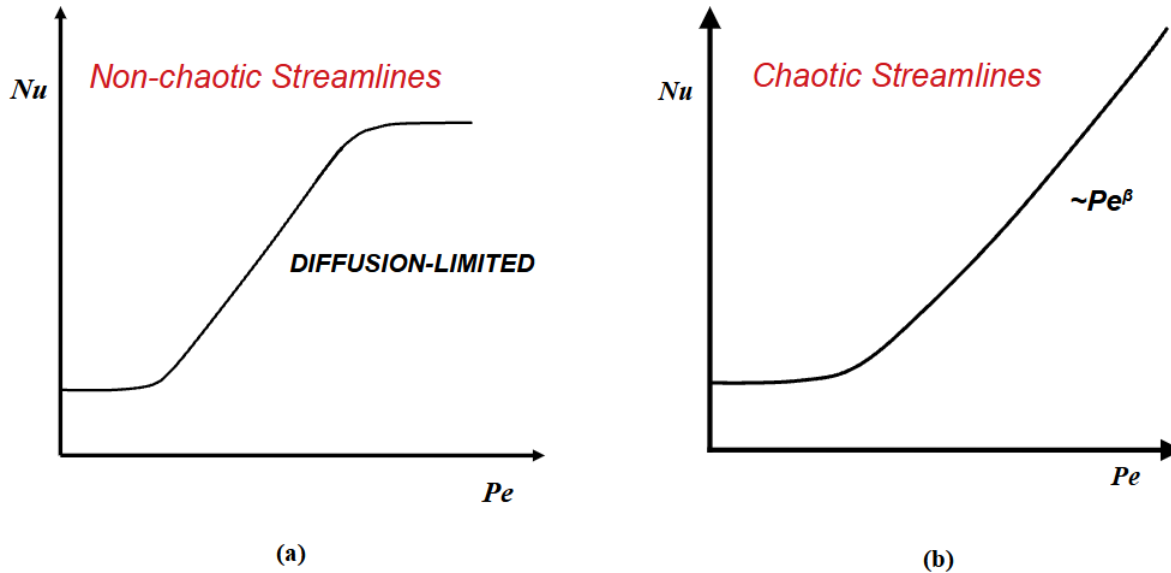
Figure 4.7: Representative plots (on log scale) of Nu versus Pe for cases with (a) regular and (b) chaotic streamlines in the interior of the drop. Regular streamlines lead to diffusion-limited transport, while chaotic streamlines lead to a diverging Nu with Pe, where the scale β is specific to the flow parameters. One expects $\beta = 1/2$ when the chaos is space-filling as far as the interior of the drop is concerned.

In this section, we will calculate the Nusselt number for the different flows that we encountered in the streamline analysis, to illustrate the convective enhancement due to chaotic streamlines, and thereby, calculate the exponent β that defines the scaling relation between Nu and Pe at $Pe \gg 1$. To that end, Langevin Dynamics simulations are performed using a parallel in-house code, written in the $C^{®}$ programming language, to calculate the Nusselt number for a drop in a linear flow. Such calculations for the chaotic flows encountered earlier do not appear in earlier studies and are reported here for the first time. However, we should also mention that these calculations are of a preliminary nature and the entirety of parameter space (of linear flows) have not been explored. Nevertheless, these calculations serve to show strong evidence for the existence of an internal boundary layer when chaotic streamlines are present in the interior.

---

[1]This diffusion problem will be 1D for translation (Kronig and Brink (1950)), and 2D for planar linear flows.

4.3.1 Deterministic Description of Transport

The fundamental equation governing transport is the convection-diffusion equation, given by:

$$\frac{\partial c}{\partial t} + \boldsymbol{u}.\boldsymbol{\nabla} c = \frac{1}{Pe}\nabla^2 c, \tag{4.13}$$

with $c(\boldsymbol{x}, t)$ being the concentration of passive tracers, which are the fundamental units of heat or mass: for the mass transfer case, the passive tracers resemble solute particles. This equation is in the dimensionless form, with a the drop radius and $|\boldsymbol{\Gamma}|a$ the characteristic magnitude of ambient velocity, being used as the length and velocity scales. The equation is subject to the following conditions:

$$c = 1 \text{ at } t = 0 \text{ (Initial condition)} \tag{4.14}$$

$$c \begin{cases} = 0 \text{ at } r = 1 \; \forall \; t \\ \neq 0 \text{ at } r = 0 \; \forall \; t \end{cases} \quad \text{(Boundary conditions)} \tag{4.15}$$

The first of these is the initial condition, corresponding to a uniform distribution of solute. The second one corresponds to an absorption boundary condition at the interface. This is the limiting form the flux continuity condition used by Bryden and Brenner (1999), where the limit corresponds to the exterior conductivity $k_e \to \infty$ and therefore represents negligible transport resistance in the exterior phase. The third boundary condition avoids a singularity at the centre of the drop. For the calculation of Nu, it is sufficient to consider the total concentration inside the drop ($C(t)$), because, the Nusselt number by definition is the rate of change of bulk concentration in the interior. The total (bulk) concentration can be obtained from $c(\boldsymbol{x}, t)$ as:

$$C(t) = \oint_V c(\boldsymbol{x}, t)d\boldsymbol{x} \tag{4.16}$$

The solution of the convection-diffusion equation (Eq.4.13), can be written as a series in terms of it's eigenvalues and eigenmodes, provided the convection-diffusion operator is separable in a suitable coordinate system. For a drop in an arbitrary $3D$ linear flow, the separability is not immediately obvious, but one can comment on the separability of the operator for flows with regular streamlines and for the case of pure diffusion. For diffusion ($Pe = 0$), the operator reduces to a diffusion operator, which is separable and self-adjoint and therefore leads to eigenvalues which are real. Since the concentration in the drop depletes with time in the absence of an source, we can conclude that the eigenvalues of the diffusion operator must be real and negative. Thus, one can write the resulting (bulk) concentration profile as a series of exponentials of these eigenvalues and the exact relation is given by (Kronig and Brink (1950)):

$$C(t) = \frac{1}{4\pi}\int c(\boldsymbol{x}, t)\sin\theta d\theta d\phi = 6\sum_{n=1}^{n=\infty}\frac{e^{\frac{-n^2\pi^2 t}{2}}}{n^2\pi^2} \tag{4.17}$$

where the time t is in units of a^2/D, the diffusion time scale, the only time-scale available for $Pe = 0$. This expression suggests that the concentration in the interior decreases monotonically with time. However, when $Pe \neq 0$, the convection-diffusion operator is not self-adjoint, but still separable for flows with regular streamlines. In this case, one can expect the eigenvalues to be imaginary, which would suggest a non-monotonic (oscillatory) behavior of concentration with time for finite Pe (as we shall see later, for the case of translating drop and drop in an axisymmetric extensional flow). Therefore, for this case, the concentration profile in general can be written as:

$$C(t) \sim \sum_{n=0}^{n=\infty} e^{\frac{-\lambda_n t}{Pe}} \tag{4.18}$$

with the time now given in units of $|\mathbf{\Gamma}|a$, the convection time scale. Nevertheless, the concentration in the interior depletes with time and, at long times, the profile eventually reaches a quasi-steady state with a constant exponential decay in the bulk concentration. This is because, for these regular streamline flows, there is a separation in the magnitudes of these eigenvalues, especially at large Pe, in that the imaginary eigenvalues responsible for oscillatory behavior have a larger magnitude of $O(Pe^{1/3})$, while the smallest (real) eigenvalue, responsible for the exponential decay at large times is $O(1)$ in inverse diffusion time scale. Thus, at long times, it is only the smallest eigenvalue (λ_0) that dominates the summation and in the asymptotic limit $t \to \infty$, corresponding to the quasi-steady state, we have:

$$C(t) \sim e^{\frac{-\lambda_0 t}{Pe}} \tag{4.19}$$

Thus, after an initial transient, the concentration inside the drop decays as a simple exponential, with a decay rate proportional to the smallest eigenvalue λ_0 of the convection-diffusion operator. This decay rate can be used as a measure of the transport rate at steady state (Kronig and Brink (1950)), which leads to a Nusselt number definition of the form:

$$Nu = \frac{4}{3}\lambda_0 = \frac{4}{3}\frac{1}{C(t)}\frac{dC}{dt} \tag{4.20}$$

where the factor $4/3$ is chosen, so as to reproduce the exact solution for the case of pure diffusion ($Pe = 0$) (Kronig and Brink (1950)). We shall calculate this decay rate (λ_0) from our numerical simulations, which will give us the Nusselt number. The aforementioned discussion only holds for flows with regular streamlines and, for cases with chaotic streamlines in the interior, the nature and distribution of the eigenvalues and, even the separability of the convection-diffusion operator, is not known. Nevertheless, the results of our simulations suggest that the concentration profiles for these cases, also exhibit a quasi-steady state at long times (a simple exponential decay) and therefore, we can use the same definition given in Eq.4.20 to calculate the Nusselt number for these flows.

4.3.2 Langevin Dynamics Simulation

In order to calculate the decay rate λ_0, we perform Langevin dynamics simulations, which numerically solves a Stochastic differential equation. There have been numerical studies carried out in the past, to calculate the Nusselt number in the interior of a drop subject to a Stokesian velocity field, using techniques like finite difference and finite element methods (Christov and Homsy (2009), Jhuncu (2010)). However, these methods are only suitable for the cases with an underlying symmetry, where, the concentration profile does not depend on all three spatial coordinates. For chaotic flows however, these techniques are not well-suited and therefore one must rely on Stochastic simulations, which are well suited for systems that exhibit random, chaotic dynamics. These techniques typically provide solutions for Stochastic differential equations, which model the chaotic behavior of the system. In Langevin Dynamics simulations, we initialise the interior of a spherical drop with multiple number (N) of passive tracers, which are uniformly distributed at $t = 0$. These tracers are governed by the Langevin equation,

$$d\boldsymbol{x} = \boldsymbol{u}(\boldsymbol{x})dt + \frac{1}{\sqrt{Pe\Delta t}}W(t)dt \tag{4.21}$$

where, $\boldsymbol{u}(\boldsymbol{x})$ is the Stokesian velocity field inside the drop and $W(t)$ is the Wiener process. The Wiener process represents the random velocity of the tracer particle. As such, the process satisfies the following properties: (i) It is a random variable with a normally distributed probability density function, whose mean $< W(t) >= 0$ and, (ii) it has independent increments i.e. for $t > 0$, the future increments $W(t + u) - W(t)$, $u > 0$ are independent of the past increments $W(s)$, $s < t$. Such a process leads to Brownian motion of the tracers. It can be easily shown that the system represented by the Langevin equation (Eq.4.21) corresponds to the Fokker-Planck equation, in that each trajectory obtained from an

integration of Eq.4.21 represents a specific realization of the stochastic process whose probability density is governed by the Fokker-Planck equation. Thus, the local average of the tracer number density can be shown to be governed by the Fokker-Planck (F-P) equation. The solution of the Langevin equation, unlike F-P, is a random function and has a probability distribution with a well-defined mean (that is, it is a stochastic differential equation or an SDE). Thus, sufficiently large number of initial tracers or taking an ensemble average ensures that the mean of the SDE solution converges to the concentration given by the Fokker-Planck equation. The convection term in F-P relates to advection term in the Langevin equation and the diffusion term relates to the Wiener process, where the diffusivity (D) that appears in F-P is related to the mean squared displacement of a tracer particle undergoing a Wiener process as $MSD = 2nDt$, n being the dimension of the system.

We use a fourth-order Runge-Kutta scheme to integrate the equations for every tracer. Since each tracer is passive and follows a unique trajectory, we can parallelize the code by splitting the total number of tracers across multiple processors, without having to communicate the positions of tracers between the processors. The tracers are uniformly distributed in the droplet to begin with. The absorption boundary condition is imposed by removing the tracer which leaves the physical domain ($r \leq 1$). At each instant, we count the number of tracers inside the drop and also find the radial distribution of tracers by radially binning the drop. This gives the bulk concentration of the tracers inside the drop at each instant as well as the angularly averaged concentration as a function of the radial coordinate. The normalized concentration is the ratio of number of tracers in the drop at an instant and the initial number of tracers. We perform these simulations for multiple ambient flows at different Pe for each of these flows. Our simulations pertain to a transient scenario, where we get the bulk concentration (C) as a function of time and from it, extract the Nusselt number, by calculating the slope $dC(t)/dt$. At long times, we reach a quasi-steady state scenario, where $C(t)$ is a simple exponential with a constant decay rate λ_0. This quasi-steady value represents the steady state transport rate (Nu). We also find the steady state radial concentration profile inside the drop, by integrating the radial profiles obtained from the transient simulations over time, which can be used to ascertain the existence of an internal boundary layer. Before we present the results for the linear flows that result in chaotic interior streamlines, we provide the results for validation cases, where we have compared our numerical simulations with results from previous works.

4.3.3 Validation

For validating our simulations, we consider the simple flows, that result in regular interior streamlines, for which the results are known, either from analysis (pure diffusion, translating drop (Kronig and Brink (1950))) or from numerical simulations (drop in axisymmetric extension (Christov and Homsy (2009))) The first case we consider is that of pure diffusion.

4.3.3.1 Pure Diffusion

In this case corresponding to $Pe = 0$, the closed-form solution for the concentration field can be easily derived by solving the diffusion equation using separation of variables and the resulting time-dependent spatially averaged concentration is given by Eq.4.17. In Fig.4.8, we have plotted the bulk concentration profiles obtained from the simulation at different values of time-step (dt) along with the profile represented by the analytical solution given in Eq.4.17. This is plotted on a semi-log scale, where for long times, corresponding to an exponential decay regime, we observe a line of constant slope for the concentration field. From the plot, we see that for a time step of size $dt = 10^{-6}$, the results are within 0.1% of the theoretical curve.
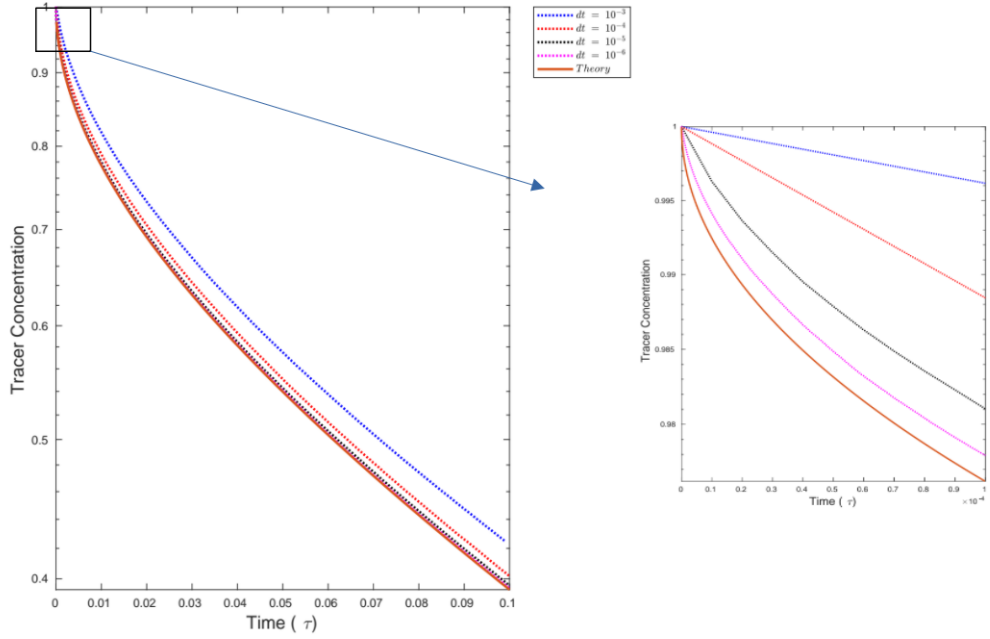
Figure 4.8: Plot of concentration profiles for the case of pure diffusion ($Pe = 0$) corresponding to different dt. The time is made non-dimensional by diffusion scale a^2/D. The initial number of tracers used is $N = 4 * 10^6$. The inset shows the magnified view at small time. The plot is in a semi-log scale and the exponential decay appears as a line of constant slope.

In Fig.4.9, we show the Nusselt number profiles, which are calculated from the corresponding concentration profiles using Eq.4.20, on a log scale. The data from the simulations show fluctuations for all dt especially at large times. This is due to the fact that our simulations are transient in nature and so, the number of tracers (N) in the drop deplete with time. The amplitude of these fluctuations are proportional to $N^{-1/2}$, and they inevitably grow as time increases. The fluctuations in the raw data also increase with decreasing dt and exhibit a pattern. The increase in amplitude is due to the fact that $Nu \sim 1/dt$ from Eq.4.20 and the patterns arise because, at small time steps, there are multiple intervals of time during which the the total concentration inside the drop remains constant and then it suddenly drop to a smaller value at an instant, resulting in such patterns. Better results can be achieved either by increasing the number of initial tracers or running multiple simulations with the same number of tracers and averaging over them. The results shown correspond to the initial number of tracers, $N = 4 * 10^6$, which gives us satisfactory results for $Pe = 0$. But for finite Pe, convection results in a faster depletion of tracers and thus increases the amplitude of fluctuations at a given t. Therefore, the amplitude of fluctuations increases with Pe. Therefore, one needs to increase N or perform multiple runs for these cases. Equivalently, one can assume that, the mean calculated from a single run is a random variable following a Students-T distribution (Arfken et al. (2012)), which enables us to quantify the error in the mean at a desired confidence level. In Fig.4.10, the smoothed Nusselt profiles are drawn on a log scale, where the exponential decay regime appears as a horizontal line (plateau). The data is smoothed by a Gaussian filter, which plots the weighted moving-time average of the raw data. The effect of the window size of this filter can be removed trial and error, wherein the window size is changed until the changes in the result are within a pre-set tolerance, which in our case was set at 0.1%. From Fig.4.10, we see that a smaller time step leads to a more accurate match with the small time asymptote, $\frac{3}{\sqrt{\pi}}t^{-1/2}$, while at longer times, it results in larger fluctuations. Nevertheless, the mean of these fluctuations match the analytical result accurately.
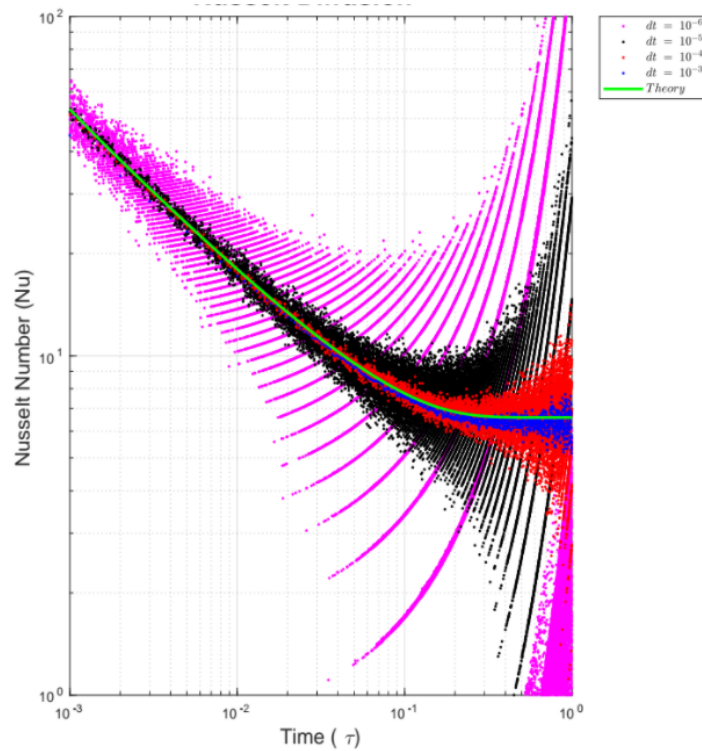
Figure 4.9: Plot of Nusselt number profiles for the case of pure diffusion. This plot shows the raw data that is not smoothed using a filter. Smaller time steps leads to a larger spread and the patterns in the spread are due to existence of multiple time intervals in which the total concentration in the drop remains unchanged.
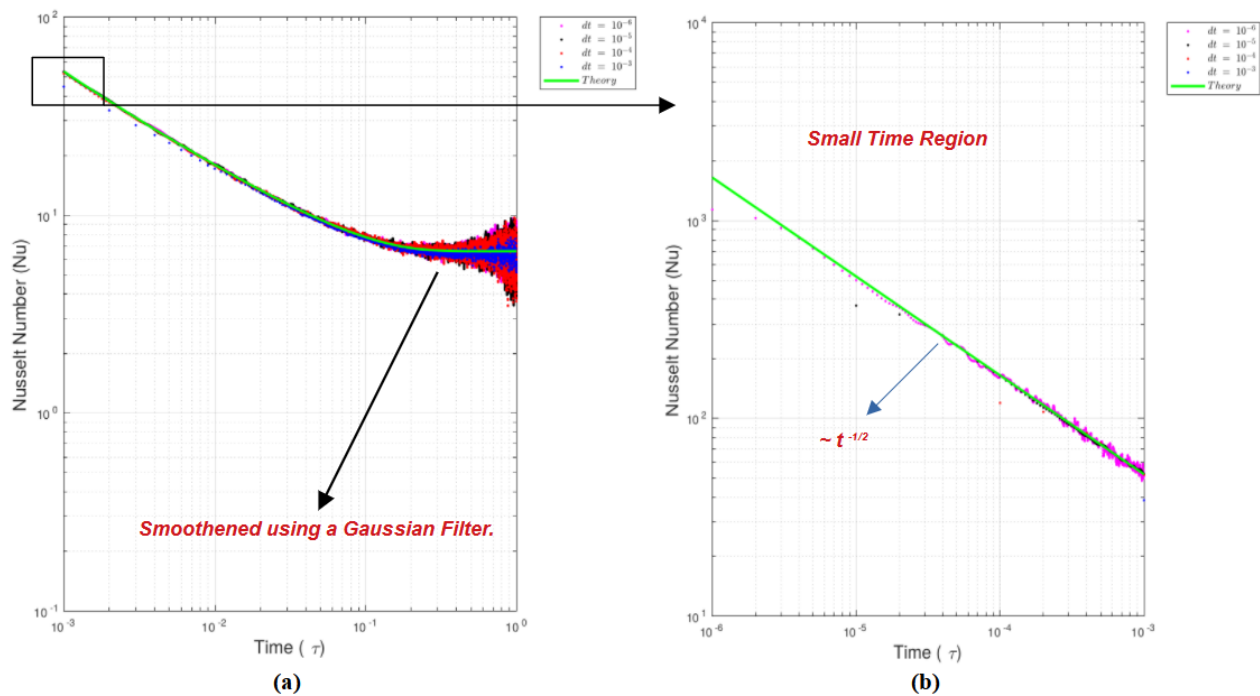
Figure 4.10: Plot of Nusselt number profiles smoothed using a Gaussian filter for the case of pure diffusion. The inset shows the profiles at small time which match with the small-time asymptote of diffusion.

The small time asymptote can be calculated exactly from Eq.4.17 and from Eq.4.20, by using the fact that for $t \ll 1$, the eigenvalues λ_n are closely spaced to each other, so the summation in Eq.4.17 can be replaced by an integral and then substituted into Eq.4.20 to get:

$$Nu = \frac{4}{3}\frac{1}{C}\frac{dC}{dt} = \frac{3\,\mathrm{erfc}(\frac{\pi\sqrt{t}}{\sqrt{2}})}{\sqrt{2\pi t}} \tag{4.22}$$

For $t \to 0$, this reduces to $Nu = \frac{3}{\sqrt{\pi t}}$ which is plotted in Fig.4.10(b).

4.3.3.2   Translating Drop

The next validation we do is for the case of translating drop, for which the large Pe plateau value of Nu was found analytically by Kronig and Brink (1950). The smoothed concentration profile for multiple Pe is shown in Fig.4.11, where we see that the plots corresponding to two time steps are converged for all Pe, suggesting that our results are independent of dt. From the plot, we see that the concentration profiles exhibit an exponential regime for long times and the concentration decreases faster as Pe increases. At larger Pe, we see that the concentration profiles collapse onto a single curve for long times, implying that the Nusselt number at steady state approaches a plateau. The plot on the right side shows that at large times, the concentration profile exhibits a step-like change, where the concentration remains unchanged for a finite time interval and abruptly drops at an instant (this is what leads to the patterns in the spread of raw data seen before in Fig.4.9).
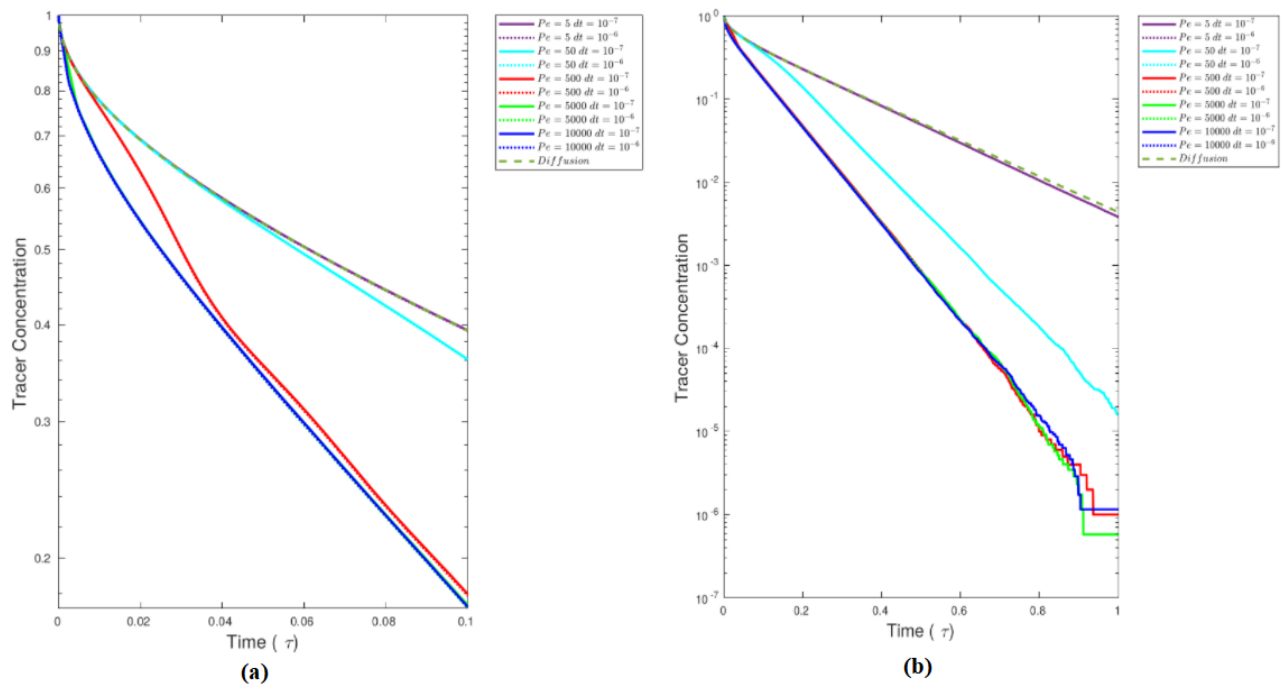
Figure 4.11: Plot of concentration profiles for the case of a translating drop. The plot on the right is for the entire range of simulated time, while the left one shows the concentration until the exponential decay regime. The plot is in a semi-log scale and the exponential decay appears as a line of constant slope and corresponds to $N = 4*10^6$ initial tracers.

Next, we plot the Nusselt number (on a log scale) for various Pe in Fig.4.12. For small Pe, the plot is very close to the diffusion curve for both small and long times. The Nu plot exhibits three regimes at large Pe. In this case, we see that the small time solution still closely follows the diffusion cure (Regime 1) and

thus initially, diffusion dominates transport. For moderate times (Regime 2), however, we see that the Nu curve oscillates. Recall that this oscillation is the physical process underlying the non-self-adjointness of the convection-diffusion operator, resulting in complex eigenvalues. These oscillations start earlier for larger Pe, where the time of onset of this regime for different Pe scales as Pe^{-1}, while the extent of this regime scales as $Pe^{1/3}$, implying that it lasts longer for higher Pe as seen in Fig.4.12. These oscillations correspond to the isopycnals (constant concentration curves) adjusting to the streamlines, before they eventually overlap (Region 3). Here, the Nu curve has reached the exponential decay regime, where the transport rate is governed by the smallest eigenvalue of the convection-diffusion operator. It is in this regime that the calculations of Kronig and Brink (1950) apply, where, they estimated the plateau value of Nu by solving the diffusion equation in streamline coordinates. As before, this decay regime appears as a plateau that corresponds to the steady state Nu. In this quasi-steady state, we can average the Nu over the plateau to find the true steady state value, which is then plotted against Pe in Fig.4.13. The plot shows that at large Pe, the Nusselt number asymptotes to a value ~ 2.7, that was calculated by Kronig and Brink (1950), which is also consistent with the previous figure, where the curves corresponding to large Pe overlapped at large t. Note that the calculated average is insensitive to the length of the plateau. This serves as a validation of our simulations. We also note that the Nusselt number rises from the diffusion value to the asymptote ~ 2.7, over a moderate range $10 < Pe < 100$. In the same plot, error bars corresponding to the Student's-T distribution of the plateau-averaged Nu are plotted at a confidence level of 99%. We see that their extent is $\approx O(10^{-2})$ at large Pe, implying that the mean calculated from a single run is within 1% of the true value. Moreover, our results for $Pe > 10$ also match well with those of Jhuncu (2010), who have used finite element method to calculate the Nusselt number in the interior. Finally in Fig.4.14, we have compared Nu versus Pe plot for multiple time steps and see that a plot of $Nu - Nu_{Diffusion}$ against Pe leads to a $O(Pe^2)$ scaling at small Pe. This is due to the fact that convection in the interior problem is a regular perturbation in the neighbourhood of diffusion limit, as opposed to the exterior problem, where convection effects are singular.
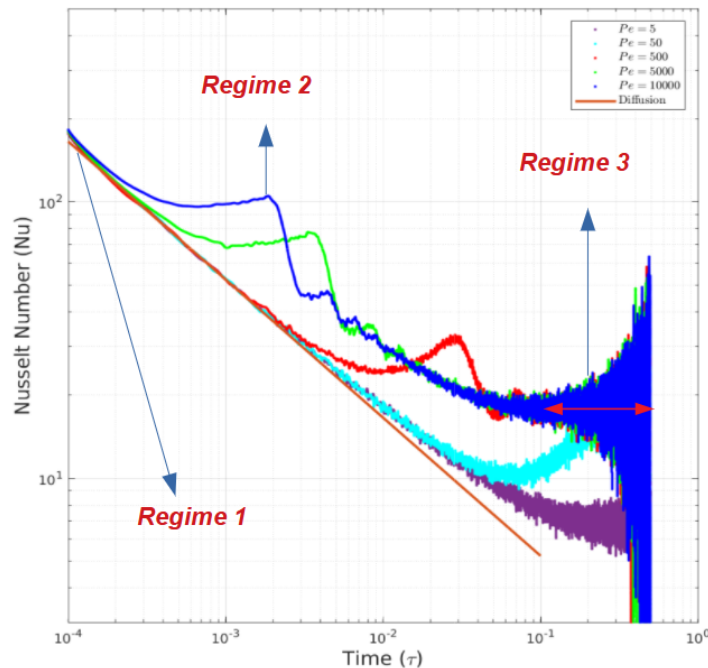
Figure 4.12: Plots of Nu for a translating drop on a log-log scale. The plot exhibits three regimes corresponding to small, moderate and long times. At small t the plots for all Pe follow the diffusion curve and at large t, the Nu curve plateaus to a finite value, corresponding to the exponential decay regime. These plots are smoothed using a Gaussian filter and correspond to $dt = 10^{-7}$.
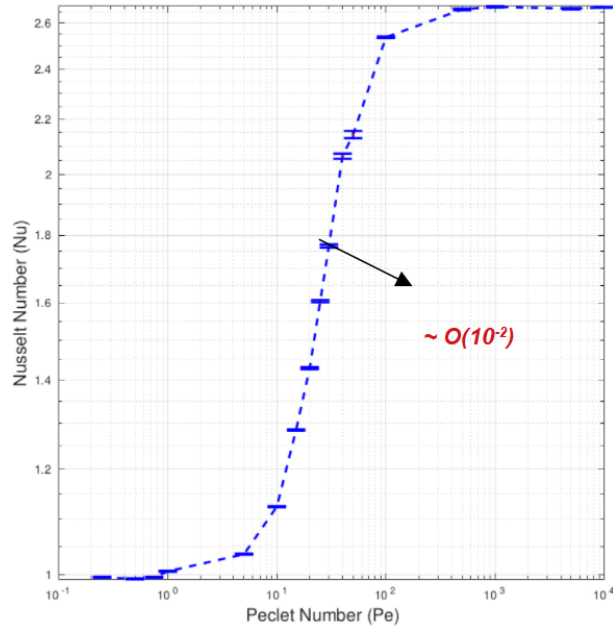
Figure 4.13: Plot of Nu at steady state against Pe for a translating drop. The error bars are drawn assuming that Nu at steady state (the mean over the plateau from Fig.4.12), is a random variable following a Student's - T distribution. The error corresponds to a confidence level of 99% and is $\approx O(10^{-2})$ for large Pe. At large Pe, $Nu \to 2.7$, implying diffusion-limited transport.
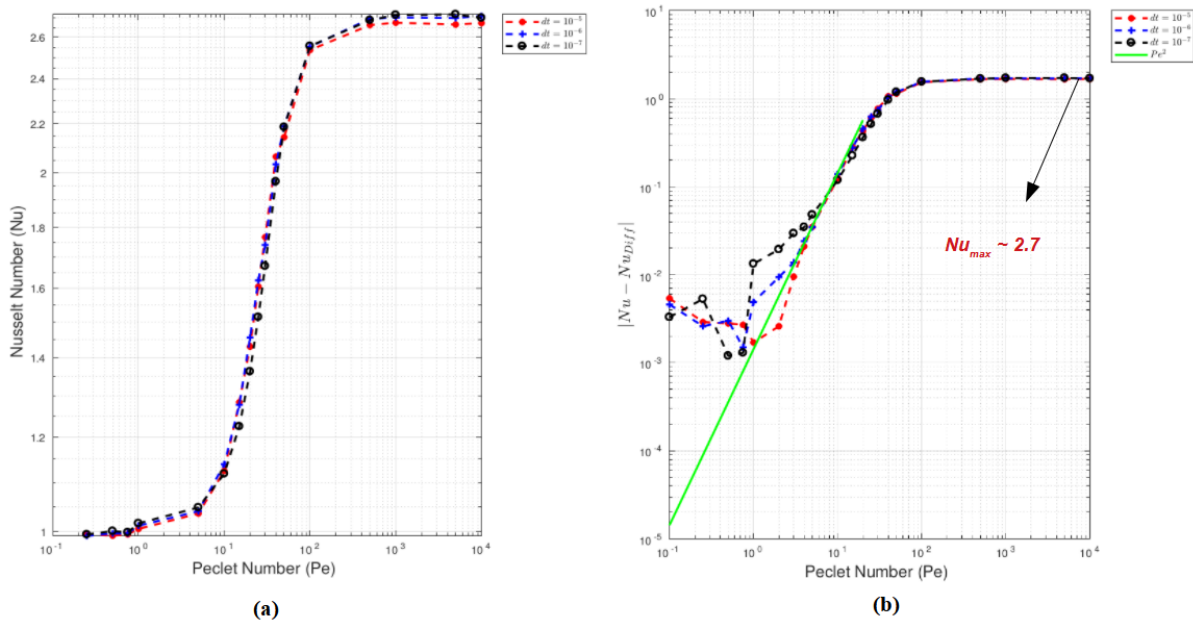
Figure 4.14: Plot of (a) Nu at steady state against Pe for multiple time steps and (b) $Nu - Nu_{Diffusion}$ against Pe. At small Pe, $Nu - Nu_{Diffusion}$ scales as Pe^2, which is computationally hard to capture owing to large signal-to-noise ratio at small Pe.

So, using arguments of flow-reversal symmetry and a smooth dependence of Nu on Pe, one can show that the Nusselt number scales as $O(Pe^2)$ in the interior.Even though our simulations confirm this scaling at small Pe, we see from the plot that Nu at $Pe < 1$ are more error-prone owing to large signal-to-noise

ratios at this limit.

4.3.3.3 Drop in Axisymmetric Extension

The final validation case we consider is that of a drop in an axisymmetric extensional flow for which the velocity field in the interior is given in Eq.4.9 - 4.11. Correspondingly, we again have closed streamlines in the interior, which are organised into four-cells as shown in Fig.4.2. Thus like the case of a translating drop, this case will also lead to a Pe independent plateau for Nu at large Pe. The smoothed concentration profiles plotted in Fig.4.15 suggests that this is the case, as the curves corresponding to $Pe \gg 1$, collapse onto a single curve.
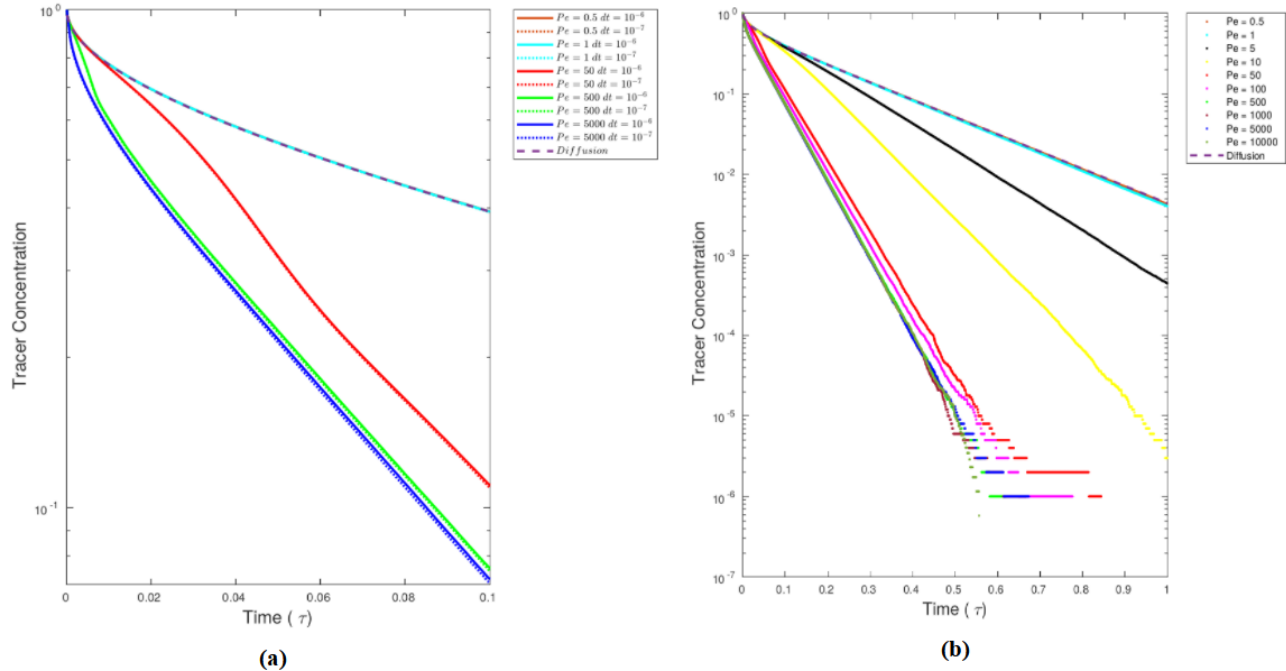
Figure 4.15: Plot of concentration profiles for the case of a drop in an axisymmetric extensional flow. The plot on the right is for the entire range of simulated time. The plots are on a semi-log scale and the exponential decay appears as a line of constant slope and corresponds to $N = 4 * 10^6$ initial tracers.

In Fig.4.16, we plot the corresponding Nu profiles, which are analogous to the case of a translating drop, exhibiting three distinct regimes, with plots corresponding to large Pe collapsing onto a single plateau for long times. The plateau-average of Nu is plotted against Pe in Fig.4.17, and at large Pe, it asymptotes to the value ~ 4.5 reported by Christov and Homsy (2009). The analog of Kronig and Brink (1950) calculation does not exist for this case to estimate this asymptote, owing to the fact that the functions of streamline coordinate cannot be derived in closed form. The error bars in this case, have an extent of about 10^{-3} and correspond to a confidence level of 99% cementing the accuracy of our simulations. Finally, we plot Nu versus Pe in Fig.4.18, where we compare the plots for different time steps and show that our results are independent of dt. The large Pe asymptote $Nu \sim 4.5$ is twice as that of a translating drop. Owing to this increased rate of transport, large Pe requires smaller time steps to obtain converged results, as can be seen from the first plot. The second plot of $Nu - Nu_{Diffusion}$ against Pe again suggests a Pe^2 scaling at small Pe, which again loses it's accuracy for $Pe < O(1)$ owing to large signal-to-noise ratios. Although not shown here, the same results also apply for the case of axisymmetric extension with vorticity aligned along the axis of symmetry. In this case the Nusselt number at large Pe remains independent of the vorticity magnitude (α'), as shown for the exterior case in Chapter 2.
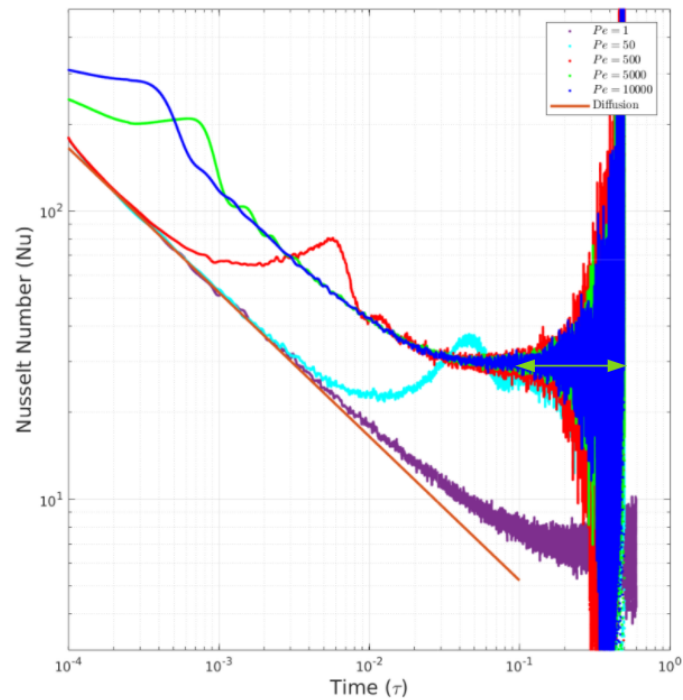
Figure 4.16: Plot of Nu profiles for a drop in axisymmetric extension on a log-log scale. The plot again exhibits three regimes corresponding to small, moderate and long times. These plots are smoothed using a Gaussian filter and correspond to $dt = 10^{-7}$.
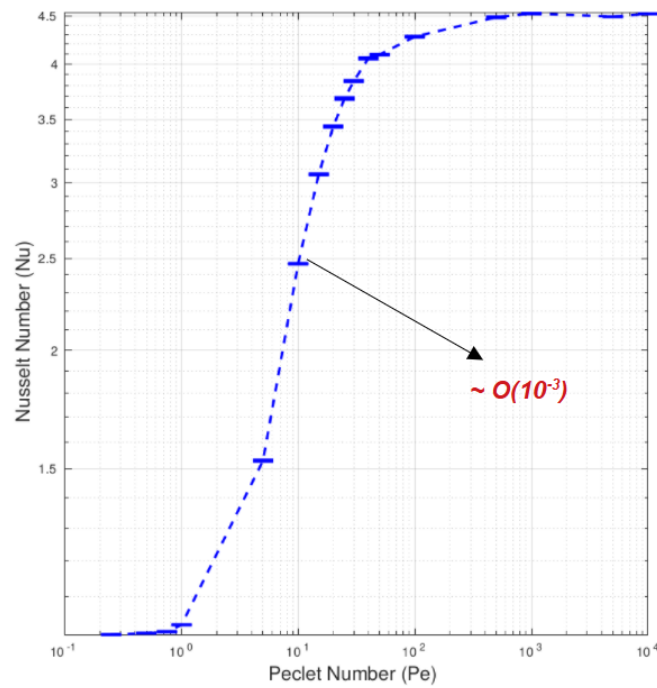
Figure 4.17: Plot of Nu at steady state for a drop in axisymmetric extension against Pe. The error bars are drawn assuming that Nu at steady state (the mean over the plateau from Fig.4.16), is a random variable following a Student's - T distribution. They are plotted for a confidence level of 99% and are of $O(10^{-3})$.
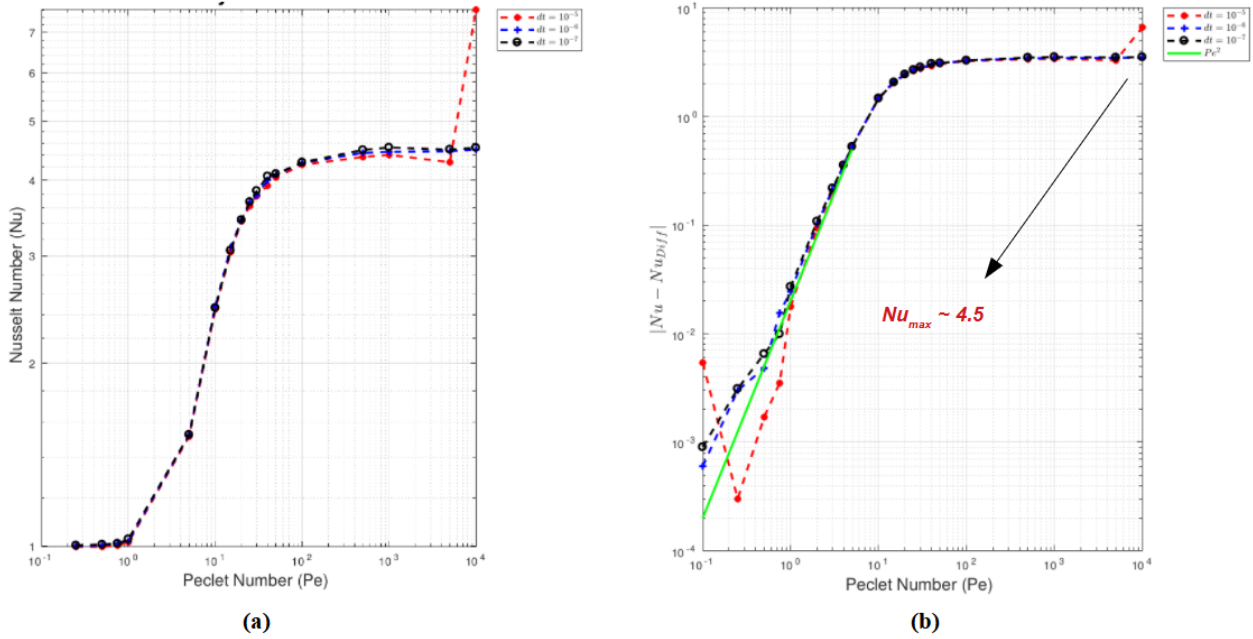
Figure 4.18: Plot of (a) Nu at steady state against Pe for multiple time steps and (b) $Nu - Nu_{Diffusion}$ against Pe for a drop in axisymmetric extension. At small Pe, $Nu - Nu_{Diffusion}$ scales as Pe^2.

In all the aforementioned cases, we have considered a spherical drop and neglected drop deformation. For flows with chaotic streamlines, drop deformation only has a perturbative effect on Nu, regardless of Pe, but for the aforementioned flows with regular streamlines, drop deformation could have a profound effect for $Pe > O(Ca^{-1})$ for $Ca \ll 1$, where Ca, the Capillary number, governs the deformation of drop. For these linear flows, specifically, for the family of $3D$ extensional flows, the regular streamlines are closed curves on a family of nested tori in each octant of the drop, owing to the eight-fold symmetry of these extensional flows. For small Ca, this streamline topology in the interior would change to a spiralling one, where each streamline densely winds around these nested invariant tori in each octant, since deformation also respects this eight-fold symmetry. Therefore, the transport rate for this case will again be diffusion limited, with Nu plateauing at large Pe. But, the deformation-induced plateau of Nu will differ from the $Ca = 0$ plateau by order unity, for $Pe > O(Ca^{-1})$. So, in these cases, Nu would increase from 1, saturating at the expected $Ca = 0$ value for $1 \ll Pe \ll Ca^{-1}$, but then increase to a second order-unity plateau for $Pe \gg Ca^{-1}$. For the special case of axisymmetric extension without vorticity, weak deformation would not have any effect on the Nu asymptote, because of the underlying symmetry of the flow, which inhibits streamlines winding over a tori and so they remain closed curves even for finite Ca. However, when vorticity is added to all the aforementioned base flows, deformation may lead to chaotic streamlines in the interior, where the extent of chaos may be greater than the case of a spherical drop ($Ca = 0$) suspended in these flows.

4.3.4   Results for Flows with Chaotic Streamlines

Having validated our simulations using the cases with regular interior streamlines, we shall now present the results for linear flows which lead to chaotic streamlines in the interior, and discuss the scaling behavior of Nu for large Pe, a result which is presented here for the first time.

4.3.4.1   Drop in $3D$ Extension with Aligned Vorticity

The first case we simulate is that of a drop in a $3D$ extensional flow with aligned vorticity. Recall that a representative plot of Poincaré sections for this case was shown in Fig.4.3, for $\epsilon = -0.25$ and for $O(1)$

values of α', the streamlines were seen to be chaotic, with multiple regular islands interspersed among the chaotic region. The Nusselt number profile for $\epsilon = -0.25$, $\alpha' = 1$ is shown in Fig.4.19, where we see that the profiles again exhibit a plateau at long times, implying an exponential decay regime (a quasi-steady state). Importantly, the signature of chaos is visible in the form of subdued oscillations of the Nusselt curves at intermediate times (Region 2). Recall that in the previous cases, the Nusselt curve exhibited oscillations for all Pe, even for $Pe \gg 1$, but in Fig.4.19, we see that for the largest Pe plotted ($Pe = 10^5$), the oscillations are almost non-existent. This suggests that an almost uniform concentration exists inside the drop owing to chaotic streamlines inside it. In Figs.4.20a - 4.20c, we have plotted the steady state value of $Nu - Nu_{Diff}$ (averaged over the plateau corresponding to the exponential decay regime of the Nu profile), against Pe for $\alpha' = 0.5, 1.0, 2.0$ and $\epsilon = -0.25$ for multiple time steps and we see from the plot that that Nu grows with Pe as $Pe \to \infty$ and this growth scales as Pe^β; unlike the usual cases, β here is a function of flow parameters. For the three α' considered above, the parameter $\beta \sim 0.075$, $0, 08$, 0.0775 respectively. We also observe that the plots corresponding to smaller time-steps coincide, implying that our simulation results are independent of dt.
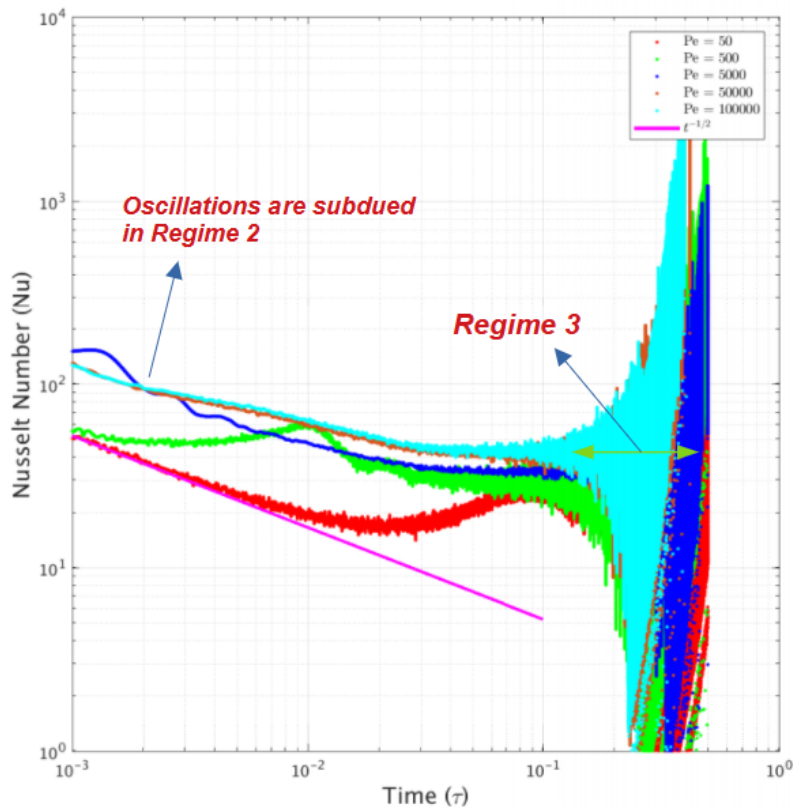
Figure 4.19: Plot of Nusselt number as a function of time for $\epsilon = -0.25$, $\alpha' = 1.0$. The plot shows that at long times, there exists a quasi-steady state, corresponding to simple exponential decay (the plateau) of Nu and at intermediate times, the oscillations of the Nusselt profile are highly subdued, a visual signature of chaos in the interior.

In Fig.4.21, we plot Nu versus Pe plots for the aforementioned values of α' on a single plot. The maximum Nusselt number obtained in this case is roughly $O(10)$ corresponding to $\alpha' = 1$, which is more than twice the value for axisymmetric extension without vorticity. Going back to the Poincaré sections in Fig.4.3, we see that $\alpha' = 1$ appears more chaotic owing to a smaller number of non-chaotic islands. Although $\alpha' = 2$, appears visually more chaotic, it also has more number of non-chaotic islands. The correlation between the extent of chaos and Nu can be established by calculating the fraction of area

traversed by chaotic streamlines to the total area and correlating it to Nu. However, one must note that the Poincaré sections have been generated over a time that is much longer than the average time taken for a tracer to be absorbed. Thus, it is not obvious that the Lyapunov exponents that characterise the chaotic behavior for long times, directly relate to the enhancement factor.
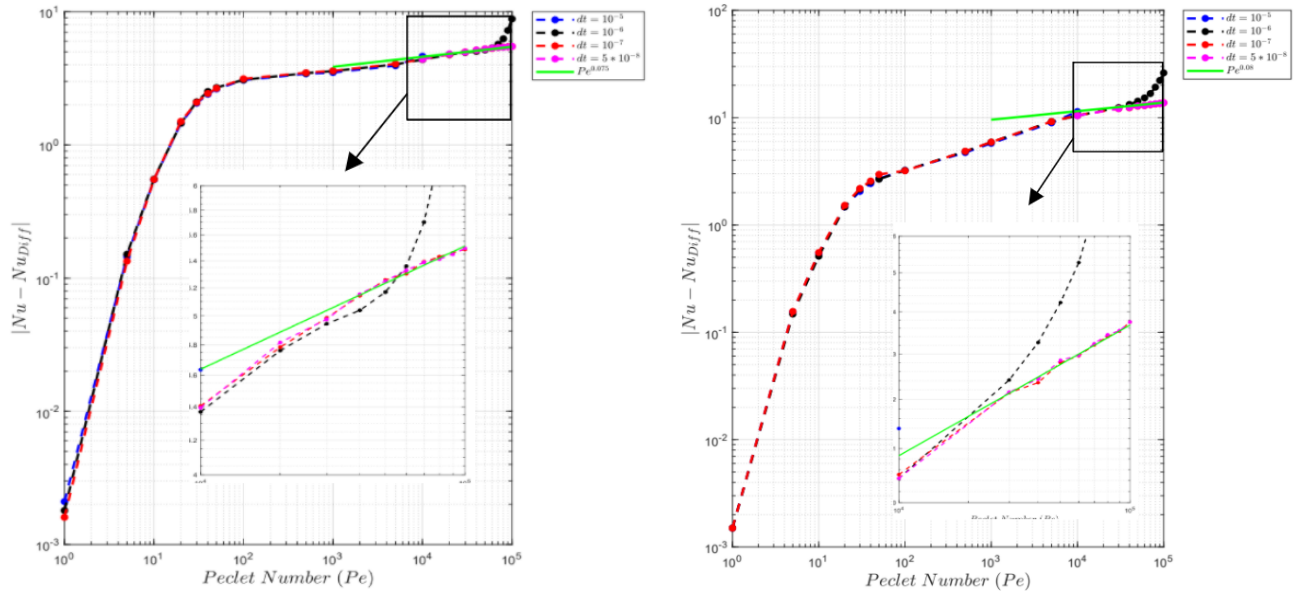
(a) $\alpha' = 0.5$

(b) $\alpha' = 1.0$
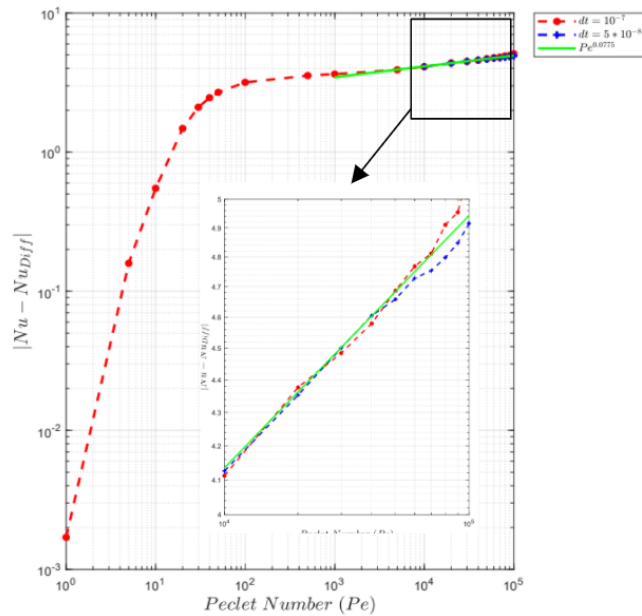
(c) $\alpha' = 2.0$

Figure 4.20: Plot of $Nu - Nu_{Diffusion}$ against Pe for three different values of α' and $\epsilon = -0.25$. Unlike the previous cases, Nu grows with Pe as $Pe \to \infty$. The exponent at large Pe is different for each case.
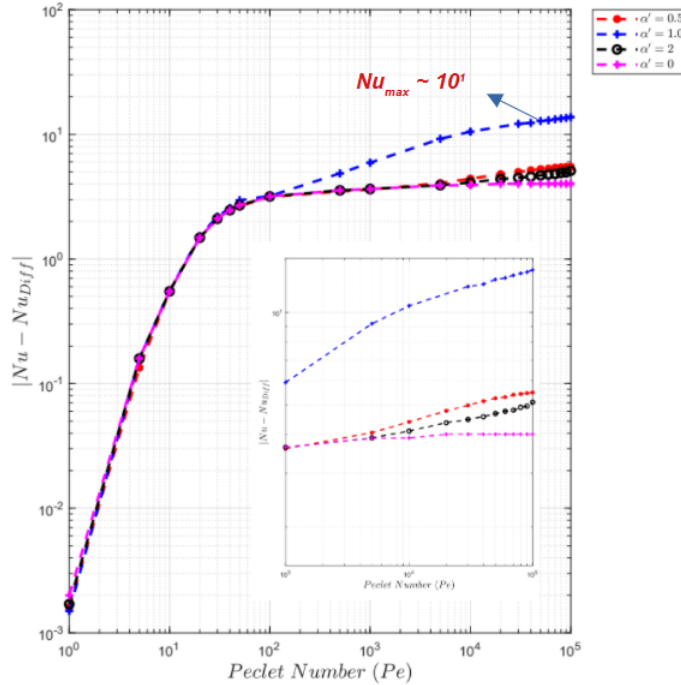
Figure 4.21: Plot of $Nu - Nu_{Diffusion}$ at steady state against Pe for three different α' at $\epsilon = -0.25$. The rise in Nu at large Pe is due to the presence of chaotic streamlines in the drop. The inset shows the magnified image for large Pe, where the magenta curve ($\alpha' = 0$) corresponds to $3D$ extension with no vorticity ($\epsilon = -0.25$) and the Nusselt number plateaus at large Pe for this case as there is no chaos.

4.3.4.2 Drop in Axisymmetric Extension with Inclined Vorticity

The final case we simulate is the one considered by Stone et al. (1991), and the Poincaré sections for which are shown in Fig.4.4. In this case, chaos could fill up the entire drop depending on the parameters chosen, as can be seen in the plot for $\alpha' = 0.1$, $\theta_\omega = 0.304\pi$. But this picture corresponds to a coarse-grained description, as, theoretically, regular islands are known to exist at all scales down to the smallest one. So, we cannot exclude the possibility of there being islands having small cross-sections, which correspond to stable periodic orbits with high periods (Stone et al. (1991)). Recall that this value of $\theta_\omega = 0.304\pi$ corresponds to the critical value of inclination at which the dominant island (of regular flow) in the neighbourhood of the elliptic fixed point breaks down leading to complete chaos in the drop. In Fig.4.22, we have plotted the Nusselt number for $\alpha' = 0.1$ and three different values of θ_ω, including the critical inclination. On the left side, we show the Poincaré sections for the three values of inclination considered so as to correlate the enhancement to the degree of chaos. The cases $\theta_\omega = 0.304\pi$ and 0.35π, have chaotic regions filling the entire drop. These two inclinations give rise to $Pe^{1/2}$ scaling of Nu at $Pe \gg 1$, which is what one expects from boundary layer based arguments. In this state of complete chaos, the situation is exactly analogous to the case of a drop surrounded by open streamlines in the exterior where, the entire resistance to transport is confined to a boundary layer of thickness $Pe^{-1/2}$. For $\theta_\omega = 0.25\pi$, for which islands of regular flow exist, the scaling changes to $Pe^{1/4}$, as this case offers more resistance to transport than the other two due to the existence of such islands.
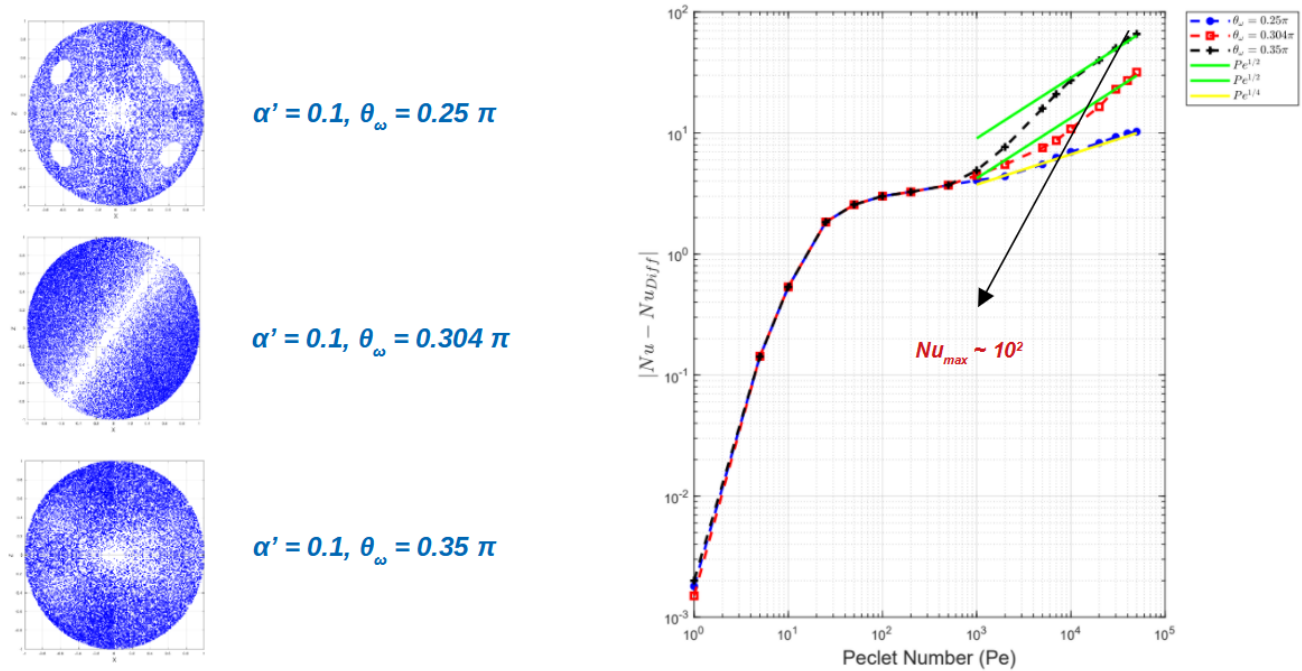
Figure 4.22: Plot of $Nu - Nu_{Diffusion}$ at steady state against Pe for three different inclinations at $\alpha' = 0.1$. The rise in Nu at large Pe is due to the presence of chaotic streamlines in the drop where the exponent β is exactly $1/2$ for the cases with no islands of regular flow (maximum chaos).

An important thing to note here is the significant enhancement of Nu at large Pe. For $\theta_\omega = 0.35\pi$ and $\alpha' = 0.1$, we see that $Nu_{max} \sim 10^2$, which is more than an order of magnitude higher than the case of axisymmetric extension with no vorticity (see Fig.4.18). This enhancement is crucial as it occurs for an α' as small as 0.1. The nature of flow inside the drop, when it is subjected to a general linear flow, is similar to this case (Fig.4.6), with the chaotic regions having a greater spatial extent at corresponding parameter values than the case of axisymmetric extension with inclined vorticity (Fig.4.3). Thus, one can expect analogous enhancements for a spherical drop in an arbitrary linear flow. As we will see later, for cases with completely chaotic interior, the $C - \tau$ formalism developed for the exterior transport analysis, can be easily extended to solve the conjugate transport problem, for which the resistances in the interior and exterior are of comparable magnitude.

4.4 Existence of Internal Boundary Layer

In the last section, we showed that the existence of chaos leads to $Nu \sim O(Pe^\beta)$ for $Pe \gg 1$, where β was an exponent dependent on flow type. This implies that, at steady state, there exists a boundary layer in the interior of the drop whose thickness is $O(Pe^{-\beta})$. To show the existence of this internal boundary layer, one can make use of the radial distribution of concentration at the steady state. Our Langevin simulations are inherently transient in nature and we have been extracting quantities of interest from an assumed quasi-steady state at long times and the validity of this assumption was provided by a plateauing Nusselt number from the Nu profiles at long times. However, a true steady state can be achieved by adding a constant source term in the interior that replenishes the tracers at a constant rate. For long times, one would eventually settle into a steady state where the depletion adjusts to match the rate of replenishment. Thus the governing equation to be solved for this case is given by:

$$\frac{\partial c}{\partial t} + \boldsymbol{u} \boldsymbol{.} \boldsymbol{\nabla} c = \frac{1}{Pe} \nabla^2 c + \mathcal{F}(r, \theta, t) \tag{4.23}$$

where $\mathcal{F}(r, \theta, t) = 1$, and therefore, it represents a uniform source. Correspondingly in the simulations, one needs to introduce new tracers with a uniform probability in the domain at each time step, until the steady state is reached. Such a simulation would require huge amounts of memory to store and track the tracers that were introduced initially and also at subsequent times. But this isn't needed, as one can use the results of our transient simulation (specifically, the angularly averaged radial concentration profile at each instant $(c(r,t))$), to obtain the steady state solution $c(r)$, by integrating $c(r,t)$ over time. We show this explicitly for the simpler cases of diffusion and translation for which analytical solutions to the convection-diffusion equation exist. We then extend this method to plot the radial distribution of the tracer concentration at the steady state from the transient simulations for other flows, particularly for those flows which lead to chaotic streamlines in the interior, thereby enabling us to show the existence of an internal boundary layer.

4.4.1 The Steady State Solution

The idea that the steady state solution can be derived from the transient solution can be established by the fact that the initial condition (Eq.4.14) of the convection-diffusion equation (Eq.4.13), can be realised by enforcing an impulsive forcing at time $t = 0$ as:

$$\frac{\partial c}{\partial t} + \boldsymbol{u.\nabla} c - \frac{1}{Pe} \nabla^2 c = \delta(t). \tag{4.24}$$

where $\delta(t)$ is the Dirac delta function. Integrating both sides with respect to time from 0^- to 0^+ gives us,

$$c(0^+) - c(0^-) = 1 \Rightarrow c(0^+) = 1 \tag{4.25}$$

which is the desired initial condition (since $c(0^-) = 0$). The solution corresponding to the steady forcing $\mathcal{F}$ in Eq.4.23, can be obtained from the superposition of impulse-response solutions at successive instants of time s, with s ranging from 0 to t^-. Thus, the impulse-response solution $c_I(t-s)$ satisfies,

$$\frac{\partial c_I}{\partial t} + \boldsymbol{u.\nabla} c_I - \frac{1}{Pe} \nabla^2 c_I = \delta(t - s), \tag{4.26}$$

with the solution corresponding to the onset of a steady source being given by:

$$c_s(t) = \int_0^{t^-} c_I(t - s) \tag{4.27}$$

where the upper limit is chosen as t^-, since the impulse-response function is only defined starting at 0^+. Keeping in mind the relation above, one operates with $\int_0^{t^-}$ on both sides of Eq.4.26, to get:

$$\int_0^{t^-} \frac{\partial c_I}{\partial t} + \boldsymbol{u.\nabla} \int_0^{t^-} c_I - \frac{1}{Pe} \nabla^2 \int_0^{t^-} c_I = \int_0^{t^-} \delta(t - s) \tag{4.28}$$

where the right hand side is 0, as the argument of the delta function isn't in the range of integration. Applying the Leibnitz rule (of differentiation under the integral sign) for the first term, we get:

$$\frac{\partial c_s}{\partial t} - c_I(0^+) + \boldsymbol{u.\nabla} c_s - \frac{1}{Pe} \nabla^2 c_s = 0 \tag{4.29}$$

where $c_I(0^+) = 1$, which can be rewritten as a Heaviside function i.e. $c_I(0^+) = \mathcal{H}(t)$, since $c_I(0^-) = 0$. So, we have,

$$\frac{\partial c_s}{\partial t} + \boldsymbol{u.\nabla} c_s - \frac{1}{Pe} \nabla^2 c_s = \mathcal{H}(t). \tag{4.30}$$

Thus, we have established that the time-dependent solution corresponding to a Heaviside forcing (steady forcing) is given in terms of the solution of an impulsive forcing by the relation in Eq.4.27. The limiting solution at steady state is then given by,

$$\lim_{t\to\infty} c_s(t) = \lim_{t\to\infty} \int_0^{t^-} c_I(t-s). \tag{4.31}$$

Changing the variable of integration from $t-s$ to $\hat{t}$, we finally have:

$$\lim_{t\to\infty} c_s(t) = \int_0^\infty c_I(\hat{t})d\hat{t} \tag{4.32}$$

which is the desired relation between the steady state and transient solutions subject to the impulsive forcing. The latter is equivalent to the system of equations we solve in the Langevin simulations, with a uniform initial condition. This shows that regardless of the flow, we can derive the steady state concentration profile from our transient simulations. We now validate the aforementioned discussion by comparing the analytical steady state solution and the one obtained from our transient simulation for the case of diffusion and a translating drop, before showing the results for other flows.

4.4.2 Pure Diffusion

The governing equation for this case, where there is no flow of the ambient fluid is:

$$\frac{\partial c}{\partial t} = \frac{1}{r^2}\frac{\partial}{\partial r}(r^2\frac{\partial c}{\partial r}) \tag{4.33}$$

where $\frac{\partial c}{\partial \phi} = \frac{\partial c}{\partial \theta} = 0$ owing to spherical symmetry. The solution of the above equation can be found by separation of variables by assuming $c = G(r)F(t)$, which gives rise to solution of the form (Kronig and Brink (1950)):

$$c(r,t) = 2\sum_{n=1}^{n=\infty}\left((-1)^{n+1}e^{-n^2\pi^2 t}\frac{\sin(n\pi r)}{n\pi r}\right) \tag{4.34}$$

The steady state solution can be derived from this solution by integrating over time to give:

$$c(r) = 2\sum_{n=1}^{n=\infty}\left((-1)^{n+1}\frac{\sin(n\pi r)}{n^3\pi^3 r}\right). \tag{4.35}$$

This solution can be shown to be the same as

$$c(r) = \frac{1}{6}(1 - r^2), \tag{4.36}$$

which is the solution of the equation with a source term,

$$\frac{\partial c}{\partial t} = \frac{1}{r^2}\frac{\partial}{\partial r}(r^2\frac{\partial c}{\partial r}) + \mathcal{F}(r) \tag{4.37}$$

where, as before, $\mathcal{F}(r) = 1$, denoting a spatially uniform source. We can see that this is the case from Fig.4.23, where the two solutions given by Eq.4.35 and 4.36 are plotted against the result from the transient simulation. The plot shows that the solution at the steady state $(c(r))$, can be calculated from the transient simulation by adding up (integrating) the (angularly averaged) radial concentration profile corresponding to each instant $(c(r,t))$.
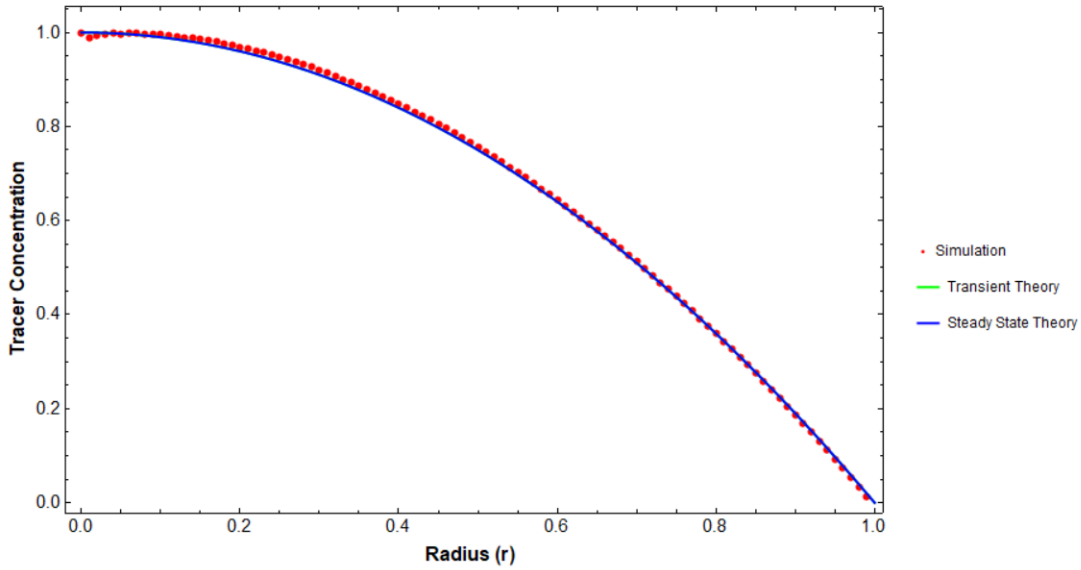
Figure 4.23: Steady state radial concentration profile for diffusion from the transient simulations compared with the solutions given in Eq.4.35 (green) and Eq.4.36 (blue).

4.4.3 Translating Drop

The problem of translating drops was solved exactly by Kronig and Brink (1950) in the limit $Pe \gg 1$ using streamline coordinates, where the authors showed the the concentration is only a function of the streamline coordinate for $Pe \gg 1$. The governing equation at steady state is given by:

$$\frac{\partial}{\partial \xi}\left(P(\xi)\frac{\partial c}{\partial \xi}\right) = -\frac{1}{16}Q(\xi) \tag{4.38}$$

where ξ is the streamfunction (streamline coordinate) defined as $\xi = 4r^2(1 - r^2)\sin^2\theta$. The quantities $P(\xi)$ and $Q(\xi)$ are given by:

$$P(\xi) = \int \frac{(2r^2 - 1)^2 \sin^2\theta}{r\cos^3\theta}d\zeta \tag{4.39}$$

$$Q(\xi) = \int \frac{(2r^2 - 1)^2}{4r^3\cos^3\theta\Delta}d\zeta \tag{4.40}$$

with $\Delta = (2r^2 - 1)^2\sin^2\theta + (1 - r^2)^2\cos^2\theta$ and $\zeta = (r^4\cos^4\theta)/(2r^2 - 1)$, the orthogonal coordinate of ξ. The boundary conditions are given by:

$$c(\xi = 0) = 0 \tag{4.41}$$

$$c(\xi = 1) = 1 \tag{4.42}$$

The solution of Eq.4.38, subject to Eqs.4.41 and 4.42, is:

$$c(\xi) = \frac{1}{16}\int_0^\xi \frac{1}{P(\xi')}\int_{\xi'}^1 Q(u)dud\xi' \tag{4.43}$$

We now wish to calculate the radial distribution of the concentration, which is given as:

$$\bar{c}(r) = \int_0^\pi c(r, \theta)\sin\theta d\theta. \tag{4.44}$$

Rewriting the integral in terms of ξ, we have,

$$\bar{c}(r) = \frac{2}{8r^2(1-r^2)} \int_0^{4r^2(1-r^2)} c(\xi) \frac{d\xi}{\left(1 - \frac{\xi}{4r^2(1-r^2)}\right)^{1/2}} = \frac{1}{r\sqrt{1-r}} \int_0^{4r^2(1-r^2)} \frac{c(\xi)d\xi}{\sqrt{4r^2(1-r^2) - \xi}} \qquad (4.45)$$

It can be shown that $c(\xi) = \xi$ to within a constant from Eq.4.43, which then reduces the above equation to,

$$\bar{c}(r) = \frac{1}{r\sqrt{1-r}} \frac{4}{3} \left(4r^2(1-r^2)\right)^{3/2} = 4r^2(1-r^2) \qquad (4.46)$$

to within a constant, which can be set to 1, making it a normalised distribution. This solution corresponds to the steady state distribution of tracer concentration inside the translating drop, and is compared to the one obtained from the numerical simulations in Fig.4.24. Note that, the maximum in this profile occurs at a radial position of $r = 1/\sqrt{2}$, which corresponds to the radial location of the elliptic fixed point in the interior (Fig.4.1). The simulation results asymptote to the theoretical curve as $Pe \to \infty$ and all the profiles at large Pe have a maximum at $r = 1/\sqrt{2}$, which further validates the fact that, one can obtain steady state profiles from the transient ones by integration. For cases, without the exact solution, the matching of the maximum in the profile with the location of the stagnation point serves as a validation. The key observation from the figure is that the profile changes from a monotonically decreasing function of r to a non-monotonic one with a maximum at the stagnation point as Pe increases. This transition in the profile occurs over the same range of Pe, over which Nu rose from the diffusion limit to the large Pe asymptote in Fig.4.13. Importantly, for large Pe, $O(1)$ change in the concentration profile (from c_{max} to 0) occurs as r changes from $1/\sqrt{2}$ to 1. This immediately implies that there is no boundary layer, since the length scale $r = 1 - 1/\sqrt{2}$, over which the concentration changes by $O(1)$ is independent of Pe.
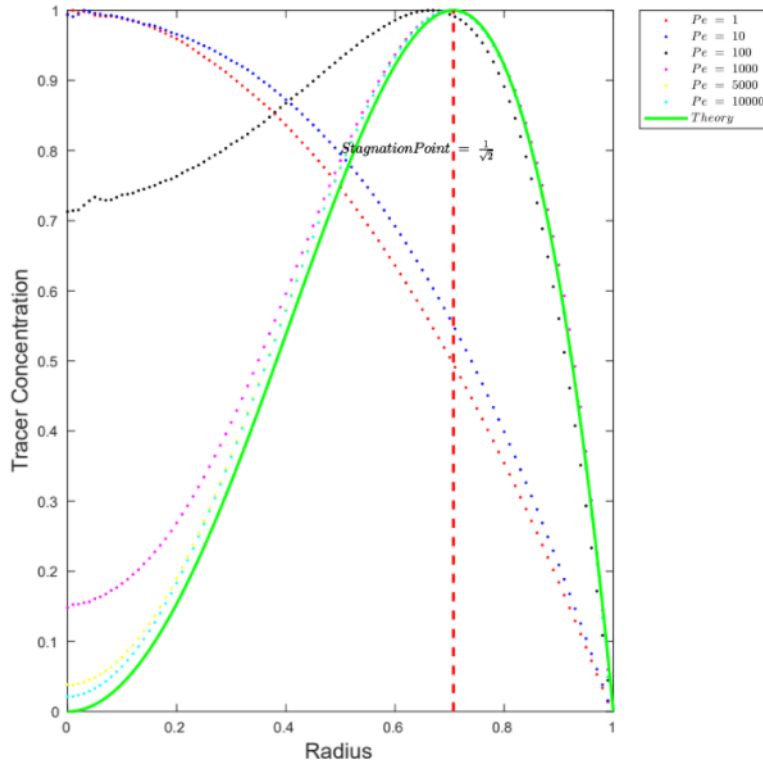
Figure 4.24: Steady state radial concentration profile for a translating drop from the transient simulations compared with the solution given in Eq.4.46. At small Pe, the solution is very similar to the solution for diffusion given in Eq.4.35.

4.4.4 Drop in Axisymmetric Extension

For a drop in an axisymmetric extension, the solution, at steady state, of the convection-diffusion equation is not known in closed form. This is due to the fact that the quantities analogous to $P(\xi)$ and $Q(\xi)$ in Eq.4.38 are not known in closed form, despite the fact the concentration is only a function of the streamline coordinate just like the case of a translating drop. Nevertheless, one can still plot the steady state radial profile from the transient simulation by adding the radial profiles corresponding to successive instants of time, until the quasi-steady state is reached. This has been done for several Pe from the Langevin simulations and the results are plotted in Fig.4.25. We see from the figure that the solution corresponding to small Pe is very close to the solution for pure diffusion given in Eq.4.35 and at large Pe all profiles collapse onto a single curve. This transition is analogous to one observed in Fig.4.24 for the case of a translating drop. The maximum for all the profiles occurs at $r = \sqrt{3/5}$, which corresponds to the radial location of the elliptic fixed point. Again, the crucial thing to note in Fig.4.25 is that, an $O(1)$ change in concentration occurs over a radial length scale $1 - \sqrt{3/5}$, which is independent of Pe for $Pe \gg 1$. This again implies that there is no internal boundary layer.
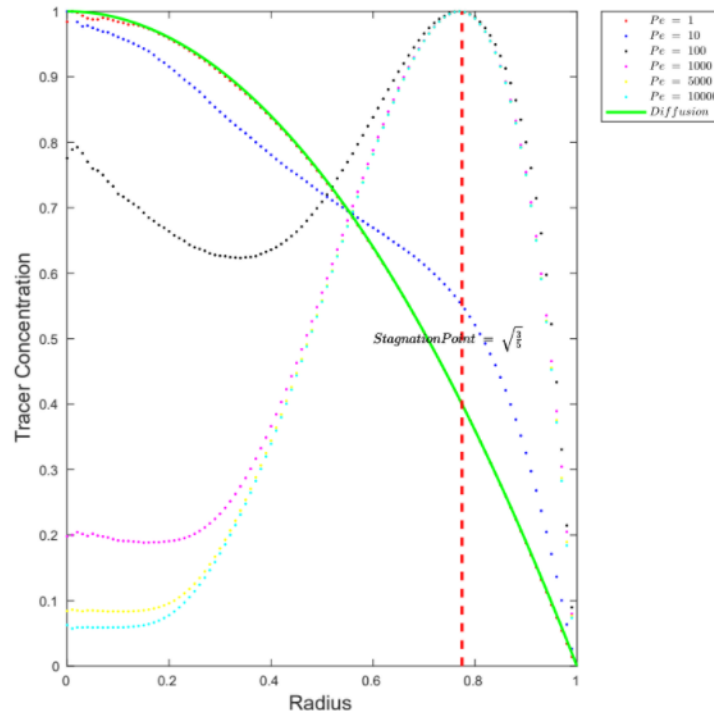
Figure 4.25: Steady state radial concentration profile for a drop in an axisymmetric extension from the transient simulations. This plot is analogous to the case of a translating drop in Fig.4.24, where at large Pe, the concentration changes by $O(1)$ over a radial length scale $r = 1 - \sqrt{3/5}$, for all $Pe \gg 1$, implying the absence of an internal boundary layer.

4.4.5 Flows with Chaotic Streamlines

Having validated the steady state results derived from our transient simulations, we now move on to extending the same for flows with chaotic interior streamlines, in a bid to show the existence of an internal boundary layer, at large Pe.

4.4.5.1 Drop in $3D$ Extension with Aligned Vorticity

For this case, transient simulations showed Nu to be a weakly growing function of Pe in Fig.4.21, with the apparent exponent (β) being a function of α'. We plot the steady state radial profiles corresponding to $\epsilon = -0.25, \alpha' = 1.0$ in Fig.4.26 for different Pe, which had the maximum enhancement among the three cases considered in Fig.4.21. In Fig.4.26, we have plotted the concentration as a function of $1 - r$, and a magnified image near the origin shows that unlike previous cases, the plots don't collapse onto a single curve at large Pe. Here, the slope of the radial profile is larger for larger Pe and this implies that, an $O(1)$ change in concentration occurs over a radial distance that is dependent on Pe. This shows that an internal boundary layer exists for this case, whose thickness is $O(Pe^{-\beta})$, β, being a function of the flow parameters. In Fig.4.27, we have plotted the same profile but with a scaled radial distance given by $(1 - r)Pe^{0.08}$, where $Pe^{0.08}$ is the growth rate of Nu for this case (see Fig.4.20b). In this re-scaled plot we see that all the curves corresponding to large Pe collapse onto a single curve near the origin ($r = 1$) confirming the existence of an internal boundary layer, whose thickness is roughly $(1 - r) = \delta_{BL} \sim 0.075Pe^{-0.08}$. In contrast, for the previous cases involving regular interior streamlines, the plots collapsed onto a single curve at large Pe despite any re-scaling of the radial distance, which suggests that there is no boundary layer for those cases.
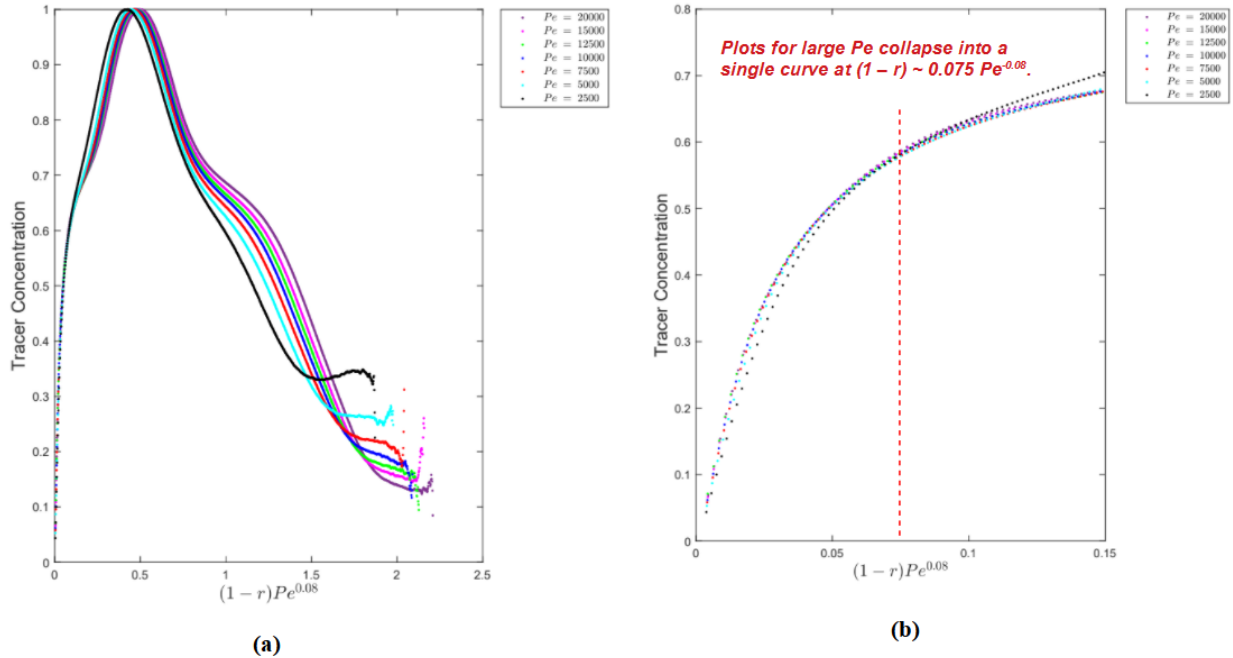
Figure 4.26: Steady state radial concentration profile for a drop in $3D$ extension with aligned vorticity with $\epsilon = -0.25, \alpha' = 1.0$. The magnified image shows that at large Pe, the curves don't collapse onto one another and the curves for larger Pe exhibit larger slopes, implying the existence of a boundary layer, whose thickness depends on Pe.
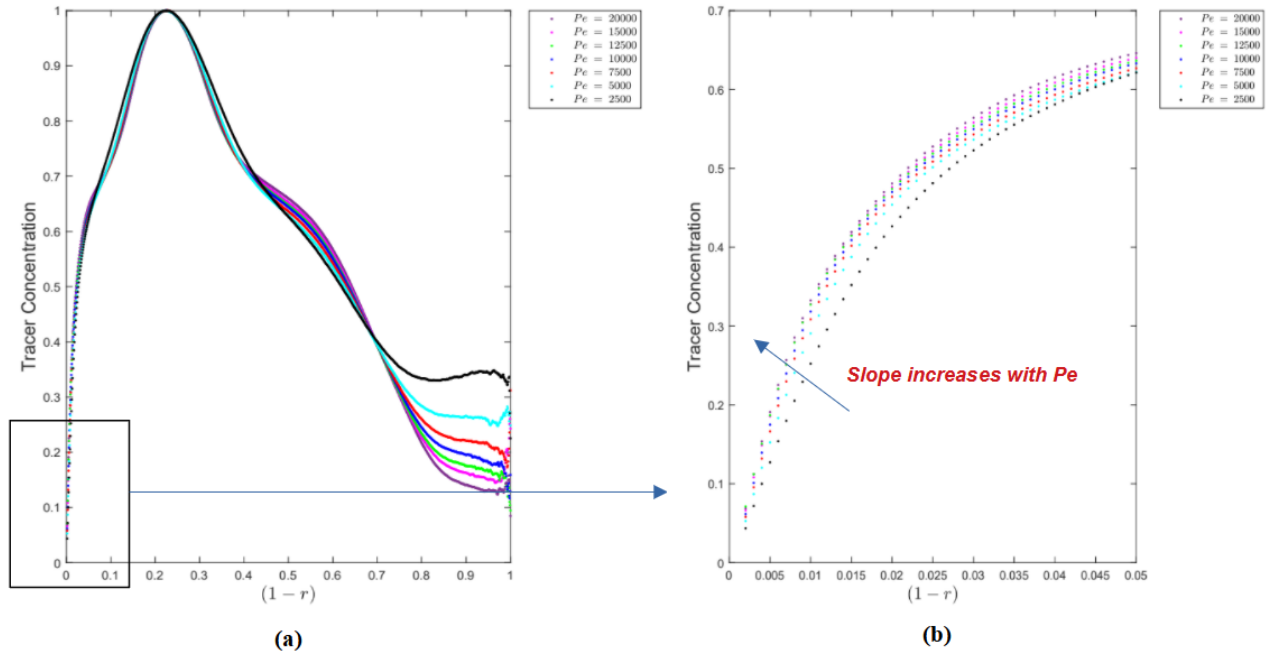
Figure 4.27: Steady state radial profile for a drop in $3D$ extension with aligned vorticity for $\epsilon = -0.25, \alpha' = 1.0$. The concentration is plotted against re-scaled radial distance $(1-r)Pe^{0.08}$, where 0.08 is the exponent for this case.

4.4.5.2 Drop in Axisymmetric Extension with Inclined Vorticity

In this case, the interior exhibited completely chaotic states for particular values of the parameters α' and θ_ω (see Fig.4.22). The steady-state radial concentration profiles for the parameters considered in Fig.4.22, where $Nu \sim O(Pe^\beta)$ for $Pe \gg 1$, are plotted in Fig.4.28 and Fig.4.30. In Fig.4.28 (for $\theta_\omega = 0.304\pi, \alpha' = 0.1$), we have plotted the concentration as a function of $1 - r$, and a magnified image near the origin shows that the plots don't collapse onto a single curve at large Pe and the slope of the profile increases with Pe, just like the previous case. In Fig.4.29, the same profile is plotted with a scaled radial distance given by $(1 - r)Pe^{1/2}$, where $Pe^{1/2}$ is the growth rate of Nu for this case (see Fig.4.22). Here again, we see that all the curves corresponding to large Pe collapse onto a single curve near the origin ($r = 1$) suggesting the existence of an internal boundary layer, whose thickness is roughly $(1 - r) = \delta_{BL} \sim 0.25 Pe^{-1/2}$.

A similar plot in re-scaled coordinates is plotted for the case $\theta_\omega = 0.25\pi, \alpha' = 0.1$ in Fig.4.30, for which the growth rate is Nu was $Pe^{1/4}$ (from Fig.4.22). Thus, for this case the re-scaled radial distance should be $(1 - r)Pe^{1/4}$, and in this re-scaled coordinate the curves for large Pe collapse onto a single curve again implying the existence of an internal boundary layer of thickness $Pe^{-1/4}$, analogous to the aforementioned scenario. We see from these results that as the interior exhibits more non-chaotic islands i.e. when the extent of chaotic region is smaller, the thickness of the boundary layer increases eventually becoming $O(1)$ for cases without chaotic streamlines.
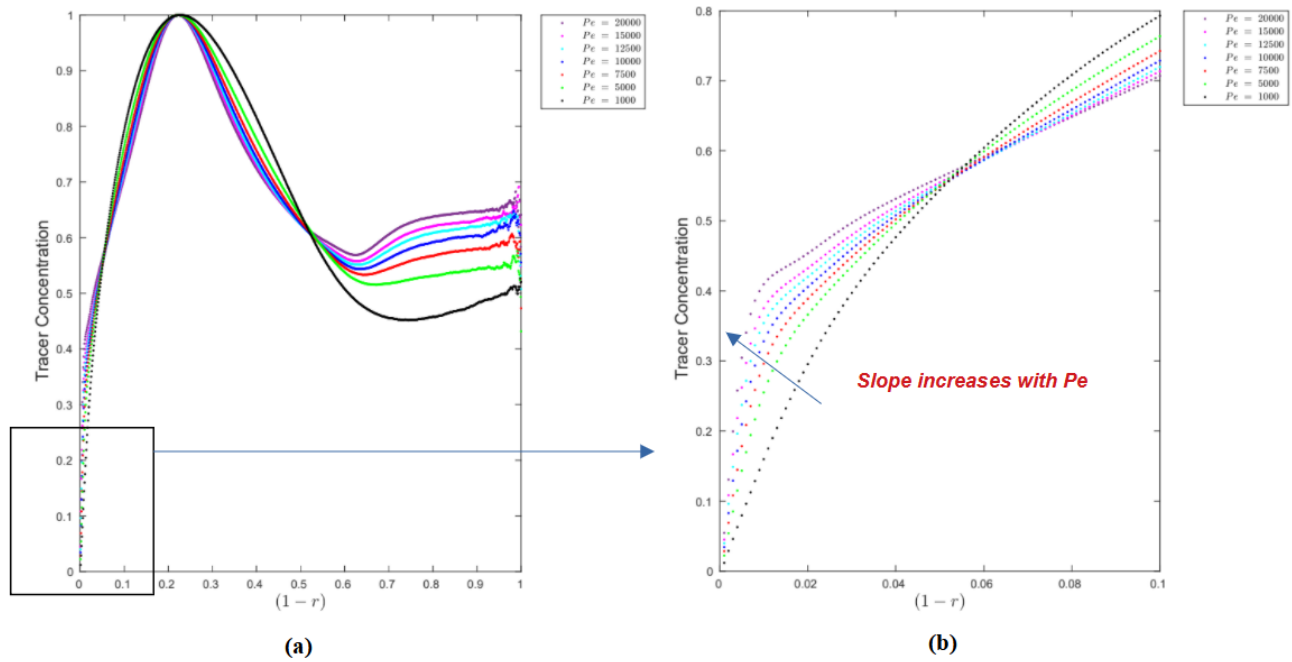
Figure 4.28: Steady state radial concentration profile for a drop in axisymmetric extension with inclined vorticity for $\theta_\omega = 0.304\pi, \alpha' = 0.1$. The magnified image shows that at large Pe, the curves don't collapse onto one another and near $r = 1$, curves for larger Pe exhibit larger slopes.
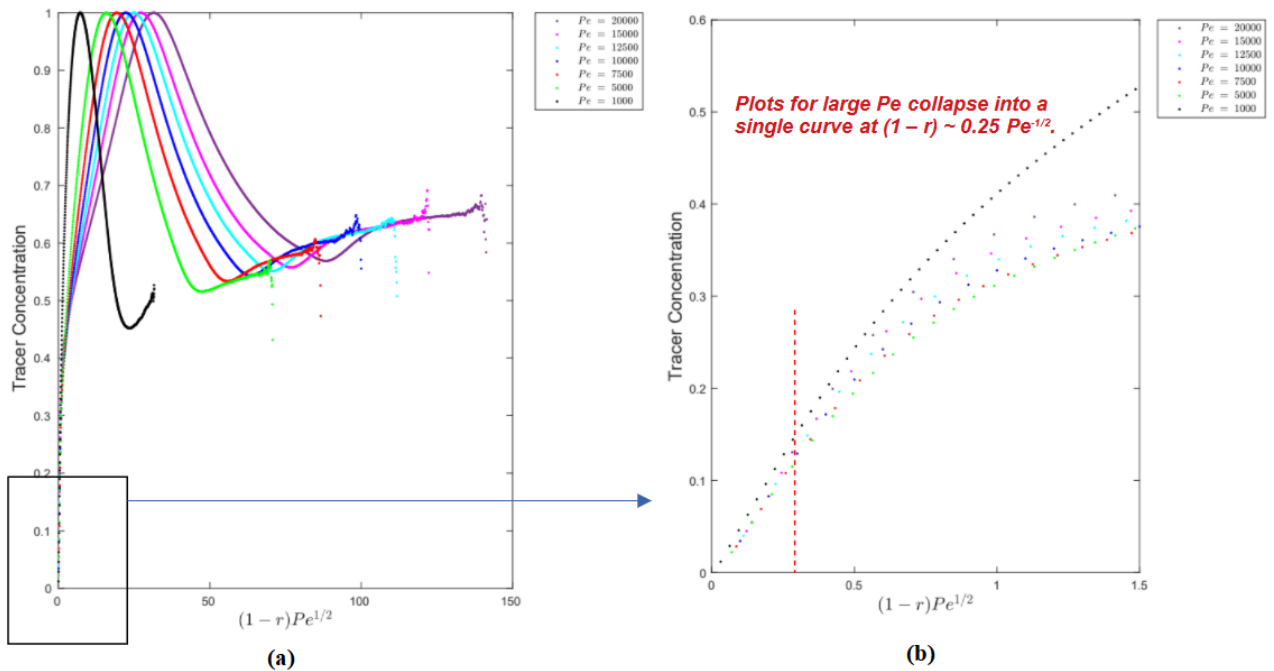
Figure 4.29: Steady state radial profile for a drop in axisymmetric extension with inclined vorticity for $\theta_\omega = 0.304\pi, \alpha' = 0.1$. The concentration is plotted against re-scaled radial distance $(1 - r)Pe^{1/2}$, where $1/2$ is the exponent for this case. In this re-scaled coordinates, the curves for large Pe collapse onto a single curve implying the existence of boundary layer.
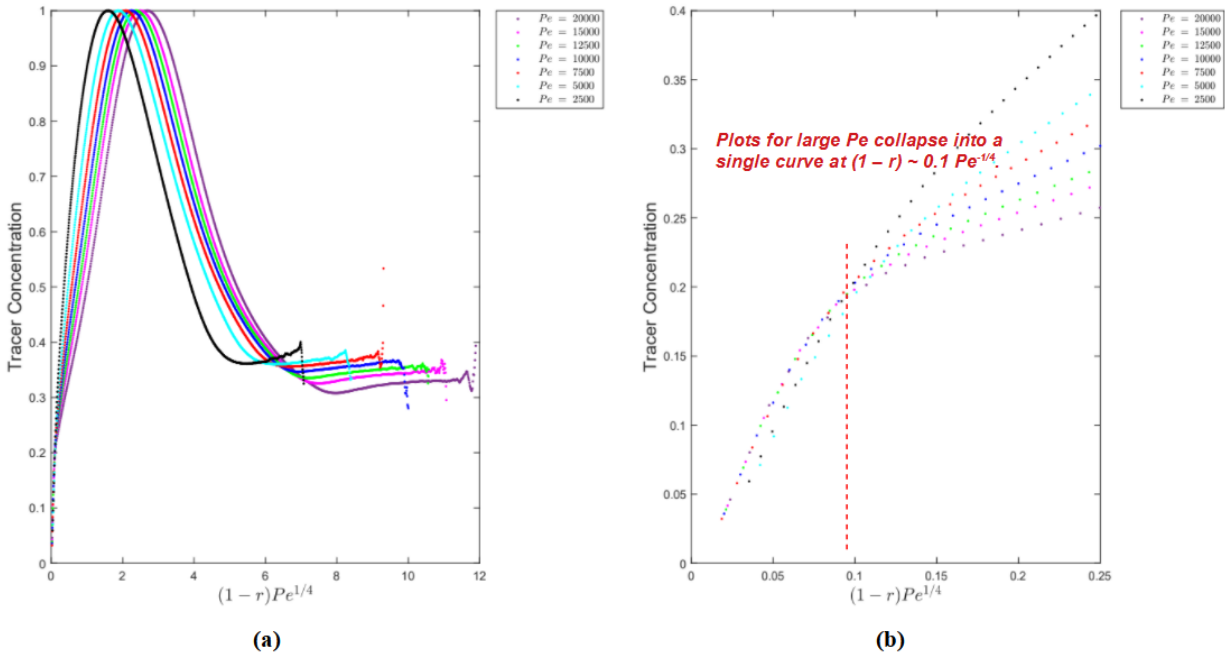
Figure 4.30: Steady state radial profile for a drop in axisymmetric extension with inclined vorticity for $\theta_\omega = 0.25\pi, \alpha' = 0.1$. The concentration is plotted against re-scaled radial distance $(1-r)Pe^{1/4}$, where $1/4$ is the exponent for this case.

The results shown above are of course preliminary, and there is a huge swathe of parameter values to explore along the same lines. But these results are also strong indicators of the existence of a boundary layer. More detailed analysis with simulations of higher accuracy will enable us to calculate the thickness of this boundary layer for each parameter value to a higher precision. This will be taken up in the near future, as this is one of the crucial calculations needed to explain the mechanism of interior transport that leads to a flow-dependent exponent for chaotic flows.

4.5 Concluding Remarks

At the beginning of this section, it was mentioned that the aim of this chapter was to show the existence of an internal boundary layer, which would enable us to take up the problem of conjugate heat or mass transfer from the drop using the flow-aligned coordinate system, the $C - \tau$ system, for certain special cases. The special case pertains to scenarios with completely chaotic interior that leads to a $Pe^{1/2}$ growth in Nu. The fact that the flow-aligned coordinate system can be used to solve the conjugate problem for this case was shown by Krishnamurthy and Subramanian (2018a) who, assuming the existence of an internal boundary layer of thickness $O(Pe^{-1/2})$, showed that such a case can be solved rigorously using the $C - \tau$ system. This generalisation is possible because, the governing equation in the interior and exterior can be reduced to the same form by a suitable similarity variable, provided these variables are defined based on the corresponding Peclet numbers Pe_i and Pe in the interior and exterior respectively. Since the boundary satisfies continuity of velocity, it leads to the same expression for boundary layer thickness $g(C, \tau)$ as was obtained for the exterior analysis. These features combined with the appropriate boundary conditions of temperature and flux continuity at the drop surface, will lead to the Nusselt number given by:

$$Nu = \frac{Pe^{1/2}}{2\pi^{3/2}} \left[\frac{(k_i/k_e)^{1/2}}{(k_i/k_e)^{1/2} + 1} \right] \int_S \frac{dS}{g(C\tau)} \tag{4.47}$$

where k_i and k_e are the interior and exterior conductivities.

The aforementioned expression, as already mentioned, is valid only when the boundary layer thickness scales as $Pe^{-1/2}$, which from the analysis presented in this chapter seems to be possible only for cases where the chaos is space-filling. Nevertheless, our streamline analysis suggests that the flows that give rise to completely chaotic interior, would constitute a significant fraction of the full $4D$ parameter space of three-dimensional linear flows, which makes the $C - \tau$ analysis all the more indispensable, for it enables one to rigorously calculate Nu for the conjugate problem analytically. But for flows where chaos isn't space-filling, numerical analysis is the only option available. Our preliminary results in this chapter suggest a computationally effective way to analyse the problem of transport in the interior, where there are still multiple open avenues to explore. This shall be the subject of a separate study to be taken up in the future, which will undoubtedly be rich in physics.

Chapter 5

Drop in Canonical Planar Linear Flows - Effect of Deformation on Streamline Topology

In the preceding chapters, the primary focus was on the calculation of the Nusselt number for the exterior and interior problems for cases where the exterior streamlines were open, and the interior streamlines were chaotic (the interior flows with regular streamlines were only analyzed as a baseline scenario). We now turn our attention to the case where the exterior streamlines in the vicinity of the drop are closed curves. Recall that a vanishingly small subset of linear flows in the four-dimensional parameter space (but, nevertheless an important set from the rheological perspective), namely the one-parameter family of canonical planar linear flows, exhibit closed streamlines in the near-field around a (spherical) drop, depending on the flow parameter $\hat{\alpha}$ and the viscosity ratio λ. Note that this parameter $\hat{\alpha}$ for canonical planar linear flows has a different definition compared to α and both are related by Eq.2.6. The significance of closed exterior streamlines is known from the works of Acrivos (1971), Poe and Acrivos (1976), that for a rigid particle in the aforementioned planar flows, the Nusselt number plateaus to a Pe-independent value for $Pe \gg 1$, which suggests a diffusion-limited transport. This was also seen to be the case for the interior problem (Chapter 4) with regular closed streamlines. Note that, these closed streamlines are consequences of Stokesian reversibility. Inertial effects in the exterior problem are known to destroy the Stokesian closed-streamline topology, leading to convective enhancement of transport for both solid bodies (Subramanian and Koch (2006a), Subramanian and Koch (2006b)) and drops (Krishnamurthy and Subramanian (2018b)) alike; for Pe large enough that $Re\,Pe \gg 1$ ($Re \ll 1$), Nu scales as $O(Re\,Pe)^{1/3}$ for rigid particles and as $O(Re\,Pe)^{1/2}$ for drops. While inertia is the only source of irreversibility that leads to convective enhancement in the case of rigid particles, one also has irreversible effects arising from interfacial tension for the case of drops. Thus interfacial tension and the associated drop deformation offers another route to destroy the closed streamlines surrounding the drop, although this has not been investigated properly in previous works by several authors. While earlier effects have focused on the role deformation plays in the rheology of the suspension, fewer focus on the streamline topology, despite the fact that the velocity field in the exterior for a deformed drop has been known for a long time, accurate to the second order in the Capillary number that measures the drop deformation. The cause for this lack of attention to the streamline topology may perhaps be attributed to the fact that the experimental work by Torza et al. (1971) had ruled out the possibility of a deformation-induced alteration of the streamline topology. Rather surprisingly, the existence of closed streamlines even at Capillary numbers of order unity was shown by Kennedy and Pozrikidis (1994), using Boundary Element (BEM) simulations and also by some recent numerical simulations using modern techniques like Lattice Boltzmann Method (LBM) (Komrakova et al. (2014)). However, the known analytical velocity field has never been used in any of these studies to investigate the streamline topology, either in the interior or exterior domain.

In this chapter, we revisit this problem, with specific focus on the streamline topology in the exterior of a deformed drop. We use both analytical and numerical tools to to examine the streamline topology around a deformed drop for small but finite Ca, and show that drop deformation indeed alters the nature of streamlines by destroying the Stokesian closed streamline topology. This would imply that, like inertia, deformation too can lead to convective enhancement in the rate of transport (Nu). While inertia converts the closed streamlines into open spiralling ones (that run from upstream to downstream infinity), we find that deformation leads to a more complicated scenario, where a subset of the original closed streamline region contains open spiralling streamlines akin to the inertial case, while, in the remaining part, the spiralling streamlines wind around a configuration of nested invariant tori. The results for the finite-Ca streamline topology have important implications to the problem of heat or mass transfer from a deformed drop, which are briefly discussed in the conclusion to this chapter.

5.1 Drop in Canonical Planar Linear Flows - Streamline Topology

For a drop in a ambient flow that is a member of the canonical planar linear flows, one may either have open or closed streamlines around the drop depending on the relation between viscosity ratio (λ) and the parameter $\hat{\alpha}$. The parameter $\hat{\alpha}$ is a measure of the strength of vorticity to extension and is defined in Eq.3.3. As already noted, the parameter $\hat{\alpha}$, ranges from -1 (solid-body rotation) to 1 (planar extension), with $\hat{\alpha} = 0$, corresponding to simple shear flow. From the work of Powell (1983), it is known that the streamlines around a drop in hyperbolic planar linear flows, are closed for $\lambda > \lambda_c = 2\hat{\alpha}/(1-\hat{\alpha})$, while for drop in elliptic linear flows, all the streamlines remain closed regardless of λ. Therefore, we restrict our discussion to planar hyperbolic linear flows.

In this section, we briefly outline the works of Powell (1983) and Krishnamurthy and Subramanian (2018a), who have analysed the streamline topology in the exterior of the drop suspended in a hyperbolic planar linear flow, in order to lay the ground work for our analysis later in the chapter. As in our previous chapters, the starting point is again the Stokesian velocity field for the drop, which for this particular case is given by:

$$u_r = (1 + \hat{\alpha})(Ar^2 + B)\sin^2\theta\sin 2\phi \tag{5.1}$$

$$u_\theta = \frac{(1 + \hat{\alpha})}{2}rB\sin 2\theta\sin 2\phi \tag{5.2}$$

$$u_\phi = (1 + \hat{\alpha})r\sin\theta(B\cos 2\phi - \beta) \tag{5.3}$$

where $\beta = (1 - \hat{\alpha})/(1 + \hat{\alpha})$. Here the quantities A and B are defined as:

$$\text{Interior} \begin{cases} A &= \frac{-3\lambda}{2(1+\lambda)} + \frac{5\lambda}{2(1+\lambda)}r^2 \\ B &= \frac{-\lambda}{1+\lambda}r^2 \end{cases} \qquad \text{Exterior} \begin{cases} A &= 1 - \frac{\lambda}{(1+\lambda)r^5} \\ B &= \frac{5\lambda}{2(1+\lambda)r^7} - \frac{(5\lambda)+2}{2(1+\lambda)r^5} \end{cases} \tag{5.4}$$

The Stokes streamlines corresponding to Eq.5.1-5.3 may be regarded as the curves of intersection of invariant streamsurfaces (an approach first used in the context of rigid particles by Cox et al. (1968)), and are defined by:

$$\frac{dr}{u_r} = \frac{rd\theta}{u_\theta} = \frac{r\sin\theta d\phi}{u_\phi} \tag{5.5}$$

Integrating the relations between velocities in the r and θ directions, and θ and ϕ directions, one obtains

the equations for the streamsurfaces characterizing the exterior flow as:

$$x_2 = \pm r \left[\frac{\hat{\alpha}}{(1 + \hat{\alpha})} + Ef(r)^2 + \frac{\beta\lambda}{1 + \lambda} f(r)^2 g(r) \right]^{1/2} \tag{5.6}$$

$$x_3 = rCf(r) \tag{5.7}$$

where C and E are the streamsurface labels. Thus the streamlines for a drop in planar linear flows are characterised by two invariants, unlike the case of drop in axisymmetric flows, where a single invariant, the Stokes streamfunction ψ_s characterises the velocity field. Here,

$$f(r) = \left[r^3 + \frac{3\lambda}{2(1 + \lambda)r^2} - \frac{5\lambda + 2}{2(\lambda + 1)} \right]^{-1/3} \tag{5.8}$$

$$g(r) = \int_r^\infty \frac{f(y)}{y^3} dy \tag{5.9}$$

The function $f(r)$ diverges as $r \to \infty$ (i.e. at the drop surface), while $g(r)$ is finite in this limit. Note from Eq.5.6 and 5.7, the constant-C and constant-E surfaces are surfaces of revolution about x_3 and x_2 axes. Similarly for the interior flow, the streamsurfaces are given by:

$$x_2 = \pm r \left[\frac{1}{2} - \frac{\beta(1 + \lambda)}{2r^2} + \hat{E}r^{-2}(1 - r^2)^{-2/3} \right]^{1/2} \tag{5.10}$$

$$x_3 = \hat{C}(1 - r^2)^{-1/3} \tag{5.11}$$

Just like the exterior case, for the interior case too, constant-$\hat{C}$ and constant-$\hat{E}$ surfaces are surfaces of revolution about x_3 and x_2 axis respectively. Since, we are going to be dealing with exterior streamlines in this chapter, we shall only focus on the exterior domain from this point onward and the interested reader is directed to Krishnamurthy and Subramanian (2018a) for the complete characterisation of both interior and exterior streamlines. To characterise the streamlines in terms of these invariants (C, E), we first consider the case of $C = 0$, which is equivalent to $x_3 = 0$ (the equatorial plane). One may nevertheless extract features outside this plane by virtue of the axial symmetry properties of the constant-E and constant-$\hat{E}$ surfaces. Note that $C = 0$, despite denoting the equatorial plane is also the label for the drop surface. Thus the drop corresponds to $(C, E) = (0, E_0 = E|_{r=1})$. Also, note that the vorticity axis x_3, corresponds to a line of fixed points for all $\hat{\alpha}$ and λ.

To begin with, we find the conditions that need to be satisfied by the streamsurface label E in the equatorial plane $C = 0$. In this case, we have the constraint that $0 \le |x_2| \le r$, which leads to the following constraints on E from Eq.5.10:

$$E \le \frac{1}{f(r)^2(\hat{\alpha} + 1)} - \frac{\beta\lambda g(r)}{1 + \lambda} = F_1(r, \hat{\alpha}, \lambda) \tag{5.12}$$

$$E \ge \frac{-\hat{\alpha}}{f(r)^2(\hat{\alpha} + 1)} - \frac{\beta\lambda g(r)}{1 + \lambda} = F_2(r, \hat{\alpha}, \lambda) \tag{5.13}$$

The spatial extent and nature of the streamlines can now be understood based on the behaviour of the functions F_1 and F_2. For a given streamline (identified by the pair of streamline labels, $(C = 0, E)$), one may calculate the interval in the radial coordinate, (r_{min}, r_{max}), for which the above relationships are satisfied. When the lower and upper bounds for the radial coordinate of a streamline are both finite, the streamline must be closed. Open streamlines, on the other hand, are characterized by an interval in the radial coordinate where the upper bound is infinity and the lower bound corresponds to the distance of closest approach.

The behavior of the exterior bounding functions is sketched in Fig.5.1 for $\hat{\alpha} = 0.25$, $\lambda = 10$. From the figure, we see that the exterior bounding function F_1 is a strictly increasing function, starting from $E_0 = -\beta g(1)\lambda/(1 + \lambda)$ at $r = 1$. $F_2(r)$ has the same starting point at $r = 1$, but is non-monotonic, with a maximum E_{sep}, at $r_0 = ((\lambda(1 + \hat{\alpha}))/((1 + \lambda)2\hat{\alpha}))^{1/5}$ (r_0 diverges for simple shear; $\hat{\alpha} = 0$). One can deduce from Eq.5.1-5.3, and owing to the axisymmetry of constant E surfaces, that this location is a fixed circle of the exterior field, lying in the $x_1 - x_3$ plane at a location $(r, \theta, \phi) = (r_0, \theta, (0, \pi))$. Thus, the streamlines with $E > E_{sep}$, have $r_{max} = \infty$ and so correspond to open streamlines running from downstream to upstream ∞. For streamlines with $E_0 \leq E \leq E_{sep} = F_2(r_0)$, fall into two types: (i) for $r < r_0$, they correspond to streamlines with both the bounding radial coordinates (r_{min}, r_{max}) being finite and hence closed streamlines and (ii) for $r > r_0$, they have a finite r_{min}, but $_{max}$ is infinite, and so one has open reversing streamlines. For $E = E_{sep}$, the open and closed branches are part of a separatrix curve, that separates the open streamlines from the closed and reversing streamlines. For this case, we observe that the region of closed streamlines is finite in extent. Finally, when $E < E_0$, the streamlines again have a finite r_{min}, while $r_{max} = \infty$ and they also correspond to open reversing streamlines.

Note that for the special case of $\hat{\alpha} = 0$ (simple shear), since $r_0 = \infty$, $F_2(r_0) = E_{sep} = 0$, any constant-E line with $E_0 < E < E_{sep} = 0$, now corresponds only to a closed streamline. Also, $E < E_0$ for this case lies outside the physical domain and so they do not correspond to any physical streamline. Thus the case of $\hat{\alpha} = 0$ has no open reversing streamlines with the region of closed streamlines and hence the separatrix extending to ∞.
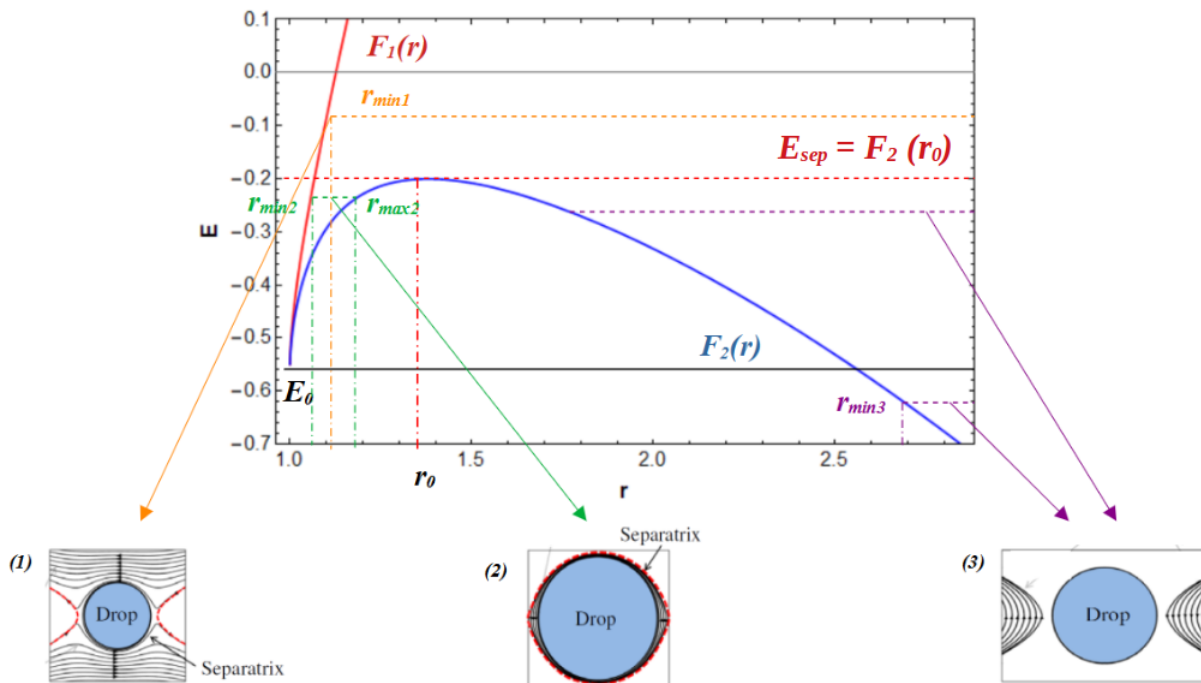
Figure 5.1: Plot of the bounding functions $F_1(r)$, $F_2(r)$ for $\lambda = 10$, $\hat{\alpha} = 0.25$. The red dashed line passing through the maximum of F_2 corresponds to $E = E_{sep}$, the label for separatrix surface. The streamlines corresponding to three different values of E are shown. The first one corresponds to $E > E_{sep}$ (orange dashed line), with open streamlines, the second one corresponds to $E_0 < E < E_{sep}$ with streamlines being closed (green) or open (reversing) ones (purple). For $E < E_0$, (purple line) the streamlines are open (reversing).

While the behavior of the bounding function was analysed for a particular set of parameters before, we

now look at their behavior when $\hat{\alpha}$ is fixed and λ is changed. This is shown in Fig.5.2 for the same value of $\hat{\alpha} = 0.25$, from which we see that as λ is decreased, F_2 transitions from a non-monotonic dependence to becoming a strictly decreasing function (with its maximum value at $r = 1$) for λ below a threshold value (λ_c). The value of this threshold λ_c can be obtained by setting $r_0 = 1$ to give the same expression given in Eq.2.113, which, for the chosen value of $\hat{\alpha} = 0.25$ corresponds to $\lambda_c = 2/3$ (Fig.5.2)(c).
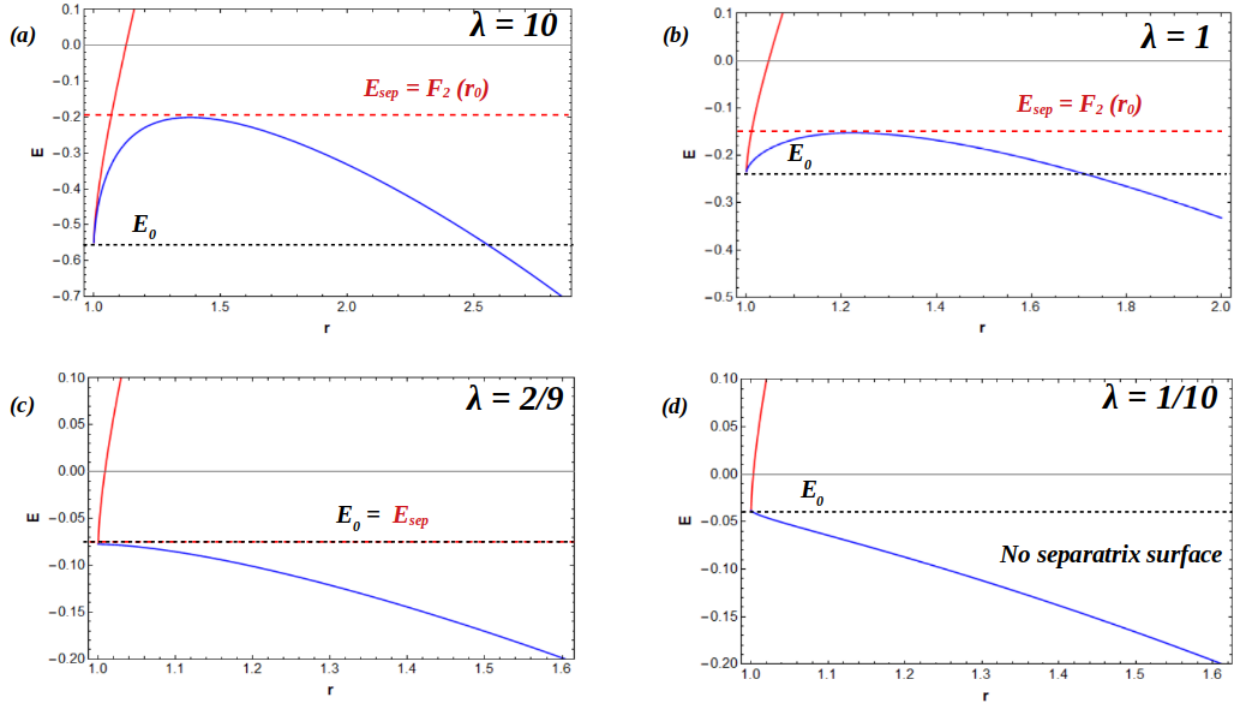
Figure 5.2: Plot of the bounding functions $F_1(r)$ (red), $F_2(r)$ (blue) for $\hat{\alpha} = 0.25$ at different λ. At $\lambda = 2/9 = \lambda_c$ (c), the function $F_2(r)$ becomes strictly decreasing with a maximum at $r = 1$, and for $\lambda < \lambda_c$, the function is no longer non-monotonic, implying that there are no closed streamlines.

Although not shown here, the same thing happens when λ is fixed and $\hat{\alpha}$ is changed and the threshold $\hat{\alpha}_c$ can be similarly obtained by inverting Eq.2.113 as:

$$\hat{\alpha}_c = \frac{\lambda}{2 + \lambda} \tag{5.14}$$

Therefore, in the $\hat{\alpha} - \lambda$ plane, there exists a critical curve that separates closed and open streamline topologies corresponding to $Re = Ca = 0$. This curve is shown in Fig.5.3, and when $\lambda > \lambda_c$ at a given $\hat{\alpha}$, the streamline topology in the near-field around the drop is closed and when $\lambda < \lambda_c$, it is open. Equivalently, when $\hat{\alpha} < \hat{\alpha}_c$ at a given λ, we have closed streamlines around the drop, otherwise the topology consists of open streamlines. From the plot, we see that for $\hat{\alpha} = 1$ (planar extension), all the streamlines around the drop are open as expected and for $\hat{\alpha} = 0$ (simple shear), closed streamlines exist for all λ. Moreover at this value of $\hat{\alpha}$, the radius of the fixed circle r_0 diverges implying that the closed streamlines occupy an infinite volume for simple shear flow. The critical λ given in Eq.2.113 was derived by Powell (1983) and was re-derived by Krishnamurthy and Subramanian (2018a) along the lines mentioned in the previous paragraph.
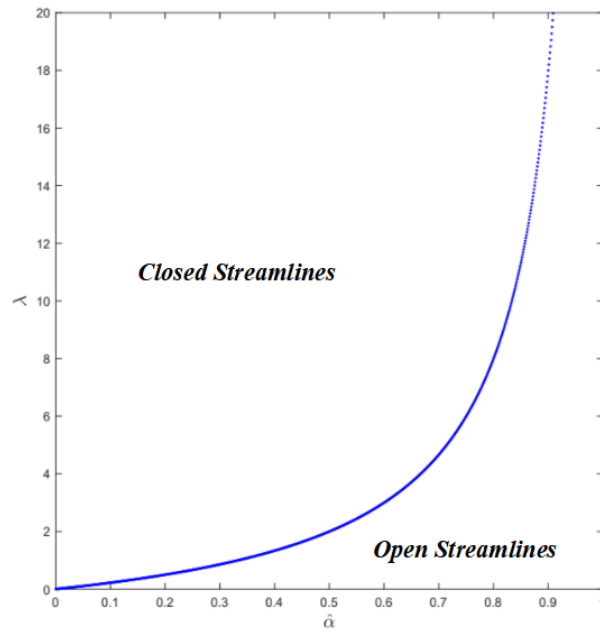
Figure 5.3: Plot of the critical curve in $\hat{\alpha} - \lambda$ plane that demarcates open and closed streamline topologies around the drop.
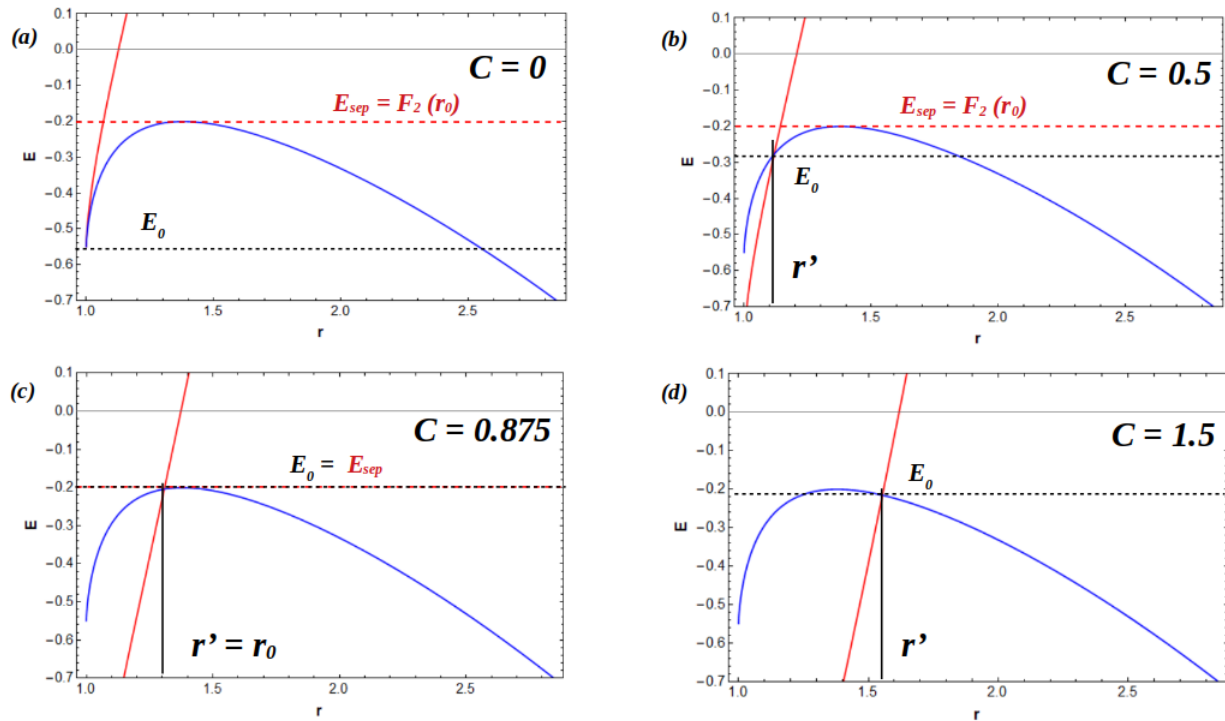
Figure 5.4: Plot of the bounding functions $F_1(r)$ (red), $F_2(r)$ (blue) for $\hat{\alpha} = 0.25$, $\lambda = 10$ at different C values. The streamlines only exist to the right of the intersection between F_1 and F_2 (i.e. $r > r'$). At a critical C value (c), the functions F_1 and F_2 intersect at $r = r_0$, implying that beyond this value of C there are no closed streamlines.

While the aforementioned discussion was restricted to $C = 0$, one can, nevertheless, extend the same

arguments for $C \neq 0$, owing to the axisymmetry of the constant-E surfaces and the relations that need to be satisfied by a streamline whose labels are given by (C, E) is:

$$E \leq \frac{1}{f(r)^2(\hat{\alpha}+1)} - \frac{\beta \lambda g(r)}{1+\lambda} - c^2 = F_1(r, \hat{\alpha}, \lambda) \tag{5.15}$$

$$E \geq \frac{-\hat{\alpha}}{f(r)^2(\hat{\alpha}+1)} - \frac{\beta \lambda g(r)}{1+\lambda} = F_2(r, \hat{\alpha}, \lambda) \tag{5.16}$$

which is derived by subjecting x_2 to the constraint $0 \leq |x_2| \leq \sqrt{r^2 - x_3^2}$. Thus for any finite value of C, the bounding values of E are given by the above equations. In Fig.5.4, we have plotted F_1 and F_2 for $\hat{\alpha} = 0.25$ and $\lambda = 10$, at different values of C. We see from the plot that streamlines only exist beyond the intersection of F_1 and F_2, that happens at $r = r'$. There is a critical value of C at which the intersection coincides with r_0 and beyond this critical value of C, we only have open streamlines. Except for this change, the analysis mentioned before is equally valid for non-zero values of C.

Finally, we put together the results from our discussion of the $C - E$ interpretation of the Stokesian velocity field to plot the physical streamlines in the exterior in Fig.5.5a - 5.6. Keeping in line with our preceding analysis, we first plot the streamlines on the equatorial plane ($x_3 = 0$) before showing the corresponding $3D$ streamlines.
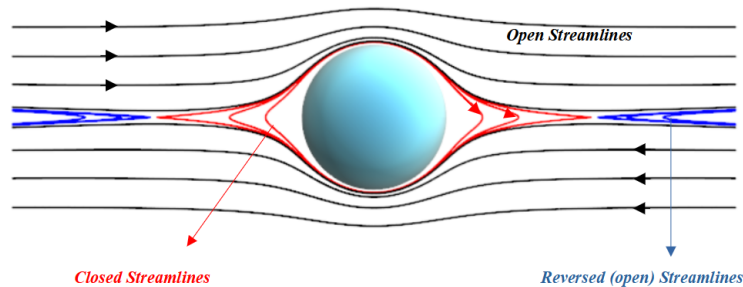
(a) Streamlines on the equatorial plane $x_3 = 0$.
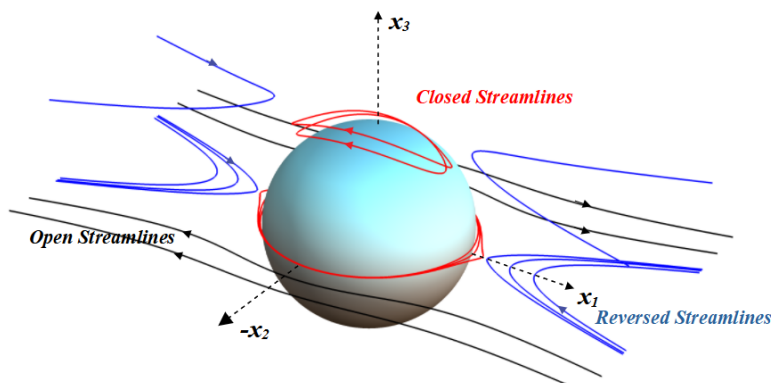
(b) Three-dimensional streamlines.

Figure 5.5: Stokesian streamlines around a drop for $\hat{\alpha} = 0.25$, $\lambda = 10$ (a) on the equatorial plane and (b) the complete three-dimensional topology. Note that for this $\hat{\alpha}$, the extent of closed streamlines is finite.
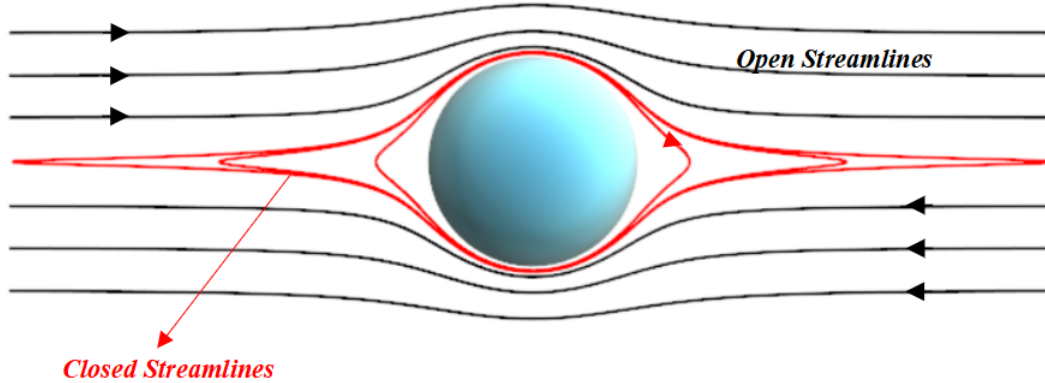
Figure 5.6: Streamlines on the equatorial plane for $\hat{\alpha} = 0$, $\lambda = 10$. For this case, there are no reversed streamlines and the closed streamlines occupy a volume of infinite extent.

We saw earlier that for $\hat{\alpha} \neq 0$, the region of closed streamlines is finite and that there are open reversing streamlines along with streamlines that run from upstream to downstream infinity. This can be seen in Fig.5.5a-5.5b, where the closed streamlines are plotted in red and the reversing streamlines in blue. For $\hat{\alpha} = 0$, the region of closed streamlines is infinite in extent and the topology does not contain open reversing streamlines as seen in Fig.5.6.

The aforementioned analysis suggests that there is an equivalent description for the Stokesian streamlines in terms of these labels C and E, and that one may organize the regions of closed and open streamlines on the $C - E$ plane. In order to do that, we first plot the boundary in this plane, that encloses the closed streamlines, which can be derived from the fact that closed streamlines exist when $E \in [E_0, E_{sep}]$, where E_0 is the intersection of F_1 and F_2, which at $C = 0$ occurred at $r = 1$. For other values of C, we find this intersection E_0 by solving, $F_1(r) = F_2(r)$, to get r', which corresponds to a point on the vorticity axis (and so $r' = x_3$). Therefore, $E_0 = F_1(r')(or\ F_2(r'))$ corresponds to the smallest or minimal closed streamline at a given C. We can plot a curve joining the points (C, E_0) corresponding to each C which gives us the desired boundary and this boundary terminates when $E_0 = E_{sep}$. This point of termination is finite for $\hat{\alpha} \neq 0$ but is infinity for $\hat{\alpha} = 0$. The $C - E$ plane with this boundary marked is shown in Fig.5.7. From the plot, we see that the curve constituting the locus of E_0 until $E_0 = E_{sep}$, along with the horizontal line $E = E_{sep}$ and the line $C = 0$, bound the region of closed streamlines. The region above E_{sep} correspond to open streamlines running from upstream to downstream ∞ and the region below E_{sep} (excluding the closed streamline region corresponds to reversed open streamlines. Also, the point of intersection of this bounding curve with $C = 0$ marks the drop surface.

The advantage of the $C - E$ plane will become apparent once we begin the analysis of the streamline topology for the perturbed system, with either inertia or deformation acting as the perturbation, where we will see that inferring the nature of the streamlines, and organizing them, is more easily done in terms of their representations in the $C - E$ plane (because this representation reduces the dimensionality of the streamlines by one). Note that our focus is on the case where near-field closed streamlines are present around the drop, which corresponds to drop in planar hyperbolic flows $(0 \leq< \hat{\alpha} < 1)$, when $\lambda > \lambda_c$. From the transport perspective, for this case, convection is incapable of transporting heat away on account of the near-field closed streamline topology, and the transport remains diffusion limited even for $Pe \to \infty$. But, when the Stokesian field is subject to these perturbations the closed streamline topology is destroyed, and there is no diffusion limitation and Nusselt will grow as $Pe^{1/2}$, just like in the open streamline regime (Chapter 2). The scaling would actually be $(Re\ Pe)^{1/2}$ for inertia, where the flow-type dependent pre-

factor was already found by Krishnamurthy and Subramanian (2018b), and would be $(Ca\,Pe)^{1/2}$ for the case of drop-deformation, although this analysis has not been done in any of the earlier efforts.
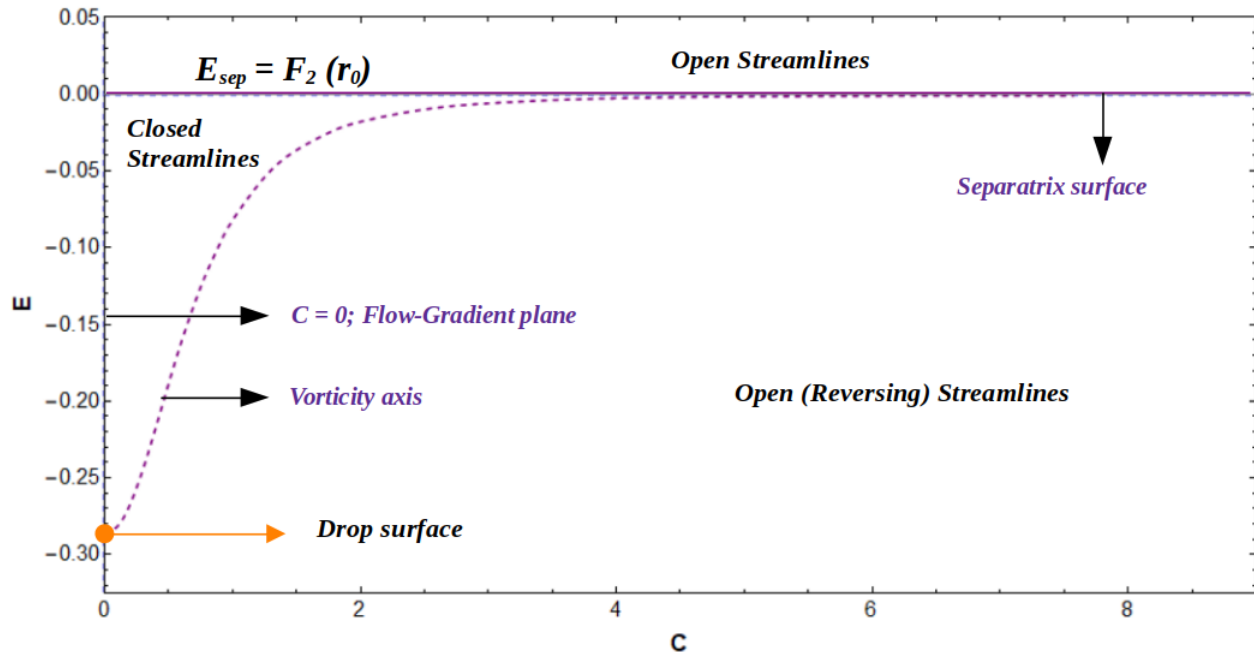
Figure 5.7: The $C - E$ plane for $\hat{\alpha} = 10^{-3}$, $\lambda = 1 > \lambda_c$ showing the various streamline topologies and their region of occurrence.

5.2 Drop in Canonical Planar Linear Flows - The Effect of Inertia

In this section, we will focus on the first one, detailing the nature of the streamlines and its implications for scalar transport to/from the drop. Although the effect of inertia on a drop suspended in a linear flow has been well studied since the pioneering effort of Peery (1966), who derived the first order inertial correction to the Stokesian field for both rigid particles and drops in shear flow, the implication for the Stokesian streamline topology was not recognized at the time. The inertial alteration of the closed streamline topology, where the Stokesian closed streamlines in the vicinity of the drop become spiralling streamlines, and the resulting convective enhancement of transport driven by the inertial flow was first analyzed by Subramanian and Koch (2006b). The authors solved the transport problem for a solid particle suspended in a planar linear flow, in the limit $Re \ll 1$, $RePe \gg 1$ and found that the new 'convective channels' due to inertia, lead to a Nusselt number increasing with Pe as $Nu = 0.325(1 + \hat{\alpha})^{2/3}(Pe\,Re)^{1/3}$ for sufficiently large Pe. Thus, for any Re however small, Nu far exceeds the geometrically determined upper bound attained in the limit $Re = 0$, $Pe \to \infty$ (for $\hat{\alpha} = 0$, this upper bound equals 4.5). Unlike the open streamline regime, where the effects of inertia are perturbative in nature, in the closed streamline regime, inertia modifies the heat transport at leading order. This discovery was crucial because earlier attempts at this problem by (Poe and Acrivos (1975)), have erroneously concluded that weak inertia will not lead to convective enhancement, as they were lead to believe so owing to the fact that in two dimensions the closed-streamlines do not open up due to incompressibility (Robertson and Acrivos (1970a), Kossack and Acrivos (1974)).

More recently, the case of drops in planar linear flows was examined by Krishnamurthy and Subramanian (2018b) in the same limit of $Re \ll 1$, $RePe \gg 1$. As already seen, the Stokesian scenario exhibits both closed and open streamline topologies (depending on whether $\lambda > \lambda_c$ or $\lambda < \lambda_c$ respectively). Trans-

port in the latter case is convectively enhanced leading to the usual $Pe^{1/2}$ scaling. On the other hand, the convective enhancement on the closed-streamline side relies on an inertia-induced alteration of the streamline topology just as for the rigid particle case above. In this section, we first describe the analysis of Krishnamurthy and Subramanian (2018b), in order give a clear picture of the inertia-induced alteration of the Stokesian streamline topology. This will help one better appreciate the streamline topology around a deformed drop and its implications on transport, which is described in the second half of this chapter.

The effect of weak inertia is a well known singular perturbation problem for particle motion in an unbounded domain, as is familiar from the canonical case of a translating sphere for small but finite Re (G. L. Leal (2007)). For a drop in a simple shear flow, the scenario is analogous, although the leading order $O(Re)$ correction to the velocity field on length scales of order the drop size is a regular one. For small but finite Re, the velocity field around the drop can be written as:

$$\boldsymbol{u}(\boldsymbol{x}) = \boldsymbol{u}^{(0)}(\boldsymbol{x}) + Re\boldsymbol{u}^{(1)}(\boldsymbol{x}) + O(Re^{3/2}) \tag{5.17}$$

where the singular role of inertia enters at $O(Re^{3/2})$, and requires explicit consideration of the outer region (Raja et al. (2010)). The $O(Re)$ correction has has been derived by Raja et al. (2010), who have updated the results by Peery (1966), correcting a few minor errors therein. Although only valid for distances from the drop smaller than the inertial screening length of $O(Re^{-1/2})$, this first order correction evidently suffices for purposes of the large-Pe boundary layer analysis which only involves the exterior field in the immediate vicinity of the drop.

As mentioned above, the first order inertial correction to the Stokesian field can be determined using a regular expansion to $O(Re)$, and is given by:

$$\boldsymbol{u}^{(1)}(\boldsymbol{x}) = u_1(r,\lambda)(\boldsymbol{\Gamma}:\boldsymbol{xx})^2\boldsymbol{x} + u_2(r,\lambda)(\boldsymbol{\Gamma}:\boldsymbol{xx})\boldsymbol{\Gamma}.\boldsymbol{x} + u_3(r,\lambda)(\boldsymbol{\Gamma}:\boldsymbol{xx})\boldsymbol{\Gamma^T}.\boldsymbol{x} + u_4(r,\lambda)(\boldsymbol{\Gamma}.\boldsymbol{x})(\boldsymbol{\Gamma}.\boldsymbol{x})\boldsymbol{x}$$

$$+ u_5(r,\lambda)(\boldsymbol{\Gamma}.\boldsymbol{x})(\boldsymbol{\Gamma^T}.\boldsymbol{x})\boldsymbol{x} + u_6(r,\lambda)(\boldsymbol{\Gamma^T}.\boldsymbol{x})(\boldsymbol{\Gamma^T}.\boldsymbol{x})\boldsymbol{x} + u_7(r,\lambda)\boldsymbol{\Gamma}.(\boldsymbol{\Gamma}.\boldsymbol{x}) + u_8(r,\lambda)\boldsymbol{\Gamma^T}.(\boldsymbol{\Gamma^T}.\boldsymbol{x})$$

$$+ u_9(r,\lambda)\boldsymbol{\Gamma^T}.(\boldsymbol{\Gamma}.\boldsymbol{x}) + u_{10}(r,\lambda)\boldsymbol{\Gamma}.(\boldsymbol{\Gamma^T}.\boldsymbol{x}) + u_{11}(r,\lambda)\left(\boldsymbol{\Gamma}:\boldsymbol{\Gamma^T} + \boldsymbol{\Gamma}:\boldsymbol{\Gamma}\right)\boldsymbol{x}$$

$$\tag{5.18}$$

where $\boldsymbol{\Gamma}$ is the transpose of the velocity-gradient tensor of the ambient flow, which for the case of planar linear flows is:

$$\boldsymbol{\Gamma} = \begin{bmatrix} 0 & 2 & 0 \\ 2\hat{\alpha} & 0 & 0 \\ 0 & 0 & 0 \end{bmatrix} \tag{5.19}$$

In Eq.5.18, $\boldsymbol{x}$ is the position vector and the functions $u_i(r,\lambda)$ are functions of the radial distance and viscosity ratio and are given in Raja et al. (2010). This velocity field can be used to plot the exterior streamlines, and those on the drop surface. These are then compared to the Stokesian streamlines already shown in Figs. 5.5a-5.6. We first begin by showing the nature of the $3D$ and surface streamlines for small but finite Re, and then depict them on the $C - E$ plane. We shall borrow many of the results in the inertial streamline topology from the work of Krishnamurthy and Subramanian (2018b) and interpret them in terms of their representation on the $C - E$ plane. Note that, as already mentioned, the results for the inertial alteration of streamlines are only valid on distances smaller than the inertial screening length. Although these suffice for calculating the transport rate at large Pe, the nature of the velocity field in the outer region remains an open question, and is not taken up here.

5.2.1   Exterior Streamlines

We begin by plotting the exterior streamlines (close to the drop) using the velocity field in Eq.5.18. We have plotted the streamlines using $Mathematica^{\circledR}$, which uses an in-built numerical integrator. We

proceed by first choosing a value of λ and then choose a sequence of $\hat{\alpha}$ values extending until $\hat{\alpha}_c$, plotting the streamline pattern for each of these cases. In Fig.5.8-5.10, we have plotted the exterior streamlines for $\lambda = 2$, where we have also showed the separatrix boundary, the curve of intersection of the separatrix surface with the $x_1 - x_3$ plane (red circle of radius $r = r_0$). In Fig.5.8, we have plotted one such spiralling streamline for $\hat{\alpha} = 0$ and $Re = 0.5$, corresponding to simple shear, for which the separatrix boundary is at ∞. Here, we see that the streamline spirals in from infinity along x_3 (vorticity axis) and then escapes to infinity along the flow-gradient plane. In Figs.5.9 and 5.10, corresponding to $\hat{\alpha} = 10^{-4}$ and $\hat{\alpha} = 10^{-1}$, we see that the streamlines still spiral in along the vorticity axis towards the drop and escape along the flow-gradient plane. The key difference with that of Fig.5.8, is that the separatrix boundary is now finite and the streamline is scattered in the vicinity of the boundary $(r = r_0)$, more precisely the saddles on this boundary, which populate this circle. Therefore, the actual topology can be interpreted as follows: an open streamline, that lies outside the separatrix, scatters into the region bound by the separatrix and spirals down along the vorticity axis, before it scatters out again along the flow gradient plane, in the vicinity of another saddle point on the separatrix boundary, to become an open streamline again. As $\hat{\alpha} \to \hat{\alpha}_c$ the region of spiralling streamlines (bound by the separatrix of the Stokesian field) shrinks in size and disappears at $\hat{\alpha}_c$.
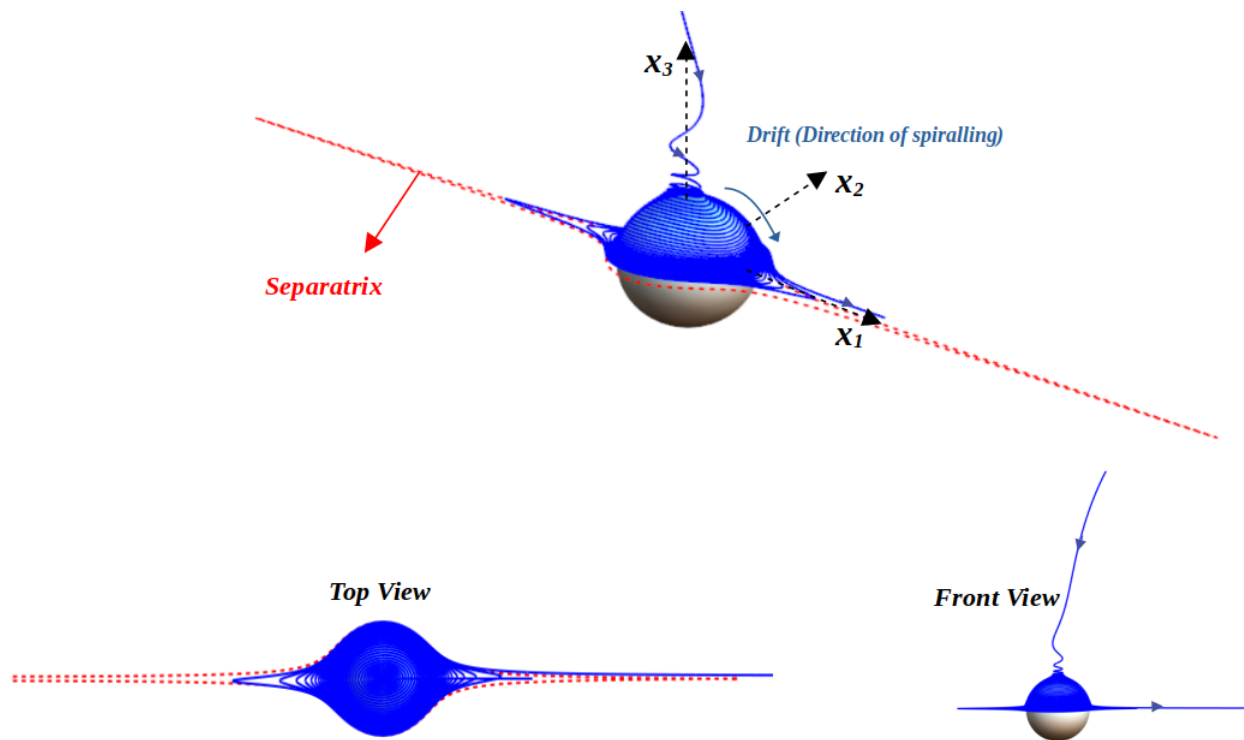
Figure 5.8: Streamline topology in the exterior of the drop for $Re = 0.5$, $\lambda = 2$, $\hat{\alpha} = 0$. The closed streamline topology of the Stokesian field is transformed into spiralling streamlines.
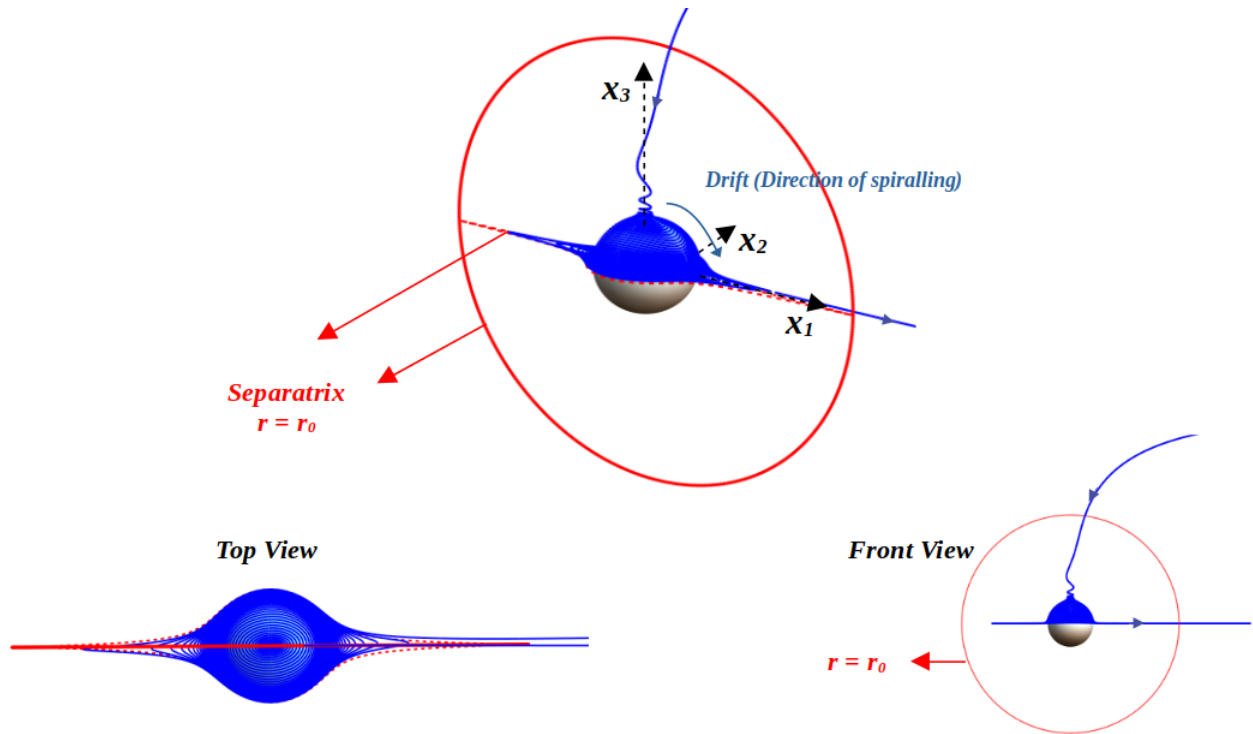
Figure 5.9: Streamline topology in the exterior of the drop for $Re = 0.5$, $\lambda = 2$, $\hat{\alpha} = 10^{-4}$. For this case the streamlines scatter in and out in the vicinity of the saddle point on the separatrix boundary.
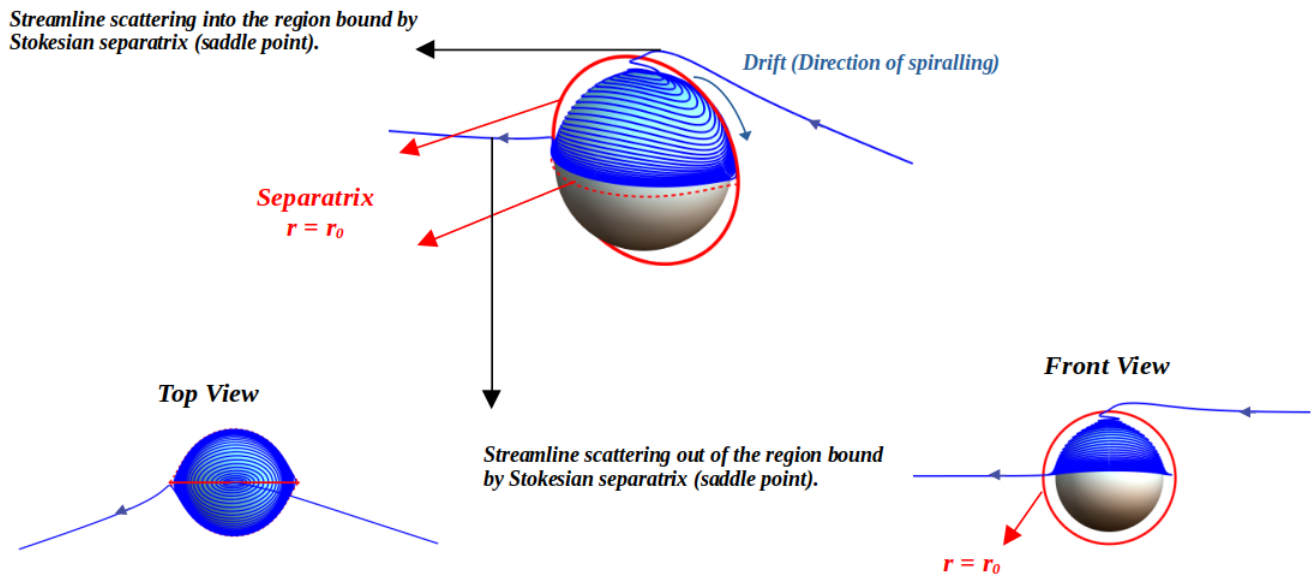
Figure 5.10: Streamline topology in the exterior of the drop for $Re = 0.5$, $\lambda = 2$, $\hat{\alpha} = 10^{-1}$. For this case the streamlines scatter in and out in the vicinity of the saddle point on the separatrix boundary.

When the viscosity ratio λ is increased, the behavior of streamlines is qualitatively similar to the aforementioned one (for $\lambda = 2$), except that the region bound by separatrix (r_0) at a given $\hat{\alpha}$, which encloses the spiralling streamlines, increases in size. The threshold value $\hat{\alpha}_c$ also corresponds to a larger value at a larger λ implying that spiralling streamlines now exist for an extended range of $\hat{\alpha}$. As $\lambda \to \infty$

(solid particle), we see that spiralling streamlines exist for all values of $\hat{\alpha}$ except $\hat{\alpha} = 1$, which is planar extension, consistent with the observation of Subramanian and Koch (2006b). Thus, we see that the original closed streamline topology of the Stokesian field has been destroyed, with the streamlines exhibiting a spiralling character upon addition of inertia.

While the streamline topology described above corresponds to a vast majority of parameter values $(\hat{\alpha}, \lambda)$ in the $\hat{\alpha} - \lambda$ plane above the critical curve ($\lambda = \lambda_c$), Krishnamurthy and Subramanian (2018b) showed that there is a finite region in this plane where the topology is qualitatively different. This region is bounded by two critical curves $\lambda = \lambda_{bif}(\hat{\alpha})$ and $\lambda = \lambda_c(\hat{\alpha})$. In this region ($\lambda_{bif} \geq \lambda \geq \lambda_c$) shown in Fig.5.11 (reproduced from Krishnamurthy and Subramanian (2018b)), which the authors call the 'bifurcated wake regime', the streamlines that spiral down along the vorticity axis, scatter off and escape to infinity at an intermediate location instead of along the flow-gradient plane. Correspondingly, to satisfy incompressibility, the streamlines now spiral toward the drop on the flow-gradient plane and scatter off to infinity along the same intermediate location.
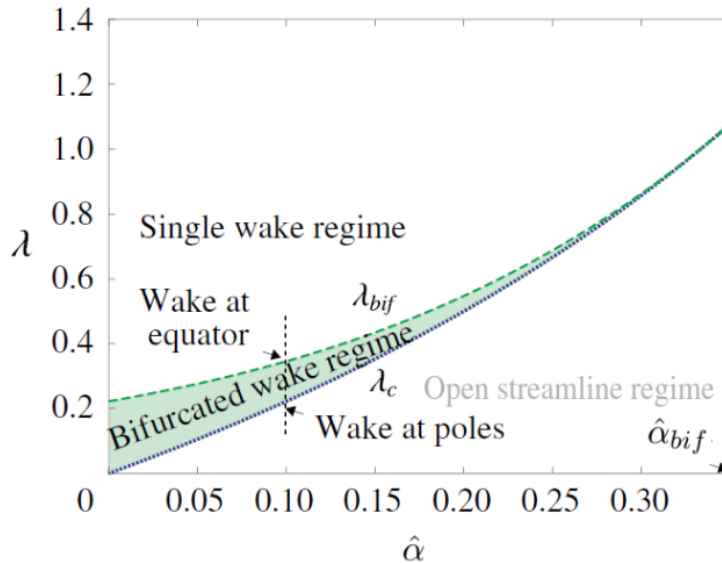
Figure 5.11: The $\hat{\alpha} - \lambda$ plane showing the single and bifurcated wake regime. This figure is reproduced from Krishnamurthy and Subramanian (2018b) with permission.

Thus, in this case, the fluid particles flow towards the drop along two different directions and escape to infinity at an intermediate direction. This is shown in Fig.5.12 for $Re = 0.5$, $\hat{\alpha} = 0.1$ and $\lambda = 0.3$, which conforms to $\lambda < \lambda_{bif} \approx 0.35$. Krishnamurthy and Subramanian (2018b) showed that $\lambda_c = \lambda_{bif}$ at $\hat{\alpha} = \hat{\alpha}_{bif} \approx 0.35$, beyond which, the bifurcated wake regime does not exist. The reason for calling this regime the bifurcated wake regime is rooted in the fact that the boundary corresponding to this regime exhibit two inlets and a wake, which bifurcates and is lifted off the symmetry plane.
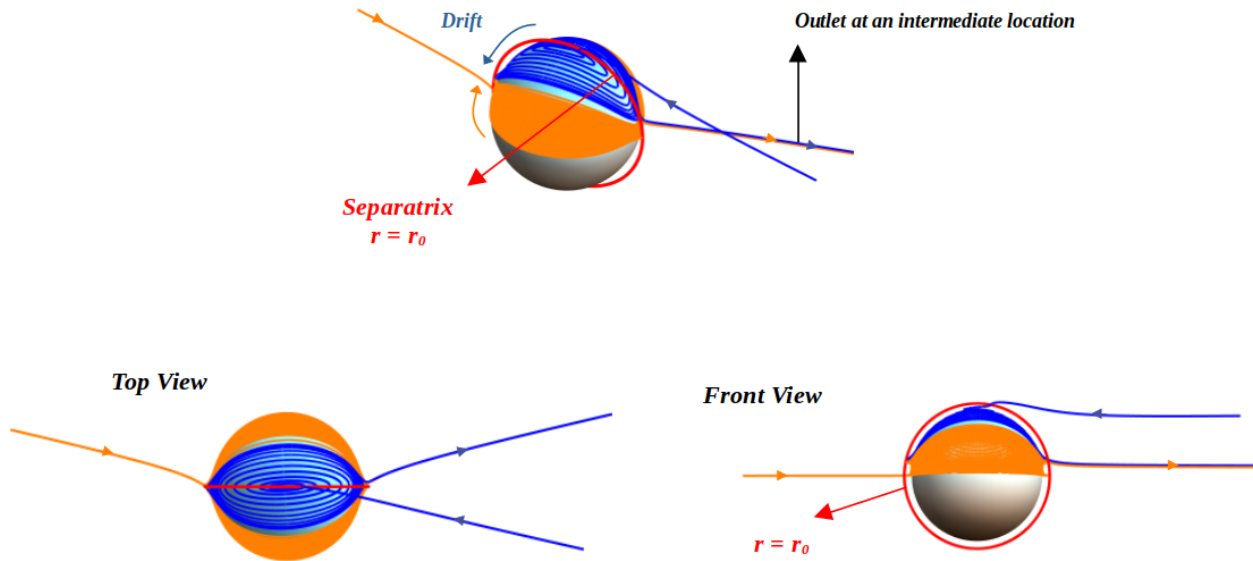
Figure 5.12: Streamline topology in the exterior of the drop for $Re = 0.5$, $\lambda = 0.3$, $\hat{\alpha} = 0.1$, corresponding to the bifurcated wake regime. For this case the streamlines spiral in along both vorticity axis and the flow-gradient plane and leave along an intermediate direction.

5.2.2   Surface Streamlines

Even though we had explained the nature of exterior streamlines for a weakly inertial drop in planar linear flow, it is the surface streamlines that is of interest to the transport problem at large Pe, as in the case of the drop in open streamline flows (for instance, those examined in Chapter 2). A detailed analysis of the inertial surface-streamline topology was carried out by Krishnamurthy and Subramanian (2018b) and the interested reader is directed to their work. Here we shall briefly describe the surface-streamline topology and how it connects with the exterior topology described in Section 5.2.1. Recall that in the exterior, the velocity field used was invalid outside a region of $r \sim O(Re^{-1/2})$, but this restricted validity is of no consequence to the surface velocity field. Krishnamurthy and Subramanian (2018b) use this velocity field to examine the surface flow, and observed that the surface streamlines exactly mirror the behavior the exterior streamline topology. Like the exterior streamlines, the surface streamlines also exhibit two kinds of behavior. For $\lambda > \lambda_{bif}$, the streamlines are spirals running from the pole ($\theta = 0$) to the equator ($\theta = \pi/2$) of the spherical drop. In the bifurcated wake regime, the streamlines spiral down from the pole and spiral up from the equator and both branches terminate at an intermediate curve $\theta = f(\phi)$ on the spherical drop surface, that serves as the wake. These features are shown in Figs.5.13-5.14, for $\hat{\alpha} = 0$, and $\hat{\alpha} = 0.1$ respectively with $Re = 0.5$. From the plots, we observe that the wake is bifurcated when $\lambda < \lambda_{bif}$ and is otherwise located on the equator. The spiralling character of surface streamlines can be interpreted as inertia-induced drifts across the closed orbits associated with the Stokesian field of a drop suspended in planar linear flows.
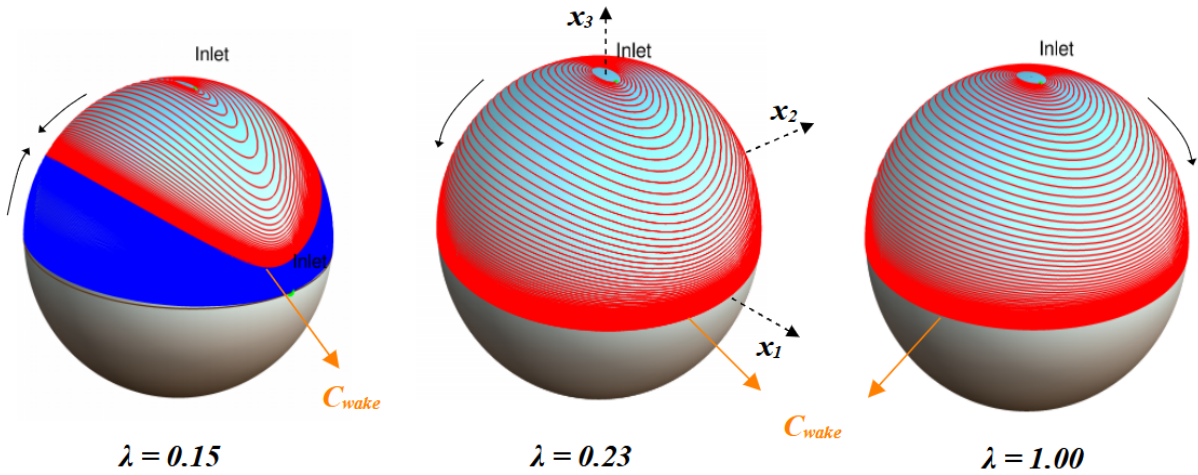
Figure 5.13: Surface streamlines for $Re = 0.5$, $\hat{\alpha} = 0$. The threshold viscosity ratio $\lambda_{bif} \approx 0.21$.
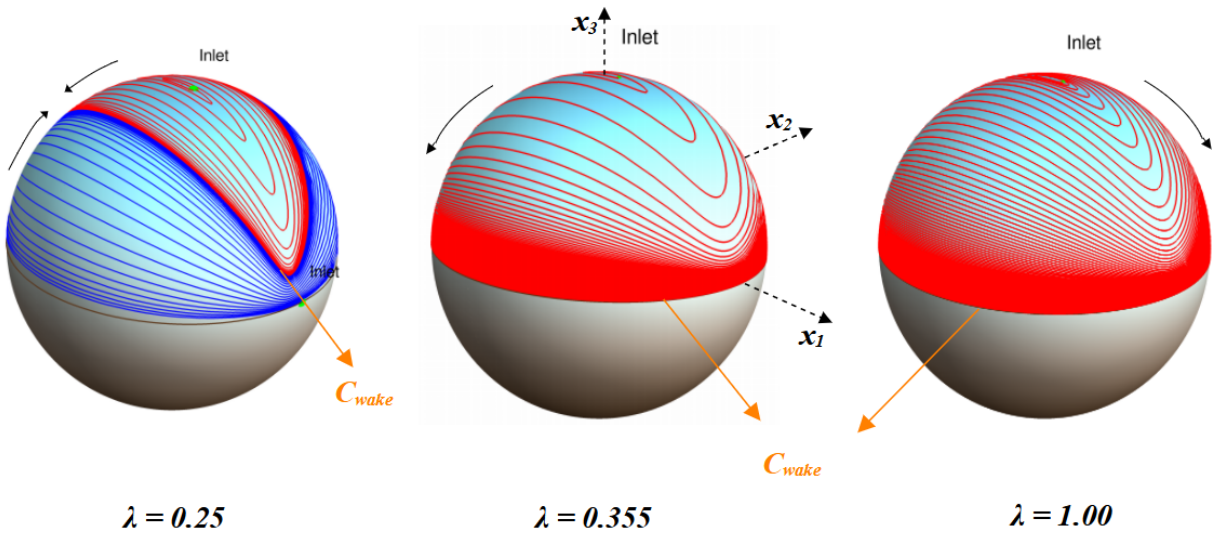
Figure 5.14: Surface streamlines for $Re = 0.5$, $\hat{\alpha} = 0.1$. The threshold viscosity ratio $\lambda_{bif} \approx 0.35$.

The authors use insights from the surface streamline topology described above, and develop a surface-streamline-aligned $\hat{C} - \tau$ coordinate system, to solve the problem of convective transport from a drop. Here $\hat{C}$ is the analog of the orbit constant for Jeffery orbits, which now acts as a label for surface streamlines for planar linear flows (the coordinate $\hat{C}$ is the same as the coordinate C used earlier in Chapters 2 and 3, but restricted to the case of planar linear flows). Thus, the wake of the boundary layer (the limiting curve at which the surface streamlines terminate) corresponds to a Stokesian surface streamline (a Jeffery orbit). Thus is terms of the surface streamline coordinates ($\hat{C} - \tau$ coordinates), the location of the wake corresponds to an orbit constant $\hat{C}_{wake}$. The location of the wake arising from the inertial convection may be calculated using the fact that the tangential flux (at the surface) goes to zero, and in addition, the fluid drifts radially outwards at this location. Thus, $\hat{C}_{wake}$ is determined by the equation:

$$\int u_{\hat{C}}^{(1)}(\hat{C}_{wake}, \tau) \, d\tau \;=\; 0 \tag{5.20}$$

where $u_{\hat{C}}^{(1)}$ is the inertia-induced correction to the drift velocity on the drop surface. The aforementioned equation, together with the fact that the wake moves from an intermediate closed orbit (for $\lambda_c < \lambda < \lambda_{bif}$

to the equator at λ_{bif}, i.e. $\hat{C}_{wake} \to \infty$ as $\lambda \to \lambda_{bif}$, was used by the authors to determine the boundary separating the bifurcated and single wake regimes in the $\hat{\alpha} - \lambda$ plane.

5.2.3 The $C - E$ Representation for the Inertial Streamlines

Recall that the Stokesian streamlines were intersections of two streamsurfaces of revolution (the constant-C and constant-E surfaces, and in this regard, the $C - E$ plane was introduced (see Fig.5.7) to organize the different Stokesian streamlines. In this plane a point (C, E) corresponded to a particular Stokesian streamline. We had seen that with the addition of inertia, the Stokesian closed streamlines become spiralling ones. There are two time scales associated with a spiralling inertial streamline: (i) the Stokesian time scale $t_f \sim \dot{\gamma}^{-1}$, which characterises the circulation around a closed streamline and, (ii) the drift time scale $t_d \sim O(\dot{\gamma}^{-1}Re)$ characterising the inertia-induced drift across the closed streamlines. As can be seen, these two timescales are widely separated with $t_d \gg t_f$. While C and E, by definition, were constants of motion in the Stokesian limit, for small but finite Re, they are no longer constant but instead slowly varying functions of time, the variation being on the aforementioned drift time scale of $O(\dot{\gamma}^{-1}Re)$ and are termed adiabatic invariants. The equations governing the variation of these invariants may derived using the method of averaging (Bajer and Moffat (1990)). This method exploits the separation between the underlying time scales, so as to average out the dynamics on the fast time scale, leading to equations governing the adiabatic invariants on the slow time-scale.

Therefore, while the Stokesian closed streamlines corresponded to a point (C, E) on the $C - E$ plane, the inertial streamlines, as characterised by a time-varying C and E, will correspond to curves in the plane. In order to plot these trajectories in the $C - E$ plane, one must derive the equation governing C and E in terms of the velocity field and time t. To derive this equation, we start with the definitions of C and E given in Eq.5.10 and Eq.5.11, which we can rewrite as:

$$C = \frac{\cos\theta}{f(r)} \tag{5.21}$$

$$E = \frac{1}{f(r)^2}\left(\sin^2\theta\sin^2\phi - \frac{\hat{\alpha}}{(1+\hat{\alpha})} - \frac{\beta\lambda}{1+\lambda}f(r)^2 g(r)\right) \tag{5.22}$$

where we have written x_2 and x_3 in terms of spherical coordinates (r, θ, ϕ). This equation gives the relation between the spherical coordinates and the invariants C and E, and can be used to rewrite the velocity field,

$$\frac{d\boldsymbol{x}}{dt} = \boldsymbol{u}^{(0)}(\boldsymbol{x}) + Re\,\boldsymbol{u}^{(1)}(\boldsymbol{x}) \tag{5.23}$$

in terms of these invariants. This can be done by differentiating differentiating Eqs.5.21-5.22 with respect to time and substituting for the velocity field to get:

$$\frac{dC}{dt} = \mathcal{F}_0(C, E, r) + Re\,\mathcal{F}_1(C, E, r) \tag{5.24}$$

$$\frac{dE}{dt} = \mathcal{G}_0(C, E, r) + Re\,\mathcal{G}_1(C, E, r) \tag{5.25}$$

where the functions $\mathcal{F}_0(C, E, r)$, $\mathcal{G}_0(C, E, r)$, $\mathcal{F}_1(C, E, r)$ and $\mathcal{G}_1(C, E, r)$ are given by:

$$\mathcal{F}_0(C, E, r) = \frac{1}{f(r)^2} \left(\sin\theta f(r) u_\theta^{(0)} + \cos\theta f'(r) u_r^{(0)} \right) = 0, \tag{5.26}$$

$$\mathcal{F}_1(C, E, r) = \frac{1}{f(r)^2} \left(\sin\theta f(r) u_\theta^{(1)} + \cos\theta f'(r) u_r^{(1)} \right) = 0, \tag{5.27}$$

$$\mathcal{G}_0(C, E, r) = u_\theta^{(0)} I_1 + u_r^{(0)} I_2 + u_\phi^{(0)} I_3, \tag{5.28}$$

$$\mathcal{G}_1(C, E, r) = u_\theta^{(1)} I_1 + u_r^{(1)} I_2 + u_\phi^{(1)} I_3, \tag{5.29}$$

with,

$$I_1 = f(r)^2 \sin^2\phi \sin(2\theta), \tag{5.30}$$

$$I_2 = (2f(r)f'(r))(\frac{\alpha}{1+\alpha} - \sin^2\phi \sin^2\theta)) + (\frac{\beta\lambda f(r)^5}{(1+\lambda)r^3}), \tag{5.31}$$

$$I_3 = f(r)^2 \sin^2\theta \sin(2\phi). \tag{5.32}$$

Here, $u_i^{(0)}$ and $u_i^{(1)}$ correspond to the components of Stokesian field (Eq.5.1-5.3) and the inertial correction (Eq.5.18) respectively. The leading order terms are identically zero because, C and E are invariants for the Stokesian field and so Eq.5.24-5.25 reduce to:

$$\frac{dC}{dt} = Re\ \mathcal{F}_1(C, E, r), \tag{5.33}$$

$$\frac{dE}{dt} = Re\ \mathcal{G}_1(C, E, r). \tag{5.34}$$

In the two equations above, one can pull Re to the LHS to give $\hat{t} = Re\ t$, which is the slow time scale in our scenario. In order to get the averaged equations, we average over the fast time scale (t) to get:

$$\frac{dC}{d\hat{t}} = \bar{\mathcal{F}}_1(C, E, r) = \frac{1}{t_{period}} \int_0^{t_{period}} \mathcal{F}_1(C, E, r)\ dt, \tag{5.35}$$

$$\frac{dE}{d\hat{t}} = \bar{\mathcal{G}}_1(C, E, r) = \frac{1}{t_{period}} \int_0^{t_{period}} \mathcal{G}_1(C, E, r)\ dt. \tag{5.36}$$

Note that the integration over t can be equivalently converted to an integration over r, by a change of variables as:

$$\int_0^{t_{period}} dt = \int_{r_{min}}^{r_{max}} \frac{dt}{dr} dr = \int_{r_{min}}^{r_{max}} (u_r)^{-1} dr, \tag{5.37}$$

where, to the first order u_r can be taken as $u_r^{(0)}$. Thus using the velocity field in Eq.5.18, we get:

$$\frac{dC}{d\hat{t}} = -\frac{\int_{r_{min}}^{r_{max}} \left(\sin\theta f(r) u_\theta^{(1)} + \cos\theta f'(r) u_r^{(1)} \right) f(r)^{-2} (u_r^{(0)})^{-1} dr}{\int_{r_{min}}^{r_{max}} (u_r^{(0)})^{-1} dr}, \tag{5.38}$$

$$\frac{dE}{d\hat{t}} = \frac{\int_{r_{min}}^{r_{max}} \left(u_\theta^{(1)} I_1 + u_r^{(1)} I_2 + u_\phi^{(1)} I_3 \right) (u_r^{(0)})^{-1} dr}{\int_{r_{min}}^{r_{max}} (u_r^{(0)})^{-1} dr}. \tag{5.39}$$

The limits that occur in the integration are again functions of C and E, which makes Eqs.5.38-5.39 a $2D$ autonomous system of ODEs at leading order, whose natural representation is in the $C - E$ plane. One can find the limits r_{min} and r_{max} by solving the equations:

$$\left[\frac{\hat{\alpha}}{(1 + \hat{\alpha})} + Ef(r_{min})^2 + \frac{\beta\lambda}{1 + \lambda} f(r_{min})^2 g(r_{min}) \right] = 0, \tag{5.40}$$

$$\left[\frac{\hat{\alpha}}{(1 + \hat{\alpha})} + Ef(r_{max})^2 + \frac{\beta\lambda}{1 + \lambda} f(r_{max})^2 g(r_{max}) \right] = 1 - C^2 f(r_{max})^2 \tag{5.41}$$

which are again derived from the definitions of C and E by setting $\phi = 0$ and $\phi = \pi/2$ in Eq.5.10 respectively.

Having derived the governing differential equations, we proceed with the integration of $dC/d\hat{t}$ and $dE/d\hat{t}$ numerically. We first choose an initial condition on a given spiralling streamline, and determine the corresponding initial point (C_0, E_0) in the $C - E$ plane. Using these initial conditions, Eq.5.38-5.39 are integrated using $Mathematica^{\circledR}$ and the solution trajectories in the $C - E$ plane are plotted. In Fig.5.15 and Fig.5.16, we have show the trajectories corresponding to multiple initial conditions (multiple spiralling streamlines) for $\hat{\alpha} = 10^{-3}$, $\lambda = 1 > \lambda_{bif}$ and $\hat{\alpha} = 10^{-3}$, $\lambda = 0.1 < \lambda_{bif}$, corresponding to the single wake and the bifurcated wake regimes respectively. From the plot we see that the trajectories in the $C - E$ plane are open, where they originate and terminate at the separatrix, which is represented by a horizontal line E_{sep} (see discussion in Section 5.1 on the Stokesian streamline topology) and are consistent with the spiralling character of the streamlines. The trajectories from the method of averaging do not cross this boundary as the period of rotation diverges as the streamline approaches the separatrix $(E \to E_{sep})$.
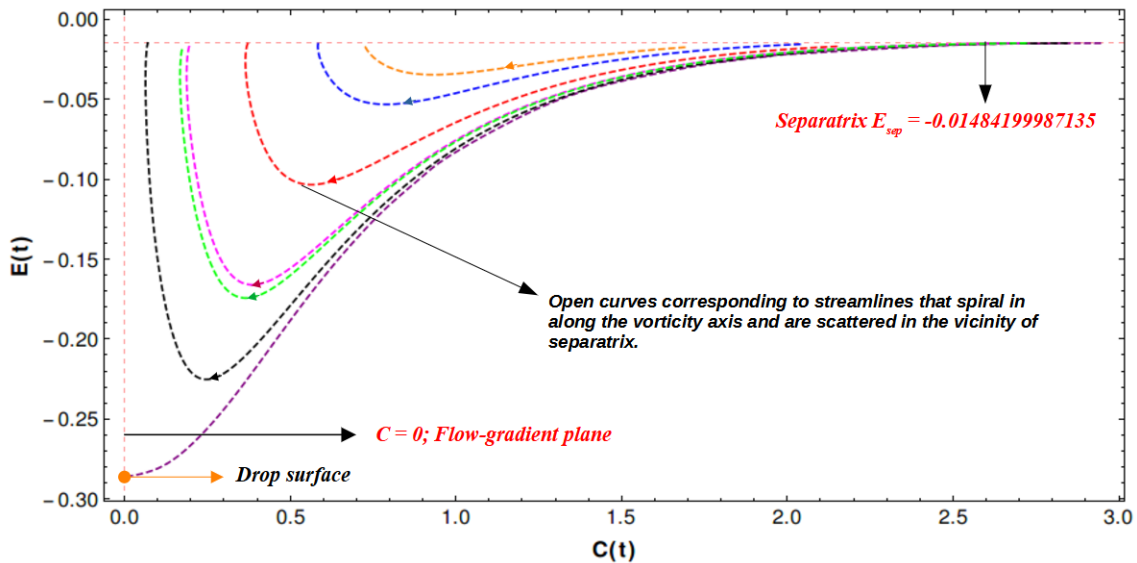
Figure 5.15: $C - E$ plane for $\hat{\alpha} = 10^{-3}$, $\lambda = 1 > \lambda_{bif}$. This corresponds to the single wake regime, and in the $C - E$ plane the spiralling streamlines appear as open trajectories running to and from the separatrix surface (horizontal red dashed line).
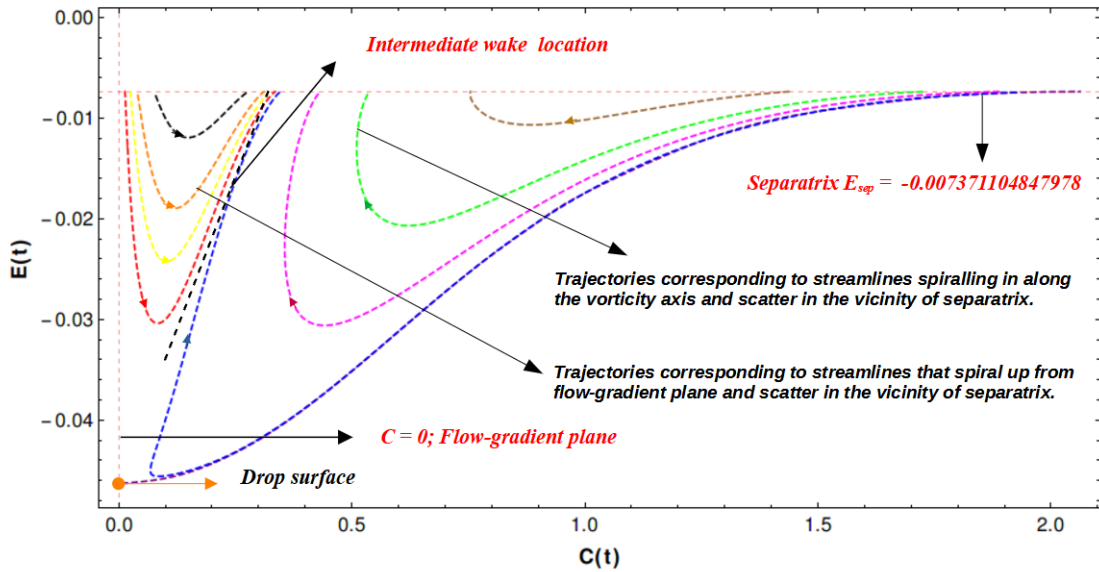
Figure 5.16: $C - E$ plane for $\hat{\alpha} = 10^{-3}$, $\lambda = 0.1 < \lambda_{bif}$. This corresponds to the bifurcated wake regime, and in the $C - E$ plane the spiralling streamlines appear as trajectories running to and from the separatrix surface (horizontal red dashed line), but with two sets of curves running in opposite direction, corresponding to the two inlet streams.

We also compare the trajectories in the $C - E$ plane obtained by the averaging analysis with the ones calculated using the full velocity field in Fig.5.17. Note that in the latter, the trajectories not only cross the separatrix, but also continue to move along vertical lines (i.e constant-C lines). This however is not a physical behavior as, in the physical domain, once the spiralling streamlines scatter from the separatrix, they merge with a Stokesian open streamline and escape to infinity. This would imply that the corresponding trajectory in the $C - E$ plane terminate at a point. This is, however, not what we observe and it can be attributed to the fact that the inertial velocity field Eq.5.18, does not decay to zero as $r \to \infty$ and is therefore invalid outside the inertial screening length ($O(Re^{-1/2})$). This leads to the aforementioned unphysical behavior in the $C - E$ plane.
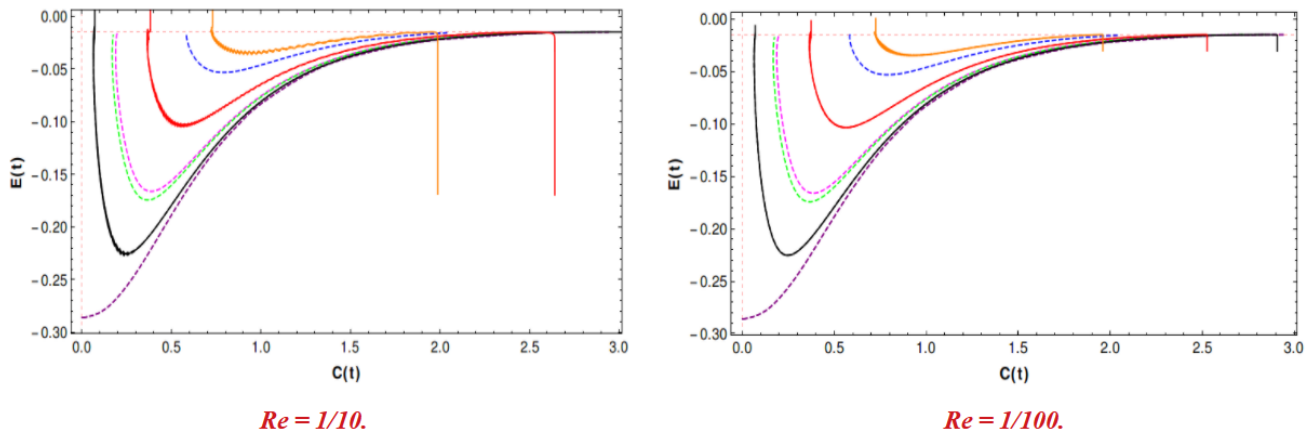
Figure 5.17: $C - E$ plane for $\hat{\alpha} = 10^{-3}$, $\lambda = 1 > \lambda_{bif}$. The trajectories from the averaging analysis are compared with solution from full integration for two different Re. Note as Re decreases, the fluctuations on the full-integration trajectories decrease in amplitude.

This behavior, however, would be absent for the case of simple shear $\hat{\alpha} = 0$, as the separatrix for this case extends to infinity and thus the trajectories in the $C - E$ plane (both the averaged and actual ones) never cross the separatrix line ($E_{sep} = 0$ for $\hat{\alpha} = 0$).

The divergence of time period of a Stokesian streamline in the vicinity of the separatrix can be shown rigorously using the definitions we have encountered before. The time period of a Stokesian streamline is given by:

$$
\begin{aligned}
t_{period} &= 4 \int_{r_{min}}^{r_{max}} (u_r^{(0)})^{-1} dr \\
&= \int_{r_{min}}^{r_{max}} \frac{r^2 f(r) \, dr}{\left[\frac{\hat{\alpha}}{(1+\hat{\alpha})f(r)^2} + \beta \left(E + \frac{\beta\lambda}{1+\lambda} g(r) \right) - f(r)^2 \left(E + \frac{\beta\lambda}{1+\lambda} g(r) \right)^2 \right]^{1/2}}.
\end{aligned}
\tag{5.42}
$$

The denominator D of the integrand diverges as $r \to r_{min}$ and $r \to r_{max}$. The nature of the divergence can be extracted by expanding the denominator about r_{min} and r_{max} as:

$$
D = (D)_{r_{max}} + \left(\frac{dD}{dr} \right)_{r_{max}} (r - r_{max}) + O(r - r_{max})^2
\tag{5.43}
$$

$$
D = (D)_{r_{min}} + \left(\frac{dD}{dr} \right)_{r_{min}} (r - r_{min}) + O(r - r_{min})^2
\tag{5.44}
$$

One can easily show that:

$$
\left(\frac{dD}{dr} \right)_{r_{max}} = - \left(\frac{dF_2(r)}{dr} \right)_{r_{max}},
\tag{5.45}
$$

$$
\left(\frac{dD}{dr} \right)_{r_{min}} = - \left(\frac{dF_2(r)}{dr} \right)_{r_{min}},
\tag{5.46}
$$

where,

$$
F_2(r) = \frac{\hat{\alpha}}{(1 + \hat{\alpha})f(r)^2} - \frac{\beta\lambda}{1 + \lambda} g(r).
\tag{5.47}
$$

Therefore, one has:

$$
\left(\frac{dF_2(r)}{dr} \right)_{r_{max}} = \begin{cases} 0 \text{ as } E \to E_{sep} \\ \text{finite } \forall \ E \neq E_{sep} \end{cases}
\tag{5.48}
$$

$$
\left(\frac{dF_2(r)}{dr} \right)_{r_{min}} = \text{finite} \ \forall \ E.
\tag{5.49}
$$

This implies that the integrand,

$$
\frac{f(r)r^2}{D^{1/2}} \begin{cases} \sim O(r - r_{max})^1 \text{ for } E \to E_{sep}, \\ \sim O(r - r_{max})^{1/2} \text{ for } E \neq E_{sep}, \end{cases}
\tag{5.50}
$$

$$
\frac{f(r)r^2}{D^{1/2}} \sim O(r - r_{min})^{1/2} \ \forall \ E.
\tag{5.51}
$$

This has been verified by calculations and can be seen in Fig.5.18, where $D^{1/2}$ is plotted as a function of $r - r_{min}$ and in Fig.5.19, where we plot it against $r_{max} - r$. The change of scaling from $1/2$ to 1 is clearly

seen as $E \to E_{sep}$ when $r \to r_{max}$. This shows that a trajectory approaching the separatrix undergoes a logarithmic divergence in the time period, i.e. $t_{period} \sim \log((r_{max} - r)(E - E_{sep}))$. Thus, the trajectories calculated using the method of averaging never cross the separatrix, even though the actual streamlines will.
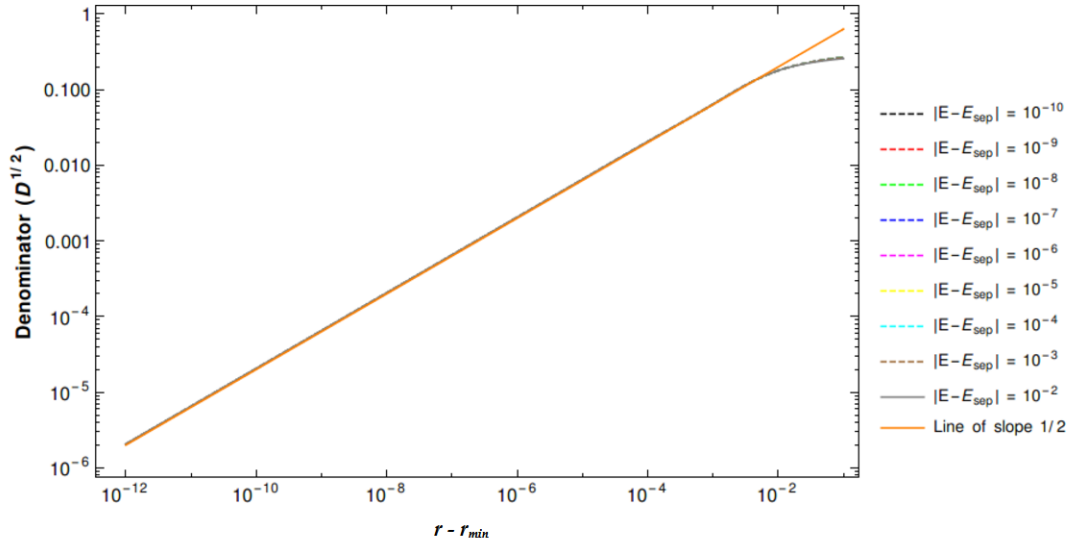
Figure 5.18: The denominator of the integrand $D^{1/2}$ plotted against $r - r_{min}$ for $\hat{\alpha} = 10^{-1}$, $\lambda = 1$. As $E \to E_{sep}$, the denominator scales as $O(r - r_{min})^{1/2}$, implying an integrable singularity.
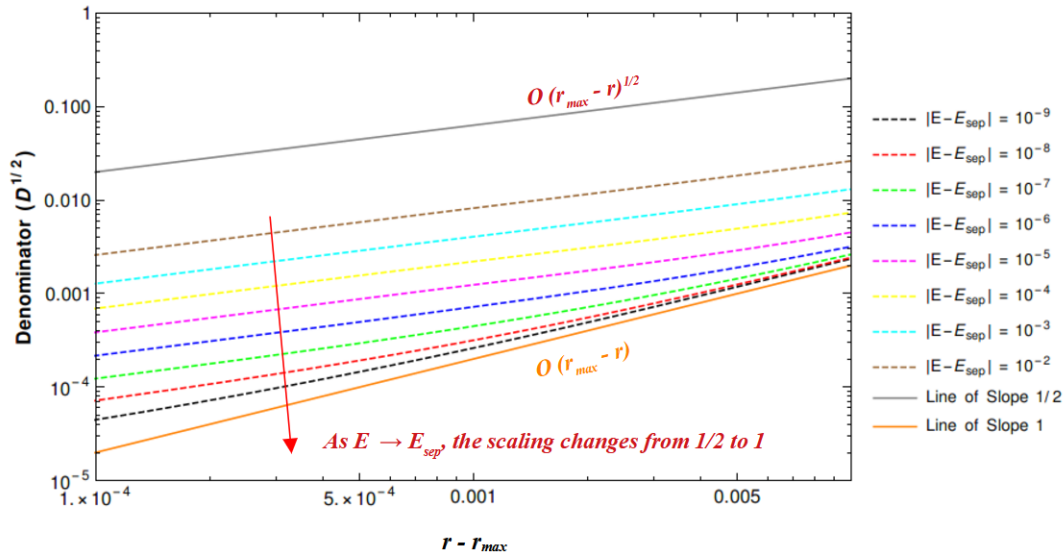
Figure 5.19: The denominator of the integrand $D^{1/2}$ plotted against $r_{max} - r$ for $\hat{\alpha} = 10^{-1}$, $\lambda = 1$. As $E \to E_{sep}$, the denominator scales as $O(r - r_{min})$, implying a logarithmic divergence of t_{period}.

This concludes the discussion on the effect of weak inertia ($Re \ll 1$) on the Stokesian streamline topology. We now move on to consider the effect of drop deformation ($Ca \ll 1$) on the Stokesian topology and it's implications to transport.

5.3 A Weakly Deformed Drop in Canonical Planar Linear Flows - Effect of Drop Deformation

The fact that weak inertial effects induce a non-trivial alteration of the Stokesian closed streamline topology points to the non-trivial role of drop deformability. Both are departures from the reversible Stokesian scenario. That the drop deformability, or equivalently, interfacial tension forces, is a source of irreversibility may be seem from the fact that these forces drive a drop towards sphericity regardless of the sense of the ambient shear flow. The role of drop deformability was one of the issues addressed by Torza et al. (1971) in their experimental effort, and the authors concluded, rather surprisingly, that weak drop deformation does not alter the streamline topology. This conclusion appeared to be validated by later computational efforts of Kennedy and Pozrikidis (1994) and, Komrakova et al. (2014). But there have been no confirmation of this fact or otherwise by any analytical studies on suspension of drops, of which there have been many. G. I. Taylor (1932) was the first to analytically calculate the steady state deformation of the drop in simple shear flow, which later extended by him to the case of drop in planar extension (G. I. Taylor (1934)). It is important to note here that drop deformation can be controlled either due to a small Ca or a large λ. Ca is the Capillary number defined as $Ca = \mu a |\mathbf{\Gamma}|/\sigma$, which is the ratio of viscous forces to surface (interfacial) tension forces and λ is the viscosity ratio. Thus, the deformation of the drop can be due to small Ca (with $\lambda \sim O(1)$; interfacial tension is dominant) or large λ (with Ca arbitrary; viscosity is dominant). Taylor had considered both the cases of dominant interfacial tension ($Ca \ll O(1)$, $\lambda \sim O(1)$, such that $\lambda.Ca \ll 1$) and dominant viscosity ($1/\lambda \ll O(1)$, $Ca \gg 1$, such that $\lambda.Ca \gg 1$) and had calculated the deformation for each of these cases. In the former case, Taylor found that the drop is a triaxial ellipsoid with its longest axis aligned with the extensional axis of simple shear and in the latter case it is an ellipsoid with its longest axis aligned along the flow direction. The above clearly shows that the inclination of the principal axis is a function of $\lambda.Ca$, asymptoting to $\pi/4$ for $\lambda.Ca \ll 1$, and to 0 for $\lambda.Ca \gg 1$.

Cox (1969) extended Taylor's work and demonstrated that, at steady state, the inclination of the principal axis could be oriented at any angle between 0 and $\pi/4$ depending on $\lambda.Ca$. He derived the time-dependent inclination of the principal axis (and deformation of the drop) and showed that when $\lambda.Ca \ll 1$ the approach to steady state inclination ($\pi/4$) was an overdamped (monotonic) one, while for $\lambda.Ca \gg 1$ the approach to steady state (0) was an underdamped one with the drop (on short time scales) exhibiting shape oscillations in shape similar to Jeffery orbits of a nearly spherical particle. His analysis was nevertheless restricted to first order in the relevant small parameter (Ca or $1/\lambda$) and the relaxation time reported at this order is erroneous. Following his work, several authors made efforts to calculate higher order corrections to deformation in terms of ϵ. Note that, unlike inertia, both Ca and $1/\lambda$ constitute a regular perturbation of the Stokesian field. Frankel and Acrivos (1970) calculated the deformation up to second order in Ca, which was again extended by Barthes-Biesel and Acrivos (1973) to $O(Ca^3)$. Even though both the authors had developed their theory for a general deformation parameter ϵ, exact solutions were possible only for $\epsilon = Ca$. For $\epsilon = 1/\lambda$, one needed to account for terms that jump order from higher orders in this limit and thus an exact solution eluded these authors. This was pointed out by Rallison (1980), who also suggested an efficient way to exactly calculate higher order corrections in $O(1/\lambda)$, albeit for $\lambda.Ca \gg 1$. More recently Vlahovska et al. (2009) have extended this analysis to surfactant-laden drops in the limit of surface incompressibility, where the Marangoni number is an additional parameter involved. Greco (2002) recognised that the higher order corrections to the fields involved a characteristic combination, that always characterised the dependence of these corrections on the vorticity tensor, that resulted in an algebraically simpler procedure to calculate higher order corrections. The procedure was adopted by Olivera and daCunha (2015) to solve for higher order corrections in $1/\lambda$, although subject to few restrictive assumptions, which shall be discussed at a later stage. Even though all of the aforementioned authors have analyzed the drop-deformation-induced correction to the leading order Stokesian velocity field of G. I. Taylor (1932), the focus was on the deformation of the drop and its effect on emulsion rheology. Thus none of the aforementioned efforts had analysed

the streamline topology in the exterior of the drop due to its deformation, which is our focus in this study.

To begin with, we shall restrict ourselves to the case of dominant interfacial tension, $Ca \ll O(1)$, $\lambda \sim O(1)$, and briefly discuss the derivation of the velocity field in the exterior to $O(Ca)$ using the method of tensor harmonics (Greco (2002)). An analysis of streamline topology using this field reveals that the Stokesian topology is altered in a non-trivial fashion, similar to inertia. This deformation-induced alteration of the streamline topology is reported here for the first time, and seemingly in contradiction to the experimental effort of Torza et al. (1971). In light of the contradiction, we confirm this result by performing boundary integral simulations, which again point to an alteration of streamline topology and match well with our analytical predictions. Finally we move on to the case of $\lambda Ca \sim O(1)$, and our preliminary results show that the alteration of streamline topology also persists in this limit. A detailed analysis in this latter limit, along the lines of the small Ca case above, will be taken up in the near future. Nevertheless, our results yield a reasonably complete picture of the streamline topology in the exterior of a weakly deformed drop immersed in an ambient canonical hyperbolic flow.

5.3.1 Drop in a Planar Linear Flow: The limit of large Interfacial Tension ($Ca \ll O(1)$; $\lambda \sim O(1)$)

When interfacial forces are are dominant over viscous forces, Ca is the small parameter, and the shape of the drop may be written as:

$$F(r, \lambda, Ca, \hat{\alpha}, t) = r - \left(1 + Ca\,\Im(\lambda, \hat{\alpha}, t) + Ca^2\,\Re(\lambda, \hat{\alpha}, t) + O(Ca^3)\right) = 0 \qquad (5.52)$$

where r is the drop radius, and $\hat{\alpha}$ characterizes the one-parameter family of planar linear flows, analyzed in the inertial context, in Section 5.2. As before, the Stokes equations (in dimensionless form) governing the fluid motion are given by (see Eq.2.7 of Chapter 2):

$$\begin{aligned}\nabla.\mathbf{u} &= 0 \\ \nabla^2\mathbf{u} &= \nabla p\end{aligned} \quad (Exterior\ Problem) \qquad \begin{aligned}\nabla.\hat{\mathbf{u}} &= 0 \\ \lambda\nabla^2\hat{\mathbf{u}} &= \nabla\hat{p}\end{aligned} \quad (Interior\ Problem) \quad (5.53)$$

Here, $\hat{\mathbf{u}}$ and $\mathbf{u}$ are the velocity fields in the drop interior and exterior, respectively; $\hat{p}$ and p are the associated pressure fields; $\lambda = \hat{\mu}/\mu$ is the drop to ambient fluid viscosity ratio. The boundary conditions in dimensionless terms are given by:

$$\mathbf{u} \to \bar{\mathbf{\Gamma}}.\mathbf{x} \quad as\ r \to \infty \qquad (5.54)$$

$$\left.\begin{aligned} \mathbf{u} &= \hat{\mathbf{u}} \\[1em] \mathbf{u}.\mathbf{n} &= \hat{\mathbf{u}}.\mathbf{n} = \frac{1}{\nabla F}\frac{\partial F}{\partial t} \\[1em] (2(\bar{\mathbf{E}} - \lambda\hat{\bar{\mathbf{E}}}) - (p - \hat{p})).\mathbf{n} &= \frac{1}{Ca}\mathbf{n}(\mathbf{\nabla}.\mathbf{n}) \end{aligned}\right\} At\ r = 1 + Ca\,\Im(\lambda, \hat{\alpha}) + O(Ca^2). \qquad (5.55)$$

where, $\bar{\mathbf{E}} = \nabla\mathbf{u} + (\nabla\mathbf{u})^T = f(\mathbf{E}, \mathbf{\Omega})$, $\hat{\bar{\mathbf{E}}} = \nabla\hat{\mathbf{u}} + (\nabla\hat{\mathbf{u}})^T = f(\mathbf{E}, \mathbf{\Omega})$ and, the term $\mathbf{n}(\mathbf{\nabla}.\mathbf{n})$ in the last boundary condition denotes the curvature of the interface. As can be seen the factor $1/Ca$ in this boundary condition relates the velocity field at $O(Ca^i)$ to the deformation at $O(Ca^{i+1})$ through the curvature term. This suggests that, one can find the velocity field at a given order, and then use it to find the deformation at the next order; the shape being spherical at the leading order. One can now, expand

all the relevant fields in terms of Ca as:

$$\boldsymbol{u} = \boldsymbol{u}^{(0)} + Ca\ \boldsymbol{u}^{(1)} + O(Ca^2) \tag{5.56}$$

$$\hat{\boldsymbol{u}} = \hat{\boldsymbol{u}}^{(0)} + Ca\ \hat{\boldsymbol{u}}^{(1)} + O(Ca^2) \tag{5.57}$$

$$p = p^{\infty} + p^{(0)} + Ca\ p^{(1)} + O(Ca^2) \tag{5.58}$$

$$\hat{p} = \hat{p}^{\infty} + \hat{p}^{(0)} + Ca\ \hat{p}^{(1)} + O(Ca^2) \tag{5.59}$$

where p^{∞} and $\hat{p}^{\infty}$ are the pressure in the exterior and interior phase when there is no flow outside and from the Young-Laplace equation $\hat{p}^{\infty} - p^{\infty} = 2/Ca$ (G. L. Leal (2007)). Likewise, one can also expand the normal vetor $\boldsymbol{n}$ as:

$$\boldsymbol{n} = \boldsymbol{n}^{(0)} + Ca\ \boldsymbol{n}^{(1)} + O(Ca^2) \tag{5.60}$$

where $\boldsymbol{n^{(0)}}$ is the unit radial vector (normal to the spherical drop surface). Now to calculate the corrections to the normal vector $\boldsymbol{n}$, one should first find the functional form of $\Im$. One can find this, by using symmetry arguments (G. L. Leal (2007)). $\Im(\lambda, \hat{\alpha})$ is a true scalar where the flow parameter can only enter the function $\Im$ through the ambient velocity-gradient tensor $\bar{\boldsymbol{\Gamma}}$. The governing Stokesian equations are linear and since the boundary conditions also are linear in $\bar{\boldsymbol{\Gamma}}$, to the first order in Ca, the only possible way $\Im$ (a scalar) can be related to $\bar{\boldsymbol{\Gamma}}$ (a second rank tensor) is by:

$$\Im(\lambda, \hat{\alpha})\ =\ s_0 \bar{\boldsymbol{\Gamma}} : \boldsymbol{nn}\ =\ s_0 (\boldsymbol{E} + \boldsymbol{\Omega}) : \boldsymbol{nn}\ = = s_0 \boldsymbol{E} : \boldsymbol{nn} \tag{5.61}$$

where, $\boldsymbol{E}$ and $\boldsymbol{\Omega}$ are the symmetric and anti-symmetric parts of $\bar{\boldsymbol{\Gamma}}$, $\boldsymbol{n}$ is the unit-normal vector to the drop surface and $\boldsymbol{\Omega} : \boldsymbol{nn} = 0$. Using this, one can calculate $\boldsymbol{n}^{(1)}$ as:

$$\boldsymbol{n}^{(1)} = 2(\boldsymbol{E} : \boldsymbol{n}^{(0)} \boldsymbol{n}^{(0)} - \boldsymbol{E}.\boldsymbol{n}^{(0)}). \tag{5.62}$$

This can then be used to calculate $\boldsymbol{n}(\boldsymbol{\nabla}.\boldsymbol{n})$ to $O(Ca)$. We now substitute these expressions into Eq.5.53 and the boundary conditions to get the system of differential equations at $O(1)$ as:

$$\nabla^2 \boldsymbol{u}^{(0)} = \nabla p^{(0)} \tag{5.63}$$

$$\nabla^2 \hat{\boldsymbol{u}}^{(0)} = \nabla \hat{p}^{(0)} \tag{5.64}$$

$$\boldsymbol{\nabla}.\boldsymbol{u}^{(0)} = \boldsymbol{\nabla}.\hat{\boldsymbol{u}}^{(0)} = 0 \tag{5.65}$$

with,

$$\boldsymbol{u}^{(0)} = \hat{\boldsymbol{u}}^{(0)} \tag{5.66}$$

$$\boldsymbol{u}^{(0)}.\boldsymbol{n}^{(0)} = \hat{\boldsymbol{u}}^{(0)}.\boldsymbol{n}^{(0)} = 0 \tag{5.67}$$

$$(\hat{p}^{(0)} - p^{(0)})\boldsymbol{n}^{(0)} + 2(\bar{\boldsymbol{E}}^{(0)} - \lambda \hat{\bar{\boldsymbol{E}}}^{(0)}).\boldsymbol{n}^{(0)} = 4s_0 \boldsymbol{E} : \boldsymbol{n}^{(0)} \boldsymbol{n}^{(0)} \tag{5.68}$$

where $\bar{\boldsymbol{E}}^{(0)} = \boldsymbol{\nabla}\boldsymbol{u}^{(0)} + (\boldsymbol{\nabla}\boldsymbol{u}^{(0)})^T = f(\boldsymbol{E}, \boldsymbol{\Omega})$ and $\hat{\bar{\boldsymbol{E}}}^{(0)} = \boldsymbol{\nabla}\hat{\boldsymbol{u}}^{(0)} + (\boldsymbol{\nabla}\hat{\boldsymbol{u}}^{(0)})^T = f(\boldsymbol{E}, \boldsymbol{\Omega})$. Note that the last boundary condition is given after simplification and can be obtained by substituting for $\boldsymbol{n}^{(1)}$. To solve this system of equations, one can now use the boundary condition Eq.5.68 to guess the form of $\boldsymbol{u}^{(0)}$ and $\hat{\boldsymbol{u}}^{(0)}$ and substitute them back into the governing equation to get the constants that are needed. From the boundary condition Eq.5.68, where $\bar{\boldsymbol{E}}^{(0)}$ and $\hat{\bar{\boldsymbol{E}}}^{(0)}$ are both functions of $\boldsymbol{E}$ and $\boldsymbol{\Omega}$, one can show using symmetry arguments that the interior and exterior velocity fields have to be of the form:

$$\boldsymbol{u}^{(0)} = c_1(r, \lambda)(\boldsymbol{E} : \boldsymbol{n}^{(0)} \boldsymbol{n}^{(0)})\boldsymbol{n}^{(0)} + c_2(r, \lambda)\boldsymbol{E}.\boldsymbol{n}^{(0)} + r\boldsymbol{\Omega}.\boldsymbol{n}^{(0)} \tag{5.69}$$

and similarly for $\hat{\boldsymbol{u}}^{(0)}$, which have the same functional form as the Stokesian field given in Eq.2.10 of Chapter 1. When this is substituted into Eq.5.64 and 5.65, we get back the solutions given by G. I. Taylor (1932) for $\boldsymbol{u}^{(0)}$ and $\hat{\boldsymbol{u}}^{(0)}$, which are given in Eq.5.1-5.3 and obtain,

$$s_0 = \frac{19\lambda + 16}{8(1 + \lambda)} \tag{5.70}$$

which was also first calculated by G. I. Taylor (1932) for the shape constant at $O(Ca)$. We can now move to the next order, i.e. $O(Ca)$, to find the first correction to this velocity field using similar arguments.

To begin with, we first need the shape function F for the drop to $O(Ca^2)$, which is given by:

$$F(r, \lambda, Ca, \hat{\alpha}) = r - \left(1 + Ca\,\frac{19\lambda + 16}{8(1 + \lambda)}\boldsymbol{E} : \boldsymbol{n}^{(0)}\boldsymbol{n}^{(0)} + Ca^2\,\Re(\lambda, \hat{\alpha})\right) \tag{5.71}$$

The form of $\Re$ can again be guessed by using the same arguments of tensor harmonics used to get $\Im$, in that it has to be a true scalar and that it can be quadratic in $\boldsymbol{\Gamma}$ for $O(Ca^2)$. This gives us:

$$\Re = s_1(\lambda)(\boldsymbol{E} : \boldsymbol{n}^{(0)}\boldsymbol{n}^{(0)})^2 + s_2(\lambda)\boldsymbol{E}.\boldsymbol{E} : \boldsymbol{n}^{(0)}\boldsymbol{n}^{(0)} + s_3(\lambda)\boldsymbol{E} : \boldsymbol{E} + s_4(\lambda)\boldsymbol{A}_2 : \boldsymbol{n}^{(0)}\boldsymbol{n}^{(0)} \tag{5.72}$$

where $\boldsymbol{A}_2$ is the Rivlin-Erickson tensor given by $\boldsymbol{A}_2 = 2(\boldsymbol{E}.\boldsymbol{\Omega} - \boldsymbol{\Omega}.\boldsymbol{E}) + 4\boldsymbol{E} : \boldsymbol{E}$ (Greco (2002)). Using this expression one can calculate the $O(Ca^2)$ correction to $\boldsymbol{n}$ and $\boldsymbol{n}.\boldsymbol{\nabla}\boldsymbol{n}$, which when substituted into the boundary conditions gives us at $O(Ca)$:

$$\boldsymbol{u}^{(1)} + \Im\frac{\partial \boldsymbol{u}^{(0)}}{\partial r} - \left(\hat{\boldsymbol{u}}^{(1)} + \Im\frac{\partial \hat{\boldsymbol{u}}^{(0)}}{\partial r}\right) = 0 \tag{5.73}$$

$$\boldsymbol{u}^{(1)}.\boldsymbol{n}^{(0)} + \boldsymbol{u}^{(0)}.\boldsymbol{n}^{(1)} + \Im\frac{\partial \boldsymbol{u}^{(0)}}{\partial r} = 0 \tag{5.74}$$

$$(\hat{p}^{(0)} - p^{(0)})\boldsymbol{n}^{(1)} + \left[(\hat{p}^{(1)} - p^{(1)}) + \Im\frac{\partial(\hat{p}^{(0)} - p^{(0)})}{\partial r}\right]\boldsymbol{n}^{(0)} +$$
$$2(\bar{\boldsymbol{E}}^{(0)} - \lambda\hat{\bar{\boldsymbol{E}}}^{(0)}).\boldsymbol{n}^{(1)} + 2\left[(\bar{\boldsymbol{E}}^{(1)} - \lambda\hat{\bar{\boldsymbol{E}}}^{(1)}) + \Im\frac{\partial(\bar{\boldsymbol{E}}^{(0)} - \lambda\hat{\bar{\boldsymbol{E}}}^{(0)})}{\partial r}\right].\boldsymbol{n}^{(0)} = \boldsymbol{g} \tag{5.75}$$

where $\boldsymbol{g}$ is $\boldsymbol{n}.\boldsymbol{\nabla}\boldsymbol{n}$ to $O(Ca^2)$, whose detailed expression is given in Greco (2002). One can then show, based on the aforementioned boundary conditions and the solutions at $O(1)$, that both $\boldsymbol{u}^{(1)}$ and $\hat{\boldsymbol{u}}^{(1)}$ will be of the form:

$$\begin{aligned}
\boldsymbol{u}^{(1)} =\,&c_1(r, \lambda)(\boldsymbol{E} : \boldsymbol{n}^{(0)}\boldsymbol{n}^{(0)})^2\boldsymbol{n}^{(0)} + c_2(r)(\boldsymbol{E} : \boldsymbol{n}^{(0)}\boldsymbol{n}^{(0)})\boldsymbol{E}.\boldsymbol{n}^{(0)} + c_3(r, \lambda)(\boldsymbol{E} : \boldsymbol{E})\boldsymbol{n}^{(0)} + \\
&c_4(r, \lambda)(\boldsymbol{E}.\boldsymbol{E} : \boldsymbol{n}^{(0)}\boldsymbol{n}^{(0)})\boldsymbol{n}^{(0)} + c_5(r, \lambda)\boldsymbol{E}.\boldsymbol{E}.\boldsymbol{n}^{(0)} + c_6(r, \lambda)(\boldsymbol{A}_2 : \boldsymbol{n}^{(0)}\boldsymbol{n}^{(0)})\boldsymbol{n}^{(0)} + \\
&c_7(r, \lambda)\boldsymbol{A}_2.\boldsymbol{n}^{(0)}
\end{aligned} \tag{5.76}$$

This can be substituted into the governing equation at $O(Ca)$, which is of the same form as Eq.5.64, to get the constants $c_i(r, \lambda)$, which is given in Appendix 1. Note that this velocity field has the same tensorial form as the inertial correction given in Eq.5.18 but unlike that, this is valid everywhere in the exterior domain. Now, we shall again proceed in the same fashion as in the case of inertial correction by first plotting the $3D$ streamlines and then characterising them using the $C - E$ description, so a rigorous comparison can be made between these two perturbations.

5.3.1.1 Exterior Streamlines

We first plot the exterior streamline topology associated with the total velocity field, that includes both the $O(1)$ (Eq.5.69) and $O(Ca)$ (Eq.5.76) contributions. We proceed in the same manner as we did for the inertial case, by first fixing a value of $\hat{\alpha}$ and then plotting the streamlines for various λ. We start with the case of $\hat{\alpha} = 0$, for which the separatrix surface extends until ∞. The plot in Fig.5.20 shows a typical streamline topology for $\hat{\alpha} = 0$, $\lambda = 1$. Firstly, we note that the streamlines with their initial points in the region bound by the Stokesian separatrix surface have a spiralling character, much like the inertial case. Secondly, depending on the direction of approach towards the drop, a given finite-Ca streamline can either approach the flow-gradient plane, spiralling off to infinity in the process, or move in the other direction and head off along the vorticity axis. This is, in some sense, opposite of what was observed for the inertial case, corresponding to the bifurcated wake regime. But, surprisingly, the streamline does not head off to infinity along the vorticity axis, but instead turns around and comes back towards the flow-gradient plane. This, for long times, leads to the streamline winding around an invariant torus, and part of the domain being foliated by nested tori. Third, there are no streamline configurations with a single inlet and an outlet, like the single wake configuration of inertial streamlines. Although not shown here, all viscosity ratios, that correspond to the range of validity of the $O(Ca)$ velocity field, i.e. $\lambda \leq O(1/Ca)$, exhibit the same configuration with nested tori foliating a part of the (separatrix) domain and open spiralling streamlines in the other.
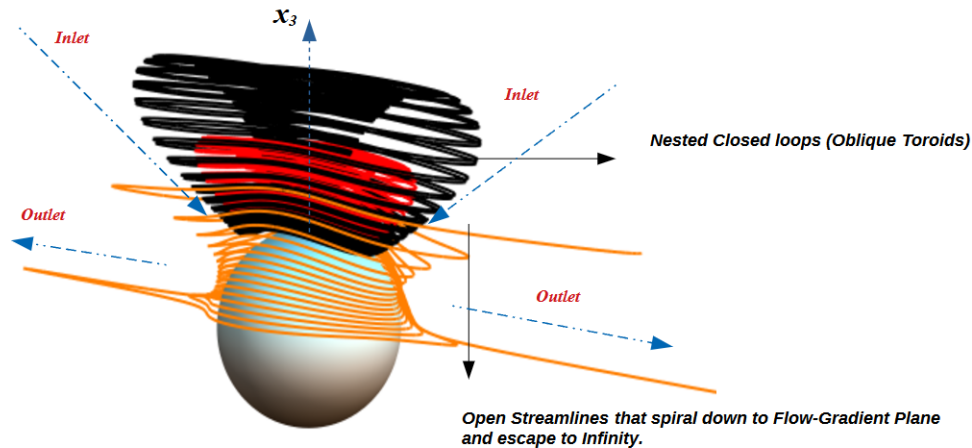
Figure 5.20: Streamlines in the exterior for $\hat{\alpha} = 0$, $\lambda = 1$ and $Ca = 1/30$. The topology contains nested tori foliating a part of the (separatrix) domain and open spiralling streamlines in the other. The black and red streamlines wind over an oblique torus, while the orange one escapes to infinity along the flow-gradient plane. The separatrix for this case lies at ∞ and there is no scattering of streamlines.

Thus, the streamline topology associated with a deformed drop, contains nested invariant tori in the physical domain. In Fig.5.21, we analyse one such torus, by plotting the Cartesian coordinates of a streamline winding over it with time and, we see that they are doubly-periodic functions of time. This implies that there are two time scales, $t_d \sim O(\dot{\gamma}^{-1}Ca)$ and $t_f \sim O(\dot{\gamma}^{-1})$, which are widely separated in magnitude, and therefore, these spiralling streamlines may be interpreted as trajectories that slowly drifts across the Stokesian closed streamlines. We also see from the plot that, the torus stretches along the flow direction (x_1) and shrinks along the gradient direction (x_2) as we move along the vorticity axis (x_3), thereby making it an oblique configuration. The nested configuration suggests that one has two limiting surfaces bounding this configuration; a singular curve (a ring) being the limiting surface on the inside and an outermost torus, that extends to ∞ along x_3 and x_1 directions, with its x_2 extent shrinking to zero. The outer limiting torus, seemingly mimics the separatrix surface of $\hat{\alpha} = 0$, in it's infinite spatial

extent.
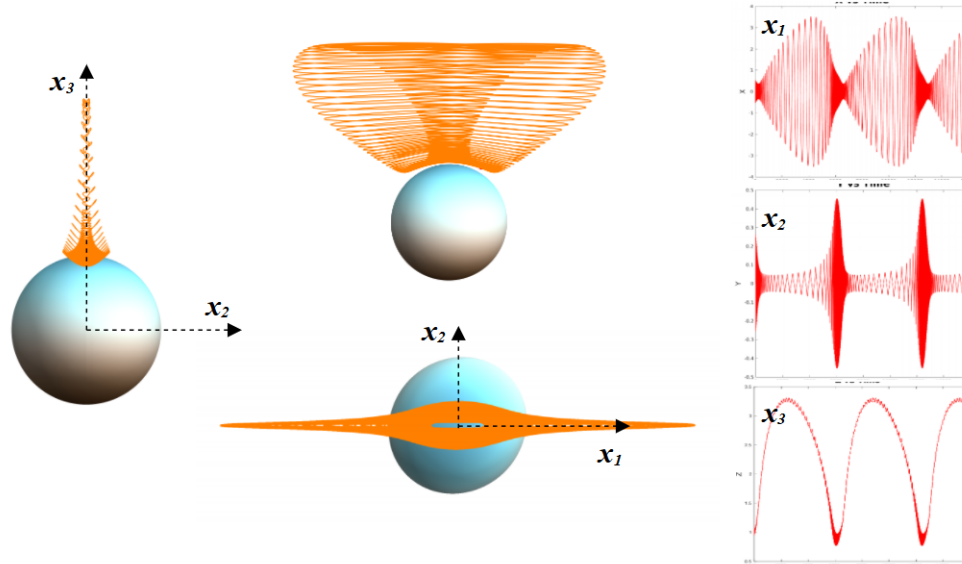
Figure 5.21: A streamline for $\hat{\alpha} = 0$, $\lambda = 1$ and $Ca = 1/30$ that winds over a deformed torus. The figure shows the cross section of one such torus. As can be seen the spatial extent of a torus in x_2 reduces as one moves along x_3, while the extent along x_1 increases. The figures on the right show the variation of the Cartesian coordinates with time and they are doubly-periodic functions.
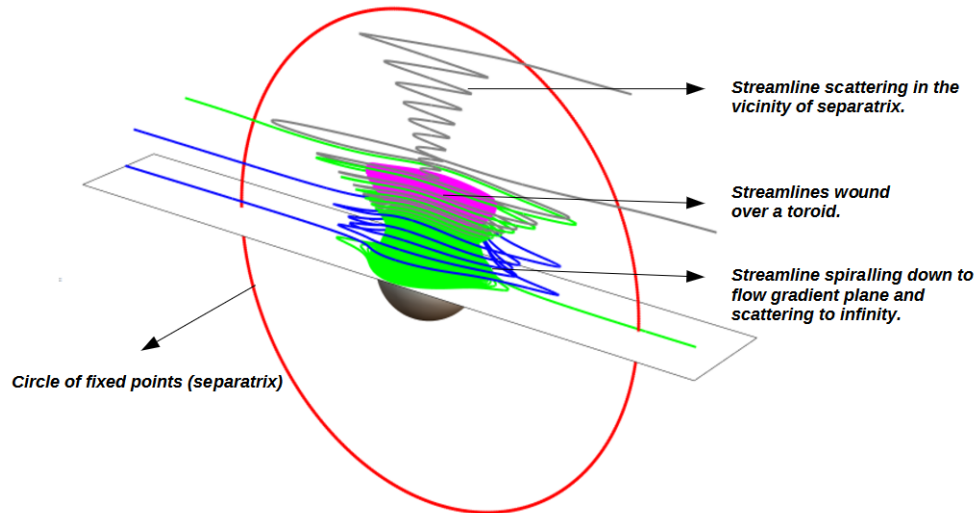
Figure 5.22: Streamlines in the exterior for $\hat{\alpha} = 10^{-4}$, $\lambda = 1$ and $Ca = 1/30$. The separatrix surface for this case is finite in extent and its intersection with $x_1 - x_3$ plane is the red circle in figure. Apart from the existence of nested tori, the topology contains streamlines that scatter in the vicinity of saddle points on the separatrix surface regardless of the direction of spiralling.

For non-zero $\hat{\alpha}$ (Fig.5.25), we find that the streamline topology remains qualitatively similar to the case of $\hat{\alpha} = 0$ described above, except for the presence of streamlines that scatter off to infinity in the vicinity of the saddle points on the separatrix surface. Recall from the discussion on Stokesian streamline topology in Section 5.1, that the separatrix surface has a finite extent for planar hyperbolic flows. The nested tori configuration survives even for the planar hyperbolic flows, but these tori do not fill up

the entire region within the separatrix surface. Instead streamlines within a certain distance from the separatrix surface scatter off to infinity. This is attributed to the fact that despite the boundary of the separatrix surface shrinking to a finite extent, the inner limiting torus (the ring) also approaches the drop, making it possible for nested tori structures to exist in its vicinity. We also observe that the streamlines scatter off to infinity in the vicinity of the separatrix surface, regardless of the direction in which they spiral (towards or away from the flow-gradient plane). Although not shown here, the topology remains same for all $\lambda \sim O(1)$ and the invariant tori configuration exists for all $\hat{\alpha} \leq \hat{\alpha}_c$, with the inner limiting torus coinciding with the drop surface at $\hat{\alpha}_c$.

Thus, the key conclusion from the analysis above is that, drop deformation does destroy the Stokesian closed streamline topology, but the resulting finite-Ca streamline topology appears more complicated than the finite-Re counterpart. For instance, the simplest finite-Ca topology could have been the opposite of the inertial alteration (in the bifurcated wake regime) - in the sense that all streamlines on one side of a "critical approach surface" would end up spiralling towards the flow-gradient plane and then out to infinity, while all of those on the other side of this surface would end up spiralling out along the vorticity axis, subsequently scattering off to infinity (note that this critical approach surface would be the critical exit surface in the bifurcated wake regime). Instead, there exists a finite subset (the entire set for the specific case of simple shear flow where the separatrix surface extends to infinity) of streamlines that do not spiral out along the vorticity axis, but instead reverse and spiral back in, so they end up winding around the surface of an invariant (deformed) torus. Considering the non-triviality of this topology, we validate it by performing boundary integral simulations, before using the method of averaging to organise the finite-Ca streamlines on the $C - E$ plane, analogous to the inertial case.

5.3.1.2 Boundary Element Simulations

The exterior streamlines plotted using the $O(Ca)$ field has revealed a non-trivial alteration of the streamline topology, with closed streamlines becoming spiralling ones. As was pointed out in the introduction of this chapter, this alteration appears to go against the experiments of Torza et al. (1971) and the numerical studies of Kennedy and Pozrikidis (1994) and Komrakova et al. (2014)). Kennedy and Pozrikidis (1994) numerically analysed the problem of drop deformation in planar shear flows, by using Boundary Element Method (BEM), which is based on the boundary integral formulation of the Stokes' equations (G. L. Leal (2007))), while Komrakova et al. (2014)) had performed Lattice Boltzmann (LB) simulations to study the same. The focus of these numerical efforts was again the deformation of the drop, but the authors nevertheless plot the streamlines on the flow-gradient plane and conclude that they are closed. Even though, visually, they are not exactly closed (see Fig. 6 of Kennedy and Pozrikidis (1994) and Fig.8 of Komrakova et al. (2014)), the authors conclude that this is an "apparent" spiralling due to the accuracy issues associated with numerical simulations. Motivated by the results of our analytical velocity field, we perform independent BEM simulations, along the lines of Kennedy and Pozrikidis (1994) to confirm our theoretical predictions, since the boundary integral simulation is computationally efficient with the discretisation being applied only over the bounding surfaces than over the entire domain, so the computational expense increases as $O(N^2)$, N being the number of boundary elements.

Ladyzhenskaya (1963) first showed that the solutions of the Stokes' equation can be written down formally as an integral over the domain boundary of distribution of fundamental solutions of the Stokes' equations, namely the Stresslet and Stokeslet. She showed that the solution of the velocity field satisfying Stokes' equation can be written as (Ladyzhenskaya (1963), Pozrikidis (2002)):

$$\boldsymbol{u}(\boldsymbol{x}) = \boldsymbol{u}^{\infty}(\boldsymbol{x}) + \frac{1}{8\pi} \int_D \boldsymbol{G}(\boldsymbol{x} - \boldsymbol{x_0}).\boldsymbol{\sigma}(\boldsymbol{x_0}).\boldsymbol{n}(\boldsymbol{x_0}) \, dA(\boldsymbol{x_0}) - \frac{3}{4\pi} \int_D \boldsymbol{T}(\boldsymbol{x} - \boldsymbol{x_0}).\boldsymbol{u}(\boldsymbol{x_0}).\boldsymbol{n}(\boldsymbol{x_0}) \, dA(\boldsymbol{x_0}) \quad (5.77)$$

where $\boldsymbol{G}(\boldsymbol{x} - \boldsymbol{x_0})$ is the Stokeslet, the Green's function for the velocity and $\boldsymbol{T}(\boldsymbol{x} - \boldsymbol{x_0})$ is the Stresslet, the Green's function of the stress, both associated with a point force at $\boldsymbol{x_0}$. These fundamental solutions

are given by:

$$G(\boldsymbol{x} - \boldsymbol{x_0}) = \left(\frac{\boldsymbol{I}}{r} + \frac{(\boldsymbol{x} - \boldsymbol{x_0})(\boldsymbol{x} - \boldsymbol{x_0})}{r^3} \right) \tag{5.78}$$

$$\boldsymbol{T}(\boldsymbol{x} - \boldsymbol{x_0}) = -6 \left(\frac{(\boldsymbol{x} - \boldsymbol{x_0})(\boldsymbol{x} - \boldsymbol{x_0})(\boldsymbol{x} - \boldsymbol{x_0})}{r^5} \right) \tag{5.79}$$

with $r = |\boldsymbol{x} - \boldsymbol{x_0}|$ and $\boldsymbol{I}$ being the second rank identity tensor. The aforementioned equation suggests that the velocity at a point $\boldsymbol{u}(\boldsymbol{x})$ which satisfies the Stokes' equation in Eq.5.53 subject to certain boundary conditions and incompressibility can be obtained by integrating a distribution of the surface velocity and stress field on the boundaries of the solution domain. The first term is called the single-layer potential, with the density function being the surface stress vector $\boldsymbol{\sigma}.\boldsymbol{n}(\boldsymbol{x_0})$ and the second term is called the double-layer potential whose density function is the surface velocity $\boldsymbol{u}(\boldsymbol{x_0})$. This equation is simply an integral representation of Eq.5.53 and to find solution corresponding to a specific set of boundary conditions, we will have to apply those conditions and solve an integral equation numerically, which is the crux of BEM Simulations. For a drop in a planar flow subject to boundary conditions Eq.5.54-5.55, one can easily show that the boundary integral representation in Eq.5.77 reduces to (in dimensionless terms):

$$\begin{aligned}
\boldsymbol{u}(\boldsymbol{x}) = 2Ca\boldsymbol{u}^\infty(\boldsymbol{x}) &- \frac{1}{2\pi} \int_D \boldsymbol{G}(\boldsymbol{x} - \boldsymbol{x_0}).(\boldsymbol{\nabla}_{\boldsymbol{x_0}}.\boldsymbol{n})\boldsymbol{n}(\boldsymbol{x_0}) \, dA(\boldsymbol{x_0}) \\
&+ \frac{1 - \lambda}{(1 + \lambda)4\pi} \int_D \boldsymbol{T}(\boldsymbol{x} - \boldsymbol{x_0}).\boldsymbol{u}(\boldsymbol{x_0}).\boldsymbol{n}(\boldsymbol{x_0}) \, dA(\boldsymbol{x_0})
\end{aligned} \tag{5.80}$$

for a point $\boldsymbol{x}$ on the drop surface, where $\boldsymbol{u}^\infty$ is the velocity field of the ambient planar linear flow and therefore involves the parameter $\hat{\alpha}$ (Eq.5.1-5.3). Note here that for the case of $\lambda = 1$, the second term (the double layer potential term) drops off and the equation is no longer an integral equation. But for an arbitrary λ, one needs to solve the full integral equation to get the velocity field, which is a Fredholm integral equation of the second kind (Pozrikidis (2002)).

We write a serial $FORTRAN^\circledR$ code to solve the boundary integral equation (Eq.5.80), although our simulations are restricted to simple shear flow of the ambient ($\hat{\alpha} = 0$). We begin with an initially spherical drop, whose surface is discretised into N number of elements. This discretisation is achieved by inscribing an octahedron or icosahedron and tessellating the faces of these isotropic solids by successive division of the triangular faces along their medians. Thus, in going from level of discretization to the next, each triangular face in the original discretization is divided into four new faces, and then these faces are projected onto the sphere. Depending on whether the initial inscribed solid is a octahedron or icosahedron, one will have either $N = 8(4^n)$ or $N = 20(4^n)$ elements, at the nth level of discretisation. In our simulations we use 512, 1280 and 2048 elements to ensure grid independent solutions, while the simulations of Kennedy and Pozrikidis (1994) were limited to $N = 512$. The need for the high resolution will become evident in the sections below where we validate our simulation. Once the sphere is discretised, we initialise the velocity field to 0 everywhere and solve the Integral equation (Eq.5.80) by Gaussian Quadrature. We use 20 quadrature points for our integrations and it provides results of reasonable accuracy. For the case of $\lambda = 1$, we simply integrate the first term (single layer potential) to get the velocity field. But for an arbitrary λ, the integral equation is solved iteratively using the Gauss-Siedel method and the iterations are carried out until the solution converges to within a tolerance of 10^{-6}. This gives us the velocity field at the end of one time step. Then we march in time using a fourth order Runge-Kutta method with a time step of 10^{-3} to evaluate the field at the next instant using the solution of the previous time instant as the new guess value. We stop the simulations when the parameters of interest reach a steady state. Typically in our simulations we find that the solutions reach a steady value when the time is around two to three times the relaxation time of the system.

We calculate from the simulations the Taylor Coefficient D, which is defined as $D = (r_{max} - r_{min}/(r_{max} + r_{min})$ and is a measure of deformation. Since the Taylor coefficient (D) is a pointwise parameter, the comparison is eventually limited by the choice of our points (on the deformed interface) to measure r_{max} and r_{min}. This limits one's ability to resolve the agreement at higher order in Ca. This motivates the choice of an integral measure $F_{ij} = \int_0^{2\pi} (\delta_{ij} - n_i n_j) r_{drop} d\phi$ (that conveys the same information about the deformation) as a parameter of choice to validate the simulation results by comparison with theory at higher order in Ca. Our calculations suggest that BEM simulations cannot be reliably used to infer the detailed finite-Ca streamline topology (since one can't integrate accurately over long enough times to verify the existence of invariant tori). But, one can nevertheless establish the alteration of topology by an integral parameter based on a quantity that doesn't involve the velocity field at large distances. The quantity we calculate to show this alteration is the flux per unit length (span) of the velocity around a closed curve (circle) on the flow-gradient plane which can be easily compared with our theoretical prediction. This quantity offers an indirect evidence for spiralling streamlines as closed streamlines would have zero flux across a closed curve. We now present the results that validate our simulations.

Validation of BEM Simulations

We validate our BEM results by comparing the Taylor coefficient (D) calculated from the simulations with the analytical solution at $O(1)$. We have rederived the analytical result by solving the transient problem at $O(1)$ (Eqs.5.53-5.55), following along the lines of Cox (1969), where the only constraints placed on λ and Ca are that they result in a small deformation of the form:

$$F(r, \lambda, Ca, \hat{\alpha}, t) = r - \left(1 + \epsilon \boldsymbol{A}(t, \lambda, Ca) : \boldsymbol{n^{(0)}} \boldsymbol{n^{(0)}} + O(\epsilon^2)\right) \tag{5.81}$$

where, the deformation is governed by a parameter ϵ. The tensor $\boldsymbol{A}$ is a function of time and is, in genereal, not a linear function of $\boldsymbol{E}$, the velocity-gradient tensor of the ambient flow (that includes $\hat{\alpha}$). The solution for the Taylor coefficient D at $O(1)$ is given by:

$$D = \sqrt{A_{11}^2 + A_{12}^2}, \tag{5.82}$$

with,

$$A_{11} = \frac{5(16 + 19\lambda)e^{-\frac{t}{\tau_{rel}}}\left((16 + 19\lambda)(3 + 2\lambda)(\cos t - e^{\frac{t}{\tau_{rel}}}) + 40(1 + \lambda)Ca^{-1}\sin t\right)}{2\left((40(1 + \lambda)Ca^{-1})^2 + ((16 + 19\lambda)(3 + 2\lambda))^2\right)} = -A_{22} \tag{5.83}$$

$$A_{12} = \frac{5(16 + 19\lambda)e^{-\frac{t}{\tau_{rel}}}\left(40(1 + \lambda)Ca^{-1}(\sin t + e^{\frac{t}{\tau_{rel}}}) - (16 + 19\lambda)(3 + 2\lambda)\cos t\right)}{2\left((40(1 + \lambda)Ca^{-1})^2 + ((16 + 19\lambda)(3 + 2\lambda))^2\right)} = A_{21} \tag{5.84}$$

The aforementioned results are the corrected versions of Cox (1969), who reports an erroneous relaxation time $\tau_{rel} = 19\lambda Ca/20$, while the correct value corresponds to:

$$\tau_{rel} = \frac{(3 + 2\lambda)(19\lambda + 16)Ca}{40(1 + \lambda)} \tag{5.85}$$

As already mentioned, these results are uniformly valid for arbitrary $\lambda.Ca$, and therefore provides for a direct comparison with BEM simulations. The plot for D against (dimensionless) time is shown in Fig.5.23 for two values of Ca at different values of λ. From the plot we can see that the simulation results satisfactorily match the theoretical predictions, with the deviations remaining finite and bounded. We have also ensured convergence of our simulation results with respect to grid size and time step size.

(a) $Ca = 0.033$ (b) $Ca = 0.1$
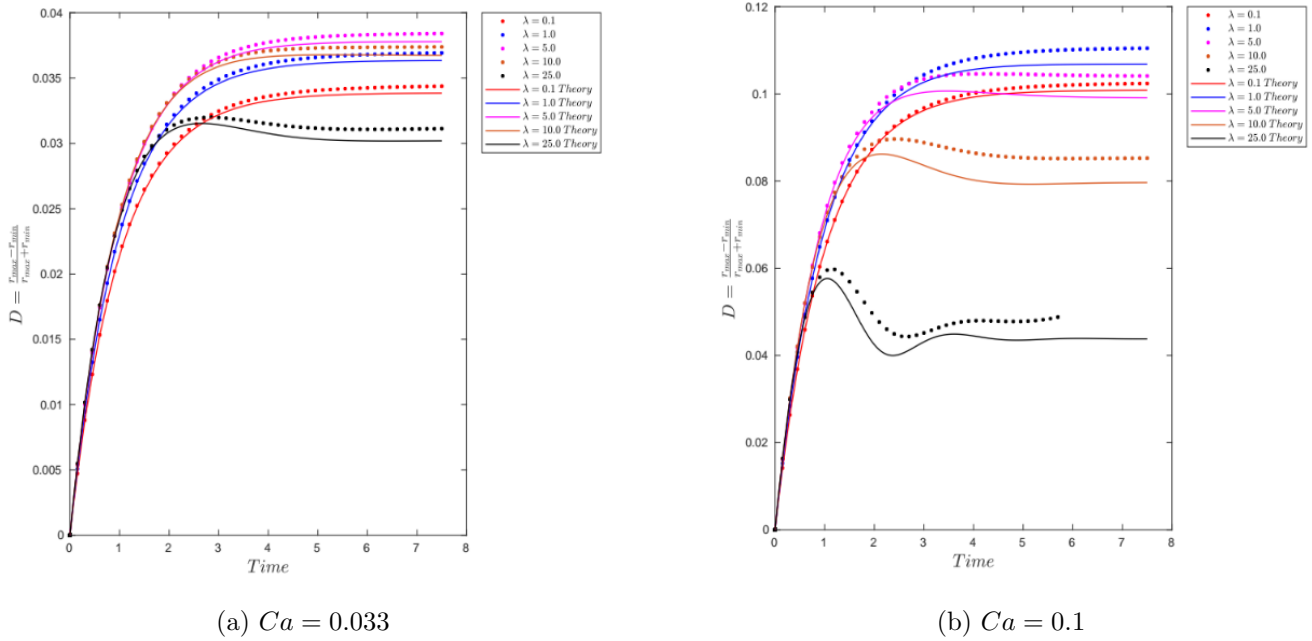
Figure 5.23: Plot of the Taylor Coefficient D against (dimensionless) time. The results of simulation agree well with the theoretical prediction for arbitrary $\lambda.Ca$.

While the transient results above have been compared with the analytical solutions at $O(1)$ valid over the entire range of parameters, we also wish to validate our results at the steady state. The steady state result that we wish to calculate is $D - D_\infty$, where D_∞ corresponds to the steady state value of Eq.5.82. This difference is expected to scale with the higher order correction $(O(\epsilon^2))$, for which we do not have (steady-state) theoretical expressions valid for arbitrary $\lambda.Ca$. Therefore we make our comparison with the steady-state results corresponding to the two limiting scenarios, $Ca \ll 1$ with $\lambda \sim O(1)$ and $\lambda \gg 1$ with $\lambda.Ca \sim O(1)$, for which analytical expressions are available. For the first case, the analytical expressions are already presented in Section 5.3.1 and for the latter scenario, they are presented at a later stage (in Section 5.3.2). From our simulations, we observe that the quantity $D - D_\infty$ does not agree well with the theoretical predictions, owing to it being a point-wise measure, as mentioned earlier. Therefore we calculate the integral measure of deformation $(F_{ij} = \int_0^{2\pi} (\delta_{ij} - n_i n_j) r_{drop} d\phi)$ and plot it as a function of Ca in Fig.5.24. This tensor F_{ij} is calculated by integrating over the perimeter (boundary) of the drop in the flow-gradient plane, which is an ellipse for small deformations. The corresponding analytical expressions for the tensorial components (in the two aforementioned limits) are given by:

$$Ca \ll 1, \lambda \sim O(1) : \begin{cases} F_{11} = Ca^2 \pi \left(\frac{16+19\lambda}{8(1+\lambda)}\right)^2 \left(\frac{3+2\lambda}{20}\right) \\ F_{12} = Ca\ \pi \left(\frac{16+19\lambda}{32(1+\lambda)}\right) \end{cases} \tag{5.86}$$

$$\lambda \gg 1, \lambda.Ca \sim O(1) : \begin{cases} F_{11} = \frac{\pi}{2\lambda} \left(\frac{1805\lambda^2 Ca^2}{1444\lambda^2 Ca^2+1600}\right) \\ F_{12} = \frac{\pi}{2\lambda} \left(\frac{1900\lambda Ca}{1444\lambda^2 Ca^2+1600}\right) \end{cases} \tag{5.87}$$

From the plot, we see that the Ca^2 scaling is accurately captured for $Ca \ll 1, \lambda \sim O(1)$ and the results match accurately with the $O(1/\lambda)$ correction in the other limit of $\lambda \gg 1$, as the effect of discretisation is averaged out by integration. Note that in Figs.5.24c-5.24d, even though the simulation result at the smallest Ca ($Ca = 1/30$), corresponding to $\lambda.Ca \ll 1$, seems to match with the theoretical curve that is valid for $\lambda.Ca \sim O(1)$, this match is not a contradiction, as one needs to go to even smaller Ca to see the deviation from the theory. But we do not have data for $Ca < 1/30$ from our simulations.

(a) $\lambda = 0.1$

(b) $\lambda = 1$

(c) $\lambda = 5$

(d) $\lambda = 10$
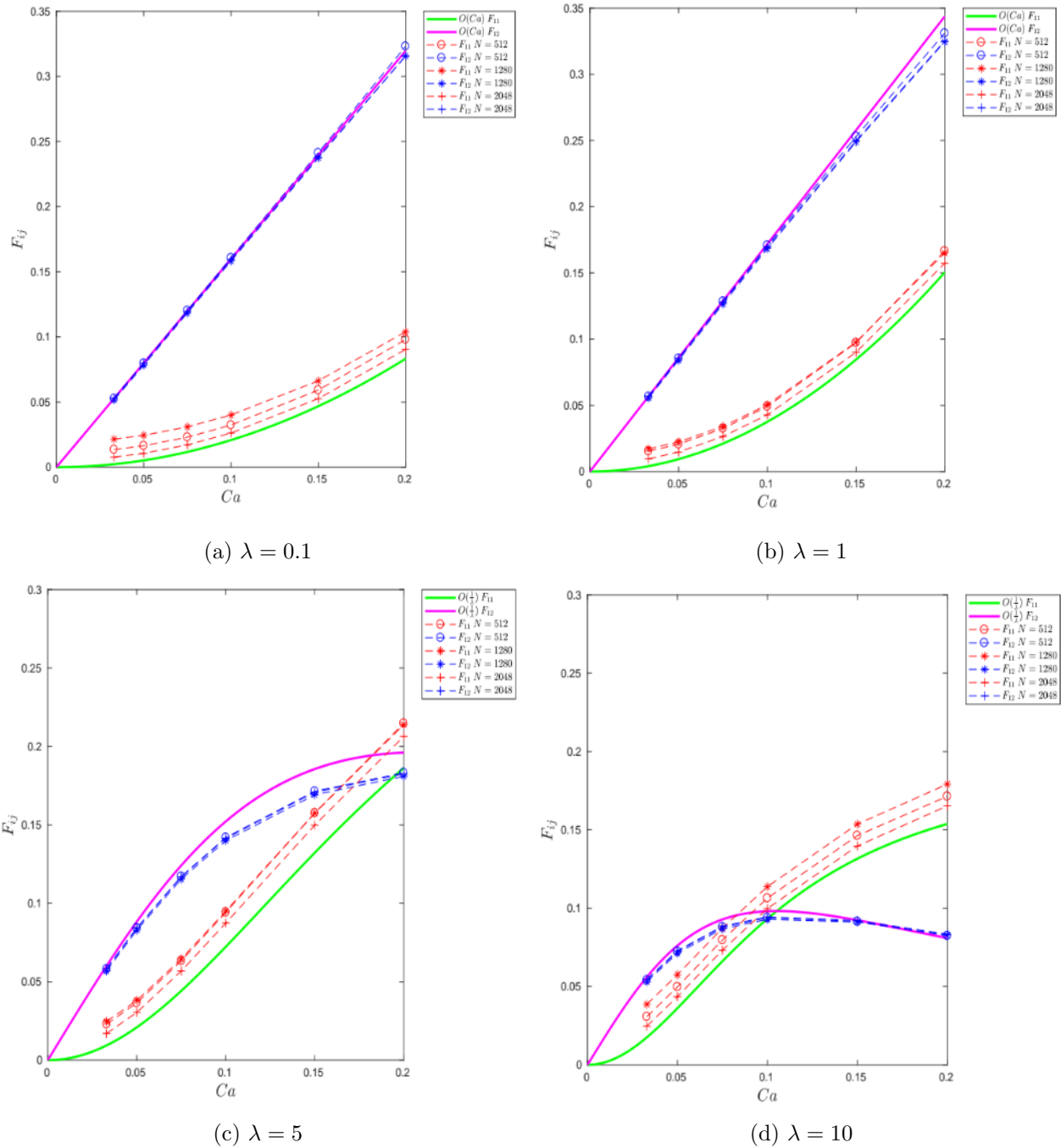
Figure 5.24: Plot of the integral deformation tensor F_{ij} against Ca. Being an integral measure, this quantity averages out the effect of discretisation and gives us the expected scaling.

Results from BEM Simulations

Having validated our simulations, we can now plot the quantity of interest which constitutes the primary evidence of deformation-induced streamline alteration. This quantity, as mentioned earlier, is the flux per unit length of velocity across a closed curve (circle of radius r_0, in the flow-gradient plane $\theta = \pi/2$) defined as $\oint \boldsymbol{u}.\boldsymbol{n} \, r_0 \, d\phi$. We compare our simulation results with the theoretical ones, where, the theoretical expressions for the transient case are available only for $Ca \ll 1$, $\lambda \sim O(1)$. The transient expressions are too complicated and are not shown here, but we present the steady state results derived from Eq.5.76,

which is given by:

$$\oint \boldsymbol{u.n}\, r_0\, d\phi = -\frac{\pi Ca(19\lambda + 16)\left(-5(\lambda + 1)(45\lambda + 4) + 12(\lambda(25\lambda + 41) + 4)r_0^4 + (182 - \lambda(75\lambda + 37))r_0^2\right)}{6720(\lambda + 1)^3 r_0^5}.$$

(5.88)

From Eq.5.88, we see that the flux per span scales as $O(Ca)$, establishing that this arises from drop deformation. We do not have the corresponding theoretical expressions for this quantity in the other regime ($\lambda \gg 1$, $\lambda.Ca \sim O(1)$) for the time being. In our simulations, we calculate this quantity with a fixed $r_0 = 1.25$, such that we aren't too far from the drop surface. If the streamlines are closed, this quantity will be identically zero. But a non-zero value of flux would imply that the streamline topology is no longer closed (and is therefore spiralling). In Fig.5.25, a representative value of the flux along a circle of radius $r_0 = 1.25$ on the flow-gradient plane for $Ca = 0.033$ and two different values of λ are shown. From the plot, we see that the steady state mass flux is $O(Ca)$, and matches with the steady state value given in Eq.5.88. Note that for $\lambda = 1$, a simulation with larger N converges to the theoretical prediction, but for $\lambda = 0.1$, it approaches the theoretical curve as N increases. This is because for $\lambda \neq 1$, we are required to solve an integral equation which is computationally more demanding than the case for $\lambda = 1$, where the double layer term in Eq.5.80 does not enter.

(a) $\lambda = 0.1$ (b) $\lambda = 1$
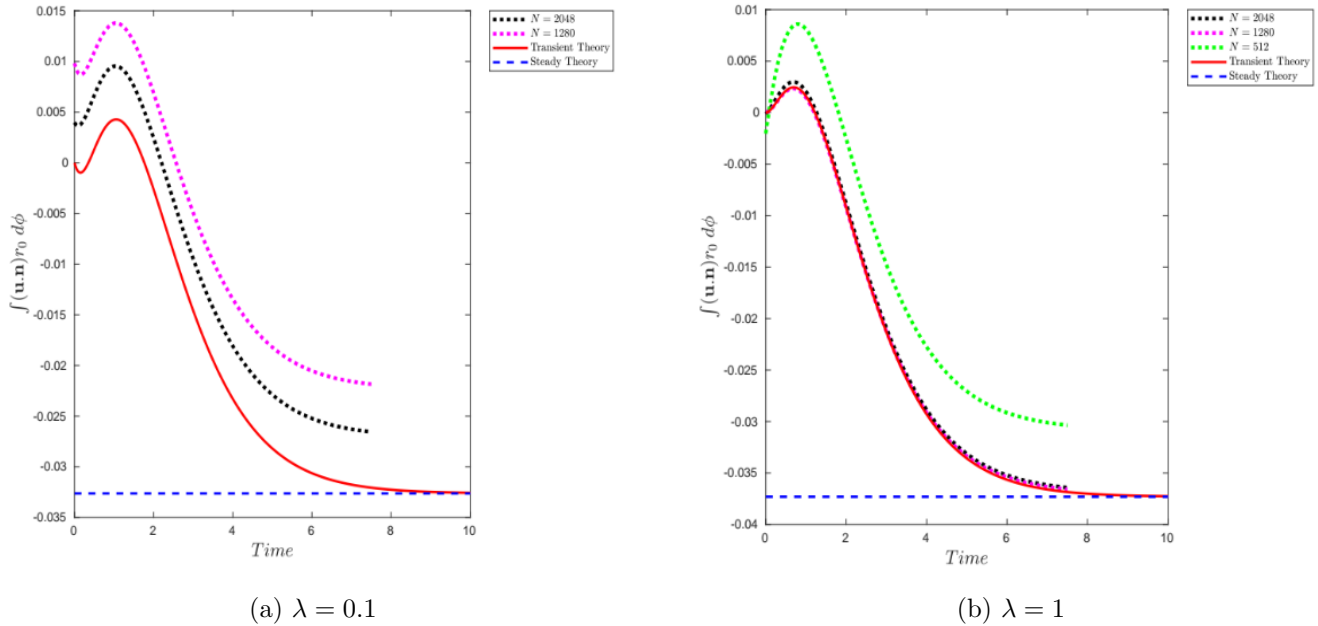
Figure 5.25: Plot of the transient flux of velocity per length against time for $Ca = 0.033$, $r_0 = 1.25$ with (a) $\lambda = 0.1$ and, (b) $\lambda = 1$. The case of $\lambda = 1$ is more accurate and the simulations converge to the theoretical prediction as this case does not involve the double layer potential term. For the other case, the simulation results approaches the theoretical curve with increasing N.

The results in Fig. 5.25 reinforce our analytical prediction that drop deformation indeed alters the Stokesian closed streamline topology. However, as was pointed out, this was not identified by any of the earlier efforts. This may perhaps be explained by observing the magnitude of the flux which is $O(10^{-2})$. Such small magnitudes mave have been easily misconstrued as an artefact of the accuracy issues associated with the simulations, thereby leading the authors to conclude otherwise in their studies. This is quite plausible in the case of Kennedy and Pozrikidis (1994), where the authors have only used $N = 512$ elements in their simulation. We find that $N = 512$ gives results that are not grid-independent, which may have affected the results of the authors. But our calculation of flux per span, although an indirect proof of the alteration in streamline topology, nevertheless agrees with theoretical predictions and provides

compelling evidence of deformation-induced alteration of the Stokesian streamline topology. As for the experiments of Torza et al. (1971), the authors use dye-visualisation techniques to show a region of closed streamlines around the drop. But we feel that, given the small magnitudes of the drift velocity, which results in spiralling streamlines, the authors didn't perform their experiments long enough to observe any discernable change in the streamline topology.

5.3.1.3 Surface Streamlines

In line with the analysis carried out for the inertial case, we plot the streamlines on the surface of the deformed drop to see if they conform to the exterior topology just described. Unlike the inertial case, here the drop surface is deformed and the $O(Ca)$ surface streamlines exist on a surface whose deformation is also $O(Ca)$. Thus, in order to plot the streamlines, one needs to integrate $\frac{d\boldsymbol{x}}{dt} = \boldsymbol{u}^{(0)} + Ca\boldsymbol{u}^{(1)}$ setting $r = 1$, which respects the deformation to $O(Ca)$, in that its normal component is zero on the $O(Ca)$ deformed drop surface. These streamlines are plotted for both $\hat{\alpha} = 0$ and $\hat{\alpha} \neq 0$ in Fig.5.26 and 5.27 respectively. These figures suggest that the surface streamline topology is consistent with the exterior topology for all $O(1)$ λ, where the surface streamlines spiral towards the polar axis and the flow-gradient plane, with the inlet being an invariant orbit on the drop surface, that corresponds to the "critical approach surface" in the exterior.

$\lambda = 0.10$ $\lambda = 0.50$ $\lambda = 1.00$
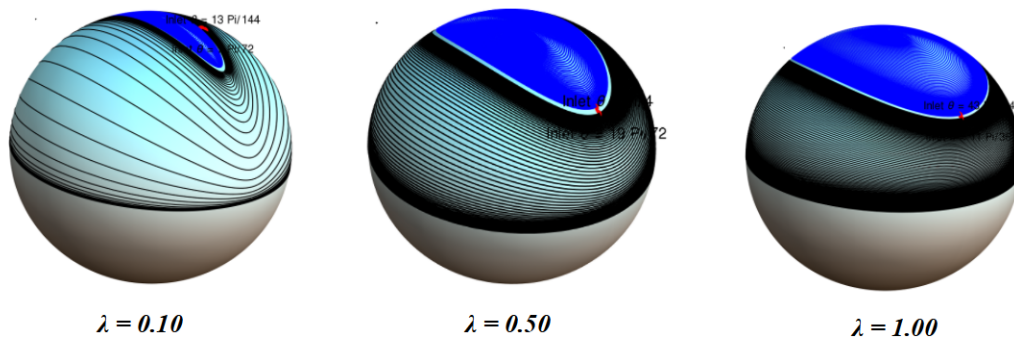
Figure 5.26: Surface streamlines for $\hat{\alpha} = 0$ and $Ca = 1/30$. $\lambda_c = 0$ for this case.

$\lambda = 0.50$ $\lambda = 0.75$ $\lambda = 1.00$
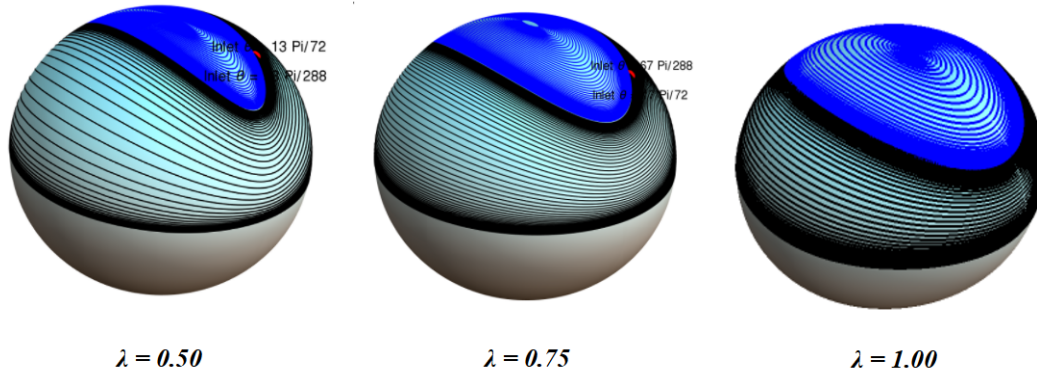
Figure 5.27: Surface streamlines for $\hat{\alpha} = 0$ and $Ca = 1/30$. $\lambda_c = 0.\bar{2}\bar{2}$ for this case.

Note that, while the exterior streamline topology associated with a deformed drop is more complicated than the inertial case, the surface-streamline topology is analogous to the latter corresponding to the bifurcated wake regime (with the exception of a reversed direction of spiralling). This suggests that a surface-streamline aligned coordinate system can be developed in an analogous manner to the inertial

case, for the purpose of finding the convective enhancement of transport (Krishnamurthy and Subramanian (2018b)), although one needs to account for the deformed interface in this scenario. The formulation of this coordinate system and the subsequent analysis of the transport problem is outside the purview of this work and will be taken up in the future. We now move on to the $C - E$ characterisation of the $O(Ca)$ streamlines depicted in Figs.5.20-5.22.

5.3.1.4 $C - E$ Plane of the Exterior Streamlines

The trajectories in the $C - E$ plane for the case of $O(Ca)$ streamlines, are obtained by the method of averaging, by solving an analogous set of equations that were used for the inertial case given in Eq.5.38-5.39, except that the expressions for $u_r^{(1)}$, $u_\theta^{(1)}$ and $u_\phi^{(1)}$ are from Eq.5.76. The slow time variable ($\hat{t}$) in these equations is now equal to $Ca\, t$ rather than $Re\, t$. Note that this set of averaged equations do not account for the deformation of the drop and is thus not valid in the vicinity (an $O(Ca)$ neighborhood) of the drop (see Fig.5.29). Nevertheless, Outside of this asymptotically small neighborhood, the averaged equations are expected to yield a faithful picture of the streamline topology for small but finite Ca. These equations are again integrated numerically in $Mathematica^\circledR$, to obtain the trajectories and we have shown the $C - E$ plane for both $\hat{\alpha} = 0$ (Fig.5.28) and $\hat{\alpha} \neq 0$ (Figs.5.29-5.30). In these plots, the nested tori appear as closed curves, while the streamlines outside the critical approach surface, that spiral to ∞ along the flow-gradient plane, appear as open curves running originating and terminating at the separatrix surface. The $C - E$ plane is similar to that in Fig.5.16 for the bifurcated wake regime of inertial streamlines, except for the presence of nested closed curves and the direction of these trajectories, which are opposite in sense to the trajectories of the inertial case.

For non-zero $\hat{\alpha}$, apart from the nested tori configuration, we also have streamlines that scatter regardless of the direction in which they spiral. In the $C - E$ plane shown in Fig.5.29 for $\hat{\alpha} = 10^{-4}$, $\lambda = 1 > \lambda_{bif}$, they correspond to the open curves (originating and terminating at the separatrix surface) which enclose the nested closed loops and those open curves, that run in the opposite sense to the aforementioned ones. In Fig.5.30, we show the $C - E$ plane for $\hat{\alpha} = 0.33$, $\lambda = 1$, which is very close to $\hat{\alpha}_c$ and we still see the existence of nested tori, which confirms that these structures exist for all $\hat{\alpha}$ until $\hat{\alpha}_c$.
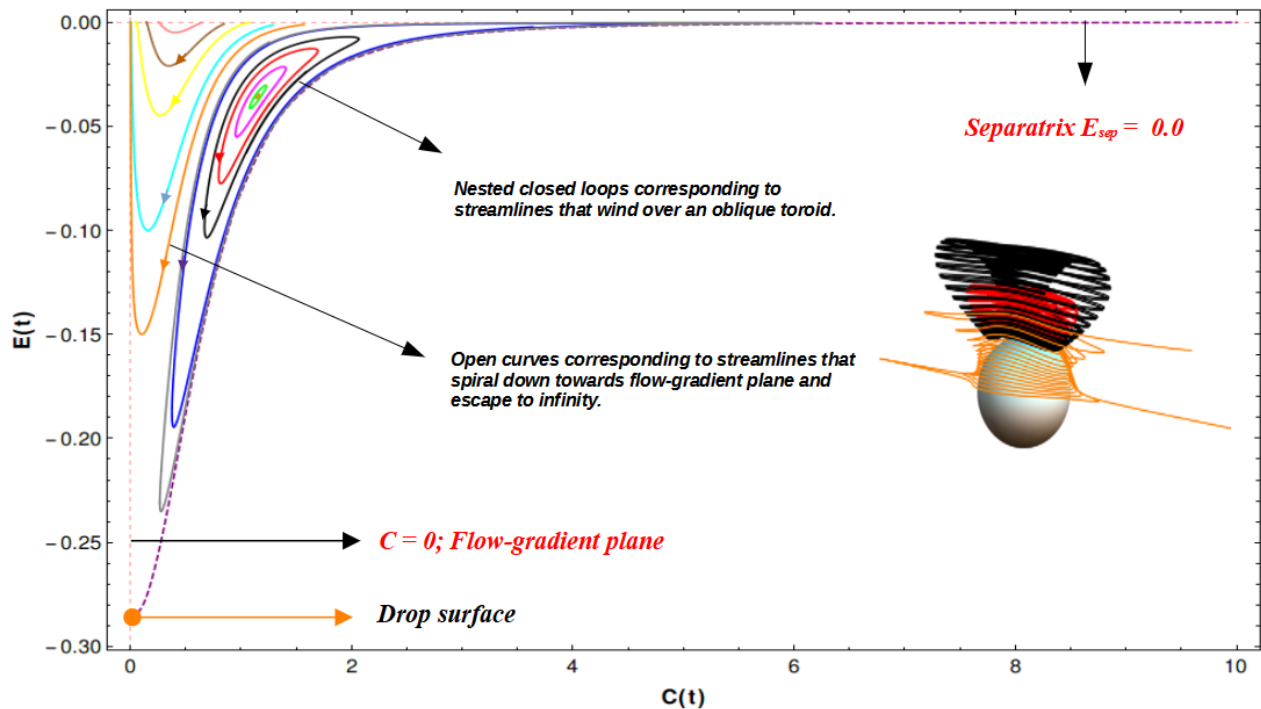
Figure 5.28: $C - E$ plane for $\hat{\alpha} = 0$, $\lambda = 1 > \lambda_c$. In the $C - E$ plane the streamlines spiralling towards flow-gradient plane appear as trajectories running to and from the separatrix surface, and nested closed loops correspond to streamlines that wind over nested tori. The inset shows the $3D$ streamlines, whose $C - E$ trajectory is shown in the same color.
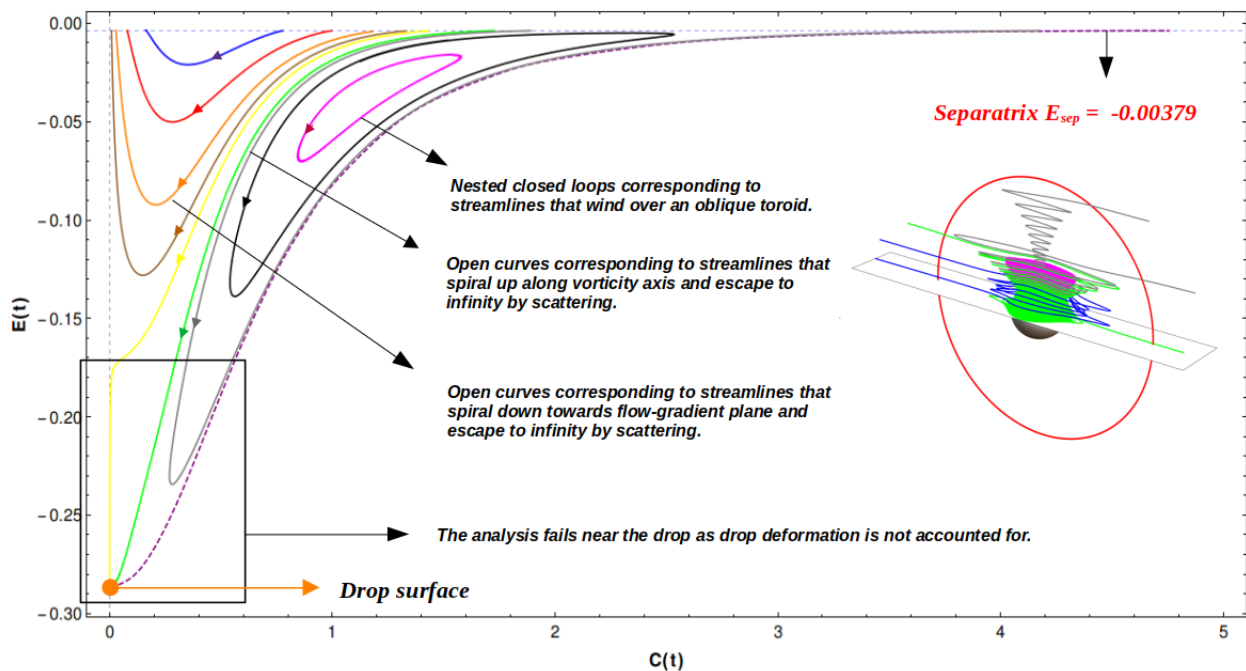
Figure 5.29: $C - E$ plane for $\hat{\alpha} = 10^{-4}$, $\lambda = 1 > \lambda_c$. This case consists of streamlines that scatter in the vicinity of the separatrix. The inset shows the $3D$ streamlines, whose $C - E$ trajectory is shown in the same color.
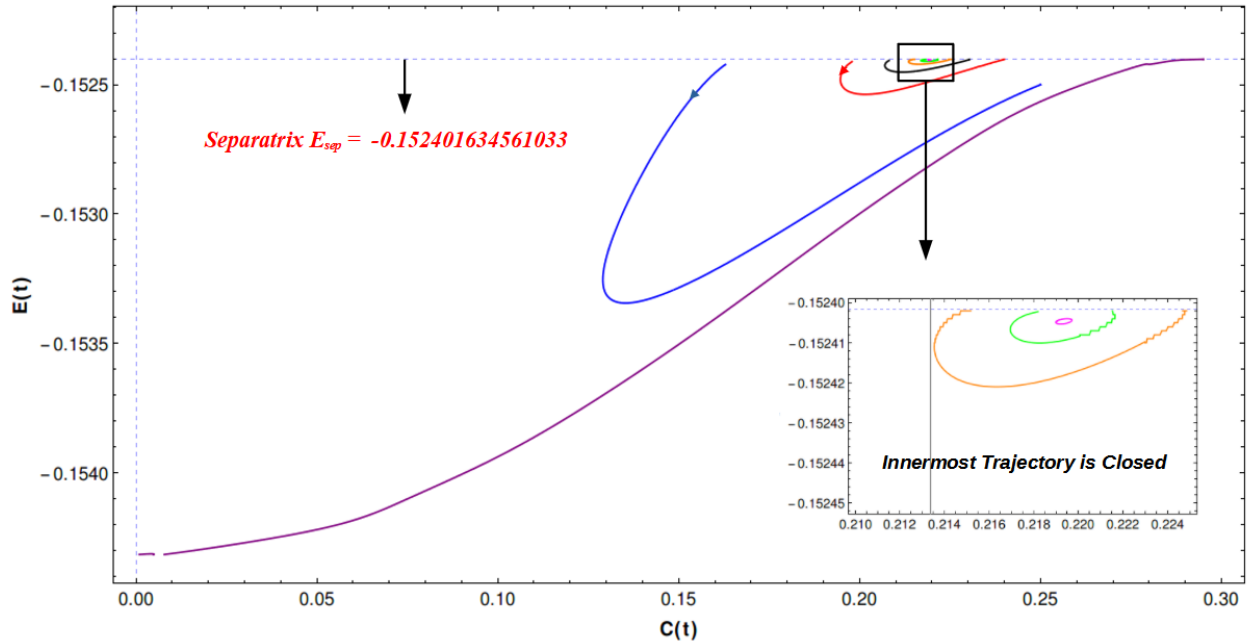
Figure 5.30: $C - E$ plane for $\hat{\alpha} = 0.33 \approx \hat{\alpha}_c$, $\lambda = 1$. We note that the closed loops exist for all values of $\hat{\alpha}$ until $\hat{\alpha}_c$. Note that as $\hat{\alpha} \to \hat{\alpha}_c$ E_{sep} and the location of the limiting torus (the innermost ring) approach the drop surface.

In Fig.5.31, we compare the trajectories obtained from the averaging analysis and the full integrations of the velocity field in the $C - E$ plane for $\hat{\alpha} = 10^{-4}$, $\lambda = 1$ for the same set of initial conditions used in Fig.5.29. From the plot, we see that the full integrations match well with our averaged trajectories, except that they cross the separatrix and escape to infinity. Note that once, the full integration trajectories cross the separatrix, they eventually stop at a point (C, E), corresponding to an open Stokesian streamline, unlike the inertial case, where the non-validity of the correction outside the screening length caused the trajectories to grow unbounded. Importantly, the trajectories obtained from full integration respect the deformation of the drop, which our averaged solutions do not. This is seen in the green curve from the full integration in Fig.5.31, which runs towards the separatrix surface. The averaging analysis fails to capture this behavior, on account of not considering drop deformation. Also, the wiggles associated with the full integrations are much larger in amplitudes for Ca having the same values as Re in Fig.5.17, suggesting that deformation exerts a stronger influence on the flow topology than inertia.

Having established the streamline topology, we now briefly describe its implication on scalar transport. Recall that for the case of drop with weak inertia, the streamlines (in the bifurcated wake regime) were spiralling in from infinity, thereby ensuring a constant replenishment of the ambient fluid, which led to convective enhancement and a boundary layer formation. In the case of a deformed drop however, we find that the streamlines spiralling out along the vorticity axis wind over an oblique torus. This implies that the same fluid is re-circulated and this re-circulation presents a possible barrier to convective enhancement. However, we also observed that the streamlines (which wound over tori far away from the limiting ring) were scattered in and out of the region, thereby bringing in new fluid material to effectively carry away the passive scalar. Thus there are two elements that govern convective enhancement. Firstly, a boundary layer (BL) exists in the usual sense, provided, the flow that goes out along the torus relaxes to the ambient concentration by the time it re-enters the boundary layer (while winding over an invariant torus). This amounts to a certain restriction on the time spent on the torus (outside the BL). Thus, there are two competing resistances (time scales), with the dominant one controlling transport. The first time scale (t_{BL}) is relevant to transport across the boundary layer and, the second one (t_{RS}) is relevant
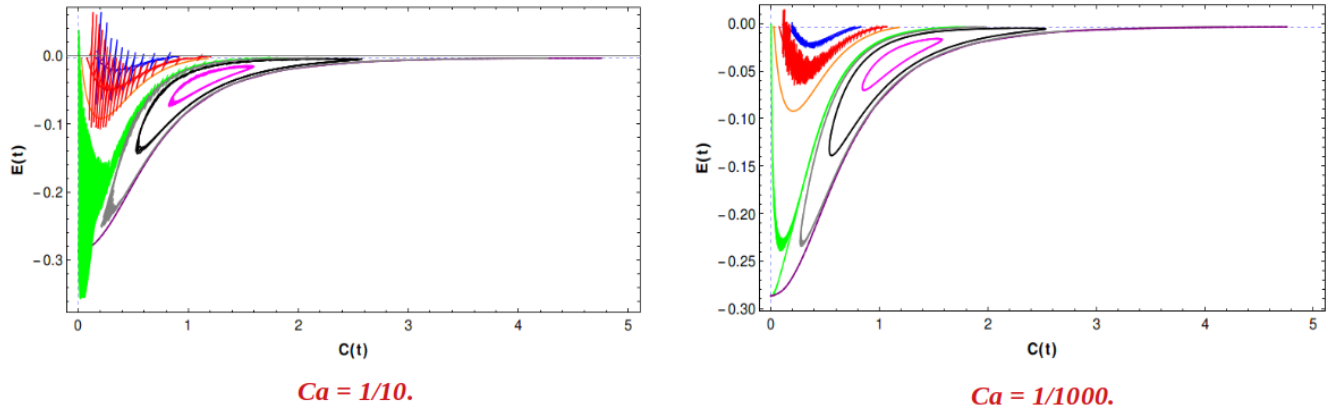
Figure 5.31: $C - E$ plane for $\hat{\alpha} = 10^{-4}$, $\lambda = 1 > \lambda_c$. The trajectories from the averaging analysis are compared with the full integration trajectories. Note the larger amplitude of fluctuations compared to the inertial case in Fig.5.17, implying that deformation is dominant of the two.

to the larger scale re-circulation around the invariant tori (with resonant scattering playing a role for streamlines that scatter). The smallest of the two will be the bottleneck that will determine the Nusselt number Nu. However, this requires a detailed analysis of this streamline topology, which is not carried out in this thesis. For the streamlines spiralling towards the flow-gradient plane, the situation is analogous to the convective channels being opened, as in the case of inertia, and so it can be subject to an analysis analogous to the one carried out by Krishnamurthy and Subramanian (2018b).

5.3.2 Drop in a Planar Linear Flow: The limit of large Viscosity ($\lambda \gg 1$; $\lambda Ca \sim O(1)$)

Until now, we had analysed the streamline topology in the exterior of the deformed drop, when interfacial tension controlled the deformation, i.e. $Ca \ll 1$; $\lambda \sim O(1)$. Now we examine the other case where the large viscosity of the drop limits its deformation from the spherical shape. G. I. Taylor (1934) was again the first to explore this limit ($\lambda \gg 1$) and he derived the steady-state deformation of the drop subject to a simple-shear flow for the limiting cases of $\lambda.Ca \ll 1$ ($Ca \ll 1$) and $\lambda.Ca \gg 1$ ($Ca \gg 1$). Cox(1969) later extended the analysis of steady state drop deformation for $\lambda.Ca \sim O(1)$, with $Ca \ll 1$. Several authors after Cox had attempted to derive the deformation and hence the velocity field at higher orders including Frankel and Acrivos (1970), Barthes-Biesel and Acrivos (1973), who were able to find the deformation to $O(Ca^2)$ and $O(Ca^3)$ respectively, but not for the corresponding large-λ case, because their expansions were not tailored for this purpose. Rallison (1980) was the first to recognise this constraint in the methods of Frankel and Barhtes-Biesel and suggested an alternate (simpler) way to derive the deformation and the velocity field at higher orders in $1/\lambda$, by starting from the solid-particle as the base state corresponding to $\lambda.Ca \gg 1$. More recently, Olivera and daCunha (2011) and Olivera and daCunha (2015), find the deformation of a drop in unsteady ambient flows at $O(1/\lambda)$ and $O(1/\lambda^2)$ respectively, but they do not account for a perturbed domain in their boundary conditions and end up with an erroneous velocity field at $O(1/\lambda)$.

We have derived the correction to the exterior velocity field at $O(1/\lambda)$, for $\lambda.Ca \sim O(1)$. Our derivation again requires us to solve the governing Stokes' equations (Eq.5.53) perturbatively subject to the boundary conditions given in Eq.5.54-5.55. We find it convenient to rescale the interior pressure field as $\hat{\mu}u_c/l_c$ as opposed to the scale $\mu u_c/l_c$ used in Eqs.5.54-5.55. This would change the governing equation to:

$$
\begin{array}{ll}
\nabla.\mathbf{u} = 0 & \\
\nabla^2\mathbf{u} = \nabla p & (Exterior\ Problem)
\end{array}
\qquad
\begin{array}{ll}
\nabla.\hat{\mathbf{u}} = 0 & \\
\nabla^2\hat{\mathbf{u}} = \nabla\hat{p} & (Interior\ Problem),
\end{array}
\quad (5.89)
$$

with,

$$\mathbf{u} \to \bar{\mathbf{\Gamma}}.\boldsymbol{x} \quad as \ r \to \infty \tag{5.90}$$

$$
\left.
\begin{array}{l}
\text{(i) } \mathbf{u} = \hat{\boldsymbol{u}} \\[2mm]
\text{(ii) } \mathbf{u}.\mathbf{n} = \hat{\boldsymbol{u}}.\boldsymbol{n} = \frac{1}{\nabla F}\frac{\partial F}{\partial t} \\[2mm]
\text{(iii) } (2(\bar{\boldsymbol{E}} - \lambda \hat{\bar{\boldsymbol{E}}}) - (p - \lambda\hat{p})).\mathbf{n} = \frac{1}{Ca}\boldsymbol{n}(\boldsymbol{\nabla}.\boldsymbol{n})
\end{array}
\right\} \text{At } r = 1 + \frac{1}{\lambda}\,\Im(\lambda,\hat{\alpha}) + O(\frac{1}{\lambda^2}), \tag{5.91}
$$

as the rescaled boundary conditions. In this case, our perturbation parameter is $1/\lambda$ and the drop surface is represented by:

$$F(r,\lambda,Ca,\hat{\alpha},t) = r - \left(1 + \frac{1}{\lambda}\,\Im(\lambda.Ca,\hat{\alpha},t) + O(\frac{1}{\lambda^2})\right) = 0 \tag{5.92}$$

The associated fields in the governing equation are expanded as:

$$\boldsymbol{u} = \boldsymbol{u}^{(0)} + \frac{1}{\lambda}\,\boldsymbol{u}^{(1)} + O(\frac{1}{\lambda^2}) \tag{5.93}$$

$$\hat{\boldsymbol{u}} = \hat{\boldsymbol{u}}^{(0)} + \frac{1}{\lambda}\,\hat{\boldsymbol{u}}^{(1)} + O(\frac{1}{\lambda^2}) \tag{5.94}$$

$$p = p^\infty + p^{(0)} + \frac{1}{\lambda}\,p^{(1)} + O(\frac{1}{\lambda^2}) \tag{5.95}$$

$$\hat{p} = \hat{p}^\infty + \hat{p}^{(0)} + \frac{1}{\lambda}\,\hat{p}^{(1)} + O(\frac{1}{\lambda^2}) \tag{5.96}$$

Similarly, one can also expand the normal vector $\boldsymbol{n}$ as:

$$\boldsymbol{n} = \boldsymbol{n}^{(0)} + \frac{1}{\lambda}\,\boldsymbol{n}^{(1)} + O(\frac{1}{\lambda^2}) \tag{5.97}$$

where $\boldsymbol{n^{(0)}}$ is the unit radial vector. Unlike the $O(Ca)$ expansion, here the shape of the drop cannot be assumed to be linear in $\boldsymbol{E}$ (see Eq.5.102), but symmetry arguments nevertheless suggest that it should be a symmetric second order tensor $\boldsymbol{A}$, thereby leading to the F of the form

$$F(r,\lambda.Ca,\hat{\alpha}) = r - \left(1 + \frac{1}{\lambda}\boldsymbol{A} : \boldsymbol{nn} + O(1/\lambda^2)\right) \tag{5.98}$$

where $\boldsymbol{A}$ is a function of $\lambda.Ca$. This leads to the expansion for the normal vector $\boldsymbol{n}$ as:

$$\boldsymbol{n} = \boldsymbol{n}^{(0)} + \frac{1}{\lambda}\,\boldsymbol{n}^{(1)} + O(\frac{1}{\lambda^2}) \tag{5.99}$$

with $\boldsymbol{n}^{(1)} = 2\left[(\boldsymbol{A} : \boldsymbol{n}^{(0)}\boldsymbol{n}^{(0)})\boldsymbol{n}^{(0)} - \boldsymbol{A}.\boldsymbol{n}^{(0)}\right]$. At leading order, the stress boundary condition Eq.5.91(iii) reduces to the interior shear stress being zero (since λ is multiplied with interior stress field) - implying that the leading order approximation is a solid-body rotation given by:

$$\hat{\boldsymbol{u}}^{(0)} = r\,\boldsymbol{\Omega}.\boldsymbol{n}^{(0)} \tag{5.100}$$

This interior field, together with the interfacial velocity boundary conditions (Eqs.5.91(i)-(ii)) and the governing equation (Eq.5.89) for the exterior field give at $O(1)$:

$$\boldsymbol{u}^{(0)} = \left[\frac{5}{2}\left(\frac{1}{r^4} - \frac{1}{r^2}\right)\right](\boldsymbol{E} : \boldsymbol{n}^{(0)}\boldsymbol{n}^{(0)})\boldsymbol{n}^{(0)} + \left(r - \frac{1}{r^4}\right)\boldsymbol{E}.\boldsymbol{n}^{(0)} \tag{5.101}$$

which is again the exterior velocity field associated with a solid-particle in a linear flow. The form of the stress boundary condition (Eq.5.91(iii)), with λ multiplying the interior stress field, suggests that one can systematically proceed by using the aforementioned $O(1)$ solution for the exterior field to find the $O(1/\lambda)$ velocity and pressure field in the drop interior. Then the deformation of the drop can be found using the kinematic boundary condition (Eq.5.91(ii)) at the interface. Finally, incompressibility and the slip boundary condition (Eq.5.91(i)) at the interface can give us the exterior field at $O(1/\lambda)$. Thus, one can find the interior field, deformation and the exterior field in a systematic fashion. This procedure is highlighted in the flow chart given in Fig.5.32. Note that this method is tailored for the large-λ expansion and one does not have to worry about terms jumping order in this procedure (as was the case with the expansions of Frankel and Acrivos (1970) and Barthes-Biesel and Acrivos (1973)) and is also analogous to the procedure suggested by Rallison (1980), although he had considered the limit of $\lambda.Ca \gg 1$.
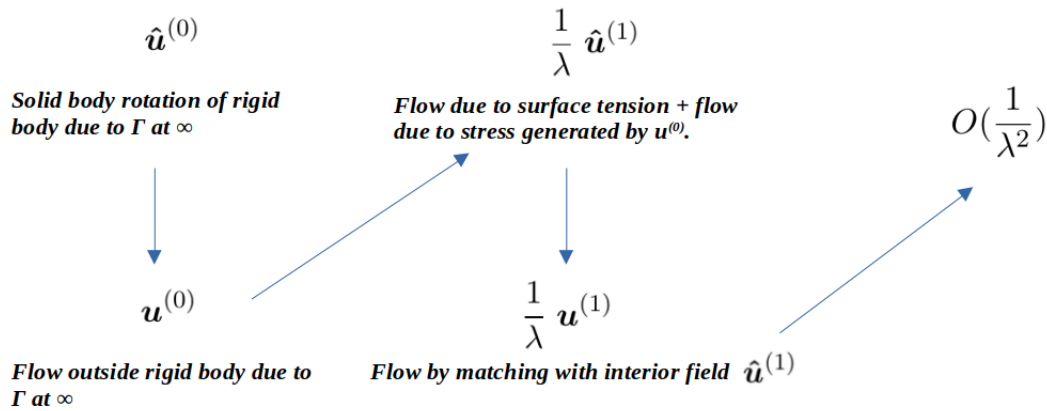
Figure 5.32: The solution procedure for finding the higher order corrections to velocity field in $1/\lambda$, starting from the velocity field for solid particle.

Now, we apply this procedure by using the $O(1)$ exterior velocity field to calculate the interior and exterior fields at $O(1/\lambda)$. At $O(1/\lambda)$, the stress boundary condition (Eq.5.91(iii)) reduces to:

$$\hat{p}^{(1)} - 2\hat{\bar{E}}^{(1)} = \frac{4}{\lambda.Ca}\boldsymbol{A} : \boldsymbol{n}^{(0)}\boldsymbol{n}^{(0)} + p^{(0)}\boldsymbol{n}^{(0)} - 2\bar{\boldsymbol{E}}^{(0)}.\boldsymbol{n}^{(0)} \tag{5.102}$$

where $\bar{\boldsymbol{E}}^{(0)} = \nabla\boldsymbol{u}^{(0)} + (\nabla\boldsymbol{u}^{(0)})^T = f(\boldsymbol{E}, \boldsymbol{\Omega})$. From the equation above, we see that the tensor $\boldsymbol{A}$ is a function of $\lambda.Ca$ and is not linear in $\boldsymbol{E}$. From the aforementioned boundary condition, one can easily show that $\boldsymbol{u}^{(1)}$ and $\hat{\boldsymbol{u}}^{(1)}$ are of the form:

$$\hat{\boldsymbol{u}}^{(1)} = \frac{5}{2}r\boldsymbol{E}.\boldsymbol{n}^{(0)} - \frac{8r^3}{19\lambda Ca}(\boldsymbol{A} : \boldsymbol{n}^{(0)}\boldsymbol{n}^{(0)})\boldsymbol{n}^{(0)} + \left(\frac{20r^3}{19\lambda Ca} - \frac{32r}{19\lambda Ca}\right)\boldsymbol{A}.\boldsymbol{n}^{(0)} \tag{5.103}$$

which is the used in the kinematic boundary condition (Eq.5.91(ii)), which at $O(1/\lambda)$ is given by:

$$\hat{\boldsymbol{u}}^{(0)}.\boldsymbol{n}^{(1)} + \hat{\boldsymbol{u}}^{(1)}.\boldsymbol{n}^{(0)} + \boldsymbol{A} : \boldsymbol{n}^{(0)}\boldsymbol{n}^{(0)}\left(\frac{\partial\hat{\boldsymbol{u}}^{(0)}}{\partial r}\right)_{r=1}.\boldsymbol{n}^{(0)} = 0. \tag{5.104}$$

Substituting for $\hat{\boldsymbol{u}}^{(1)}$ in the above equation, we get:

$$\frac{5}{2}\boldsymbol{E} - \frac{20}{19\lambda.Ca}\boldsymbol{A} + \boldsymbol{\Omega}.\boldsymbol{A} - \boldsymbol{A}.\boldsymbol{\Omega} = 0, \tag{5.105}$$

which determines the components of $\boldsymbol{A}$. Solving the above equation, using the forms of $\boldsymbol{E}$ and $\boldsymbol{\Omega}$ (Eq.5.19),

we get:

$$A_{11} = -A22 = \frac{1805(1 - \hat{\alpha}^2)\lambda^2 Ca^2}{1444(1 - \hat{\alpha})\lambda^2 Ca^2 + 1600} \tag{5.106}$$

$$A_{12} = A21 = \frac{1900(1 + \hat{\alpha})\lambda Ca}{1444(1 - \hat{\alpha})\lambda^2 Ca^2 + 1600} \tag{5.107}$$

Using these quantities in Eq.5.91(i) along with the incompressibility condition and the governing equation (Eq.5.89), one can easily show that the exterior field at $O(1/\lambda)$ has the form:

$$\begin{aligned} \boldsymbol{u}^{(1)} =& c_1(r)(\boldsymbol{E} : \boldsymbol{n}^{(0)}\boldsymbol{n}^{(0)})\boldsymbol{n}^{(0)} + c_2(r)\boldsymbol{E}.\boldsymbol{n}^{(0)} + c_3(r, \lambda Ca)(\boldsymbol{A} : \boldsymbol{n}^{(0)}\boldsymbol{n}^{(0)})\boldsymbol{n}^{(0)} + c_4(r, \lambda Ca)\boldsymbol{A}.\boldsymbol{n}^{(0)} + \\ & c_5(r)(\boldsymbol{A} : \boldsymbol{n}^{(0)}\boldsymbol{n}^{(0)})(\boldsymbol{E} : \boldsymbol{n}^{(0)}\boldsymbol{n}^{(0)})\boldsymbol{n}^{(0)} + c_6(r)(\boldsymbol{A}.\boldsymbol{E} : \boldsymbol{n}^{(0)}\boldsymbol{n}^{(0)})\boldsymbol{n}^{(0)} + c_7(r)\boldsymbol{A} : \boldsymbol{En}^{(0)} + \\ & c_8(r)(\boldsymbol{A} : \boldsymbol{n}^{(0)}\boldsymbol{n}^{(0)})\boldsymbol{E}.\boldsymbol{n}^{(0)} + c_9(r)(\boldsymbol{E} : \boldsymbol{n}^{(0)}\boldsymbol{n}^{(0)})\boldsymbol{A}.\boldsymbol{n}^{(0)} + c_{10}(r)\boldsymbol{E}.\boldsymbol{A}.\boldsymbol{n}^{(0)} + c_{11}(r)\boldsymbol{A}.\boldsymbol{E}.\boldsymbol{n}^{(0)} \end{aligned} \tag{5.108}$$
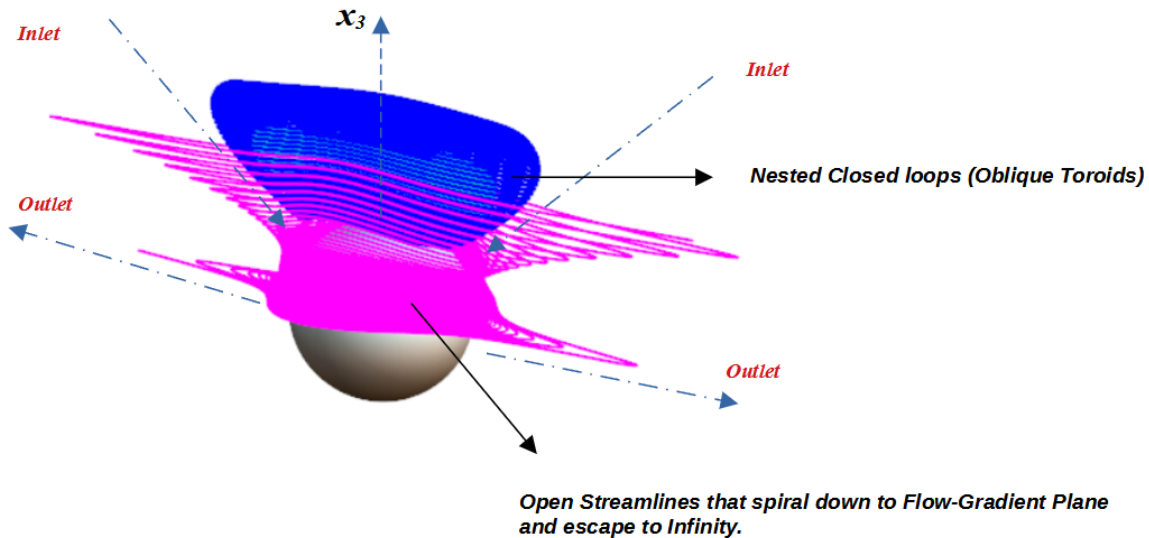
Figure 5.33: Streamlines in the exterior for $\hat{\alpha} = 0$, $\lambda = 25$ and $Ca = 1/10$. The separatrix for this case lies at ∞ and there is no scattering of streamlines. This plot shows the existence of nested tori (blue and magenta) for $\lambda \gg 1$ and $\lambda Ca \sim O(1)$ and the other features remain the same as the streamlines for $O(Ca)$ velocity field.

The coefficients that appear in these equations are given in Appendix 1. Note that an erroneous form of this exterior field was given by Olivera and daCunha (2011), whose expression does not contain terms that involve products of $\boldsymbol{A}$ and $\boldsymbol{E}$. This is because the authors have not accounted for the perturbation of the domain (drop surface) in his derivation. We can now use this velocity field, along with the leading order field, to plot the streamlines in the exterior. This streamline topology analysis is currently being undertaken and here we are only able to show preliminary results of $3D$ streamline topology, which is shown in Fig.5.33. The plot again suggests that the nested tori configuration exists in the limit of $\lambda \gg 1$, with $\lambda\,Ca \sim O(1)$. More detailed analysis and the $C - E$ description will follow in the future, but for now the initial results suggest that the existence of nested tori are not just restricted to the $O(Ca)$ correction and it seems to be an ubiquitous characteristic of drop deformation regardless of the dominant parameter.

This means that the same conclusion drawn regarding scalar transport for finite-Ca $O(1) - \lambda$ deformation will hold true for this limit.

5.4 The Combined effect of Inertia and Deformation

Herein, we briefly examine the simultaneous role of weak inertia or drop deformation, by combining the corrections to the Stokesian velocity field analyzed discussed in sections 1.2 and 1.3.

(a) $Re/Ca = \infty$

(b) $Re/Ca = 3$

(c) $Re/Ca = 0.3$

(d) $Re/Ca = 0$
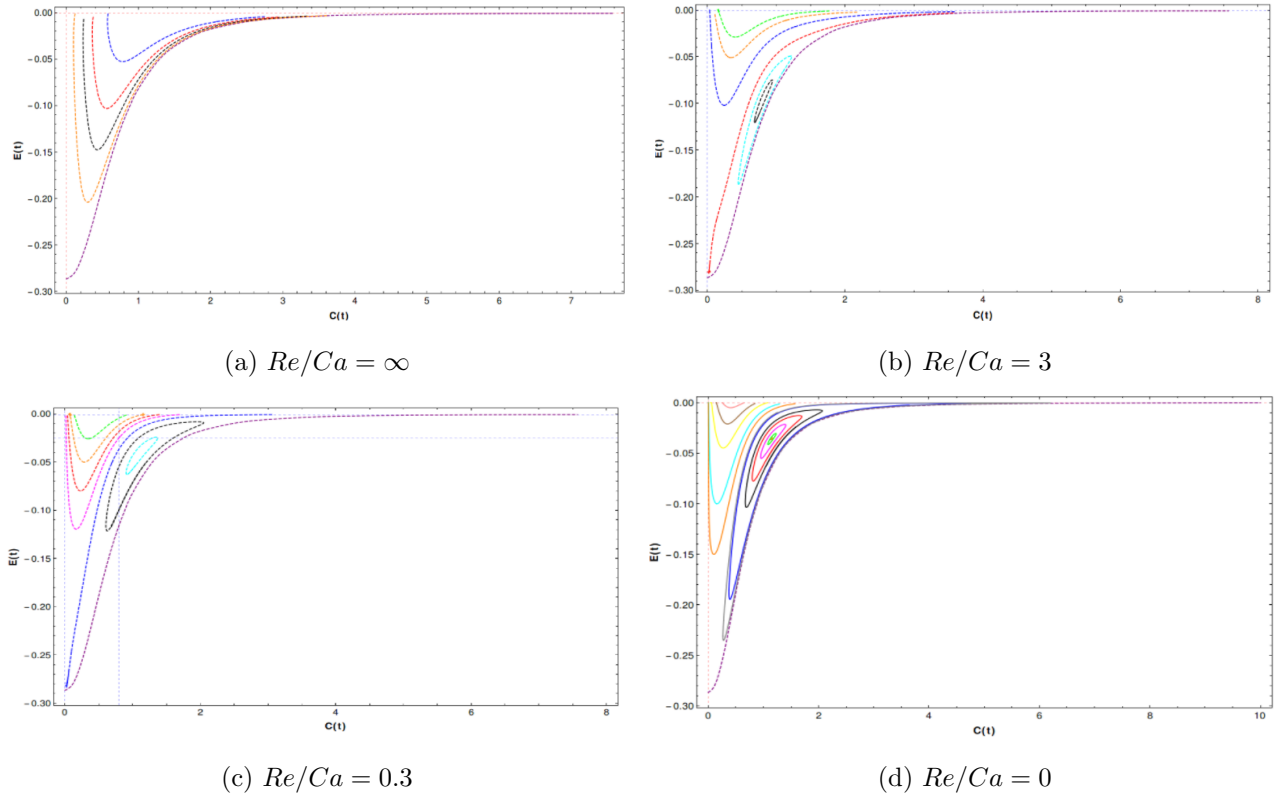
Figure 5.34: $C - E$ plane for the case of $\hat{\alpha} = 10^{-4}$, $\lambda = 1$. There is a critical $Re/Ca \sim 3 > 1$, below which the nested closed loops exist. This implies that deformation is a dominant perturbation than inertia and will therefore govern the transport rate.

One may write the combined velocity field as:

$$\boldsymbol{u} = \boldsymbol{u}^{(0)} + Ca \left(\frac{Re}{Ca} \boldsymbol{u}^{(1)}_{O(Re)} + \boldsymbol{u}^{(1)}_{O(Ca)} \right) = \boldsymbol{u}^{(0)} + Ca \ \boldsymbol{u}^{(1)}_{comb} \tag{5.109}$$

where $\boldsymbol{u}^{(1)}_{O(Re)}$ is the $O(Re)$ correction given in Eq.5.20 and $\boldsymbol{u}^{(1)}_{O(Ca)}$ is the $O(Ca)$ correction in Eq.5.76. The equations resulting, from application of the method of averaging (Eq.5.35 and 5.36), may now be written as:

$$\frac{dC}{dt} = Ca \ \mathcal{F}_1(C, E, Re/Ca, r) \tag{5.110}$$

$$\frac{dE}{dt} = Ca \ \mathcal{G}_1(C, E, Re/Ca, r) \tag{5.111}$$

where we have chosen the slow variable to be $\hat{t} = Ca \ t$, with the functions $\mathcal{F}_1$ and $\mathcal{G}_1$ being of the same form as those in Eqs.5.27-5.29, but with the velocity components $\boldsymbol{u}^{(1)}$ replaced by $\boldsymbol{u}^{(1)}_{comb}$ given above.

The $C - E$ plane for this combined velocity field is shown for $\hat{\alpha} = 10^{-4}$, $\lambda = 1$ for various values of Re/Ca in Fig.5.34, and we see that for small values of Re/Ca (Fig.5.34(c)-(d)), the $C - E$ plane resembles that of $O(Ca)$ streamlines, where, rather unexpectedly, the nested-tori still exist upon the addition of inertial perturbation, despite them being a structurally unstable configuration. We also observe there is a critical value of Re/Ca beyond which the nested tori no longer exist, but since this critical value $(Re/Ca)_c > 1$ (the tori exist for $Re/Ca = 3$ in fig.5.34(b) for this particular set of parameters), we can conclude that of the two perturbations, Ca is the dominant one that dictates the streamline topology and hence the Nusselt number. A more detailed analysis in this regard is currently under way and shall be reported in future communications. A similar comparison can be made with the $O(1/\lambda)$ field and the $O(Re)$ field with $Re\lambda$ being the governing parameter and this is also currently under investigation.

The streamline topology around a drop with weak inertia and deformation have been addressed in the work of Singh and Sircar (2011), where the authors do not observe any nested tori. But given that their simulations contained periodic boundary conditions and hence, finite box-size effects and that the analytical correction due to inertia in our velocity field is not valid outside a domain of $O(Re-1/2)$ (the inertial screening length), we are unable to make a direct comparison with their results. But, one can calculate the outer solution of the inertial correction and undertake such a comparison, which will be taken up in the near future.

5.5   Concluding Remarks

In this chapter, we have described the non-trivial changes in streamline topology, in the exterior of the drop immersed in the one-parameter family of the (canonical) hyperbolic planar linear flows, on account of either inertia or drop deformation. Such effects are only perturbative in nature when the streamlines in the baseline-scenario (spherical drop; $Ca = Re = 0$) are already open. But, when the streamlines in the immediate neighborhood of the drop are closed (as is the case for drop in a canonical hyperbolic linear flow with $\lambda > \lambda_c$), the streamline topology is altered. This has profound implications for the rate of scalar transport, arising from the aforementioned alteration in the streamline topology. The open spiralling streamlines convect heat efficiently for large enough Pe, and the transport, unlike the Stokesian scenario, will no longer be diffusion limited. Krishnamurthy and Subramanian (2018b) determined this convective enhancement at large Pe using boundary-layer analysis in a surface-flow aligned coordinate system for the case of drop with weak inertia, and the rate of transport was found to be $Nu \sim O(RePe)^{1/2}$. Our eventual aim is to be able to calculate the analogous convective enhancement for the case of a weakly deformed drop in hyperbolic linear flows. Although the streamline topology is more complicated in the deformed-drop case (that is, for finite Ca), assuming the boundary layer resistance to be dominant, one expects $Nu \sim (CaPe)^{1/2}$ in the regime $Ca \ll 1$, $\lambda \sim O(1)$. This would be the case provided $\hat{\alpha}_c - \hat{\alpha} \sim O(1)$. In the large-$\lambda$ limit, the analog of the above result viz. $Nu \sim (Pe/\lambda)^{1/2}$ does not hold since, as discussed in the section on the large-λ limit, the limit of a weakly deformed viscous perfectly miscible drop ($\lambda \gg 1$, $\lambda.Ca = \infty$) still conforms to a reversible Stokesian scenario, and therefore the streamlines around the deformed drop must still be closed, in turn implying diffusion-limited transport. Thus, for the large-λ limit, one may write $Nu = (Pe/\lambda)^{1/2}f(\lambda.Ca, \hat{\alpha})$, and for $\lambda.Ca \to \infty$, where the leading order spiralling contribution enters at $O(1/(\lambda^2 Ca))$, $Nu \sim (Pe/(\lambda^2.Ca))^{1/2}$. One can also consider the combined case with both weak inertia and deformation, for which our preliminary results again suggested a spiralling streamline topology in the exterior. For this case, $Nu = (\epsilon Pe)^{1/2}\mathcal{F}(\hat{C}, \tau, \hat{\alpha}, (Re/\epsilon), \lambda.Ca)$, $\epsilon = Ca\ or(1/\lambda)or(1/\lambda^2.Ca)$, depending on the scenario. These scaling relations and their corresponding regimes are shown in Fig.5.35.
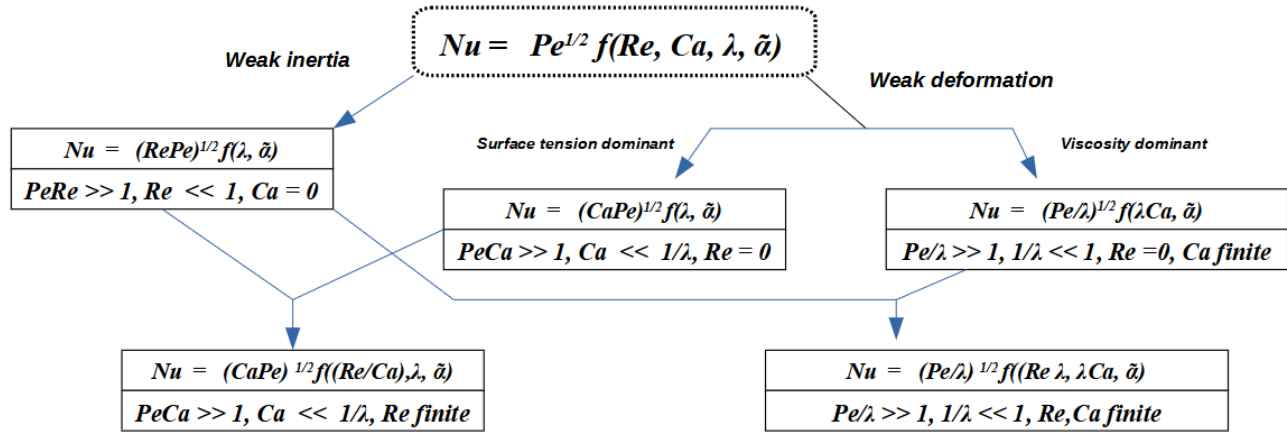
Figure 5.35: Summary of relationship between Nu and Pe corresponding to various scenarios in the closed-streamline regime.

However, as pointed out in the paragraph above, these relations are not valid everywhere in the parameter space (the $\hat{\alpha} - \lambda$ space). This is because, we saw from our streamline analysis that the exterior domain contains streamlines that wind over a torus. It was mentioned that the existence of these tori will inhibit the convective enhancement and will have a greater influence on transport for $\hat{\alpha}_c - \hat{\alpha} \ll 1$ and, for this case, one needs to do a detailed analysis of the streamline topology in order to find the relation between Nu and Pe. We conclude the chapter with this brief discussion on the expected scaling of transport rate in the closed-streamline regime, with a detailed analysis into them, being reserved for the future. This chapter marks the end of this thesis and we will summarise the results from various chapters in the epilogue and provide an outlook of future research directions.

Chapter 6

Conclusions

This thesis has been primarily concerned with the problem of transport from an isolated drop suspended in a topologically complex shearing flow, in the limit of $Pe \gg 1$. In this chapter, we briefly summarise the results of our effort in analysing this problem. Our simplifying assumptions, resulted in a physical system where an isolated spherical neutrally buoyant drop is suspended in an arbitrary $3D$ linear flow with $Re \ll 1$, corresponding to the Stokesian regime. For the exterior problem, defined by the dominant resistant to transport being in the fluid outside the drop, two distinct regimes of transport were identified, at large Pe, depending on the nature of streamlines in the neighborhood of the drop: (i) the open streamline regime, where the usual boundary-layer-enhanced transport leads to $Nu \sim O(Pe^{1/2})$ for $Pe \gg 1$ and, (ii) the closed-streamline regime, where $Nu \sim O(1)$ for $Pe \gg 1$ implying diffusion-limited transport, unless additional physics, for instance, those relating to micro-scale inertia or drop deformability are accounted for. For the interior, wherein the drop fluid offers the dominant resistance to transport, again one identified two distinct classes of flows based on the transport mechanism. Interior flows with regular streamlines (both closed curves, and open curves that densely wind around invariant tori) lead to diffusion-limited transport, while the presence of chaotic streamlines leads to convective enhancement. Below, we present a chapter-wise summary of our conclusions.

6.1 Summary of Conclusions

The analysis of the exterior transport problem, corresponding to the open streamline regime (that dominates the four-dimensional space of incompressible linear flows), was presented in **Chapter 2**. The aim is to analytically calculate the Nusselt number Nu for a drop in an arbitrary $3D$ linear flow as a function of the flow parameters ($P = \{\alpha, \epsilon, \theta_\omega, \phi_\omega\}$) and viscosity ratio ($\lambda$). This is achieved by considering a pair of two-parameter families that correspond to sub-spaces of the four-dimensional space above. These are the three-dimensional extensions with aligned vorticity (characterized by ϵ and α), and the axisymmetric extensions with inclined vorticity (characterized by θ_ω, α). A thorough analysis of the surface-streamline topology using the discriminant and invariants of an auxiliary linear system was carried out, the insights from which were used to successfully develop a surface-streamline-aligned coordinate system, the $C - \tau$ system, to calculate $Nu = f(P, \lambda)Pe^{1/2}$ for both the aforementioned two-parameter families. The calculation showed that the Nusselt number was greatly influenced by the surface-streamline topology. Importantly, it was shown that, for a subset of special flow configurations, the eccentric planar elliptic flows, the transport rate $Nu \sim O(Pe^{1/3})$ (similar to a solid particle), on account of these flows resulting in closed streamlines on the drop surface; as a result, $Nu/Pe^{1/2} \sim O(Pe^{-}1/6) \to 0$ for $Pe \to \infty$, leading to a singular furrow in the Nu-surface. This scaling is similar to that of a solid particle in a linear flow. These eccentric planar elliptic flows were identified as generalisations of the canonical planar linear flows. A preliminary investigation of the surface-streamline topology associated with a drop in an arbitrary

linear flow suggested that the resulting streamline topologies are analogous to those already found for the two-parameter families examined here. Therefore, the Nusselt surface for the general case may be obtained, in principle, by piecing together Nu curves from the aforementioned two-parameter families as an arbitrary linear flow is, qualitatively, a combination of the two-parameter families. The analysis presented in this chapter is the first of its kind to analyse the problem of transport from drops in linear flows with complex streamline topologies, whereas, most of the earlier efforts were restricted to flows which were simple and symmetric. While Krishnamurthy and Subramanian (2018a) took the first step in moving beyond the elementary symmetric surface-streamline topologies, we have taken the logical next step, that remains applicable to a general linear flow.

In **Chapter 3**, the eccentric planar linear flows, identified in Chapter 2, were analyzed in detail, with the three-dimensional subspace corresponding to their existence being identified. This subspace was represented via projections onto a pair of three-dimensional sub-spaces ($(\epsilon - \phi_\omega - \theta_\omega)$ and $(\epsilon - \phi_\omega - 1/\alpha)$ spaces); the planar linear flows occupy a finite three-dimensional region in these projections. These flows, unlike their canonical counterparts, have a non-trivial component of extension normal to the plane of flow, which led to the $3D$ streamlines projecting onto eccentrically placed surface streamlines on the unit sphere. The resulting surface streamlines, for the eccentric elliptic linear flows in particular, constitute generalizations of Jeffery orbits; this, because the projections of the streamlines in the canonical elliptic linear flows lead to the usual Jeffery orbits (Krishnamurthy and Subramanian (2018a)). In this chapter, the equation of this generalised Jeffery orbit was derived using a geometrical argument, with the Bretherton constant, governing the eccentricity of the orbits, being a function of the flow-type parameters (α, ϵ, θ_ω, ϕ_ω). Finally, we developed an alternate classification scheme for $2D$ linear flows, motivated by the fact that the eccentric and canonical flows are not distinguished in the conventional classification scheme based on scalar invariants of the velocity-gradient tensor. The domains of existence of the incompressible eccentric planar linear flows can be considered a classification that, for instance, demarcated the canonical and eccentric flows and also recognized the distance between these flows, unlike the usual $Q - R$ scheme. Thus, this new scheme was developed to achieve the same goal for $2D$ linear flows (compressible and incompressible). This new scheme consists of finite region that encloses all $2D$ linear flow topologies. Importantly, this alternate scheme provides for a notion of distance between the flow topologies, which a classification based on scalar invariants does not have.

Chapter 4 focused on the interior transport problem, where we made a first attempt at characterizing the rate of transport within a drop suspended in an arbitrary linear flow. It was shown that for a vast majority of linear flows, including almost all members of the two-parameter families considered in Chapter 2, in the context of the exterior problem, the streamlines in the interior of the drop exhibit Lagrangian chaos. Ambient linear flows that lead to interior streamlines that are regular closed curves (axisymmetric extension, or the canonical planar linear flows), or wind around invariant tori (axisymmetric extension with aligned vorticity), are known to exhibit diffusion-limited transport at large Pe (Christov and Homsy (2009)). While the transport rate is expected to be enhanced at large Pe for ambient linear flows resulting in chaotic interior streamlines (Bryden and Brenner (1999), Christov and Homsy (2009) and others), there have been no reports of the scaling behavior of Nu for large Pe. In this chapter, stochastic simulations are used to calculate the Nusselt number in the interior of a drop with chaotic interior, and identify the scaling obtained at large Pe. Our results suggest that the scaling at large Pe is not universal and is dependent on the ambient flow; the exponent appears correlated to the extent of chaos in the interior. For linear flows that lead to a chaotic interior that is space-filling (certain members of the axisymmetric-extension-inclined vorticity family being examples), Nu is found to scale as $Pe^{1/2}$, as expected from scaling arguments. For other cases, where the chaotic regions are disconnected, owing to the presence of intervening regular islands, one obtains $Nu \sim O(Pe^\beta)$ at large Pe, where $\beta(< 1/2)$ is a flow-dependent exponent. The cases of convectively enhanced transport appear to exhibit an internal boundary layer, which scales ad $O(Pe^{-\beta})$, across which temperature or concentration changes by $O(1)$.

The existence of such a boundary layer is shown for the first time in this chapter for a few representative cases.

The last chapter (**Chapter 5**) of this thesis is concerned with the vanishingly small subset of general linear flows, the canonical planar linear flows, that lead to closed streamlines in the immediate neighborhood of a drop immersed in such a flow; the existence of closed streamlines depends on the viscosity ratio λ and the flow-parameter $\hat{\alpha}$. As was noted earlier, closed streamlines lead to diffusion-limited transport, as is, in fact, well known from earlier analyses of problems involving rigid particles (Poe and Acrivos (1976), Acrivos (1971)). Convective enhancement at large Pe will result from the alteration of the exterior closed-streamline topology. for drops, this may be achieved with the addition of inertia or deformation. While the effect of inertia was analyzed by Krishnamurthy and Subramanian (2018b), earlier studies on drop deformation appeared to have ruled out this possibility (Torza et al. (1971), Kennedy and Pozrikidis (1994)). In this chapter, we use analytical and numerical techniques to show that deformation indeed alters the streamline topology by destroying the symmetry of Stokesian closed streamlines. Moreover, the deformation-induced alteration is found to be more complicated than its inertial counterpart: while a part of the fluid domain contains open spiralling streamlines similar to the inertial case, the remainder of the domain consists of spiralling streamlines that wind around nested invariant tori. This deformation-induced alteration of the streamline topology was confirmed by boundary integral simulations. The method of averaging was used to characterise these streamlines in terms of adiabatic invariants (C and E) in their natural plane of representation, the $C - E$ plane.

6.2   Future Directions

Having summarised the primary results of the various chapters, we now provide possible research avenues, that one can pursue in light of our results. While we have already discussed these ideas briefly in the corresponding chapters, we summarise and provide more details here. The analysis carried out in Chapter 2, has shown that one can calculate the Nusselt number for a drop suspended in an arbitrary $3D$ linear flow. The analysis may be generalized in at least two directions. One of these is to account for the deviation from neutral buoyancy. This would involve a new classification of surface streamline topologies that arise from a superposition of the meridional surface-streamline topology arising from translation, and the streamline topologies already seen for a linear flow. The other direction in which this analysis may be generalized is to a drop in an ambient turbulent flow. In fact, the analysis in Chapter 2 for the large-Pe transport from a drop in an arbitrary linear flow is analogous to that of Batchelor (1979), who calculated the transport rate associated with a neutrally buoyant solid particle in an arbitrary linear flow at large Pe. Next, Batchelor (1980) analyzed transport from a solid particle in a turbulent flow. This generalization to a turbulent flow is a natural one for sub-Kolmogorov particles since, on the scale of the particle, the turbulence appears as a stochastic linear flow with known statistics for the velocity gradient tensor (Meneveau (2011)). Batchelor (1980) showed that the rate of transport at large Pe, in turbulence, still scales as $Pe^{1/3}$, as for a laminar flow with regular open streamlines, but with the velocity gradient being given by the average rate of extension projected along the vorticity (that is, $< \hat{\boldsymbol{\omega}}.\boldsymbol{E}.\hat{\boldsymbol{\omega}} >$, with $\hat{\boldsymbol{\omega}}$ denoting the unit vector along the vorticity direction); note that this average is non-zero in turbulent on account of vortex-stretching. It is thus natural for one to seek an analysis of the averaged rate of transport from a drop in a turbulent flow. For a particle, this turbulent transport problem is simplified on account of two factors: (i) the tightly spiralling nature of the near-surface streamlines around a rotating particle that leads to the contribution of the extensional components, other than the one projected along ω, being asymptotically small; (ii) the asymptotically large time scale of $O(\dot{\gamma}^{-1}Pe^{1/3})$ associated with the rigid particle boundary layer to achieve a quasi-steady state, for large Pe, which allows for the transport to only be controlled by the long-time or ensemble average of the vorticity-aligned extension rate. Neither of these is true for the drop. On one hand, as already seen in Chapter 2, the surface streamline topology for a drop can be quite non-trivial depending on the ambient linear flow parameters (and λ); on the other

hand, the time scale for the development of the boundary layer is now $O(\dot{\gamma}^{-1})$.

Thus, the original averaging procedure used by Batchelor (1980), for a particle, does not work anymore. Thus, the general problem for a drop in an ambient turbulent flow may have to be solved numerically. One may nevertheless bound the rate of transport by considering two limiting cases: These correspond to the extremes where the correlation time characterizing the (Kolmogorov) velocity gradient is much greater or much lesser than the time scale of boundary layer development. The first limit allows for a quasi-steady approximation, where the Nu obtained as a function of the flow parameters as in Chapter 2, may be averaged a accounting for the probability distributions characterizing the occurrence of these flow parameters in (homogeneous isotropic) turbulence. The other limit should allow for the derivation of a turbulence-averaged convection-diffusion equation with a diffusivity that now includes an additional flow-induced contribution (that arises from the random walk executed by a tracer under the influence of a fluctuating velocity field with a short-correlation time; this latter approach might proceed along the lines of Brunk et al., 1997. The statistical average of Nu in the actual turbulent flow, is expected to be within these two bounds, but the calculation of this Nu can only be achieved numerically.

In Chapter 3, we had identified a novel class of eccentric planar elliptic flows, where we had commented briefly on their relevance to other problems in microhydrodynamics. One such scenario, we highlighted was the orientation dynamics of anisotropic particles suspended in these flows. The orientation of an anisotropic particle in canonical planar linear flows results in Jeffery orbits, provided $\hat{\alpha} \in [-1, 1/\kappa^2]$ (L. G. Leal and Hinch (1972),Marath and Subramanian (2018)), where the nature of the orbits is governed by a Bretherton constant $B = f(\hat{\alpha}, \kappa)$, κ being the geometric aspect ratio of the particle. When $\hat{\alpha}$ goes outside the range, there is a transition from closed orbits to open ones, the transition point corresponding to meridional trajectories on a unit sphere. This critical curve is given by: $\hat{\alpha} = 1/\kappa^2$ (for prolate spheroids) and $\hat{\alpha} = \kappa^2$ (for oblate spheroids) Marath and Subramanian (2018). One can extend this to the case of eccentric planar linear flows, where the transition will now be across a three-dimensional hypersurface demarcating four-dimensional volumes corresponding to closed and open trajectories (separated by parabolic topologies). Another scenario that one may consider is the coil-stretch dynamics of single-strand long polymeric molecules in these flows, which have applications in biological processes (Shaqfeh (2005)).

Our preliminary results of Chapter 4 suggest that the Nusselt number in the interior, $Nu \sim O(Pe^\beta)$, where β is a flow-dependent exponent. Even though, we have calculated the Nusselt number for a few representative cases, undertaking such a calculation for the entire four-dimensional parameter space of linear flows is a non-trivial task that also involves developing a correlation between the exponent and the nature of the chaotic (interior) dynamics. This in turn requires a characterization of the chaotic state using tools from the dynamical systems literature. From the analysis of Chapter 5, it is clear that drop deformation will exert a significant influence on transport rate, and will likely lead to a convectively enhanced transport at large Pe. While, we have only examined the streamline topology, the calculation of transport range in the various regimes highlighted in Fig.5.34, is again an interesting future direction.

Appendices

Appendix A

Expressions for $O(Ca)$ and $O(1/\lambda)$ Fields

A.1 $O(Ca)$ Corrections to Stokesian fields

The coefficients that appear in Eq.5.72 of Chapter 5, that describes the $O(Ca^2)$ correction to the shape are given by:

$$s1 = \frac{(19\lambda + 16)(751\lambda + 656)}{1728(\lambda + 1)^2} \tag{A.1}$$

$$s2 = \frac{(19\lambda + 16)\left(3591\lambda^3 + 16360\lambda^2 + 17967\lambda + 4712\right)}{15120(\lambda + 1)^3} \tag{A.2}$$

$$s3 = -\frac{(19\lambda + 16)\left(5855\lambda^2 + 8835\lambda + 2656\right)}{30240(\lambda + 1)^3} \tag{A.3}$$

$$s4 = -\frac{(2\lambda + 3)(19\lambda + 16)^2}{640(\lambda + 1)^2} \tag{A.4}$$

The corresponding coefficients that appear in the $O(Ca)$ exterior velocity field in Eq.5.76 of Chapter 5 are:

$$c_1(r) = -\frac{(19\lambda + 16)\left(7(45\lambda + 22)r^2 - 9(45\lambda + 4)\right)}{144(\lambda + 1)^2 r^6} \tag{A.5}$$

$$c_2(r) = -\frac{(19\lambda + 16)\left(35(\lambda + 1)(45\lambda + 4) + 18\left(52\lambda^2 + 92\lambda + 31\right)r^4 - 15(\lambda(159\lambda + 233) + 56)r^2\right)}{1260(\lambda + 1)^3 r^6} \tag{A.6}$$

$$c_3(r) = \frac{(19\lambda + 16)\left(r^2 - 1\right)\left(9\left(25\lambda^2 + 41\lambda + 4\right)r^2 - 5\left(45\lambda^2 + 49\lambda + 4\right)\right)}{2520(\lambda + 1)^3 r^6} \tag{A.7}$$

$$c_4(r) = \frac{(19\lambda + 16)\left(-90\lambda + (45\lambda + 22)r^2 - 8\right)}{72(\lambda + 1)^2 r^6} \tag{A.8}$$

$$c_5(r) = -\frac{(19\lambda + 16)\left(\left(639\lambda^2 + 929\lambda + 182\right)r^2 - 10\left(45\lambda^2 + 49\lambda + 4\right)\right)}{1260(\lambda + 1)^3 r^6} \tag{A.9}$$

$$c_6(r) = \frac{(19\lambda + 16)\left((19\lambda + 16)r^2 - 5(3\lambda + 2)\right)}{160(\lambda + 1)^2 r^4} \tag{A.10}$$

$$c_7(r) = \frac{(3\lambda + 2)(19\lambda + 16)}{80(\lambda + 1)^2 r^4} \tag{A.11}$$

Analogous expressions exist for the interior field and can be found in Greco (2002).

A.2 $O(\frac{1}{\lambda})$ Corrections to Stokesian fields

The expressions for the coefficients that appear in the $O(1/\lambda)$ exterior velocity field in Eq.5.108 of Chapter 5 are given by:

$$c_1(r) = \frac{25}{4r^2} - \frac{25}{4r^4} \tag{A.12}$$

$$c_2(r) = \frac{5}{2r^4} \tag{A.13}$$

$$c_3(r) = \frac{30}{19\mathrm{Ca}\lambda r^4} - \frac{2}{\mathrm{Ca}\lambda r^2} \tag{A.14}$$

$$c_4(r) = -\frac{12}{19\mathrm{Ca}\lambda r^4} \tag{A.15}$$

$$c_5(r) = \frac{45}{2r^6} - \frac{35}{2r^4} \tag{A.16}$$

$$c_6(r) = \frac{85}{7r^4} + \frac{-\frac{270r^4}{7} - 180}{18r^6} \tag{A.17}$$

$$c_7(r) = \frac{5}{7r^6} - \frac{10}{7r^4} + \frac{5}{7r^2} \tag{A.18}$$

$$c_8(r) = -\frac{5}{r^6} \tag{A.19}$$

$$c_9(r) = \frac{5}{r^4} - \frac{5}{r^6} \tag{A.20}$$

$$c_{10}(r) = \frac{10}{7r^6} - \frac{3}{7r^4} - \frac{1}{r^2} \tag{A.21}$$

$$c_{11}(r) = \frac{10}{7r^6} - \frac{17}{7r^4} + \frac{1}{r^2} \tag{A.22}$$

Analogous expressions for the interior field are given in Eq.5.103 of Chapter 5.

References

Abramzon, B., & Borde, I. (1980). Conjugate unsteady heat transfer from a droplet in creeping flow. *AIChE J.*, *26*(4), 536–544.

Abramzon, B., & Elata, C. (1984). Unsteady heat transfer from a single sphere in stokes flow. *Int. J. Heat Mass Trans.*, *27*(5), 687–695.

Abramzon, B., & Fishbein, G. A. (1977). Some convective-diffusion problems to a spherical particle for moderate peclet number. *J. Engg. Phys. (USSR)*, *30*(6), 1053.

Acrivos, A. (1971). Heat transfer at high peclet number from a small sphere freely rotating in a simple shear field. *J. Fluid Mech.*, *46*(2), 233–240.

Acrivos, A. (1980). A note on the rate of heat or mass transfer from a small particle freely suspended in a linear shear field. *J. Fluid Mech.*, *98*(2), 299–304.

Acrivos, A., & Goddard, G. D. (1965). Asymptotic expansions for laminar forced-convection heat and mass transfer. *J. Fluid Mech.*, *23*(2), 273–291.

Acrivos, A., & Taylor, T. D. (1962). Heat and mass transfer from single spheres in stokes flow. *Phys. Fluids*, *5*(4), 387–394.

Alexandrova, S. et al. (2014). Effect of the viscosity ratio on the mass transfer into a spherical drop in liquid-liquid dispersions. *J. Chem. Tech. Metall.*, *49*(5), 429–434.

Anand, P., Ray, S. S., & Subramanian, G. (2020). Orientation dynamics of sedimenting anisotropic particles in turbulence. *Phys. Rev. Lett.*, *125*, 034501.

Anczurowski, E., & Mason, S. G. (1967). The kinetics of flowing dispersions: Iii. equilibrium orientations of rods and discs (experimental). *J. Collo. Interf. Sci.*, *23*(4), 533–546.

Aref, H. et al. (2017). Frontiers of chaotic advection. *Rev. Mod. Phys.*, *89*, 025007.

Aref, H., & Balachandar, S. (1986). Chaotic advection in a stokes flow. *Phys. Fluids*, *29*, 3515.

Arfken, G., Weber, H., & Harris, F. E. (2012). *Mathematical methods for physicists*. Elsevier.

Aris, R. (2012). *Vectors, tensors and the basic equations of fluid mechanics*. Dover Publications.

Ashurst, W. T. et al. (1987). Alignment of vorticity and scalar gradient with the strain rate in simulated navier-stokes turbulence. *Phys. Fluids*, *30*, 2343–2353.

Bajer, K., & Moffat, H. K. (1990). On a class of steady confined stokes flow with chaotic streamlines. *J. Fluid Mech.*, *212*, 337–363.

Barthes-Biesel, D., & Acrivos, A. (1973). Deformation and burst of a liquid droplet freely suspended in a linear shear field. *J. Fluid Mech.*, *61*, 1–21.

Batchelor, G. K. (1979). Mass transfer from a particle suspended in fluid with a steady linear ambient velocity distribution. *J. Fluid Mech.*, *95*(2), 369–400.

Batchelor, G. K. (1980). Mass transfer from small particles suspended in turbulent fluid. *J. Fluid Mech.*, *98*(3), 609–623.

Batchelor, G. K., & Greene, T. J. (1972). The hydrodynamic interaction of two small freely-moving spheres in a linear flow field. *J. Fluid Mech.*, *56*(2), 375–400.

Beard, K. V., & Pruppacher, H. R. (1971). A wind tunnel investigation of the rate of evaporation of small water drops falling at terminal velocity in air. *J. Atmos. Sci.*, *28*(8), 1455–1464.

Bentley, B. J., & Leal, L. G. (1986). An experimental investigation of drop deformation and breakup in steady, two-dimensional linear flows. *J. Fluid Mech.*, *167*, 241–283.

Blackburn, H. M. (2002). Mass and momentum transport from a sphere in steady and oscillatory flows. *Phys. Fluids*, *14*(11), 3997–4011.

Bohr, T. et al. (1998). *Dynamical systems approach to tutbulence*. Cambridge University Press.

Brenner, H. (1963). Forced convection heat and mass transfer at small péclet numbers from a particle of arbitrary shape. *Chem. Engg. Sci.*, *18*, 109–122.

Brooks, B. (2010). Suspension polymerization processes. *Chem. Engg. Tech.*, *33*(11), 1737–1744.

Brounshtein, B. I., Zheleznyak, A. S., & Fishbein, G. A. (1970). Heat and mass transfer in interaction of spherical drops and gas bubbles with a liquid flow. *Int. J. Heat Mass Trans.*, *13*, 963.

Brown, A. (1965). Diffusion of heat from a sphere to a surrounding medium. *Aust. J. Phys.*, *18*, 483.

Brunk, B. K., Koch, D. L., & Lion, L. W. (1997). Hydrodynamic pair diffusion in isotropic random velocity fields with application to turbulent coagulation. *Phys. Fluids*, *9*, 2670.

Brunn, H. O. (1984). Inertia effects for slow forced scalar transfer from a sphere. *Acta Mech.*, *50*, 271–284.

Bryden, M. D., & Brenner, H. (1999). Mass-transfer enhancement via chaotic laminar flow within a droplet. *J. Fluid Mech.*, *379*, 319–331.

Chao, B. T. (1969). Transient heat and mass transfer of a translating droplet. *J. Heat Trans.*, *273*.

Chaotic mixer for microchannels (Vol. 295). (2002).

Chong, M. S., Perry, A. E., & Cantwell, B. J. (1990). A general classification of three?dimensional flow fields. *Phys. Fluids A*, *2*(5), 765–777.

Christov, C. I., & Homsy, G. M. (2009). Enhancement of transport from drops by steady and modulated electric fields. *Phys. Fluids*, *21*, 083102.

Cooper, F. (1977). Heat transfer from a sphere to an infinite medium. *Int. J. Heat Mass Trans.*, *26*, 991.

Cox, R. G. (1969). Deformation of a drop in a general time dependent fluid flow. *J. Fluid Mech.*, *37*, 601–623.

Cox, R. G., Zia, I. Y. Z., & Mason, S. G. (1968). Particle motions in sheared suspensions xxv: Streamlines around cynlinders and spheres. *J. Collo. Interf. Sci.*, *21*(1), 7–18.

Dehdashti, E., & Masoud, H. (2020). Forced convection heat transfer from a particle at small and large péclet numbers. *J. Heat Trans.*, *142*(6), 1–9.

Duguid, H. A., & Stampfer, J. F. (1971). The evaporation rates of small, freely falling water drops. *J. Atmos. Sci.*, *28*(7), 1233–1243.

Favelukis, M., & Lavrenteva, O. M. (2013). Mass transfer around prolate spheroidal drops in an extensional flow. *Can. J. Chem. Engg.*, *91*, 1190–1199.

Favelukis, M., & Lavrenteva, O. M. (2014). Mass transfer around oblate spheroidal drops in a biaxial stretching flow. *Can. J. Chem. Engg.*, *92*, 964–972.

Feng, Z., & Michaelides, E. E. (1996). Unsteady heat transfer from a sphere at small peclet numbers. *J. Fluid. Engg.*, *108*(1), 96–102.

Feng, Z., & Michaelides, E. E. (2001). Heat and mass transfer coefficients of viscous spheres. *Int. J. Heat Mass Trans.*, *44*, 4445–4454.

Feng, Z., & Michaelides, E. E. (2000b). Mass and heat transfer from fluid spheres at low reynolds numbers. *Powder Tech.*, *112*, 63–69.

Feng, Z., & Michaelides, E. E. (2000a). A numerical study on the transient heat transfer from a sphere at high reynolds and peclet numbers. *Int. J. Heat Mass Trans.*, *43*, 219–229.

Frankel, N. A., & Acrivos, A. (1968). Heat and mass transfer from small spheres and cylinders freely suspended in shear flow. *Phy. Fluids*, *11*(1913).

Frankel, N. A., & Acrivos, A. (1970). The constitutive equation for a dilute emulsion. *J. Fluid Mech.*, *44*, 65–78.

Greco, S. (2002). Second order theory for deformation of a newtonian drop in stationary flow field. *Phys. Fluids*, *14*, 946–954.

Guasto, J. S., Rusconi, R., & Stocker, R. (2012). Fluid mechanics of planktonic microorganisms. *Ann. Rev. Fluid Mech.*, *44*, 373–400.

Guido, S. et al. (1999). Experimental determination of drop shape in slow steady shear flow. *J. Collo. Interf. Sci.*, *219*, 298–309.

Gulitski, G. (2007). Velocity and temperature derivatives in high-reynolds-number turbulent flows in the atmospheric surface layer. part 1. facilities, methods and some general results. *J. Fluid Mech.*, *589*, 57–81.

Gupalo, I. P., & Riazantsev, I. S. (1972). Diffusion on a particle in the shear flow of a viscous fluid. approximation of the diffusion boundary layer. *J. Appl. Math. Mech.*, *36*(3), 447–451.

Gupalo, I. P., Riazantsev, I. S., & Ulin, V. I. (1975). Diffusion on a particle in a homogeneous translational-shear flow. *Prikl. Mat. Mekh.*, *39*, 497–504.

Hudson, S. D. et al. (2004). Microfluidic analog of the four-roll mill. *Appl. Phys. Lett.*, *85*, 335–337.

Jeffery, G. B. (1922). The motion of ellipsoidal particles immersed in a viscous fluid. *Proc. Roy. Soc. Lond. A*, *102*(715), 161–179.

Jhuncu, G. (2010). A numerical study of the unsteady heat/mass transfer inside a circulating sphere. *Int. J. Heat Mass Trans.*, *53(15)*, 3006–3012.

Kao, S., Cox, R. G., & Mason, S. (1977). Streamlines around single spheres and trajectories of pairs of spheres in two-dimensional creeping flows. *Chem. Engg. Sci.*, *32*(12), 150–1515.

Kaper, T. J., & Wiggins, S. (1993). An analytical study of transport in stokes flows exhibiting large-scale chaos in the eccentric journal bearing. *J. Fluid Mech.*, *253*, 211–243.

Karp-Boss, L. et al. (1996). Nutrient fluxes to planktonic osmotrophs in the presence of fluid motion. *Oceano. Marine Bio.: An Ann. Rev.*, *34*, 71–107.

Ke, C. et al. (2018). On the drag coefficient and averaged nusselt number of an ellipsoidal particle in a fluid. *Powder Tech.*, *325*, 134–144.

Kennedy, M. R., & Pozrikidis, C. (1994). Motion and deformation of liquid drops and the rheology of dilute emulsions in simple shear flow. *Comp. Fluids*, *23*, 251–278.

Kinzer, G. D., & Gunn, R. (1951). The evaporation, temperature and thermal relaxation-time of freely falling water drops. *J. Metrol.*, *8*(2), 71–83.

Kishore, N., & Sai, G. (2011). Momentum and heat transfer phenomena of spheroid particles at moderate reynolds and prandtl numbers. *Int. J. Heat Mass Trans.*, *54*(11), 2595–2601.

Komrakova, M. R. et al. (2014). Lattice boltzmann simulations of drop deformation and breakupin shear flow. *Int. J. Multi. Flow*, *59*, 24–43.

Konpoliv, N., & Sparrow, E. M. (1970). Transient heat transfer between a moving sphere and a fluid. *4th International Heat Transfer Conference, Paris-Versailles.*

Konpoliv, N., & Sparrow, E. M. (1971). Temperature and heat transfer history of a solid body in a forced convection flow. *Quat. Appl. Math.*, *29*, 225–235.

Konpoliv, N., & Sparrow, E. M. (1972). Unsteady heat transfer for stokesian flow about a sphere. *J. Heat Trans.*, *94*(3), 266–272.

Kossack, C. A., & Acrivos, A. (1974). Steady simple shear flow past a circular cylinder at moderate reynolds numbers. a numerical solution. *J. Fluid Mech.*, *66*(2), 353–376.

Krishnamurthy, D., & Subramanian, G. (2018a). Heat or mass transport from drops in shearing flows. part 1. the open-streamline regime. *J. Fluid Mech.*, *850*, 439–483.

Krishnamurthy, D., & Subramanian, G. (2018b). Heat or mass transport from drops in shearing flows. part 2. inertial effects on transport. *J. Fluid Mech.*, *850*, 484–524.

Kronig, R., & Brink, J. C. (1950). On the theory of extraction from falling droplets. *Appl. Sci. Res.*, *2*, 142–154.

Kroujiline, D., & Stone, H. A. (1999). Chaotic streamlines in a steady bounded three-dimensional stokes flow. *Physica D*, *130*, 105–132.

Kumar, S., & Homsy, G. M. (1996). Chaotic advection in creeping flow of viscoelastic fluids between slowly modulated eccentric cylinders. *Phys. Fluids*, *8*, 1744.

Ladyzhenskaya, O. (1963). *The mathematical theory of viscous incompressible flow*. Martino Publishing.

Law, C. K. (1982). Recent advances in droplet vaporization and combustion. *Prog. Energy Combust. Sci.*, *8*(3), 171–201.

Lawson, J. M. (2020). Mass transfer to freely suspended particles at high peclet number. *J. Fluid Mech.*, *913*(A32).

Leal, G. L. (2007). *Advanced transport phenomena: Fluid mechanics and convective transport processes*. Cambridge University Press.

Leal, L. G., & Hinch, E. J. (1971). The effect of weak brownian rotations on particles in shear flow. *J. Fluid Mech.*, *46*, 685–703.

Leal, L. G., & Hinch, E. J. (1972). The effect of brownian motion on the rheological properties of a suspension of non-spherical particles. *J. Fluid Mech.*, *52*, 683–712.

Lee, J. S. et al. (2007). Microfluidic four-roll mill for all flow types. *Appl. Phys. Lett.*, *90*, 335–337.

Levich, V. G. (1962). *Physicochemical hydrodynamics*. Prentice Hall.

Levich, V. G., Krylov, V. S., & Vorotilin, V. P. (1965). On the theory of unsteady diffusion from moving droplets. *Dok. Akad. Nauk SSSR*, *161*, 648.

Liu, A. et al. (2019). Unsteady conjugate mass and heat transfer from/to a prolate spheroidal droplet in uniaxial extensional creeping flow. *Int. J. Heat Mass Trans.*, *134*, 1180–1190.

Ma, H., & Zhao, Y. (2020). Convective heat transfer coefficient for a rod-like particle in a uniform flow. *Int. J. Heat Mass Trans.*, *147*(118742).

Magar, V., Goto, T., & Pedly, T. J. (2003). Nutrient uptake by a self-propelled steady squirmer. *Quat. J. Mech. Appl. Math.*, *56*(1), 65–91.

Marath, N. K., & Subramanian, G. (2018). The inertial orientation dynamics of anisotropic particles in planar linear flows. *J. Fluid Mech.*, *844*, 357–402.

Masliyah, J. H., & Epstein, N. (1972). Numerical solution of heat and mass transfer from spheroids in steady axisymmetric flow. In G. Hestroni & S. Sideman (Eds.), *Progress in heat and mass transfer, volume 6. proceedings of the international symposium on two-phase systems* (pp. 613–632). Oxford: Pergamon.

Mason, S. G., & Manley, R. J. (1956). Particle motions in sheared suspensions: Orientations and interactions of rigid rods. *Proc. Roy. Soc. A*, *238*, 117.

Meneveau, C. (2011). Lagrangian dynamics and models of the velocity gradient tensor in turbulent flows. *Ann. Rev. Fluid Mech.*, *43*, 219–245.

Michaelides, E. E. (2006). *Particles, bubbles and drops - their motion, heat and mass transfer.* World Scientific Publishing.

Nambiar, S. et al. (2017). Stress relaxation in a dilute bacterial suspension. *J. Fluid Mech.*, *812*, 41–64.

Nambiar, S. et al. (2019). Stress relaxation in a dilute bacterial suspension: The active–passive transition. *J. Fluid Mech.*, *870*, 1072–1104.

Neishtadt, A. I., Vainshtein, D. L., & Vasiliev, A. A. (1998). Chaotic advection in a cubic stokes flow. *Physica D*, *111*, 227.

Newman, A. B. (1931). The drying of porous solids: Diffusion calculations. *Trans. Am. Inst. Chem. Engg.*, *27*, 310–332.

Olbricht, W. L., Rallison, M. S., & Leal, G. L. (1982). Strong flow criteria based on microstructure deformation. *J. Non-Newt. fluid Mech.*, *10*, 291–318.

Oliver, D. L. R., & DeWitt, K. J. (1993). High peclet number heat transfer from a droplet suspended in an electric field: Interior problem. *Int. J. Heat Mass Trans.*, *36*(12), 3153–3155.

Olivera, T. F., & daCunha, F. R. (2011). A theoretical description of a dilute emulsion of very viscous drops undergoing unsteady simple shear. *J. Fluids Engg.*, *133*, 101208.

Olivera, T. F., & daCunha, F. R. (2015). Emulsion rheology for steady and oscillatory shear flows at moderate and high viscosity ratio. *Rheol. Acta*, *54*, 951–971.

Ottino, J. M. (1990). Mixing, chaotic advection, and turbulence. *Ann. Rev. Fluid Mech.*, *22*, 207–254.

Pahlow, M. et al. (1997). Impact of cell shape and chain formation on nutrient acquisition by marine diatoms. *Limun. and Oceano.*, *42(8)*, 1660–1672.

Peery, J. H. (1966). *Fluid mechanics of rigid and deformable particles in shear flows at low reynolds numbers* (Doctoral dissertation). Princeton University.

Perry, A. E., & Chong, M. S. (1987). A description of eddying motions and flow patterns using critical-point concepts. *Ann. Rev. Fluid Mech.*, *19*, 125–155.

Philip, J. R. (1964). Transient heat conduction between a sphere and a surrounding medium of different thermal properties. *Aust. J. Phys.*, *17*, 423–430.

Poe, G., & Acrivos, A. (1975). Closed-streamline flows past rotating single cylinders and spheres: Inertia effects. *J. Fluid Mech.*, *72*(4), 605–623.

Poe, G., & Acrivos, A. (1976). Closed streamline flows past small rotating particles: Heat transfer at high peclet numbers. *Int. J. Multi. Flows*, *2*(4), 365–377.

Polyanin, A. (1984). Three-dimensional diffusive boundary-layer problems. *J. Appl. Mech. Tech. Phys.*, *25*(4), 562–571.

Powell, R. L. (1983). External and internal streamlines and deformation of drops in linear twodimensional flows. *J. Coll. Interf. Sci.*, *95*(1), 148–162.

Pozrikidis, C. (1997). Unsteady heat or mass transport from a suspended particle at low péclet numbers. *J. Fluid Mech.*, *334*, 111–133.

Pozrikidis, C. (2002). *A practical guide to boundary element methods*. Chapman; Hall.

Raja, R., Subramanian, G., & Koch, D. L. (2010). Inertial effects on the rheology of a dilute emulsion. *J. Fluid Mech.*, *646*, 255–296.

Rallison, J. M. (1980). Note on the time-dependent deformation of a viscous drop which is almost spherical. *J. Fluid Mech.*, *98*, 625–633.

Robertson, C., & Acrivos, A. (1970a). Low reynolds number shear flow past a rotating circular cylinder. part 1. momentum transfer. *J. Fluid Mech.*, *40*(4), 685–703.

Robertson, C., & Acrivos, A. (1970b). Low reynolds number shear flow past circular cylinder. part 2. heat transfer. *J. Fluid Mech.*, *40*(4), 705–718.

Saboni, A. et al. (2016). Mass transfer into a spherical bubble. *Chem. Engg. Sci.*, *152*, 109–115.

Sehlin, R. C. (1969). *Forced-convection heat and mass transfer at large peclet numbers from an axisymmetric body in laminar flow: Prolate and oblate spheroids* (Doctoral dissertation). Carnegie-Mellon University, Pittsburgh, PA.

Shaqfeh, E. S. G. (2005). The dynamics of single-molecule dna in flow. *J. Non-Newt. Fluid Mech.*, *130*, 1–28.

Singh, R. K., & Sircar, K. (2011). Inertial effects on the dynamics, streamline topology and interfacial stresses due to a drop in shear. *J. Fluid Mech.*, *683*, 149–171.

Stocker, R. (2012). Marine microbes see a sea of gradients. *Science*, *338*(1), 628–633.

Stone, H. A., Nadim, A., & Strogatz, S. (1991). Chaotic streamlines inside drops immersed in steady stokes flow. *J. Fluid Mech.*, *232*, 629–646.

Strogatz, S. (1994). *Nonlinear dynamics and chaos*. Westview Press.

Subramanian, G., & Koch, D. L. (2006a). Centrifugal forces alter streamline topology and greatly enhance the rate of heat and mass transfer from neutrally buoyant particles to a shear flow. *Phys. Rev. Lett.*, *96*(13).

Subramanian, G., & Koch, D. L. (2006b). Inertial effects on the transfer of heat or mass from neutrally buoyant spheres in a steady linear velocity field. *Phys. Fluids*, *18*(7).

Taylor, G. I. (1932). The viscosity of a fluid containing small drops of another fluid. *Proc. Roy. Soc. Lond. A*, *138*(834), 41–48.

Taylor, G. I. (1934). The formation of emulsions in definable fields of flow. *Proc. Roy. Soc. Lond. A*, *146*(858), 501–523.

Torza, S., Henry, C. P., Cox, R. G., & Mason, S. (1971). Particle motions in sheared suspensions xxvi. streamlines in and around liquid drops. *J. Coll. Interf. Sci.*, *35*(4), 529–543.

Vainshtein, D. L., Vasiliev, A. A., & Neishtadt, A. I. (1996). Changes in the adiabatic invariant and streamline chaos in confined incompressible stokes flow. *Chaos*, *6*, 67.

Vivaldo-Lima, E., Wood, P. E., Hamielec, A., & Penlidis, A. (1997). An updated review on suspension polymerization. *Ind. Engg. Chem. Res.*, *36*(4), 939–965.

Vlahovska, P. M. et al. (2009). Small-deformation theory for a surfactant-covered drop in linear flows. *J. Fluid Mech.*, *624*, 293–337.

Ward, T., & Homsy, G. M. (2001). Electrohydrodynamically driven chaotic mixing in a translating drop. *Phys. Fluids*, *13*(12), 3521–3525.

Wiggins, S. (1988). *Global bifurcations and chaos*. Springer-Verlag.

Yang, C., Zhang, J., Koch, D. L., & Yin, X. (2011). Mass/heat transfer from a neutrally buoyant sphere in simple shear flow at finite reynolds and peclet numbers. *AIChE J.*, *57*(6), 1419–1433.

Yu-Fang, P., & Acrivos, A. (1968). Heat transfer at high peclet number in regions of closed streamlines. *Int. J. Heat Mass Trans.*, *11*(3), 439–444.